UNIVERSITÉ DE MONTRÉAL

SEISMIC VELOCITIES, ANISOTROPY, HYSTERESIS AND POISSON'S RATIO OF ULTRAHIGH PRESSURE (UHP) METAMORPHIC ROCKS

QIAN WANG
DÉPARTEMENT DES GÉNIES CIVIL, GÉOLOGIQUE ET DES MINES
ÉCOLE POLYTECHNIQUE DE MONTRÉAL

THÈSE PRÉSENTÉE EN VUE DE L'OBTENTION
DU DIPLÔME DE PHILOSOPHIAE DOCTOR (Ph.D.)
(GÉNIE MINÉRAL)
JUNE 2009

Your file Votre référence
ISBN: 978-0-494-53807-4
Our file Notre référence
ISBN: 978-0-494-53807-4

UNIVERSITÉ DE MONTRÉAL

ÉCOLE POLYTECHNIQUE DE MONTRÉAL

Cette thèse intitulée:

SEISMIC VELOCITIES, ANISOTROPY, HYSTERESIS AND POISSON'S RATIO OF ULTRAHIGH PRESSURE (UHP) METAMORPHIC ROCKS

présentée par: WANG Qian
en vue de l'obtention du diplôme de: Philosophiae Doctor
a été dûment acceptée par le jury d'examen constitué de:

M. CHOUTEAU Michel, Ph.D., président
M. JI Shaocheng, Ph.D., membre et directeur de recherche
M. MARTIGNOLE Jacques, Ph.D., membre et codirecteur de recherche
M. MARCOTTE Denis, Ph.D., membre
M. MARESCHAL Jean-Claude, Ph.D., membre

Acknowledgements

I would like to express my great gratitude to my supervisor Prof. Shaocheng Ji for his guidance, encouragement, help, concern and patience during my Ph.D. study. Furthermore, without his financial support, I could not come to Canada to complete my thesis. His enthusiasm, insights, diligence, persistence and hard work at science inspired me to continue my research career. I gratefully acknowledge my co-supervisor Prof. Jacques Martignole for his financial support, suggestions and discussion throughout my Ph.D. study period.

I would like to thank Dr. Matthew H. Salisbury for providing an opportunity to use his GSC/Dalhousie High Pressure Laboratory for the seismic velocity measurements and Mr. Robert Iuliucci for his technical assistance. I also express my appreciation to Prof. Denis Marcotte for his contribution to the statistic analysis of the experimental data.

I am grateful to Mrs. Manon Latour, Mrs. Carole Giguère, Mrs. Manon Leduc, Mrs. Huguette Perron and Mr. Yvéric Rousseau for their support and smile. I acknowledge École Polytechnique de Montréal for the exemption of my foreign student tuition fees. I thank the Natural Sciences and Engineering Council of Canada, the Chinese National Natural Science Foundation and the Chinese Academy of Sciences for research grants.

I also would like to thank Prof. Bin Xia (Guangzhou Institute of Geochemistry), Prof. Guan Yin and Prof. Qichun Zhang (Chengdu University of Technology) for encouraging me to study in Canada and continuous help during the past 4 years and Prof. Zhiqin Xu (Chinese Academy of Geological Sciences) for providing the CCSD core samples.

Finally, and most of all, I would like to thank my family and my friends for their love, support and trust.

Résumé

Le terrane métamorphique à ultra-haute pression (UHP) de Qinling-Dabie-Sulu, dans lequel l'éclogite contient du diamant et de la coesite, et les orthogneiss, les paragneiss, le quartzite et le marbre contiennent de la coesite, est un fragment de croûte continentale subductée à 100 kilomètres de profondeur dans le manteau supérieur, et remontée dans la croûte supérieure. Le projet chinois de forage scientifique continental (Chinese Continental Scientific Drilling: CCSD) a atteint 5158 m dans le terrane métamorphique UHP de Sulu et fourni une occasion unique et excellente de caractériser la composition chimique, la variation lithologique, les réactions métamorphiques, le recyclage géochimique des matériaux de la croûte et du manteau, les mécanismes de déformation, le comportement rhéologique, les processus tectoniques et les propriétés sismiques (par exemple, les vitesses des ondes P et S, l'anisotropie et le rapport de Poisson) des roches UHP. L'objectif principal de cette étude est de calibrer les propriétés sismiques et leurs variations en fonction de la pression hydrostatique et de la lithologie des roches métamorphiques UHP. La connaissance des propriétés sismiques des roches polyphasées qui constituent l'intérieur de la Terre est essentielle pour l'interprétation géologique des données sismiques (par exemple, profils sismiques réflexion et réfraction, fonctions télésismiques, tomographie, anisotropie sismique et biréfringence des ondes S) et pour l'établissement des modèles lithologiques et structuraux de la lithosphère.

Cette thèse, intitulée "Vitesses sismiques, anisotropie, hystérésis et rapport de Poisson des roches métamorphiques à Ultra-Haute Pression (UHP)", se compose de 2 parties. La première partie est une introduction à la théorie de l'élasticité et des lois de mélange et à leur application à la prévision des propriétés physiques des solides et des roches polyminérales (Chapitre 1), et une synthèse des principaux résultats scientifiques du projet CCSD et des investigations sur le terrane métamorphique UHP de Sulu (Chapitre 2). La deuxième partie de la thèse est constituée de quatre articles publiés ou

acceptés par des revues scientifiques internationales (Journal of Geophysical Research et Tectonophysics) (Chapitres 3 à 6).

Nous avons étudié les vitesses des ondes P, l'anisotropie et l'hystérésis dans les roches métamorphiques UHP en fonction de la pression hydrostatique (Chapitre 3). La comparaison entre les échantillons des affleurements et ceux des forages CCSD indique que l'hystérésis sismique est provoquée par les changements irréversibles des contacts de grains, par l'augmentation des rapports géométriques (largeur/longueur) des microfissures et par la réduction des vides pendant le cycle de pressurisation-dépressurisation. La variation de la vitesse sismique avec la pression est bien décrite par une équation exponentielle dérivée du principe général et définie par quatre paramètres. La signification physique de chaque paramètre de cette équation a été mise en évidence. Il est suggéré que l'équation non seulement puisse être employée dans l'interpolation et l'extrapolation des vitesses sismiques mais offre également une base pour la comparaison de résultats expérimentaux de différentes lithologies ou de différents contextes géologiques. Les propriétés statistiques des vitesses d'ondes P dans les roches UHP, obtenues au cours de cette étude, fournissent un ensemble d'informations de base pour l'interprétation des données sismiques des zones de racine, des ceintures orogéniques convergentes continentales et des zones de subduction modernes ou anciennes. Les résultats suggèrent aussi que les réflecteurs sismiques observés régionalement dans la lithosphère mantellique sous les ceintures orogéniques modernes ou anciennes, puissent représenter des matériaux de la croute continentale rapidement subductée, et préservés de façon métastable dans le manteau supérieur.

Nous avons également étudié la dépendance de la pression hydrostatique (P) sur les rapports de Poisson (υ) pour les roches métamorphiques UHP. Les résultats expérimentaux montrent deux types principaux de corrélations entre P et υ dans la gamme de 40-850 MPa: (1) υ montre peu de variation par rapport à P dans la gamme de 40-850 MPa; et (2) υ, avec l'augmentation de la pression, augmente rapidement en-

dessous de ~200 MPa et ensuite devient quasi-constante à des pressions plus élevées. On observe le Type 1 dans 22 échantillons et le Type 2 dans 32 échantillons. L'origine du Type 2 peut être raisonnablement interprétée par la présence d'une petite fraction de volume (0.1-0.5%) de pores de forme lenticulaire, distribués aléatoirement et orientés aléatoirement dans les roches. Les pores sont progressivement fermés pendant la pressurisation. Les effets de l'orientation des microfissures, des orientations préférentielles cristallographiques des minéraux, et d'une structure de litage compositionnelle devraient être pris en compte pour interpréter l'origine du Type 1. Cette étude suggère que la minéralogie et la pression de confinement jouent un rôle critique en influençant le rapport de Poisson des roches cristallines en particulier en-dessous de 200-300 MPa.

Nous avons mis l'accent sur les rapports de Poisson des minéraux et des roches communes et sur l'application des résultats expérimentaux à contraindre la composition et l'évolution tectonique de la croûte continentale chinoise en se basant sur des données [épaisseur de la croûte (H) et rapport de Poisson] mesurées à partir de 248 stations sismiques à bande large utilisant des techniques "teleseismic received functions" (Chapitre 5). On constate qu'excepté les roches monominérales telles que quartzite, serpentinite, anorthosite, calcaire et marbre, les roches ont des rapports de Poisson localisés le long d'une courbe convexe ascendante déterminée à partir des corrélations entre les modules élastiques et la densité. Les rapports de Poisson montrent une augmentation avec la densité quand la lithologie change de granite, à gneiss felsique et schiste, en passant par diorite, syénite, gneiss intermédiaire et metasediments, jusqu'aux gabbro-diabase, gneiss amphibolique et gneiss mafique, puis vient une diminution du rapport de Poisson alors que les roches deviennent ultramafiques. L'éclogite a une densité plus élevée mais un rapport de Poisson inférieur à celui de la peridotite. Les données des "teleseismic received functions" prouvent que les blocs de Chine du nord, de Yangtze, de Chine du sud et de Chine du nord-est et le Songpan-Ganzi Terrane sont dominés (>70%) par des rapports de Poisson bas ($\upsilon < 0.26$) et modérés

($0.26 \leq \upsilon < 0.28$), indiquant que la croûte est principalement felsique. Le terrane de Lhasa, le terrane de Qiangtang, et le bloc de l'Indochine sont caractérisés par des proportions élevées (33-42%) de très haut rapports de Poisson (≥ 0.30), suggérant que la croûte y est partiellement fondue. Une corrélation négative entre υ et H qu'on observe pour le bloc de Chine du sud, le bloc du nord-est, le bloc de Lhasa, le terrane de Qiangtang et le bloc de l'Indochine, indique l'épaississement tectonique de la croûte supérieure et moyenne felsique par plissement et chevauchement, et la delamination de la croûte inférieure mafique dans le manteau supérieur. Les données de "teleseismic received functions" du bloc de Chine du nord sont particulièrement intéressantes: υ augmente doucement et de façon linéaire avec la diminution de H, dans les régions de Baoding-Datong et de Guanting-Zhangjiakou-Zhangbei, tout en augmentant abruptement et de façon non-linéaire dans le reste du bloc (par exemple, le nord-est de la province de Hebei et la région méridionale de Taihangshan près de Shijiazhuang). La corrélation linéaire est interprétée comme la conséquence de deux processus qui sont l'amincissement tectonique de la croûte felsique et l'addition de roches mafiques à partir de magmas "underplated" dans la croûte inférieure. L'augmentation brusque de υ avec la diminution H implique que l'amincissement tectonique était beaucoup plus grand dans la croûte supérieure et moyenne felsique que dans la croûte inférieure mafique pendant l'extension regionale Mésozoïque-Cénozoïque. Cela implique également que l'underplating basaltique a été localisé à la région de Zhangjiakou.

Le chapitre 6 est consacré aux corrélations entre vitesses des ondes P et S (V_p et V_s) et rapports de Poisson correspondants (υ) pour 12 catégories de roches (amphibolite, anorthosite, basalte, diorite, éclogite, gneiss felsique, gabbro-diabase, granite, gneiss intermédiaire, calcaire, gneiss mafique, et peridotite) et 4 types de minerais massifs de sulfure (chalcopyrite, pyrite, sphalérite, et pyrrhotite). La corrélation linéaire fournit de bonnes descriptions pour les relations V_s-V_p et $\ln V_s - \ln V_p$. Le rapport de Poisson est linéairement corrélé avec V_s, V_p, le module de cisaillement (G) et le module de Young (E) pour ces roches et pour les minerais de sulfure. Une diminution du rapport de

Poisson est associée aux augmentations de V_s, G et E. Cependant, la variation de υ avec V_p dépend du rapport logarithmique $R_{s/p}$ (c'est-à-dire, $\partial \ln V_s / \partial \ln V_p$). Le rapport de Poisson augmente ou diminue avec V_p quand $R_{s/p}$<1 ou >1. $R_{s/p}$ s'avère varier avec la lithologie (0.300 pour le granite, 0.573 pour la diorite, 0.602 pour le gneiss felsique, 0.631 pour le gneiss intermédiaire, 0.721 pour le gabbro-diabase, 0.768 pour le gneiss mafique, 0.866 pour l'eclogite, 0.890 pour l'amphibolite, et 1.391 pour la peridotite). Donc, $R_{s/p}$ peut être employé comme un indicateur de composition de la croûte continentale profonde et du manteau supérieur. Cette étude suggère que les corrélations entre V_p et V_s, et les rapports de Poisson correspondant (υ) devront être importants en modélisant et en interprétant des données sismiques en termes de composition chimique et de lithologie.

Le dernier chapitre fournit un résumé du volume entier et un plan de travail sur les propriétés sismiques des roches des montagnes de Yunkai (la marge continentale nord de la mer de Chine du sud).

Abstract

The Qinling-Dabie-Sulu UHP metamorphic terrane, in which eclogite contains both diamond and coesite, and granitic gneiss, paragneiss, quartzite and marble contain coesite, is a slab of continental crust that was subducted to depths >100 km and then exhumated into the upper crust. The Chinese Continental Scientific Drilling (CCSD) drilled 5158 m into the Sulu UHP metamorphic terrane and provides a unique and excellent opportunity to characterize the chemical composition, lithological variation, metamorphic reactions, geochemical cycling of crust/mantle materials, deformation mechanisms, rheological behavior, tectonic processes and seismic properties (e.g., P- and S-wave velocities, anisotropy and Poisson's ratio) of UHP rocks. The main objective of the present study was to calibrate the seismic properties and their variations as a function of confining pressure and lithology of the UHP metamorphic rocks. The understanding of seismic properties of polyphase rocks that consist of the Earth's interior is fundamental for geological interpretation of in-situ seismic data (e.g., reflections, refraction, received functions, tomography, seismic anisotropy and shear-wave splitting) and for establishing lithospheric structure and composition models.

This thesis, entitled "Seismic velocities, anisotropy, hysteresis and Poisson's ratio of ultrahigh pressure (UHP) metamorphic rocks", consists of two parts. The first part presents an introduction to the general background of elasticity and mixture rules and their application to the prediction of physical properties of multiphase solids and rocks (Chapter 1), and an overview of the main scientific results achieved from the CCSD project and the investigations of the Sulu UHP metamorphic terrane (Chapter 2). The second part of the thesis is a collection of 4 research papers published or accepted in international journals (Journal of Geophysical Research and Tectonophysics) (from Chapter 3 to Chapter 6).

P-wave velocities, anisotropy and hysteresis as a function of confining pressure have been investigated in the UHP-pressure metamorphic rocks (Chapter 3). The comparison

between samples collected from surface outcrops and those from the CCSD main borehole cores indicates that the seismic hysteresis is caused by irreversible changes in grain contacts, increases in microcrack aspect ratios and reduction of void space during the pressurization-depressurization cycle. The variation of velocity with pressure can be well described by a four-parameter exponential equation derived from the general principle. The physical meaning of each parameter in the equation has been clarified. It is suggested that the equation not only can be used in the interpolation and extrapolation of seismic velocities but also offers a basis for comparison among experimental results of different lithologies or different geological settings. The statistical properties of P-wave velocities in the UHP rocks, obtained from this study, provide an important set of basic information for the interpretation of seismic data from the root zones of continental convergent orogenic belts and modern and ancient subduction zones. The results suggest that regionally extensive mantle reflectors observed beneath modern and ancient orogenic belts may imply the preservation of rapidly subducted, dry, metastable crustal mafic or felsic material within the lithospheric upper mantle.

The pressure (P) dependence of Poisson's ratios (υ) for UHP metamorphic rocks has been studied (Chapter 4). The experimental results display two main types of the $\upsilon - P$ relationships in the range of 40-850 MPa: (1) υ shows little variation with P in the range of 40-850 MPa; and (2) with increasing pressure, υ increases rapidly below ~200 MPa and then becomes quasi-constant at higher pressures. Types 1 and 2 are observed in 22 and 32 samples, respectively. The origin of Type 2 can be reasonably interpreted by a small volume fraction (0.1-0.5%) of randomly distributed and randomly oriented thin-disk shaped pores that are progressively closed during pressurization. The effects of microcrack orientation, crystallographic preferred orientations, and compositional layering should be taken into consideration for interpreting the origin of Type 1. This study suggests that both mineralogy and confining pressure play a critical role in influencing the Poisson's ratio of the crystalline rocks particularly below 200-300 MPa.

Poisson's ratios of common minerals and rocks have been outlined and the experimental results have been applied to constrain the crustal composition and tectonic evolution of the Chinese continental crust based on crustal thickness (H) and Poisson's ratio (υ) data measured from 248 broadband seismic stations using teleseismic receiver function techniques (Chapter 5). It is found that except for monomineralic rocks such as quartzite, serpentinite, anorthosite, limestone and marble, most rock types have Poisson's ratios falling along an upward convex curve determined from the correlations between elastic moduli and density. Poisson's ratios display an increase with density as the lithology changes from granite, felsic gneiss and schist, through diorite-syenite, intermediate gneiss and metasediment, to gabbro-diabase, amphibolite and mafic gneiss, and then decrease as the rocks become ultramafic in composition. Eclogite has a higher density but a lower Poisson's ratio than peridotite. The teleseismic receiver function data show that the North China, Yangtze, South China and Northeast China blocks and Songpan-Ganzi Terrane of China are dominated by low ($\upsilon < 0.26$) and moderate ($0.26 \le \upsilon < 0.28$) υ values (>70%), indicating that the crust is predominantly felsic. The Lhasa terrane, Qiangtang terrane, and Indochina block of China are characterized by high proportions (33-42%) of measurements with very high υ values (≥ 0.30), suggesting that the crust is partially molten due to high temperatures. A negative correlation between υ and H is observed for the South China block, Northeast block, Lhasa block, Qiangtang terrane and Indochina block, indicating either tectonic thickening of the felsic upper and middle crust by folding and thrusting or the removal of mafic layers from the lower crust into the upper mantle by delamination. The receiver function data from the North China block are particularly interesting: with decreasing H, υ increases gently and linearly in the Baoding-Datong and Guanting-Zhangjiakou-Zhangbei regions, while increasing abruptly and nonlinearly in the rest of the block (e.g., Northeastern Hebei province and the southern Taihangshan area near Shijiazhuang). The linear correlation is interpreted as due to the summed, opposing contribution of tectonic thinning of felsic crust and the addition of mafic rocks crystallized from underplated magmas to the bulk crustal Poisson's ratio. The abrupt increase of υ with decreasing H

implies that much larger thinning strains have taken place in the felsic upper and middle crust than in the mafic lower crust during Mesozoic-Cenozoic tectonic extension. It is further inferred that basaltic underplating has been localized mainly in the Zhangjiakou and adjacent regions.

We also investigated the correlations between P- and S-wave velocities (V_p and V_s) and corresponding Poisson's ratios (υ) for 12 common categories of rocks (amphibolite, anorthosite, basalt, diorite, eclogite, felsic gneiss, gabbro-diabase, granite, intermediate gneiss, limestone, mafic gneiss, and peridotite) and 4 types of massive sulfide ores (chalcopyrite, pyrite, sphalerite and pyrrhotite) (Chapter 6). The linear correlation provides good descriptions for the V_s-V_p and $\ln V_s - \ln V_p$ relationships. Poisson's ratio is linearly correlated with V_s, V_p, shear modulus (G) and Young's modulus (E) for these rocks and sulfide ores. A decrease in Poisson's ratio is associated with increases in V_s, G and E. However, the variation of Poisson's ratio with V_p depends on the logarithmic ratio $R_{s/p}$ (i.e., $\partial \ln V_s / \partial \ln V_p$). Poisson's ratio increases or decreases with V_p when $R_{s/p}$<1 or >1. $R_{s/p}$ is found to vary with lithology (0.300 for granite, 0.573 for diorite, 0.602 for felsic gneiss, 0.631 for intermediate gneiss, 0.721 for gabbro-diabase, 0.768 for mafic gneiss, 0.866 for eclogite, 0.890 for amphibolite, and 1.391 for peridotite). $R_{s/p}$ can be used as a proxy for the composition of the deep continental crust and the upper mantle. This study suggests that the correlations between V_p and V_s, and corresponding Poisson's ratios (υ) should be important in modeling and interpreting seismic data in terms of chemistry and lithology.

It is worthy of mention that my further work (Chapter 7) will focus on the seismic properties of rocks from the Yunkai Mountains – the northern continental margin of the South China Sea.

Condensé en français

Notre connaissance de la composition chimique, de l'état physique et de la structure de l'intérieur de la Terre est principalement issue des données séismiques. L'interprétation des données sismiques, alternativement, est en grande partie contrainte par l'extrapolation des propriétés sismiques mesurées dans un environnement géologique et physique donné sur des roches naturelles. Puisque les vitesses des ondes élastiques dépendent peu de la température, sauf s'il y a transformation de phase, déshydratation ou fusion partielle, l'étude expérimentale des vitesses sismiques en fonction de la pression hydrostatique est particulièrement importante pour l'interprétation des données sismiques. L'objectif de recherche au cours de cette thèse de Ph.D consistant à mesurer les vitesses des ondes P et des ondes S, l'anisotropie, et les rapports de Poisson de roches métamorphiques à ultra-haute pression (UHP) et de quantifier leur dépendance à l'égard de la pression, de la lithologie et des microstructures (par exemple, foliation et linéation).

Pendant les quatre dernières décennies, un grand nombre de mesures des vitesses des ondes P et S et d'anisotropie sismique ont été exécutées sur divers types de roches s'étendant des roches sédimentaires, plutoniques et métamorphiques aux enclaves du manteau supérieur. Dans un manuel de 630 pages, Ji et al. (2002) ont rassemblé les données disponibles sur les vitesses sismiques et sur l'anisotropie des minéraux, des roches et des minerais. Les échantillons étudiés proviennent principalement d'Amérique du Nord et d'Europe de l'ouest, du Japon et des bassins océaniques. Une telle distribution, non homogène, reflète essentiellement une situation socio-économique. La présente étude des échantillons provenant de la ceinture orogénique de Qinling-Dabie-Sulu (Chine) remplit un vide existant dans le continent asiatique.

L'orogène de Qinling-Dabie-Sulu a été formé par subduction et collision entre le craton de la Chine du nord et le bloc du Yangtze. Cette ceinture orogénique est l'un des

orogènes de collision continent-continent les plus intensivement étudiés dans le monde en termes de métamorphisme UHP et de subduction continentale profonde puisque la coesite a été trouvée dans les roches métamorphiques. La ceinture métamorphique UHP de Qinling-Dabie-Sulu est la plus grande ceinture métamorphique UHP identifiée à ce jour dans le monde. Afin de caractériser la structure de la croûte et de contraindre le mécanisme de formation et d'exhumation de la racine profonde orogénique continentale, le projet chinois de forage scientifique continental (Chinese Continental Scientific Drilling: CCSD) a été entrepris de 1997 à 2005 dans le village de Maobei, comté de Donghai, province de Jiangsu. Le trou principal de CCSD se situe à N34.40, E118.67, à environ 30 kilomètres à l'est de la zone de faille Tanlu, et à approximativement 70 kilomètres à l'ouest de la Mer Jaune. Le forage a pénétré toutes les couches de vitesse élevée et les réflecteurs sismiques observés dans la croûte supérieure sur des profils sismiques de réfraction et de réflexion. Le trou principal de CCSD (CCSD-MH) a atteint en avril 2005 une profondeur de 5158 mètres. Les échantillons provenant du CCSD-MH, des trous pré-pilotes et des affleurements de surface nous donnent une excellente occasion d'étudier les propriétés sismiques des roches métamorphiques UHP.

Le premier chapitre de cette thèse présente une introduction à la théorie de l'élasticité et des lois de mélange et à leur application à la prévision des propriétés physiques des solides et des roches polyminérales. Le deuxième chapitre est une synthèse des principaux résultats scientifiques du projet CCSD et des investigations sur le terrane métamorphique UHP de Sulu.

En dépit de plusieurs tentatives, on n'a atteint aucun consensus quant à l'équation susceptible d'offrir la meilleure description de la dépendance de la pression sur les vitesses sismiques dans les roches naturelles bien qu'une telle équation permette à des données d'être interpolées ou extrapolées de façon précise dans l'interprétation géologique des données sismiques. Une telle équation devrait avoir des implications physiques claires et les inclure en aussi peu de paramètres que possible. Les données

expérimentales sur des vitesses sismiques pourraient alors être décrites en termes de paramètres plutôt que d'employer des tables pour analyser les vitesses mesurées aux pressions hydrostatiques choisies pour chaque échantillon comme c'est souvent le cas. En outre, l'équation servirait d'expression standard pour adapter la relation entre les vitesses sismiques et la pression, et les paramètres résultants pourraient être employés pour des analyses statistiques et la classification des propriétés sismiques de roches en termes de chimie, de minéralogie, de lithologie et de microstructure.

Le chapitre 3 de cette thèse traite des vitesses des ondes P, de l'anisotropie et de l'hystérésis de 31 échantillons typiques de CCSD-MH et de 35 échantillons représentatifs des affleurements de la ceinture orogénique de Sulu UHP, à des pressions hydrostatiques allant jusqu'à 850 MPa. On constate que les courbes vitesse-pression peuvent être décrites par une équation exponentielle à quatre paramètres:

$$V(P) = V_0 + DP - B_0 \exp(-kP) \qquad \text{(i)}$$

où V_0 est la vitesse projetée à la pression nulle si les pores et les fissures étaient absents ; D est la dérivée de la pression par rapport à la vitesse (intrinsèque) en régime élastique linéaire; B_0 est la baisse initiale de vitesse provoquée par la présence de pores ou de fissures en extrapolant à la pression nulle ; et k est la constante d'affaiblissement de la baisse de vitesse dans le régime poro-élastique non-linéaire.

L'hystérésis sismique, à savoir le fait que les vitesses mesurées pendant la dépressurisation sont plus hautes que celles mesurées pendant la pressurisation, est bien connue mais mal comprise. L'hystérésis de vitesse est-elle une propriété importante de toutes les roches cristallines? Si une roche montre l'hystérésis, quelle est la variation directionnelle en ce qui concerne les critères structuraux tels que la foliation et la linéation? La quantité d'hystérésis est-elle liée à lithologie, à la microstructure et à l'histoire de la déformation? Afin de répondre à ces questions, nous avons comparé les

résultats de vitesses mesurées sur des échantillons de surface et celles mesurées sur des échantillons du CCSD-MH. Si l'hystérésis ne se retrouve pas dans les échantillons de CCSD-MH, ceci peut indiquer que les microfissures s'ouvrent complètement pendant que la pression est libérée. Les résultats présentés au Chapitre 3 suggèrent que l'hystérésis sismique observée est provoquée par des changements irréversibles des contacts de grains, par l'augmentation des rapports géométriques (largeur/longueur) des microfissures et par la réduction des vides pendant le cycle de pressurisation-dépressurisation. Dans ce chapitre, nous avons également souligné que les propriétés statistiques des vitesses d'ondes P dans les roches UHP, obtenues au cours de cette étude, fournissent un ensemble d'informations de base pour l'interprétation des données sismiques des zones de racine des ceintures orogéniques convergentes continentales et des zones de subduction modernes ou anciennes.

Les rapports de Poisson des roches ont été employés pour contraindre la composition de l'intérieur de la Terre. Afin d'évaluer les effets de la pression hydrostatique (P) sur les rapports de Poisson (υ), nous avons mesuré les vitesses des ondes P et S (V_p et V_s) jusqu'à 850 MPa pour 54 roches cristallines de la ceinture orogénique de Sulu-Dabie (Chine) en employant des techniques de transmission d'impulsion. Les résultats expérimentaux (Chapitre 4) montrent deux types principaux de corrélations entre P et υ dans la gamme de 40-850 MPa: (1) Type 1: υ montre peu de variation par rapport à P dans la gamme de 40-850 MPa; et (2) Type 2: υ augmente rapidement en-dessous de ~200 MPa avec l'augmentation de la pression, et devient en suite quasi-constant à des pressions plus élevées. On observe le Type 1 dans 22 échantillons et le Type 2 dans 32 échantillons. L'origine du Type 2, qui a été observé dans 59% des échantillons étudiés, peut être raisonnablement interprétée par une petite fraction de pores (0.1%-0.5%) de forme lenticulaire (ou mince-disque), distribués aléatoirement et orientés aléatoirement dans les roches. Les pores sont progressivement fermés pendant la pressurisation. Les effets de l'orientation des microfissures, des orientations préférentielles cristallographiques des minéraux, et d'une structure de litage compositionnelle devraient

être pris en compte pour interpréter l'origine du Type 1. Cette étude suggère que la minéralogie et la pression de confinement jouent un rôle critique en influençant le rapport de Poisson des roches cristallines en particulier en-dessous de 200-300 MPa.

Les données expérimentales rapportées au Chapitre 4 ont été analysées en utilisant les équations exponentielles décrites au Chapitre 3:

$$V_p = a_p + b_p P - c_p \exp(-k_p P) \qquad \text{(ii)}$$

et

$$V_s = a_s + b_s P - c_s \exp(-k_s P) \qquad \text{(iii)}$$

où les indices p et s dénotent les ondes P et S, respectivement; a est la vitesse intrinsèque à pression nulle en absence de pores et fissures; b est la dérivée intrinsèque de la pression par rapport à la vitesse dans le régime élastique linéaire; c est la baisse initiale de vitesse provoquée par la présence de pores ou de fissures à la pression nulle; et k est la constante d'affaiblissement de la baisse de vitesse, qui commande la forme des courbes de vitesse-pression dans le régime poro-élastique non-linéaire. Dans le régime élastique linéaire (P>200-300 MPa), le rapport de Poisson augmente avec l'augmentation de P si $(b_p/b_s) > (a_p/a_s)$, diminue avec l'augmentation de P si $(b_p/b_s) < (a_p/a_s)$, et reste presque constante si $(b_p/b_s) \approx (a_p/a_s)$. Dans le régime poro-élastique non-linéaire (P<200-300 MPa), cependant, la variation du rapport de Poisson dépend de la concurrence entre les valeurs $V_s(dV_p/dP)$ et $V_p(dV_s/dP)$. Le rapport de Poisson augmente avec l'augmentation de P si $V_s(dV_p/dP) > V_p(dV_s/dP)$, diminue avec l'augmentation de P si $V_s(dV_p/dP) < V_p(dV_s/dP)$, et demeure constante si ces deux valeurs sont égales.

Afin d'obtenir des informations complètes sur les constantes élastiques [module de Young (E), module de cisaillement (μ), module de compressibilité (K) et rapport de Poisson (υ)] d'une roche, il faut avoir les mesures de sa densité et les vitesses moyennes des ondes P et S. Dans la littérature, cependant, il est relativement rare que les vitesses des ondes P et S aient déterminées sur le même ensemble d'échantillons en utilisant le même équipement de laboratoire et les mêmes méthodes. Habituellement seule la vitesse des ondes P ou la vitesse des ondes S est mesurée. Dans cette investigation, nous avons déterminé expérimentalement les vitesses des ondes P et S de 60 échantillons métamorphiques typiques de roche UHP dont 31 issus du trou principal et des trous pré-pilotes du CCSD et 29 issus des affleurements de la ceinture orogénique de Sulu-Dabie. Les mesures ont été effectuées à la température ambiante et à des pressions hydrostatiques allant jusqu'à 850 MPa (Chapitre 5). Les courbes vitesse-pression sont bien décrites par l'équation à quatre paramètres donnée au Chapitre 3. Les constantes élastiques de chaque échantillon ont donc été calculées à partir de la vitesse moyenne des ondes P et de celle des ondes S, mesurées pendant la dépressurisation. À chaque pression, la corrélation entre un module élastique (m) et la densité (ρ) peut être décrite par une équation empirique: $M = a\rho^3 + b\rho^2 + c\rho$, où a, b et c sont des coefficients variables. La synthèse des résultats expérimentaux de cette étude et des données compilées dans le manuel des propriétés séismiques des minéraux, des roches et des minerais (Ji et al., 2002) indique qu'excepté les roches monominérales telles que quartzite, serpentinite, anorthosite, calcaire et marbre, les roches ont des rapports de Poisson situées le long d'une courbe convexe ascendante déterminée à partir des corrélations entre les modules élastiques et la densité. Les rapports de Poisson augmentent avec la densité quand la lithologie change de granite, à gneiss felsique et schiste, en passant par diorite, syénite, gneiss intermédiaire et metasediments, jusqu'aux gabbro-diabase, gneiss amphibolique et gneiss mafique, puis ils diminuent quand les roches deviennent ultramafiques (c.-à-d., pyroxénite et peridotite). L'éclogite a une densité plus élevée mais un rapport de Poisson inférieur à celui de la peridotite. L'augmentation de υ avec la densité de la roche, depuis gneiss felsique jusqu'au

metagabbro, est corrélée avec la variation systématique du contenu en quartz et en feldspath. Une augmentation du contenu en quartz cause une diminution de υ tandis qu'une augmentation du contenu en feldspath cause une augmentation de υ. Une augmentation de la teneur en anorthite du plagioclase augmente également le rapport de Poisson de la roche. La serpentinisation des peridotites pose un problème parce que la serpentinite possède une de valeur élevée du υ (0.34). Les résultats suggèrent également que, en absence de mesures expérimentales, des estimations raisonnables de υ peuvent être faites pour une roche de densité donnée en utilisant les données de V_p et la ligne de tendance. Les résultats expérimentaux sont censés fournir un ensemble complet d'informations de base pour l'interprétation des données sismiques en place.

Des données sur l'épaisseur dans la croûte (H) et le rapport de Poisson (υ) déterminées pour 248 stations séismiques à bande large à travers la Chine en utilisant les techniques de l'analyse teleseismique de fonction de récepteur, ont été soigneusement examinées. Les blocs de la Chine du nord, de Yangtze, et de la Chine du sud et le Songpan-Ganzi Terrane sont dominés à ~70% par le bas ($\upsilon < 0.26$) et modéré ($0.26 \leq \upsilon < 0.28$) des rapports de Poisson (>70%), ci suggère la prédominance des compositions felsiques dans ce type de croûte.

Le terrane de Lhasa, le terrane de Qiangtang, et le bloc de l'Indochine sont caractérisés par des proportions élevées (33-42%) de mesures avec les valeurs très élevées de υ ($\geq$0.30), suggérant que la croûte profonde de la région est partiellement fondue. La fusion partielle se produit dans la croûte moyenne du terrane de Lhasa et dans la croûte inférieure du terrane de Qiangtang. La chaleur responsable de la fusion partielle est probablement l'épaississement dans la croûte du terrane de Lhasa et l'intrusion de magmas basaltiques dérivés du manteau supérieur dans le terrane de Qiangtang. La corrélation négative entre υ et H, dans le bloc de la Chine du sud, le bloc de la Chine du nord-est, le bloc de Lhasa, le terrane de Qiangtang, le terrane de Songpan-Ganzi et le bloc de l'Indochine, indique que l'épaississement tectonique de la

croûte supérieure et moyenne felsique s'est faite par plissement et chevauchement et par delamination de la croûte inférieure mafique dans le manteau supérieur.

Les données de "teleseismic received functions" sur le bloc de la Chine du nord sont particulièrement intéressantes: υ augmente doucement et de façon linéaire avec la diminution de H, dans les régions de Baoding-Datong et de Guanting-Zhangjiakou-Zhangbei, tout en augmentant abruptement et de façon non-linéaire dans le reste du bloc (par exemple, le nord-est de la province de Hebei et la région méridionale de Taihangshan près de Shijiazhuang). La corrélation linéaire est interprétée comme la conséquence de deux processus qui sont l'amincissement tectonique de la croûte felsique et l'addition de roches mafiques à partir de magmas "underplated" dans la croûte inférieure. L'augmentation brusque de υ avec la diminution de H implique que l'amincissement tectonique était beaucoup plus grand dans la croûte supérieure et moyenne felsique que dans la croûte inférieure mafique pendant l'extension regionale Mésozoïque-Cénozoïque. Cela implique également que l'underplating basaltique a été localisé à la région de Zhangjiakou.

Dans le Chapitre 6, des données de mesures expérimentales à haute pression des vitesses des ondes P et S (V_p et V_s) sont statistiquement analysées pour 12 catégories communes de roches (amphibolite, anorthosite, basalte, diorite, éclogite, gneiss felsique, gabbro-diabase, granite, gneiss intermédiaire, calcaire, gneiss mafique, et peridotite) et 4 types de minerais massifs de sulfure (chalcopyrite, pyrite, pyrrhotite, et sphalérite). L'analyse montre que la corrélation linéaire fournit des descriptions plutôt bonnes pour les relations entre V_s et Vp ou entre $\ln V_s$ et $\ln V_p$. Ces relations empiriques peuvent donner une évaluation raisonnable pour la valeur de V_s quand seules les données de V_p sont disponibles ou vise versa. Le rapport logarithmique $R_{s/p}$ ($\partial \ln V_s / \partial \ln V_p$) change systématiquement avec la lithologie: 0.300 pour le granite, 0.573 pour la diorite, 0.602 pour le gneiss felsique, 0.631 pour le gneiss intermédiaire, 0.721 pour le gabbro-diabase, 0.768 pour le gneiss mafique, 0.866 pour l'éclogite, 0.890 pour l'amphibolite, et 1.391

pour la peridotite. La tendance d'une augmentation évidente de $R_{s/p}$ avec la diminution de SiO_2 dans les roches acides à intermédiaires, ainsi que dans les roches mafiques et ultramafiques, suggère que le rapport peut être employé comme diagnostic pour la composition de la croûte continentale avec moins d'ambiguïté que les valeurs absolues de V_p ou V_s. L'éclogite montre sensiblement un rapport $R_{s/p}$ inférieur (0.866) alors que la peridotite a un rapport $R_{s/p}$ supérieur (1.391). Une masse eclogitique d'un volume assez grand, décollée (délamination) de la partie inférieure de la croûte continentale épaissie et descendue dans le manteau supérieur, devrait se distinguer du manteau peridotitique environnant par les valeurs de $R_{s/p}$. La discrimination de l'éclogite et de la peridotite est par contre impossible à partir des seules valeurs de V_p ou V_s.

Le rapport de Poisson, qui est censé fournir des contraintes beaucoup plus serrées sur la composition lithologique que V_p ou V_s seulement, s'avère linéairement corrélé avec V_s, V_p, G et E pour les roches communes et les minerais sulfurés. Une diminution du rapport de Poisson est généralement associée aux augmentations de V_s, G ou E. La variation du rapport de Poisson avec V_p dépend de la valeur de $R_{s/p}$. Les corrections positives ou négatives entre le rapport de Poisson et V_p se produisent quand $R_{s/p}<1$ ou $R_{s/p}>1$, respectivement. On constate également que la pyrrhotite et la chalcopyrite ont les valeurs négatives pour $R_{\rho/s}$ $(\partial \ln \rho / \partial \ln V_s)$ et $R_{\rho/p}$ $(\partial \ln \rho / \partial \ln V_p)$ et que la pyrite et la sphalérite, par contre, ont les valeurs positives pour $R_{\rho/s}$ $(\partial \ln \rho / \partial \ln V_s)$ et $R_{\rho/p}$ $(\partial \ln \rho / \partial \ln V_p)$. Les problèmes théoriques intéressants se posent pour expliquer les résultats présentés dans le Chapitre 6.

Le chapitre final (Chapitre 7) fournit un résumé de la thèse et également un plan de travail sur les propriétés séismiques des roches des montagnes de Yunkai - la marge continentale nord de la mer de Chine du sud.

Table of contents

List of tables

List of figures

List of initials and abbreviations

Symbol	Notation
P	Pressure
HP	High pressure
UHP	Ultrahigh pressure
P-wave	Compressional wave
S-wave	Shear wave
CCSD	Chinese Continental Scientific Drilling
MH	Main hole
ρ	Density in g/cm^3
G	Shear modulus
E	Young's modulus
K	Bulk modulus
$\boldsymbol{C}$	Stiffness tensor
$\boldsymbol{S}$	Compliance tensor
T	Temperature
V_p	Compressional wave velocity
V_s	Shear wave velocity
V_{s1}	Fast shear wave velocity in shear wave splitting
V_{s2}	Slow shear wave velocity in shear wave splitting
X	Direction parallel to the stretching lineation
Y	Direction perpendicular to the lineation and in the foliation
Z	Direction normal to the foliation
λ	Direction of wave propagation and polarization
A	Velocity anisotropy
M	Mean velocity
LPO	Lattice-preferred orientation

List of relationships among the elastic constants of isotropic materials and rocks

$$K = \frac{EG}{3(3G - E)} \qquad K = \frac{E}{3(1 - 2\upsilon)} \qquad K = \frac{2G(1+\upsilon)}{3(1-2\upsilon)}$$

$$E = \frac{9KG}{3K + G} \qquad E = 3K(1 - 2\upsilon) \qquad E = 2G(1+\upsilon)$$

$$G = \frac{3KE}{9K - E} \qquad G = \frac{3K(1-2\upsilon)}{2(1+\upsilon)} \qquad G = \frac{E}{2(1+\upsilon)}$$

$$\upsilon = \frac{3K - E}{6K} \qquad \upsilon = \frac{3K - 2G}{2(3K+G)} \qquad \upsilon = \frac{E}{2G} - 1$$

$$V_p = \sqrt{\frac{K + \frac{4}{3}G}{\rho}} \qquad V_s = \sqrt{\frac{G}{\rho}}$$

$$\upsilon = \frac{\frac{1}{2}\left(\frac{V_p}{V_s}\right)^2 - 1}{\left(\frac{V_p}{V_s}\right)^2 - 1} \qquad \frac{V_p}{V_s} = \sqrt{\frac{2(1-\upsilon)}{1-2\upsilon}}$$

Chapter 1
Introduction

1.1 Objective and organization of the thesis

Our knowledge of the chemical composition, physical state and structure of the Earth's interior mainly came from seismic data. Interpretation of seismic data, in turn, is largely constrained by the extrapolation of laboratory-measured seismic properties of relevant rocks thought to exist in a given geological and physical (i.e., pressure and temperature) environment. Because elastic wave velocities are not strongly temperature-dependent unless phase transformation, dehydration or partial melting has taken place, laboratory study of the confining pressure dependences of seismic velocities is particularly important for the correct interpretation of seismic data. The research objective of this Ph.D. thesis is to better understand how the seismic compressional wave (P-wave) and shear wave (S-wave) velocities, anisotropy, and Poisson's ratios of high pressure (HP) and ultrahigh pressure (UHP) metamorphic rocks are affected by their chemical and modal compositions, porosity and pore geometry, and microstructures (e.g., foliation and lineation) at various confining pressures.

During the past four decades a large number of laboratory measurements of P- and S-wave velocities and anisotropy have been performed on various types of rocks ranging from sedimentary rocks, igneous rocks and metamorphic rocks to upper mantle xenoliths. In a 630-page handbook and an internet-based database (http://texture.civil.polymtl.ca:8080/seismic-properties/index.jsp), Ji et al. (2002) have summarized the available data on seismic velocities and anisotropy in minerals, rocks and ores. The studied samples were collected mainly from North America and Western Europe, Japan and the ocean basins. Such inhomogeneous distribution reflects essentially a socioeconomic situation. The present study of the samples from the Dabie-Sulu orogenic belt (China) fills such a gap existent in the Asian continent.

The Dabie-Sulu orogen was formed by subduction and collision between North China Block and Yangtze Block. This orogenic belt is probably one of the most intensively investigated collisional orogens in the world in terms of ultrahigh pressure metamorphism and deep continental subduction since coesite was found in the metamorphic rocks (Xu, 1987; Wang et al., 1989; Liou and Zhang, 1996; Cong et al., 1996; Wallis et al., 1997). The Dabie-Sulu UHP metamorphic belt is the largest UHP metamorphic belt recognized in the world. In order to unravel the subsurface structure and to further constrain the mechanism of formation and exhumation of the continental orogenic deep root, the Chinese Continental Scientific Drilling (CCSD) project was undertaken from 1997 to 2005 in the Maobei village, Donghai County, Jiangsu Province. The CCSD main hole is located at a site (N34.40, E118.67), about 30 km east of the Tan-Lu fault zone and approximately 70 km west of the Yellow Sea. The borehole penetrated through all of the high velocity layers and seismic reflectors observed within the uppermost crust on seismic refraction and reflection profiles (Yang et al., 1999; Yang, 2002). The CCSD Main Hole (CCSD-MH) was completed in April, 2005 with a final depth of 5158 m. The core samples from the CCSD main and pre-pilot holes and surface samples collected from the surrounding areas offer us an excellent opportunity to study the seismic properties of UHP metamorphic rocks. Chapter 2 of this thesis will present an introduction to the Sulu ultrahigh pressure (UHP) metamorphic terrane (China) and give a succinct summary of the main scientific results achieved from the CCSD.

Despite several attempts (Zimmerman et al., 1986; Shapiro, 2003; Wepfer and Christensen, 1991; Wang et al., 2005a and b), no consensus has been reached as to which equation can offer the best description of the pressure dependence of seismic velocities in natural rocks although such an equation would allow data to be accurately interpolated and extrapolated in the geological interpretation of seismic data. Such an equation should have clear physical implications and include as few parameters as

possible. Then experimental data on seismic velocities could be published in terms of these parameters rather than using tedious tables to list the velocities measured at selected confining pressures for each sample as is currently done (e.g., Christensen, 1974; Kern et al., 1999; Ji et al., 2003; Wang et al., 2005a and b). Furthermore, the equation would serve as a standard expression for fitting the seismic velocity-confining pressure relation and the resultant parameters could be used for statistical analyses and classification of rock seismic properties in terms of chemistry, mineralogy, lithology and microstructure.

Chapter 3 of this thesis will deal with P-wave velocities, anisotropy and hysteresis of 31 typical CCSD core samples and 35 representative surface samples collected from the Sulu UHP orogenic belt, measured at hydrostatic confining pressures up to 800 MPa. It is found that the velocity-pressure curves can be well described by a four-parameter exponential equation derived from theory:

$$V(P) = V_0 + DP - B_0 \exp(-kP) \qquad (1.1)$$

where V_0 is the projected velocity at zero pressure if pores/cracks were absent; D is the intrinsic pressure derivative of velocity in the linear elastic regime; B_0 is the initial velocity drop caused by the presence of pores/cracks at zero pressure; and k is the decay constant of the velocity drop in the nonlinear poro-elastic regime. The origin of the seismic hysteresis was investigated in detail for the first time.

Seismic hysteresis, namely the fact that rock velocities measured during depressurization are higher than those measured during pressurization, is well-known but poorly understood. Is velocity hysteresis an important property of all crystalline rocks? If a rock displays hyseteresis, what is the directional variation with respect to structural features such as foliation and lineation? Is the amount of hysteresis related to the lithology, microstructure and deformation history? In order to answer the above

questions, in Chapter 3, I also compared the velocity results of the samples collected from surface outcrops and from the CCSD deep drill cores. If a hysteresis lacks in the drill core samples, this may indicate that the microcracks reopen completely as the pressure is released. The results suggest that the observed seismic hysteresis is caused by irreversible changes in grain contact, increases in microcrack aspect ratios and reduction of void space during the pressurization-depressurization cycle. In chapter 3, we also emphasized that the statistical properties of P-wave velocities in the UHP rocks provide an important set of basic information for the interpretation of field seismic data from the root zones of continental convergent orogenic belts and modern and ancient subduction zones.

Chapter 4 addresses the hydrostatic pressure (P) dependence of Poisson's ratios (υ) for 54 crystalline rocks from the Sulu-Dabie orogenic belt (China). The experimental results display two main types of the $\upsilon - P$ relationships in the range of 40-850 MPa: (1) υ shows little variation with P in the range of 40-850 MPa; and (2) with increasing pressure, υ increases rapidly below ~200 MPa and then becomes quasi-constant at higher pressures. Types 1 and 2 are observed in 22 and 32 samples, respectively. The origin of type 2 can be reasonably interpreted by a small volume fraction (0.1-0.5%) of randomly distributed and randomly oriented thin-disk shaped pores that are progressively closed during pressurization. The effects of microcrack orientation, crystallographic preferred orientations, and compositional layering should be taken into consideration for interpreting the origin of type 1. The present study suggests that both mineralogy and confining pressure play a critical role in influencing the Poisson's ratio of the crystalline rocks particularly below 200-300 MPa.

The experimental data reported in Chapter 4 were analyzed using the exponential equations described in Chapter 3:

$$V_p = a_p + b_p P - c_p \exp(-k_p P) \qquad (1.2)$$

and

$$V_s = a_s + b_s P - c_s \exp(-k_s P) \qquad (1.3)$$

where the subscripts p and s denote the P- and S-waves, respectively; a is the intrinsic velocity at zero pressure if pores/cracks were absent; b is the intrinsic pressure derivative of velocity in the linear elastic regime; c is the initial velocity drop caused by the presence of pores/cracks at zero pressure; and k is the decay constant of the velocity drop, which controls the shape of the velocity-pressure curves in the nonlinear poro-elastic regime. In the linear elastic regime (P>200-300 MPa), Poisson's ratio increases with increasing P if $(b_p/b_s) > (a_p/a_s)$, decreases with increasing P if $(b_p/b_s) < (a_p/a_s)$, and remains almost unchanged if $(b_p/b_s) \approx (a_p/a_s)$. In the nonlinear poro-elastic regime (P<200-300 MPa), however, the variation in Poisson's ratio depends on the competition between terms $V_s(dV_p/dP)$ and $V_p(dV_s/dP)$. Poisson's ratio increases with increasing P if $V_s(dV_p/dP) > V_p(dV_s/dP)$, decreases with increasing P if $V_s(dV_p/dP) < V_p(dV_s/dP)$, and remains constant if the two terms are equal.

Chapter 5 is devoted to Poisson's ratios of common minerals and rocks. The strength of this chapter is to apply the laboratory experimental results to constrain the crustal composition and tectonic evolution of the Chinese continental crust based on crustal thickness (H) and Poisson's ratio data measured from 248 broadband seismic stations using teleseismic receiver function techniques. The high pressure experimental results, together with those compiled in Handbook of Seismic Properties of Minerals, Rocks and Ores (Ji et al., 2002), reveal that except for monomineralic rocks such as quartzite, serpentinite, anorthosite, limestone and marble, the rest of the rock types have Poisson's ratios falling along an upward convex curve determined from the correlations between

elastic moduli and density. Poisson's ratios increase with density as the lithology changes from granite, felsic gneiss and schist, through diorite-syenite, intermediate gneiss and metasediment, to gabbro-diabase, amphibolite and mafic gneiss, and then decrease as the rocks become ultramafic in composition. Eclogite has a higher density but a lower Poisson's ratio than peridotite. The North China, Yangtze, South China and Northeast China blocks and Songpan-Ganzi Terrane of China are dominated by low ($\upsilon < 0.26$) and moderate ($0.26 \leq \upsilon < 0.28$) υ values (>70%), suggesting the crust is predominantly felsic. The Lhasa terrane, Qiangtang terrane, and Indochina block of China are characterized by high proportions (33-42%) of measurements with very high υ values (≥ 0.30), suggesting that the crust is partially molten due to high temperatures. A negative correlation between υ and H is found for the South China block, Northeast block, Lhasa block, Qiangtang terrane and Indochina block, indicating either tectonic thickening of the felsic upper and middle crust by folding and thrusting or the removal of mafic layers from the lower crust into the upper mantle by delamination.

Chapter 5 also reported two types of correlation between υ and H in the North China block: with decreasing H, υ increases gently and linearly in the Baoding-Datong and Guanting-Zhangjiakou-Zhangbei regions, while increasing abruptly and nonlinearly in the rest of the block (e.g., Northeastern Hebei province and the southern Taihangshan area near Shijiazhuang). The linear correlation is interpreted as due to the summed, opposing contribution of tectonic thinning of felsic crust and the addition of mafic rocks crystallized from underplated magmas to the bulk crustal υ. The abrupt increase of υ with decreasing H suggests that much larger thinning strains have taken place in the felsic upper and middle crust than in the mafic lower crust during Mesozoic-Cenozoic tectonic extension. It is further inferred that basaltic underplating has been localized mainly in the Zhangjiakou and adjacent regions.

Chapter 6 analyzed the correlations between P- and S-wave velocities (V_p and V_s) and corresponding Poisson's ratios (υ) for 12 common categories of rocks (amphibolite,

anorthosite, basalt, diorite, eclogite, felsic gneiss, gabbro-diabase, granite, intermediate gneiss, limestone, mafic gneiss, and peridotite) and 4 types of massive sulfide ores (chalcopyrite, pyrite, sphalerite and pyrrhotite). The analysis reveals that the linear correlation provides good descriptions for the V_s - V_p and $\ln V_s - \ln V_p$ relationships. Poisson's ratio is linearly correlated with V_s, V_p, shear modulus (G) and Young's modulus (E) for these rocks and sulfide ores. A decrease in Poisson's ratio is associated with increases in V_s, G and E. However, the variation of Poisson's ratio with V_p depends on the logarithmic ratio $R_{s/p}$ (i.e., $\partial \ln V_s / \partial \ln V_p$). Poisson's ratio increases or decreases with V_p when $R_{s/p}$<1 or >1. $R_{s/p}$ varies systematically with lithology (0.300 for granite, 0.573 for diorite, 0.602 for felsic gneiss, 0.631 for intermediate gneiss, 0.721 for gabbro-diabase, 0.768 for mafic gneiss, 0.866 for eclogite, 0.890 for amphibolite, and 1.391 for peridotite). It is suggested that $R_{s/p}$ can be used as a proxy for the composition of the deep continental crust and the upper mantle. It is believed that the correlations between V_p and V_s, and corresponding Poisson's ratios (υ) are important in modeling and interpreting seismic data in terms of chemistry and lithology.

Chapter 7 presented a succinct summary of the results and discussed the further work needed to perform.

In order to facilitate the reading of this thesis, a brief review of basic principles is provided below.

1.2 Elasticity

Many materials including rocks can be approximately considered perfectly linear elastic without appreciable error when the deformations are small, as is the case for seismic waves except near a seismic source. The theory of elasticity deals with the relations between the stress (σ_{ij}) and the resulting strain (ε_{ij}) on a body, where i, j may

take the values 1, 2, or 3, parallel to the coordinate axes x_1, x_2, x_3, respectively, the first suffix denotes the direction of the stress component and the second indicates the direction of the normal to the plane under consideration (Nye, 1957, Figure 1.1). Stresses of σ_{11}, σ_{22} and σ_{33} are normal stresses, whereas those of the type σ_{12}, σ_{13} and σ_{23} are shear stresses.

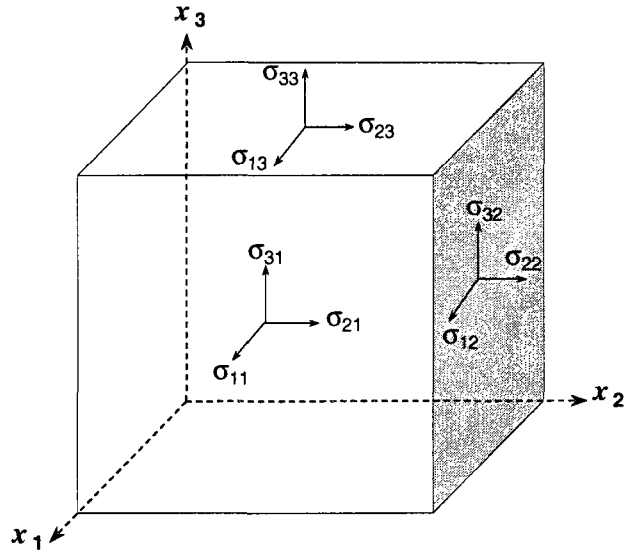

Figure 1.1 Stress components acting on the faces of a unit cube.

A perfect elastic body deforms as linear elasticity, which is stated by Hooke's law:

$$\sigma_{ij} = C_{ijkl}\varepsilon_{kl} \tag{1.4}$$

Or

$$\varepsilon_{ij} = S_{ijkl}\sigma_{kl} \tag{1.5}$$

where C_{ijkl} and S_{ijkl} are the elastic stiffness and compliance, respectively, and $i, j, k, l = 1$, 2, or 3. Because the conditions for zero rotation of the body are $\sigma_{12} = \sigma_{21}$, $\sigma_{13} = \sigma_{31}$ and

$\sigma_{23} = \sigma_{32}$, σ_{ij} contains only 6 independent components and the stiffness C_{ijkl} can be expressed by a 6×6 tensor:

$$C_{qr} = \begin{pmatrix} C_{11} & C_{12} & C_{13} & C_{14} & C_{15} & C_{16} \\ C_{21} & C_{22} & C_{23} & C_{24} & C_{25} & C_{26} \\ C_{31} & C_{32} & C_{33} & C_{34} & C_{35} & C_{36} \\ C_{41} & C_{42} & C_{43} & C_{44} & C_{45} & C_{46} \\ C_{51} & C_{52} & C_{53} & C_{54} & C_{55} & C_{56} \\ C_{61} & C_{62} & C_{63} & C_{64} & C_{65} & C_{66} \end{pmatrix} \tag{1.6}$$

The stiffnesses C_{qr} can be further simplified into 21 independent elastic coefficients due to the reciprocal relations $C_{qr} = C_{rq}$ imposed by thermodynamic requirements. The components of compliance S_{ijkl} can be specified in a similar way to the stiffnesses. The compatibility between C_{qr} and S_{qr} requires

$$C_{qr} \bullet S_{q_r} = I \tag{1.7}$$

where $\boldsymbol{I}$ is the unit tensor. The 21 stiffnesses (or compliances) of the generalized Hooke's law describe the elastic behavior of a material belonging to the triclinic crystal system (e.g., plagioclase). The existence of symmetry will reduce the number of independent elastic constants to 13 for monoclinic (e.g., hornblende, clinopyroxene, coesite and muscovite), 9 for orthorhombic (e.g., sillimanite, olivine and orthopyroxene), 7 or 6 for trigonal (e.g., dolomite, alpha-quartz, calcite) or tetragonal (e.g., rutile and zircon), 5 for hexagonal (e.g., graphite and nepheline), and 3 for cubic crystal systems (e.g., garnets, spinel, magnetite, halite, pyrite, and sphalerite). Table 1.1 lists elastic constants for common minerals in high pressure (HP) and ultrahigh pressure (UHP) metamorphic rocks such as quartz (Lakshtanov et al., 2007a), stishovite (Lakshtanov et al., 2007b), majorite (Pacalo and Weidner, 1997), aragonite (Liu et al., 2005), lawsonite (Sinogeikin et al., 2000), zoisite (Mao et al., 2007), orthopyroxene (Perrillat et al., 2007), clinopyroxene (Collins and Brown, 1998), pyrope, calcite,

ilmenite, rutile, olivine, coesite, muscovite and epidote (Ahrens, 1995). The full set of 21 elastic constants for triclinic albite ($NaAlSi_3O_8$), which is the sodic end-member of the plagioclase solid solution series, was reported by Brown et al. (2006) for the first time.

$$\begin{pmatrix} 69.9 & 34.0 & 30.8 & 5.1 & -2.4 & -0.9 \\ 34.0 & 183.5 & 5.5 & -3.9 & -7.7 & -5.8 \\ 30.8 & 5.5 & 179.5 & -8.7 & 7.1 & -9.8 \\ 5.1 & -3.9 & -8.7 & 24.9 & -2.4 & -7.2 \\ -2.4 & -7.7 & 7.1 & -2.4 & 26.8 & 0.5 \\ -0.9 & -5.8 & -9.8 & -7.2 & 0.5 & 33.5 \end{pmatrix}$$

For a statistically isotropic (i.e., texture-free polycrystalline rocks and amorphous glasses), linearly elastic solid, only two of the following elastic constants are required to characterize the seismic properties: the Young's (E), shear (G) and bulk (K) moduli and Poisson's ratio (υ). Once two independent constants are known, other constants can be calculated according to the well-known equations in elastic mechanics. The magnitudes of the elastic constants reflect crystal interatomic bonding, grain boundary strength, and microstructural characteristics (e.g., microcracks, porosity, phase connectivity and continuity) of rocks during uniaxial extension/compression, simple shear and hydrostatic compression.

Young's modulus E is defined as the ratio of compressional stress to the resultant longitudinal strain for a small cylinder under compression at both ends:

$$E = \frac{\sigma_{11}}{\varepsilon_{11}} \qquad (1.8)$$

Shear modulus G, which reflects the resistance of a body to shearing strain, is defined as:

$$G = \frac{\sigma_{12}}{2\varepsilon_{12}} \tag{1.9}$$

Bulk modulus is defined as:

$$K = V\frac{\partial P}{\partial V} \tag{1.10}$$

where P is pressure, V is volume, and $\partial P/\partial V$ denotes the partial derivative of pressure with respect to volume.

$$K = \frac{EG}{3(3G - E)} \tag{1.11}$$

The elastic constants of an isotropic rock are usually determined through acoustic measurements of P- and S-wave velocities (V_p and V_s) using the pulse transmission technique (Birch, 1960; Christensen, 1974; Ji et al., 1993; Ji and Salisbury, 1993), along with the density (ρ).

$$G = \rho V_s^{\,2} \tag{1.12}$$

$$K = \rho\left(V_p^{\,2} - \frac{4}{3}V_s^{\,2}\right) \tag{1.13}$$

$$E = \frac{\rho V_s^{\,2}\left(3V_p^{\,2} - 4V_s^{\,2}\right)}{V_p^{\,2} - V_s^{\,2}} \tag{1.14}$$

Table 1.1 Independent single-crystal stiffness coefficients at room conditions

Symmetry	Monoclinic				Orthorhombic					Tetragonal			Trigonal			Cubic
Crystal	epidote	muscovite	coesite (SiO_2)	Cpx	Opx	Zoisite	Lawsonite	Aragonite ($CaCO_3$)	Olivine ($Fo_{93}Fa_7$)	Majorite ($MgSiO_3$)	Stishovite (SiO_2)	Rutile (TiO_2)	Ilmenite ($MgSiO_3$)	Calcite ($CaCO_3$)	α-Quartz (SiO_2)	Pyrope
Density (g/cm^3)	3.40	2.844	2.911	3.327			3.090		3.311	3.522	4.21	4.26	3.795	2.712	2.649	3.567
N*	13	13	13	13	9	9	9	9	9	7	6	6	7	6	6	3
C_{11} (GPa)	211.8	184.3	160.8	237.8	224.4	279.8	226	171.1	323.7	286.4	453	269	472	144.0	86.9	296.2
C_{22} (GPa)	238.7	178.4	230.4	183.6	165.8	249.2	214	110.1	197.6							
C_{33} (GPa)	202.0	59.1	231.6	229.5	202.9	209.4	259	98.4	235.1	280.1	776	480	382	84.0	106.4	
C_{44} (GPa)	39.1	16.0	67.8	76.5	82.2	51.8	65	39.3	64.6	85.0	252	124	106	33.5	59.5	91.6
C_{55} (GPa)	43.2	17.6	73.3	73.0	73.8	81.4	60	24.2	78.1							
C_{66} (GPa)	77.5	72.4	58.8	81.6	77.1	66.3	17	40.2	79.0	93.2	302	192				
C_{12} (GPa)	66.3	48.3	82.1	83.5	71.4	94.7	69	60.3	66.4	83.0	211	177	168	53.9	7.6	111.1
C_{13} (GPa)	45.2	23.8	102.9	80.0	52.7	88.7	65	27.8	71.6	104.9	203	146	70	51.1	12.0	
C_{14} (GPa)													-27	-20.5	-17.8	
C_{15} (GPa)	0.0	-2.0	-36.2	9.0									24			
C_{16} (GPa)										1.4						
C_{23} (GPa)	45.6	21.7	35.6	59.9	45.2	27.5	82	41.9	75.6							
C_{25} (GPa)	-8.2	3.9	2.6	9.5												
C_{35} (GPa)	-14.3	1.2	-39.3	48.1												
C_{46} (GPa)	-3.4	0.5	9.9	8.4												

N* is the number of independent elastic constants of each crystal symmetry.

1.3 V_p/V_s and Poisson's ratio

1.3.1 Definitions and implications

Poisson's ratio (υ) was defined by a French mathematician Simeon Poisson in 1829 as the negative of the ratio of transverse strain (ε_{jj}) to the axial strain (ε_{ii}) when an isotropic elastic solid is subjected to uniaxial stress (σ_{ii}) only (Gercek, 2007).

$$\upsilon = -\frac{\varepsilon_{jj}}{\varepsilon_{ii}} \qquad (1.15)$$

For an isotropic material at a given temperature and a given pressure, there is only one V_p/V_s ratio because V_p is the same for all propagation directions and there is only one V_s value. In this case, Poisson's ratio is a constant that does not depend on the choice of *i* and *j*, and lies between -1 and 0.5. Liquids have no resistance to shear but are incompressible and hence $\upsilon = 0.5$. Materials with $\upsilon < 0$ are called auxetic materials (e.g., foams) because there is an increase in volume when compressed (Lakes, 1987). A negative value of Poisson's ratio implies that a cylinder undergoing compression along its axis would contract simultaneously in all directions, which has been observed for certain directions in single crystals (Svetlov et al., 1988). For most rocks, Poisson's ratio is about 0.25-0.26. The values of Poisson's ratio range from 0.05 for very hard, rigid rocks to about 0.45 for soft, poorly consolidated materials.

Poisson's ratio is generally determined from measurements of P- and S-wave velocities (V_p and V_s) of an isotropic solid:

$$\upsilon = 0.5\left[1 - (\phi^2 - 1)^{-1}\right] \qquad (1.16)$$

where

$$\phi = V_p / V_s \qquad (1.17)$$

In an isotropic material, Poisson's ratio (υ) has the following relationships with the other elastic constants:

$$\upsilon = \frac{3K - 2G}{6K + 2G} \qquad (1.18)$$

$$\upsilon = \frac{E}{2G} - 1 \qquad (1.19)$$

$$\upsilon = 0.5 - \frac{E}{6K} \qquad (1.20)$$

For a fixed value of G, υ increases with increasing K. For a fixed value of K, however, υ decreases with increasing G.

Compared with other elastic constants such as Young's modulus, shear modulus and bulk modulus, Poisson's ratio (υ) is much less studied for rocks. Recently Poisson's ratio has received more attention in materials science. For metals, Poisson's ratio shows a systematic variation with crystalline structure: $\upsilon = 0.330 \pm 0.054$ for the f.c.c. (face-centered cubic) metals, $\upsilon = 0.317 \pm 0.064$ for b.c.c. (body-centered cubic) metals, and $\upsilon = 0.281 \pm 0.032$ for h.c.p. (hexagonal close-packed) metals (Koster and Franz, 1961; Ledbetter, 1977). Generally speaking, the Poisson's ratio increases with increasing ionicity (Dunn and Ledbetter, 1995), $\upsilon = 0.215$ for pure covalency (zero ionicity), 0.266 for phosphides, arsenides and antimonides, 0.336 for oxides, sulfides, selenides, and tellurides, and 0.391 for halides (Cl, Br, I). In geophysical survey, Poisson's ratio has

been used as an important indicator to distinguish quartz-dominated sandstone from calcite-dominated limestone in oil reservoirs (Figs. 1.2-1.3). As shown in Figure 1.2, it is almost impossible to distinguish sandstone from limestone in terms of P-wave velocity and density in certain areas. However, the distinguishing between sandstone and limestone becomes easy in term of Poisson's ratio or V_p/V_s (Figure 1.3) because calcite (0.32) has a much higher Poisson's ratio or V_p/V_s value than quartz (0.08). Poisson's ratios have been also used to distinguish quartz-dominated rocks from the feldspar-dominated rocks in the deep crust (e.g., Holbrook et al., 1988; Clarke and Silver, 1993; Zandt and Ammon, 1995; Owens and Zandt, 1997; Chevrot and van der Hilst, 2000; Xu et al., 2007).

Figure 1.4 illustrates the Poisson's ratio values of 23 common categories of rocks. The rocks rich in quartz (e.g., quartzite, sandstone, and siltstone) show clearly lowest Poisson's ratios compared with other rocks. Using the Poisson ratios we can distinguish quartz-rich rocks from calcite-rich rocks in the sedimentary basins or from feldspar-rich rocks in the crystalline basements. Moreover, serpentine, which is a hydrated peridotite and distributed mainly along the water-infiltrated faults or shear zones, has the highest Poisson-ratio. This feature provides an excellent opportunity for the Earth scientists to investigate the subduction zones and fault zones within an oceanic lithosphere.

The non-linear increase in V_p and V_s with increasing confining pressure reflects both the reduction of porosity and the change in the aspect ratios of microcracks in the rocks. How does the Poisson's ratio vary with the confining pressure for a given rock? How does the Poisson's ratio change with increasing or decreasing porosity and variation in the length/width ratios of micropores? Is it possible to obtain information about the state of microcracks from the in-situ measured V_p/V_s ratios or the Poisson's ratios? These are important questions scientifically deserved to be addressed.

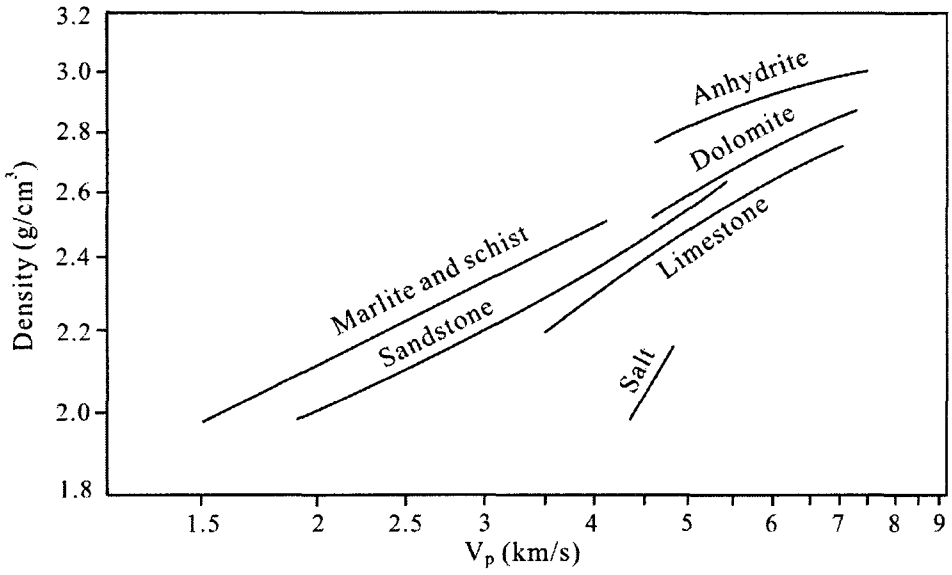

Figure 1.2 P-wave velocities of common sedimentary rocks as a function of density. (After Gardner et al., 1974)

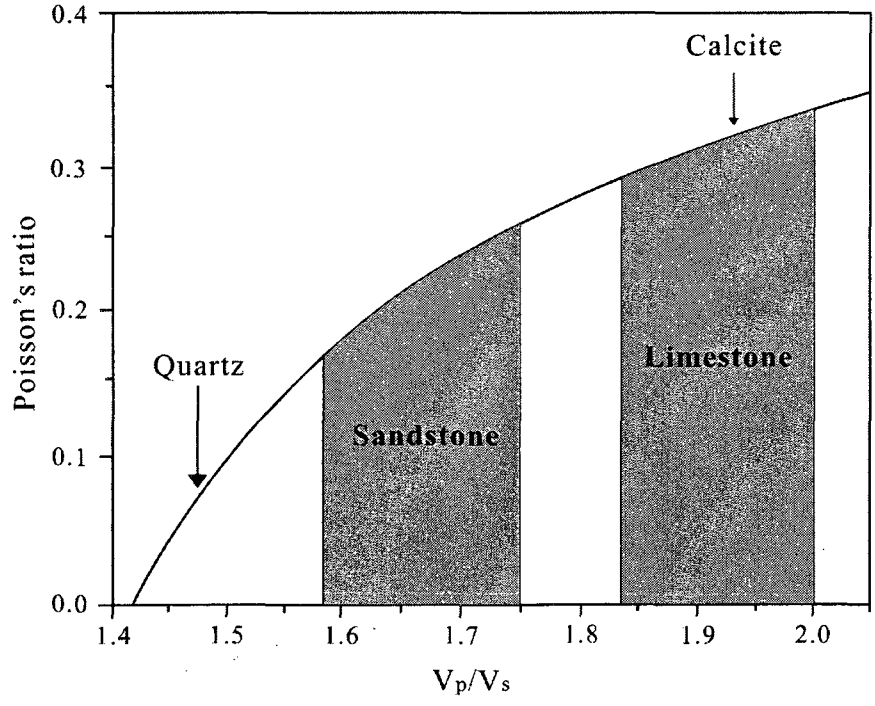

Figure 1.3 V_p/V_s ratios as a function of Poisson's ratio. (After Guéguen and Palciauskas, 1992)

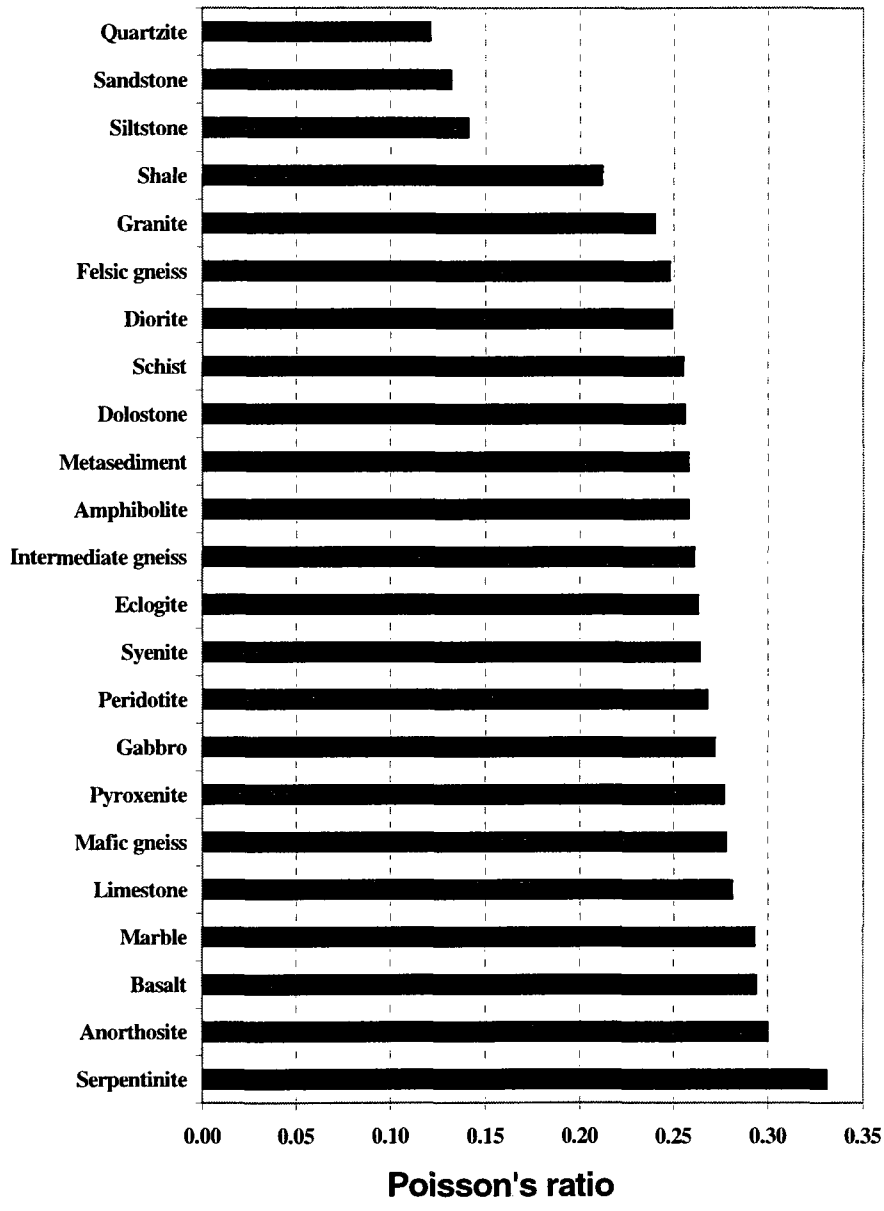

Figure 1.4 Mean Poisson's ratios of 23 main lithological categories (Ji et al., 2002)

Yeheskel and Tevet (2000) found a nonlinear decrease in the effective Poisson's ratio with increasing porosity, and a nonlinear increase in the effective Poisson's ratio with increasing the ratio of E/E_0 or V_p/V_{p0} where E_0 and V_{p0} are the Young's modulus and the P-wave velocity of the non-porous solid. The variation of the effective

Poisson's ratio with increasing porosity was also confirmed by the study of Phani and Sanyal (2005).

If the experimental data can be fitted by least squares expressions of the form:

$$E = E_0(1 - a_E\phi) \tag{1.21}$$

$$G = G_0(1 - a_G\phi) \tag{1.22}$$

where ϕ is the porosity, E_0 and G_0 are the Young's and shear moduli of the non-porous solid, and a_E and a_G are two constants. According to the theoretical analyses of Dewey (1947), Mackenzie (1950) and Hashin (1962) on the effect of spherical porosity on the Young's and shear moduli,

$$a_E = 3(9 + 5\upsilon_0)\frac{(1-\upsilon_0)}{2(7-5\upsilon_0)} \tag{1.23}$$

$$a_G = \frac{15(1-\upsilon_0)}{7-5\upsilon_0} \tag{1.24}$$

where υ_0 is the Poisson's ratio of the non-porous material or rock.

If the equation $M = M_0\frac{1-\phi}{1+d\phi}$ is used to describe the porosity dependence of elastic moduli, then

$$d_E = \frac{(13-15\upsilon_0)(1-\upsilon_o)}{(14-10\upsilon_0)} \tag{1.25}$$

$$d_K = \frac{1+\upsilon_0}{2-4\upsilon_0} \tag{1.26}$$

$$d_G = \frac{8-10\upsilon_0}{7-5\upsilon_0} \tag{1.27}$$

where E, K and G refer, respectively, the Young's, bulk and shear moduli, respectively.

If $M = M_0 \frac{1-\phi}{1+(a-1)\phi}$ is used, where a is a coefficient that depends on the pore aspect ratio (α) and the Poisson's ratio of the non-porous material (υ_0). Then, in the case of oblate pores ($\alpha << 1$),

$$a = \frac{8}{15\pi\alpha}\frac{(1-\upsilon_0)(5-\upsilon_0)}{2-\upsilon_0}$$ for the shear modulus, and

$$a = \frac{4}{3\pi\alpha}\frac{\left(1-\upsilon_0^{\,2}\right)}{1-2\upsilon_0}$$ for the bulk modulus.

In the case of needle shaped pores ($\alpha >> 1$),

$$a = \frac{8}{15(5-3\upsilon_0)}$$ for the shear modulus, and

$$a = \frac{5-4\upsilon_0}{3(1-2\upsilon_0)}$$ for the bulk modulus.

In the case of spherical pores,

$$M = M_0\left[1-\frac{\phi}{1-\phi}a\right] \tag{1.28}$$

where

$$a=\frac{2(4-5\upsilon_0)}{15(1-\upsilon_0)} \qquad \text{for the shear modulus, and}$$

$$a=\frac{1+\upsilon_0}{3(1-\upsilon_0)} \qquad \text{for the bulk modulus.}$$

Using the Mori-Tanaka mean-field approach, Dunn and Ledbetter (1995) theoretically analyzed the effective Poisson's ratio of macroscopically isotropic solids containing randomly distributed and randomly oriented spherical pores. The pore shape varies from spherical to penny-shaped and needle-shaped. For the material containing spherical voids (α=1, where α is the ratio of length to width of the voids),

$$\upsilon=\frac{2\upsilon_0(5\upsilon_0-7)+\phi(5\upsilon_0-3)(\upsilon_0+1)}{2(5\upsilon_0-7)+\phi(15\upsilon_0-13)(\upsilon_0+1)} \tag{1.29}$$

For the material containing penny-shaped cracks (α=0),

$$\upsilon=\frac{45\upsilon_0(2-\upsilon_0)+16\upsilon_0\eta(1-\upsilon_0^{\,2})}{45(2-\upsilon_0)+16\eta(1-\upsilon_0^{\,2})(10-3\upsilon_0)} \tag{1.30}$$

where η is the crack density parameter that was defined by Budiansky and O'Connell (1976) as the number of cracks of unit radius per unit volume:

$$\eta = \frac{3\phi}{4\pi\alpha} \tag{1.31}$$

For the material containing needle-shape pores ($\alpha \to \infty$),

$$\upsilon = \frac{-15\upsilon_0 + \phi(8\upsilon_0 - 5)(\upsilon_0 + 1)}{-15 + 4\phi(4\upsilon_0 - 5)(\upsilon_0 + 1)} \tag{1.32}$$

Equations (29)-(32) suggest that the effective Poisson's ratio depends only on porosity, pore shape and the Poisson's ratio of the solid medium. In other words, the effective Poisson's ratio of a given porous material is independent on any other elastic constants than the Poisson's ratio of the solid medium.

Using Eq. (29), we calculated the effects of spherical pores on the Poisson's ratio values for calcite ($\upsilon_0 = 0.32$) and quartz ($\upsilon_0 = 0.08$) monomineralic aggregates (Fig. 1.5a). Interestingly, the effective Poisson's ratio decreases with increasing porosity in calcite aggregates while it increases with increasing porosity in quartz aggregates. For a material with $\upsilon_0 = 0.20$ (e.g., staurolite, diallage and enstatite), the effective Poisson's ratio remains constant as a function of porosity. For any materials with $\upsilon_0 > 0.20$ (e.g., plagioclase, biotite, muscovite, hornblende, diopside, olivine and garnet), the effective Poisson's ratio decreases with increasing porosity. For any materials with $\upsilon_0 < 0.20$ (pyrite, quartz), the effective Poisson's ratio increases with increasing porosity. For the same reason, the ratio of V_P/V_S decreases with increasing porosity for calcite aggregates such as limestone and marble but increases with increasing porosity for quartz aggregates such as sandstone and quartzite (Fig. 1.5b).

As discussed in Chapter 5, thickening of the felsic upper-middle crust by folding and thrusting causes a decrease of crustal bulk Poisson's ratio with an increase of crustal thickness. The removal of mafic component from the lower crust by delamination

results in a decrease of crustal bulk Poisson's ratio. In contrast, addition of mafic component into the lower crust by magmatic underplating increases the crustal bulk Poisson's ratio. So far the interpretation of crustal Poisson's ratios in term of lithology has been essentially based on an assumption that Poisson's ratios depend primarily on quartz or SiO_2 content [$\upsilon \leq 0.26$ ($V_p/V_s \leq 1.756$) for felsic rocks, $0.26 < \upsilon \leq 0.28$ ($1.756 < V_p/V_s \leq 1.809$) for intermediate rocks, $0.28 < \upsilon \leq 0.32$ ($1.809 < V_p/V_s \leq 1.944$) for mafic rocks] and fluid content [$\upsilon > 0.32$ ($V_p/V_s > 1.944$) for fluid-filled porous/fractured or partially molten rocks] but is relatively insensitive to pressure, temperature, and wave propagation-vibration paths (e.g., Zandt and Ammon, 1995; Owens and Zandt, 1997; Chevrot and van der Hilst, 2000). The average V_p/V_s value proposed for the continental crust is 1.78 (Zandt and Ammon, 1995). On the basis of the V_p/V_s ratios, for example, a significant difference has been found between the lower crusts of the Appalachian (1.70-1.77 with a mean value of 1.73) and Grenville (1.77-1.85 with a mean value of 1.81) terranes. Musacchio et al. (2004) inferred a dioritic composition and a gabbroic composition for the lower crusts of the Appalachian and Grenville terranes, respectively. It is worthy to point out that the above lithology discrimination holds true for homogeneous isotropic and nearly isotropic rocks in the scale of in-situ seismic wave propagations.

1.3.2 V_p/V_s and Poisson's ratio anisotropy

However, most of crustal rocks are elastically anisotropic due to the presence of compositional layering, lattice preferred orientation (LPO), shape preferred orientation (i.e., foliation and lineation) of rock-forming minerals (e.g., Meissner et al., 2006), and alignment of microcracks (e.g., Crampin and Peacock, 2005, 2008). In an anisotropic medium, there are three velocities (V_p, V_{s1} and V_{s2}, see this chapter 1.5) and thus two ratios V_p/V_{s1} and V_p/V_{s2} for each direction. Furthermore, these ratios vary with direction. Unfortunately, it has been a common practice to use a single V_p/V_s ratio measured for only a selected pair of propagation-vibration directions in the potentially anisotropic

crust (i.e., seismic refraction/wide-angle reflection experiments and analyses of teleseismic receiver functions using single station techniques) to calculate the Poisson's ratio according to Eq. (1.16) (e.g., Clarke and Silver, 1993; Zandt and Ammon, 1995; Owens and Zandt, 1997; Chevrot and van der Hilst, 2000; Xu et al., 2007). A fundamental assumption of Eq. (1.16), isotropy, is not fulfilled for strongly anisotropic crustal rocks such as serpentinite, mica schist. The value obtained from Eq. (1.16), hereafter referred to as the apparent Poisson's ratio, corresponds to neither the isotropic (υ_0) nor anisotropic (υ_{ii}) Poisson's ratios. The anisotropic Poisson's ratio for the longitudinal direction i and the transverse direction j is given by: $\upsilon_{ij} = -\varepsilon_{ii}/\varepsilon_{jj} = -S_{iijj}/S_{iiii}$ ($i \neq j$), where S_{ijkl} are the components of the elastic compliance tensor, and ε_{ii} and ε_{jj} are the strain components in the i and j directions, respectively. An anisotropic material can have an arbitrarily large positive or negative υ_{ii} (Ting and Chen, 2005). Obviously, the anisotropic Poisson's ratio varies with direction in a complex manner. The lack of S_{ijkl} data precludes a detailed analysis of anisotropic Poisson's ratios for the crust at each depth interval of interest. Hence the apparent Poisson's ratio is not a physically sound parameter if the isotropy of the crust is uncertain, and at best only represents a mathematic substitution for V_p/V_s.

It is also necessary to point out that in anisotropic medium the V_p/V_{s1} and V_p/V_{s2} ratios measured for a particular propagation direction does not correspond to the anisotropic Poisson's ratio because S-wave involves shear strains and P-wave involves more complex strains composed of both compression and shear components whereas the definition of Poisson's ratio only contains axial and transverse pure strains (Mainprice et al., 2008; Wang et al., 2009). Therefore, it is not good practice to define the V_p/V_s ratio via the Poisson's ratio because V_p/V_s ratio is a physically sound parameter that can be really measured while the Poisson's ratio is neither directly observable nor corresponds to the characteristics of wave propagation in anisotropic rocks.

In the following, I will show that the V_p/V_s ratio of some common crustal rocks can be strongly anisotropic and vary over the whole range displayed by the entire spectrum of common rocks. In these special cases, neither very high V_p/V_s values (>1.944) with V_p>6.5 km/s necessarily imply the presence of melt or fluids (water or volatile components) nor low V_p/V_s values (<1.756) are indicative of felsic composition, as proposed for presumably isotropic rocks (e.g., Zandt and Ammon, 1995; Owens and Zandt, 1997; Chevrot and van der Hilst, 2000; Xu et al., 2007).

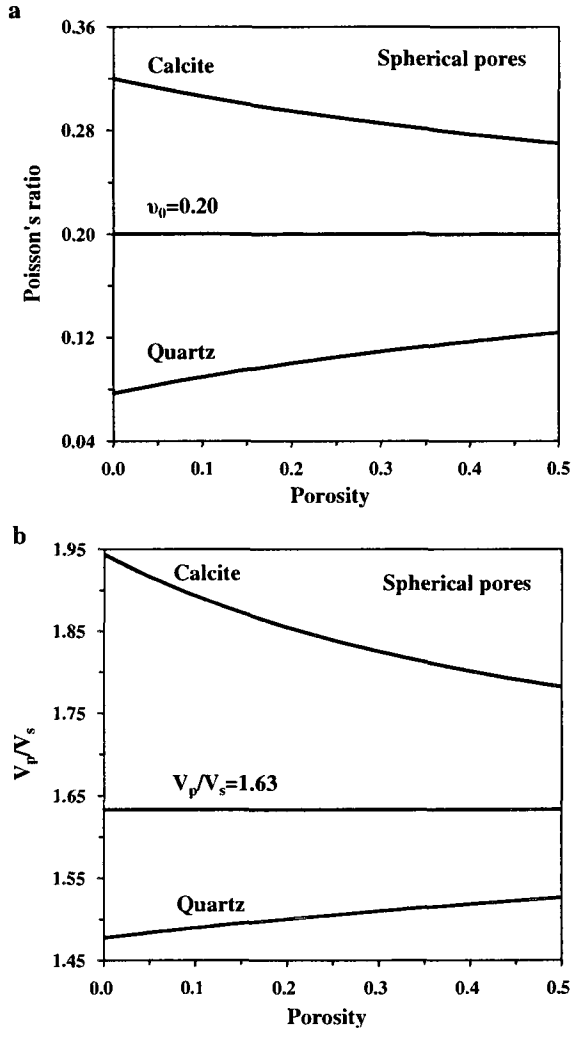

Figure 1.5 Poisson's ratios and V_p/V_s ratios of polycrystalline aggregates of quartz and calcite containing spherical pores.

Anorthosite is an important component of many Precambrian cratons such as the Grenville Province. An anorthosite sample (Fig. 1.6a), which was from the Precambrian Grenvillian (1.1 Ga) basement in Oklahoma (USA), contains 90 vol.% plagioclase (An65-68) and 10 vol.% olivine. The plagioclase crystals are tabular with length/width ratios >4 and developed remarkable magmatic foliation but no lineation. LPO measurements (Seront et al., 1993) display that (010) planes of plagioclase form a strong preferred orientation parallel to the foliation and the (001) pole and [100] direction each form a nearly perfect girdle in the foliation. The same LPO pattern has been observed for plagioclase in the Sept-Iles Neoproterozoic layered mafic intrusion, Quebec (Zhao, 1997). The LPO formed when the plagioclase crystals floated and accumulated at the top of the basaltic magma chamber. The anorthosite is transversely isotropic in V_p (Seront et al., 1993): $V_p(Z)>>V_p(X)=V_p(Y)$. However, this sample is orthorhombic in V_s: $V_s(XZ)=V_s(YZ)>V_s(XY)=V_s(YX)>>V_s(ZX)>V_s(ZY)$. In the range of 100-1000 MPa, $\upsilon_{ZY}>\upsilon_{ZX}>>\upsilon_{XY}=\upsilon_{YX}>\upsilon_{XZ}=\upsilon_{YZ}$ (Fig. 1.6a). With respect to υ_0 (0.330), υ_{ZY}, υ_{ZX}, υ_{XY}, υ_{YX}, υ_{XZ}, and υ_{YZ} increase, respectively, 19.31%, 16.64%, -7.84%, -7.84%, -10.13% and -10.13%. Obviously, υ_{ij} varies considerably with the propagation direction: 0.39 ± 0.05 perpendicular to the foliation and 0.30 ± 0.04 parallel to the foliation. The anisotropy coefficients for V_p, V_s and υ are 13.96%, 11.18% and 29.44%, respectively. Using the conventional criteria (e.g., Zandt and Ammon, 1995; Owens and Zandt, 1997; Chevrot and van der Hilst, 2000; Xu et al., 2007), υ_{ZY} and υ_{ZX} (0.39) may be easily mistaken as indicative of the presence of partial melt and fluids.

Amphibolite is one of the most common lithologies in the middle and lower crust. Sample J313C, collected from the Snowbird tectonic zone (Canada), consists of 61.2% hornblende, 37.0% plagioclase, 0.6% clinopyroxene, 0.6% biotite and 0.6% garnet. Deformation took place at ~700 MPa and ~700 °C. This amphibolite displays typically orthorhombic symmetry in V_p (Ji et al., 1993): $V_p(X)>V_p(Y)>V_p(Z)$. However, it is nearly transversely isotropic in V_s (Ji and Salisbury, 1993): $V_s(YX)\approx V_s(XY)>V_s(XZ)$

$\approx V_s(YZ) \approx V_s(ZX) \approx V_s(ZY)$. At P>100 MPa, $\upsilon_{XZ} > \upsilon_{YZ} > \upsilon_{XY} > \upsilon_{ZY} \approx \upsilon_{ZX} > \upsilon_{YX}$ (Fig. 1.6b). Apparent Poisson's ratios in the XY, XZ, YX, YZ, ZX and ZY directions increase, respectively, 5.36%, 17.81%, -13.33%, 7.55%, -9.08%, and -8.31% with respect to υ_0 (0.262) at 600 MPa. The apparent Poisson's ratios measured along the YX (0.227), ZX (0.239) and ZY (0.241) directions may be mistaken as indicative of felsic rocks although those along the XZ (0.309), XY (0.276) and YZ (0.283) paths are typical for mafic rocks (Wang et al., 2009).

Seismic anisotropy of amphibolites is essentially controlled by amphibole LPO that is generally simple, consistent, and strong (e.g., Ji et al., 1993; Barberini et al., 2007): the [001] directions have a strong concentration parallel to the lineation, the (100) planes are parallel to foliation, and [010] directions are parallel to Y. This LPO pattern is produced by (100)[001] slip. The LPO formed by {110}[001] slip, which is characterized by the poles to either (100) or (010) form a girdle or partial girdle normal to the lineation, has also been reported for some amphibolites (Ji et al., 1993; Barberini et al., 2007). Monoclinic amphibole is strongly anisotropic with the highest, moderate and lowest V_p close to the a*, b and c axes, respectively. The largest S-wave splitting (ΔV_s) occurs in the (100) plane. As a result, the fastest, intermediate and slowest P-wave velocities are in the X, Y, and Z directions, respectively. P-wave anisotropy of amphibolites is generally high (>10%). The maximum ΔV_s is observed for propagation in the foliation plane and almost no shear-wave splitting is observed normal to foliation (Wang et al., 2009). Accordingly, υ_{ij} measured along the XZ and YZ directions increase significantly while those along YX, ZX and ZY decrease with respect to υ_0 (0.262).

Granitic gneiss is probably the most common lithology in the continental crust. Sample YK-28, collected from the Xinyi complex in the Yunkai Mountain (China), is granitic gneiss with porphyroclastic texture. At confining pressures above the critical value necessary to close microcracks, $V_p(Y) > V_p(X) > V_p(Z)$, and

$V_s(XY)>V_s(ZX)>V_s(YX)>V_s(ZY)>V_s(YZ)>V_s(XZ)$. At 200-800 MPa, $\upsilon_{XZ} > \upsilon_{YZ} > \upsilon_{YX} > \upsilon_{ZY} > \upsilon_{XY} > \upsilon_{ZX}$ (Fig. 1.6c). At 600 MPa, apparent Poisson's ratios measured along the XY (0.242), XZ (0.345), YX (0.310), YZ (0.338), ZX (0.217) and ZY (0.259) directions increase, respectively, -15.13%, 21.08%, 8.73%, 18.45%, -23.86%, and -9.27% with respect to υ_0 (0.285). Poisson's ratios measured in the XZ and YZ directions would be misinterpreted as due to the presence of melt and/or fluids while those in the YX direction as due to the occurrence of mafic rocks such as gabbro (Wang et al., 2009).

Sample KZ-17, which contains 42.5% quartz, 38.4% biotite, 17.6% plagioclase, 0.6% K-feldspar, 0.6% garnet, 0.2% opaque, and 0.1% zircon, is a typical paragneiss from the amphibolite-granulite facies transition zone of the Kapuskasing uplift in Ontario, Canada (Fountain et al., 1990; Salisbury and Fountain, 1994). The seismic property of this paragneiss is characterized by $V_p(X)>V_p(Y)>V_p(Z)$ and $V_s(XY)\approx V_s(YX)\approx V_s(YZ)>>V_s(XZ)\approx V_s(ZX)\approx V_s(ZY)$. At 200-600 MPa, the Poisson's ratio anisotropy is characterized by $\upsilon_{XZ} >> \upsilon_{ZY} \approx \upsilon_{ZX} > \upsilon_{XY} > \upsilon_{YX} \approx \upsilon_{YZ}$ (Fig. 1.6d). At 600 MPa, the Poisson's ratios increase -6.55%, 31.81%, -14.99%, -17.26%, 2.74% and 4.25% in the XY (0.260), XZ (0.367), YX (0.237), YZ (0.230), ZX (0.286), and ZY (0.290) directions, respectively, compared with υ_0 (0.279). The anisotropy coefficients of V_p, V_s and υ for the paragneiss are 17.52%, 22.37% and 49.07%, respectively (Wang et al., 2009).

High-grade biotite-sillimanite metapelite is an important component in the Ivrea-Verbano zone (Northern Italy), which is believed to represent a segment of continental lower crust thrust to the Earth's surface. Sample IV-77 is a typical example for the metapelite, which consists of 35.9% biotite, 25.1% sillimanite, 22.1% quartz, 9.4% garnet, 4.7% muscovite, and 2.8% plagioclase (Burlini and Fountain, 1993). Both mica and sillimanite develop strong LPOs with the mica (001) plane parallel to the foliation and the sillimanite c-axis parallel to the lineation. In the pressure range 200-600 MPa,

$V_p(X)>V_p(Y)>V_p(Z)$, and $V_s(XY)>V_s(YX)>>V_s(ZY)>V_s(ZX)>V_s(YZ)>V_s(XZ)$. At 600 MPa, the mean V_p, V_s and υ of the bulk sample are 7.52 km/s, 4.00 km/s, and 0.283, respectively; the anisotropy coefficients of V_p, V_s and υ are 26.7%, 36.6% and 69.5%, respectively (Fig. 1.7a). Apparent Poisson's ratio is strongly anisotropic: υ_{XY} =0.250, υ_{XZ} =0.404, υ_{YX} =0.237, υ_{YZ} =0.366, υ_{ZX} =0.231, and υ_{ZY} =0.207. Using the conventional criteria, υ_{XY}, υ_{YX} and υ_{ZX} would be misinterpreted as granitic rocks, υ_{ZY} as a quartz-rich rock, and υ_{XZ} and υ_{YZ} as partially molten or fluid-rich rocks (Wang et al., 2009).

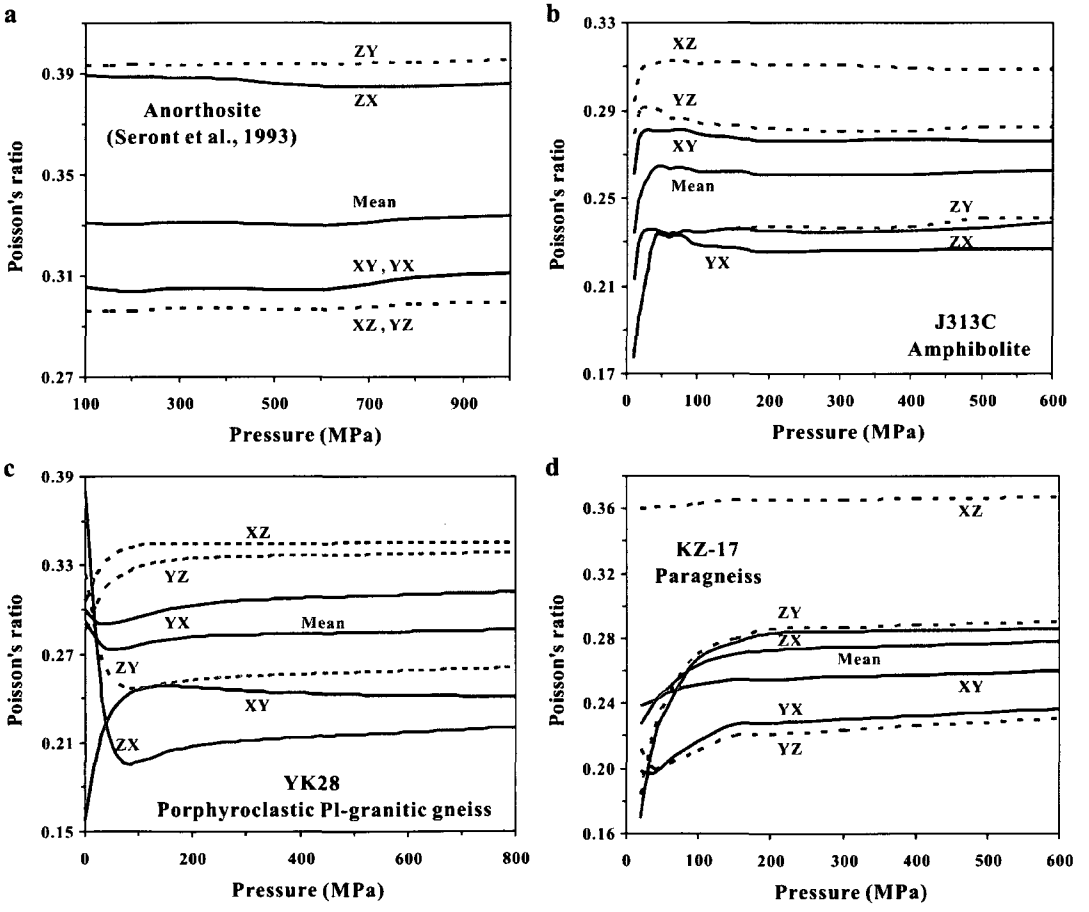

Figure 1.6 Apparent Poisson's ratios (υ_{XY}, υ_{XZ}, υ_{YX}, υ_{YZ}, υ_{ZX}, υ_{ZY}) and average Poisson's ratio (υ_0) as a function of confining pressure for anorthosite (a), amphibolite (b), granitic gneiss (c) and paragneiss (d).

Sulu-YK22 (Fig. 1.7b) is a metagabbro collected from a layered mafic and ultramafic complex at Yangkou Beach, Qingdao (China). The sample consists of 45% plagioclase, 14% clinopyroxene, 9% garnet, 10% quartz, 5% muscovite, 11% chlorite, 5% zoisite and 1% opaque. This metagabbro is characterized by $V_p(X)>V_p(Y)>V_p(Z)$ and $V_s(YX)>V_s(XY)>>V_s(ZX)>V_s(YZ)\approx V_s(ZY)>V_s(XZ)$. At 600 MPa, $\upsilon_{XY}=0.291$, $\upsilon_{XZ}=0.321$, $\upsilon_{YX}=0.257$, $\upsilon_{YZ}=0.289$, $\upsilon_{ZX}=0.241$, and $\upsilon_{ZY}=0.257$. The apparent Poisson's ratios increase 5.27%, 16.27%, -6.70%, 4.76%, -12.61% and -6.98% in the XY, XZ, YX, YZ, ZX, and ZY directions, respectively, compared with υ_0 (0.276).

Slates, which are commonly produced by the metamorphism of shales, are foliated, low-grade metamorphic rocks. Sample Chri-18 is a typical slate from Poultney, Vermont (USA). This slate shows strong transverse isotropy (Christensen, 1965, 1966): $V_p(X)\approx V_p(Y)>>V_p(Z)$, and $V_s(YX)\approx V_s(XY)>> V_s(XZ)\approx V_s(YZ)\approx V_s(ZX)\approx V_s(ZY)$. The anisotropic coefficients of V_p, V_s and υ at 600 MPa are as high as 18.36%, 32.26% and 66.91%, respectively. This slate displays orthotropic symmetry with $\upsilon_{XZ}\approx\upsilon_{YZ}>\upsilon_{ZX}=\upsilon_{ZY}>\upsilon_{XY}\approx\upsilon_{YX}$ (Fig. 1.7c). At 600 MPa, $\upsilon_{XY}\approx\upsilon_{YX}=0.190\pm0.006$, $\upsilon_{ZX}=\upsilon_{ZY}=0.278$, $\upsilon_{XZ}\approx\upsilon_{YZ}=0.365\pm0.005$ (Wang et al., 2009).

Schist is an important category of rocks in the crust. Sample 12 is a foliated and lineated staurolite-garnet schist from Highland gneiss, Litchfield, Connecticut (USA), which consists of 44% quartz, 23% biotite, 14% muscovite, 13% plagioclase (An25), 3% staurolite, 2% almandine, and 1% magnetite (Christensen, 1965). Mica forms a strong LPO with (001) planes parallel to the foliation. $V_p(X)$ is slightly higher than $V_p(Y)$ but much higher than $V_p(Z)$. $V_s(XY)\approx V_s(YX)>>V_s(ZX)=V_s(ZY)\approx V_s(YZ)\approx V_s(XZ)$ (Christensen, 1965, 1966). The Poisson's ratio anisotropy is characterized by $\upsilon_{XZ}>\upsilon_{YZ}>\upsilon_{ZX}=\upsilon_{ZY}>\upsilon_{XY}>\upsilon_{YX}$ in the pressure range 200-1000 MPa (Fig. 1.7d). At 600 MPa, the apparent Poisson's ratios increase -17.11%, 28.95%, -22.05%, 21.59%, -5.69%

and -5.69% in the XY, XZ, YX, YZ, ZX, and ZY directions, respectively, compared with υ_0 (0.310). The υ_{ij} values along the XY (0.257) and YX (0.241) paths, the ZX (0.292) and ZY (0.292) paths and the XZ (0.399) and YZ (0.376) paths may be misinterpreted as granitic (υ<0.26), mafic (υ=0.28-0.30) and partially molten (or fluid-rich) rocks (υ>0.32), respectively, if the effect of seismic anisotropy is not taken into account.

Obviously, due to the limitations of the ray path geometry, a full characterization of crustal Poisson's ratio anisotropy cannot be achieved by in-situ seismic observations. The crustal Poisson's ratio values reported in the literature were calculated from the V_p and V_s data measured along a single propagation-vibration path through a potentially anisotropic medium. The orientation of the path with respect to the structural framework (X-Y-Z) is generally unclear. The obtained "apparent" Poisson's ratios, which are sensitive to the propagation and vibration directions, can be different from the isotropic value (υ_0). As the total range of Poisson's ratios displayed by a single rock can be as large as the range displayed by the entire spectrum of common rocks (Figs. 1.6-1.7), determinations of lithology using Poisson's ratio alone are subject to considerable ambiguity. For example, if the lower crust subjected to tectonic extension is composed of a metapelite (sample IV-77) which develops regionally and pervasively horizontal foliation, the apparent Poisson's ratio can vary from 0.207 to 0.231 (implying a felsic composition) for steep propagation paths to 0.404 for horizontal propagation path parallel to lineation and S-wave vibration direction normal to foliation. If velocities for the lower crust are determined from the wide-angle reflections off the Moho and diving wave rays which turn in the lower crust due to gradients (e.g., Salisbury and Fountain, 1994), the obtained Poisson's ratio should be biased toward higher values because the wave paths are aligned with subhorizontal to moderate (45°) dips. If velocities for the crust are obtained from the analysis of teleseismic receiver functions using single station techniques (e.g., Zandt and Ammon, 1995; Owens and Zandt, 1997; Chevrot and van

der Hilst, 2000; Xu et al., 2007), the wave propagation paths are oriented with subvertical to moderate (45°) dips, causing υ to be biased toward lower values (<0.25).

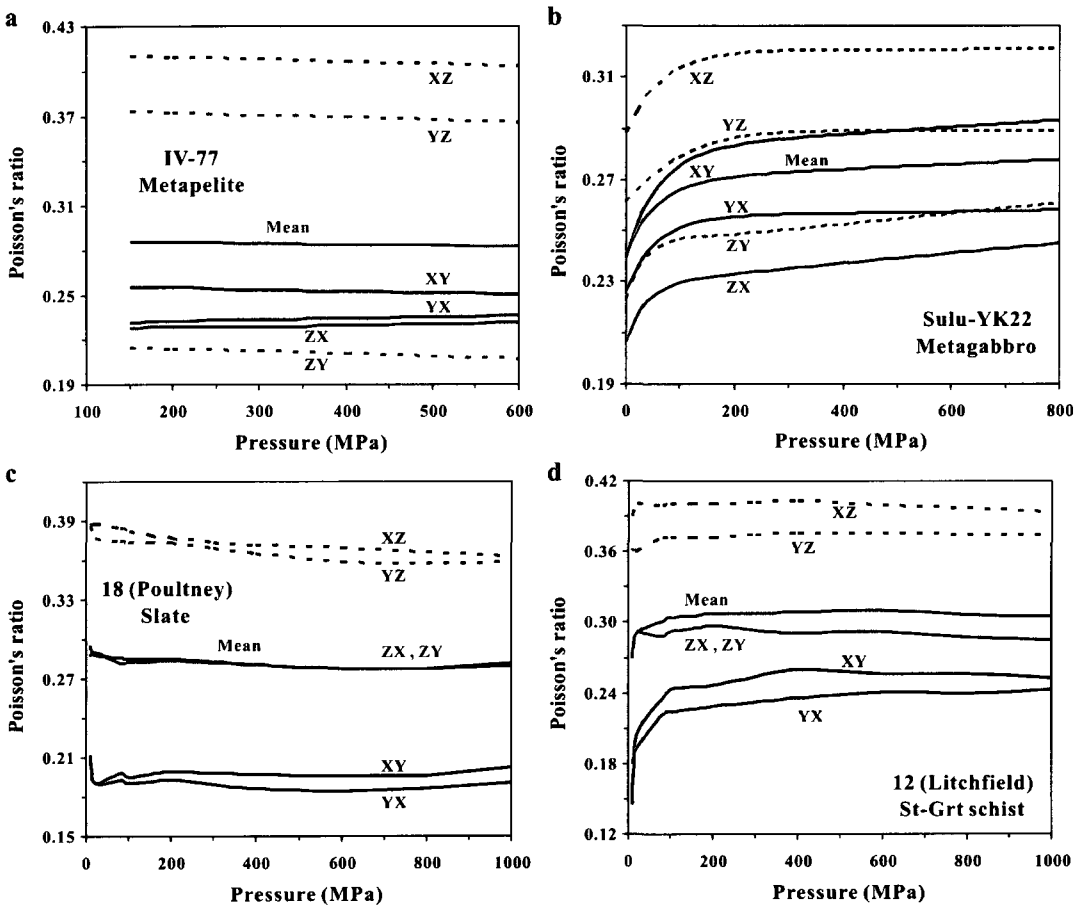

Figure 1.7 Apparent Poisson's ratios (υ_{XY}, υ_{XZ}, υ_{YX}, υ_{YZ}, υ_{ZX}, υ_{ZY}) and average Poisson's ratio (υ_0) as a function of confining pressure for metapelite (a), metagabbro (b), slate (c) and Staurolite-garnet schist (d).

1.4 Mixture rules

A terrestrial material consists of a matrix made of different minerals and pores that can be filled with various gas and fluids. Each of the constituents has their own physical

properties. The physical properties of the terrestrial material depend in some way on the relative abundance of each constituent and of their related physical properties. The prediction of the bulk physical property of the material is usually done using mixing rules.

Seismic velocities, density, magnetic susceptibility, electrical conductivity, thermal conductivity and heat generation are important physical properties of rocks in the Earth's crust and mantle. For example, gravity survey is to measure rock densities, magnetic survey is concerned with the magnetic susceptibility, seismic experiments deal with P- or S-wave velocities and anisotropy, and electrical survey is related to the electrical conductivity. Physical properties of rocks or mineral assemblages are generally calculated from laboratory measured physical properties of constituent minerals and appropriate rules of mixture. A rule of mixture or a mixing law describes the variation of a given physical property of polymineralic composite as a function of their end-member properties and volume fractions. The success of such a commonly practiced scientific approach depends not only on an accurate knowledge of the physical properties of the proposed minerals but also on the relevance of the rule of mixture used. However, the application of different rules of mixture yields different results. It is thus especially important to understand the physical meaning of each existing rule of mixture.

It is almost impossible to describe all existent mixing laws from the literature. In the following, I will list only some rules of mixture which are commonly used for statistically isotropic composite materials or rocks. For these anisotropic or heterogeneous materials, microstructure has significant effects on the bulk or effective property of the composite, and thus the mixture rule should take into consideration the effects of detailed microstructure (geometric shape, spatial arrangement, connectivity and continuity of each phase), becomes extremely complicated and accordingly will have no analytic solution (see Ji and Xia, 2002 for a review). In the latter case, tedious

numerical models (i.e., finite element, boundary element, or finite difference modeling) are needed and are beyond the scope of the present thesis.

1.4.1 Voigt average

Voigt average, which was proposed by Voigt (1928), is actually an arithmetic mean, that is,

$$M_c = \sum_{i=1}^{N} (f_i M_i) \qquad (1.33)$$

where M is a given physical property (e.g., Young's modulus, shear modulus, electrical conductivity, thermal conductivity), the subscript c stands for the composite which consists of N phases in total, f_i is the volume fraction of the ith phase.

$$\sum_{i=1}^{N} f_i = 1 \qquad (1.34)$$

Eq. (1.33) yields a linear variation of M_c with any volume fraction f_i. A dry porous rock can be considered to consist of two phases: a rock matrix and a phase of pores being filled with air. If this porous rock is partially saturated with water, then it is a 3-phase composite: rock matrix, pores filled with air, and water.

The density of a composite rock consisting of N components always obeys the mixing law given by Eq. (1.33):

$$\rho_c = \sum_{i=1}^{N} (f_i \rho_i) \qquad (1.35)$$

Using Eq. (1.35), the density of a porous rock partially saturated with water can be easily calculated.

The heat generation (A_c) of a rock containing radioactive elements (e.g., U, Th and K) with concentrations c_i also obeys the Voigt average:

$$A_c = \sum_{i=1}^{N} (c_i A_i) \tag{1.36}$$

where A_i is the heat generated by the ith radioactive element.

The bulk magnetic susceptibility (k) of an isotropic rock comprising minerals having different magnetic susceptibilities (k_i) and volume fractions (f_i) equally obeys the Voigt average:

$$k_c = \sum_{i=1}^{N} (f_i k_i) \tag{1.37}$$

(Kobranova, 1989). Because magnetite is the most common and the most magnetic mineral of the iron-titanium oxide series, there is a correction between the rock susceptibility (k_c) and magnetite volume fraction ($f_{magnetite}$):

$$k_c = a f_{magnetite}^{\,b} \tag{1.38}$$

where a and b are two empirical values. In Minnesota basalt, a=0.0475 SI unit, and b=1.08 SI unit. In Minnesota granite, a=0.0244 SI unit, and b=0.47 SI unit. In Minnesota diabase, a=0.0336 SI unit, and b=1.14 SI unit (Schon, 1996).

For the elasticity (Young's modulus, shear modulus, and bulk modulus), Eq. (1.33)

suggests that the overall stress in the composite is equal to the arithmetic weight average of the stresses in the constituent phases and the weight factors are the volume fractions of the phases, but the strain is uniform in the composite (Fig. 1.8a-b). Eq. (1.33) yields an upper bound for the bulk property of the composite.

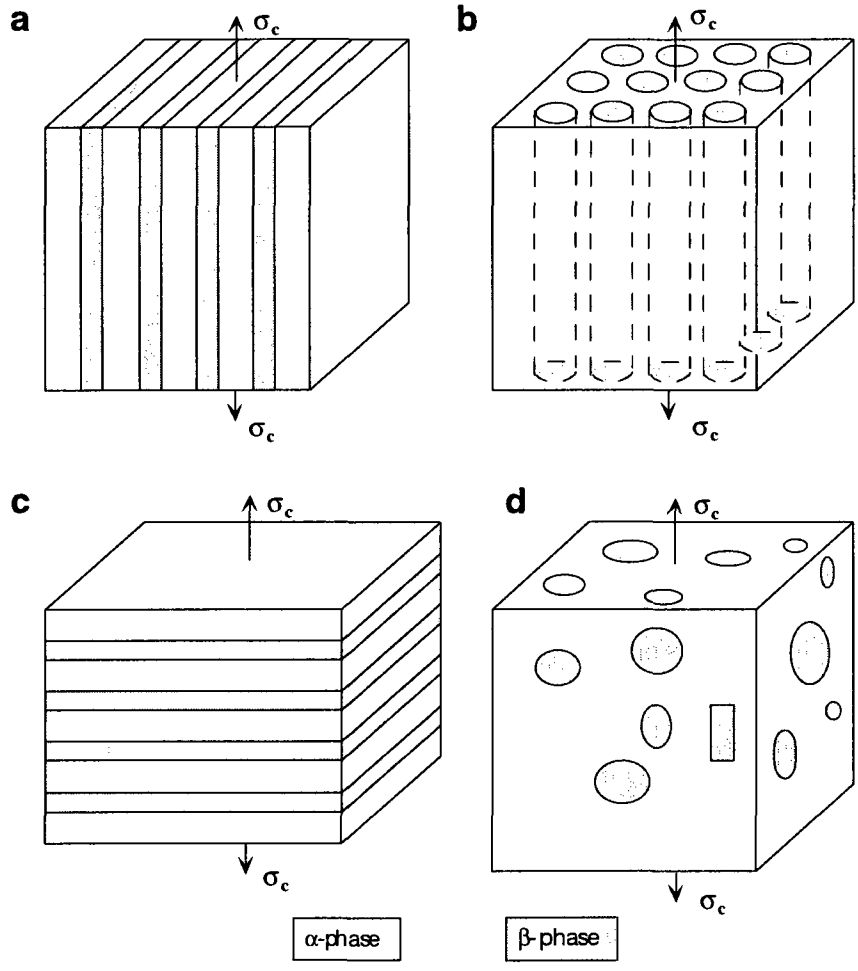

Figure 1.8 Microstructures of two-phase (α and β) composites. (a) and (b) The stress (σ_c) is applied in such a direction that the phases experience the same strains but different stresses. This is the arrangement that utilizes the strong phase to the best advantage. (c) The stress (σ_c) is applied in such a direction that the stresses borne by both phases are the same as σ_c, but they experience different strains. (d) A particulate composite in which both stresses and strains are different in both the phases.

1.4.2 Reuss average

Reuss average, which was proposed by Reuss (1929), is actually a harmonic mean.

$$\frac{1}{M_c} = \sum_{i=1}^{N} \frac{f_i}{M_i} \tag{1.39}$$

The Voigt and Reuss averages form, respectively, the upper and lower bounds for effective properties and bracket the permissible range in which the effective properties must lie. Eq. (1.39) yields a non-linear variation of M_c with any volume fraction f_i.

Fourmaintrax's (1976) equation for calculating the seismic velocities of composite rocks is actually a Reuss average. He suggested:

$$\frac{1}{V_c} = \sum_{i=1}^{N} \frac{f_i}{V_i} \tag{1.40}$$

where V is a given seismic velocity.

For a porous rock with its pores partially saturated with liquid (water or petroleum), Eq. (1.40) gives:

$$\frac{1}{V_c} = \frac{f_g}{V_g} + \frac{f_l}{V_l} + \frac{1 - f_g - f_l}{V_s} \tag{1.41}$$

where V is a given seismic velocity, the subscripts g, l, s, and c represent gas (or air), liquid (water or oil), the solid medium and the composite, respectively. In the literature, Eq. (1.41) is the celebrated so-called Wyllie's time-average equation (Wyllie et al., 1956).

For the elasticity of materials and rocks, Eq. (1.39) means that the overall strain is equal to the arithmetic weight average of the strains in the phases and the stress is uniform (Fig. 1.8c).

1.4.3 Voigt-Reuss-Hill or VRH average

Voigt-Reuss-Hill or VRH average (Hill, 1963). The upper and lower bounds defined by Voigt and Reuss averages can be widely separated if the constituent phases have a significant difference in property. For example, the electrical conductivities (σ) in silicate minerals (s) and brine water (w) are considerably different: $\sigma_s/\sigma_w \approx 10^{-10}$. The range between the Voigt and Reuss averages is then too large to be meaningful for estimating the effective conductivity of their composites.

In order to overcome the above difficulty, Hill (1963) proposed to an arithmetic mean of the Voigt and Reuss bounds, that is,

$$M_{VRH} = \frac{1}{2}\left(M_{Voigt} + M_{Reuss}\right) \qquad (1.42)$$

The VRH average have been widely used as an approximation of the overall elastic or seismic properties of polymineralic aggregates in the interpretation of worldwide seismic data (e.g., Preliminary reference Earth model, Dziewonski and Anderson, 1981; Zhao and Anderson, 1994). However, the VRH average is not of physical significance. As pointed out by Matthies and Humbert (1993), Mainprice and Humbert (1994) and Ji and Xia (2002), the VRH average does not give compatible elastic stiffness ($\mathbf{C}_{ij}$) and compliance tensors ($\mathbf{S}_{ij}$). Moreover, the VRH average failed in the test by comparing with the experimental data in both the regimes of strong-phase-supported structure and weak-phase-supported structure (Ji et al., 2004).

1.4.4 Geometrical mean

$$M_c = \prod_{i=1}^{N} M_i^{f_i} \qquad (1.43)$$

The geometrical mean was found to yield a result very close to the much more complicated iterative self-consistent micromechanical model in the predication of the bulk elastic properties for the composite materials (Matthies and Humbert, 1993; Mainprice and Humbert, 1994). As stated by Ji (2004) in a JGR paper, however, the geometrical mean becomes physically meaningless when one of the constituent phases has a null property (for example, pores have zero shear strength). In this case, the overall property of the composite materials or rocks given by the geometrical mean will always vanish for any finite volume fraction of the constituent that has a null property.

1.4.5 Generalized mixture rule (GMR)

Ji et al. (2004) and Ji (2004) put the Voigt average, Reuss mean and Geometrical mean into a unified model called the generalized means:

$$M_c^{\ J} = \sum_{i=1}^{N} \left(V_i M_i^{\ J} \right) \qquad (1.44)$$

where J is a scaling, fractal parameter, which is mainly controlled by the shape and distribution (continuity and connectivity) of the phases. The case J=1 yields the arithmetic mean or Voigt average. The case J=-1 yields the Reuss average. Variations of the composite properties with the volume fraction are nonlinear for all J values other than J=1. The GMR yields the geometrical mean as $J \rightarrow 0$.

The J value for a given type of microstructure can be calibrated by fitting the experimentally measured M_c data with the predicted curves. Ji et al. (2004), Ji et al. (2006) found that the GMR with J = 0.5 and J = -0.5 provides good agreement with the experimental data of Young's modulus for the two-phase composites (including porous materials) in which inclusions are shaped like spheres isolated in a continuous, stronger (strong-phase supported structure) and weaker (weak-phase supported structure) host mediums, respectively. For most composite materials in which the inclusions are of somewhat arbitrary geometry, however, the GMR with J = -0.25 and J = 0.25 does well at predicting the measured values of Young's modulus for those with weak-phase supported structure (the volume fraction of strong phase $V_s \leq 0.5$) and strong-phase supported structure ($V_s \geq 0.7$), respectively. In the intermediate range ($0.5 \leq V_s \leq 0.7$), J was found to vary progressively from -0.25 to 0.25 due to the transition in microstructure.

In a paper entitled "Electromagnetic propagation logging: advances in technique and interpretation" published in Soc. Petrol. Eng., AIME Paper 9267, Wharton et al. (1980) proposed a mixing law for the complex dielectric constant (K) of water-saturated sandstone:

$$K^{1/2} = \sum_{i=1}^{N} \left(f_i K_i^{1/2} \right) \tag{1.45}$$

Eq. (1.45) is called the complex refractive index method (CRIM, Freedman and Vogiatzis, 1979; Knight and Endres, 1990). The derivation of Eq. (1.45) used the concept of time-average equation. It was assumed that the layers are aligned perpendicular to the electrical conduction direction, and the thickness of each layer (L_i) are much greater than a wavelength so that total transit time t_c for a pulse moving normal to the layers is the sum of the transit time t_i in each layer:

$$t = \sum_{i=1}^{N} t_i = \sum_{i=1}^{N} \frac{L_i \sqrt{K_i}}{c} \qquad (1.46)$$

(Sen et al., 1981), where c is the velocity of light in free space.

Eq. (1.45) has the same form as Eq. (1.44) with $J = 0.5$. This indicates that the GMR can be equally applied to predict the electrical property of composite rocks.

If sandstone is composed of dry rock (r), water (w) and hydrocarbon (h), Eq. (1.45) can be rewritten as:

$$K^{0.5} = f_r K_r^{0.5} + f_w K_w^{0.5} + f_h K_h^{0.5} = (1-\phi) K_r^{0.5} + (\phi - f_h) K_w^{0.5} + f_h K_h^{0.5} \qquad (1.47)$$

where ϕ is the porosity, and $\phi = f_h + f_w$. Eq. (1.47) is exactly the same as that suggested in Knight and Endres (1990).

Sen et al. (1981) proposed the following equation for the effective dielectric constant of a composite:

$$\frac{K_r - K_c}{K_r - K_w}\left(\frac{K_w}{K_c}\right) = \phi \qquad (1.48)$$

The electrical conductivity (σ , Siemens/m) of a material or rock is defined as $\sigma = 1/\rho$, where ρ is the electrical resistivity ($\Omega \cdot m$). Geomaterials exhibit a wide range of resistivity values from 1 $\Omega \cdot m$ in clay or contaminated soil to more than 10^4 $\Omega \cdot m$ in rocks such as limestone and granite (Reynolds, 1997). Quartz, feldspar, mica, amphibole and pyroxene show an electric resistivity higher than $10^8 \Omega \cdot m$. The effective or bulk electrical conductivity (σ_c) of a wet rock which consists of dry rock with

conductivity σ_s and a brine water with conductivity σ_w is controlled mainly by the conductivity of brine water because $\sigma_s/\sigma_w \approx 10^{-10}$,

$$\sigma_c = \frac{\sigma_w}{F} \tag{1.49}$$

where $F = \rho_s/\rho_w$ is a parameter called the formation factor (Archie, 1942; Rey et al., 2006). When the porosity $\phi \to 1$, $F \to 1$ and then $\sigma_c \to \sigma_w$; When the porosity $\phi \to 0$, $F \to \sigma_w/\sigma_s$ and then $\sigma_c \to \sigma_s$. After having performed DC electrical measurements on brine-saturated sand formations, Archie (1942) established an empirical relation between F and ϕ:

$$F = \frac{\rho_s}{\rho_w} = \phi^{-m} \tag{1.50}$$

Thus,

$$\sigma_c = \sigma_w \phi^m \tag{1.51}$$

where m is a coefficient that depends on not only lithology but also microstructure of the rock (see Table 1.2). Eq. (1.51) is the famous Archie's law. The exponent m increases as the resistive particles become less spherical. According Jackson et al. (1978), m varies from about 1.2 for spheres to 1.9 for platy shell fragments. For most of sedimentary rocks, m ranges from 1.5 to 2.5.

As shown by Eq. (1.51), $\sigma_c = 0$ if $\phi = 0$, and $\sigma_c = \sigma_w$ when $\phi = 1$, σ_c increases progressively with increasing ϕ. The nature of the Archie's law indicates the absence of a percolation threshold. In other words, the fluid phase in sediments and sedimentary

rocks remains essentially interconnected whatever the porosity is. Apparently this is difficult to understand. Theoretically, the microstructural evolution of a material with increasing porosity is a 3D connectivity problem. According to the percolation theory, there should exist two critical porosity levels. When the porosity reaches the first critical value (ϕ_{c1}), a microstructural transition occurs from fully isolated and closed pores with nearly spherical or ellipsoidal shapes to open and interconnected with complex shapes. Finally, the effective mechanical strength vanishes when the porosity reaches the second critical value (ϕ_{c2}). For powder materials, the ϕ_{c2} value seems to be the apparent porosity of the powder before densification by sintering or hot pressing. Therefore, theoretically three regimes can be identified: (1) At low porosity levels ($\phi<\phi_{c1}$), pores are fully isolated and closed with nearly spherical or ellipsoidal shapes; (2) At intermediate porosity levels ($\phi_{c1}\leq\phi<\phi_{c2}$), interconnected pores with complex shapes are present; (3) The stress-supporting solid framework fails when $\phi\geq\phi_{c2}$. The absence of a percolation threshold as indicated by the Archie's law implies that microfractures and cracks filled brine water should play a much more important role than the pure pores in the electrical conduction within natural rocks.

It is noted that the Archie's law Eq. (1.51) can be directly derived from the GMR. For a two-phase or diphasic composite consisting of resistive phase (s) and conductive phase (w), Eq. (1.44) can be simplified:

$$\sigma_c^{\ J} = (1-\phi)\sigma_s^{\ J} + \phi\sigma_w^{\ J} \tag{1.52}$$

where σ is the electrical conductivity, and ϕ is the porosity. Eq. (1.52) can be rewritten as:

$$\left(\frac{\sigma_c}{\sigma_w}\right)^J = (1-\phi)\left(\frac{\sigma_s}{\sigma_w}\right)^J + \phi \tag{1.53}$$

As $\sigma_s/\sigma_w \approx 10^{-10}$, then

$$(1-\phi)\left(\frac{\sigma_s}{\sigma_w}\right)^J \to 0 \qquad (1.54)$$

Thus, Eq. (1.53) can be approximated by:

$$\left(\frac{\sigma_c}{\sigma_w}\right)^J = \phi \qquad (1.55)$$

or

$$\sigma_c = \sigma_w \phi^{1/J} \qquad (1.56)$$

Comparing Eq. (1.56) with Eq. (1.51), we obtain $m=1/J$. $m=2$ corresponds to $J=0.5$. J should depend on the geometrical shape, spatial arrangement, orientation and size distribution of pores, and in turn on the rocks and their formation processes (e.g., petrogenesis, brittle fracturing mechanisms, solution and precipitation). The exponent J or $1/m$ should depend on size distribution rather than absolute size of the resistive particles (Ji, 2004).

Besides the Archie's law, other mixing laws are also available in the literature. For example,

$$\sigma_c = \sigma_w \frac{2\phi}{3-\phi} \qquad (1.57)$$

(Sen et al., 1981).

Table 1.2 The *m* value of the Archie empirical equation.

Materials	***m* value**	**Reference**
Unconsolidated sands	m=1.3	Archie, 1942
Spherical glass beads (0.10<φ<0.25)	m=1.3	Wyllie and Gregory, 1953
Sandstone	m=2.0	Ruffet et al., 1991
Most sedimentary rocks	1.5≤m≤2.5	Ruffet et al., 1991
Sphere-shaped resistive particles	m=1.2	Jackson et al., 1978
Platy shell fragments	m=1.85	Jackson et al., 1978
Sphere-shaped resistive particles	m=1.5	Sen et al., 1981
Sphere-shaped resistive particles	m=1.5	Mendelson and Cohen, 1982
Cylindrical particles with their long axes normal to electrical field	m=2.0	Sen et al., 1981

1.4.6 Hashin-Shtrikman bounds

Hashin and Shtrikman (1963) initially derived two bounds on the elastic properties of composites by employing the variational principle that considers the change in strain energy in a loaded homogeneous body due to the insertion of inhomogeneities. In an arbitrary reference cube in the composite that is large compared with the size of the inhomogeneities, yet small compared with the whole body, the volume average of a quantity such as displacement, strain, stress or phase volume fraction is the same for the whole body and the reference cube. The lower bound is obtained from the minimum complementary energy theorem and the upper bound is obtained from the minimum potential energy theorem. The Hashin and Shtrikman bounds are given by the following equations:

$$K_c^U = K_s + \frac{f_w}{\frac{1}{K_w - K_s} + \frac{3(1-f_w)}{3K_s + 4G_s}} \tag{1.58}$$

$$K_c^L = K_w + \frac{1 - f_w}{\frac{1}{K_s - K_w} + \frac{3f_w}{3K_w + 4G_w}} \tag{1.59}$$

$$G_c^U = G_s + \frac{f_w}{\frac{1}{G_w - G_s} + \frac{6(K_s + 2G_s)(1 - f_w)}{5G_s(3K_s + 4G_s)}} \tag{1.60}$$

$$G_c^L = G_w + \frac{1 - f_w}{\frac{1}{G_s - G_w} + \frac{6(K_w + 2G_w)f_w}{5G_w(3K_w + 4G_w)}} \tag{1.61}$$

where K and G are the bulk modulus and shear modulus, respectively. The superscripts U and L denote the upper and lower bounds, respectively. The subscripts s and w represent the strong and weak phases, respectively, and f is the volume fraction.

Because the Hashin-Shtrikman bounds are significantly narrower than the Voigt and Reuss bounds, they have been widely used for calculating the overall elastic moduli and seismic velocities of polyphase aggregates in terms of phase moduli and volume fractions (e.g., Watt et al., 1976; Duffy and Anderson, 1989).

The Hashin-Shtrikman bounds can be extended to estimate the upper and lower bounds of thermal conductivity (k) in dense rocks consisting of N kinds of minerals, and each mineral has a volume fraction f_i, where $1 \le i \le N$, and $k_1 \le k_2 \le ..... \le k_N$,

$$k_{\min} = k_1 + \frac{3k_1 A_1}{3k_1 - A_1} \tag{1.62}$$

$$k_{\max} = k_N + \frac{3k_N A_N}{3k_N - A_N} \tag{1.63}$$

where,

$$A_1 = \sum_{i=2}^{N} \frac{f_i}{(k_i - k_1)^{-1} + (3k_1)^{-1}} \qquad (1.64)$$

$$A_N = \sum_{i=1}^{N-1} \frac{f_i}{(k_i - k_N)^{-1} + (3k_N)^{-1}} \qquad (1.65)$$

(Guéguen and Palciauskas, 1992).

As the thermal conductivity k does not vary much from mineral to mineral, the Hashin-Shtrikman upper and lower bounds yield a rather narrow range for the effective thermal conductivity of the polymineralic rock. The Hashin-Shtrikman upper and lower bounds can also be applied to the calculation of the effective electrical conductivity of dry rocks. For wet rocks, however, the calculated bounds are far separated because the conductivities are considerably different between the resistive dry rock and the conductive brine water.

Partially molten rocks have received extensive experimental and theoretical studies during last 2 decades (Karato, 2003). The importance of these studies is obvious because the low-velocity zone immediately beneath the lithosphere is interpreted as partially molten zone. Moreover, partial melting is an important geological process for the generation of magmas (i.e., formation of the oceanic and continental crusts) and the compositional differentiation within the Earth. However, so far there is no single mixing rule that can predict precisely the rheological properties of partially molten rocks. There are so many factors governing these properties, for example, (1) melt fraction; (2) distribution of melt; (3) melt viscosity (depending in turn on chemical composition, temperature, pressure, strain rate, and H_2O content); (4) dihedral angle (depending in

turn on composition, surface energy, viscosity contrast, H_2O content); (5) strain history (pure shear, simple shear); and (6) segregation and redistribution of melt.

In summary, I have given some brief description about commonly used, simple mixing laws for estimating the various physical properties of isotropic materials and rocks. Using the appropriate mixture laws presented above, the physical properties [e.g., elastic moduli (in turn seismic velocities), density, magnetic susceptibility, electrical resistivity, dielectric constant] can be easily calculated for a material consisting of several phases or a rock matrix and pores partially saturated with water (a 3-phase composite). More specific mixing models for physical properties of rocks can be found from a comprehensive review by Schon (1996).

1.5 Seismic anisotropy and shear-wave splitting

For compressional (P-) waves, the direction of wave propagation is parallel to that of particle displacement (oscillation). For shear (S-) waves, these two directions are perpendicular to each other. Thus, shear wave velocity can be different for different oscillation directions. The velocity of either P- or S-wave can be dependent on the orientation of wave propagation, which is referred to as azimuthal anisotropy. For S-waves, because particle motion in a plane perpendicular to the propagation direction involves a different distortion of materials dependent upon the direction of particle motion, S-wave velocity can depend on the direction of particle motion—that is, polarization. This is referred to as polarization anisotropy. When a seismic wave passing through an anisotropy layer is recorded at one station, we would find two different S-wave arrivals with different polarizations, rather than one S-wave. This is called shear wave splitting. A record of shear wave splitting contains two piece of information: the travel time difference and the direction of the polarization of the (faster) S-wave. They reflect the strength of anisotropy and geometry of anisotropic structure, respectively.

For each propagation direction the P-wave velocity (V_p), the two shear wave velocities (V_{s1} and V_{s2}, $V_{s1}>V_{s2}$), and the birefringence or shear-wave splitting (V_{s1}- V_{s2}) are usually measured from three mutual perpendicular directions in each sample. For the rocks in which both foliation and lineation are developed, these directions are parallel to the X, Y and Z axes of the tectonic framework (X-parallel to the stretching lineation, Y-perpendicular to the lineation and parallel to the foliation, and Z-normal to the foliation) or the strain ellipsoid (Fig.1.9). If the sample is foliated but not lineated (deformed by flattening strain), both X-and Y-directions are arbitrarily aligned in the foliation plane. For samples that displayed neither foliation nor lineation (e.g., undeformed isotropic igneous rocks), all three directions are aligned in an arbitrary direction or only one direction is taken because such rocks are generally isotropic.

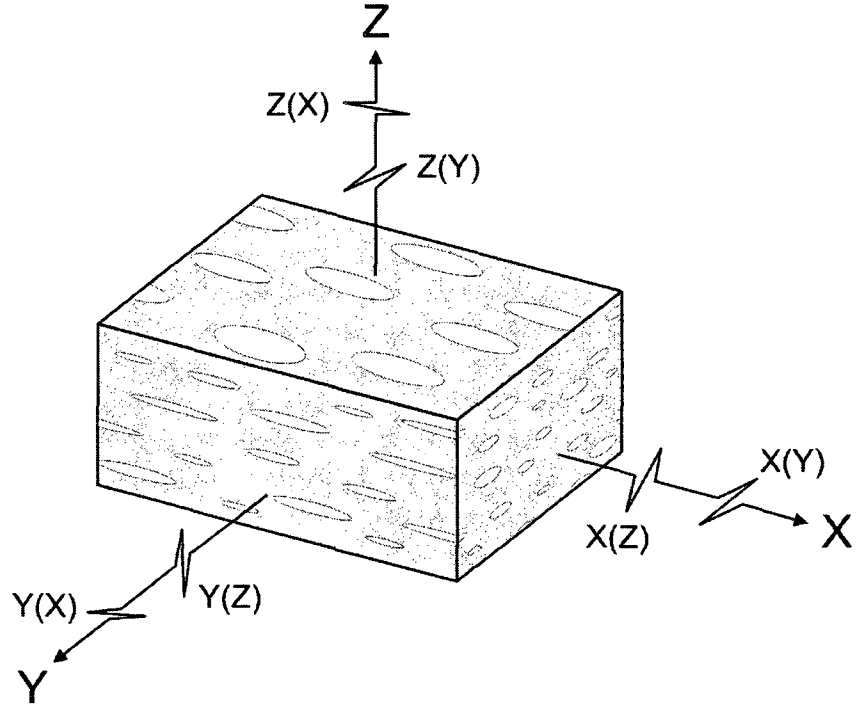

Figure 1.9 Relative orientations between rock structural framework (X-Y-Z) and seismic wave propagation and vibration directions. X is parallel to stretching lineation, Y is normal to lineation in the foliation plane, and Z is normal to foliation plane.

The V_p anisotropy, is defined as:

$$A\,(V_p) = 100\%\ (V_{max}-V_{min})\ /V_{mean} \qquad (1.66)$$

$$V_{mean} = (V_x+V_y+V_z)/3 \qquad (1.67)$$

Thus, A (V_p) depends only on the maximum and minimum velocity values and does not carry any information about their orientations. The V_s anisotropy for a given propagation direction, is defined as:

$$A\,(V_s) = 100\%\ (V_{s1}-V_{s2})/V_{s,\,mean} \qquad (1.68)$$

$$V_{s,\,mean} = (V_{s1}+V_{s2})/2 \qquad (1.69)$$

In order to determine the S-wave properties, six measurements, designated XY, XZ, YX, YZ, ZX and ZY, are generally undertaken for each sample. The first letter signifies the propagation direction; the second indicates the polarization or vibration direction. The mean S-wave velocity and anisotropy can be calculated for each propagation direction. In the Y direction, for example,

$$M_Y = (V_{YX}+V_{YZ})/2 \qquad (1.70)$$

$$A_Y = 100\%\ (V_{YX}-V_{YZ})/\,M_Y \qquad (1.71)$$

For each bulk sample, the mean S-wave velocity and anisotropy are defined by

$$M = (V_{XY}+V_{XZ}+V_{YX}+V_{YZ}+V_{ZX}+V_{ZY})/6 \qquad (1.72)$$

$$A=100\% \ (V_{max}-V_{min})/M \qquad (1.73)$$

Thus, A calculated from Eq. (1.73) depends only on the maximum and minimum S-wave velocity values and does not carry any information about their orientation, while A_X, A_Y, and A_Z are directional parameters.

How is the seismic anisotropy nature in the upper and lower crust? Generally speaking, seismic anisotropy of rocks is caused by lattice preferred orientations (LPO) of rock-forming minerals, small-scale compositional layering, and alignments of microcracks of various dimensions.

The sedimentary rocks constitute the uppermost part of the crust. Most sedimentary rocks developed layered structures which are named bedding. The layered rocks can be described as transversely isotropic media. Within a single layer of massive rocks such as sandstones, the velocities vary insignificantly in dependence on direction. However, the rocks are interlayered with other lithological layers (e.g., sandstone with mudstone or limestone), such composite media exhibit substantial anisotropy with greater velocities parallel to bedding. Anisotropy may range up to 30% and is particularly pronounced for P-wave velocities from about 2.0 to 4.2 km/s (Gebrande, 1982). The layering of sedimentary rocks has long been recognized as a source of seismic anisotropy (e.g., Riznichenko, 1949; Postma, 1955). Seismic velocities in horizontally layered media are independent of the azimuth of propagation. Such a transverse isotropy with a vertical axis of symmetry can be combined with a transverse isotropy characterized by a horizontal axis of symmetry due to parallel vertical cracks, which leads to an orthorhombic symmetry (Leary et al., 1991).

In porous sediments, velocities and their anisotropy depend largely on a degree of saturation of the pore space with fluids (e.g., brine water) and on the pressure of the pore fluid. Water saturation increases the P-wave velocities at small pressures and the effect

becomes more pronounced when the crack porosity of the rock is greater (Nur and Simmons, 1969). The difference between the velocities in dry and water-saturated states decreases with increasing pressure and may be neglected above about 200 MPa which corresponds to a depth of around 7-8 km (Fig. 1.10). In contrast to P-wave velocities, S-wave velocities are barely influenced by the pressure of pore fluids with zero pore pressure. If, however, the pore pressure equals the confining pressure, microcracks and grain boundaries are kept opened and P- as well as S-wave velocities remain much smaller with increasing pressure than the values measured in dry rocks. Thus, the ratio of P- to S-wave velocities (V_P/V_S) is an efficient indicator for pore fluid content.

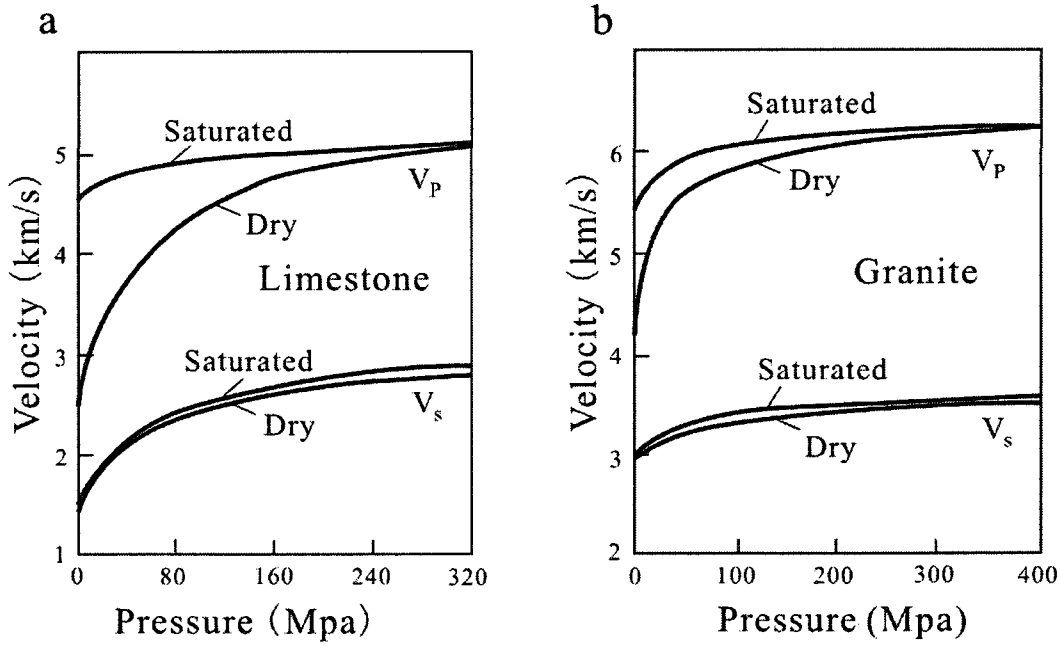

Figure 1.10 Effects of pore fluid content on velocities in limestone and granite (Nur and Simmons, 1969).

In crystalline rocks and sedimentary rocks of the upper crust, the preferred alignment of microcracks presents an important contribution to the observed seismic anisotropy. To the first approximation, we can consider such an anisotropic medium as a transverse isotropy with a symmetry axis normal to the microcrack plane which is perpendicular to the minimum principal stress (σ_3). In general, the microcracks are

vertical in the regime of tectonic extension or strike-slip (Fig. 1.11) and the symmetry axis of the seismic anisotropy is thus horizontal. For a vertical propagation this model predicts fast S waves polarized in a direction perpendicular to the symmetry axis and slow S waves if the polarization direction is parallel to the symmetry axis (Fig. 1.12).

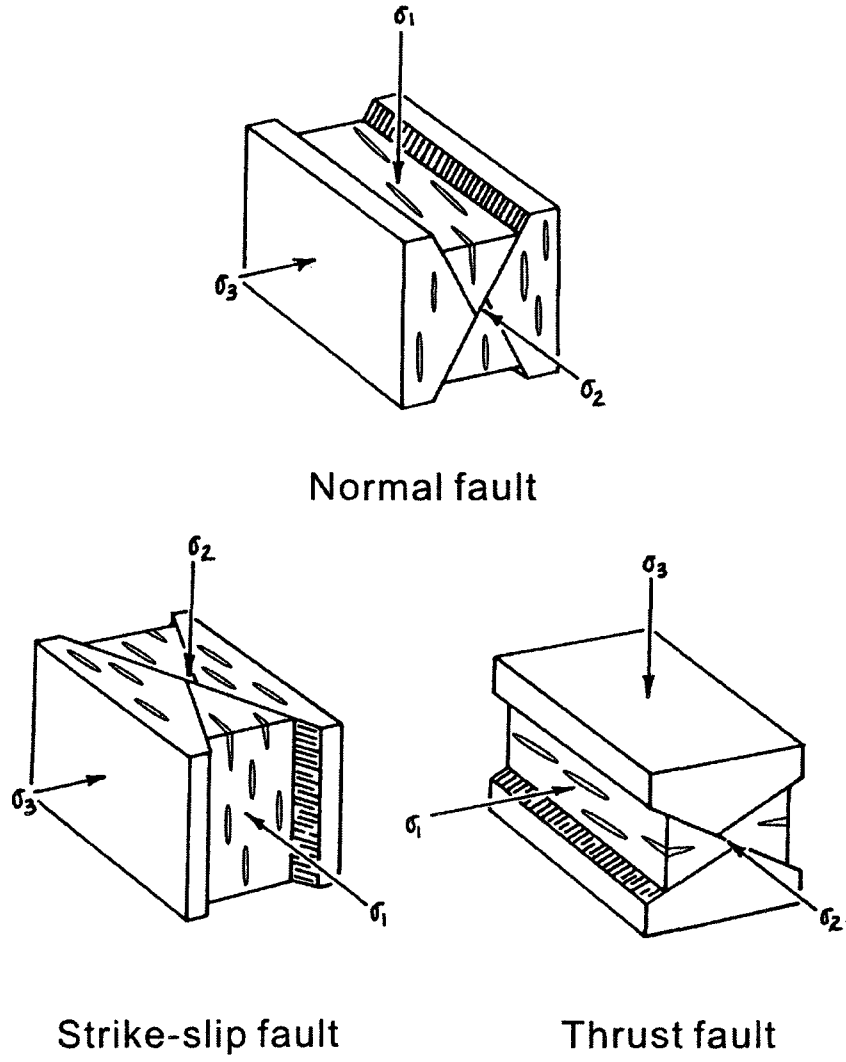

Figure 1.11 Orientations of tensile fractures in three types of faults

The crack-induced anisotropy is limited only to the brittle portion of the crust, say, the uppermost 10 to 15 km depth (Kaneshima and Ando, 1988). This critical depth corresponds to the depth of the brittle-ductile transition and decreases with increasing regional geothermal gradient.

Kaneshima (1990) studied the travel time difference between leading and slower split shear waves of crustal and upper-mantle earthquakes, and suggested that the crustal anisotropy caused by subvertically aligned cracks of fractures is limited to the upper 15 km of the crust with the maximum of fractured anisotropy rock in the uppermost crust (depths of less than 3-5 km).

In the lower crust, which consists of amphibolite-granulite facies metamorphic rocks, seismic anisotropy is caused mainly by mineral LPOs and metamorphic/structural layering (Ji et al., 1993 and Ji and Salisbury, 1993). The lower crust may also include metasedimentary and metavolcanic rocks, layered mafic complexes, gneisses and ultramafic bodies. The lower crustal rocks are often intensively deformed plastically and develop remarked lattice preferred orientations of the rock-forming minerals. The presence of isoclinal folds, boudinage structures and mylonitic shear zones in the deep cross sections attests to the dominance of ductile deformation mechanisms in the lower crust. These structures, coupled with igneous and metamorphic processes, in many cases result in a horizontally layered deep crust from centimeter to kilometer scales (Fountain, 1987). Such a layering in combination with a preferred orientation of minerals in metamorphic rocks produces appreciable seismic anisotropy within the lower continental crust.

In the amphibolite- and granulite-facies rocks, dominant minerals are mica, amphibole, feldspar, clinopyroxene and orthopyroxene. The maximum P-wave anisotropy of mica, amphibole, feldspar, clinopyroxene and orthopyroxene single crystals is, respectively, 44.2%, 23.8%, 27.4%, 25.8%, and 11.3% (Table 1.3 and Fig.1.13). They are very seismically anisotropic. If these minerals form strong lattice preferred orientations (LPOs) in the rocks, then the rocks should be anisotropic too.

In amphibolites where amphibole develops strong LPOs with [001] parallel to the stretching lineation and (100) or {110} parallel to the foliation show a prominent

anisotropy (mostly ~10%) with an orthorhombic symmetry: $V_p(X)>V_p(Y)>V_p(Z)$ (Ji et al., 1993). This is because in amphibole, the maximum V_p is parallel to [001] direction, and the minimum V_p is parallel to [010] directly. In the amphibolite, plagioclase has a negative contribution to the seismic anisotropy formed by amphibole because feldspar usually has its (010) plane parallel to the foliation (Ji and Mainprice, 1988). For feldspar, the V_p has the maximum value in the direction normal to (010). As a result, the contribution of amphibole and feldspar is opposed each other.

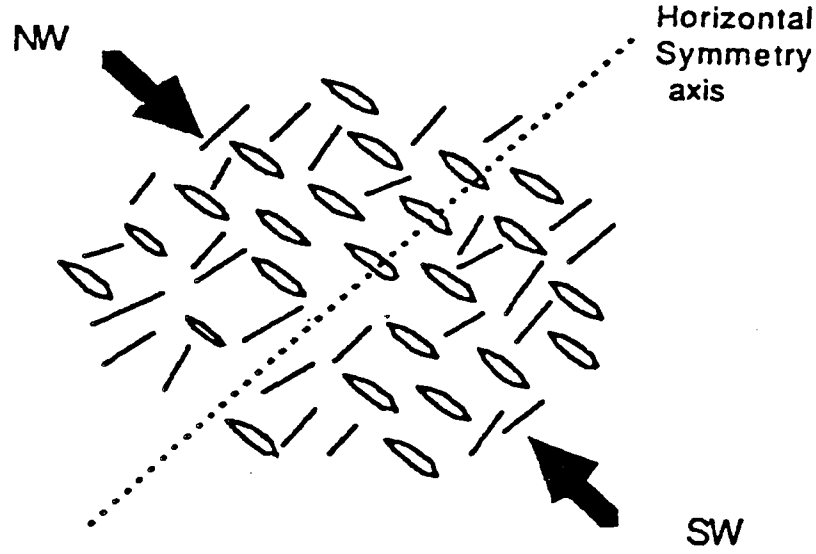

Figure 1.12 Schematic crack model which could explain the shear-wave splitting observed in the Paris Basin, developed by Babuska and Cara (1991). Thick arrows indicate the direction of maximum compression. Pre-existing cracks which are approximately parallel to the direction of maximum compressive horizontal stress may be opened while other cracks are closed. The polarization of fast shear waves propagating vertically is parallel to the direction of preferred orientation of the cracks.

In schists or phyllonites where biotite and/or muscovite develop strong LPOs with (001) parallel to the foliation show a prominent anisotropy (mostly ~8-10%) with a transversely isotropic pattern: $V_p(X)=V_p(Y)>V_p(Z)$ (Ji et al., 1993; Kern and Wenk, 1990).

Table 1.3 Anisotropic seismic properties of common mineral single crystals.

Mineral	Symmetry	V_p (km/s)		V_{s1} (km/s)		V_{s2} (km/s)		V_{s1}-V_{s2}	Anisotropy (%)		
		max	min	max	min	max	min	(km/s)	V_p	V_{s1}	V_{s2}
Albite	Triclinic	7.4	5.2	4.4	3.0	3.5	2.5	1.4	30.9	31.2	27.2
Anorthite	Triclinic	8.6	5.9	5.0	3.6	3.8	2.9	1.2	31.8	27.5	23.2
Plagioclase (An_{53})	Triclinic	7.8	5.7	4.7	3.4	3.6	2.7	1.3	27.4	27.4	24.4
K-feldspar	Triclinic	8.1	5.1	4.8	2.8	3.6	2.3	1.9	37.4	42.6	35.3
Quartz	Trigonal	7.0	5.3	5.1	3.7	4.7	3.3	1.8	24.3	26.8	29.5
Calcite	Trigonal	7.7	5.6	4.7	2.9	3.8	2.5	2.2	27.6	38.0	33.8
Dolomite	Trigonal	8.7	6.3	5.3	3.6	4.3	3.0	2.3	27.9	32.7	29.5
Hornblende	Monoclic	7.9	6.0	4.3	3.4	3.8	3.2	1.1	23.8	22.3	16.2
Muscovite	Monoclic	8.1	4.5	5.0	2.5	3.5	2.4	2.7	44.2	50.7	32.9
Epidote	Monoclic	8.4	6.7	5.0	3.5	4.6	3.4	1.4	19.9	30.7	25.9
Diopside	Monoclic	9.4	7.0	5.0	4.3	4.8	4.0	0.9	25.8	13.7	16.2
Jadeite	Monoclic	9.5	7.9	5.7	4.9	5.6	4.3	1.0	16.8	12.7	23.9
Omphacite	Monoclic	9.4	7.6	5.4	4.8	5.3	4.3	0.8	18.6	12.0	18.3
Enstatite	Orthorhombic	8.4	7.5	5.1	4.9	5.0	4.4	0.5	11.3	4.1	11.4
Olivine	Orthorhombic	10.0	7.7	5.6	4.9	4.9	4.4	1.0	22.9	12.7	9.4
Rutile	Tetragonal	10.6	7.9	6.7	5.4	5.4	3.3	2.1	25.1	19.5	38.5
Spinel	Cubic	10.6	8.9	6.6	5.2	6.6	4.2	2.3	16.3	20.4	35.5
Garnet	Cubic	8.6	8.5	4.8	4.7	4.8	4.7	0.1	0.9	2.1	1.5

In plagioclase-dominated metamorphic rocks as anorthositic mylonites, anisotropic pattern is characterized by $V_p(Z)>V_p(X)>V_p(Y)$ (Ji and Mainprice, 1988; Ji et al., 1993).

Pyroxene-bearing mafic or felsic granulites and deformed tonalite and granites generally display very low anisotropy (Commonly <3-4%) (Ji et al., 1993; Burke and Fountain, 1990; Kern 1990). This is due to a fact that the contribution of plagioclase and clinopyroxene/orthopyroxene cancel one another to produce low anisotropy. Similarly, the contribution of plagioclase and quartz cancel also one another to produce low anisotropy.

Quartz SiO_2

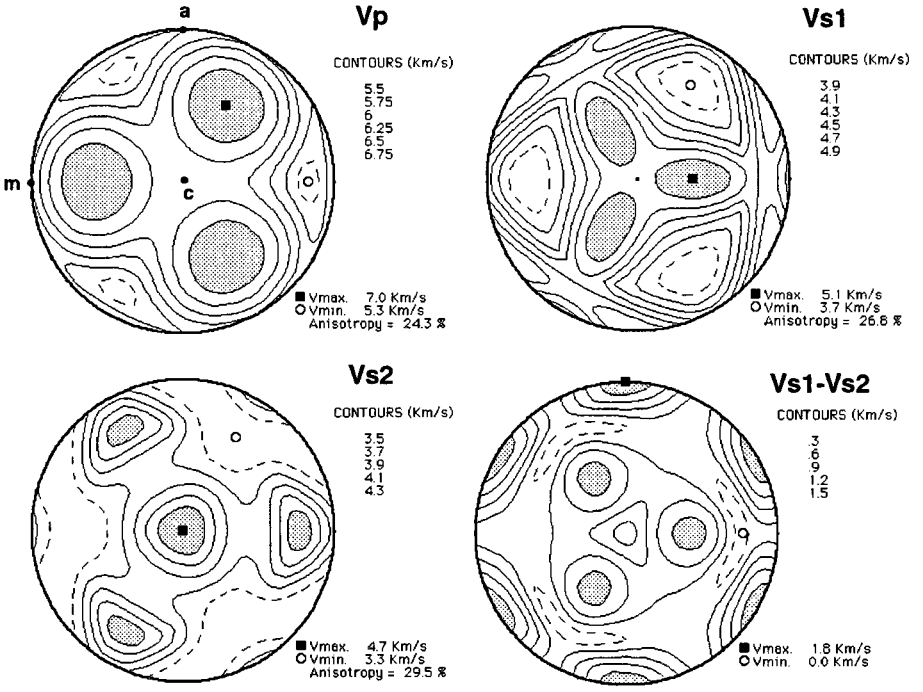

Muscovite $KAl_3Si_3O_{10}(OH)_2$

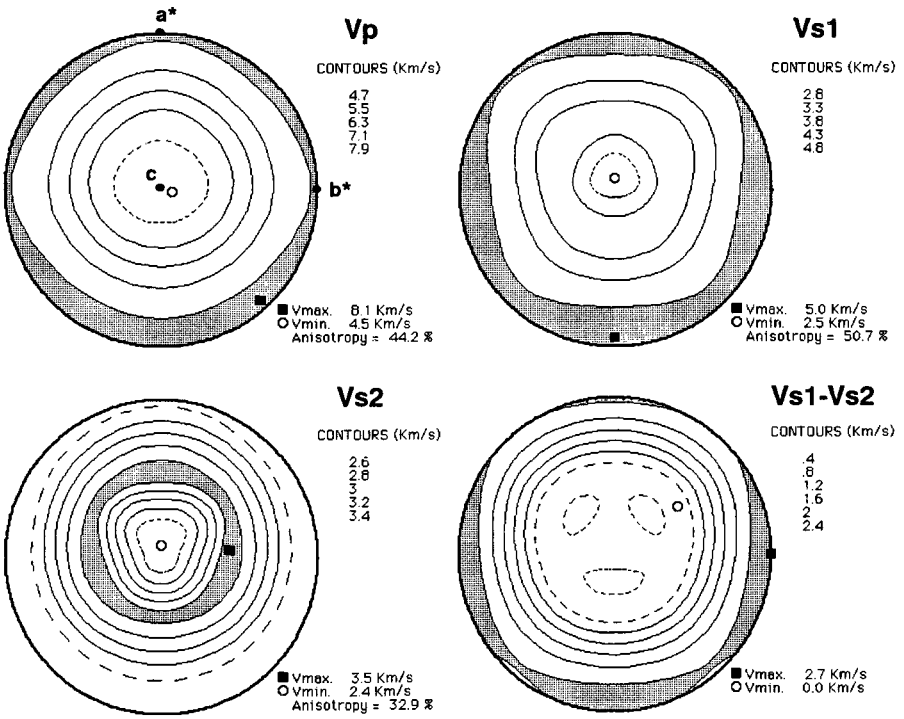

K-feldspar $KAlSi_3O_8$

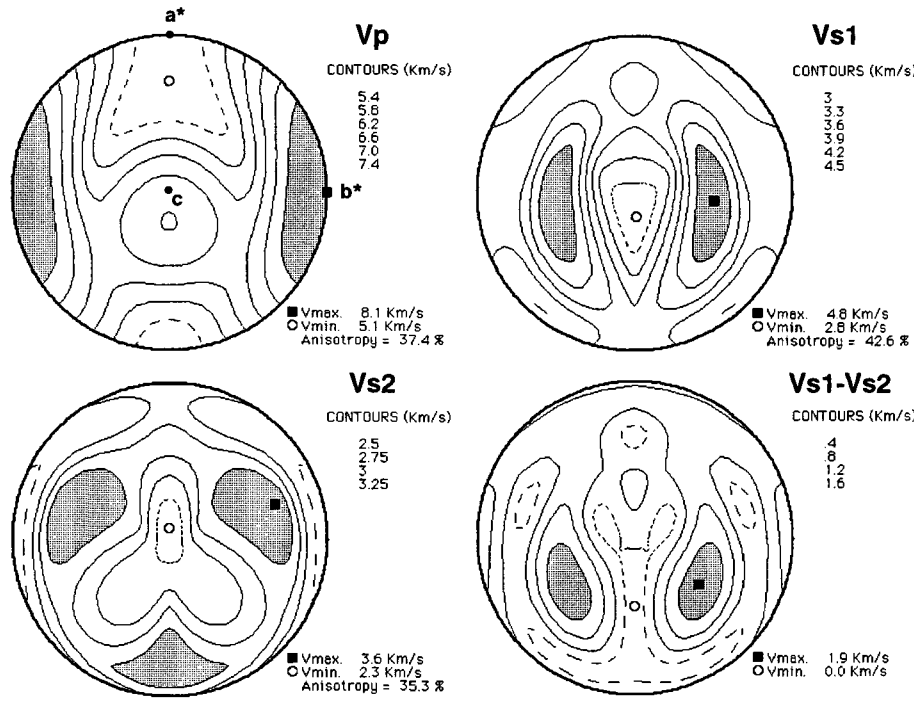

Albite $NaAlSi_3O_8$

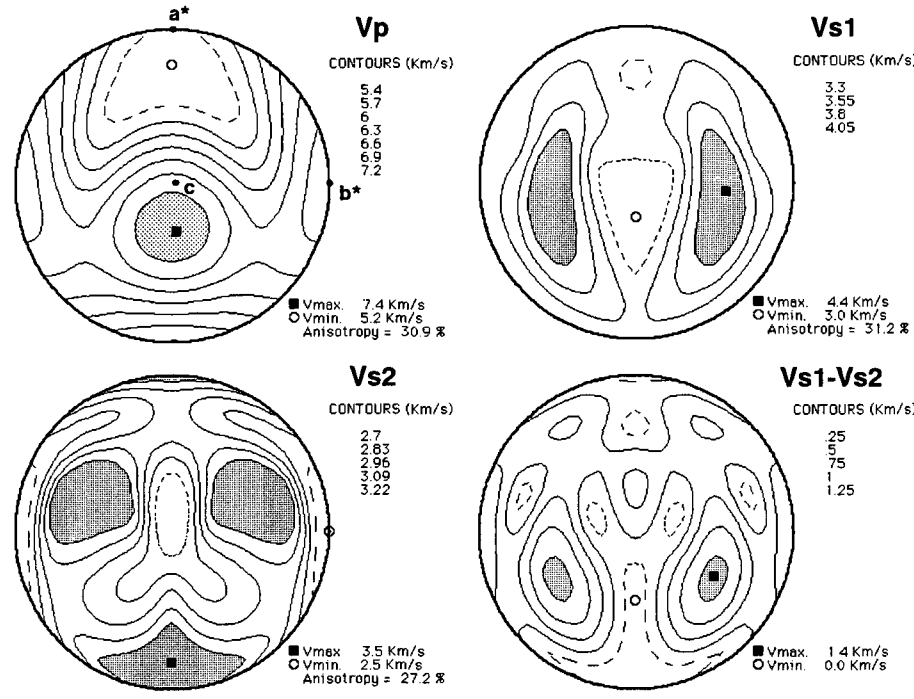

Hornblende $(Ca,Na)_{2-3}(Mg,Fe,Al)_5(Al,Si)_8O_{22}(OH)_2$

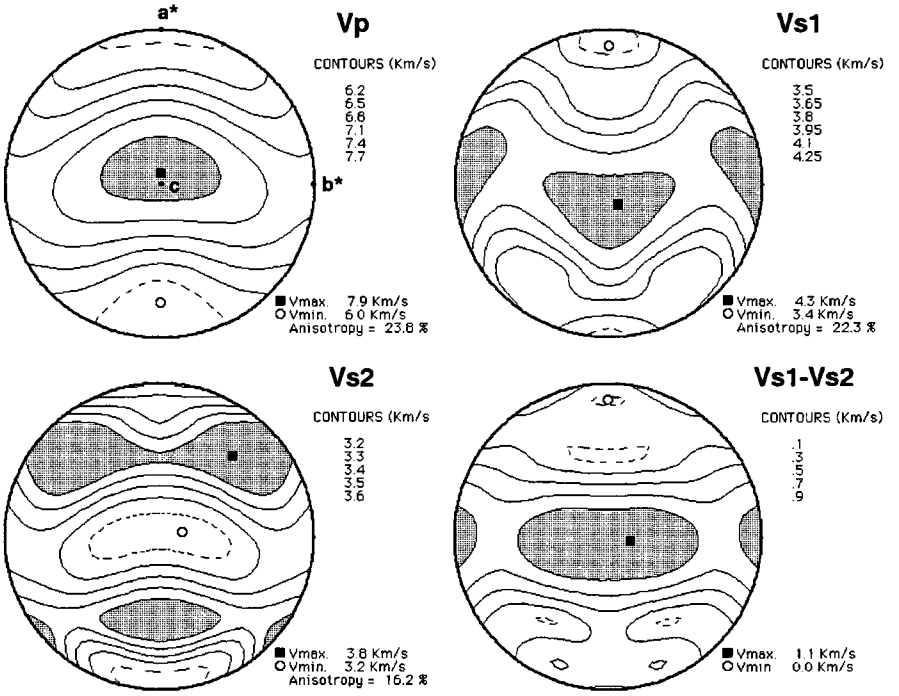

Diopside $CaMgSi_2O_6$

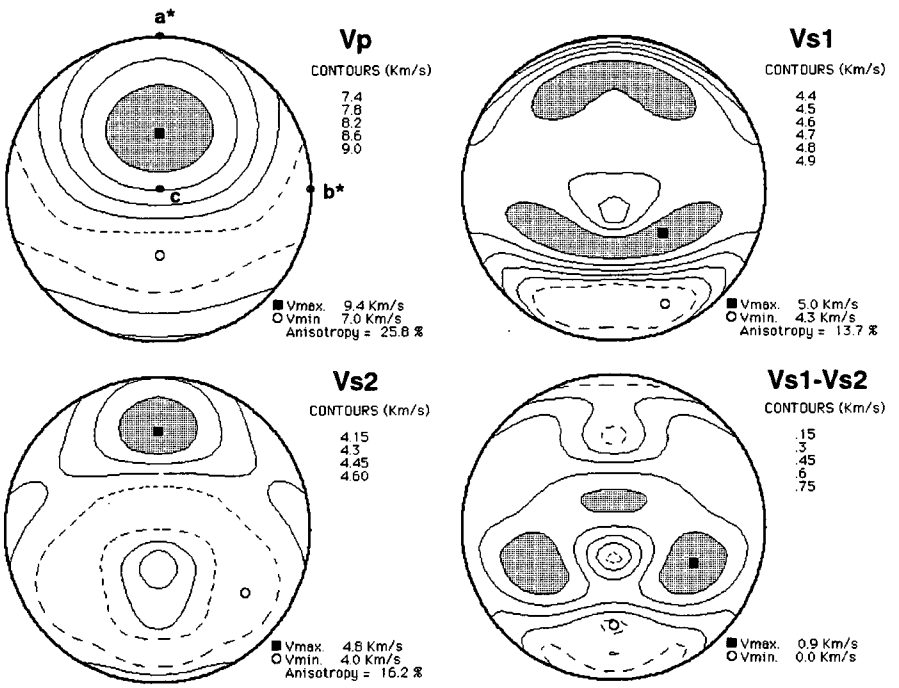

Enstatite ($MgSiO_3$)

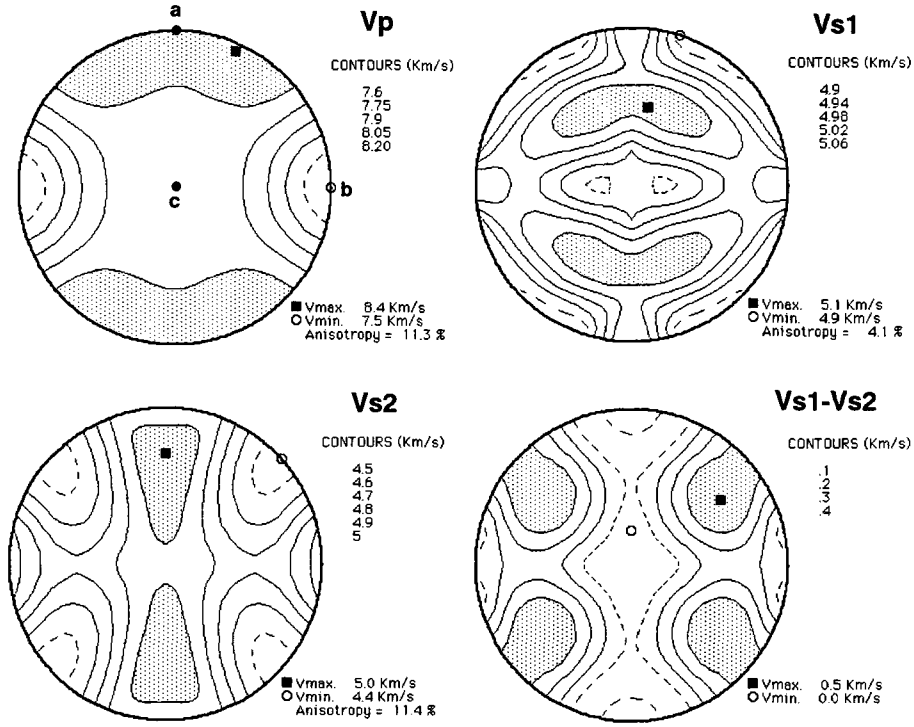

Plagioclase An53

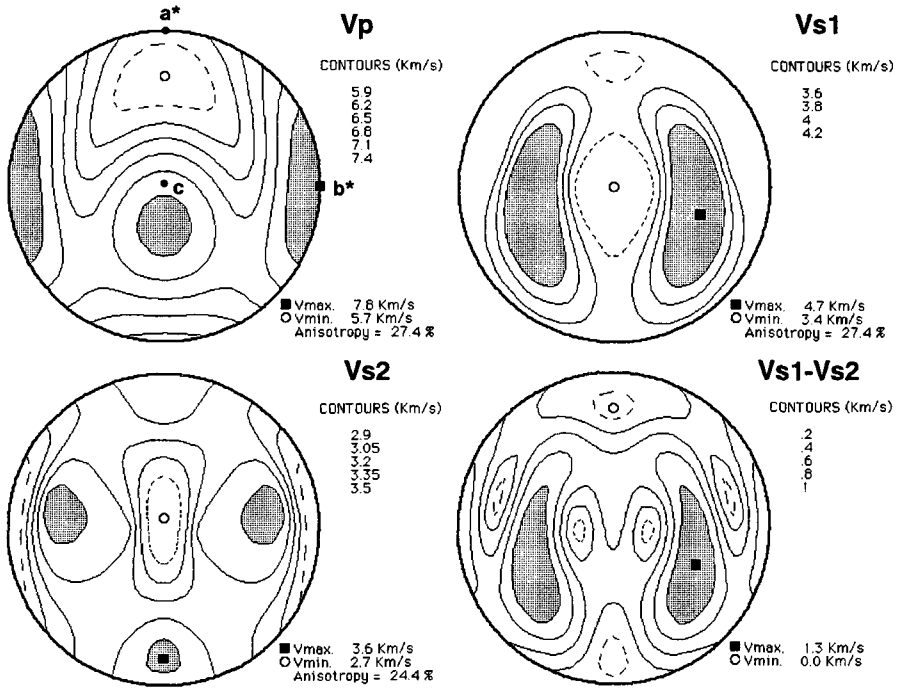

Sillimanite Al_2SiO_5

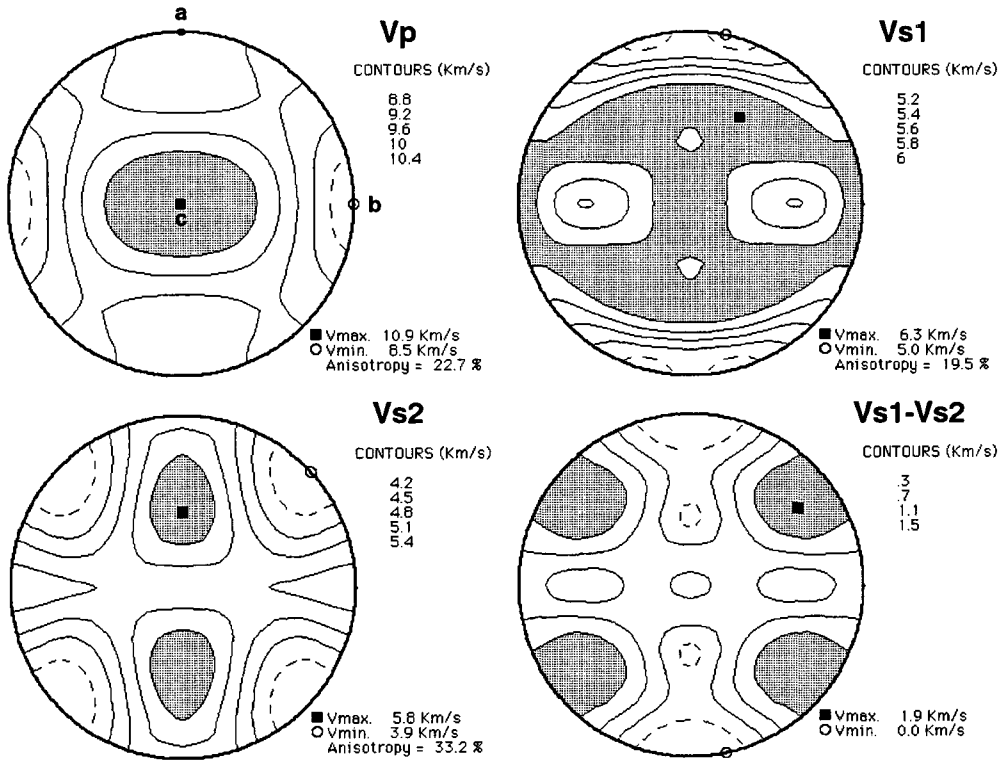

Figure 1.13 P- and S-wave properties of 9 main minerals in the lower crust. The P-wave phase velocities (V_p, up-left), the fast S-wave velocities (V_{s1}, up-right), the slow S-wave velocities (V_{s2}, low-left), and the S-wave birefringence or shear-wave splitting (V_{s1}-V_{s2}, low-right) are shown in equal area stereographic projection with respect to the crystallographic orientations of a, b, c, a* and b*, where a* and b* are the directions normal to (100) and (010) planes, respectively. The maximum velocity (in km/s) is marked by a solid square and the minimum by an open circle. The anisotropy is in per cent. Notice that the contour intervals are not the same for every diagram. Shaded areas correspond to directions of high P- or S-wave velocities.

1.6 Effects of chemical composition and metamorphic facies on seismic properties of rocks

The rocks in the deep crust and mantle, where pressure and temperature are sufficiently high to close almost fully microcracks and pores, can be considered as dense aggregates of minerals. The seismic or elastic properties of such dense aggregates depend primarily on the seismic or elastic properties of the rock-forming minerals and their volume fractions (i.e., modal compositions). Figures 1.14 and 1.15 show, respectively, the P- and S- wave velocities (V_p and V_s) for 11 main common constituent minerals for the crust and upper mantle. For V_p, an order from lower to higher velocities is: Quartz/K-feldspar/Plagioclase (An9)/Mica < Calcite/Plagioclase (An53) < Amphibole < Clino- or Orthopyroxene < Olivine < Garnet (Fig. 1.14). A similar trend can be found for V_s (Fig. 1.15). Following the same logic, we can easily obtain the following conclusions: a granite composed of quartz, K-feldspar, albite and mica should have a lower V_p or V_s than a gabbro consisting of plagioclase (An53) and clinopyroxene, and further the gabbro should have a lower V_p or V_s than a peridotite composed of olivine, orthopyroxene and clinopyroxene. This conclusion is consistent with laboratory measurement results as shown in Fig. 1.16. In consequence, the upper crust dominated with granites has lower seismic velocities than the lower crust if the latter consists of mainly mafic rocks. The boundary between the upper crust and lower crust should be seismic reflective (Conrad discontinuity). The lower crust and the upper mantle, which are separated by a seismic discontinuity named Moho, have also significantly different seismic velocities.

As different rock-forming minerals have different chemical compositions, there are some general correlations between the bulk composition and seismic properties of rocks. In Sulu ultrahigh metamorphic rocks (e.g., granitic gneiss, paragneiss, amphibolite, eclogite, eclogitized gabbro and peridotite), for example, seismic velocities increase with increasing MgO+FeO, and CaO contents and decreasing SiO_2 and Na_2O+K_2O

contents (Fig. 1.17). The trend reflects a fact that the seismic velocities increase with increasing the mafic components and decrease with increasing the felsic components.

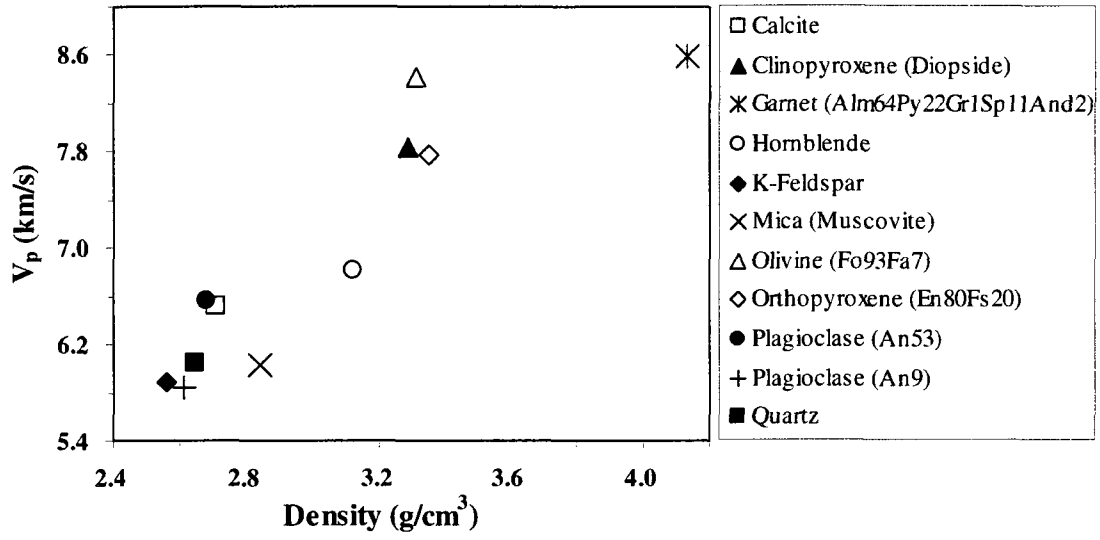

Figure 1.14 Monomineralic aggregate P-wave velocities versus density for 11 common rock-forming minerals (Data calculated from the single crystal elastic constants listed in Ji et al., 2002)

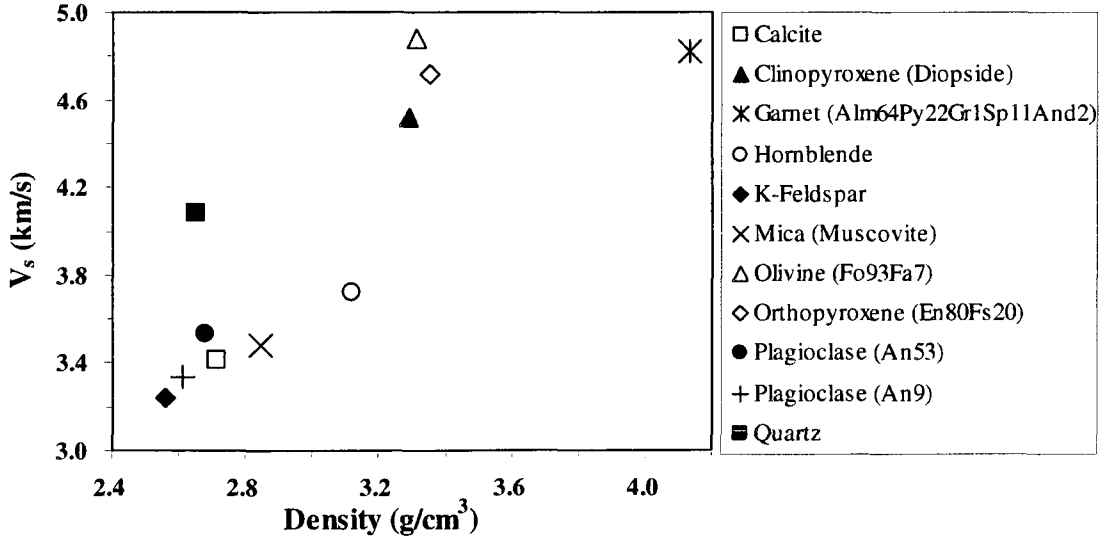

Figure 1.15 Monomineralic aggregate S-wave velocities versus density for 11 common rock-forming minerals (Data calculated from the single crystal elastic constants listed in Ji et al., 2002)

However, the seismic properties are more controlled by minerals than by the bulk compositions. For example, alpha-quartz (V_p=6.15 km/s) and coesite (V_p=8.50 km/s) have the same bulk composition but considerably different seismic properties (Fig. 1.18). The best example is the transition of graphite to diamond. Diamond has an average $V_p \approx 18$ km/s while $V_p \approx 7$ km/s for graphite. Therefore, the metamorphic facies transition plays an important role in the change in seismic properties of rocks. An abrupt rise in V_p and V_s should occur across the metamorphic facies boundary, for example, from amphibolite to granulite, and then to eclogite facies. This can be clearly seen from Fig. 1.16 The velocity increases are caused by the replacement of lower velocity, lower density, water-bearing content minerals by higher velocity, high density and lower water content dry minerals in response of rising metamorphic conditions (i.e., pressure and temperature). Thus, modern seismological techniques can provide constraints on the lithological compositions and physical state of rocks in the in-situ crust and upper mantle.

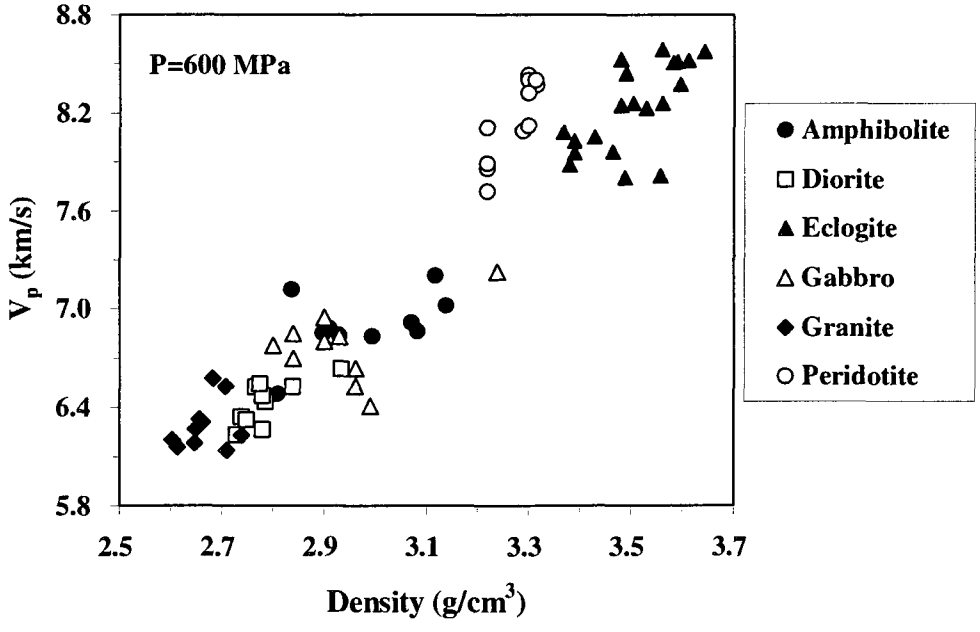

Figure 1.16 Mean P-wave velocity versus density for 6 main lithological categories at 600 MPa and room temperature (Data from Ji et al., 2002)

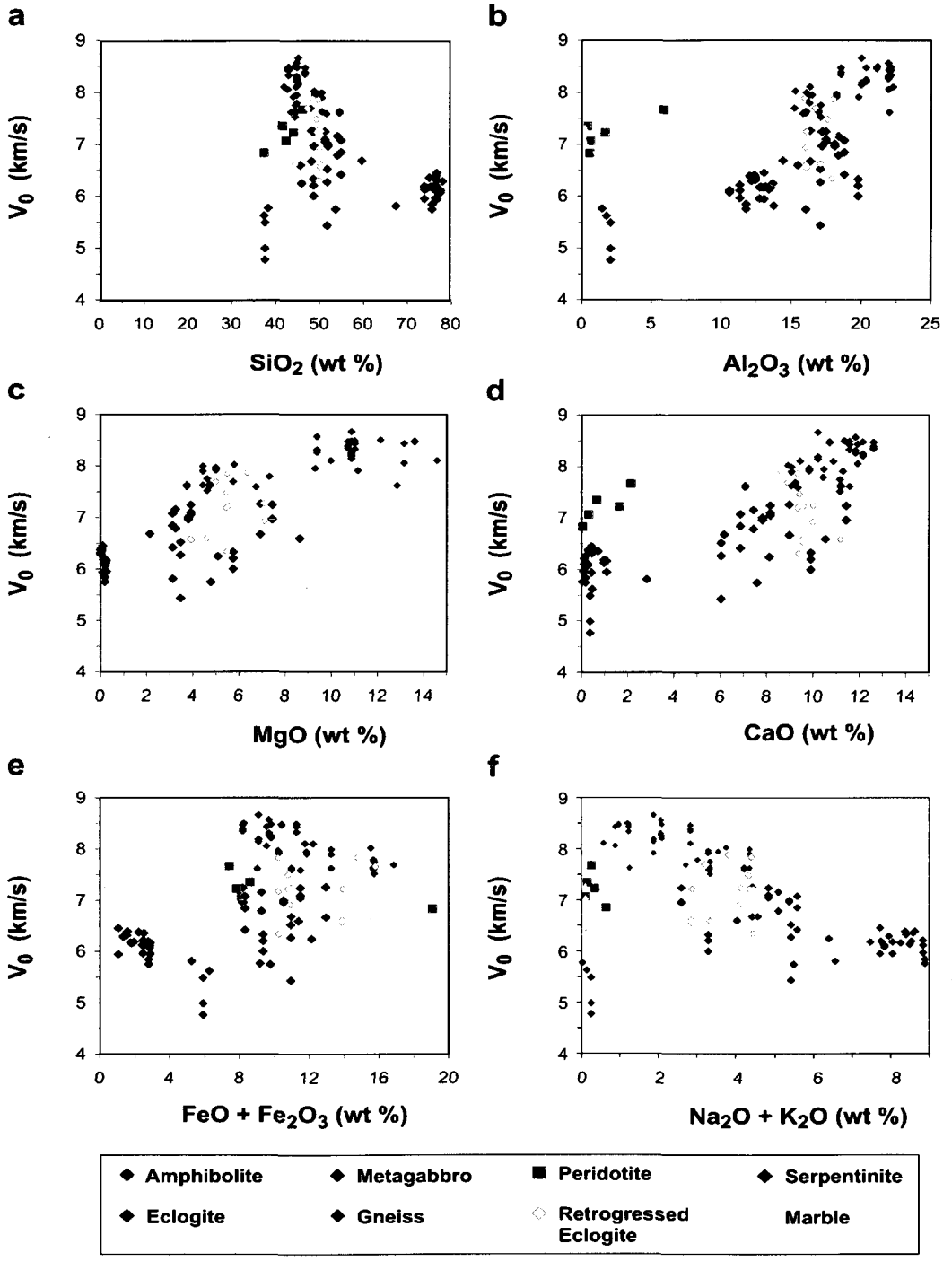

Figure 1.17 Relationship between V_0 and chemical compositions for 122 UHP metamorphic rocks. V_0 is the zero-pressure P-wave velocity of dense rocks presumably free of cracks or pores. Data measured by both Qian Wang (this study) and Qin Wang et al. (2005a).

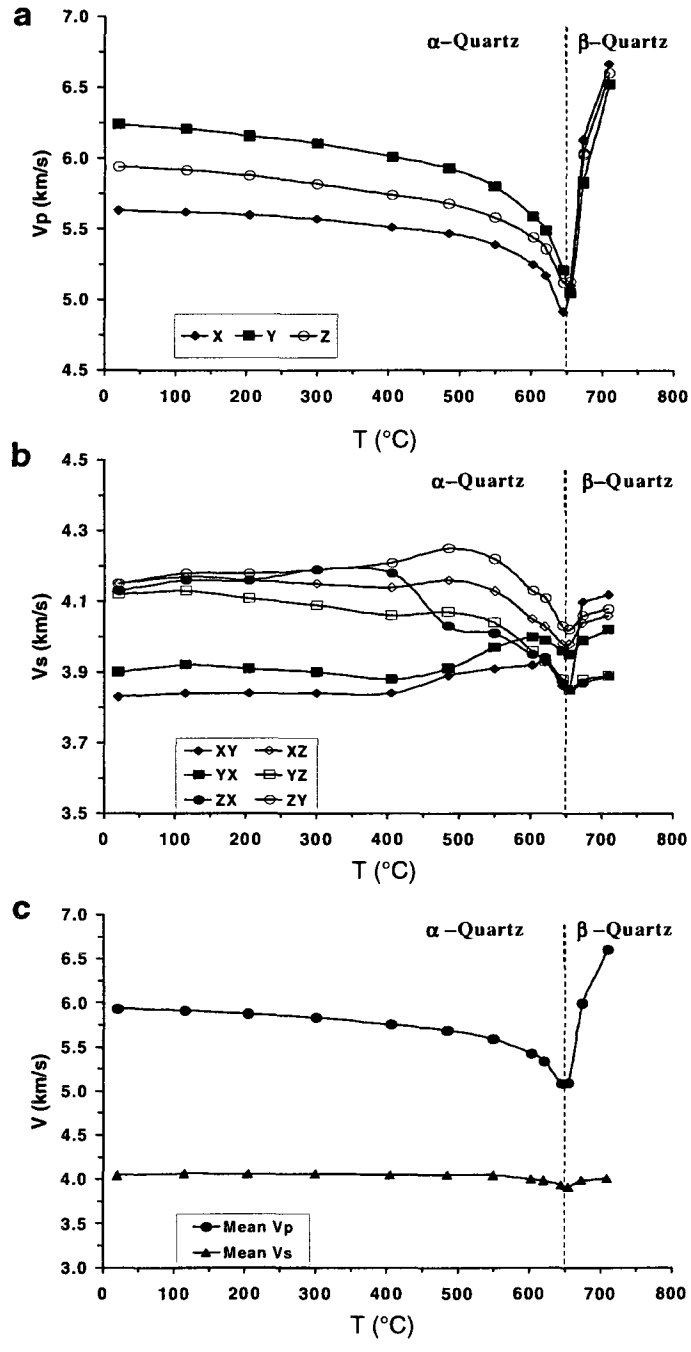

Figure 1.18 Variations of seismic properties in a quartzite due to the α-β quartz transition with changing temperature. (a) P-wave velocities in the X, Y and Z directions, (b) S-wave velocities propagating and vibrating in the X, Y, and Z directions, and (c) the mean P- and S-wave velocities. Original experimental data from Barruol (1993) (Ji et al., 2002).

1.7 Summary

In this chapter, I gave a succinct overview of the elasticity, V_p/V_s and Poisson's ratio, mixture rules, seismic anisotropy and shear-wave splitting, and effects of chemical composition and metamorphic facies on seismic properties of rocks. I also presented a brief introduction to each of the following chapters included in this thesis. In summary, this thesis is a proof for my research interest in the seismic properties of polymineralic rocks at all scales, from hand specimens to continents. The seismic properties are influenced by various factors such as mineral properties (chemical composition and crystal structure), confining pressure, temperature, porosity and pore/microcrack geometry, and microstructure (layering and lattice preferred orientation, phase connectivity and continuity). Determining how the factors affect the seismic velocities, anisotropy and elastic moduli is of a critical importance for the geological interpretation of in-situ seismic data (refraction, reflection and shear-wave splitting). Since I arrived in École Polytechnique de Montréal in July 2005, I have not only received training at the forefront of the research field, but also benefited from being involved in challenging interdisciplinary projects which enriched my research experience in natural observations, high-pressure experimentation and computation.

Chapter 2
The Sulu ultrahigh pressure (UHP) metamorphic terrane (China) and the Chinese Continental Scientific Drilling (CCSD) project

2.1 The Sulu ultrahigh pressure metamorphic terrane

One of the most important geoscience discoveries during the last three decades is the finding of a major ultrahigh pressure (UHP) metamorphic belt, more than 1000 km long, in the Sulu-Dabie-Qinling region of central eastern China (the central orogenic belt of China). Both coesite and diamond have been found in eclogite, and coesite has also been reported in granitic gneiss, paragneiss, quartzite and marble in this belt (Xu, 1987; Wang et al., 1989; Okay et al., 1989; Xu et al., 1992; Yang et al., 1999), indicating that the supracrustal material was subducted to depths >100-150 km (Cong and Wang, 1999; Liou et al., 2000).

The Sulu-Dabie UHP metamorphic belt was formed by continent-continent collision between the North China Block and the Yangtze Block during the Triassic (Li et al., 1989, 1996, 2000a, 2000b; Ames et al., 1993; Liou et al., 1998; Hacker et al., 1998). Recently diamond- and coesite-bearing eclogites and gneisses were also discovered in an Ordovician (500-440 Ma) metamorphic belt that extends northwestward along the north side of the Dabie-Qinling Mountain belt, through the Qilian-Altyn Mountains, to northern Tibet (Yang et al., 2001, 2002, Fig. 2.1). In northwestern China, this older belt, referred to as the North Qaidam-south Altyn UHP metamorphic belt, is offset ~400 km by the left-lateral strike-slip Altyn Tagh fault. The Triassic Sulu-Dabie UHP metamorphic belt and the Ordovician North Qaidam-south Altyn UHP metamorphic belt together form a huge UHP metamorphic belt ~4000 km long (Fig. 2.1), the largest UHP metamorphic belt recognized in the world (Yang et al., 2002).

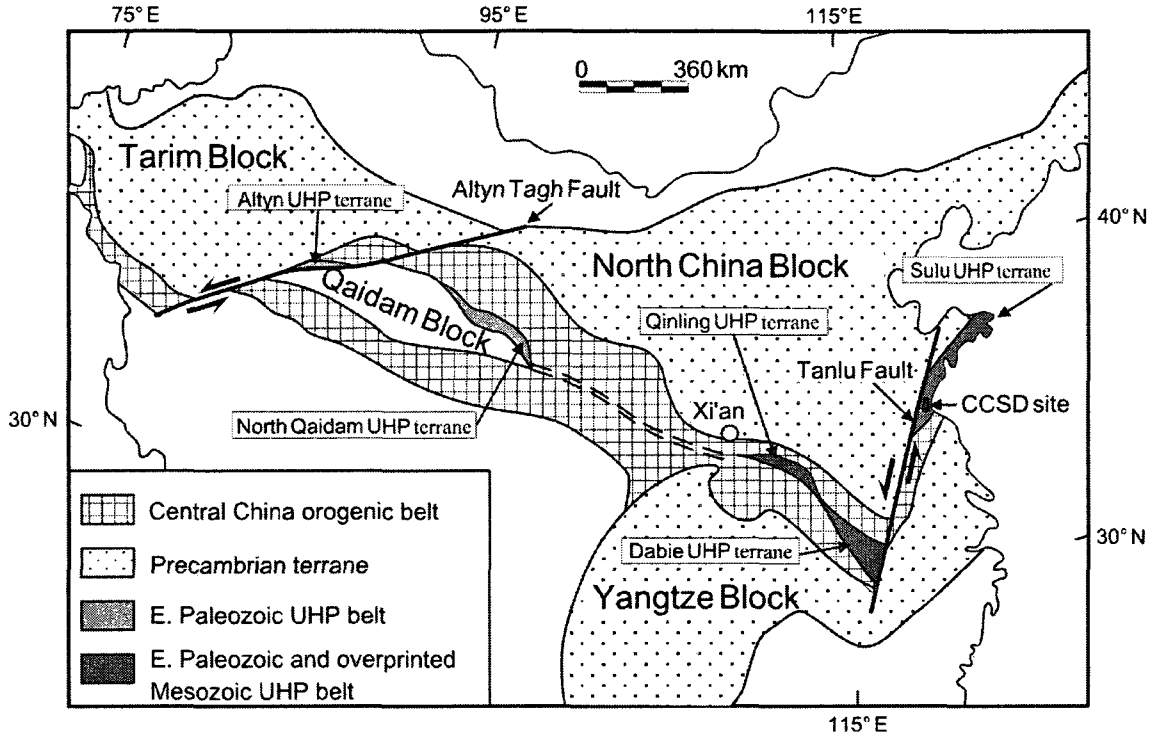

Figure 2.1 Geologic map showing the central UHP metamorphic belt of China. This huge belt consists of the Triassic Sulu-Dabie-Qinling UHP metamorphic terranes and the Ordovician North Qaidam and Altyn UHP metamorphic terranes.

The Sulu-Dabie UHP metamorphic terrane is actually a part of the deep orogenic root formed by collision between the North China Block and the Yangtze Block during the Triassic. This root, which consists of deeply buried UHP metamorphic rocks (e.g., Hacker et al., 2000; Rathschbacher et al., 2000), is now exposed on the surface. These UHP rocks provide an excellent and unique opportunity for investigating the seismic properties of the deep orogenic root. The results of the investigation may yield important constrains on the geological interpretation of in-situ seismic refraction/reflection and anisotropy data from the continental collision belts. Detailed petrological, geochemical, and structural studies of these UHP rocks equally provide important constraints on the tectonic processes that first formed and then exhumed the root. All the studies mentioned above can also lead to a better understanding of the metamorphic reactions at great depth, geochemical cycling of crust/mantle materials, rheology of the crust and the

nature and extent of crustal fluids. Below an introduction is given to tectonic setting of the Sulu HP-UHP metamorphic terrane.

The Sulu UHP metamorphic terrane, which extends NE-SW for ~750 km and is ~180 km wide, has been offset about 530 km from the Dabie UHP metamorphic terrane by the sinistral strike-slip Tanlu fault (Fig. 2.1). According to previous researchers (Ji et al., 2003, 2007; Wang et al., 2005a, b; Xu et al., 2005, 2006; Zhang et al., 2004, 2006), the UHP metamorphic rocks in the Sulu terrane are garnet peridotite, garnet pyroxenite, eclogite, schist, jadeite quartzite, kyanite (garnet) phengite schist, kyanite quartzite, omphacite-bearing marble and various orthogneisses and supracrustal gneisses. Numerous lenses of eclogite and ultramafic rocks (~vol. 5%) are intercalated in metamorphosed supracrustal country rocks (~vol. 25%) and granitic gneiss (~vol. 70%). Coesite and other UHP minerals (e.g., omphacite, phengite, garnet and kyanite) occur as inclusions within zircons from the eclogite and gneisses, suggesting that huge volumes of continental material were subducted to depths of more than 150 km and then exhumed to the surface (Liu et al., 2001, 2003a,b).

According to Xu et al. (2009), the Sulu metamorphic terrane consists of four parallel and imbricate HP-UHP metamorphic slices with foliation dipping gently to the SE (Fig. 2.2). An antiformal structure in the northwest part of the terrane (Fig. 2.3) was modified by emplacement of Triassic–Cretaceous granites (Cheng and Chang, 2004; Lin et al., 2006). Figure 2.3, which is based on seismic reflection data, is a schematic tectonic profile showing an extrusion-nappe structure formed by the exhumation of the Sulu orogenic deep root. These imbricate tectonic slices occur from top to bottom as:

(1) the southern Sulu high pressure (HP) tectonic slice composed of high pressure and low temperature (HP-LT) metamorphic rocks (P=0.7-0.85 GPa, T=300-360°C) (Qiu et al., 2002);

(2) the southern Sulu very high pressure (VHP) tectonic slice composed of very

high pressure (VHP, P=1.5-2.5 GPa, T=500-600°C) metamorphic rocks (Zhang et al., 2002);

(3) the southern Sulu UHP (P>2.8 GPa, T=650-900 °C) tectonic slice (UHPS in Fig. 2.2) mainly composed of supracrustal gneiss and granitic gneiss intercalated with eclogite and ultramafic lenses;

(4) the northern Sulu UHP tectonic slice (UHPN in Fig. 2.2) dominantly composed of granitic gneiss (Xu et al., 2006a). This tectonic unit is characterized by the emplacement of Triassic–Cretaceous granites.

These imbricate slices are separated by ductile shear zones. The shear zones in the southeast (i.e., the upper part) of the HP-UHP terrane are characterized by thrusts with top-to-the-NW sense of shear, whereas those in the northwest (i.e., the lower part) of the terrane are normal faults with top-to-the-SE sense of shear. These normal shears, which formed during exhumation of the UHP rocks, have been dated at 218-200 Ma by ^{40}Ar-^{39}Ar thermochronology (Xu et al., 2006).

The North Sulu detachment (NSLD), which constitutes the southern boundary of the Laiyang Basin (Fig. 2.2) and marks the northern boundary of the Sulu HP-UHP terrane, dips gently NW or WNW. This detachment contains mylonitic gneiss, marble and schist, all formed at 148-146 Ma (Yang et al., 2002) and then overprinted by Cretaceous movement of the Wulian-Yantai normal fault.

2.2 The Chinese Continental Scientific Drilling (CCSD) project

The CCSD project was the largest fundamental geoscientific research program ever been supported financially by the Chinese government before 2007. This project was also supported by the International Continental Drilling Program (ICDP). The CCSD project was designed to study the composition, geophysical properties, deep

structure, tectonic evolution and geodynamic processes of this unusual orogenic belt by means of drilling a deep borehole into hard crystalline rocks (e.g., eclogite, felsic gneiss, garnet peridotite) in the southern part of the Sulu UHP metamorphic terrane. The main borehole (34.40° N, 118.67° E) is located in Maobei village, about 12 km southwest of Donghai County in Jiangsu Province, China (Fig. 2.1).

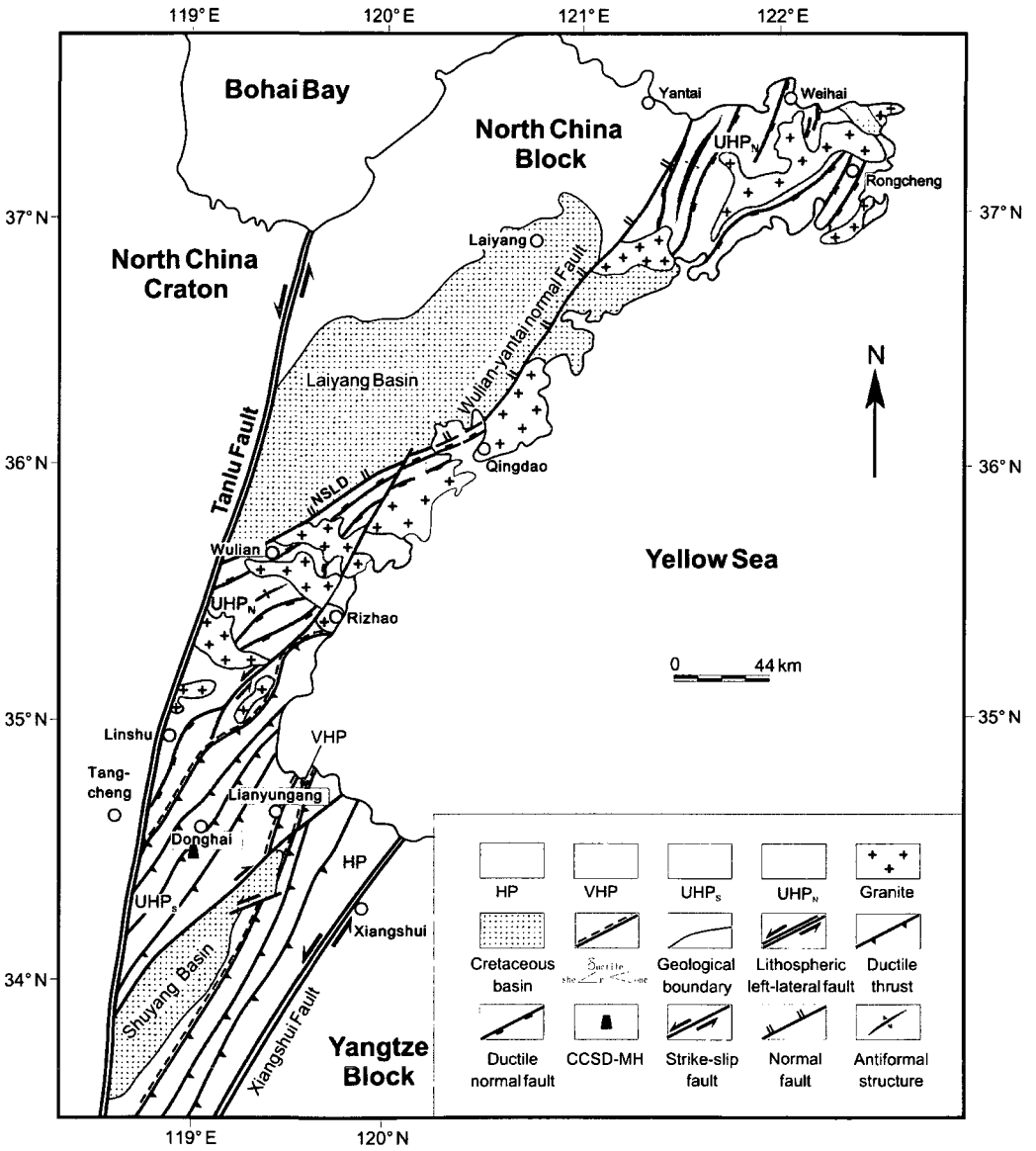

Figure 2.2 Simplified structural map of the Sulu HP-UHP metamorphic terrane.

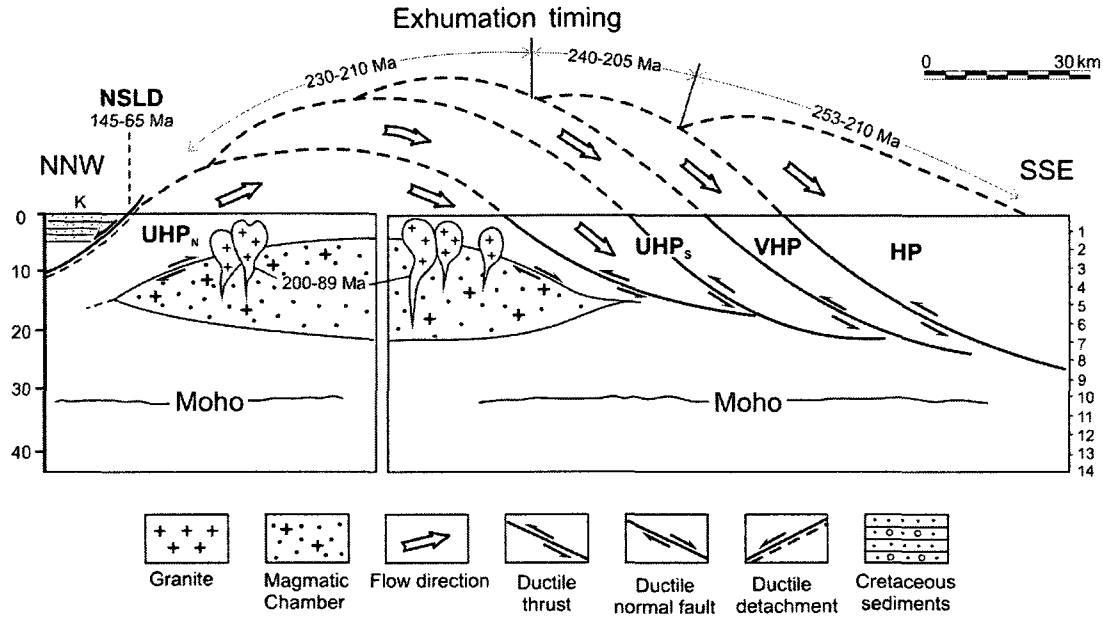

Figure 2.3 Schematic tectonic profiles showing the extrusion nappe structure formed during the exhumation of the Sulu orogenic deep root. (Modified from Xu et al., 2009)

According to Xu (2004) and Xu et al. (2009), the major research themes of the CCSD project were to:

(1) Determine the three-dimensional (3D) composition, structure and geophysical character of this continental collision belt;

(2) investigate the nature and timing of the UHP metamorphism;

(3) investigate crust–mantle interactions involved in the formation and exhumation of UHP rocks;

(4) study the process of fluid circulation and mineralization in the subduction and subsequent exhumation stages;

(5) study the rheological properties of the various rocks during subduction and

exhumation;

(6) calibrate the physical properties (i.e., seismic or elastic properties and anisotropy, densities, thermal conductivity, magnetic susceptibility, electrical properties, and radioactivity) of the UHP and HP metamorphic rocks;

(7) develop and test dynamic models for deep subduction and exhumation of the crustal rocks;

(8) establish a long-term, natural laboratory for the study of present-day crustal dynamics (i.e., stress, strain, fluid activity) and the evolution of deeply buried rocks.

The main hole of the CCSD project (hereafter "CCSD-MH") was spudded in June, 2001 and reached its target depth of 5158 m in April, 2005. The hole was continuously cored, with an average recovery of 85% (Xu et al., 2009). The Chinese geoscientists have run a full suite of petrophysical logs including gamma ray, geochemistry, fluid, sonic, and vertical seismic profiling (VSP). Using the down-hole logs, the core has been oriented viably based on visible fractures and/or foliation.

Chinese scientists involved in the CCSD project have established precise and oriented profiles of the entire borehole for lithology, geochemistry, oxygen isotopes, structural deformation, rheology, mineralization, physical properties of rocks, logging, seismic VSP and underground fluids. Using logging data, microstructural elements for the entire core have been accurately characterized. Three-dimensional (3D) seismic surveys of the CCSD site, as well as calibration of the CCSD-MH geophysical data, revealed the 3D distribution of lithological units and crustal structures, which provided further constraints on the "subduction deep root dynamics" of the Sulu collision orogen.

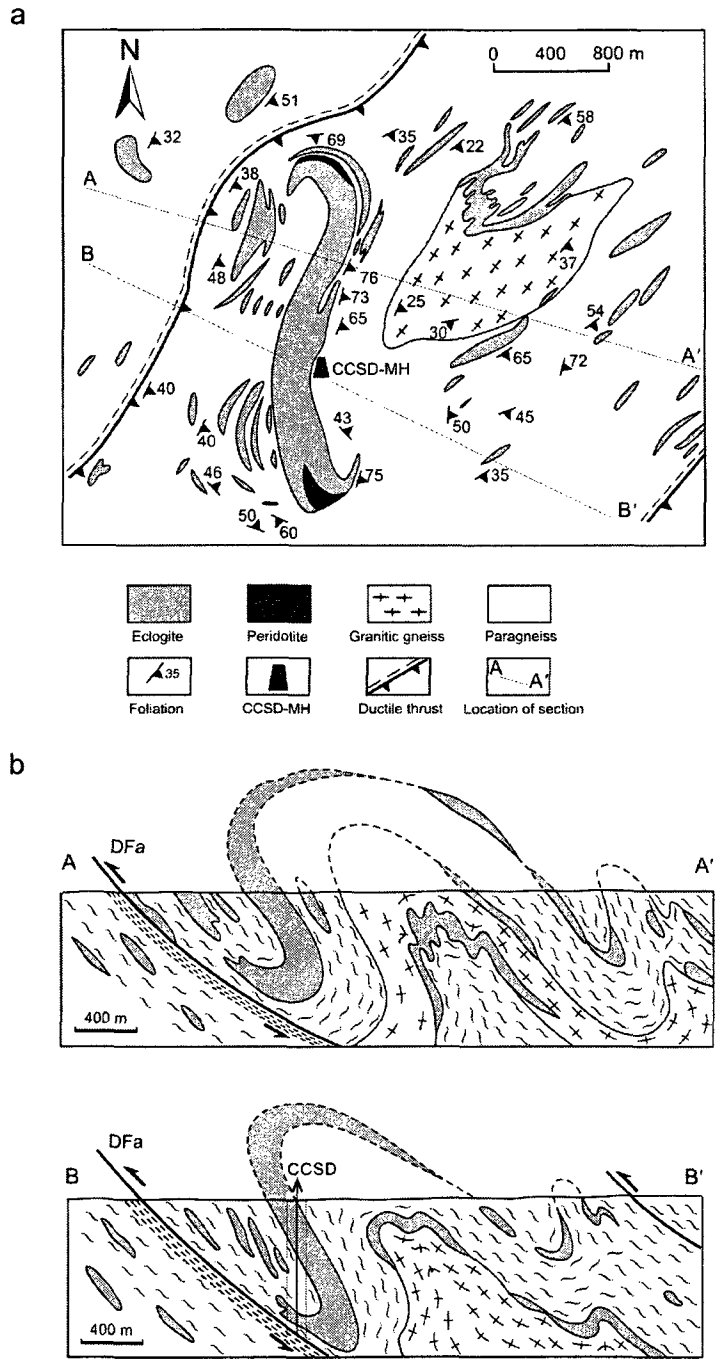

Figure 2.4 Folded and boudinaged eclogite layers intercalated with ultramafic lenses lie in a matrix of paragneiss and granitic gneiss in the CCSD region. (a) Simplified structural map. The CCSD main hole is located at 34.40° N, 118.67° E. (b) NW-SE profiles indicated in (a). (Modified from Xu et al., 2009)

The main borehole of the CCSD is located in the sigmoid-shaped Maobei eclogite/ultramafic complex in the northern Sulu UHP upper tectonic slice (Fig. 2.4a). The folded, boudinaged, and rootless eclogite layer, intercalated with ultramafic lenses, lies in a matrix of paragneiss and granitic gneiss. These rocks together form an overturned syncline to the northwest and an overturned anticline to the southeast (Fig. 2.4b-c).

2.3 Lithostructural profile of the CCSD-main borehole

Tectonophysics will publish a special issue on the main results obtained from the CCSD project (edited by S.C. Ji and Z.Q. Xu, 2009). Here I take an opportunity to summarize succinctly the main results of the CCSD-main borehole.

The CCSD main borehole has a core recovery of ~85%. Core from the CCSD-MH consists mainly of granitic gneiss, paragneiss and eclogite or retrogressed eclogite, with lesser amounts of amphibolite, ultramafic rock, and minor mica schist, mica-quartz schist, kyanite quartzite, granite and mylonite (Fig. 2.5).

Eclogites have a total cumulated thickness of about 1600 m, and mainly occur at depth intervals of 100 to 1100 m, 1600 to 2050 m and 2500 to 3500 m (Fig. 2.5). Gneisses mainly occur at depths between 1100 to 1600 m and below 2050 m. Other rock types include garnet-peridotite with a thickness of ~70 m, rarely, schist and quartzite occurring as thin layers within eclogites and gneisses.

According to the spatial distribution, association, and compositional variation of the rocks, the CCSD-MH can be divided into five lithological units. With increasing depths, they are: unit 1 (from 0 to 710 m) which consists mainly of eclogite, intercalated layers of gneiss and peridotite; unit 2 (from 710 to 1190 m) which is composed mainly of

eclogite with abundant interlayers of gneiss; unit 3 (from 1190 to 1505 m) consisting of gneiss with minor eclogite as thin layers; unit 4 (from 1505 to 3460 m) which is composed mainly of gneiss with abundant interlayers of eclogite and retrograded eclogite (amphibolite); and unit 5 (below 3460 m) consisting mainly of gneiss with rare interlayers of eclogite and amphibolite.

Eclogites from the CCSD-MH have variable mineral assemblages with different modal abundance. Quartz-rich, rutile-rich, ilmenite-rich, phengite-rich and MgO-rich eclogite were recognized (Zhang et al., 2009). Rt- and/or Ilm-rich eclogites that occur in unit 1 have a typical mineral assemblage of Grt + Omp + Rt (or Ilm) ± Ap; Qtz-rich eclogite occurs mainly in unit 1 and contains quartz up to 20 vol. % with minor rutile; Phn-rich eclogite occurs mainly in units 1 and 2, and is characterized by relatively high contents of phengite ± kyanite; MgO-rich eclogite occurs as thin layers, lenses or blocks within ultramafic rocks of unit 1, which can be distinguished by absence of minor minerals except for rutile.

Inclusions of polycrystalline quartz pseudomorph after coesite are common in the eclogitic garnet and omphacite. Coesite, garnet, omphacite and phengite are also found as inclusions in zircons from fresh and retrograde eclogites (Zhang et al., 2006), indicating that all eclogites have been subjected to UHP metamorphism. Some eclogites, especially those that occur as thin layers in gneisses from units 3, 4 and 5, have been subjected to amphibolite-facies retrogression to various extents, i.e., omphacite is partly or completely replaced by amphibole + sodic plagioclase symplectite, garnet by amphibole + plagioclase symplectite, and phengite by biotite + plagioclase symplectite or corona.

Ultramafic rocks, including garnet-peridotite and garnet-pyroxenite, occur at the depth interval of 600 to 680 m. They consist of garnet, olivine, clinopyroxene, and orthopyroxene with or without minor Ti-clinohumite and phlogopite. Most ultramafic

rocks exhibit variable degrees of hydration alteration as indicated by partial to complete serpentinization.

Gneisses occur in all units, and consist of plagioclase, K-feldspar and quartz with minor and variable amounts of biotite, amphibole, muscovite, epidote (or allanite), garnet, apatite, and zircon. The gneisses from units 3 and 5 are characterized by relatively high contents of feldspar and quartz, and relatively low abundances of ferromagnesian minerals, showing only weak foliation or even massive texture. In general, gneisses from the CCSD-MH have amphibolite-facies mineral assemblages. However, symplectite of amphibole + plagioclase after jadeite, and plagioclase + biotite after phengite were recognized in some gneiss samples, implying that their UHP counterparts are phengite-bearing jadeite-quartzite. As an important indicator for the UHP metamorphism, coesite inclusions are common in gneissic zircons. Other minerals, such as phengite, garnet, jadeite (or omphacite), rutile and apatite also occur as inclusions in gneissic zircons as shown by previous studies (Liu et al., 2004, Zhang et al., 2006). These observations strongly suggest that the gneisses have been subjected to early UHP metamorphism before they were overprinted by amphibolite-facies metamorphism, which is consistent with the results obtained from non-mafic rocks from some shallow holes and surface outcrops in the Donghai area (Liu et al, 2002; Zhang et al., 2006).

Schists occur usually as thin layers (<1 m) within gneiss and eclogite. Three types of schists can be recognized according to their mineralogy (Zhang et al., 2009): garnet-phengite-quartz schist, garnet two-mica schist, and garnet epidote biotite quartz schist. The schists have mineral assemblages similar to the gneisses but with higher amounts of mica and quartz. Symplectite of biotite + plagioclase after phengite is recognized in some schists. Coesite and other eclogite-facies mineral inclusions are also present as inclusions within zircon of the schists, suggesting an early stage of UHP metamorphism.

As shown in Fig. 2.5, the folded eclogite layer, in which the foliation dips steeply to the east, lies at 0-700 m in the CCSD-MH. Several thin layers of paragneiss are intercalated with the eclogite and an ultramafic band, ~80 m thick, occurs in the lower part of the eclogite layer. A 400-m-thick interval between 1600-2000 m consists of rutile eclogite. Gneisses are dominant below 2000 m.

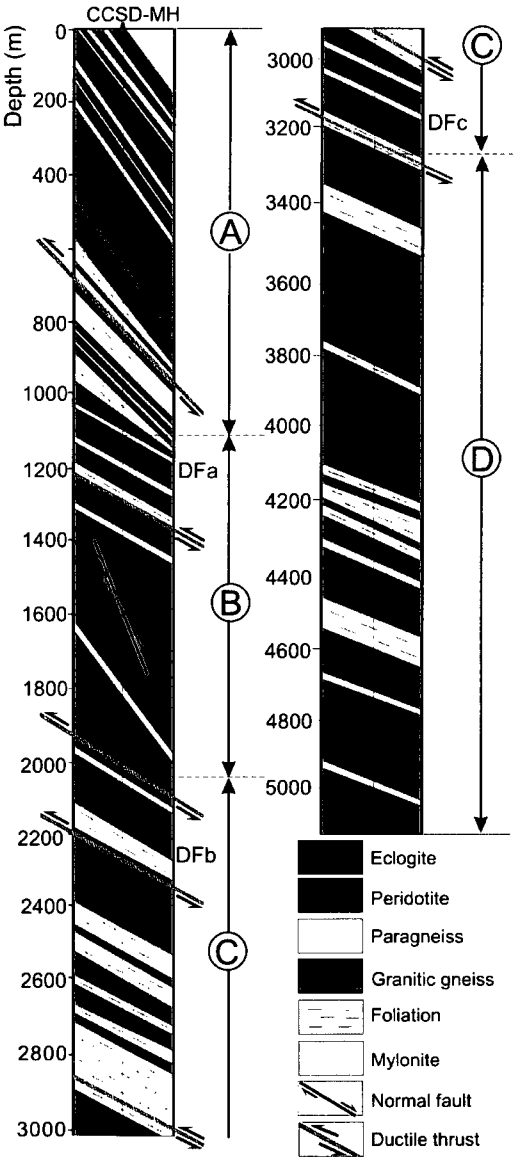

Figure 2.5 Structural profiles revealed by the CCSD main hole (0-5118 m).

According to a series of studies by Zhang et al. (2004, 2006a, b), eclogites in the CCSD-MH have a wide range of composition, suggesting that their protoliths vary from andesite and basalt to picrite. Paragneisses represent a suite of clastic sedimentary and silicic pyroclastic rocks. Protoliths of the orthogneiss are interpreted to be A-type granite (Liu et al., 2004; Xu et al., 2006). Thus, the protoliths of the UHP metamorphic rocks were continental basaltic rocks, supracrustal rocks and granites. Coesite inclusions are widespread in zircon from various rocks throughout the borehole (Liu et al., 2007) and surface outcrops, suggesting that the crustal materials in the area were indeed subducted to depths >100 km.

The structural profile of the CCSD-MH shown in Fig. 2.5 is characterized by 4 imbricate fault slices dipping gently SE or ESE, separated by ductile shear zones. Each slice is described below:

(1) Slice A comprises the upper 1113.14 m of the drilled section and consists of eclogite and ultramafic rocks in the upper 735.76 m and supracrustal gneiss intercalated with retrograded eclogite and ultramafic rocks in the lower 377.38 m (Fig. 2.5). In this slice, the foliation changes progressively from steeply eastward-dipping in the upper portion (0-735.76 m) to gently SE- or ESE-dipping below 735.76 m.

(2) Slice B has a total thickness of 825.26 m and consists of granitic gneisses intercalated with thin layers of supracrustal gneiss in the upper part (1113.14-1596.22 m) and phengite eclogite in the lower part (1596.22-2038.34 m, Fig. 2.5).

(3) Slice C (2038.34-3225.00 m) is composed of supracrustal gneisses intercalated with thin layers of granitic gneiss and eclogite (Fig. 2.5).

(4) Slice D (3225-5158 m) consists of granitic gneiss intercalated with thin layers of supracrustal gneiss and eclogite (Fig. 2.5).

The upper three units (slices A, B and C) in the main hole belong to tectonic slice UHP_S (Fig. 2.2) whereas the lower unit (slice D) correlates with tectonic slice UHP_N. These 4 tectonic units are separated by ductile shear zones (DFa, DFb and DFc) with NE-SW (or NNE-SSW) striking foliation, NW-SE or WNW-ESE oriented stretching lineation, large finite strain and intense mylonitization (Fig. 2.5). Each shear zone is composed of a series of small, parallel ductile zones, all indicating thrust shear during early high pressure and high temperature deformation and normal shear during later low pressure and low temperature deformation.

2.4 Calibration of crustal seismic structure for the upper crust of the Sulu Terrane

In order to calibrate the crustal seismic structure with the lithology and understanding the origin of the seismic reflections within the upper crust of the Sulu Terrane, Wang et al. (2005a) and Xu et al. (2009) have compared the lithological/structural profile (Fig. 2.6a) with the velocity profile of the CCSD-MH (Fig. 2.6b) and the seismic reflection profile (Fig. 2.6d) to define the spatial distribution of reflectors and to constrain their origin in terms of petrophysical, compositional and structural properties. These authors computed a reflection coefficient (R_c) profile (Fig. 2.6c) based on laboratory measurements of bulk densities and seismic velocities of the cores from various depths in the CCSD-MH (Wang et al., 2005a and b; Ji et al., 2007) (Tables 2.1 and 2.2). The main features of the profile are summarized below:

(1) Eclogite is the most important lithology in tectonic slice A. The largest

reflection coefficients (R_c=0.18-0.26) are associated with interfaces between eclogite and paragneiss (64-157 m) and between eclogite and amphibolite (466-525 m). The lithological interfaces of eclogite and retrograde eclogite and eclogite and serpentinized peridotite (523-738 m) also have very large reflection coefficients (R_c>0.1).

(2) The lower boundary of the ductile shear zone DFa (738-1103 m) also has an extremely large reflection coefficient (R_c=0.20-0.23).

(3) Tectonic slice B, which is characterized by granitic gneiss intercalated with paragneiss (1183-1597 m), and eclogite intercalated with retrograded eclogite or granitic gneiss (1664-1783 m and 1852-2038 m), has a reflection coefficient R_c generally <0.1, but some, eclogite layers are strong reflectors against paragneiss (R_c=0.23-0.30).

(4) There is a very large reflection coefficient (R_c=0.20-0.29) for the ductile shear zone DFb (2038-2320 m).

(5) In the upper part of tectonic slice C, granitic gneiss is intercalated with paragneiss (2320-2675 m), in the middle part paragneiss is interlayered with eclogite (2675-2770 m) and in the lower part paragneiss is intercalated with granitic gneiss (2770-3010 m). The upper, middle and lower parts yield R_c<0.1, R_c=0.23 and R_c<0.1, respectively.

(6) The R_c for ductile shear zone DFc (3010-3240 m) at the bottom of slice C ranges from 0.23 to 0.26.

(7) In tectonic slice D (3240-5158 m), consisting of granitic gneiss interlayered with paragneiss, R_c is <0.1 except for the interfaces between retrogressed eclogite and

granitic gneiss (5080-5105 m, R_c=0.22). The reflection coefficient for the ductile shear zone (4265-4310 m) in slice D is 0.15.

As shown in Fig. 2.6d, there are a series of seismic reflectors dipping 20-30° to the southeast in the upper crust. According to Xu et al. (2009), 4 types of seismic reflectors are recognized:

(1) Continuous and strong seismic reflectors (e.g., DFa at 835-1280 m, DFb at 2010-2280 m, and DFc at 2920-3220 m). These reflectors are attributed to ductile shear zones composed of eclogite layers in a matrix of mylonitized gneiss. Fountain et al. (1984) demonstrated that constructive interference in mylonitized/unmylonitized layers in a shear zone can double and sometimes even triple the peak-to-trough amplitude of a complex reflection so that appreciable reflections can arise even if the seismic impedance contrasts are moderate. Large strains may develop strong shape preferential orientations (SPO) and lattice preferential orientations (LPO) within shear zones, and result in seismic anisotropy. The anisotropic effect, however, is often complex, and can either enhance or mute reflections, but in general, the anisotropy alone is not strong enough to cause strong seismic reflections, except possibly in the case of amphibolite, serpentinite and mica schist (Ji et al., 1993). The role of thin layer clusters in the seismic reflectivity of ductile shear zones has been highlighted by a detailed investigation of Ji et al. (1997). For the same reason, the strong reflectivity from ductile shear zones in the upper crust beneath the CCSD-MH area appears to reflect the presence of thin layer clusters of subhorizontal or gently dipping eclogite/retrogressed eclogite within dominantly felsic gneisses.

(2) Short reflectors. Strong seismic reflection events consisting of relatively short reflectors occur in slice C (Fig. 2.6d), which is a thick-layered complex consisting of paragneiss intercalated with discontinuous layers or lenses of

eclogite and granitic gneiss. The petrophysical properties of this dominantly paragneiss suite display relatively high reflection coefficients: R_c =0.20-0.30 and 0.20-0.25 for the upper part (2260-2330 m) and lower part (3000-3225 m) of the slice, respectively.

(3) Irregular and dispersive weak seismic reflections. These reflectors are observed in slices B and D, which consists of granitic gneiss with minor eclogite and paragneiss at 1113-1596 m and 3225-5000 m. The felsic gneisses have lower densities (2.60-2.80 g/cm3) than any other rocks in the lithological profile (Wang et al., 2005a and b; Ji et al., 2007). Borehole logging and field observations indicate that the granitic gneiss and paragneiss developed complex, multi-order folds in a great variety of shapes from close, tight folds to inclined and overturned folds. The axial planes of folds commonly dip gently to the SE. Ji and Long (2006) carried out forward synthetic modeling and found that complex, multi-order folds cannot be correctly imaged by conventional reflection techniques. The reflections from steeply dipping fold limbs tend to be muted, leaving the crest and troughs that merge laterally into discontinuous, pseudo-subhorizontal or gently dipping reflections. Therefore, the irregular, dispersive, discontinuous, weak seismic reflections most likely correspond to complex folded structures in granitic gneiss and paragneiss.

(4) Very weak seismic reflections. These reflections represent homogeneous eclogite. As shown in Wang et al. (2005a, b), the eclogite has high densities (3.26-3.64) while the retrograded eclogite has relatively low densities (2.90-3.24). A homogeneous eclogite layer occurs at 1664-2038 m in the CCSD-MH, coinciding exactly with the very weak seismic reflections. These data confirm the existence of a 3-km-long and 442-600-m thick eclogite body embedded within granitic gneiss and paragneiss above ductile shear zone DFb.

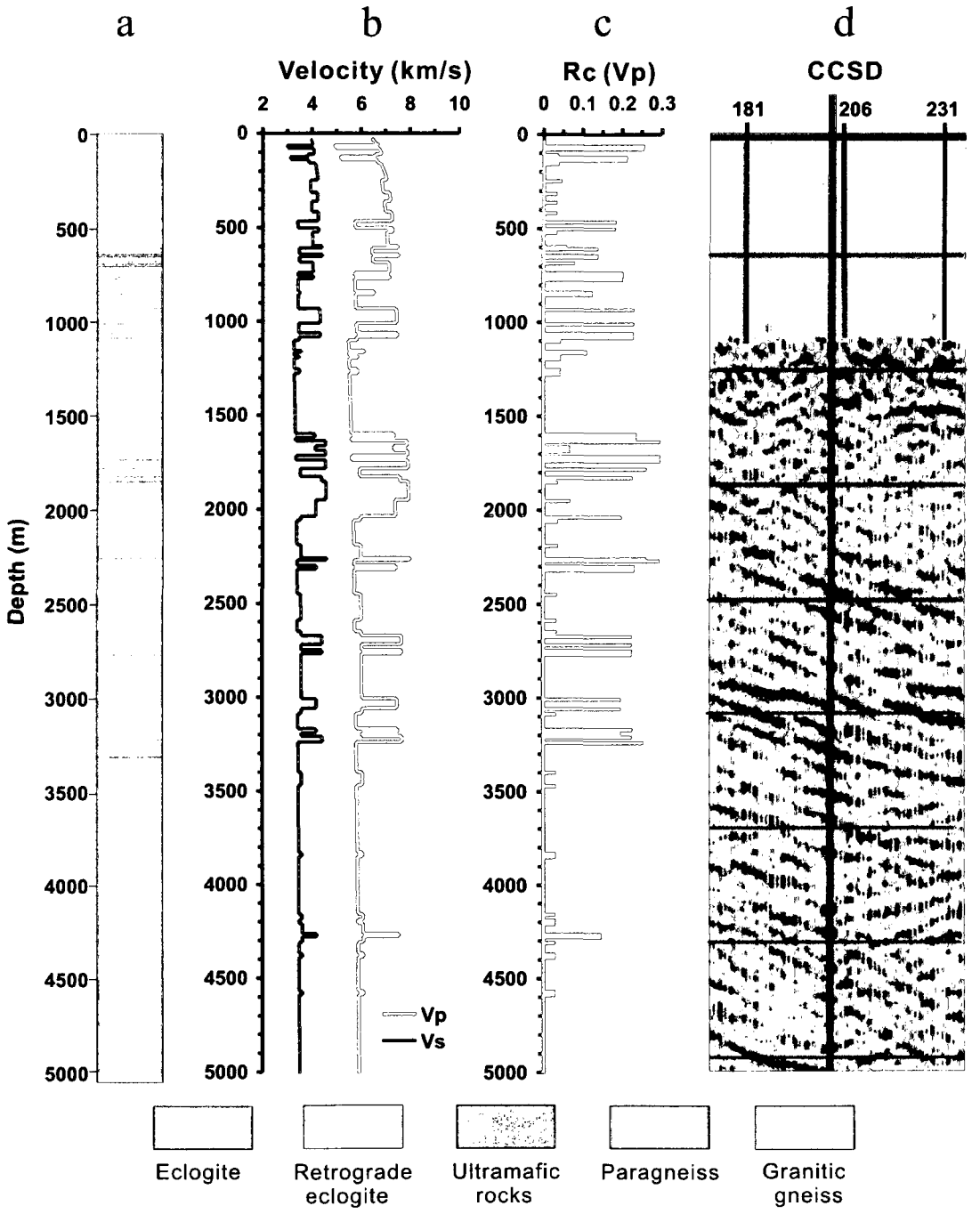

Figure 2.6 Seismic parameters of the CCSD-MH. (a) Lithologic profile; (b) P- and S-wave velocity profiles; (c) Reflection coefficients (V_p); and (d) 2D seismic reflection section. (After Xu et al., 2009)

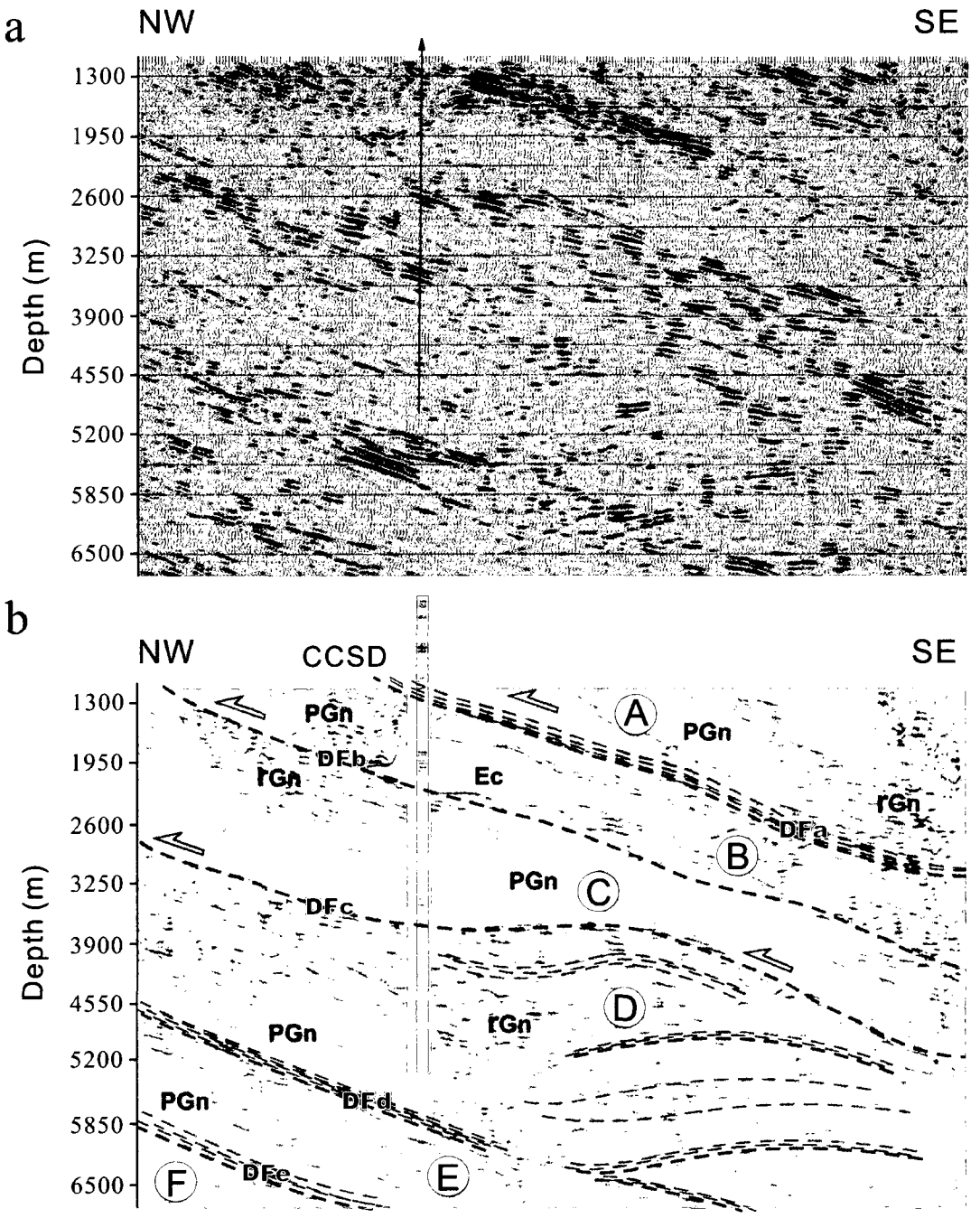

Figure 2.7 Seismic reflection profile (a) and geological interpretation (b) across the CCSD-MH (see Fig. 2.3 for location). A, B, C, D, E and F represent UHP rock slices. Dashed lines: ductile shear zones (DFa, DFb, DFc, DFd, and DFe). Ec: eclogite; PGn: paragneiss; rGn: granitic gneiss. The upper 1000 m of the drilled section is not included. (After Xu et al., 2009)

Table 2.1 Reflection coefficients (R_c) at possible lithological interfaces in the Dabie-Sulu UHP belt at 50 MPa and 600 MPa

Lithology	ρ (g/cm^3)	V_p (km/s)		Eclogite	Peridotite	Srp peridotite	Mafic granulite	Amphibolite	Marble	Paragneiss	Quartzite	Felsic gneiss	Serpentinite
		50 MPa	600 MPa										
Eclogite	3.57	7.87	8.51		0.06	0.13	0.17	0.22	0.22	0.24	0.29	0.31	0.36
Peridotite*	3.31	7.55	8.24	-0.05		0.07	0.19	0.16	0.17	0.19	0.23	0.26	0.31
Srp peridotite*	3.18	6.82	7.32	-0.13	-0.08		0.04	0.09	0.10	0.12	0.17	0.19	0.24
Mafic granulite*	3.15	6.65	6.98	-0.16	-0.11	-0.03		0.08	0.08	0.10	0.15	0.17	0.23
Amphibolite	3.00	5.99	6.65	-0.21	-0.16	-0.08	-0.09		0.00	0.03	0.07	0.10	0.15
Marble	2.86	6.24	6.87	-0.21	-0.16	-0.08	-0.11	-0.01		0.02	0.07	0.09	0.15
Paragneiss*	2.85	5.99	6.51	-0.24	-0.19	-0.11	-0.16	-0.04	-0.03		0.05	0.07	0.13
Quartzite*	2.65	5.86	6.24	-0.29	-0.24	-0.17	-0.25	-0.09	-0.09	-0.06		0.03	0.08
Felsic gneiss	2.66	5.56	6.16	-0.30	-0.25	-0.17	-0.26	-0.10	-0.09	-0.06	-0.01		0.06
Serpentinite	2.61	5.08	5.50	-0.36	-0.31	-0.24	-0.35	-0.16	-0.16	-0.13	-0.07	-0.07	

R_c derived from average densities at ambient conditions and velocities measured at 50 MPa (the upper matrix) and 600 MPa (the lower matrix), respectively.
The bold numbers refer to possible lithologic interfaces that may generate strong seismic reflections.
* Data from *Handbook of Seismic Properties of Minerals, Rocks and Ores* (Ji et al., 2002)

Table 2.2 Reflection coefficients (R_c) at the lithological interfaces in the CCSD-MH

No.	Depths (m)	Lithological unit	Lithological interface	Structure	R_c
1	64-157	A	Eclogite/paragneiss		0.21-0.26
2	157-466	A	Eclogite/retrogressed eclogite		0.03-0.05
3	466-523	A	Eclogite/amphibolite		0.18
4	523-608	A	Eclogite/retrogressed eclogite		0.03-0.06
5	608-738	A	Eclogite/Serpentine peridotite		0.08-0.14
6	738-840	A	Retrogressed eclogite/paragneiss	Ductile shear zone (DFa)	0.2
7	840-931	A	Serpentine peridotite/paragneiss	Ductile shear zone (DFa)	0.12
8	931-1103	A	Eclogite/paragneiss	Ductile shear zone (DFa)	0.23
9	1103-1183	B	Amphibolite/granitic gneiss		0.11
10	1183-1597	B	Granitic gneiss/paragneiss		0.04
11	1597-1664	B	Retrogressed eclogite/granitic gneiss		0.24-0.30
12	1664-1716	B	Eclogite/retrogressed eclogite		0.07
13	1716-1783	B	Eclogite/granitic gneiss		0.3
14	1783-1852	B	Eclogite/paragneiss		0.23-0.26
15	1852-2038	B	Eclogite/retrogressed eclogite		0.04-0.07
16	2038-2060	B	Retrogressed eclogite/paragneiss	Ductile shear zone (DFb)	0.2
17	2060-2260	B	Granitic gneiss/paragneiss		0.04
18	2260-2320	B	Eclogite + retrogressed eclogite/ granitic gneiss	Ductile shear zone (DFb)	0.23-0.29
19	2320-2675	C	Granitic gneiss/paragneiss		0.03-0.04
20	2675-2770	C	Eclogite/paragneiss		0.23
21	2770-3010	C	Paragneiss/granitic gneiss		<0.05
22	3010-3240	C	Eclogite/paragneiss + granitic gneiss	Ductile shear zone (DFc)	0.23-0.26
23	3240-4265	D	Granitic gneiss/paragneiss		0.03
24	4265-4310	D	Amphibolite/paragneiss	Ductile shear zone (DFd)	0.15
25	4310-5080	E	Granitic gneiss/paragneiss		0.03
26	5080-5105	E	Retrogressed eclogite/granitic gneiss		0.22
27	5105-5158	E	Granitic gneiss		

Figure 2.7a shows a seismic reflection profile in the Maobei area (Donghai county), which goes through the CCSD site. Its geological interpretation is given in Fig. 2.7b with identification of different lithological units. Paragneiss layers occur mainly in the upper part of the profile whereas granitic gneiss predominates in the lower part. A large eclogite body lies in the second slice (B). The tectonic slices usually dip gently to SE or ESE. Four slices (A, B, C and D) are separated by three subparallel ductile shear zones (DFa, DFb and DFc). The continuous and densely distributed layers with very strong seismic reflections at 5200-5500 m are interpreted as a large-scale ductile shear zone (DFd). There is apparently a 2-km-thick layer of granitic gneiss immediately beneath the DFd. The sigmoid-shaped eclogite lens as shown in Fig. 2.4 are intercalated with ultramafic rocks and extend from the surface down to 700 m in the CCSD-MH (Fig.

2.7b). The structure of the Maobei area is characterized by these overturned folds with NNE-subhorizontal axes and axial planes dipping steeply to the ESE.

2.5 Age data of CCSD core and surface samples

In order to determine the ages of protoliths, continental subduction, peak metamorphism, exhumation and uplift of the UHP metamorphic rocks, the CCSD researchers have utilized zircon SHRIMP U-Pb, LA-ICP-MS, ^{40}Ar-^{39}Ar and apatite fission track (AFT) chronologic methods. Their results are summarized below.

2.5.1 Protolith ages

Zircon SHRIMP U-Pb dating of various UHP metamorphic rocks in the CCSD-MH yields ages of 780-680 Ma for the protoliths of the granitic gneisses, and 765-730 Ma for the protoliths of the eclogites and garnet amphibolites. The latter are interpreted as regressed eclogites (Zhang et al., 2004; Yang et al., 2004). Inherited detrital and magmatic zircons from the paragneisses display younger ages (730 Ma, 680 Ma, and 621 Ma). SHRIMP U/Pb dating also reveals similar protolith ages of 715-780 Ma and 700-765 Ma for granitic gneiss and eclogite from the southern Sulu UHP belt. The protoliths of paragneisses from the southern UHP belt have U-Pb zircon SHRIMP ages of 730 Ma, 680 Ma, and <680 Ma. However, the protoliths of granitic gneiss and eclogite from the northern Sulu UHP belt were derived from an ancient crystalline basement with an age ≥2.4 Ga, and since then they have been overprinted by at least 2 metamorphic events at 1.7-1.8 Ga and 218-234 Ma. This crystalline basement has formation age similar to the North China Block north of the Wulian-Yantai fault and west of the Tanlu fault. Thus, the Sulu HP-UHP terrane has two basement sequences: an early-middle Proterozoic (≥2.4 Ga) assemblage in the northern UHP belt and a Neoproterozoic (700-800 Ma) assemblage in the southern HP-UHP belt (Fig. 2.8).

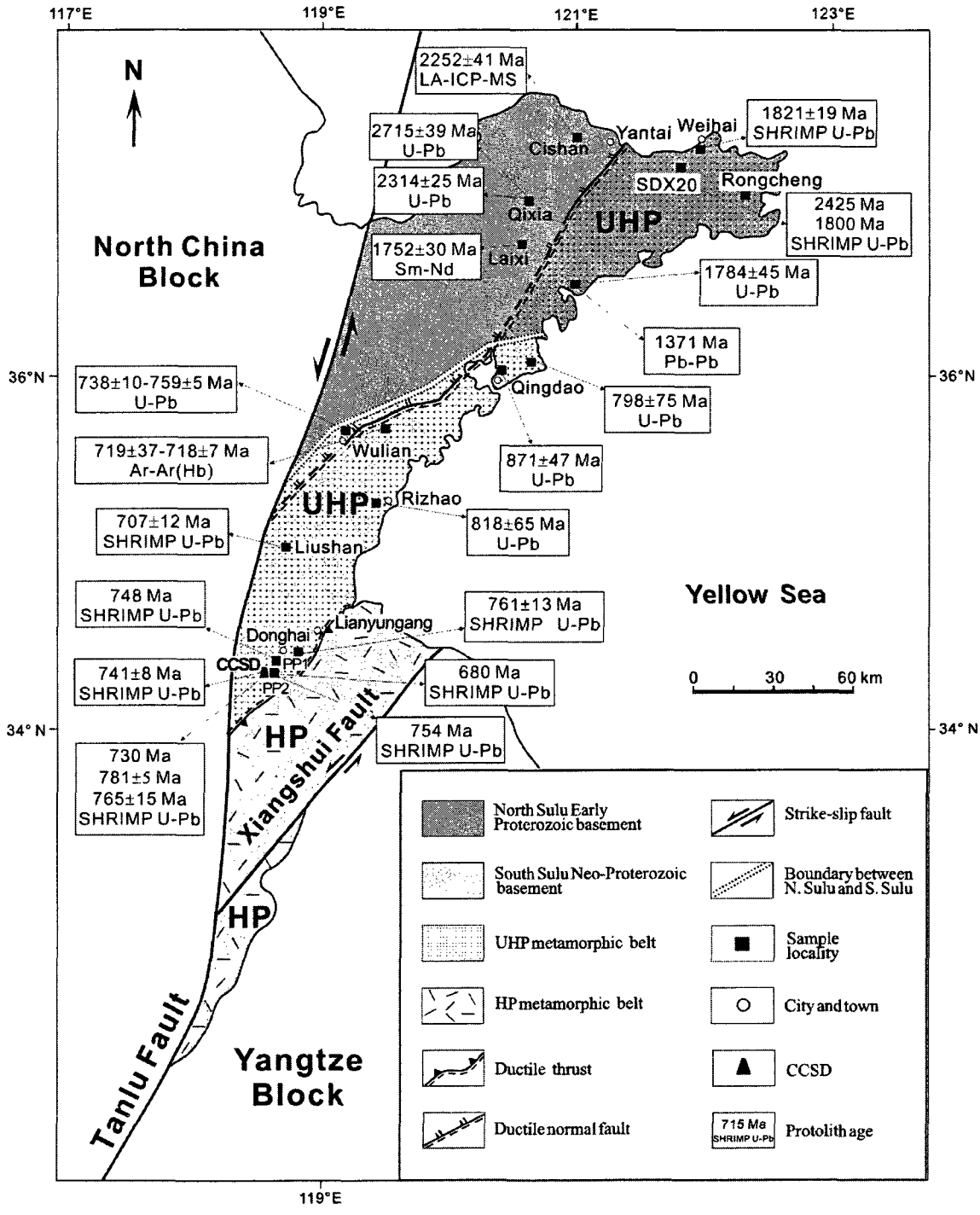

Figure 2.8 Map showing protolith ages of the HP and UHP metamorphic rocks in the Sulu collision belt.

2.5.2 Age of UHP metamorphism

SHRIMP U-Pb dating of zircons from paragneiss, granitic gneiss and eclogite of the CCSD-MH (Table 2.3) indicates that the UHP peak metamorphic event took place at 239-222 Ma or 243-221 Ma (Liu et al., 2004; Xu et al., 2006a). The UHP rocks were later overprinted by amphibolite-facies retrograde metamorphism at 207-219 Ma, 209-220 Ma, or 214-221 Ma (Xu et al., 2009). SHRIMP U-Pb dating of zircons from the coesite-bearing calcite and dolomite marbles also identifies three discrete and meaningful age groups: the prograde quartz eclogite facies metamorphism at 240-252 Ma, the UHP peak metamorphic event at 230-237 Ma and amphibolites facies metamorphism at 207-218 Ma (Liu et al., 2006).

2.5.3 ^{40}Ar-^{39}Ar ages of ductile shear zones

Xu et al. (2006a, 2009) determined ^{40}Ar-^{39}Ar ages of biotite crystals formed in the foliation planes of the ductile shear zones and other metamorphic rocks in various UHP slices of the CCSD-MH. The ^{40}Ar-^{39}Ar plateau ages of biotite from the mylonitic gneisses of the ductile shear zone DFc range from 203.26±0.83 Ma to 213.38±0.81 Ma, and the isochron ages vary from 202.5±1.1 Ma to 218.7±4.4 Ma. The shear zone DFa displays similar ^{40}Ar-^{39}Ar plateau and isochron ages to DFc (Xu et al., 2006a). The ^{40}Ar-^{39}Ar plateau ages of biotite from gneisses in the tectonic slice B between shear zones DFa and DFb range from 203.0±1.1 Ma to 212.3±1.0 Ma, and the isochron ages vary from 201.9±3.2 Ma to 223.0±3.3 Ma (Fig. 2.8 and Table 2.3). Therefore, these ductile shear zones formed during the exhumation stage.

It is worthy to mention that ^{40}Ar-^{39}Ar plateau ages of the ductile normal shear zones in the north of the UHP metamorphic slice UHP_N (e.g., samples from Weihai, the south Linshu and the southeast Linshu) are 116.9±0.8 Ma, 130.3±4.3 Ma, and 138.8±0.9 Ma. These ages correspond to the formation of normal shear zones during the doming stage of post exhumation.

Table 2.3 Age spectrum of cores from the CCSD-MH

No.	Depth (m)	Petrology	Protolith age (Ma)	UHP metamorphic age (Ma)	Uplift ages (Ma)	Method	Reference
1	0.00	Eclogite			87.1	AFT	Liu et al., 2009
2	101.00	Eclogite			89.0	AFT	Liu et al., 2009
3	131.60	Garnet/feldspar-amphibolite	659-520	239-225		SHRIMP U-Pb	Liu et al., 2007
				219-210			
4	249.50	Eclogite		220±11		SHRIMP U-Pb	Zhang et al., 2007
5	256.02	Eclogite			84.9	AFT	Liu et al., 2009
6	316.73	Eclogite			79.3	AFT	Liu et al., 2009
7	368.00	Eclogite		221.6±3.8		LA-ICP-MS	Zhang et al., 2007
8	369.00	Eclogite		222.0±4.7		LA-ICP-MS	Zhang et al., 2007
9	424.61	Eclogite			56.4	AFT	Liu et al., 2009
10	521.75	Eclogite			50.6	AFT	Liu et al., 2009
11	643.80	Eclogite		216.8±8.7		SHRIMP U-Pb	Zhang et al., 2007
12	728.00	Eclogite		220.0±13		SHRIMP U-Pb	Zhang et al., 2007
13	812.30	Gneiss		220.0±8		SHRIMP U-Pb	Zhang et al., 2007
14	824.00	Paragneiss	659-313	239-222		SHRIMP U-Pb	Liu et al., 2006
				219-207			
15	891.00	Mylonitic paragneiss (DF1)		210.90±1.05		^{40}Ar-^{39}Ar (bi)	Xu et al., 2009
				218.73±4.37			
16	904.10	Gneiss (DF1)	730.5±23	232±6		SHRIMP U-Pb	Xu et al., 2006a,b
17	930.20	Gneiss (DF1)		220.5±9.4		SHRIMP U-Pb	Zhang et al., 2007
18	960.10	Mylonitic paragneiss (DF1)		214.12±4.28		^{40}Ar-^{39}Ar (bi)	Xu et al., 2009
				214.12±4.28			
19	963.20	Eclogite		243.0±8		SHRIMP U-Pb	Xu et al., 2006a,b
				220.0±7			
20	959.20	Gneiss (DF1)	621±14	238±8		SHRIMP U-Pb	Xu et al., 2006a,b
				219±5			
21	1043.40	Gneiss (DF1)	680±14	211±6		SHRIMP U-Pb	Xu et al., 2006a,b
22	1074.30	Eclogite (DF1)		221.5±3.3		LA-ICP-MS	Zhang et al., 2007
23	1097.10	Mylonitic paragneiss (DF1)		200.86±1.14		^{40}Ar-^{39}Ar (bi)	Xu et al., 2009
				198.22±3.96			
24	1109.30	Gneiss (DF1)		217.4±3.6		LA-ICP-MS	Zhang et al., 2007
25	1130.10	Mylonitic paragneiss (DF1)		202.40±1.04		^{40}Ar-^{39}Ar (bi)	Xu et al., 2009
				201.14±3.02			
26	1147.70	Paragneiss			40.0	AFT	Liu et al., 2007
27	1148.50	Granitic gneiss		203.14±1.04		^{40}Ar-^{39}Ar (bi)	Xu et al., 2009
				202. 41±3.04			
28	1174.30	Granitic gneiss	780.7±4.9			SHRIMP U-Pb	Xu et al., 2006a,b
29	1262.10	Granitic gneiss		202. 95±1.05		^{40}Ar-^{39}Ar (bi)	Xu et al., 2009
				201.89±3.23			
30	1262.30	Orthogneiss			36.9	AFT	
31	1264.30	Granitic gneiss		212.34±1.01		^{40}Ar-^{39}Ar (bi)	Xu et al., 2009
				222.95±3.34			
32	1302.10	Granitic gneiss		211.74±1.04		^{40}Ar-^{39}Ar (bi)	Xu et al., 2009
				220.14±3.00			
33	1325.20	Granitic gneiss	800-810	236-220		SHRIMP U-Pb	Liu et al., 2004a,b
				215-203			
34	1417.10	Orthogneiss			32.7	AFT	Liu et al., 2009
35	1425.40	Gneiss		223.0±16		SHRIMP U-Pb	Zhang et al., 2007
36	1531.00	Orthogneiss			34.7	AFT	Liu et al., 2009
37	2204.50	Gneiss			26.4	AFT	Liu et al., 2009
38	2299.00	Amphibolite			25.2	AFT	Liu et al., 2009
39	2566.00	Gneiss	767±29			LA-ICP-MS	Zhang et al., 2007
40	2687.00	Eclogite		214.2±2.7		LA-ICP-MS	Zhang et al., 2007

Table 2.3 (continued)

No.	Depth (m)	Petrology	Protolith age (Ma)	UHP metamorphic age (Ma)	Uplift ages (Ma)	Method	Reference
41	2698.90	Gneiss		217.2±1.8		LA-ICP-MS	Zhang et al., 2007
42	2710.60	Eclogite		218.2±3.3		LA-ICP-MS	Zhang et al., 2007
43	2800.30	Gneiss			20.0	AFT	Liu et al., 2009
44	2899.40	Gneiss			25.0	AFT	Liu et al., 2009
45	2925.40	Granitic gneiss (DF3)		203.26±0.85		^{40}Ar-^{39}Ar (bi)	Xu et al., 2009
				202.48±1.07			
46	2949.30	Granitic gneiss (DF3)		213.38±0.81		^{40}Ar-^{39}Ar (bi)	Xu et al., 2009
				212.35±0.85			
47	2997.90	Gneiss			12.7	AFT	Liu et al., 2009
48	3062.10	Gneiss		217.3±3.4		LA-ICP-MS	Zhang et al., 2007
49	3299.90	Eclogite			25.8	AFT	Liu et al., 2009
50	3325.80	Gneiss		221.2±3.7		SHRIMP U-Pb	Zhang et al., 2007
51	3400.00	Gneiss			19.1	AFT	Liu et al., 2009
52	3500.30	Gneiss			8.7	AFT	Liu et al., 2009
53	3600.10	Gneiss			3.4	AFT	Liu et al., 2009
54	3899.30	Gneiss			3.2	AFT	Liu et al., 2009
55	3949.70	Gneiss	776±19			LA-ICP-MS	Zhang et al., 2007
56	5084.90	Garnet-amphibolite	765±15	218.0±8Ma		SHRIMP U-Pb	Xu et al., 2006a,b

2.5.4 Apatite fission track (AFT) ages

Recently, Liu et al. (2009) carried out an apatite fission track (AFT) analysis of the core samples from the CCSD mainhole between 0 and 4000 m depth. The AFT age varies from 87.1 ± 11.2 Ma at the surface to 3.2 ± 1.3 Ma at 3899 m, showing a general trend of decreasing AFT age with depth (Fig. 2.9a). This observation is consistent with previous data from the KTB (German Continental Deep Drilling Project) that the AFT age decreases gradually with increasing depth from the surface to about 4000 m (Coyle et al., 1997, Fig. 2.9b). The AFT age of the surface rock from the CCSD site is comparable with those from the other sites in the Sulu HP and UHP metamorphic belts (Fig. 2.10). As the complete annealing of fission tracks in apatite needs keeping the rock at about 110 °C for a period of about 10 Ma, the critical temperature above which fission tracks are annealed is generally set to be 120 °C (Ketcham et al., 1999). Thus, an AFT age represents the time when the rock sample cooled below the temperature of effective track retention (say 110-120 °C). According to Liu et al. (2009), the depths between 0 and 1810 m represent a stable region for AFT (<60 °C), between 1810 and 4150 m is a partially stable region (60-120 °C), and the region below 4150 m is a complete AFT

annealing zone. From the above data, Liu et al. (2009) obtained an average uplift rate of ~35 m/Ma between 90 and 30 Ma for the Sulu region.

Furthermore, the present-day geothermal gradient in the Sulu region is about 24.8±3.4 °C/km (He et al., 2006). Temperature at the bottom of the CCSD main borehole (5118 m) is measured to be 110 °C. Approximately, 1.6 km of the uppermost crustal rocks at the CCSD site has been exhumed since the Oligocene.

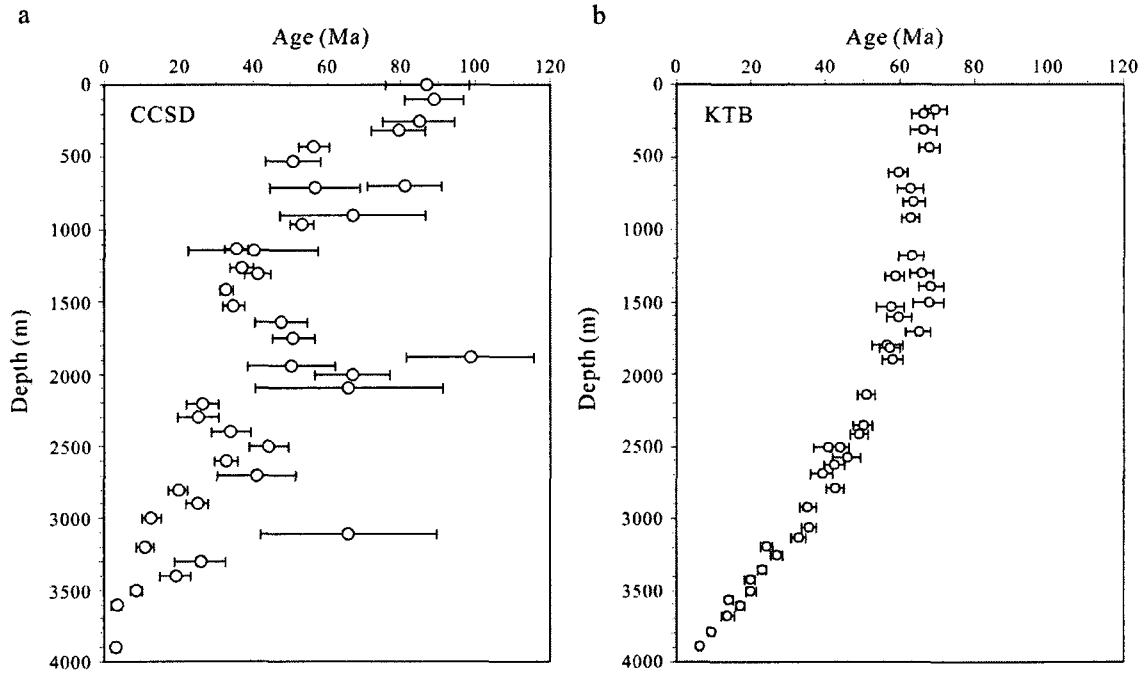

Figure 2.9 Comparation of apatite fission track (AFT) data between the CCSD and KTB projects.

2.6 Garnet peridotite

The main hole (MH), and pre-pilot holes PP1, and PP3 of the CCSD Project penetrated three different garnet peridotite bodies in the Sulu ultrahigh pressure (UHP) metamorphic belt, which are 80 m, 120 m, and 430 m thick, respectively. The bodies

occur as tectonic blocks hosted in eclogite (MH peridotite) and gneisses (PP1 and PP3 peridotites).

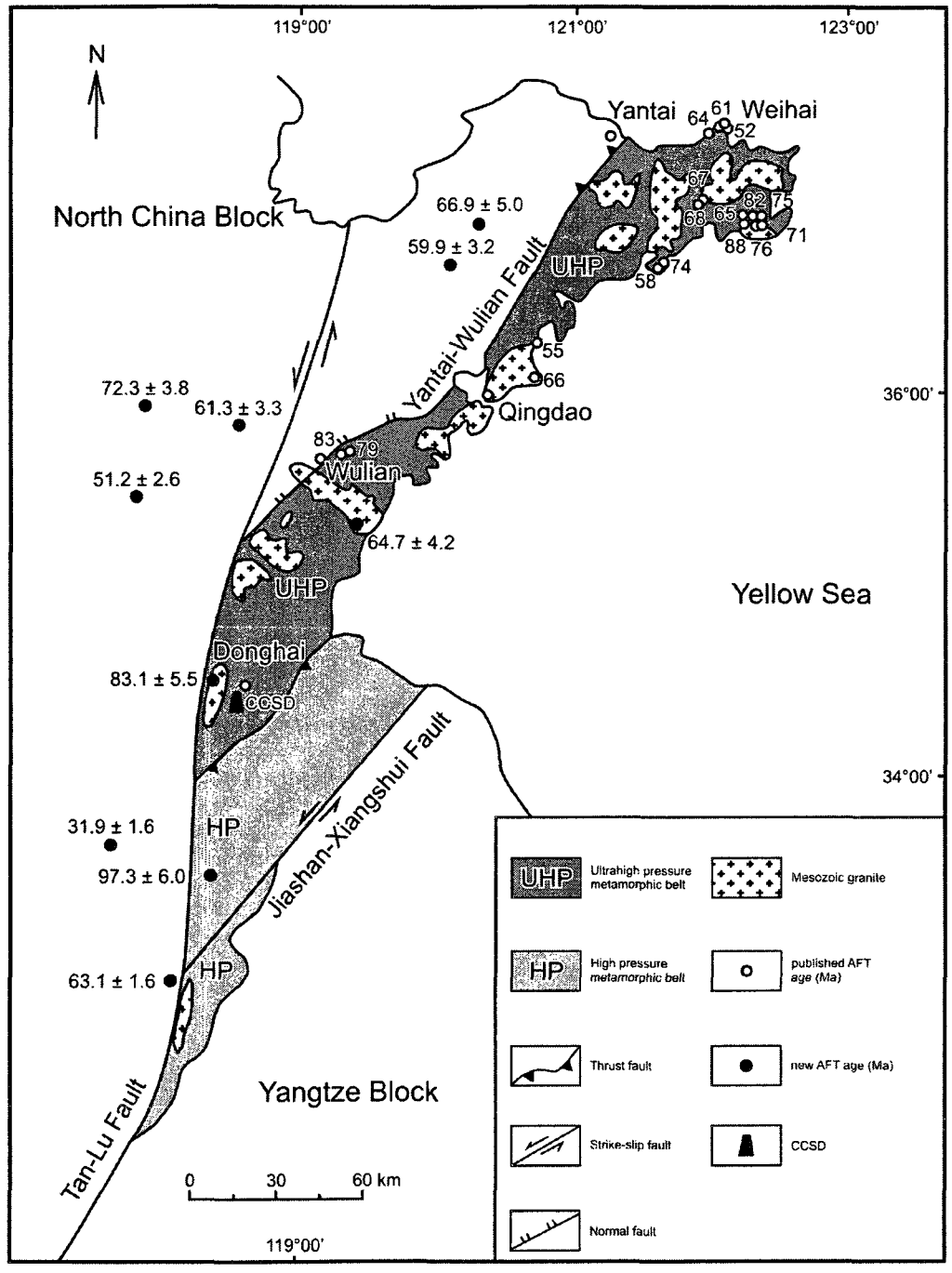

Figure 2.10 Distribution of AFT ages in the Sulu region (Modified from Xu et al., 2006)

The peridotites in MH are garnet wehrlites, whose protoliths were ultramafic, cumulates based on olivine compositions (Fo79-89) and other geochemical features (Yang et al., 2009). Zoned garnet and omphacite (with 4-5 wt% Na_2O) are typical metamorphic minerals in these ultramafic rocks. P-T estimates based on mineral pairs suggest that the rocks have undergone ultrahigh pressure metamorphism. SHRIMP U-Pb isotope dating zircon from the garnet wehrlite (Yang et al., 2009) yielded a Paleozoic protolith age (346-461 Ma), and a Mesozoic UHP metamorphic age (ca. 220-240 Ma).

The peridotites in PP1 consist of interlayered garnet (Grt)-bearing and garnet-free (GF) peridotite. Both types of peridotite have depleted mantle compositions ($Mg^{\#}$=90-92) and display transitional geochemical variations between them. The intercalated layers probably reflect variations in partial melting rather than pressure variations during metamorphism, and the garnets may have been formed by exsolution from orthopyroxene during exhumation. According to Yang et al. (2009), these peridotites were probably part of the mantle wedge above the subduction zone and thus belonged to the North China Block before its tectonic emplacement. The exhumation of the subducted Yangtze Block brought these mantle fragments to shallow crustal levels (Zhang et al., 2000, 2005; Yang et al., 2003).

The ultramafic rocks in PP3 are dominantly dunite with minor garnet dunite (Yang et al., 2009). Their high $Mg^{\#}$ (92-93) and relatively uniform chemical compositions indicate that they are part of a depleted mantle sequence. The presence of garnet replacing spinel and enclosing pre-metamorphic minerals such as olivine, clinopyroxene and spinel suggests that these rocks have undergone progressive metamorphism. SHRIMP U-Pb isotope dating of zircon from these rocks yielded two age groups: 726±56 Ma for relic magmatic zircon grains and 240±2.7 Ma for the newly formed metamorphic zircon. The older group is similar in age to granitic intrusions within the Dabie-Sulu belt, suggesting that the PP3 garnet peridotite may record the early

emplacement of the peridotite into the crust. The younger dates coincide with the age of UHP metamorphism during continent-continent collision between the Yangtze and North China Blocks, suggesting that these peridotites were subducted to depths equivalent to the coesite facies and later exhumed (Yang et al., 2007).

Figure 2.11 schematically illustrates a model proposed recently by Yang et al. (2009) for the history of the garnet peridotites from the main hole (MH), and pre-pilot holes PP1, and PP3 of the CCSD Project. According the authors, the MH and PP3 peridotites were originally located in the subducted slab while the PP1 rocks, which were a piece of the mantle wedge above the subducted slab, were brought to the surface during exhumation of the subducted slab. In other words, the PP1 peridotite would originally have been part of the North China Block. The model shown in Fig. 2.11 explains 3 stages of geological processes:

(1) The Yangtze Block started to subduct beneath the North China Block at about 250 Ma when the MH and PP3 peridotites were located in the subducting crust and PP1 peridotites were located in the mantle wedge above the subduction zone.

(2) The MH and PP3 peridotites were subducted into the mantle where they underwent UHP metamorphism at ~250-220 Ma. The PP1 peridotites remained in their original position.

(3) During exhumation of the subducted slab the peridotites of PP1 were plucked from the mantle wedge and brought to the surface together with the MH and PP3 peridotites at about 220-200 Ma.

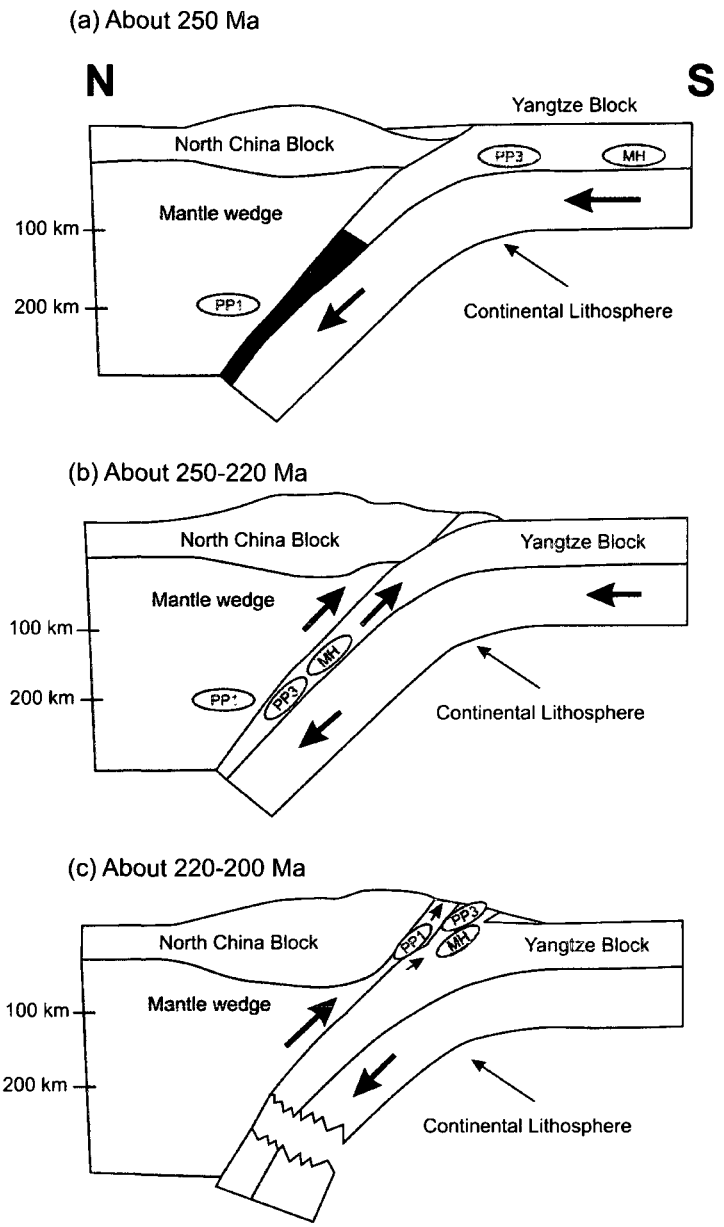

Figure 2.11 Generalized cross-sections showing possible models for emplacement of the garnet peridotites from the CCSD MH, PP1 and PP3. (a) The Yangtze Block started to subduct beneath the North China Block at about 250 Ma when the MH and PP3 peridotites were located in the subducting crust and PP1 peridotites were located in the mantle wedge above the subduction zone. (b) The MH and PP3 peridotites were subducted into the mantle where they underwent UHP metamorphism at ~250-220 Ma. The PP1 peridotites remained in their original positions. (c) During exhumation of the subducted slab the peridotites of PP1 were plucked from the mantle wedge and brought to the surface together with the MH and PP3 peridotites at about 220-200 Ma. (Modified from Yang et al., 2009)

2.7 Rheology during formation and exhumation of the orogenic deep root

Petrofabrics and microstructures of omphacite, garnet, olivine, and quartz in samples collected from the CCSD-MH, the pilot hole CCSD-PP1 and surface outcrops have been analyzed by Ji et al. (2003), Xu et al. (2006, 2009), Ji et al. (2007) and Wang et al. (2007, 2009) using both optical microscope and SEM-electron back-scattered diffraction techniques. The studied samples are mainly UHP eclogite and garnet peridotite, and amphibolite-facies mylonites from exhumation-related ductile shear zones.

Observations of optical microstructures, petrofabrics and TEM structures by Ji et al. (2003) have distinguished two types of eclogites from the Sulu UHP metamorphic belt: the coarse-grained (Type-1) and fine-grained (Type-2) eclogites, which recorded two distinct plastic deformations: constrictional strain (L>>S) in Type-1 eclogites while plane strain in Type-2 eclogites. Omphacite, which could be only a few times lower in flow strength than garnet, deformed mainly by dislocation creep as demonstrated by the occurrence of CPOs. Plastic deformation of garnet in Type-1 eclogites was dominated by recovery-accommodated dislocation creep as testified by the pervasive presence of dislocation walls and networks, whereas garnet in Type-2 eclogites was deformed by recrystallization-accommodated dislocation creep as indicated by the presence of porphyroclastic texture. As <111> dislocations are commonly dissociated into two partials 1/2<111> in bcc garnet, the cross slip of <111> dislocations, which is sensitive to the hydrostatic pressure, may be the factor that controls the transition from recovery-accommodated dislocation creep at higher pressures (P>~3.2 GPa) to recrystallization-accommodated dislocation creep at lower pressures (P<~2.8 GPa). According to these authors, Type-1 eclogites represent the subducted mafic rocks deformed at the peak metamorphic conditions while Type-2 eclogites resulted from recrystallization of Type-1 eclogites along some shear zones which were active during the exhumation of the UHP metamorphic rocks.

Because both garnet and omphacite in these eclogites deformed plastically and the flow strength contrast between these two constituent minerals is apparently much less than an order of magnitude under the UHP metamorphic conditions. Ji et al. (2003) suggest that plasticity of eclogites under UHP conditions may effectively facilitate channeled flow along the interplate shear zone. The enhanced counterflow within a wedge-shaped flow channel may force the subducted crustal rocks to be rapidly exhumed.

The SEM-EBSD measurements of the eclogites reveal random lattice-preferred orientations (LPO) for garnet and pronounced LPO for omphacite: [001] sub-parallel to the lineation and (010) subparallel to the foliation (Ji et al., 2003; Xu et al., 2006, 2009). The fabric asymmetry of omphacite with respect to the structural framework (i.e., foliation and lineation) recorded a top-to-south shear event during subduction of the Yangtze Block. In the eclogite samples, the calculated fastest P-wave velocity (V_p) is generally sub-parallel to the lineation, but subsequent deformation events during exhumation could have added second-order variations to the LPO pattern of omphacite and further affect the V_p distribution in eclogites (Xu et al., 2009). Comparison between measured and calculated seismic properties indicates that the LPO of omphacite controls the seismic anisotropy of eclogites, and the presence of compositional layering and retrograde minerals will increase the anisotropy (Ji et al., 2003). In addition to the fabric-induced anisotropy, the direction-dependence of pressure and temperature derivatives of V_p may significantly increase seismic anisotropy of eclogites with depth (Wang et al., 2009), making deformed eclogites a potential candidate for the source of seismic anisotropy in the upper mantle.

As described previously, the packages of interlayered eclogite, marble, quartzite, pelitic and felsic gneisses from the Dabie-Sulu UHP metamorphic belt, which were pieces of the continental crust, were subducted to mantle depths greater than 80-100 km and then tectonically exhumed to the Earth's surface. Field and laboratory studies of

these UHP metamorphic rocks provided some important hints for understanding the origin of mantle reflections. As long as these interlayered UHP rocks remain within the present upper mantle, the interfaces between eclogite (or peridotite) and their wall rocks such as quartzite, marble, pelitic and felsic gneisses should be strong seismic reflectors. The continuous boundaries between garnet- and omphacite-rich layers or between peridotite and garnet-rich eclogite layers can also be seismically reflective. Thus, the regionally extensive seismic reflectors from the upper mantle may indicate the preservation of relict crustal materials subducted within the continental lithosphere.

2.8 Subduction/exhumation/uplift history of the Sulu UHP rocks

As described in Section 2.5, SHRIMP U-Pb ages of zircons from the Sulu UHP metamorphic rocks suggests that voluminous pre-Triassic continental material experienced prograde metamorphism under eclogite-facies at 240-252 Ma, UHP peak metamorphic event followed at 230-237 Ma, and later amphibolite-facies retrograde metamorphism took place at 207-218 Ma. The major ductile shear zones in the metamorphic rocks formed at 200-210 Ma under the amphibolite-greenschist facies (650 - <350 °C) and corresponded to about 20-15 km depth within the crust, indicating that these shear zones were active at the late exhumation stage.

^{40}Ar-^{39}Ar dating on biotite from the HP metamorphic rocks indicates that the exhumation age of the HP metamorphic rocks ranges from 253-243 to 214 Ma (Xu et al., 2006a, 2009). The subduction age of the HP rocks, which is >253 Ma, is older than that of the UHP rocks. Combining the geochronological data with the P-T estimations for HP-LT, HP-MT and UHP rocks, recently Xu et al. (2009) proposed a P-T-t-D (Pressure-Temperature-Time-Deformation) path (Fig. 2.12) for the HP-UHP metamorphic rocks of the Sulu terrane. The continental slab was subducted from ~30 km (HP peak metamorphism) to 150 km (UHP peak metamorphism) at 260-254 Ma to 237-230 Ma. The subduction rate is estimated to be about 4.8-6.1 km/Ma (Fig. 2.9). The

continental slab was exhumed from about 150 km to 15-20 km, accompanied by the formation of ductile shear zones (amphibolite-greenschist facies), from ~237-230 Ma to 220-200 Ma. The exhumation rate was about 5.2- 5.4 km/Ma (Fig. 2.9). These data show that the Sulu UHP metamorphic terrane underwent a fast subduction and a rapid exhumation. Because the North UHP metamorphic slice was intruded by the 225-205 Ma Shidao potassic granitic complex (Guo et al., 2005; Cheng and Chang, 2004; Yang et al., 2005; Lin et al., 1992), crustal partial melting and magma activities were coeval with exhumation.

The P-T-t path for the HP belt (Fig. 2.10) shows that the continental slab was subducted to a depth of 30 km to form HP metamorphism (0.7-0.85 GPa, 300-360 °C) before 253 Ma and then the HP slab started to be exhumed through the formation and development of ductile shear zones at 253-210 Ma. The P-T-t path for the very high pressure (VHP) belt (Fig. 2.10) shows that the continental slab was subducted to a depth of ~60 km at which the VHP metamorphism (1.5-2.5 GPa, 500-600 °C) took place. The precise age of the exhumation of the VHP slab is not yet available. The peak UHP metamorphism (4-5 GPa, 800-900 °C) occurred when the continental slab was subducted to a depth of ~150 km at about 230 Ma (Fig. 2.10). The subduction rate was about 4.8-6.0 km/Ma. Subsequently, the UHP slab was uplifted to the upper crust during 230-200 Ma at a rate of 4.0-4.5 km/Ma. The associated ductile shear zones formed mainly at 210-200 Ma.

During the post exhumation stage, large-scale granitic complexes were intruded into the North UHP metamorphic slice at 200-85 Ma. The North Sulu detachment (NSLD) was active at 145-65 Ma and the Laiyang Cretaceous basin formed during this period. Under tectonic extension, the exhumed crust formed a dome structure (Fig. 2.12). The uplift rates at 200-90 Ma and 90-30 Ma are estimated to be about 0.96 and 0.035 km/Ma, respectively (Fig. 2.10). It is thus inferred that the UHP metamorphic rocks

were subjected successively to fast subduction, fast uplift, slow early uplift and very slow late uplift (unroofing) processes (Figs. 2.9-2.10).

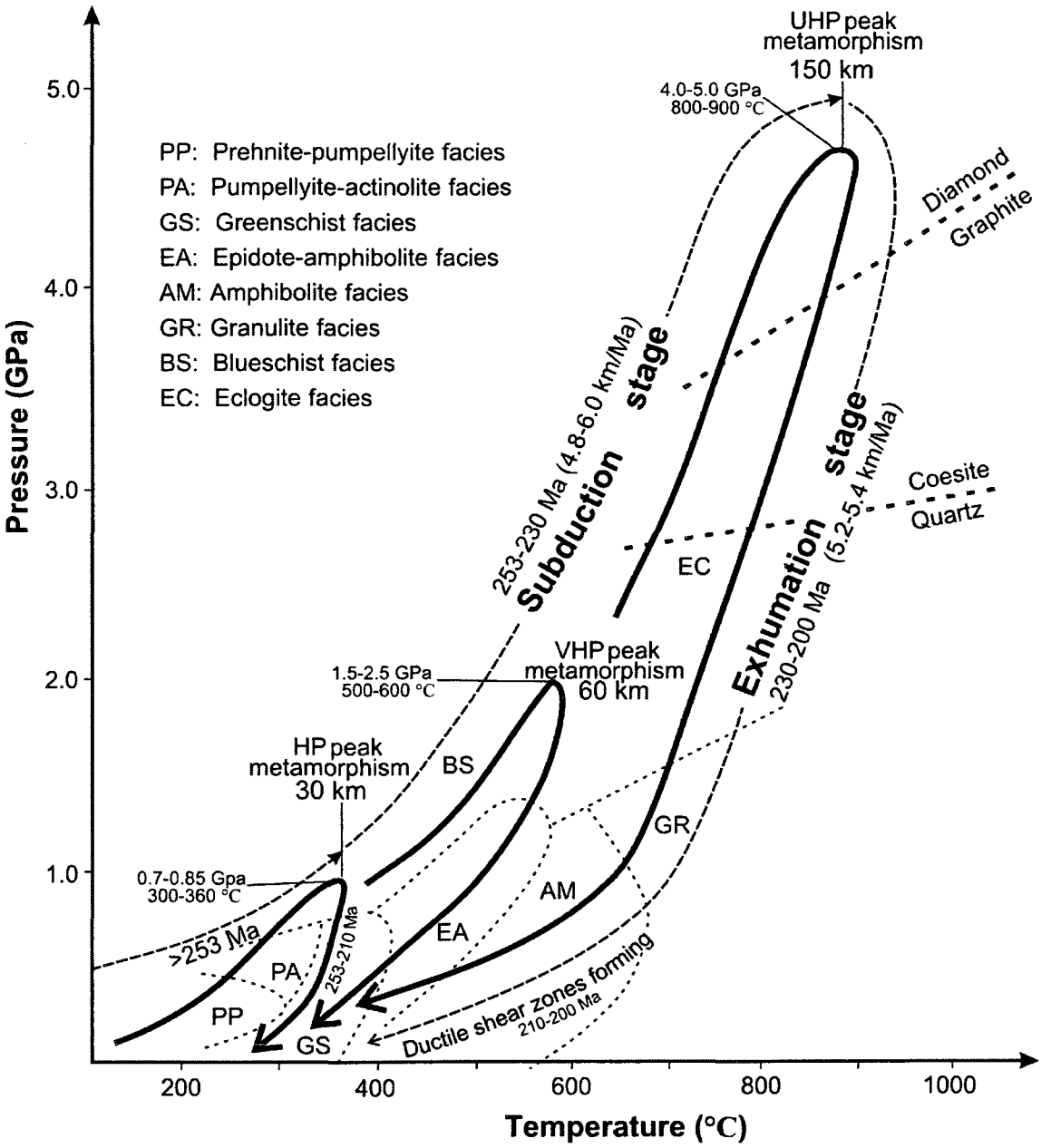

Figure 2.12 P-T-t paths of the HP, VHP and UHP metamorphic rocks in the Sulu terrane. (After Xu et al., 2009)

2.9 Exhumation structure of the Sulu orogenic deep root

The seismic reflection profiling of the CCSD project has allowed Xu et al. (2009) to conclude that the HP-UHP metamorphic slab in the Sulu terrane occurs as an eroded rootless dome structure (Fig. 2.3). The dome structure, which is composed of 4 tectonic slices from the south to north: HP (high metamorphic slice), VHP (very high pressure metamorphic slice), UHP_S (south UHP metamorphic slice) and UHP_N (north UHP metamorphic slice), is interpreted as an extrusion nappe. Translucent reflection lens, which appear beneath the nappe, probably represent a low density and low velocity magmatic chamber. This magmatic chamber could have been the source of the large-scale Mesozoic granite in the slice UHP_N.

The upper and lower parts of the extruded or napped Sulu orogenic deep root were deformed by normal shearing and thrusting, respectively (Fig. 2.3). The whole zone formed an exhumation channel along which the UHP metamorphic rocks flowed upwards. Subsequent doming modified the polarities of the channel boundaries; the normal sheared portion became the lower part while the thrust portion became the upper part (Xu et al., 2009). The subduction and exhumation of the HP and VHP metamorphic slices occurred earlier than that of the UHP metamorphic slices. Because of post-uplift unroofing and erosion, units HP, VHP and UHP_S were preserved in the south Sulu terrane and unit UHP_N was preserved as an antiformal structure in the north Sulu terrane (Fig. 2.3).

A tectonic model, which was proposed by Xu et al. (2009) for the formation and exhumation of the Sulu HP-UHP metamorphic slab (orogenic deep root), is summarized below:

(1) The upper crustal material of the Yangtze Block was first subducted to depths of ~30 km where they formed the HP metamorphic slice under the conditions of P=0.7-0.85 GPa and T=300-360 °C at 253 Ma, and then uplifted to the shallow crust at 253-210 Ma.

(2) The middle crustal material was subducted to depths of ~60 km and formed the VHP metamorphic slice under conditions of P=1.5-2.5 GPa and T=500-600 °C at ~253 Ma before being uplifted into the shallow crust.

(3) The lower crustal material was subducted to depths of >150 km and formed the UHP metamorphic slice under conditions of P=4.0-5.0 GPa and T=800-900 °C at ~230-237 Ma. From 237-200 Ma, the UHP metamorphic slice was progressively uplifted, subjected to retrograde metamorphism and developed amphibolite-greenschist facies ductile shear zones. Therefore, the superacrustal material in the Sulu orogenic belt did not act as a single block during either the subduction or exhumation. They were sliced into pieces by ductile shear zones and each piece developed its own subduction-exhumation history (Fig. 2.3). Neither subduction nor exhumation of the slices was initiated or ended at the same time. They were subducted or exhumed one after the other. These slices were independently extruded upwards from the deep root of the collision belt into the shallow crust as a dome-shaped nappe (Fig. 2.3). The upper and lower parts of the nappe are characterized by thrusting and normal shearing, respectively.

2.10 Summary

The Chinese Continental Scientific Drilling program (CCSD), which was designed to study the physical and chemical properties and tectonic processes of a continental orogenic deep root, drilled a 5158 m deep borehole into the Sulu UHP metamorphic terrane in Maobei village (Donghai County, Jiangsu Province, China). The deep drilling

was accompanied by various surface observations, horehole logs measuring petrophysical properties and chemical compositions, and comprehensive laboratory studies on core samples. The present investigation as an important part of the CCSD project was mainly focused on high pressure seismic P- and S- velocities, anisotropy, shear wave splitting, and Poisson's ratios of the HP and UHP metamorphic rocks. By comparing the lithological/structural profile and seismic reflection profile of the CCSD-MH, we can determine the spatial distribution of seismic reflectors and establish some reliable constraints on their origin in terms of petrophysical, compositional and structural properties. The CCSD main borehole results together with geological and geophysical data from the region allow us to build a 3D compositional and structural model for the deep root of the Sulu UHP orogenic belt. The exhumation structure of the Sulu orogenic deep root is characterized by a dome-extrusion nappe composed of 4 imbricate slices dipping gently to the SE. The slices are bounded by ductile shear zones. Ages of protolith, subduction, exhumation and uplift have been determined using zircon SHRIMP U-Pb, LA-ICP-MS, ^{40}Ar-^{39}Ar and AFT chronologic methods. The geochronological results reveal: (1) The Sulu HP-UHP terrane is composed of two basements: an early-middle Proterozoic (≥2.4 Ga) basement in the north and a Neoproterozoic (700-800 Ma) basement in the south. (2) UHP metamorphic rocks experienced successively a series of geological events; fast subduction (~4.8-6.1 km/Ma at 240-252 Ma, UHP peak metamorphism at 230-237 Ma, fast exhumation (~5.2- 5.4 km/Ma) at 230-200 Ma, slow uplift associated with tectonic extension (0.96 km/Ma) at 200-89 Ma, and unroofing (<35 m/Ma) since 89 Ma.

Chapter 3

P-wave velocities, anisotropy and hysteresis in ultrahigh-pressure metamorphic rocks as a function of confining pressure

3.1 Abstract

The Chinese Continental Drilling Project (CCSD) has drilled to a depth of 5100 m at Maobei (N34.40, E118.67), Donghai County, Jiangsu Province in the eastern segment of the Dabie-Sulu ultrahigh pressure (UHP) metamorphic terrane. The borehole, which penetrated through all of the high velocity layers and seismic reflectors observed within the uppermost crust on seismic refraction and reflection profiles, reveals the main lithologies to be coesite-bearing felsic gneisses, metabasic rocks (i.e., amphibolite, retrogressed and non-retrogressed eclogites) and ultramafic rocks (i.e., garnet peridotite and serpentinite). P-wave velocities, anisotropy and hysteresis of 31 typical CCSD core samples and 35 representative surface samples collected from the Sulu UHP belt were measured at hydrostatic confining pressures up to 800 MPa. The velocity-pressure curves can be well described by a four-parameter exponential equation derived from theory: $V(P) = V_0 + DP - B_0 \exp(-kP)$, where V_0 is the projected velocity at zero pressure if pores/cracks were absent; D is the intrinsic pressure derivative of velocity in the linear elastic regime; B_0 is the initial velocity drop caused by the presence of pores/cracks at zero pressure; and k is the decay constant of the velocity drop in the nonlinear poro-elastic regime. The seismic hysteresis is caused by irreversible changes in grain contact, increases in microcrack aspect ratios and reduction of void space during the pressurization-depressurization cycle. The statistical properties of P-wave velocities in

the UHP rocks provide an important set of basic information for the interpretation of field seismic data from the root zones of continental convergent orogenic belts and modern and ancient subduction zones.

3.2 Introduction

Our knowledge of the chemical composition, physical state and structure of the Earth's interior mainly comes from seismic data. Interpretation of seismic data, in turn, is largely constrained by the extrapolation of laboratory-measured seismic properties of relevant rocks thought to exist in a given geological and physical (i.e., pressure and temperature) environment. Apart from phase transformation, metamorphic reaction, dehydration and partial melting, temperature and confining pressure are two critical factors to affect elastic wave properties of dry crystalline rocks. Thus, laboratory studies of the temperature- and pressure-dependences of seismic velocities are particularly important for correct interpretation of seismic data.

During the past four decades a large number of laboratory measurements of P- and S-wave velocities and anisotropy have been performed on various types of rocks ranging from sedimentary rocks, igneous rocks and metamorphic rocks to upper mantle xenoliths. Recently in a 630-page handbook, Ji et al. (2002) summarized the available data on seismic velocities and anisotropy in minerals, rocks and ores. The studied samples were collected mainly from North America and Western Europe, Japan and the ocean basins (Figure 3.1). Despite several attempts, no consensus has been reached as to which equation can offer the best description of the pressure dependence of seismic velocities in natural rocks (e.g., Zimmerman, 1986; Wepfer and Christensen, 1991; Greenfield and Graham, 1996; Shapiro, 2003; Wang et al., 2005a) although such an equation would allow data to be accurately interpolated and extrapolated in the geological interpretation of seismic data. Such an equation should have clear physical meaning and include as few parameters as possible. Moreover, the equation would serve

as a standard expression for fitting the seismic velocity-confining pressure relation and the resultant parameters could be used for statistical analyses and classification of rock seismic properties in terms of chemistry, mineralogy, lithology and microstructure.

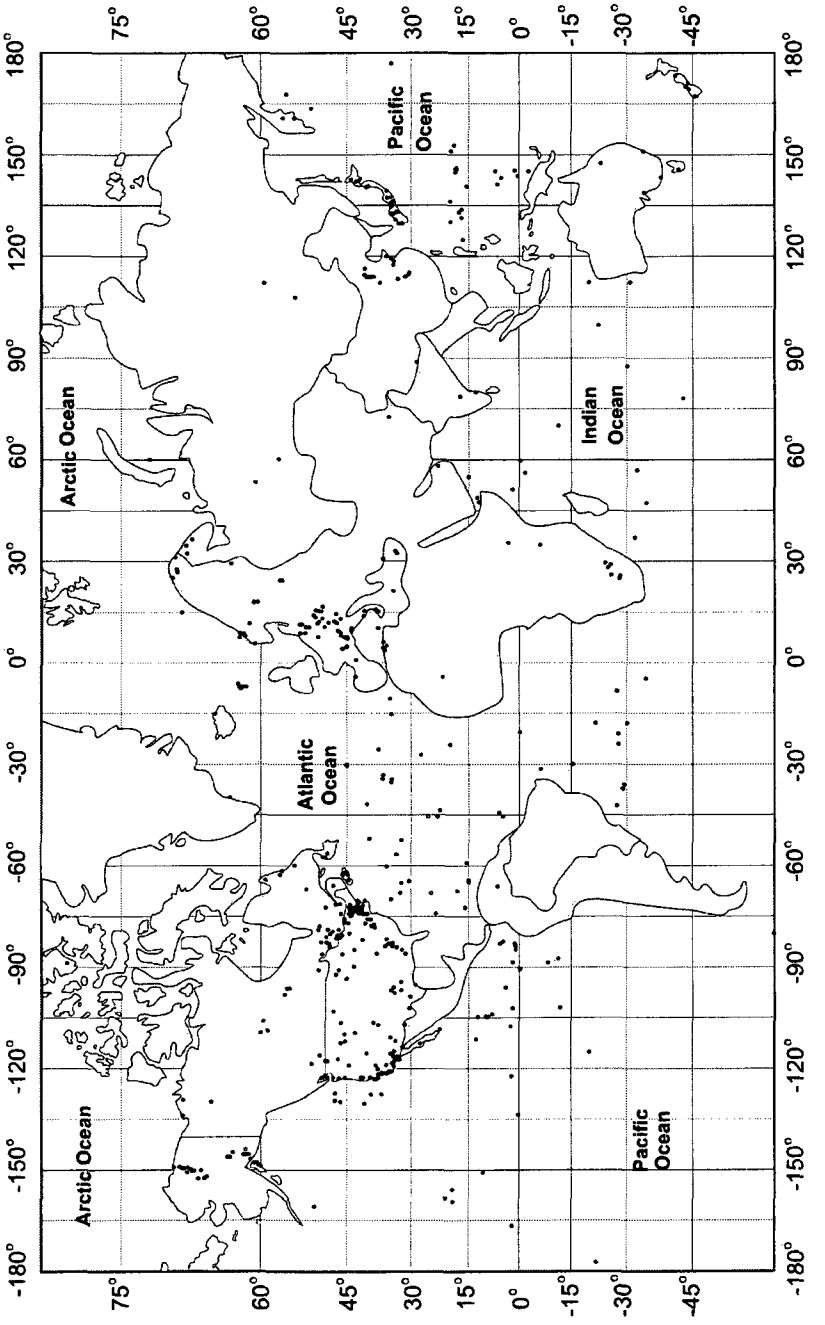

Figure 3.1 Map showing the locations of rock samples whose acoustic velocities have been experimentally measured during last 4 decades worldwide.

Seismic hysteresis, which is a physical phenomenon that rock seismic velocities measured during depressurization are higher than those measured during pressurization, is well-known but still poorly understood (Birch, 1960; Burke and Fountain, 1990). Is velocity hysteresis an important property of the UHP metamorphic rock samples collected from either the surface outcrops or boreholes? If a dry, highly compact, crystalline rock displays hysteresis, what is the directional variation with respect to structural features such as foliation and lineation? Is the amount of hysteresis related to the lithology, microstructure and exhumation history? Answers to these questions are critically important for understanding the origin and potential implications of seismic hysteresis.

Eclogites and related HP and UHP rocks are believed to comprise the high velocity layers and seismic reflectors in ancient and modern subducted slabs and in the root zones of continental convergent orogenic belts (e.g., Calvert et al., 1995; Bostock, 1997; Cook et al., 1999; Xu et al., 2001; Ji et al., 2003). Nevertheless, relatively few laboratory studies of seismic velocities and anisotropy have been made in these rocks because they are rarely found exposed on the surface (e.g., Kern et al., 1999 and 2002; Ji et al., 2003; Wang et al., 2005a and b). The Chinese Continental Drilling Project (CCSD) has drilled to a depth of 5100 meters at Maobei, Donghai County, Jiangsu Province in the eastern segment of the Dabie-Sulu UHP belt which is the largest UHP metamorphic belt recognized in the world (Figure 3.2). The CCSD main hole (N34.40, E118.67) is located about 30 km east of the Tan-Lu fault zone and approximately 70 km west of the Yellow Sea. The borehole penetrated through all of the high velocity layers and seismic reflectors observed within the uppermost crust on seismic refraction and reflection profiles (Yang et al., 1999; Yang, 2002). The lithological section in the depth 0-5100 m depth interval revealed by the CCSD main hole (Figure 3.3) consists of felsic orthogneiss and paragneiss, metabasic rocks such as amphibolite, retrogressed eclogite and non-retrogressed eclogite, and ultramafic rocks such as serpentinized garnet peridotite and serpentinite. Zircon SHRIMP U-Pb dating suggests that these rocks,

which have protolith ages of 700-780 Ma, were subjected to a peak UHP metamorphism at 220-240 Ma, closely followed by an amphibolite-facies retrograde metamorphism at 205-215 Ma (Liu et al., 2003; Zhang et al., 2005; Xu et al., 2006). The core samples from the CCSD pre-pilot and main holes (Figure 3.4) and surface samples collected from the surrounding areas offer an excellent opportunity to study the seismic properties of UHP metamorphic rocks.

In this chapter, we present new results on P-wave velocities (Vp), anisotropy and hysteresis as a function of confining pressure for representative CCSD core samples and Sulu surface rock samples, and discuss the implications of the results. We will derive from first principles a 4-parameter expression which has been used by previous authors as an empirical equation to describe the relationship between seismic velocity and confining pressure for crystalline rocks (e.g., Stierman et al., 1979; Greenfield and Graham, 1996; Wang et al., 2005a) and porous sedimentary rocks (e.g., Zimmerman et al., 1986; Eberhart-Phillips et al., 1989; Freund, 1992; Shapiro, 2003). Our derivation will clarify the physical meaning of each parameter in the equation. It will be shown that the equation can provide an excellent description of seismic velocities in the UHP metamorphic rocks. The data reported in this chapter provide an important set of basic information for the interpretation of seismic field studies from the root zones of continental convergent orogenic belts and modern and ancient subduction zones.

3.3 Samples

Table 3.1 gives the locality, recovery depth, lithology, density and modal composition for each of 37 samples studied. The modal composition was determined by point counting on thin sections cut perpendicular to the foliation and parallel to the lineation. The samples all are dry, highly compact rocks with porosities less than 0.1-0.2%. Twelve of the 37 samples were collected from the CCSD main borehole cores between 3000 and 4600 m depth. These core samples represent typical lithologies

(orthogneiss, paragneiss, amphibolite and retrogressed eclogite) in this depth interval (Figure 3.3). Nineteen samples were collected from the pre-pilot hole between 10-700 m. In this uppermost zone of the crust beneath the CCSD site, the typical lithologies are eclogites with various degrees of retrogression, ultramafic rocks (e.g., dunite, Grt harzburgite, lherzolite) with various degrees of serpentinization, and felsic orthogneiss (Figure 3.3). Sample MB-OU-14 from a fresh surface outcrop in a quarry at Maobei village near the CCSD site is a coarse-grained garnetite with a high density (3.56 g/cm^3). The petrological, geochemical and microstructural features of the UHP rocks from the study area were described in previous references (e.g., Ji et al., 2003; Zhang et al., 2003; You et al., 2004; Liu and Jin, 2006; Xu et al., 2004; Wang et al., 2005a and b; Zhang et al., 2005).

Five samples were collected from a layered UHP complex at Yangkou Beach which lies on Laoshan Bay, about 50 km northeast of Qingdao City. The complex consists of eclogites-facies metagabbro and serpentinized garnet peridotite blocks enclosed in granitic gneiss. The latter is a strongly deformed mylonite with well-developed foliation and stretching lineation. The metagabbro blocks show various degrees of transformation from incipiently metamorphosed gabbro with relict igneous textures and mineral assemblages to completely recrystallized coesite-bearing eclogite-facies rocks. Details of metamorphic reactions in these rocks were described in Zhang and Liou (1997). There are two special reasons for which the Yangkou samples were selected for the study: (1) the eclogitized metagabbro is regarded as a product of sluggish eclogitization which took place in a fluid-deficient environment because some of the primary igneous minerals and low-P assemblages persisted metastably under peak UHP conditions. (2) The complex was possibly subducted to depths greater than 200 km (P>7 GPa) as inferred from exsolutions of clinopyroxene, rutile and apatite in garnet (Ye et al., 2000) within the Yangkou eclogitized metaggabro although Zhang and Liou (1997) estimated the peak metamorphism at T = 800-850 °C and P≥3.0 GPa according to the overall mineral assemblages.

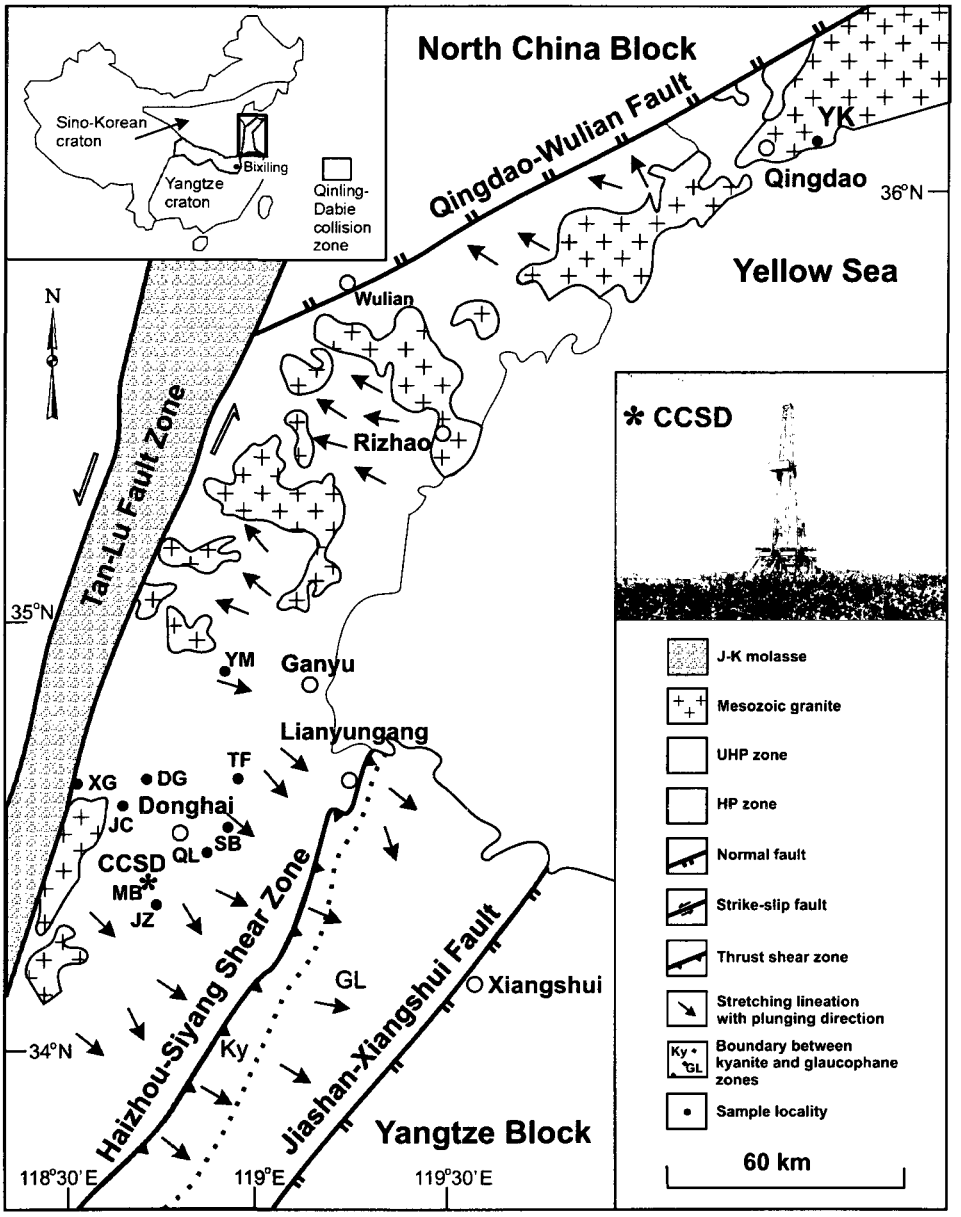

Figure 3.2 Simplified geological map of the Sulu metamorphic terrane, eastern China. Star shows location of drill site (Maobei, Donghai County, Jiangsu Province) of the Chinese Continental Scientific Drilling (CCSD) program. Sample localities are: DG, Dugou; JC, Jianchang; JZ, Jiangzhuang; MB, Maobei; QL, Qinglongshan; SB, Shanbeitou; TF, Tuofeng; XG, Xugou; YK, Yangkou, Qingdao; YM, Yanmachang.

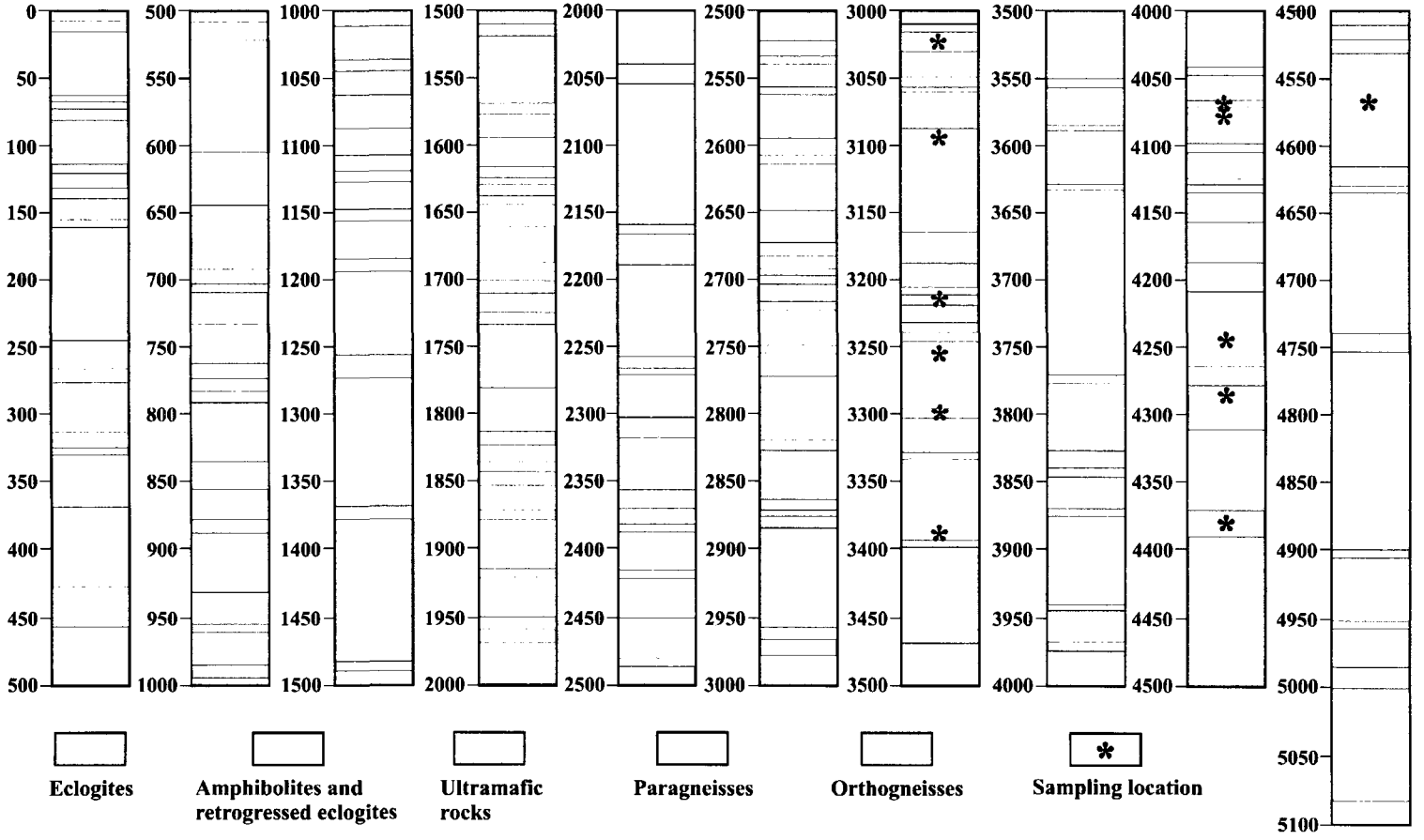

Figure 3.3 Lithological profile revealed by the CCSD main hole (0-5100 m). Stars indicate sample locations. Modified from Key Laboratory of continental Geodynamics, Ministry of Lands and Resources, China. 2006, Acta Geologica Sinica. 80. 12. 2-4. Scientific results from CCSD.

Table 3.2 lists the major element compositions for the 37 Sulu samples used in the study. The compositions were determined by X-ray fluorescence (XRF) in Guangzhou Institute of Geochemistry (China). The construction of Figure 3.5 was based on these results together with those of 29 other Sulu samples for which our group has reported velocities, modal and chemical compositions (Wang et al., 2005a). Figure 3.5a is a plot of Al_2O_3 versus SiO_2 for 8 major lithological categories: amphibolite, eclogite, gneiss, dolomitic marble, metagabbro, peridotite, retrogressed eclogite, and serpentitite. Three groups of chemical compositions can be clearly distinguished: (1) The ultramafic rocks (i.e., peridotite and serpentinite) are characterized by low contents of SiO_2 (< 46.5 wt%) and Al_2O_3 (mostly < 2 wt%). (2) The felsic orthogneiss and paragneiss samples are characterized by high contents of SiO_2 (mostly > 70 wt%) and intermediate contents of Al_2O_3 (10.5%-13.5%). Two samples (703-29 and 178-6-6) fall into the domain of intermediate rocks. (3) Eclogites and particularly retrogressed eclogites have compositions similar to metagabbros and amphibolites, all having high contents of Al_2O_3 (13.6-22.3 wt%) and intermediate contents of SiO_2 (41.8-59.0 wt%). The chemical characteristics of the eclogites display an affinity to continental basalts. The plots of MgO versus SiO_2 and Na_2O are illustrated in Figs. 3.5b and 3.5e, respectively. All of the studied rocks other than dolomitic marbles fall along a trend line showing a decrease in MgO with increasing SiO_2 and Na_2O. For all of the rocks except peridotites, serpentinites and dolomitic marbles, the CaO content decreases with increasing SiO_2 (Figure 3.5c). As shown in Figure 3.5d, $Na_2O + K_2O$ also increases gradually with increasing SiO_2 from ultramafic through mafic to felsic rocks. Furthermore, CaO contents increase with increasing MgO contents in felsic gneisses and mafic rocks such as amphibolite, metagabbro, eclogite and retrogressed eclogite (Figure 3.5f).

Bulk density data for 122 cylindrical samples from Sulu UHP metamorphic rocks are given in Figure 3.6. These data display several features. (1) Eclogites ($\overline{\rho}$=3.50) have significantly higher densities than their country rocks, for example, gneiss ($\overline{\rho}$=2.66), dolomitic marble ($\overline{\rho}$=2.86), amphibolite ($\overline{\rho}$=2.99), metagabbro ($\overline{\rho}$=3.02),

serpentinized peridotite ($\overline{\rho}$ =3.18) and serpentinite ($\overline{\rho}$ =2.58). (2) Metagabbro and amphibolite show similar densities and so do peridotite and retrogressed eclogite. (3) Metamorphic retrogression, which overprinted during exhumation, may lead to a continuous reduction in density from eclogite ($\overline{\rho}$ =3.50), through retrogressed eclogite ($\overline{\rho}$ =3.35), to amphibolite ($\overline{\rho}$ =2.99). This reflects the fact that with increasing retrogression, higher density garnet and omphacite, which are the main constituent minerals in eclogites, are progressively replaced by lower density plagioclase, amphibole, quartz, phengite, kyanite and epidote.

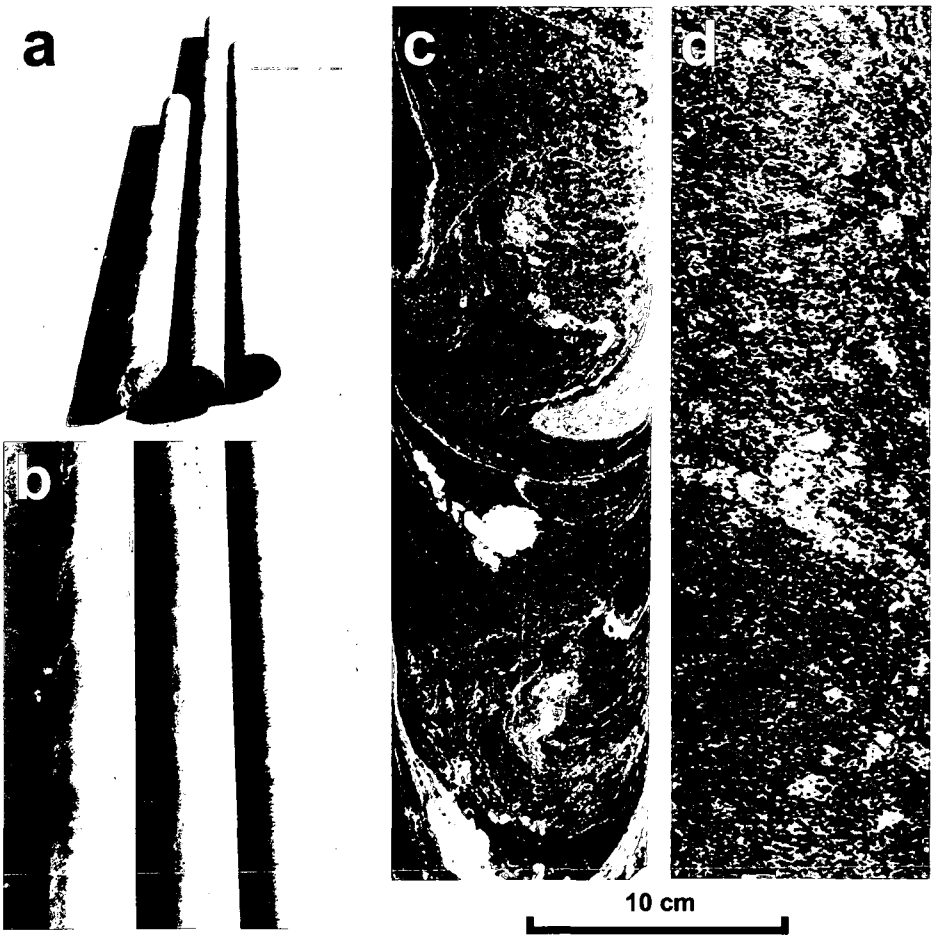

Figure 3.4 Typical cores from the CCSD main hole. The longest core in Figure 3.4a is 4.25 m. The core diameter is 10 cm (a-d). (c) gneiss, and (d) eclogite.

Table 3.1 Description of the study samples [a]

No.	Sample	Locality	Depth (m)	Lithology	Density (g/cm^3)	Modal composition (vol. %)
1	19-13-13	CCSD pre-pilot hole	14.42	Porphyroclastic granitic gneiss	2.64	Pl 31.0, Kfs 30.0, Qtz 34.0, Bt 4.0, Opq 1.0
2	26-10-17	CCSD pre-pilot hole	23.00	Porphyroclastic granitic gneiss	2.64	Pl 32.0, Kfs 31.0, Qtz 33.0, Bt 3.0, Opq 1.0
3	125-8-18	CCSD pre-pilot hole	128.30	Coarse-grained Qtz eclogite	3.38	Grt 40.0, Cpx 35.0, Amp 4.0, Symp 12.0, Qtz 7.0, Phn 1.5, Rt 0.5
4	125-15-18	CCSD pre-pilot hole	131.00	Coarse-grained Qtz eclogite	3.48	Grt 45.0, Cpx 31.0, Amp 6.5, Qtz 12.0, Phn 5.0, Rt 0.5
5	147-2-11	CCSD pre-pilot hole	168.50	Coarse-grained dunite	3.16	Ol 88.0, Srp11.0, Opq 1.0
6	150-3-20	CCSD pre-pilot hole	177.00	Coarse-grained lherzolite	3.12	Ol 70.0, Opx 8.0, Cpx 11.0, Srp 10.0, Opq 1.0
7	151-14-16	CCSD pre-pilot hole	184.00	Coarse-grained Grt harzburgite	3.21	Ol 68.0, Opx 14.0, Cpx 8.0, Grt 5.0, Srp 4.0, Phl 1.0
8	160-12-11	CCSD pre-pilot hole	210.50	Coarse-grained Grt harzburgite	3.17	Ol 67.0, Opx 10.0, Cpx 13.0, Grt 4.0, Srp 4.0, Phl 2.0
9	166-42-43	CCSD pre-pilot hole	227.00	Coarse-grained Phl dunite	3.25	Ol 86.0, Opx 2.0, Phl 4.0, Srp 5.0, Opq 3.0
10	703-29	CCSD pre-pilot hole	242.00	Fine-grained Grt-Bt-Hbl dioritic gneiss	2.93	Pl 44.0, Qtz 38.0, Amp 5.0, Grt 7.0, Bt 6.0,
11	178-6-6	CCSD pre-pilot hole	257.21	Fine-grained Bt dioritic gneiss	2.74	Pl 49.0, Qtz 37.0, Bt 12.0, Opq 2.0
12	203-5-15	CCSD pre-pilot hole	284.53	Fine-grained amphibolite	3.07	Pl 35.0, Amp 41.0, Bt 15.0, Qtz 8.0, Chl 1.0
13	210-15-21	CCSD pre-pilot hole	299.68	Porphyroclastic granitic gneiss	2.63	Pl 30.0, Kfs 35.0, Qtz 31.0, Bt 3.0, Opq 1.0
14	219-1-2	CCSD pre-pilot hole	304.77	Porphyroclastic granitic gneiss	2.63	Pl 32.0, Kfs 31.0, Qtz 30.0, Amp 3.0, Bt 3.0, Opq 1.0
15	315-1-11	CCSD pre-pilot hole	422.50	Moderate-grained Phn eclogite	3.43	Grt 36.0, Cpx 40.0, Amp 5.0, Phn 17.0, Qtz 1.0, Rt 1.0
16	315-4-11	CCSD pre-pilot hole	422.50	Fine-grained Phn eclogite	3.53	Grt 44.0, Cpx 46.0, Phn 5.0, Qtz 2.0, Rt 2.0, Opq. 1.0
17	C397 PC 2a	CCSD pre-pilot hole	679.90	Coarse-grained retrogressed Phn-Qtz eclogite	3.39	Grt 40.0, Cpx 30.0, Symp 15.0, Amp 3.5, Qtz 5.0, Phn 5.0, Rt 1.5
18	C398 PC 5b	CCSD pre-pilot hole	683.50	Coarse-grained Qtz eclogite	3.39	Grt 41.0, Cpx 39.0, Symp 8.0, Amp. 5.0, Phn 2.0, Qtz 5.0
19	C399 PC c1	CCSD pre-pilot hole	684.40	Moderate-grained retrogressed Qtz eclogite	3.24	Grt 35.0, Symp 34.0, Amp 8.0, Qtz 20.0, Bt 2.0, Rt 1.0
20	B1536R6P41e	CCSD main hole	3019.63	Fine-grained Hbl-Phn eclogite	3.11	Grt 26.0, Symp 47.0, Amp 9.0, Qtz 12.0, Phn 5.0, Rt. 1.0
21	B1578R14P18t	CCSD main hole	3092.00	Fine-grained Bt-Ms-Pl-Kfs orthogneiss	2.65	Pl 40.0, Kfs 25.0, Qtz 25.0, Ms 4.0, Bt 3.0, Grt 1.0, Opq 2.0
22	B1608R27P12e	CCSD main hole	3211.97	Fine-grained Grt-Bt-Pl amphibolite	2.98	Pl 42.0, Amp 40.0, Grt 4.0, Bt 8.0, Qtz 4.0, Chl 2.0
23	B1628R33P24	CCSD main hole	3254.50	Porphyroclastic Hbl-Mag felsic orthogneiss	2.65	Pl 38.0, Kfs 15.0, Qtz 35, Amp 7.0, Grt 1.5, Opq 2.0
24	B1651R37P41c	CCSD main hole	3297.21	Fine grained amphibolite	3.00	Amp 48.0, Chl 13.0, Grt 3.0, Cpx 15, Pl 12.0, Qtz 5.0, Ep 2.0, Opq 2.0
25	B1694R49P7s	CCSD main hole	3393.86	Porphyroclastic felsic orthogneiss	2.63	Pl 30.0, Kfs 42.0, Qtz 21.0, Cpx 4.0, Amp1.5, Opq 1.0, Rt 0.5
26	B2068R61P20h	CCSD main hole	4072.78	Fine-grained Bt-Pl amphibolite	2.85	Pl 39.0, Amp 39.0, Bt 12.0, Qtz 7.0, Chl 3.0
27	B2078R63P9r	CCSD main hole	4078.86	Porphyroclastic felsic orthogneiss	2.63	Pl 31.0, Kfs 35.0, Qtz 25.0, Bt 4.0, Amp 4.0, Opq 1.0
28	B2168R85P2a	CCSD main hole	4249.05	Fine-grained Bt-Hbl-Pl-Kfs paragneiss	2.65	Pl 39.0, Kfs 20.0, Qtz 30.0, Amp 6.0, Bt 4.0, Opq 1.0
29	B2184R88P4s	CCSD main hole	4276.28	Porphyroclastic Bt-Hbl-Pl-Kfs paragneiss	2.66	Pl. 40.0, Kfs 15.0, Qtz 40.0, Bt 4.0, Opq 1.0
30	B2242R100P16a	CCSD main hole	4385.74	Porphyroclastic Hbl-Bt-Pl-Kfs paragneiss	2.66	Pl 38, Kfs 18.0, Qtz 35.0, Amp 7.5, Opq 1.5
31	B2339R122P1f	CCSD main hole	4561.67	Porphyroclastic Hbl-Pl-Kfs paragneiss	2.65	Pl 42.0, Kfs 21.0, Qtz 25.0, Amp 8.0, Grt. 3.0, Opq 1.0
32	MB-OU-14	Maobei, Donghai	0.00	Coarse-grained Garnetite	3.56	Grt 82.0, Cpx 8.0, Phn 7.0, Rt 1.0, Qtz 2.0
33	Sulu-YK1	Yangkou, Qingdao	0.00	Fine-grained metagabbro	3.08	Pl 62.0, Cpx 5.0, Grt 15.0, Qtz 5.0, Ms 9.0, Chl 4.0
34	Sulu-YK2A	Yangkou, Qingdao	0.00	Fine-grained metagabbro	3.07	Pl 64.0, Cpx 5.0, Grt 12.0, Qtz 5.0, Ms 10.0, Chl 4.0
35	Sulu-YK3B	Yangkou, Qingdao	0.00	Fine-grained metagabbro	3.00	Pl 72.0, Cpx 4.0, Grt 8.0, Qtz 4.0, Ms 9.0, Chl 3.0
36	Sulu-YK9	Yangkou, Qingdao	0.00	Fibrous serpentinite	2.60	Srp 85.0, Tlc 10.0, Opq 5.0
37	Sulu-YK22	Yangkou, Qingdao	0.00	Fine-grained metagabbro	2.96	Pl 45.0, Cpx 14.0, Grt 9.0, Qtz 10.0, Ms 5.0, Chl 11.0, Zo 5.0, Opq. 1.0

[a] Abbreviations: Amp: amphibole; Bt: biotite; Chl: chlorite; Cpx: clinopyroxene; Ep: epidote; Grt: garnet; Hbl: hornblende; Kfs: K-feldspar; Mag: magnetite; Ms: muscovite; Ol: olivine; Opq: opaques; Opx: orthopyroxene; Phl: phlogopite; Phn: phengite; Pl: plagioclase; Qtz: quartz; Rt: rutile; Srp: serpentine; Symp: symplectite; Tlc: talc; Zo: zoisite.

Table 3.2 Chemical composition (wt.%) of UHP samples from Sulu

Sample	Lithology	SiO_2	TiO_2	Al_2O_3	Fe_2O_3	FeO	MnO	MgO	CaO	Na_2O	K_2O	P_2O_5	LOI	Total
19-13-13	Granitic gneiss	75.27	0.21	13.19	1.31	0.63	0.04	0.13	1.00	4.12	3.63	0.02	0.47	100.02
26-10-17	Granitic gneiss	75.69	0.23	12.84	0.92	0.82	0.05	0.18	1.01	4.00	3.47	0.02	0.44	99.66
125-8-18	Qtz eclogite	47.99	1.70	15.22	5.27	11.59	0.29	5.75	9.25	2.44	0.27	0.00	0.26	100.02
125-15-18	Qtz eclogite	48.78	1.45	15.29	6.38	9.16	0.25	5.80	8.92	2.82	0.93	0.07	0.39	100.24
147-2-11	Dunite	41.52	0.06	0.44	2.41	6.18	0.10	46.16	0.66	0.08	0.08	0.00	2.41	100.09
150-3-20	Lherzolite	42.36	0.04	0.63	2.61	5.50	0.10	45.48	0.31	0.04	0.04	0.00	2.92	100.01
151-14-16	Grt harzburgite	46.10	0.04	5.90	2.08	5.34	0.14	37.09	2.15	0.04	0.22	0.00	1.47	100.56
160-12-11	Grt harzburgite	44.06	0.04	1.70	1.96	5.89	0.09	42.08	1.65	0.25	0.10	0.00	2.21	100.02
166-42-43	Phl dunite	37.33	0.03	0.58	8.61	10.46	0.17	40.68	0.05	0.06	0.56	0.00	1.93	100.46
703-29	Grt-Bt-Hbl dioritic gneiss	59.59	1.18	14.42	3.96	7.02	0.40	2.13	6.18	3.38	1.18	0.49	0.21	100.14
178-6-6	Bt dioritic gneiss	67.38	0.56	13.76	1.92	3.32	0.12	3.12	2.83	2.93	3.63	0.08	0.42	100.08
203-5-15	Amphibolite	53.67	1.03	16.04	4.86	4.91	0.18	4.79	7.59	3.10	2.40	0.49	0.86	99.92
210-15-21	Granitic gneiss	74.43	0.28	13.53	0.85	0.96	0.04	0.23	1.04	4.28	3.98	0.03	0.25	99.90
219-1-2	Granitic gneiss	77.97	0.08	12.17	0.71	0.61	0.01	0.01	0.23	3.93	4.02	<0.01	0.21	99.97
315-1-11	Phn eclogite	44.80	1.25	16.48	3.93	7.91	0.18	9.31	10.46	2.27	1.29	0.66	1.27	99.80
315-4-11	Fine-grained Phn eclogite	44.65	1.35	16.34	3.56	8.68	0.19	9.99	10.87	2.22	0.62	0.56	0.55	99.56
C397 PC 2a	Retrogressed Phn-Qtz eclogite	48.42	1.72	15.94	5.29	9.46	0.21	6.39	8.39	3.01	0.80	0.11	0.71	100.45
C398 PC 5b	Qtz eclogite	44.79	1.77	16.29	4.52	11.19	0.23	7.32	10.44	2.75	0.27	0.12	0.71	100.39
C399 PC c1	Retrogressed Qtz eclogite	47.32	1.72	16.77	5.63	10.22	0.43	4.95	8.87	2.64	0.56	0.18	0.63	99.91
B1536R6P41e	Hbl-Phn eclogite	49.71	0.95	16.00	4.54	6.38	0.15	7.09	10.03	3.22	0.89	0.20	0.60	99.76
B1578R14P18t	Bt-Ms-Pl-Kfs orthogneiss	76.69	0.19	13.07	0.13	0.91	0.03	0.10	0.43	3.01	4.70	0.01	0.64	99.92
B1608R27P12e	Grt-Bt-Pl amphibolite	48.15	1.42	16.36	7.22	5.75	0.18	6.93	8.98	2.94	1.48	0.24	0.75	100.38
B1628R33P24	Hbl-Mag felsic orthogneiss	76.27	0.20	12.30	1.59	0.62	0.06	0.01	0.28	3.97	4.41	0.01	0.14	99.87
B1651R37P41c	Amphibolite	45.62	1.20	15.47	4.91	6.49	0.15	8.64	10.53	2.34	1.69	0.25	2.87	100.15
B1694R49P7s	Felsic orthogneiss	76.41	0.20	12.31	1.11	0.45	0.03	0.02	0.46	3.87	4.75	0.00	0.55	100.17
B2068R61P20h	Bt-Pl amphibolite	45.95	1.40	13.68	4.12	8.02	0.16	5.09	8.12	3.67	2.74	0.43	6.86	100.24
B2078R63P9r	Felsic orthogneiss	76.51	0.09	12.45	0.60	0.93	0.02	0.00	0.44	3.86	4.53	0.00	0.35	99.79
B2168RP85P2a	Bt-Hbl-Pl-Kfs paragneiss	73.88	0.25	13.40	0.95	1.46	0.03	0.21	0.98	3.54	4.95	0.03	0.31	100.00
B2184R88P4s	Bt-Hbl-Pl-Kfs paragneiss	73.84	0.29	12.75	1.46	1.41	0.04	0.26	1.10	3.49	4.57	0.04	0.47	99.71
B2242R100P16a	Hbl-Bt-Pl-Kfs paragneiss	75.00	0.22	12.46	1.10	1.40	0.05	0.05	0.72	3.65	4.94	0.02	0.46	100.06
B2339R122P1f	Hbl-Pl-Kfs paragneiss	73.86	0.28	13.09	1.22	1.52	0.04	0.20	1.00	3.93	4.61	0.03	0.39	100.18
MB-OU-14	Garnetite	44.02	0.16	19.81	3.01	8.86	0.18	11.16	11.29	1.88	0.01	0.01	0.27	100.65
Sulu-YK1	Metagabbro	51.25	1.20	17.48	6.42	5.08	0.21	3.91	8.16	3.78	1.06	0.29	0.98	99.82
Sulu-YK2A	Metagabbro	51.89	1.10	18.10	4.31	6.21	0.18	3.80	7.82	4.02	1.37	0.36	0.59	99.74
Sulu-YK3B	Metagabbro	54.09	1.06	18.36	3.33	5.94	0.17	3.24	7.44	3.88	1.22	0.29	0.79	99.80
Sulu-YK9	Serpentinite	38.28	0.06	1.48	6.95	2.22	0.12	38.15	0.02	0.02	0.01	0.00	12.51	99.82
Sulu-YK22	Metagabbro	54.88	0.99	18.78	3.78	4.53	0.16	3.12	6.88	3.96	1.62	0.39	0.71	99.80

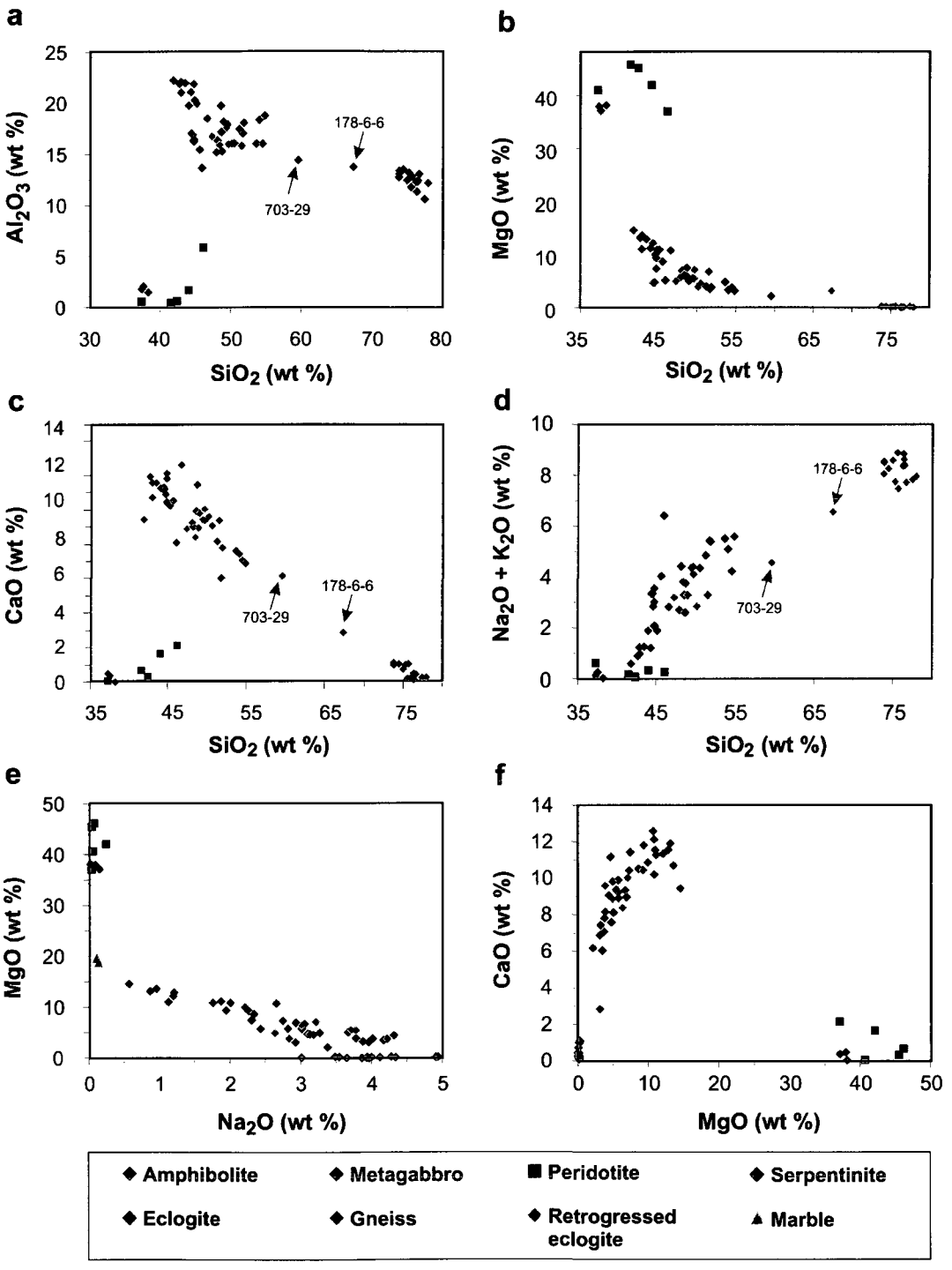

Figure 3.5 Plots of major element contents for Sulu UHP metamorphic rocks.

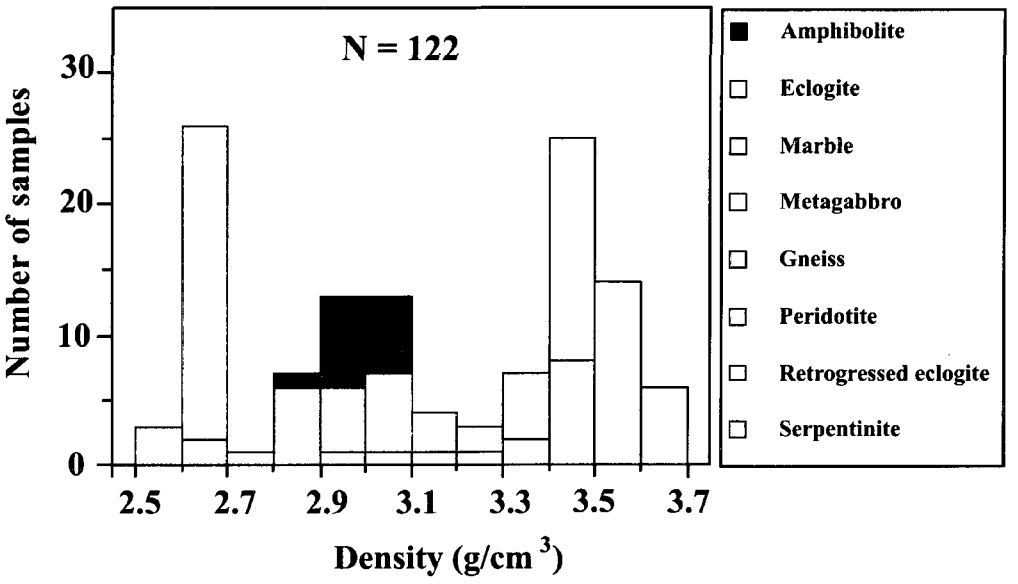

Figure 3.6 Histogram of density distribution for Sulu UHP metamorphic rocks.

3.4 Experimental techniques

Measurements of Vp were performed at confining pressures ranging from 10 to 800 MPa using the pulse transmission technique (Birch, 1960; Christensen, 1974). For each run, velocity measurements were performed first during pressurization and then depressurization in order to characterize the seismic hysteresis. All the studied samples display clearly defined foliation and lineation (e.g., Ji et al., 2003; Wang et al., 2005a; Xu et al., 2006). For most of the surface samples, three cylinders, 2.54 cm in diameter and 3-5 cm in length, were cut in orthogonal directions from each sample in order to study the seismic anisotropy, with the X direction parallel to the stretching lineation, the Y direction perpendicular to lineation and parallel to foliation, and the Z direction normal to foliation. For the core samples, only one (usually the Z-direction) or two directions (usually parallel to X and Z) were taken. Each cylinder was trimmed to ensure possession of two polished plan-parallel ends.

The Vp measurements were made on jacketed samples under hydrostatic conditions at the GSC/Dalhousie High Pressure Laboratory in Halifax, Nova Scotia (Ji et al., 1993; Salisbury and Fountain, 1994; Ji et al., 1997; Wang et al., 2005a and b). The pressure vessel is a seven-ton, double-walled steel vessel with a 40 cm long × 10 cm diameter working chamber, which can operate to a pressure up to 1.4 GPa. The pressure was generated using an air-driven fluid pump in conjunction with a multi-stage fluid intensifier system. An ester (Monoplex DOS: Di-2-ethylhexyl sebacate) was used as the pressure medium. At 25 °C, the ester has a viscosity of 0.17, 1.35, 10.81, 86.52 and 692.54 Poises at 0.1, 200, 400, 600 and 800 MPa (Figure 3.7), respectively (ASME, 1953). Temperature rise due to adiabatic compression from 0.1 MPa to 800 MPa is estimated to be about 30 °C. This rise in temperature results in a reduction in the viscosity by a factor of 2.5 (Figure 3.8). P-waves were generated and received by lead zirconate transducers with a 1 MHz resonance frequency. To prevent the pressure medium from invading the sample during the pressure run, the cylinders were sheathed in thin copper foil and the entire sample/transducer/electrode assembly was enclosed in neoprene tubing (Figure 3.9). Once the sample assembly was sealed in the pressure vessel and the pressure was raised, a high voltage spike from a pulse generator excited the sending transducer and the time of flight to the receiving transducer was measured using a digital oscilloscope.

The signal from the receiving transducer was stacked over 400 pulse repetitions in order to reduce the signal to noise ratio before being displayed on the digital oscilloscope. Errors in velocity measurement may arise from several sources: (1) Errors in measuring core length and travel time. Core lengths are accurate to 0.005 cm and travel time to 2.5 nanoseconds. This results in velocity measurements which are accurate to 0.4 per cent for standard length cores (Burke, 1991). (2) Changes in sample length at elevated confining pressure. No corrections were made for this effect in the present study because it is significant only at extremely high pressures (e.g., Brace, 1965). The absolute error associated with the pulse transmission technique is generally regarded to

be less than 0.5-1.0% for Vp and 1% for Vs (Christensen and Shaw, 1970). The dry densities of the samples (Table 3.1) were determined using the immersion method with an accuracy of ±0.005 g/cm^3 at room conditions.

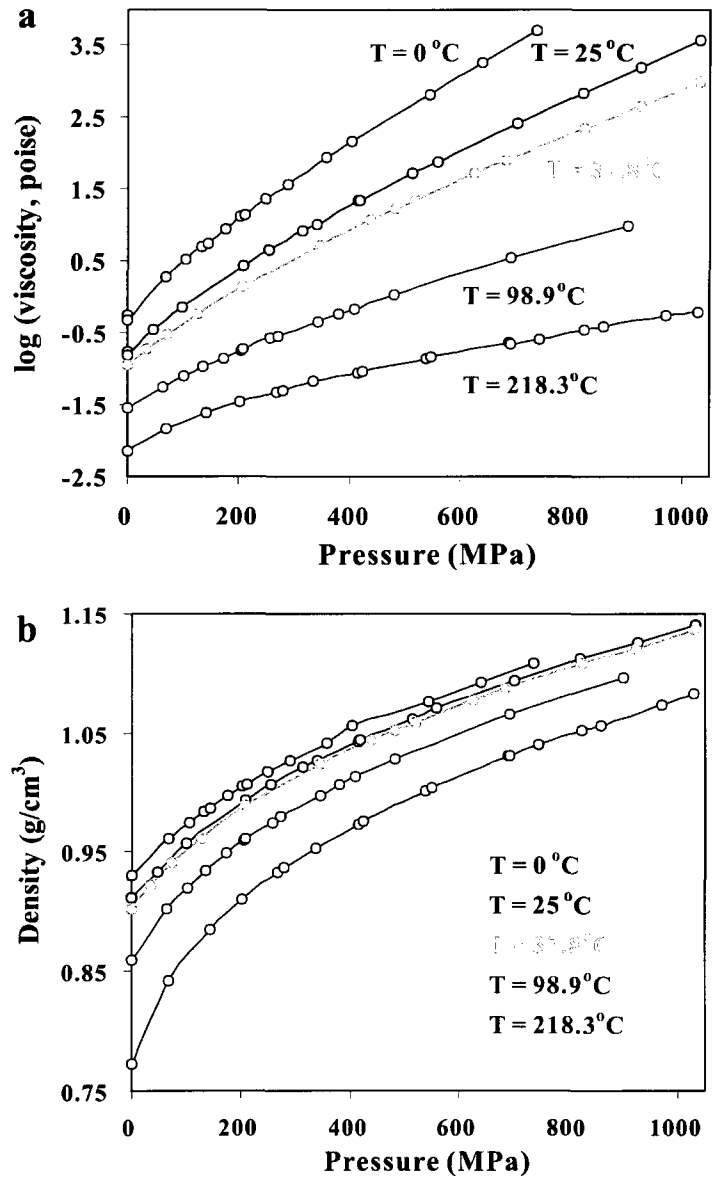

Figure 3.7 Variations in viscosity (a) and density (b) of pressure medium (Monoplex DOS: Di-2-ethylhexyl sebacate) with pressure. Each curve is for a different temperature.

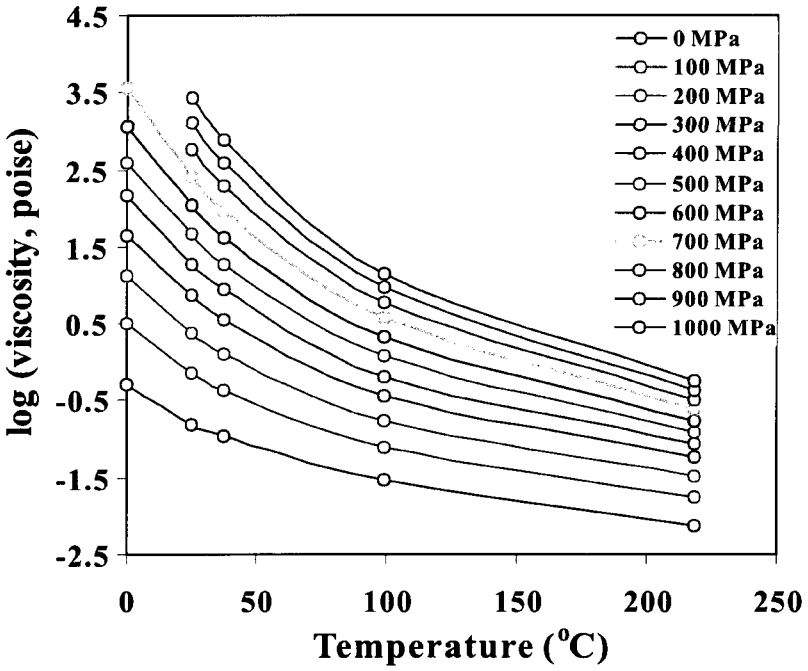

Figure 3.8 Variation in viscosity of pressure medium (Monoplex DOS: Di-2-ethylhexyl sebacate) with temperature. Each curve is for a different pressure.

3.5 Experimental results and discussion

3.5.1 Vp hysteresis

Typical variations of P-wave velocities measured during a cycle of pressurization and subsequent depressurization are shown in Figures 3.10-3.12 for samples from depths of 3000-4600 m and 10-700 m in the CCSD boreholes and Yangkou surface outcrops, respectively. During initial pressurization, the velocity-pressure curves display a rapid, nonlinear rise in velocity below a critical pressure (P_c-up), followed by a slow nearly-linear rise above P_c-up. On depressurization, the velocity decreases first nearly-linearly above a critical pressure (P_c-down), and then strongly nonlinearly with

decreasing pressure below P_c-down. In all cases, the depressurization curve lies on or above the pressurization curve, and P_c-down is equal to or lower than P_c-up. For a given specimen, the pressure derivative (dV/dP) in the high pressure regime is always lower for the depressurization curve than the pressurization curve. The above phenomenon is known as seismic velocity hysteresis (Birch, 1960; Gardner et al., 1965). The magnitude of the hysteresis at a given pressure can be described by the velocity difference ($\Delta V=V_{down}-V_{up}$) between the depressurization and pressurization curves. $\Delta V=0$ in the perfectly linear-elastic regime (i.e., nonporous or crack-free material) while $\Delta V>0$ in the nonlinear poro-elastic regime (porous or microcrack-bearing material).

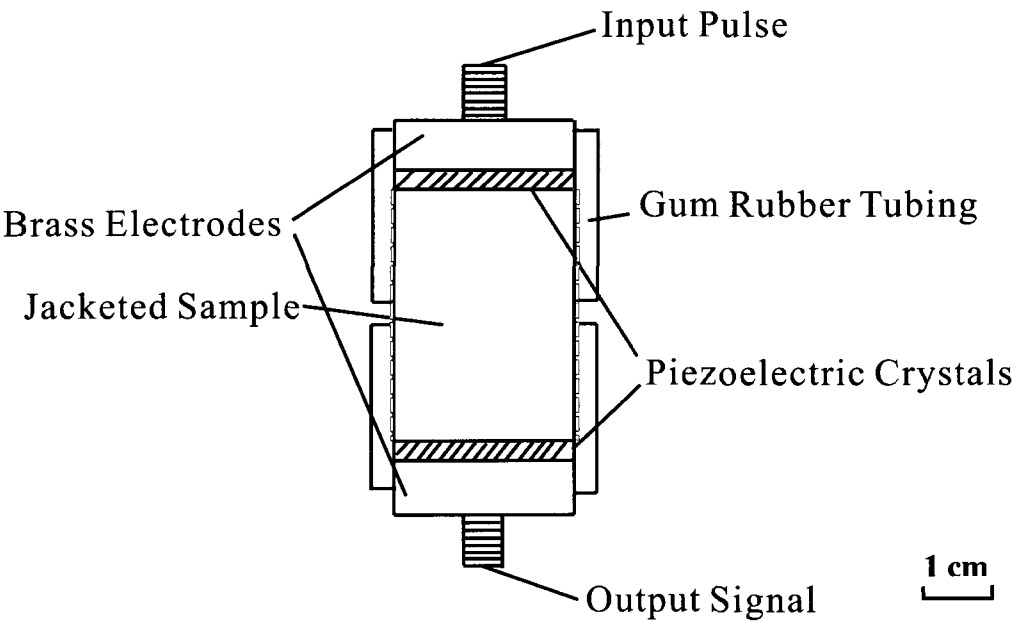

Figure 3.9 Sample assembly for seismic wave velocity measurements.

Seismic hysteresis, which displays a dependence of seismic velocity on the past pressure history of the sample, has been attributed to modifications of microstructures, particularly porosity and the geometry of microcracks, during pressurization and subsequent depressurization (Birch, 1960; Burke and Fountain, 1990). Figure 3.13 shows the variations of seismic hysteresis during successive pressurization-

depressurization cycles in two samples from depths of 3254.5 m (B1628R33P24-Z: Hbl-Mag felsic gneiss) and 4385.74 m (B2242R100P16a-X: Hbl-Bt-Pl-Kfs paragneiss) in the CCSD main hole. Each cycle was separated in time by an interval of 48 hours. The results are inconsistent with our initial expectation that the hysteresis loop would stabilize after one or two pressurization-depressurization cycles and reach an equilibrium value for the imposed confining pressure. The data do not confirm Burke and Fountain's (1990) observation of a marble that re-pressurization results in velocities intermediate between the up and down pressure curves of the first cycle, with the down pressure measurements of the first run being reproduced during the second depressurization. The present results show that only the nearly-linear segment of the velocity-pressure curves (>400 MPa) can be reproducible and reversed in the laboratory while those below 300 MPa vary from run to run and are probably very sensitive to the state of microcracks within the sample. The second pressurization-depressurization cycle displays lower velocities at low pressures, indicating probably the formation of new microcracks by pore collapse during the first pressurization-depressurization cycle. Thus, the rocks possess a discrete memory of their past pressure history.

Compared with the specimens sampled from the pre-pilot hole (10-700 m) and particularly those from the main hole (3000-4600 m) of the CCSD project, the Yangkou samples from the surface outcrops display much pronounced seismic hysteresis at each pressure. In the samples from the deep part of the main hole, for instance, the Vp values measured during pressurization and subsequent depressurization are nearly the same at P>400 MPa (Figure 3.10). For the Yangkou surface samples, however, the Vp values measured during pressurization and subsequent depressurization become close only when P>700 MPa (Figure 3.12).

Crack-free single crystals and glasses (McSkimin and Andreatch, 1962; Peselnick and Wilson, 1968) do not show any acoustic hysteresis while the hysteresis phenomenon is typical for porous materials such as sandstone (e.g., Holcomb, 1981; Guyer and

Johnson, 1999), concrete and soils (e.g., Lu, 2005), and compact crystalline rocks (e.g., Birch, 1960; Burke and Fountain, 1990; Ji et al., 1993; Burlini and Kunze, 2000). The observed non-elastic response may be caused or modified by the following processes. (1) Irreversible closure of microcracks or the effect of so-called crack lip adhesion: the microcracks closed during pressurization do not reopen during subsequent depressurization (Birch, 1960). Details of the adhesion mechanism have not been made clear. (2) Irreversible compaction of pore spaces: the pores which collapsed at higher pressures do not recover their original shapes or dimensions at lower pressures. This mechanism is more likely in sedimentary rocks such as shale and sandstone (Jones and Wang, 1981) than in high grade metamorphic rocks that are highly compact. (3) Improvement of contact conditions: the contact conditions are modified by local ductile cushions of weak, alteration materials (e.g., chlorite, sericite or serpentine) along grain boundaries, interfaces and microcracks. Generally speaking, in a natural rock, grains themselves act as perfectly elastic units while the contacts between these grains – grain boundaries and interfaces – often display non-linear elastic behavior. As a result, the rock will show an overall elastically non-linear behavior characterized by hysteresis. The classical theory of linear elasticity and the resulting averaging approaches (e.g., Hill, 1963; Hashin and Shtrikman, 1963) thus may not do an accurate job of describing the overall elastic properties of these so-called nonlinear mesoscopic elastic materials (Guyer and Johnson, 1999; Ji and Wang, 1999; Salje, 2007).

The surface samples are not affected by the rapid decompression processes that introduce microcracks into core samples during drilling and core retrieval. These newly formed microcracks, which are fresh and clean with no alteration products, are closed during pressurization and then reopened completely when the pressure is released. However, the rocks at the surface experienced a more gradual exhumation through tectonic processes. Microcracks and grain boundaries in surface samples are often altered and filled up with alteration products such as sericite, chlorite, or serpentine. These alteration materials serve as ductile cushions and tend to improve grain-to-grain

contact conditions. This explains why seismic velocity hysteresis is much less pronounced in the core samples than the surface samples.

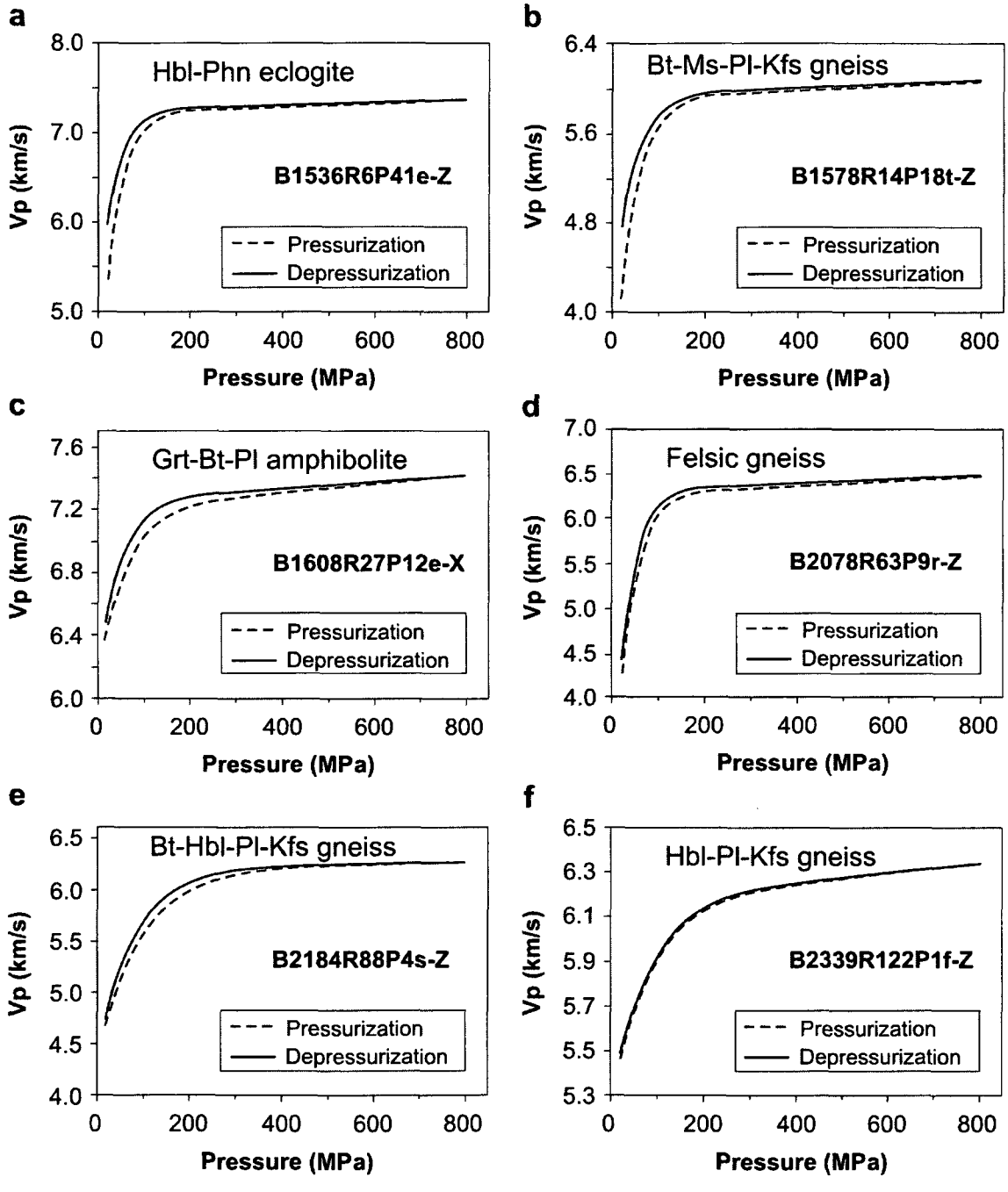

Figure 3.10 Vp-P curves for representative core samples from 3000-4600 m in the CCSD main hole.

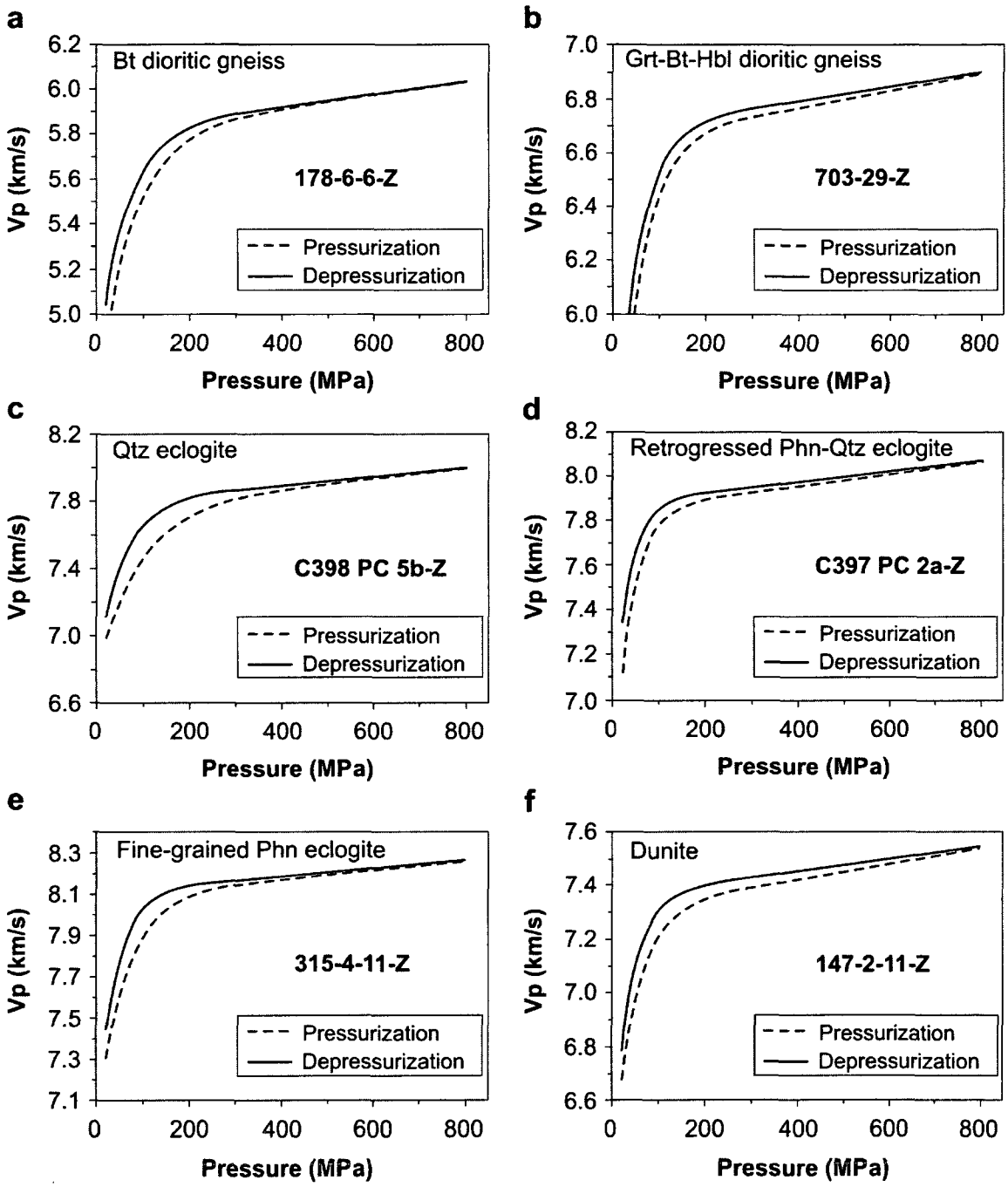

Figure 3.11 Vp-P curves for representative core samples from 10-700 m in the CCSD pre-pilot hole.

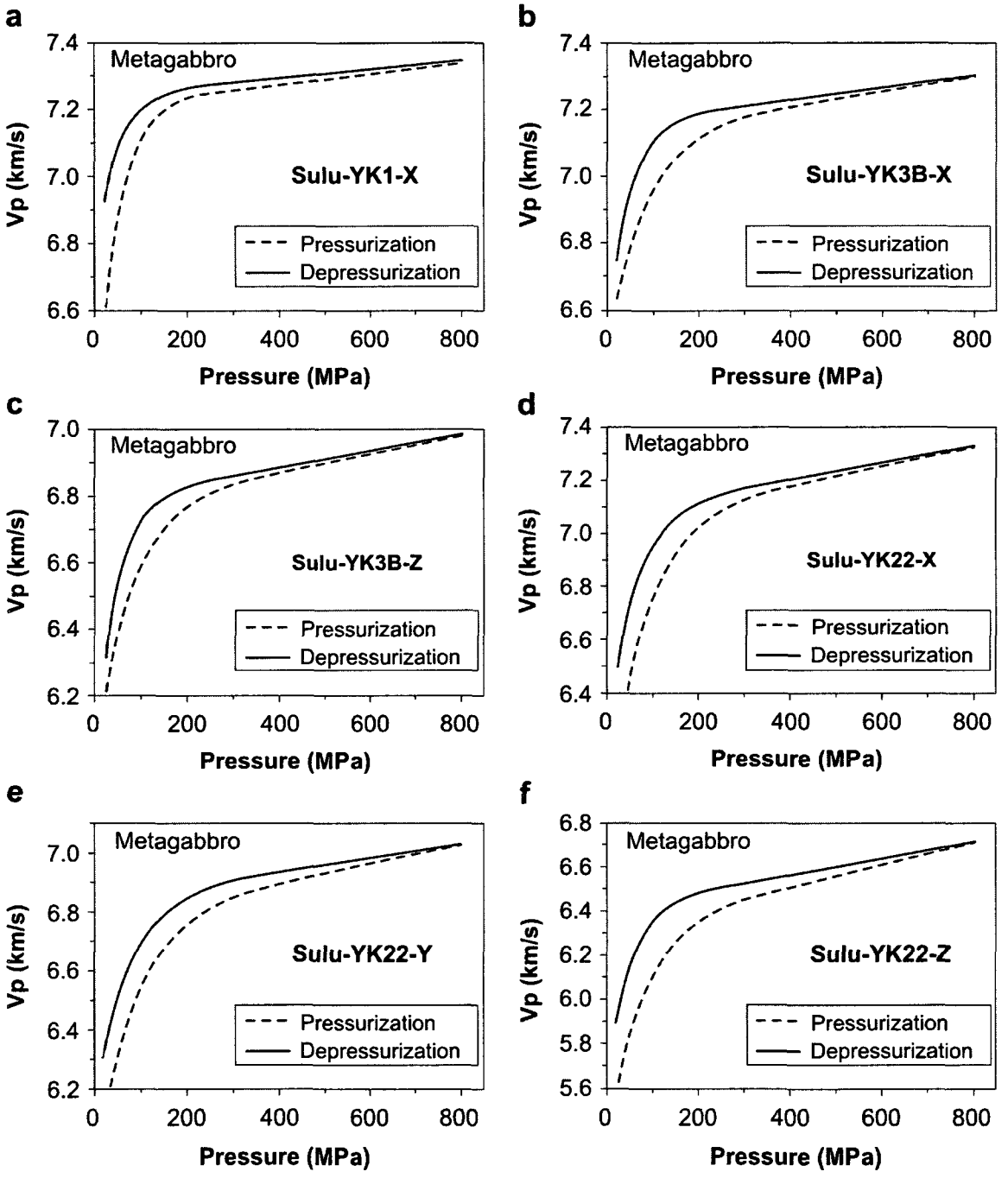

Figure 3.12 Vp-P curves for representative surface samples of eclogitized metagabbro from Yangkou, Qingdao.

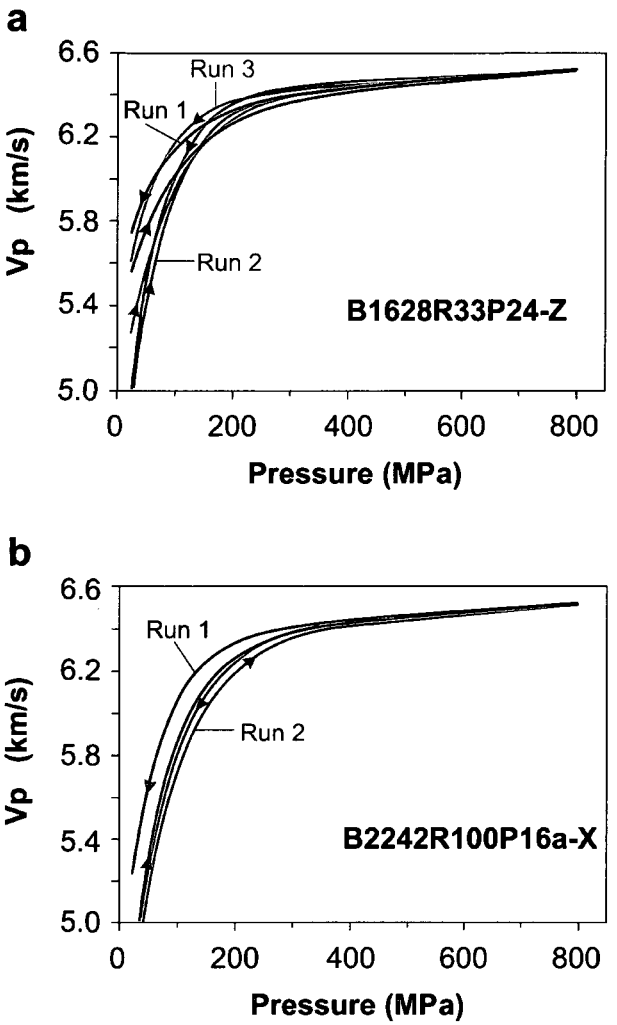

Figure 3.13 Vp-P curves for pressurization-depressurization cycles of samples B1628R33P24-Z (a) and B2242R100P16a-X (b).

3.5.2 Seismic anisotropy

Vp anisotropy (A) is defined by the equation: $A=100\%\times(Vp_{max}-Vp_{min})/Vp_m$, where Vp_{max}, Vp_{min} and Vp_m are, respectively, the maximum, minimum and arithmetic mean values of the P-wave velocities measured in a given sample along different propagation directions. It is noted that the anisotropy varies strongly with pressure. Three patterns have been distinguished (Figures 3.14a-b). Pattern 1: With increasing pressure, the

anisotropy decreases rapidly below ~150 MPa and then slowly above this pressure (e.g., samples Sulu-YK1 and Sulu-YK3B). This pattern, which has been reported previously by Kern et al. (1999), Burke and Fountain (1990), Wepfer and Christensen (1991), and Wang et al. (2005a), can be attributed to the closure of the aligned microcracks which reinforce the anisotropy induced by the lattice-preferred orientation (LPO) of anisotropic minerals such as omphacite, plagioclase, amphibole and mica (Ji et al., 1993). Pattern 2: The anisotropy increases rapidly with increasing pressure in the low-pressure range (< ~150 MPa), and then decreases (Figures 3.14c-d, samples B1608R27P12e and B1536R6P41e) or reaches a constant value (Figure 3.14e, sample B1578R14P18t) in the high pressure range (>~200 MPa). This pattern can be attributed to a rapid closure at low pressures of aligned microcracks which oppose the LPO-induced anisotropy (Ji et al., 1993; Wang et al., 2005a). Pattern 3: The anisotropy decreases with increasing pressure at low pressures (<~100 MPa), then increases at moderate pressures (200-300 MPa) and finally decreases again at high pressures (>~300 MPa, Figure 3.14f, sample Sulu-YK22). This pattern, which was also observed by Wang et al. (2005a), seems to be caused by a complex interaction between the effects of the closure of oriented microcracks, LPO and confining pressure. The anisotropy reduction at low pressures has probably the same origin as Pattern 1. The slight increase in seismic anisotropy at moderate pressures may result from differences in the pressure sensitivity of Vp in different structural directions. The gradual reduction in anisotropy at high pressures may be due to the closure of oriented pores with relatively large aspect-ratios (width/length).

Figure 3.15 is a plot of $100\%\times[Vp(X)-Vp(Z)]/Vp_m$ versus pressure for a Bt-Hbl-Pl-Kfs paragneiss (sample B2184R88P4s). Vp(X)>Vp(Z) below ~200 MPa while Vp(X)<Vp(Z) above this pressure. Above ~400 MPa, the value of $100\%\times[Vp(X)-Vp(Z)]/Vp_m$ is almost constant. The above variation indicates the effect of microcrack closure, which opposes that of rock-forming mineral LPOs, diminishes gradually with increasing confining pressure and finally vanishes at P > ~400 MPa when the closure is complete. In the high pressure regime, the seismic anisotropy is fully controlled by the

LPOs of plagioclase and K-feldspar with their (010) planes parallel to foliation and [100] directions parallel to lineation, as confirmed by optical observations. In both plagioclase and K-feldspar, the maximum and minimum Vp occur, respectively, parallel to the normal to (010) and close to the [100] direction (e.g., Ji and Mainprice, 1988; Ji et al., 2002, p. 23). Consequently, Vp(Z) >Vp(X) at P>400 MPa.

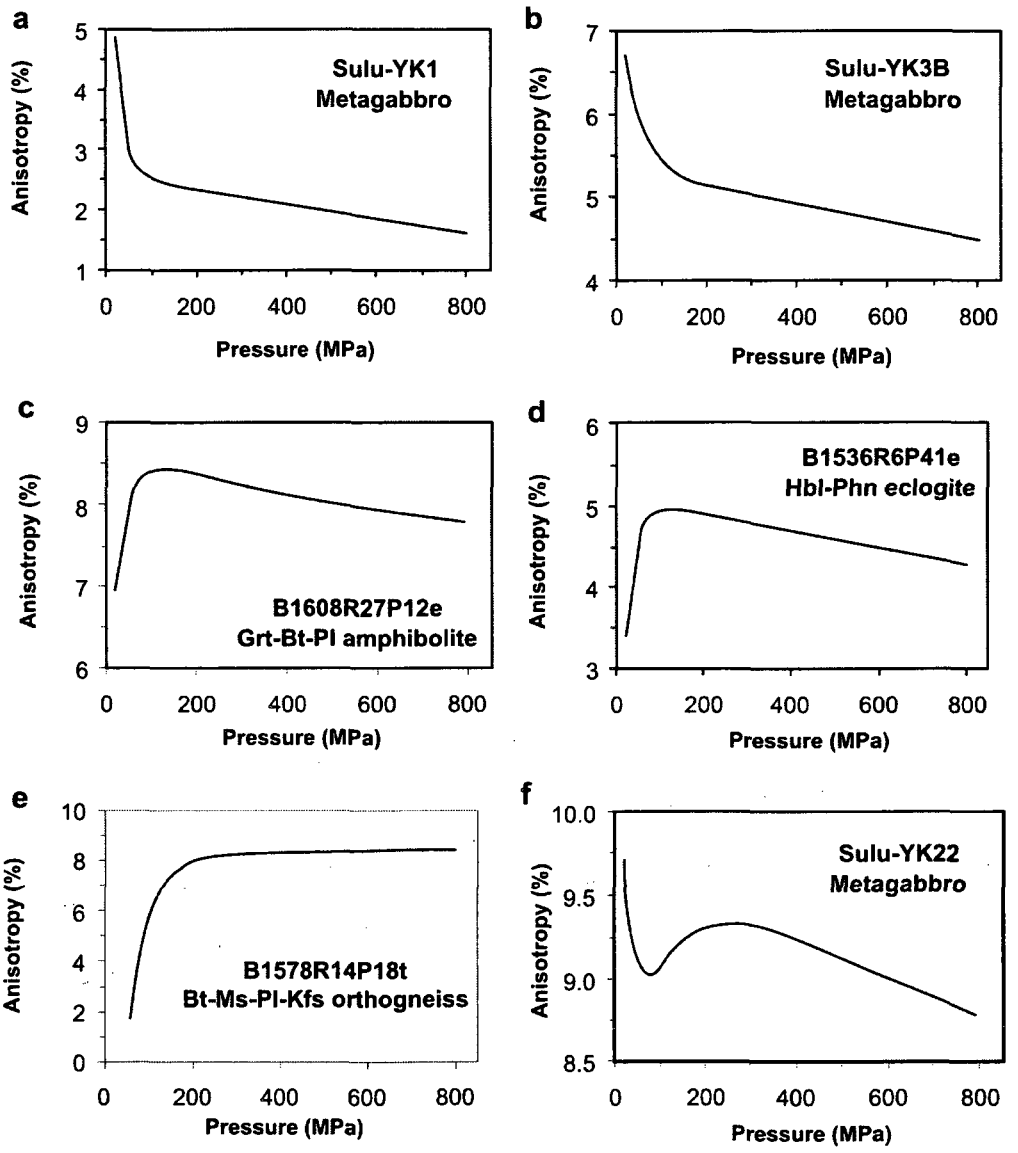

Figure 3.14 Vp anisotropy as a function of pressure for Sulu UHP rocks.

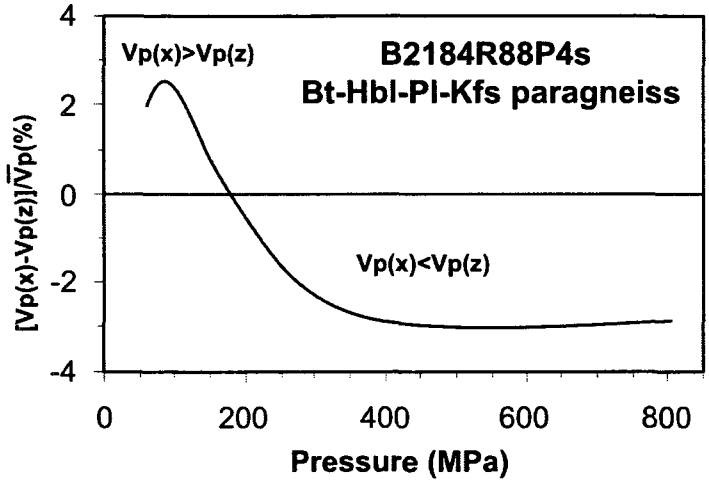

Figure 3.15 $[Vp(X)-Vp(Z)]/\overline{Vp}$ versus pressure for a Bt-Hbl-Pl-Kfs paragneiss (sample B2184R88P4s).

3.5.3 Pressure dependence of Vp

It is well known that seismic velocities in compact crystalline rocks that contain neither pores nor open microcracks increase linearly with increasing confining pressure (P).

$$V(P) = V_0 + DP \qquad (3.1)$$

where V_0 is the velocity at zero pressure, and D is the pressure derivative of velocity. The linear increase in velocities marks an elastic volume contraction under hydrostatic compression. Generally Eq. (3.1) does an excellent job in describing the velocity-pressure relationship only at very high pressures ($P \geq P_c$) where all microcracks and pores have fully been closed in the rocks (e.g., Ji et al. 1993; Wang et al., 2005a). Equation (3.1) breaks down when phase transformation, metamorphic reaction or partial melting occurs.

However, seismic velocities of rocks at low pressures are considerably affected by porosity and pore/microcrack geometry. Rocks containing pores/microcracks always have lower velocities than the same rocks with no porosity (e.g., Ji et al., 2006). The difference between the velocities of a nonporous material and its porous counterpart at a given confining pressure is called the velocity drop (B). B is a physical quantity that can be experimentally measured, which has a maximum value (B_0) at P=0 and then decays progressively with increasing confining pressure (P) at a rate proportional to the value of the velocity drop (i.e., B) at the applied confining pressure. Mathematically, the decay can be expressed as the following differential equation:

$$\frac{dB}{dP} = -kB \qquad (3.2)$$

where k is a positive number called the decay constant. Equation (3.2) then gives

$$\ln\frac{B}{B_0} = -kP \qquad (3.3)$$

that is,

$$B = B_0 \exp(-kP) \qquad (3.4)$$

where B_0 denotes the initial difference in velocities between the nonporous material and its porous counterpart at P=0. Equation (3.4) possesses the same form of the expression that is commonly used to describe natural phenomena such as radioactive decay, cooling, and vibration attenuation.

Figure 3.16 shows the effect of varying the decay constant k on the B value. The solid curve is the curve generated using k=0.025 MPa^{-1} and B_0=0.8 km/s which are typical values for eclogitized metagabbro from Yangkou. The other four dashed curves are calculated using a constant value B_0=0.8 km/s and different decay constants (k =

0.005, 0.01, 0.05 and 0.1). A larger value of k indicates that the B value decays or decreases more rapidly as the confining pressure increases (Figure 3.16). Based on the theory of continuum elasticity, Walsh (1965) shows that the closure pressure (P_c) for cracks with an aspect ratio α is approximated by

$$P_c = \frac{\pi \alpha E}{4(1-\upsilon^2)} \qquad (3.5)$$

where E and υ are the Young's modulus and Poisson's ratio of the rock, and $\alpha = b/a$, where a and b are the length and width of the cracks, respectively. At a constant porosity, flatter cracks with small aspect ratios (α) are more readily closed by the application of pressure than more spherical voids with $\alpha \approx 1$. Consequently, flatter cracks yield a larger k value while more spherical pores yield a smaller k value. Thus, the decay constant k is a parameter to quantify the facility of the successive closure and collapse of cracks of varying aspect-ratio spectra with increasing pressure.

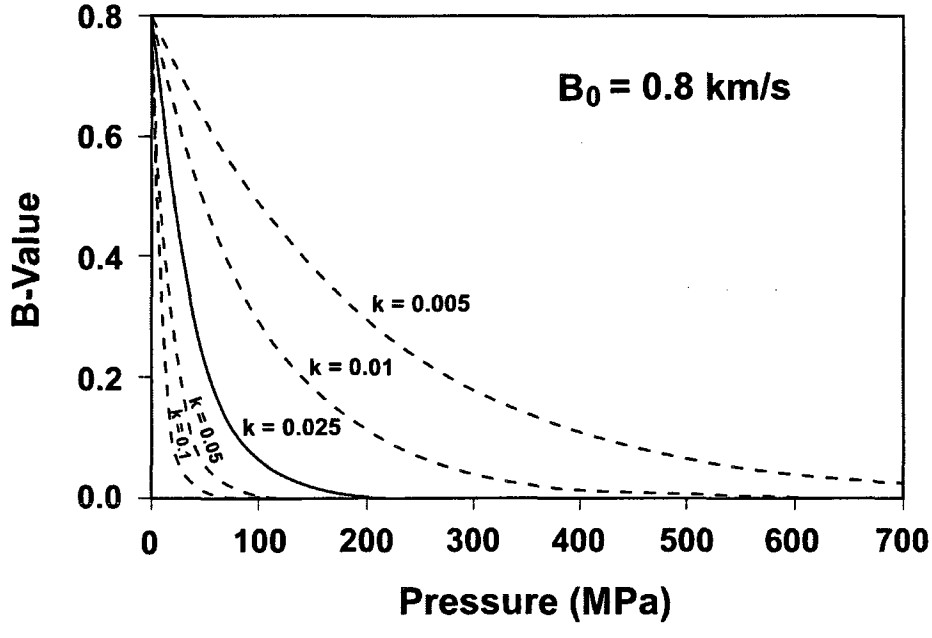

Figure 3.16 B value as a function of pressure and decay constant k.

When the pressure is higher than a critical value (P_c), such that $B/B_0 \leq 0.2\%$, then the B value becomes very small. Thus, P_c can be defined as:

$$P_c = -\frac{\ln 0.002}{k} \approx \frac{6.215}{k} \qquad (3.6)$$

Above P_c, the rock sample can be regarded as a nearly crack-free aggregate and the seismic velocities increase almost linearly with increasing pressure. Clearly, the critical pressure to fully close the microcracks and pores in the rock depends on the k value. A rock containing more spherical pores has a high P_c value than the same rock but containing flatter cracks. Thus, the k value should be a coefficient which provides a statistical measurement of the geometrical shape or sphericity of pores (e.g., α). Equation (3.6) also provides an explanation why Greenfield and Graham (1996) observed a linear relationship between the so-called crack closure parameter τ (i.e., $\tau = 1/k$) and the crack closure pressure P_c. However, the P_c value suggested by these authors is about 5 times τ, indicating that they took implicitly the pressure value at $B/B_0 \approx 0.67\%$ as the crack closure pressure P_c.

Another important characteristic of the exponential decay of B with increasing P is the pressure required for the velocity drop to equal one half of its initial value B_0. This characteristic pressure can be called the half-pressure ($P_{1/2}$). Thus,

$$e^{-kP_{1/2}} = \frac{B}{B_0} = 0.5 \qquad (3.7)$$

that is,

$$P_{1/2} = \frac{\ln 2}{k} \approx \frac{0.693}{k} \qquad (3.8)$$

The notion of half-pressure is analogous to the half-life of radioactive elements.

The variation of seismic velocities with confining pressure (Figures 3.10-3.12) is attributed to not only the gradual closure of microcracks and pore spaces with different aspect-ratios but also the lattice contraction of the rock-forming minerals in the sample. Therefore, the velocity-pressure relationship in the full range of pressure should be governed by an equation that combines both Equations (3.1) and (3.4), that is,

$$V(P) = V_0 + DP - B_0 \exp(-kP) \qquad (3.9)$$

The physical meaning of Equation (3.9) is illustrated in Figure 3.17. V_0 is the projected velocity of a non-porous or crack-free rock at zero pressure, which can be determined from extrapolation of the linear velocity-pressure relationship obtained at high pressures to zero pressure; D, which is the intrinsic pressure derivative of velocity in the linear elastic regime, determines the slope of velocity-pressure curve at high pressures ($P>P_c$); B_0, which is the initial velocity drop caused by the presence of pores/microcracks at zero pressure, represents the maximum velocity increase due to the closure of pores and microcracks; (V_0-B_0) is the zero-pressure velocity of the rock containing microcracks and pores; k, which is the decay constant of the velocity drop, controls the shape of the nonlinear segment of the velocity-pressure curve. B_0 and k are two important parameters that depend on the porosity and geometrical shape of pores (e.g., aspect ratio, spatial arrangement, orientation and size distribution), which in turn depend on the formation and deformation processes of the rocks. At a given porosity, the seismic velocity of a rock can be considerably varied by a change in pore geometry (e.g., Ji et al., 2006).

Equation (3.9) has been used as an empirical relationship between seismic velocity and confining pressure for crystalline rocks (Stierman et al., 1979; Wang et al., 2005) and sedimentary rocks (e.g., Zimmerman et al., 1986; Eberhart-Phillips et al., 1989; Freund, 1992; Shapiro, 2003). In the above, we have shown that this equation can be derived from general principles.

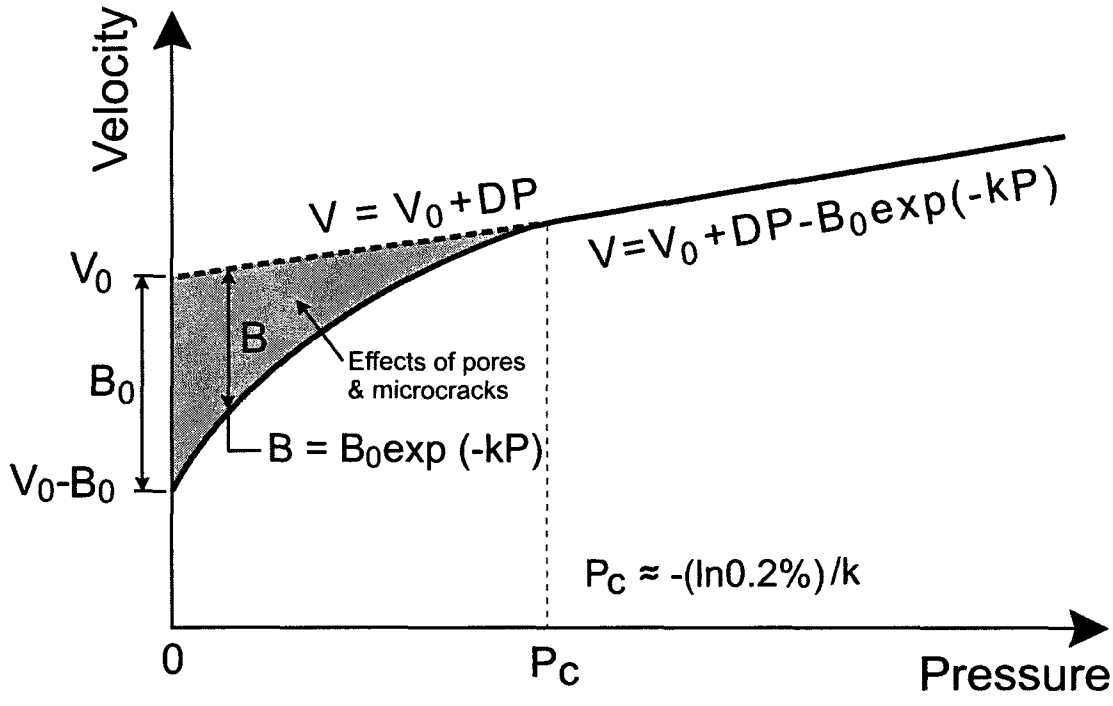

Figure 3.17 Physical significance of four parameters in Equation (3.9). Each parameter is defined in the text. The effects of microcracks/pores on the velocity are illustrated by the shadowed area.

The pressure derivative of the velocity (dV/dP) is given by:

$$\frac{dV}{dP} = D + B_0 k e^{-kP} \qquad (3.10)$$

The pressure derivative dV/dP decreases most rapidly as the confining pressure initially increases. When the pressure is sufficiently large, say above P_c defined by Equation (3.6), the pressure derivative reaches a nearly constant value equal to D (Figure 3.18). The variation marks that the pores with relatively small aspect-ratios (i.e., grain boundary cracks, transgranular cracks and flat pores) are rapidly closed at lower pressures.

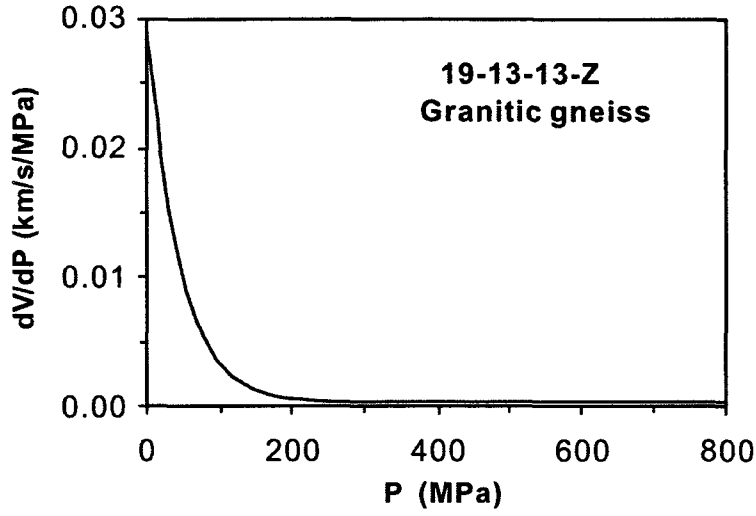

Figure 3.18 Pressure derivative (dV/dP) as a function of pressure for a granitic gneiss (sample 19-13-13-Z)

Equation (3.9), hereafter called Model 1, is a four-parameter exponential equation. These parameters can be readily determined for each given set of experimental data using a least squares regression method (Table 3.3). A goodness-of-fit coefficient (R^2) is used as a statistical measure of how well the experimental data fit the theoretically predicted values. As shown in Figures 3.19a-b, both the up-going and down-going pressure-velocity curves can be well fitted by Equation (3.9), with more than 90% of 52 cylindrical samples having $R^2 \geq 0.96$.

It is interesting to compare Equation (3.9) with empirical expressions proposed by other authors. Wepfer and Christensen (1991) fitted laboratory data using the following empirical formula:

$$V(P) = AP^a + B(1 - e^{-bP}) \qquad (3.11)$$

where V is the seismic velocity (Vp or Vs), P is the confining pressure, and a, b, A and B are four adjustable parameters. Equation (3.11), hereafter called Model 2, is based

purely on mathematical curve fitting, but its physical meaning is unclear. As shown in Figures 3.19c-d, the ability of Equation (3.11) to fit the velocity-pressure curves for the same 52 cylindrical samples is significantly lower than Equation (3.9).

Table 3.3 Model 1 parameters of Vp-pressure curves measured during depressurization for Sulu UHP rocks listed in Table 3.1 [a]

Sample	Lithology	λ	Density	V_0	D	B_0	k	R^2	P_c	$P_{1/2}$
			(g/cm^3)	(km/s)	(10^{-4} km/s/MPa)	(km/s)	(10^{-2} MPa^{-1})		(MPa)	(MPa)
19-13-13	Granitic gneiss	Z	2.64	6.186	2.548	1.273	2.241	0.997	277	31
26-10-17	Granitic gneiss	Z	2.64	6.172	2.871	0.932	2.988	0.995	208	23
125-8-18	Qtz eclogite	Z	3.38	7.694	3.188	2.174	2.559	0.979	243	27
125-15-18	Qtz eclogite	Z	3.48	8.024	3.669	1.106	1.814	0.912	343	38
147-2-11	Dunite	Z	3.16	7.356	2.408	0.947	2.495	0.989	249	28
150-3-20	Lherzolite	Z	3.12	7.070	2.152	1.455	1.528	0.996	407	45
151-14-16	Grt harzburgite	Z	3.21	7.670	2.580	1.150	1.487	0.923	418	47
160-12-11	Grt harzburgite	Z	3.17	7.229	2.441	2.049	3.137	0.972	198	22
166-42-43	Phl dunite	Z	3.25	6.835	2.114	0.932	2.139	0.966	291	32
703-29	Grt-Bt-Hbl dioritic gneiss	Z	2.93	6.685	2.721	1.436	1.988	0.995	313	35
178-6-6	Bt dioritic gneiss	Z	2.74	5.814	2.729	1.072	1.599	0.995	389	43
203-5-15	Amphibolite	Z	3.07	5.746	3.088	1.479	1.732	0.988	359	40
210-15-21	Granitic gneiss	Z	2.63	6.157	1.902	0.597	2.029	0.993	306	34
219-1-2	Granitic gneiss	Z	2.63	6.290	2.528	1.586	2.171	0.996	286	32
315-1-11	Phn eclogite	Z	3.43	7.952	1.637	1.220	1.682	0.988	369	41
315-4-11	Fine-grained Phn eclogite	Z	3.53	8.107	2.007	1.068	2.358	0.959	264	29
C397 PC 2a	Retrogressed Phn-Qtz eclogite	Z	3.39	7.879	2.455	0.964	2.870	0.997	217	24
C398 PC 5b	Qtz eclogite	Z	3.39	7.796	2.691	0.971	1.746	0.945	356	40
C399 PC c1	Retrogressed Qtz eclogite	Z	3.24	7.695	2.428	1.658	1.786	0.990	348	39
B1536R6P41e	Hbl-Phn eclogite	X	3.11	7.250	1.383	2.302	2.881	0.996	216	24
B1536R6P41e	Hbl-Phn eclogite	Z	3.11	6.924	2.053	2.003	2.820	0.998	220	25
B1578R14P18t	Bt-Ms-Pl-Kfs orthogneiss	X	2.65	6.452	1.855	3.373	2.214	0.996	281	31
B1578R14P18t	Bt-Ms-Pl-Kfs orthogneiss	Z	2.65	5.944	1.527	1.885	2.286	0.996	272	30
B1608R27P12e	Grt-Bt-Pl amphibolite	X	3.01	7.259	1.676	1.132	1.798	0.923	346	39
B1608R27P12e	Grt-Bt-Pl amphibolite	Z	2.95	6.670	2.108	0.879	1.620	0.999	384	43
B1628R33P24	Hbl-Mag felsic orthogneiss	Y	2.65	6.375	2.329	2.394	2.654	0.999	234	26
B1628R33P24	Hbl-Mag felsic orthogneiss	Z	2.65	6.381	1.516	1.057	1.553	0.995	400	45
B1651R37P41c	Amphibolite	Z	3.00	6.592	1.708	0.691	2.483	0.981	250	28
B1694R49P7s	Felsic orthogneiss	Z	2.63	6.394	1.710	1.500	0.739	0.871	841	94
B2068R61P20h	Bt-Pl amphibolite	Z	2.85	6.244	1.313	0.890	2.843	0.998	219	24
B2078R63P9r	Felsic orthogneiss	Z	2.63	6.315	1.932	3.449	3.012	0.997	206	23
B2168R85P2a	Bt-Hbl-Pl-Kfs paragneiss	Z	2.65	6.129	1.870	2.171	2.522	0.978	246	27
B2184R88P4s	Bt-Hbl-Pl-Kfs paragneiss	X	2.66	5.954	1.739	2.203	2.149	0.997	289	32
B2184R88P4s	Bt-Hbl-Pl-Kfs paragneiss	Z	2.66	6.170	1.264	1.782	1.088	0.951	571	64
B2242R100P16a	Hbl-Bt-Pl-Kfs paragneiss	X	2.66	6.357	1.970	1.545	1.592	0.998	390	44
B2339R122P1f	Hbl-Pl-Kfs paragneiss	Z	2.65	6.193	1.779	0.902	1.173	0.951	530	59
MB-OU-14	Garnetite	Z	3.56	7.914	6.224	1.079	0.595	0.867	1044	116
Sulu-YK1	Metagabbro	X	3.07	7.245	1.225	0.498	2.144	0.994	290	32
Sulu-YK1	Metagabbro	Y	3.09	7.098	2.692	0.788	2.668	0.975	233	26
Sulu-YK1	Metagabbro	Z	3.07	7.050	2.163	0.819	2.880	0.996	216	24
Sulu-YK2A	Metagabbro	X	3.06	7.008	2.214	0.717	2.631	0.983	236	26
Sulu-YK2A	Metagabbro	Z	3.07	6.963	2.442	0.720	5.186	0.998	120	13
Sulu-YK3B	Metagabbro	X	3.04	7.158	1.864	0.634	2.131	0.995	292	33
Sulu-YK3B	Metagabbro	Y	2.98	6.792	2.262	0.712	2.142	0.981	290	32
Sulu-YK3B	Metagabbro	Z	2.98	6.788	2.503	0.738	2.168	0.996	287	32
Sulu-YK9	Serpentinite	Z	2.60	5.766	2.760	0.300	2.379	0.992	261	29
Sulu-YK22	Metagabbro	X	2.96	7.078	3.190	0.815	1.652	0.988	376	42
Sulu-YK22	Metagabbro	Y	2.95	6.847	2.300	0.715	1.358	0.986	458	51
Sulu-YK22	Metagabbro	Z	2.96	6.418	3.732	0.798	2.023	0.990	307	34

[a] λ is the propagation direction.

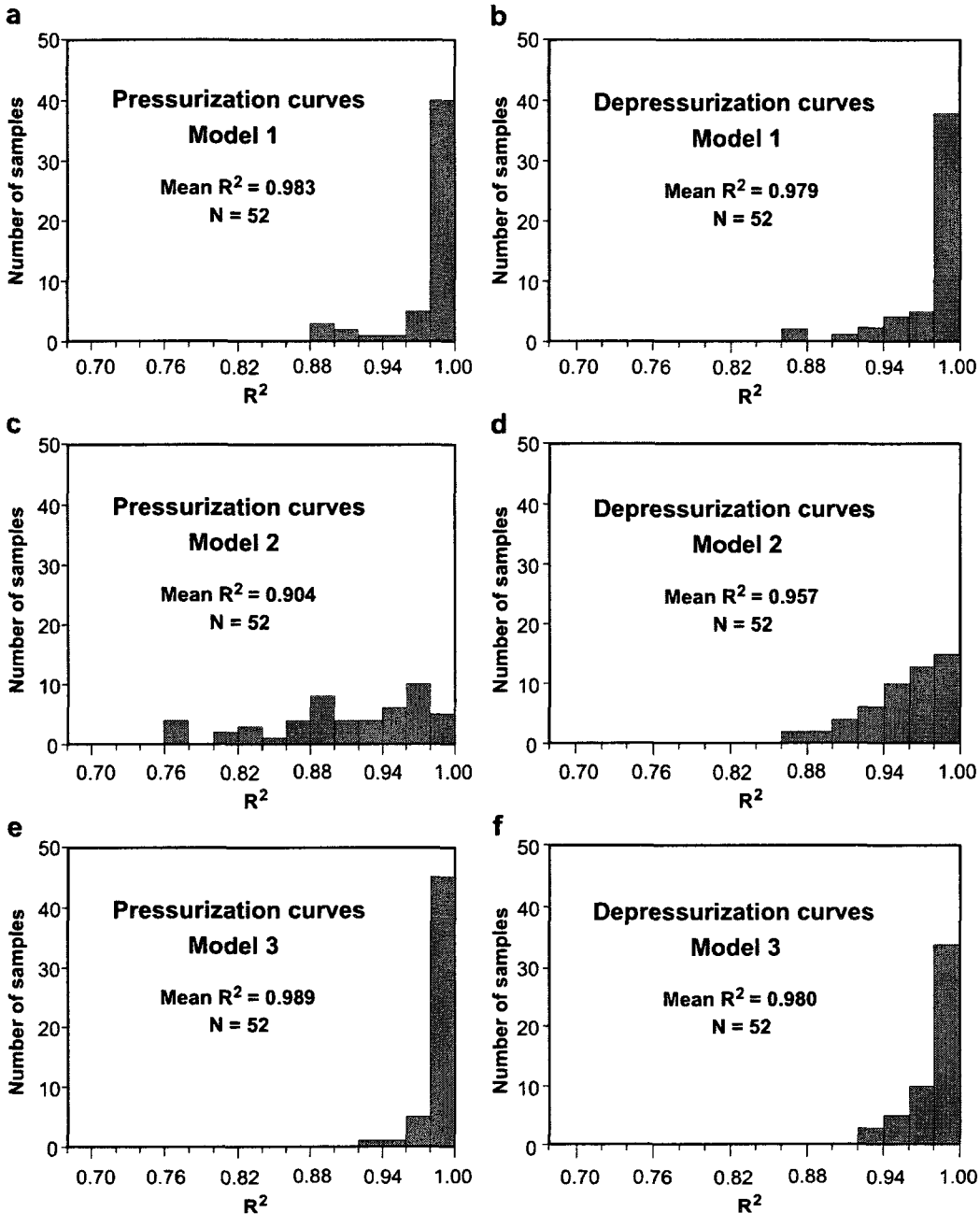

Figure 3.19 Histograms of goodness-of-fit coefficient (R^2) for 3 models discussed in the text.

Wang et al. (2005a and b) used Equation (3.1) and Equation (3.12), hereafter called Model 3, to describe the linear elastic behavior at $P \geq P_c$ and the nonlinear poro-elastic behavior at $P < P_c$, respectively.

$$V(P) = a(\ln P)^2 + b\ln P + c \qquad (0 < P < P_c) \qquad (3.12)$$

In Equation (3.12), a and b are constants, and c is the velocity when P is equal to unity (e.g., one MPa). Like Equation (3.11), Equation (3.12) has no obvious physical significance. Although Model 3 shows a good fit to the velocity-pressure curves for the Sulu UHP rocks (Figures 3.19e-f), it is more complicated to apply because a total of 5 parameters is needed to describe the pressure dependence of velocity. Moreover, the curve calculated from the derived parameters is often not smooth around P_c because the calculated pressure derivatives of velocity (dV/dP) for the nonlinear and linear regimes are often not the same when $P=P_c$. In addition, P cannot equal zero in Equation (3.12) and when P approaches zero, Equation (3.12) yields a negative velocity which is physically meaningless.

The velocity values measured during depressurization correspond to the more stable (i.e., reproducible) microstructural state (e.g., Burke and Fountain, 1990; Ji et al., 1993; Wang et al., 2005a, b), and thus have been used for the statistical analysis of the physical properties of the Sulu UHP rocks. The least-square solutions of the Model 1 parameters V_0, D, B and k for each cylinder measured during depressurization in this study are given in Table 3.3. The tabulated parameters will enable the reader to reproduce the Vp-P curves with adequate precision. The experimental data reported in Wang et al. (2005a) were also analyzed in order to obtain Model 1 parameters (Table 3.4). Based on the Model 1 parameters of a total of 122 cylindrical samples, statistical analysis can be performed for the seismic properties of the Sulu UHP rocks. The best-fit relationship between V_0 and density (ρ) is: $V_0 = 2.286\rho - 0.077$ with R^2=0.79 (Figure 3.20). The average values of V_0, D, B_0, k, P_c and $P_{1/2}$ for major rock types in the Sulu UHP orogenic belt are given in Table 3.5. As shown in Figure 3.21a, eclogites have clearly higher values of V_0 ($\overline{V_0}$=8.07 km/s) than other rocks in the Sulu belt such as

serpentinite ($\overline{V_0}$=5.33 km/s), orthogneiss and paragneiss ($\overline{V_0}$=6.15 km/s), dolomitic marble ($\overline{V_0}$=6.73 km/s), metagabbro ($\overline{V_0}$=6.95 km/s), amphibolite ($\overline{V_0}$=6.46 km/s), retrogressed eclogite ($\overline{V_0}$=7.14 km/s) and serpentinized peridotite ($\overline{V_0}$=7.23 km/s). Serpentinized peridotite and retrogressed eclogites have similar V_0 values, making them difficult to distinguish using in-situ seismic data.

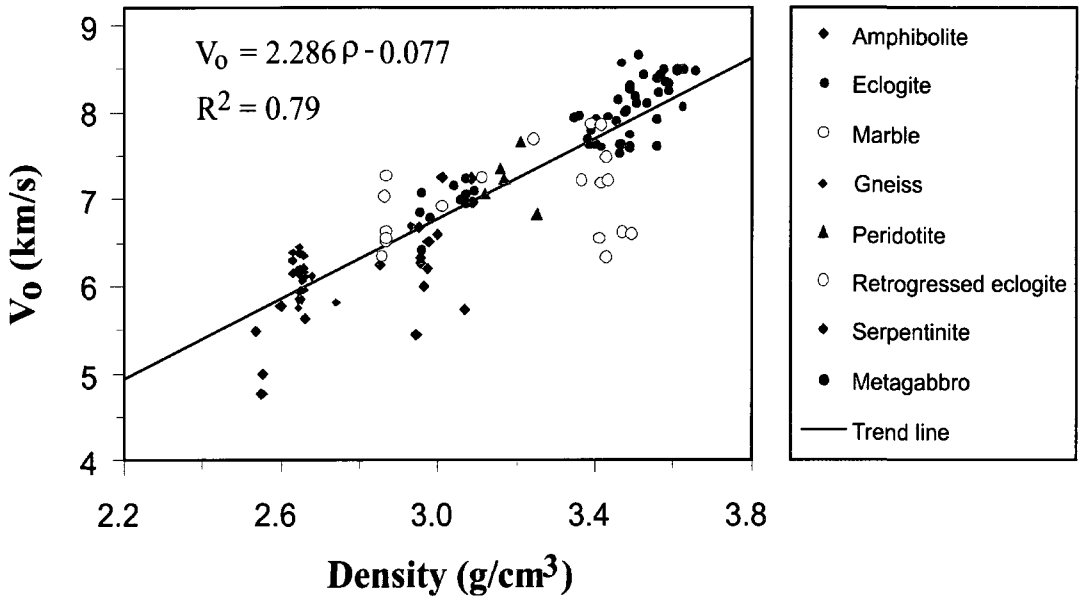

Figure 3.20 V_0 versus density for Sulu UHP metamorphic rocks. The solid line is the best-fit solution for the V_0-density relationship.

V_0 as an intrinsic property of rocks shows certain correlations with lithology and chemical composition (Figure 3.22). Eclogites are only slightly more depleted in SiO_2 but have significantly higher V_0 values than retrogressed eclogites, metagabbros and amphibolites (Figure 3.22a). During a prograde UHP metamorphism (i.e., subduction), amphibolite and metagabbro will first partially and then completely transformed to eclogites. Both the P-wave velocity and density of the rocks will significantly increase although their chemical compositions remain almost the same. During exhumation, however, an eclogite will be partially and then completely retrogressed to amphibolite,

resulting in a significant reduction in both Vp and density. Therefore, an intensively retrogressed zone, which formed during the exhumation of UHP rocks within the continental crust due to the infiltration of fluids along fractures or shear zones, should be a seismic low velocity zone. Such a retrogressed zone within UHP eclogites should be seismically reflective as long as it meets the geometric constraints needed for reflection. Peridotite and serpentinite have similar contents of SiO_2, Al_2O_3, CaO and $Na_2O + K_2O$ but distinct V_0 values (Figure 3.22). From felsic gneiss, through amphibolite and metagabbro, to retrogressed eclogite and finally to eclogite, V_0 gradually increases with increasing Al_2O_3, MgO and CaO contents (Figures 3.22b-d), but decreases with increasing $Na_2O + K_2O$ (Figure 3.22f).

The pressure derivative of velocity (D) is an important parameter for relating laboratory measurements to in-situ rock seismic properties in the Earth's interior. As shown in Table 3.5, the Sulu UHP rocks can be classified into two categories: amphibolite, retrogressed eclogite and serpentinite have higher D values (2.9×10^{-4} - 3.1×10^{-4} km/s/MPa), while gneiss, dolomitic marble, metagabbro, eclogite, and peridotite have lower D values (2.3×10^{-4} - 2.4×10^{-4} km/s/MPa). The pressure derivative D of a rock does not seem to depend on its chemical composition. It is more probable that increasing the content of retrograde minerals such as serpentine, amphibolite and mica leads to an increase in D.

Kern et al. (1999, 2002) measured the seismic properties of some UHP metamorphic rocks from the Dabie and Sulu orogenic belt, using an apparatus in which the confining pressure (up to only 600 MPa) was achieved by pressing six pyramidal pistons in three orthogonal directions on the unjacketed cubic specimen. As shown in Figure 3.23, their data display systematically lower V_0 and appreciably higher D values than our results. For the same type of rocks, their D value is almost twice larger than that obtained by the present study. Both underestimation of V_0 and overestimation of D are probably due to the nature of their apparatus in which the pressure was not perfectly hydrostatic and the resultant differential stress may keep some microcracks open. Furthermore, the pressure

of 600 MPa is not high enough to fully close all cracks in the metamorphic rocks that formed under UHP and HP conditions.

B_0 describes the crack-induced velocity drop (Figure 3.17). As shown in Figure 3.21c and Table 3.5, the Sulu UHP rocks have an average B_0 value of 1.1 km/s with small B_0 values for serpentinite (0.5 km/s) and large B_0 values for peridotite (1.3 km/s), retrogressed eclogite (1.3 km/s) and felsic gneiss (1.4 km/s). Moderate B_0 values occur in metagabbro (0.7 km/s), amphibolite and eclogite (0.9 km/s), and dolomitic marble (1.0 km/s). B_0 is an indicator of microcrack density and geometry in rocks. But the quantitative relationship between them is unclear and needs further investigation.

The decay constant k is an important parameter governing the shape of the velocity-pressure curve in the nonlinear poro-elastic regime. The k value varies from 1.3×10^{-2} MPa^{-1} (eclogite) to 2.5×10^{-2} MPa^{-1} (metagabbro) with a mean of 1.6×10^{-2} MPa^{-1} (Table 3.5 and Figure 3.21d). Amphibolite and serpentinite have the same average k values (1.6×10^{-2} MPa^{-1}). The mean k values for eclogite, retrogressed eclogite, dolomitic marble, gneiss, and peridotite are 1.3×10^{-2}, 1.5×10^{-2}, 1.7×10^{-2}, 1.8×10^{-2} and 2.2×10^{-2} MPa^{-1}, respectively.

Tables 3.3 and 3.4 also list the critical pressure (P_c) for each cylindrical sample, above which all microcracks in the rock appear to be closed and the behavior of seismic waves should only be influenced by the intrinsic properties (i.e., volume fractions and LPOs) of the constituent minerals rather than by microcracks and grain contacts. For eclogites, $\overline{E}$ =191 GPa and $\overline{\upsilon}$=0.26, the critical pressures required to close cracks with aspect ratios α=0.01 and 0.1 are estimated to be 1.61 and 16.1 GPa, respectively, according to Equation (3.5). These values are much higher than our observed value of ~0.53 GPa (Table 3.5). The comparison suggests that Walsh's (1965) equation, which was derived from the theory of continuum elasticity, may significantly overestimate the P_c value; alternatively, some pores with relatively large aspect ratios (e.g., α>0.1) may remain open at higher pressures (Christensen, 1974).

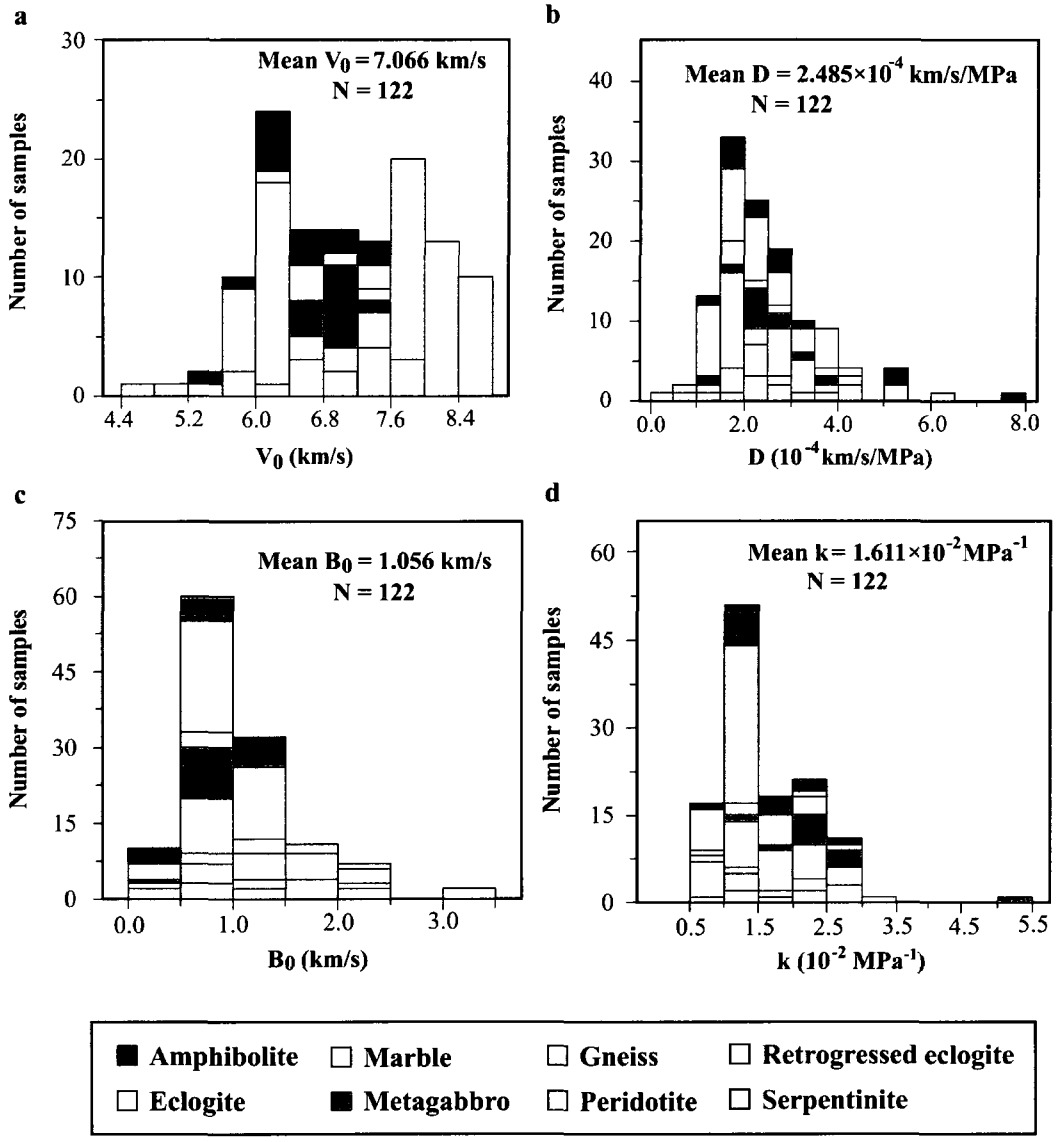

Figure 3.21 Statistical properties of P-wave velocity for Sulu UHP metamorphic rocks. (a) V_0, (b) D, (c) B_0 and (d) k.

As shown in Tables 3.3 and 3.4, the half-pressure, $P_{1/2}$, which is the pressure required for B to equal one half of its initial value B_0, is on average only about 50 MPa for the UHP rocks. $P_{1/2}$ is much smaller than P_c. This reflects the fact that microcracks with small aspect ratios, which are closed at pressures lower than 50 MPa, have a greater influence on the P-wave velocities of the rocks.

Table 3.4 Model 1 parameters of Vp-pressure curves measured during depressurization for Sulu UHP rocks reported in Wang et al. (2005a) [a]

Sample	Lithology	λ	Density (g/cm^3)	V_0 (km/s)	D (10^{-4} km/s/Mpa)	B_0 (km/s)	k (10^{-2} MPa^{-1})	R^2	P_c (MPa)	$P_{1/2}$ (MPa)
86351	Coarse-grained eclogite	X	3.51	8.667	1.415	1.114	1.352	0.986	460	51
86351	Coarse-grained eclogite	Y	3.46	8.147	2.346	1.050	0.846	0.916	735	82
86351	Coarse-grained eclogite	Z	3.50	8.192	1.545	0.492	1.091	0.993	570	64
98401	Retrogressed eclogite	X	3.47	7.642	1.175	0.826	1.415	0.978	439	49
98401	Retrogressed eclogite	Y	3.49	7.613	1.567	0.694	1.295	0.987	480	54
98501	Retrogressed eclogite	X	3.49	7.753	1.999	0.493	1.098	0.925	566	63
98501	Retrogressed eclogite	Y	3.46	7.524	1.104	0.672	0.969	0.993	641	71
98501	Retrogressed eclogite	Z	3.47	6.621	1.919	0.495	1.303	0.971	477	53
DG1	Fine-grained eclogite	X	3.48	7.997	1.098	1.209	1.907	0.892	326	36
DG1	Fine-grained eclogite	Y	3.45	7.899	2.278	0.729	0.861	0.970	722	80
DG1	Fine-grained eclogite	Z	3.46	7.631	2.495	0.644	1.198	0.951	519	58
JC1	Retrogressed eclogite	X	3.49	6.614	0.851	0.982	0.810	0.838	767	86
JC1	Retrogressed eclogite	Y	3.41	6.555	1.809	0.702	0.937	0.892	664	74
JC1	Retrogressed eclogite	Z	3.36	7.230	3.575	0.524	1.375	0.983	452	50
JC2	Fine-grained eclogite	X	3.40	7.638	1.387	1.139	1.063	0.998	584	65
JC2	Fine-grained eclogite	Y	3.38	7.630	1.483	1.133	1.451	0.963	428	48
JC2	Fine-grained eclogite	Z	3.41	7.602	1.253	0.695	1.454	0.992	427	48
JZ1	Fine-grained eclogite	Z	3.49	7.590	3.671	1.205	0.867	0.984	717	80
MB2B	Coarse-grained garnetite	X	3.61	8.506	0.252	0.853	1.293	0.975	481	54
MB22	Coarse-grained eclogite	X	3.50	8.111	2.446	0.950	1.300	0.995	478	53
MB23	Coarse-grained eclogite	X	3.46	8.572	1.225	1.402	1.281	0.990	485	54
MB23	Coarse-grained eclogite	Y	3.49	8.268	3.663	1.200	1.066	0.961	583	65
MB23	Coarse-grained eclogite	Z	3.49	8.314	2.363	0.800	1.215	0.976	511	57
MB25	Coarse-grained eclogite	X	3.56	8.214	3.635	1.647	1.672	0.995	372	41
MB25	Coarse-grained eclogite	Y	3.59	8.251	3.560	1.584	1.389	0.980	448	50
MB25	Coarse-grained eclogite	Z	3.62	8.483	2.694	0.944	1.427	0.900	436	49
MB26	Coarse-grained eclogite	X	3.59	8.332	4.182	0.603	1.026	0.836	606	68
MB26	Coarse-grained eclogite	Y	3.52	8.434	2.183	1.051	1.106	0.997	562	63
MB26	Coarse-grained eclogite	Z	3.58	8.491	2.252	0.588	1.154	0.996	538	60
MB27B	Coarse-grained eclogite	X	3.56	8.391	1.909	0.562	1.044	0.892	595	66
MB27B	Coarse-grained eclogite	Y	3.61	8.475	1.316	0.869	1.072	0.875	580	65
MB27B	Coarse-grained eclogite	Z	3.58	8.349	1.921	0.622	0.980	0.877	634	71
MB30	Coarse-grained eclogite	X	3.57	8.439	0.672	0.882	1.045	0.969	595	66
MB30	Coarse-grained eclogite	Z	3.63	8.062	3.466	0.779	1.218	0.875	510	57
MB34	Coarse-grained garnetite	X	3.63	8.486	1.721	0.459	1.076	0.859	578	64
MB34	Coarse-grained garnetite	Z	3.66	8.466	1.703	1.136	1.034	0.995	601	67
MB62	Coarse-grained garnetite	X	3.56	7.621	3.219	0.640	1.399	0.956	444	50
QL2	Retrogressed eclogite	X	3.41	7.858	3.152	1.687	0.934	0.993	666	74
QL2	Retrogressed eclogite	Y	3.42	7.195	1.823	1.855	1.031	0.991	603	67
QL2	Retrogressed eclogite	Z	3.43	6.332	4.993	1.143	0.976	0.971	637	71
QL3	Retrogressed eclogite	X	3.43	7.489	5.499	1.186	0.971	0.986	640	71
QL3	Retrogressed eclogite	Z	3.43	7.220	5.382	1.783	0.958	0.996	649	72
QL4	Amphibolite	X	2.96	6.329	5.128	1.060	1.022	0.987	608	68
QL4	Amphibolite	Y	2.97	6.202	5.492	1.236	0.923	0.972	673	75
QL4	Amphibolite	Z	2.97	6.000	7.541	1.229	1.073	0.982	579	65
QL5	Amphibolite	X	2.98	6.520	2.471	0.462	1.264	0.928	492	55
QL5	Amphibolite	Y	2.95	6.271	2.719	0.618	1.271	0.957	489	55
QL5	Amphibolite	Z	2.94	5.434	2.996	1.071	1.337	0.990	465	52
SB1	Fine-grained eclogite	X	3.36	7.972	2.707	0.547	1.012	0.891	614	68
SB1	Fine-grained eclogite	Y	3.34	7.939	1.753	0.679	0.871	0.975	714	80
SB1	Fine-grained eclogite	Z	3.40	7.920	2.517	0.614	1.033	0.885	602	67
TF1	Granitic gneiss	X	2.66	6.074	1.776	0.678	1.090	0.990	570	64
TF1	Granitic gneiss	Y	2.68	6.118	3.083	1.135	1.763	0.985	353	39
TF1	Granitic gneiss	Z	2.66	6.112	2.347	0.549	1.043	0.953	596	66
TF2	Granitic gneiss	X	2.65	5.843	3.766	0.971	1.131	0.989	549	61
TF2	Granitic gneiss	Y	2.65	5.844	3.123	0.899	1.214	0.991	512	57
TF2	Granitic gneiss	Z	2.65	5.752	3.410	0.870	1.091	0.968	569	63
TF3	Granitic gneiss	X	2.66	6.215	2.666	0.886	1.782	0.978	349	39
TF3	Granitic gneiss	Y	2.66	5.963	3.064	0.861	1.842	0.992	337	38
TF3	Granitic gneiss	Z	2.66	6.109	1.850	0.887	1.106	0.896	562	63
XG1	Serpentinite	X	2.54	5.489	4.168	0.441	1.044	0.929	595	66
XG1	Serpentinite	Y	2.56	4.991	2.561	0.533	1.086	0.963	572	64
XG1	Serpentinite	Z	2.55	4.769	4.275	0.515	0.986	0.946	631	70
XG3	Serpentinite	X	2.66	5.622	1.683	0.587	2.287	0.974	272	30
YM1	Dolomitic marble	X	2.86	7.042	1.578	1.017	2.118	0.987	293	33
YM1	Dolomitic marble	Y	2.87	6.643	2.307	0.881	2.239	0.957	278	31
YM1	Dolomitic marble	Z	2.86	6.347	1.841	0.989	2.438	0.978	255	28
YM2	Dolomitic marble	X	2.87	7.265	1.861	1.417	1.192	0.994	521	58
YM2	Dolomitic marble	Y	2.87	6.523	3.919	1.040	0.946	0.985	657	73
YM2	Dolomitic marble	Z	2.87	6.565	2.892	0.942	1.175	0.996	529	59
YM4	Amphibolite	X	3.09	7.241	1.593	0.334	1.180	0.986	527	59
YM4	Amphibolite	Y	3.09	6.958	2.945	0.494	1.179	0.984	527	59
YM4	Amphibolite	Z	3.09	6.968	1.520	0.817	2.063	0.938	301	34

[a] λ is the propagation direction.

Table 3.5 Average Model 1 parameters for Sulu UHP metamorphic rocks [a]

Lithology	N	Density	V_0	D	B_0	k	P_c	$P_{1/2}$	Z
		(g/cm^3)	(km/s)	(10^{-4} km/s/MPa)	(km/s)	(10^{-2} MPa^{-1})	(MPa)	(MPa)	(10^5 $g/cm^2/s$)
Amphibolite	14	2.99	6.460	3.021	0.885	1.556	444	50	19.3
Eclogite	42	3.50	8.074	2.276	0.932	1.270	529	59	28.3
Dolomitic marble	6	2.86	6.731	2.400	1.048	1.685	422	47	19.3
Metagabbro	11	3.02	6.949	2.417	0.723	2.453	282	32	21.0
Gneiss	26	2.66	6.154	2.303	1.419	1.771	401	49	16.4
Peridotite	5	3.18	7.232	2.339	1.307	2.157	313	35	23.0
Retrogressed eclogite	13	3.35	7.143	2.871	1.330	1.512	504	56	23.9
Serpentinite	5	2.58	5.328	3.089	0.475	1.556	466	52	13.7

[a] N is the number of samples. Data are from this study and Wang et al., (2005a). Z is calculated acoustic impedance.

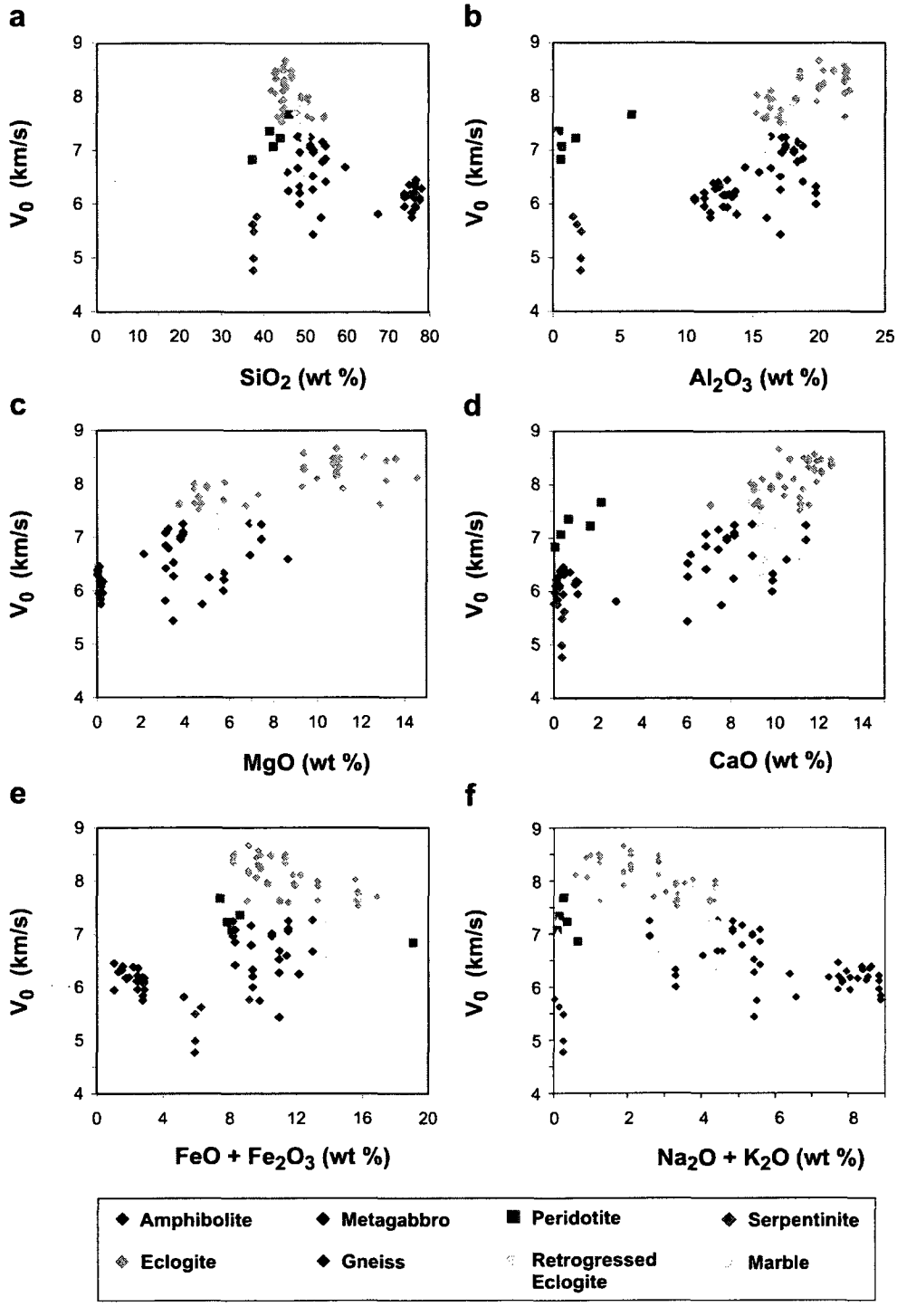

Figure 3.22 Relationship between V_0 and chemical composition for Sulu UHP metamorphic rocks.

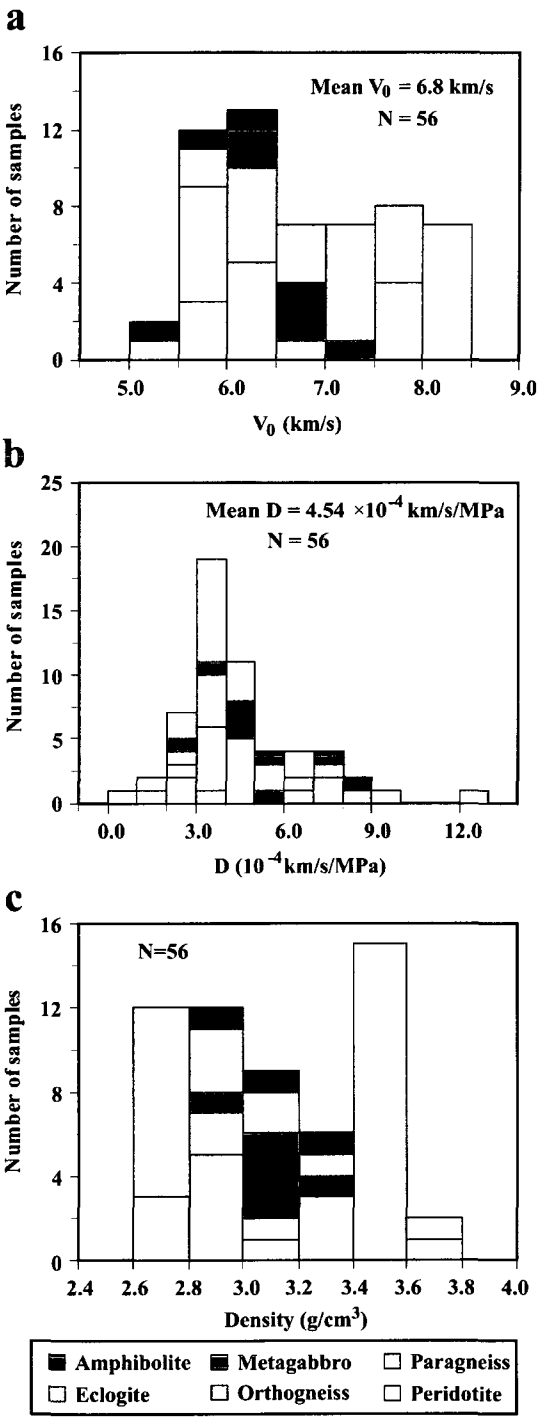

Figure 3.23 V_0 (a) and D (b) reported in Kern et al. (1999, 2002) for Dabie-Sulu UHP metamorphic rocks.

3.6 Conclusions

We have experimentally determined the P-wave velocities of 66 typical UHP metamorphic rock samples of which 31 were collected from the main and pre-pilot holes of the CCSD (Chinese Continental Scientific Drilling) project and 35 were from surface outcrops in the Sulu orogenic belt (China). The velocities were measured at ambient temperature and hydrostatic confining pressures up to 800 MPa. The velocity-pressure curves can be well described by a simple expression: $V(P) = V_0 + DP - B_0 e^{-kP}$, where V_0 is the projected velocity at zero pressure if both pores/cracks were absent; D is the intrinsic pressure derivative of velocity in the linear elastic regime; B_0 is the initial velocity drop from V_0 caused by the presence of pores and cracks at zero pressure; and k is the decay constant of the velocity drop, which controls the shape of the velocity-pressure curves in the nonlinear poro-elastic regime. This equation was used by previous workers as an empirical formula. Here we have shown that the equation can be directly derived from general principles, while the common-sense derivation provides clarification of the physical meaning of each parameter in the equation. The statistical properties of P-wave velocities in the Sulu UHP rocks provide an important set of basic information for the interpretation of field seismic data from the root zones of convergent continental orogenic belts and modern and ancient subduction zones when temperature and pore pressure effects have also been taken into consideration.

P-wave velocities in the Sulu UHP metamorphic rock samples from surface outcrops and shallow depths (10-700 m) in the CCSD pre-pilot hole generally display hysteresis between 0-400 MPa. The presence of a hysteresis loop introduces a considerable complication: there are two velocity values corresponding to each pressure, with the higher value always observed during depressurization. The hysteresis indicates that the porosity, the distribution spectrum of pore aspect ratios and the state of grain contacts are different during pressurization and depressurization. During several successive

pressurization-depressurization cycles, superimposition of the velocity-pressure curves could not be achieved in the nonlinear poro-elastic regime (P<300-400 MPa), and only the curves in the linear regime (>400 MPa) could be reproduced and reversed in the laboratory. Compared with the samples from surface outcrops, those from 3000-4600 m in the CCSD main hole display much less pronounced hysteresis. Most of the microcracks in the drill cores, which are newly formed by decompression during drilling and core retrieval, can reopen completely as pressure is released. However, the cracks and grain boundaries in the surface samples are often altered and filled with alteration products such as sericite or chlorite. The soft materials act as a ductile cushion which improves the contacts between grains. Thus, velocity hysteresis is mainly caused by irreversible change in grain contact conditions, increases in microcrack aspect ratios and reduction of void space during the pressurization-depressurization cycle.

The Yangkou metagabbro is characterized by the occurrence of intragranular coesite and the exsolution of clinopyroxene, rutile and apatite in garnet, indicating that eclogitization was so sluggish in the complex that the dry metagabbro was metastable at depths greater than 200 km (Ye et al., 2000). The eclogite-facies metagabbros display much lower densities and P-wave velocities, and thus acoustic impedances (Z) than eclogites and most peridotites (Table 3.5, Christensen, 1974; Holbrook et al., 1992; Ji et al., 2002). Since an impedance contrast of $\sim 2.5 \times 10^5$ g/s/cm^2 is sufficient to give a reflection coefficient R=5%, the minimum value required to yield strong seismic reflections in the crust, the boundaries between metagabbros and peridotites or eclogites should be strongly seismically reflective. Thus, regionally extensive mantle reflectors observed beneath modern and ancient orogenic belts (e.g., Calvert et al., 1995; Cook et al., 1999) may indicate the preservation of rapidly subducted, dry, metastable crustal mafic or felsic material within the lithospheric upper mantle.

Chapter 4

Poisson's ratios of crystalline rocks as a function of hydrostatic confining pressure

4.1 Abstract

The hydrostatic pressure (P) dependence of Poisson's ratios (υ) has been investigated for 54 samples of the crystalline rocks from the Sulu-Dabie orogenic belt (China) using pulse transmission techniques. The experimental results display 2 main types of the $\upsilon - P$ relationships in the range of 40-850 MPa: (1) υ shows little variation with P in the range of 40-850 MPa; and (2) with increasing pressure, υ increases rapidly below ~200 MPa and then becomes quasi-constant at higher pressures. Types 1 and 2 are observed in 22 and 32 samples, respectively. The origin of type 2 can be reasonably interpreted by a small volume fraction (0.1-0.5%) of randomly distributed and randomly oriented thin-disk shaped pores that are progressively closed during pressurization. The effects of microcrack orientation, crystallographic preferred orientations, and compositional layering should be taken into consideration for interpreting the origin of type 1. The present study suggests that both mineralogy and confining pressure play a critical role in influencing the Poisson's ratio of the crystalline rocks particularly below 200-300 MPa.

4.2 Introduction

Poisson's ratio (υ), named after a French mathematician Simeon Poisson who first analyzed it in 1829, is the negative of the ratio of transverse strain to the axial strain when an isotropic material is subjected to uniaxial stress only (Gercek, 2007). For an isotropic material at a given temperature and a given pressure, υ is a constant which must lie between -1 and 0.5. Materials with $\upsilon < 0$ are called auxetic materials (e.g., foams) because there is an increase in volume when compressed (Lakes, 1987). If materials are elastically anisotropic, Poisson's ratio is not constant but can be any value depending on the orientations of two specified orthogonal directions i and j, where i is the longitudinal direction along which the stress is uniaxially applied and j is the transverse direction in which the transverse strain is measured (Ting and Chen, 2005; Norris, 2006). In other words, Poisson's ratio of an anisotropic rock obtained for a selected pair of orthogonal directions is an apparent value (υ_{ij}) that is significantly different from the true value for its isotropic counterpart (υ). Here only the Poisson's ratios of isotropic rocks are considered.

υ can be calculated from the P- and S-wave velocities (V_p and V_s) of an isotropic rock:

$$\upsilon = 0.5\left(1-\left(\phi^2-1\right)^{-1}\right) \qquad (4.1)$$

where

$$\phi = V_p/V_s \qquad (4.2)$$

υ varies between 0.05 and 0.40 for most rocks.

Poisson's ratio is a helpful hint to overcome the nonuniqueness of the interpretation of either V_p or V_s alone in terms of petrological composition. To obtain the crustal Poisson's ratio requires the knowledge of both V_p or V_s. Seismic refraction and wide-angle reflection experiments often report only V_p data (Brocher, 2005) because the experiments commonly use short period vertical seismometers from which it is difficult to pick the S arrivals (Chevrot and van Hilst, 2000). In addition, the experimental results usually suffer from limited lateral resolution as the structure is averaged along the entire refraction line (Chevrot and van Hilst, 2000). During the last decade, crustal Poisson's ratio information became increasingly available through the analysis of teleseismic receiver functions using single station techniques (Clarke and Silver, 1993; Zandt and Ammon, 1995). The principle of these techniques is to analyze the travel times of phases converted at the Moho and their multiples (e.g., Pms, PpPms, PpSms). The Poisson's ratio measured from the receiver functions is the average value for the whole crust beneath a seismic station. The interpretation of such crustal Poisson's ratio results (e.g., Owens and Zandt, 1997; Chevrot and van der Hilst, 2000; Nair et al., 2006) has been largely based on an assumption that Poisson's ratio depends primarily on SiO_2 content (with more mafic rocks corresponding to higher υ values) and fluid content but does not vary significantly with pressure or temperature (Tarkov and Vavakin, 1982; Christensen, 1996; Owens and Zandt, 1997). If the Poisson's ratios of various rocks display a significant dependence on the depth (i.e., pressure and temperature), the interpretation of the Poisson's ratio data in terms of composition will be complicated. The goal of this investigation is to constrain the effects of hydrostatic confining pressure on the Poisson's ratios for crystalline rocks.

4.3 Samples

In total, 54 crystalline rocks collected from the Dabie-Sulu ultrahigh pressure metamorphic terrane have been used for this study. P- and S-wave velocities for 23 samples were reported in Wang et al. (2005a and b), among which 21 were collected

from fresh surface outcrops in quarries at Dugou, Jianchang, Jiangzhuang, Qinglongshan, Maobei and Xugou of Donghai County, Yanmachang of Ganyu County, Tuofeng of Lianyungang City in the Sulu Terrane, and 2 from the Bixiling complex in the Dabie Mountains. The other 31 samples for which P- and S-wave velocities were determined, respectively, by Ji et al. (2007) and this study were collected from the Chinese Continental Scientific Drilling (CCSD) main borehole cores between 3000 and 4600 m depth (9 samples), the CCSD pre-pilot hole in the depth interval of 0-700 m (17 samples), and a layered UHP complex at Yangkou Beach, Qingdao (5 samples). These core samples represent typical lithologies (felsic orthogneiss, paragneiss, amphibolite, eclogites with various extents of retrogression, and ultramafic rocks such as dunite, garnet harzburgite and lherzolite) in the depth intervals. The UHP complex at Yangkou Beach consists of eclogite-facies metagabbro and serpentinized garnet peridotite blocks enclosed in granitic gneiss. The metagabbro blocks display various degrees of transformation from incipiently metamorphosed gabbro with relict igneous textures and mineral assemblages (i.e., plagioclase + augite + bronzite + biotite + ilmenite) to completely recrystallized coesite-bearing eclogite-facies rocks (omphacite + zoisite + kyanite + garnet + phengite). Locality, recovery depth, lithology, density, bulk chemical and modal compositions as well as geological setting for each of 54 samples were given in Ji et al. (2007), and Wang et al. (2005a and b).

Figures 4.1a, b, and c show plots of rock densities as a function of SiO_2, MgO, Na_2O+K_2O, respectively. Two groups of rocks can be clearly distinguished: the eclogite group and the normal series that includes all other types of rocks with exception of eclogites. For a given content of SiO_2, MgO, Na_2O+K_2O, the eclogite group always exhibits remarkably higher densities than the normal series. For both the groups, the densities increase nearly linearly with decreasing SiO_2 (Fig. 4.1a) and Na_2O+K_2O (Fig. 4.1c). Figure 4.1b demonstrates a nonlinear increase of ρ with increasing MgO. The variation of rock densities as a function of CaO is more complicated: eclogite and

peridotite seem to form a series and all the other types of rocks constitute another series. In both series, rock densities increases rather linearly with CaO (Fig. 4.1d).

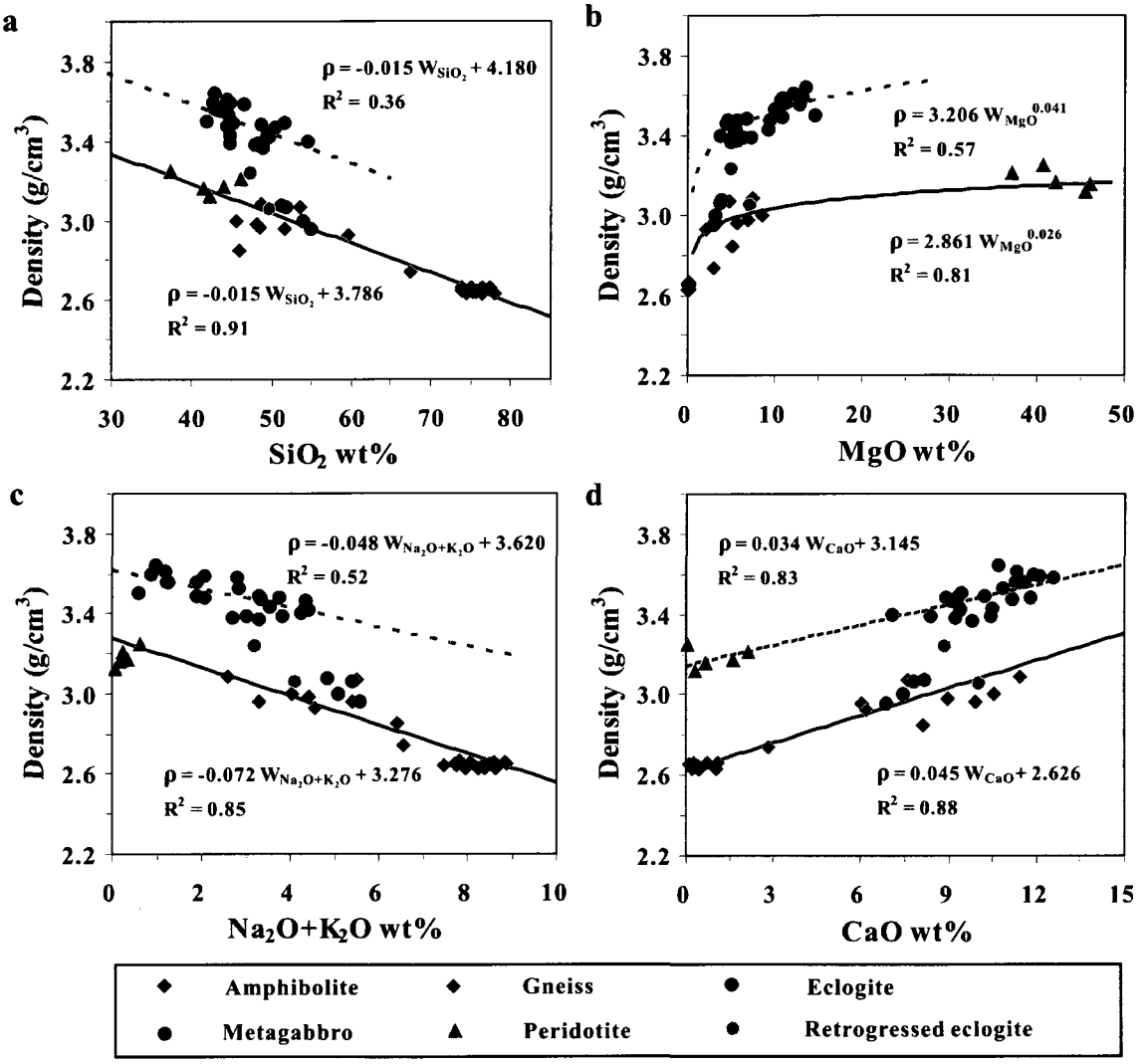

Figure 4.1 Density as a function of SiO_2 (a), MgO (b), Na_2O+K_2O (c) and CaO (d) contents for Sulu-Dabie UHP metamorphic rocks.

4.4 Experimental details

The study involved laboratory measurements of P- and S-wave velocities at hydrostatic pressure ranging from 10 to 850 MPa on jacketed dry samples using the

pulse transmission technique (Birch, 1960; Christensen, 1974; Kern, 1990). Three cylindrical mini-cores (2.54 cm in diameter and 3-5 cm in length) were cut from each sample in orthogonal directions with the X direction parallel to the stretching lineation, the Y direction perpendicular to lineation and parallel to foliation, and the Z direction normal to foliation. The mini-core samples were prepared to ensure two polished plan-parallel end-faces. The high pressure experiments were carried out at the GSC/Dalhousie High Pressure Laboratory in Halifax, Nova Scotia (Ji et al., 1993, 1997; Wang et al., 2005a and b). The apparatus is a seven-ton, double-walled steel vessel with a 40 cm long × 10 cm diameter working chamber, which can operate to a pressure up to 1.4 GPa. The pressure medium consists of light hydraulic oil pumped into the working chamber by means of a two-stage intensifier. Waves were generated and received by lead zirconate transducers with a 1 MHz resonance frequency. To prevent the pressure medium from invading the sample during the pressure run, the mini cores were sheathed in impermeable thin copper foil and the entire sample/transducer/electrode assembly was enclosed in neoprene tubing. Once the sample assembly was sealed in the pressure vessel and the pressure was raised, a high voltage spike from a pulse generator excited the sending transducer and the time of flight to the receiving transducer was measured using a digital oscilloscope. The accuracy is estimated to be 0.5% for V_p and 1% for V_s (Christensen, 1985; Ji et al., 1993; Ji and Salisbury, 1993; Kern et al., 1999, 2002) and 2.5% for calculated Poisson's ratio (Christensen, 1996). The densities of the samples (Table 4.1) were determined using the immersion method with an accuracy of ±0.005 g/cm^3 at room conditions.

4.5 Experimental results

Although the velocity measurements were performed during first pressurization and then depressurization, only the velocity values measured during depressurization corresponded to the stable microstructural state (Burke and Fountain, 1990; Ji et al., 2007) and thus were used for the computations of Poisson's ratios. As shown in Fig. 4.2,

either V_p-P or V_s-P curves display a rapid, nonlinear rise in velocity below a critical pressure (P_c), which is referred as the "crack-closing pressure" (Kern, 1990; Peacock et al., 1994), followed by a slow nearly-linear rise above this critical pressure. This characteristic has been attributed to closure of microcracks in the samples with increasing pressures to P_c, above which the rocks can be regarded as compacted aggregates (Birch, 1960). Due to the presence of microcrack-preferred orientations in each sample, the P_c value may be direction-dependent (Ji et al., 2007).

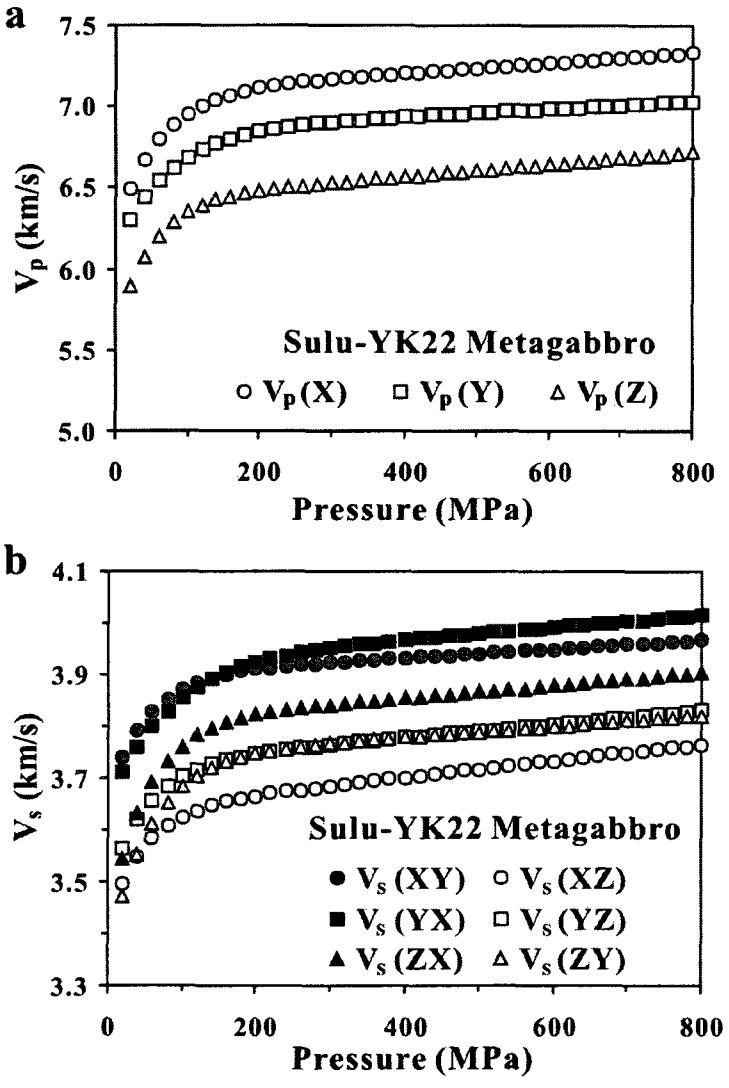

Figure 4.2 P- (a) and S- (b) wave velocities versus confining pressure in metagabbro Sulu-YK22.

Table 4.1 Parameters of V_p-pressure and V_s-pressure curves measured during depressurization for 54 samples from the Dabie-Sulu UHP metamorphic terrane

Sample No.	Lithology	Density	a_p	b_p	c_p	k_p	R^2	a_s	b_s	c_s	k_s	R^2	α	E_0	υ_0	a_p/a_s	b_p/b_s	υ-P
		(g/cm^3)	(km/s)	(10^{-4} km/s/MPa)	(km/s)	(10^{-2} MPa^{-1})		(km/s)	(10^{-4} km/s/MPa)	(km/s)	(10^{-2} MPa^{-1})		(10^{-3})	(GPa)				curve
315-4-11 *	Fine-grained Phn eclogite	3.53	8.107	2.007	1.068	2.358	0.959	4.635	1.720	0.687	2.792	0.998	2.40	131	0.257	1.749	1.167	Type 1
86351 **	Coarse-grained eclogite	3.49	8.335	1.769	0.885	1.096	0.965	4.652	1.849	0.514	1.705	0.959	4.71	142	0.274	1.792	0.957	Type 1
98401 **	Eclogite	3.48	7.627	1.371	0.760	1.355	0.983	4.277	1.863	0.367	1.725	0.964	4.61	117	0.271	1.783	0.736	Type 1
98501 **	Eclogite	3.47	7.299	1.674	0.553	1.123	0.963	4.145	1.373	0.269	1.728	0.975	6.22	106	0.262	1.761	1.219	Type 1
B1628R33P24 *	Hbl-Mag felsic orthogneiss	2.65	6.378	1.923	1.726	2.103	0.997	3.667	0.804	1.213	2.495	0.980	5.84	60	0.253	1.739	2.392	Type 1
B1651R37P41e *	Amphibolite	3.00	6.592	1.708	0.691	2.483	0.981	3.675	0.648	0.618	3.599	0.962	3.86	76	0.275	1.794	2.636	Type 1
B2068R61P20h *	Bt-Pl amphibolite	2.85	6.244	1.313	0.890	2.843	0.998	3.544	0.701	0.368	2.895	0.993	4.09	63	0.262	1.762	1.873	Type 1
C399PCc1 *	Retrogressed Qtz eclogite	3.24	7.695	2.428	1.658	1.786	0.990	4.149	1.022	0.936	2.043	0.996	3.44	117	0.295	1.855	2.376	Type 1
DG1 **	Fine-grained eclogite	3.46	7.842	1.957	0.861	1.322	0.938	4.393	2.099	0.357	1.379	0.983	4.48	124	0.271	1.785	0.932	Type 1
MB22 **	Coarse-grained eclogite	3.50	8.111	2.446	0.950	1.300	0.995	4.715	1.307	0.617	1.377	0.964	4.52	127	0.245	1.720	1.872	Type 1
MB26 **	Coarse-grained eclogite	3.56	8.419	2.873	0.747	1.096	0.943	4.775	1.336	0.349	1.341	0.973	4.67	144	0.263	1.763	2.151	Type 1
MB27B **	Coarse-grained eclogite	3.58	8.405	1.715	0.684	1.032	0.881	4.817	1.014	0.308	1.162	0.961	5.04	142	0.255	1.745	1.692	Type 1
MB2B **	Coarse-grained garnetite	3.61	8.506	0.252	0.853	1.293	0.975	4.912	0.756	0.298	1.040	0.892	3.96	145	0.250	1.731	0.333	Type 1
MB30 **	Coarse-grained eclogite	3.60	8.250	2.069	0.831	1.132	0.922	4.720	1.581	0.380	1.243	0.980	4.74	138	0.257	1.748	1.309	Type 1
MB62 **	Coarse-grained garnetite	3.56	7.621	3.219	0.640	1.399	0.956	4.805	1.388	0.346	1.330	0.974	5.66	97	0.170	1.586	2.319	Type 1
QL4 **	Amphibolite	2.96	6.177	6.053	1.175	1.006	0.980	3.489	2.497	0.728	1.336	0.983	11.25	65	0.266	1.770	2.424	Type 1
SB1 **	Fine-grained eclogite	3.37	7.943	2.325	0.613	0.972	0.917	4.448	1.578	0.247	1.681	0.982	6.10	124	0.272	1.786	1.474	Type 1
Sulu-YK1 *	Metagabbro	3.08	7.131	2.027	0.702	2.564	0.988	4.052	0.964	0.415	2.328	0.968	3.23	89	0.262	1.760	2.103	Type 1
Sulu-YK2A *	Metagabbro	3.07	6.985	2.328	0.718	3.909	0.990	3.967	1.137	0.275	2.245	0.978	2.21	85	0.262	1.761	2.048	Type 1
Sulu-YK3B *	Metagabbro	3.00	6.912	2.210	0.695	2.147	0.991	3.942	1.182	0.247	1.983	0.987	4.24	81	0.259	1.754	1.870	Type 1
YM1 **	Dolomitic marble	2.86	6.678	1.909	0.962	2.265	0.974	3.889	1.247	0.312	1.840	0.981	4.70	70	0.243	1.717	1.530	Type 1
YM4 **	Amphibolite	3.09	7.056	2.019	0.548	1.474	0.969	3.972	1.205	0.236	1.590	0.973	5.62	89	0.268	1.776	1.676	Type 1
147-2-11 *	Dunite	3.16	7.356	2.408	0.947	2.495	0.989	3.963	1.184	0.388	3.519	0.943	2.76	105	0.296	1.856	2.033	Type 2a
151-14-16 *	Grt harzburgite	3.21	7.670	2.580	1.150	1.487	0.923	4.085	1.044	0.570	2.694	0.993	4.12	117	0.302	1.878	2.472	Type 2a
166-42-43 *	Phl dunite	3.25	6.835	2.114	0.932	2.139	0.966	3.697	0.924	0.796	5.081	0.977	3.66	93	0.293	1.849	2.289	Type 2a
210-15-21 *	Granitic gneiss	2.63	6.157	1.902	0.597	2.029	0.993	3.567	0.826	0.302	3.754	0.970	6.65	55	0.247	1.726	2.303	Type 2a
26-10-17 *	Granitic Gneiss	2.64	6.172	2.871	0.932	2.988	0.995	3.611	1.073	0.460	4.072	0.959	4.57	55	0.240	1.709	2.676	Type 2a
B1536R6P41e *	Hbl-Phn eclogite	3.11	7.087	1.718	2.152	2.850	0.997	4.050	0.623	0.861	2.549	0.998	2.94	88	0.257	1.750	2.756	Type 2a
B1608R27P12e *	Grt-Bt-Pl amphibolite	2.98	6.965	1.892	1.006	1.709	0.961	3.875	0.815	0.568	2.949	0.995	5.04	85	0.276	1.797	2.320	Type 2a
MB34 **	Coarse-grained garnetite	3.64	8.476	1.712	0.797	1.055	0.927	4.846	1.161	0.275	1.418	0.968	4.75	148	0.257	1.749	1.475	Type 2a
Sulu-YK22 *	Metagabbro	2.96	6.781	3.074	0.776	1.678	0.988	3.788	1.190	0.290	1.789	0.993	5.50	79	0.273	1.790	2.584	Type 2a
Sulu-YK9 *	Serpentinite	2.60	5.766	2.760	0.300	2.379	0.992	2.923	0.563	0.053	6.734	0.972	5.23	57	0.327	1.972	4.898	Type 2a
TF3 **	Granitic gneiss	2.66	6.096	2.527	0.878	1.577	0.955	3.575	1.296	0.314	1.421	0.946	8.86	53	0.238	1.705	1.949	Type 2a
XG3 **	Serpentinite	2.66	5.622	1.683	0.587	2.287	0.974	2.879	0.464	0.077	1.827	0.984	5.67	55	0.322	1.953	3.628	Type 2a
125-15-18 *	Qtz eclogite	3.48	8.024	3.669	1.106	1.814	0.912	4.512	1.489	0.250	3.018	0.982	3.12	130	0.269	1.779	2.464	Type 2b
125-8-18 *	Qtz eclogite	3.38	7.694	3.188	2.174	2.559	0.979	4.277	1.192	0.447	2.211	0.896	2.43	118	0.276	1.799	2.675	Type 2b
160-12-11 *	Grt harzburgite	3.17	7.229	2.441	2.049	3.137	0.972	3.944	1.071	0.214	4.056	0.978	2.32	100	0.288	1.833	2.278	Type 2b

Table 4.1 (continued)

Sample No.	Lithology	Density	a_p	b_p	c_p	k_p	R^2	a_s	b_s	c_s	k_s	R^2	α	E_0	υ_0	a_p/a_s	b_p/b_s	υ-P
		(g/cm^3)	(km/s)	(10^{-4} km/s/MPa)	(km/s)	(10^{-2} MPa^{-1})		(km/s)	(10^{-4} km/s/MPa)	(km/s)	(10^{-2} MPa^{-1})		(10^{-3})	(GPa)				curve
178-6-6 *	Bt dioritic gneiss	2.74	5.814	2.729	1.072	1.599	0.995	3.277	1.083	0.407	2.518	0.984	8.61	53	0.267	1.774	2.519	Type 2b
203-5-15 *	Amphibolite	3.07	5.746	3.088	1.479	1.732	0.988	3.363	1.764	0.638	2.063	0.999	7.83	55	0.239	1.709	1.750	Type 2b
315-1-11 *	Phn eclogite	3.43	7.952	1.637	1.220	1.682	0.988	4.463	1.502	0.382	4.378	0.984	3.47	126	0.270	1.782	1.090	Type 2b
B2078R63P9r *	Felsic orthogneiss	2.63	6.315	1.932	3.449	3.012	0.997	3.743	1.212	1.170	2.355	0.982	4.47	56	0.229	1.687	1.594	Type 2b
B2168R85P2a *	Bt-Hbl-Pl-Kfs paragneiss	2.65	6.129	1.870	2.171	2.522	0.978	3.393	1.319	0.757	2.556	0.997	4.92	59	0.279	1.807	1.418	Type 2b
JC2 **	Fine-grained eclogite	3.40	7.623	1.375	0.989	1.323	0.984	4.507	1.344	0.373	1.838	0.979	5.37	106	0.231	1.692	1.023	Type 2b
MB23 **	Coarse-grained eclogite	3.48	8.384	2.417	1.134	1.187	0.976	4.669	1.389	0.356	1.390	0.963	4.29	144	0.275	1.796	1.740	Type 2b
MB25 **	Coarse-grained eclogite	3.59	8.316	3.296	1.392	1.496	0.958	4.746	1.587	0.397	1.390	0.970	3.52	140	0.258	1.752	2.077	Type 2b
TF1 **	Granitic gneiss	2.66	6.101	2.402	0.787	1.299	0.976	3.852	0.907	0.308	1.598	0.952	12.75	46	0.169	1.584	2.649	Type 2b
150-3-20 *	Lherzolite	3.12	7.070	2.152	1.455	1.528	0.996	3.857	1.255	0.506	3.774	0.976	5.05	94	0.288	1.833	1.715	Type 2c
19-13-13 *	Granitic Gneiss	2.64	6.186	2.548	1.273	2.241	0.997	3.632	1.372	0.381	6.812	0.755	6.11	55	0.237	1.703	1.856	Type 2c
219-1-2 *	Granitic gneiss	2.63	6.290	2.528	1.586	2.171	0.996	3.482	0.963	0.326	3.767	0.996	5.46	62	0.279	1.807	2.626	Type 2c
703-29 *	Grt-Bt-Hbl dioritic gneiss	2.93	6.685	2.721	1.436	1.988	0.995	3.824	1.305	0.771	6.336	0.984	5.04	74	0.257	1.748	2.085	Type 2c
B1578R14P18t *	Bt-Ms-Pl-Kfs orthogneiss	2.65	6.198	1.691	2.629	2.250	0.996	3.692	0.608	1.063	2.156	0.952	6.23	54	0.225	1.679	2.779	Type 2c
B2184R88P4s *	Bt-Hbl-Pl-Kfs paragneiss	2.66	6.062	1.502	1.992	1.618	0.974	3.619	0.753	1.233	2.793	0.987	9.06	51	0.223	1.675	1.993	Type 2c
JZ1 **	Fine-grained eclogite	3.49	7.590	3.671	1.205	0.867	0.984	4.410	1.326	0.453	1.782	0.988	7.76	111	0.245	1.721	2.768	Type 2c
QL2 **	Eclogite	3.42	7.128	3.323	1.562	0.980	0.985	4.267	2.331	0.620	1.335	0.966	8.47	91	0.221	1.671	1.426	Type 2c

* This study; ** (Wang et al., 2005 a and b).

Natural rocks are generally orthorhombic or transversely isotropic in seismic velocities with respect to the structural framework defined by foliation and lineation. The spatial distribution of seismic speeds in a rock can be described by a velocity ellipsoid whose three principal axes are parallel to the X, Y, and Z directions. If $V_p(X)$, $V_p(Y)$ and $V_p(Z)$ are, respectively, the P-wave velocities along the propagation directions X, Y and Z, the mean P-wave velocity of each sample (i.e., V_p if the rock were isotropic) can be calculated according to the following equation:

$$V_p{}^G = \left[V_p(X) \times V_p(Y) \times V_p(Z)\right]^{1/3} \tag{4.3}$$

where G represents the geometrical mean. In the literature, however, only the arithmetical mean were used (e.g., Birch, 1960; Christensen, 1966; Kern et al., 2002).

$$V_p{}^A = \left[V_p(X) + V_p(Y) + V_p(Z)\right]/3 \tag{4.4}$$

where A represents the arithmetical mean. The relative difference between these two averaging methods, which is defined as $100\% \times \left(V_p{}^A - V_p{}^G\right)/V_p{}^G$, increases consistently with the coefficient of V_p anisotropy which is defined as:

$$A(V_p) = \frac{V_p(\max) - V_p(\min)}{V_p{}^A} \times 100\% \tag{4.5}$$

For these 54 samples with $A(V_p) \leq 20\%$ (Fig. 4.3a), the replacement of the geometrical mean by the arithmetical mean results in a difference <0.35%, which is within the experimental errors. Figure 4.3b, which analyzed a database of seismic velocities of 81 crustal and mantle rocks with $A(V_p) \leq 28\%$ (Ji et al., 2002), displays that the replacement of the geometrical mean by the arithmetical mean results in a difference

<0.70%. The above analysis explains why the mean V_p values calculated from Eq. (4.4) give values very close to true isotropic elastic properties even in highly anisotropic rocks (Christensen and Ramananantoandro, 1971; Ji et al., 2003).

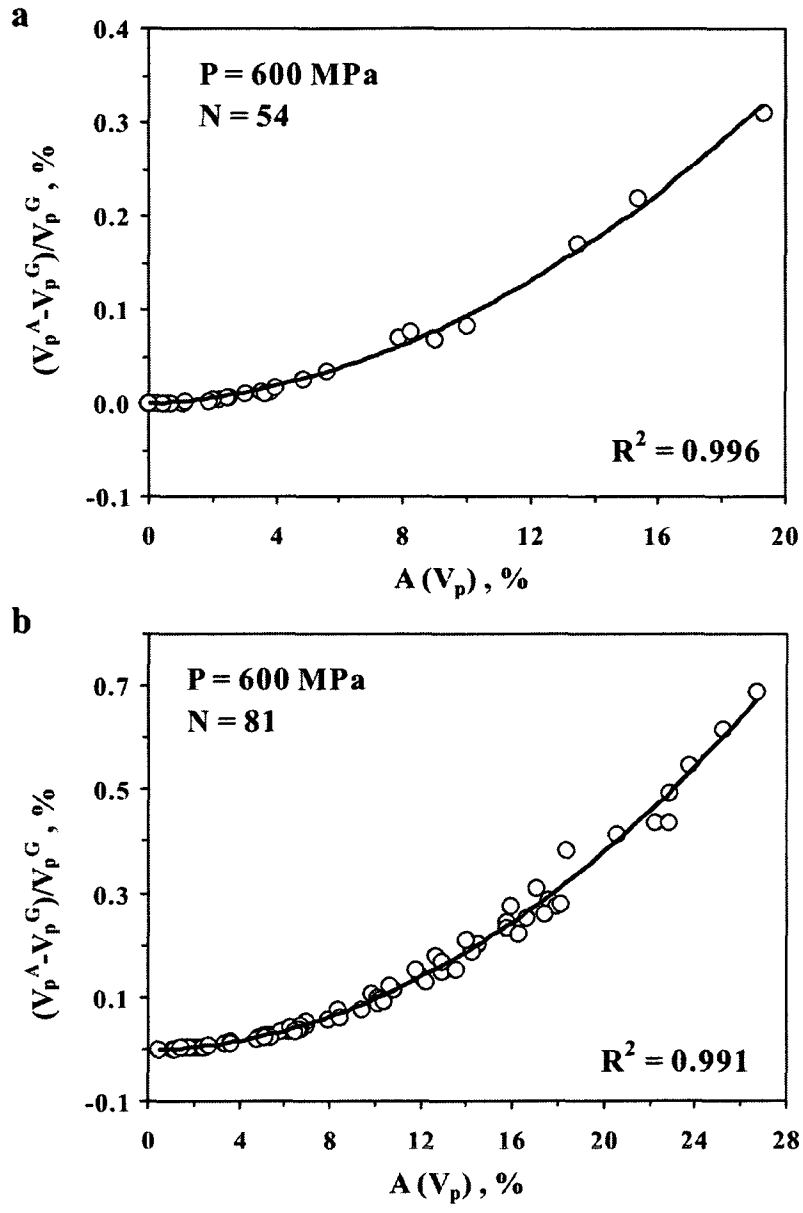

Figure 4.3 Relative differences between the geometrical and arithmetical means of P-wave velocities as a function of seismic anisotropy. Data from this study (a) and Handbook of Seismic Properties of Minerals, Rocks and Ores (Ji et al., 2002) (b). N is the number of samples.

For the same reason described above, the mean S-wave of each sample was obtained by arithmetically averaging the results of six measurements which are designed XY, XZ, YX, YZ, ZX, and ZY. The first letter refers to the propagation direction and the second to the polarization direction.

$$V_s = [V_s(XY) + V_s(XZ) + V_s(YX) + V_s(YZ) + V_s(ZX) + V_s(ZY)]/6 \qquad (4.6)$$

The mean P- and S-wave velocities as a function of confining pressure were described by the following equation:

$$V(P) = a + bP - c\exp(-kP) \qquad (4.7)$$

where a is the projected velocity of a non-porous or crack-free compacted rock at zero pressure, which is determined from extrapolation of the linear velocity-pressure relationship obtained at high pressures to zero pressure; b, which is the pressure derivative of velocity in the linear elastic regime; c, which is the ambient velocity drop caused by the presence of pores/microcracks at zero pressure, determines the maximum magnitude of the velocity increases due to the closure of pores and microcracks; k, which is a decay constant of the velocity drop, controls the shape of the nonlinear segment of the velocity-pressure curve. The zero-pressure velocity of the rock containing microcracks and pores equals (a-c). In Eq. (4.7), a and b are two parameters which describe the seismic property of the microcrack- or pore-free solid matrix, while c and k are two parameters related to the porosity and geometrical shape of pores (e.g., aspect ratio, spatial arrangement, orientation and size distribution), and in turn on the formation and deformation processes of the rocks. Eq. (4.7) was used by previous workers as an empirical formula (Stierman et al., 1979; Zimmerman et al., 1986; Eberhart-Phillips et al., 1989; Freund, 1992; Shapiro, 2003; Wang et al., 2005a, b). Recently, Ji et al. (2007) derived this equation based on an assumption that the difference between the velocities of a nonporous material and its porous counterpart at a

given confining pressure has a maximum value (c) at P=0 and then decays progressively with increasing P at a rate proportional to the value of the velocity at the applied confining pressure. The last term of Eq. (4.7) possesses the same form of the expression that is commonly used to describe natural phenomena such as radioactivity decay, cooling, and vibration attenuation.

Parameters a, b, c and k for the mean P- and S-wave velocities of each sample during depressurization, determined using a least square regression method, are given in Table 4.1. As indicated by the goodness-of-fit coefficients (R^2), the pressure-velocity curves for mean P- and S-waves can be well fitted by Eq. (4.7) with more than 98% and 94% of 54 samples having their $R^2 \geq 0.90$, respectively (Table 4.1).

The Poisson ratio (υ) of each bulk sample is computed from the arithmetical mean V_p and V_s values at each confining pressure according to Eq. (4.1). The calculated results for the 54 crystalline rocks are given in Table 4.2. Two types of the variations of Poisson's ratio with the hydrostatic pressure have been distinguished:

Type 1: Poisson's ratio shows little variation with pressure in the range of 40-850 MPa (Fig. 4.4). The difference ($\delta\upsilon$) between the υ values measured at 600 MPa and 40 MPa is within ± 0.015. This range is set because presently many refraction, vertical reflection and teleseismic measurements are hardly to offer better resolution in υ than ± 0.015. 22 among the 54 samples (41%) belong to this category. These samples are: MB2B and MB62 (garnetite), MB22, MB26, MB27B, MB30, SB1, 315-4-11, 98401, 98501, 86351 and DG1 (eclogites), C399PCc1 (retrogressed Qtz eclogite), Sulu-YK1, Sulu-YK2A and Sulu-YK3B (metagabbros), YM4, B1651R37P41c, B2068R61P20h, QL4 (amphibolite), YM1 (dolomitic marble), and B1628R33P24 (Hbl-Mag felsic orthogneiss).

Type 2: With increasing pressure, Poisson's ratio increases rapidly below about 200 MPa and then becomes quasi-constant at higher pressures (Fig. 4.5). 32 among the 54

samples (59%) belong to this category. According to the difference ($\delta\upsilon$) between the υ values measured at 600 MPa and 40 MPa, the 32 samples are further classified into three groups: Group 2a ($\delta\upsilon = 0.015 - 0.030$), Group 2b ($\delta\upsilon = 0.030 - 0.060$), and Group 2c ($\delta\upsilon > 0.060$). Samples belonging to each group are listed in Table 4.2. The metamorphic and intrusive rock samples from the San Gabriel-Mojava region, southern California, reported in McCaffree and Christensen (1998), also belong to this category.

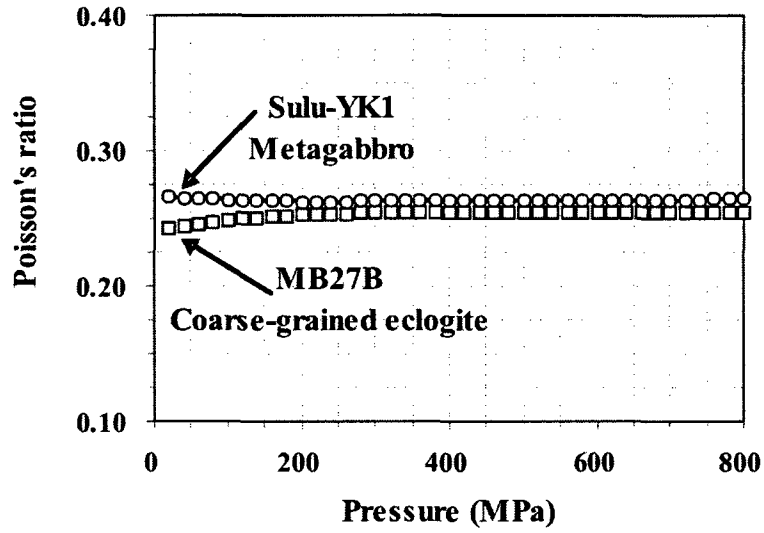

Figure 4.4 Poisson's ratios plotted as a function of pressure (Type 1). (a) Metagabbro Sulu-YK1, (2) Coarse-grained eclogite MB27B.

4.6 Discussion

4.6.1 Pressure-dependence of Poisson's ratio

The differential relationship of υ with P is:

$$\frac{d\upsilon}{dP} = \frac{d\upsilon}{d\phi}\frac{d\phi}{dP} \qquad (4.8)$$

Eq. (4.1) yields:

$$\frac{d\upsilon}{d\phi} = \frac{\phi}{(\phi^2 - 1)^2} \tag{4.9}$$

Because both ϕ and $(\phi^2 - 1)^2$ are always positive, $d\upsilon/d\phi > 0$. Hence Eq. (4.8) indicates that the variation in Poisson's ratio should depend upon the variation of ϕ or V_p/V_s with confining pressure P.

From Eq. (4.2), we obtain:

$$\frac{d\phi}{dP} = \frac{\frac{dV_p}{dP}V_s - \frac{dV_s}{dP}V_p}{V_s^2} \tag{4.10}$$

As $V_s^2 > 0$, the variation in Poisson's ratio depends upon the competition between terms $V_s(dV_p/dP)$ and $V_p(dV_s/dP)$.

In Eq. (4.10),

$$V_p = a_p + b_p P - c_p \exp(-k_p P) \tag{4.11}$$

$$V_s = a_s + b_s P - c_s \exp(-k_s P) \tag{4.12}$$

where the subscripts p and s denote the P- and S-waves, respectively. Differentiating Equations (4.11)-(4.12), we can obtain:

$$\frac{dV_p}{dP} = b_p + c_p k_p \exp(-k_p P) \tag{4.13}$$

$$\frac{dV_s}{dP} = b_s + c_s k_s \exp(-k_s P) \tag{4.14}$$

Substituting Eqs. (4.11)-(4.14) into Eq. (4.10), we obtain:

$$\frac{d\phi}{dP} = \frac{b_P + c_P k_P \exp(-k_P P)}{a_S + b_S P - c_S \exp(-k_S P)} - \frac{(a_P + b_P P - c_P \exp(-k_P P))(b_S + c_S k_S \exp(-k_S P))}{(a_S + b_S P - c_S \exp(-k_S P))^2} \tag{4.15}$$

Poisson's ratio increases with pressure if $d\phi/dP > 0$. υ remains quasi-constant if $d\phi/dP \approx 0$. υ decreases with increasing pressure if $d\phi/dP < 0$.

The results computed according to Eq. (4.15) are shown in Table 4.3. Four samples are selected to display two patterns of the variations of $d\phi/dP$ or $d(V_p/V_s)/dP$ as a function of P (Fig. 4.6). For samples MB27B (coarse-grained eclogite) and Sulu-YK1 (metagabbro), $d\phi/dP \approx 0$ in the full range from 40 MPa to 800 MPa (Figs. 4.6a-b). For samples 125-8-18 (Qtz eclogite) and 160-12-11 (Grt-harzburgite), with increasing P, $d\phi/dP$ decreases rapidly below ~200 MPa and then gradually becomes nearly zero above this pressure (Figs. 4.6a-b). In the nonlinear, poro-elastic regime, $d\phi/dP > 0$, that is, υ increases with increasing pressure for this category of samples.

At lower pressures where rocks contains open microcracks, both P- and S-wave velocities display a nonlinear rise with increase in pressure (Fig. 4.2), and thus the variation of V_p/V_s or ϕ with pressure depends on all the parameters in Eq. (4.15) at each given pressure (Table 4.3). For a compact rock that contains neither pores nor open microcracks, however, the relation between seismic velocities and confining pressure is linear. In this so-called linear elastic regime, c_p=0 and c_s=0, Eq. (4.15) is simplified as:

$$\frac{d\phi}{dP} = \frac{a_s b_p - a_p b_s}{(a_S + b_S P)^2} \tag{4.16}$$

$(a_S + b_S P)^2$ is always positive. The sign of the partial derivative of ϕ with P depends on the relative magnitude of $a_s b_p$ with respect to $a_p b_s$.

Poisson's ratio remains constant for compact rocks if

$$\frac{b_p}{b_s} = \frac{a_p}{a_s} = \sqrt{\frac{2(1-\upsilon_0)}{1-2\upsilon_0}} \qquad (4.17)$$

where υ_0 is the Poisson's ratio of the non-porous material at zero pressure.

Poisson's ratio increases with increasing pressure for compact rocks if

$$\frac{b_p}{b_s} > \frac{a_p}{a_s} = \sqrt{\frac{2(1-\upsilon_0)}{1-2\upsilon_0}} \qquad (4.18)$$

Poisson's ratio decreases with increasing pressure for compact rocks if

$$\frac{b_p}{b_s} < \frac{a_p}{a_s} = \sqrt{\frac{2(1-\upsilon_0)}{1-2\upsilon_0}} \qquad (4.19)$$

Eqs. (4.17)-(4.19) indicate that in the linearly elastic regime, the variation of Poisson's ratio with pressure depends only on the magnitude of b_p/b_s with respect to υ_0. For the compact rocks in which both pores and microcracks are closed, (a_p/a_s) is almost always larger than $\sqrt{2}$ (i.e., $0<\upsilon_0<0.5$). Among 54 samples studied (Table 4.1, Fig. 4.7), 23 samples (~42.6%) show $b_p/b_s \approx a_p/a_s$ with $(b_p/b_s - a_p/a_s)$ values are within ± 0.4, 9 samples (~16.7%) show clearly $b_p/b_s < a_p/a_s$ with $(b_p/b_s - a_p/a_s)$ values range from -1.399 to -0.439, and 22 samples (~40.7%) display unambiguously $b_p/b_s > a_p/a_s$ with $(b_p/b_s - a_p/a_s)$ values range from 0.441 to 2.925.

Table 4.2 Poisson's ratios at various hydrostatic confining pressures for 54 samples from the Dabie-Sulu UHP metamorphic terrane

Sample No.	Lithology	Pressure (MPa)																	v-P curve
		0	20	40	60	80	100	120	140	160	180	200	250	300	400	500	600	700	800	
315-4-11	Fine-grained Phn eclogite	0.270	0.259	0.255	0.253	0.253	0.254	0.254	0.255	0.255	0.255	0.255	0.255	0.254	0.254	0.253	0.252	0.251	0.250	Type 1
86351	Coarse-grained eclogite	0.277	0.269	0.264	0.262	0.262	0.262	0.262	0.263	0.264	0.265	0.266	0.267	0.268	0.268	0.267	0.266	0.265	0.264	Type 1
98401	Eclogite	0.260	0.259	0.259	0.260	0.261	0.262	0.262	0.263	0.264	0.264	0.265	0.265	0.265	0.264	0.262	0.260	0.259	0.257	Type 1
98501	Eclogite	0.254	0.251	0.250	0.250	0.251	0.252	0.253	0.254	0.255	0.256	0.256	0.258	0.258	0.259	0.258	0.258	0.257	0.256	Type 1
B1628R33P24	Hbl-Mag felsic orthogneiss	0.307	0.273	0.258	0.252	0.250	0.249	0.250	0.251	0.252	0.252	0.253	0.254	0.255	0.256	0.256	0.257	0.257	0.258	Type 1
B1651R37P41c	Amphibolite	0.317	0.287	0.275	0.272	0.272	0.272	0.273	0.274	0.274	0.275	0.275	0.276	0.276	0.277	0.277	0.278	0.278	0.279	Type 1
B2068R61P20h	Bt-Pl amphibolite	0.229	0.245	0.253	0.257	0.259	0.261	0.262	0.262	0.262	0.262	0.263	0.263	0.263	0.263	0.263	0.263	0.263	0.263	Type 1
C399PCc1	Retrogressed Qtz eclogite	0.302	0.295	0.291	0.291	0.291	0.291	0.292	0.293	0.293	0.294	0.295	0.295	0.296	0.297	0.297	0.297	0.298	0.298	Type 1
DG1	Fine-grained eclogite	0.249	0.254	0.258	0.260	0.262	0.264	0.265	0.265	0.266	0.266	0.267	0.267	0.266	0.265	0.264	0.262	0.261	0.259	Type 1
MB22	Coarse-grained eclogite	0.257	0.252	0.250	0.248	0.247	0.246	0.245	0.245	0.245	0.245	0.245	0.245	0.245	0.245	0.246	0.246	0.246	0.246	Type 1
MB26	Coarse-grained eclogite	0.250	0.251	0.252	0.253	0.254	0.256	0.257	0.258	0.259	0.260	0.260	0.262	0.263	0.264	0.265	0.265	0.266	0.266	Type 1
MB27B	Coarse-grained eclogite	0.241	0.243	0.245	0.246	0.247	0.249	0.250	0.250	0.251	0.252	0.252	0.253	0.254	0.255	0.255	0.255	0.255	0.255	Type 1
MB2B	Coarse-grained garnetite	0.214	0.226	0.233	0.238	0.242	0.244	0.246	0.247	0.247	0.248	0.248	0.248	0.247	0.246	0.245	0.244	0.243	0.242	Type 1
MB30	Coarse-grained eclogite	0.240	0.242	0.244	0.246	0.248	0.249	0.250	0.251	0.252	0.252	0.253	0.253	0.254	0.254	0.254	0.253	0.252	0.252	Type 1
MB62	Coarse-grained garnetite	0.155	0.161	0.164	0.167	0.168	0.170	0.171	0.171	0.172	0.172	0.173	0.174	0.174	0.176	0.177	0.178	0.180	0.181	Type 1
QL4	Amphibolite	0.281	0.270	0.263	0.259	0.257	0.257	0.257	0.258	0.259	0.260	0.262	0.265	0.267	0.271	0.274	0.276	0.277	0.279	Type 1
SB1	Fine-grained eclogite	0.255	0.254	0.254	0.255	0.256	0.258	0.260	0.261	0.262	0.264	0.265	0.267	0.268	0.269	0.269	0.269	0.269	0.268	Type 1
Sulu-YK1	Metagabbro	0.265	0.266	0.265	0.265	0.264	0.264	0.263	0.263	0.263	0.263	0.262	0.262	0.263	0.263	0.263	0.263	0.264	0.264	Type 1
Sulu-YK2A	Metagabbro	0.234	0.260	0.267	0.268	0.267	0.266	0.265	0.264	0.264	0.263	0.263	0.263	0.263	0.263	0.264	0.264	0.264	0.264	Type 1
Sulu-YK3B	Metagabbro	0.227	0.241	0.248	0.253	0.255	0.257	0.258	0.259	0.259	0.259	0.259	0.259	0.260	0.260	0.260	0.260	0.260	0.260	Type 1
YM1	Dolomitic marble	0.178	0.210	0.226	0.235	0.239	0.241	0.243	0.243	0.243	0.243	0.243	0.243	0.243	0.242	0.242	0.242	0.242	0.241	Type 1
YM4	Amphibolite	0.254	0.257	0.260	0.261	0.263	0.264	0.265	0.266	0.266	0.266	0.267	0.267	0.267	0.268	0.267	0.267	0.267	0.267	Type 1
147-2-11	Dunite	0.274	0.276	0.281	0.285	0.289	0.291	0.293	0.294	0.295	0.295	0.295	0.296	0.296	0.296	0.296	0.296	0.297	0.297	Type 2a
151-14-16	Grt harzburgite	0.295	0.283	0.280	0.282	0.285	0.288	0.291	0.294	0.296	0.298	0.299	0.301	0.302	0.304	0.304	0.305	0.305	0.305	Type 2a
166-42-43	Phl dunite	0.341	0.286	0.274	0.276	0.281	0.285	0.288	0.290	0.291	0.292	0.293	0.294	0.294	0.295	0.295	0.295	0.296	0.296	Type 2a
210-15-21	Granitic gneiss	0.237	0.227	0.228	0.232	0.236	0.240	0.242	0.244	0.246	0.247	0.247	0.248	0.249	0.250	0.250	0.251	0.251	0.252	Type 2a
26-10-17	Granitic Gneiss	0.217	0.216	0.223	0.229	0.234	0.237	0.239	0.240	0.241	0.242	0.242	0.243	0.244	0.245	0.246	0.248	0.249	0.250	Type 2a
B1536R6P41e	Hbl-Phn eclogite	0.142	0.216	0.241	0.251	0.256	0.257	0.258	0.259	0.259	0.259	0.259	0.259	0.259	0.260	0.261	0.261	0.262	0.262	Type 2a
B1608R27P12e	Grt-Bt-Pl amphibolite	0.277	0.260	0.256	0.257	0.260	0.264	0.267	0.269	0.271	0.273	0.274	0.276	0.276	0.277	0.278	0.278	0.279	0.279	Type 2a
MB34	Coarse-grained garnetite	0.226	0.230	0.233	0.237	0.240	0.242	0.245	0.247	0.248	0.250	0.251	0.253	0.254	0.255	0.256	0.255	0.255	0.255	Type 2a
Sulu-YK22	Metagabbro	0.243	0.252	0.258	0.263	0.266	0.268	0.270	0.271	0.272	0.273	0.274	0.275	0.276	0.277	0.278	0.278	0.279	0.280	Type 2a
Sulu-YK9	Serpentinite	0.310	0.314	0.318	0.322	0.324	0.326	0.327	0.328	0.329	0.329	0.329	0.330	0.331	0.332	0.333	0.335	0.336	0.337	Type 2a
TF3	Granitic gneiss	0.180	0.201	0.214	0.222	0.228	0.231	0.234	0.235	0.237	0.237	0.238	0.239	0.239	0.240	0.240	0.240	0.241	0.241	Type 2a
XG3	Serpentinite	0.276	0.296	0.308	0.314	0.318	0.320	0.321	0.322	0.323	0.323	0.323	0.324	0.324	0.325	0.326	0.326	0.327	0.327	Type 2a
125-15-18	Qtz eclogite	0.194	0.215	0.230	0.242	0.250	0.256	0.260	0.263	0.265	0.267	0.268	0.270	0.271	0.272	0.273	0.274	0.275	0.275	Type 2b
125-8-18	Qtz eclogite	0.036	0.181	0.231	0.253	0.264	0.270	0.274	0.276	0.277	0.277	0.278	0.279	0.279	0.280	0.281	0.282	0.282	0.283	Type 2b
160-12-11	Grt harzburgite			0.237	0.263	0.275	0.281	0.285	0.287	0.288	0.288	0.289	0.289	0.289	0.290	0.290	0.290	0.291	0.291	Type 2b
178-6-6	Bt dioritic gneiss	0.211	0.216	0.225	0.234	0.242	0.248	0.253	0.257	0.260	0.263	0.265	0.267	0.269	0.271	0.272	0.273	0.274	0.274	Type 2b
203-5-15	Amphibolite	0.156	0.179	0.195	0.206	0.215	0.221	0.226	0.230	0.232	0.234	0.236	0.238	0.239	0.240	0.240	0.240	0.240	0.240	Type 2b
315-1-11	Phn eclogite	0.210	0.207	0.219	0.231	0.242	0.249	0.255	0.259	0.261	0.263	0.265	0.266	0.267	0.266	0.266	0.265	0.264	0.263	Type 2b
B2078R63P9r	Felsic orthogneiss			0.184	0.216	0.228	0.231	0.232	0.232	0.231	0.231	0.230	0.229	0.229	0.229	0.228	0.228	0.228	0.228	Type 2b
B2168R85P2a	Bt-Hbl-Pl-Kfs paragneiss	0.101	0.204	0.240	0.257	0.266	0.271	0.274	0.276	0.277	0.277	0.277	0.278	0.278	0.277	0.277	0.276	0.275	0.275	Type 2b
JC2	Fine-grained eclogite	0.183	0.189	0.196	0.202	0.207	0.211	0.215	0.218	0.220	0.222	0.223	0.226	0.227	0.227	0.226	0.226	0.225	0.224	Type 2b
MB23	Coarse-grained eclogite	0.226	0.237	0.245	0.251	0.256	0.260	0.263	0.265	0.267	0.269	0.270	0.272	0.273	0.274	0.275	0.275	0.275	0.275	Type 2b
MB25	Coarse-grained eclogite	0.174	0.203	0.221	0.233	0.241	0.246	0.250	0.253	0.255	0.256	0.257	0.259	0.259	0.260	0.261	0.261	0.262	0.262	Type 2b
TF1	Granitic gneiss	0.099	0.114	0.125	0.134	0.142	0.148	0.153	0.157	0.160	0.163	0.165	0.169	0.172	0.175	0.177	0.179	0.180	0.182	Type 2b
150-3-20	Lherzolite	0.224	0.214	0.224	0.238	0.250	0.260	0.268	0.273	0.277	0.280	0.282	0.285	0.287	0.287	0.287	0.287	0.287	0.287	Type 2c
19-13-13	Granitic Gneiss	0.110	0.118	0.159	0.189	0.207	0.219	0.226	0.230	0.233	0.234	0.236	0.237	0.237	0.238	0.238	0.238	0.239	0.239	Type 2c
219-1-2	Granitic gneiss	0.091	0.167	0.210	0.236	0.252	0.262	0.269	0.273	0.276	0.277	0.279	0.280	0.281	0.282	0.283	0.284	0.285	0.285	Type 2c
703-29	Grt-Bt-Hbl dioritic gneiss	0.244	0.170	0.183	0.206	0.223	0.235	0.243	0.248	0.251	0.253	0.255	0.257	0.258	0.259	0.259	0.260	0.260	0.261	Type 2c
B1578R14P18t	Bt-Ms-Pl-Kfs orthogneiss			0.168	0.194	0.208	0.216	0.220	0.223	0.225	0.226	0.226	0.227	0.228	0.229	0.230	0.230	0.231	0.232	Type 2c
B2184R88P4s	Bt-Hbl-Pl-Kfs paragneiss	0.238	0.170	0.152	0.156	0.168	0.179	0.190	0.198	0.205	0.210	0.213	0.219	0.222	0.224	0.225	0.225	0.225	0.226	Type 2c
JZ1	Fine-grained eclogite	0.188	0.184	0.186	0.191	0.197	0.203	0.209	0.215	0.220	0.224	0.228	0.235	0.241	0.247	0.250	0.253	0.254	0.256	Type 2c
QL2	Eclogite	0.124	0.136	0.148	0.158	0.167	0.175	0.182	0.188	0.192	0.197	0.200	0.207	0.211	0.215	0.216	0.216	0.216	0.215	Type 2c

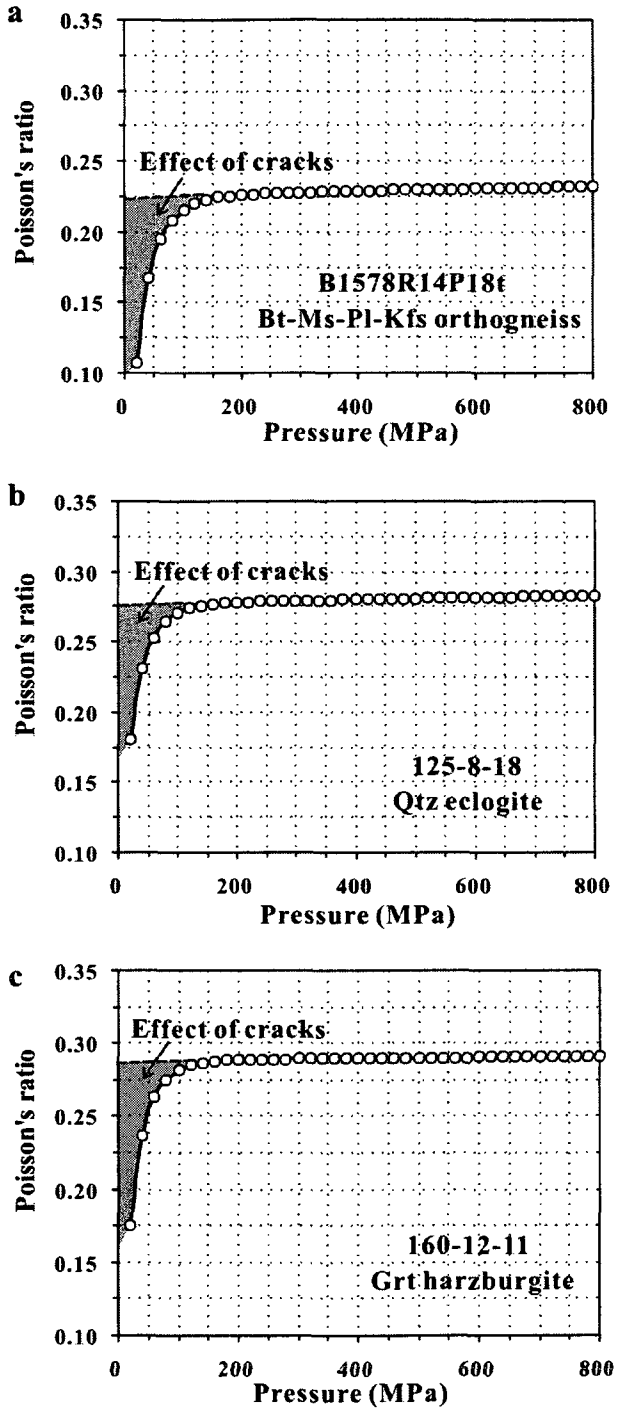

Figure 4.5 Poisson's ratio versus confining pressure (Type 2). (a) Bt-Ms-Pl-Kfs othogneiss B1578R14P18t; (b) Qtz eclogite 125-8-18; (c) Grt harzburgite 160-12-11. The linear slopes at higher pressures reflect the intrinsic elastic properties of crack-free rocks. The non-linear curves result from the progressive closure of microcracks.

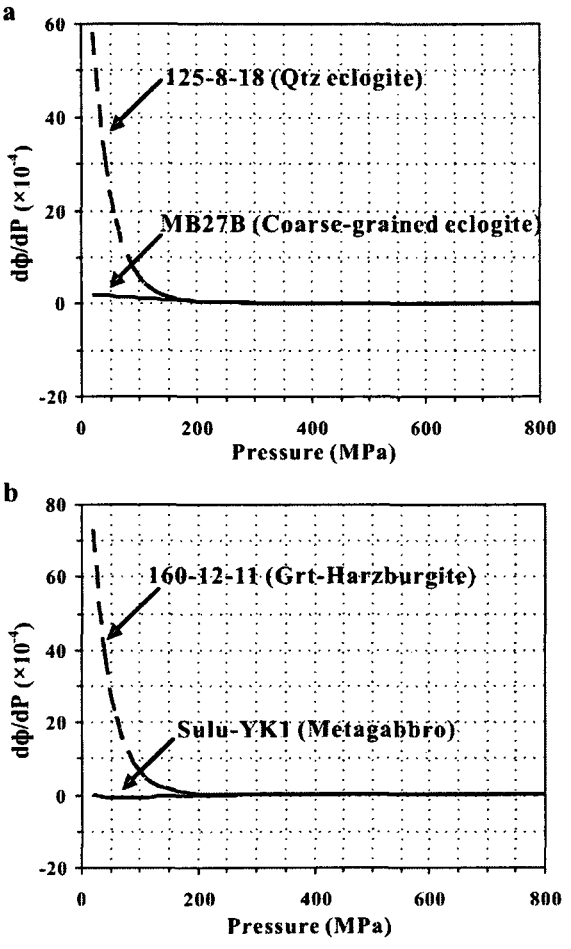

Figure 4.6 Pressure derivative of V_p/V_s ratio (ϕ) versus confining pressure. (a) samples 125-8-18 (Qtz eclogite), and MB27B (coarse-grained eclogite); (b) samples 160-12-11 (Grt harzburgite), and Sulu-YK1 (metagabbro).

Six representative samples were selected to illustrate the variations of Poisson's ratio with hydrostatic pressure (0-4.0 GPa) when porosity was assumed to be absent (Fig. 4.8). QL4 (amphibolite), B1536R6P41e (Hbl-Phn eclogite) and TF1 (granitic gneiss) show a continuous and considerable increase in Poisson's ratio with increasing pressure. Poisson's ratios for MB27B (coarse-grained eclogite) and B2078R63P9r (felsic orthogneiss) remain almost unchanged in the range of 0-4.0 GPa. Eclogite 98401

displays a pronounced decrease in Poisson's ratio with increasing pressure. Christensen (1996) averaged the Poisson's ratio values measured for each lithologic category and reported a slight increase in the mean υ with increasing P from 200 MPa to 1000 MPa for anorthosite, amphibolite, basalt, granite gneiss, felsic granulite, mafic granulite and pyroxenite. This indicates that $(a_p/a_s)<(b_p/b_s)$ over the pressure range for the investigated rocks. Obviously, the υ_0 values of samples QL4, B1536R6P41e, TF1 and 98401 cannot represent those of the same lithologies in the in-situ subduction zone or in the deep root of the continental orogenic belt. Hence the effects of confining pressure should be taken into account in the interpretation of seismic data (e.g., teleseismic received functions) in terms of Poisson's ratio.

Eqs. (4.16)-(4.19) can be applied when the confining pressure is higher than the crack-closing pressure (P_c) above which the seismic velocities increase linearly with increasing pressure. P_c depends on the k_p, and k_s values. According to Ji et al. (2007), P_c is defined as the pressure at which the difference between the velocities of a nonporous material and its porous counterpart is only 0.2% of the value at P=0. Above P_c, the difference disappears and the rock sample can be regarded as a nearly crack-free aggregate. For P-waves,

$$P_c(P) = -\frac{\ln 0.002}{k_P} \approx \frac{6.215}{k_P} \tag{4.20}$$

and for S-waves,

$$P_c(S) = -\frac{\ln 0.002}{k_S} \approx \frac{6.215}{k_S} \tag{4.21}$$

It is expected that $k_p \approx k_s$ and $P_c(P) \approx P_c(S)$ for the same rock.

Table 4.3 Pressure derivatives of the ratio of V_p to V_s at various confining pressure for 54 samples from the Dabie-Sulu UHP metamorphic terrane

Sample No.	Lithology	$d(V_p/V_s)/dP$ ($\times 10^{-4}$) (/MPa)																v-P
		40	60	80	100	120	140	160	180	200	250	300	400	500	600	700	800	curve
315-4-11	Fine-grained Phn eclogite	-2.799	-0.508	0.316	0.515	0.468	0.341	0.207	0.091	0.001	-0.129	-0.182	-0.206	-0.208	-0.207	-0.205	-0.204	Type 1
86351	Coarse-grained eclogite	-3.920	-1.508	-0.124	0.629	0.995	1.125	1.115	1.027	0.900	0.547	0.249	-0.101	-0.240	-0.289	-0.305	-0.309	Type 1
98401	Eclogite	0.576	1.043	1.181	1.140	1.007	0.835	0.653	0.479	0.321	0.016	-0.182	-0.361	-0.415	-0.427	-0.428	-0.426	Type 1
98501	Eclogite	-0.351	0.591	1.064	1.253	1.274	1.200	1.077	0.934	0.788	0.465	0.227	-0.028	-0.123	-0.156	-0.166	-0.169	Type 1
B1628R33P24	Hbl-Mag felsic orthogneiss	-11.897	-4.205	-0.909	0.453	0.930	1.008	0.921	0.782	0.640	0.378	0.240	0.156	0.142	0.140	0.139	0.138	Type 1
B1651R37P41c	Amphibolite	-8.681	-1.846	0.483	1.090	1.079	0.888	0.683	0.515	0.391	0.230	0.172	0.149	0.146	0.145	0.145	0.144	Type 1
B2068R61P20h	Bt-Pl amphibolite	6.738	3.811	2.187	1.267	0.740	0.437	0.262	0.161	0.102	0.043	0.027	0.022	0.022	0.021	0.021	0.021	Type 1
C399PCc1	Retrogressed Qtz eclogite	-2.693	-0.328	0.723	1.122	1.199	1.125	0.990	0.840	0.699	0.432	0.276	0.158	0.132	0.126	0.124	0.124	Type 1
DG1	Fine-grained eclogite	3.744	2.809	2.097	1.549	1.126	0.796	0.538	0.336	0.178	-0.081	-0.225	-0.342	-0.374	-0.381	-0.381	-0.378	Type 1
MB22	Coarse-grained eclogite	-2.557	-1.663	-1.068	-0.670	-0.404	-0.227	-0.110	-0.034	0.014	0.065	0.074	0.060	0.049	0.043	0.041	0.041	Type 1
MB26	Coarse-grained eclogite	1.282	1.424	1.446	1.397	1.307	1.196	1.078	0.960	0.849	0.613	0.437	0.238	0.155	0.123	0.111	0.106	Type 1
MB27B	Coarse-grained eclogite	1.726	1.550	1.378	1.214	1.062	0.923	0.798	0.686	0.588	0.393	0.255	0.100	0.034	0.007	-0.004	-0.008	Type 1
MB2B	Coarse-grained garnetite	6.370	4.498	3.141	2.158	1.446	0.933	0.564	0.301	0.115	-0.135	-0.231	-0.255	-0.237	-0.223	-0.215	-0.212	Type 1
MB30	Coarse-grained eclogite	2.166	1.848	1.565	1.315	1.096	0.906	0.742	0.601	0.480	0.254	0.104	-0.049	-0.108	-0.129	-0.136	-0.138	Type 1
MB62	Coarse-grained garnetite	2.068	1.487	1.086	0.807	0.613	0.479	0.387	0.323	0.280	0.226	0.206	0.201	0.203	0.204	0.203	0.202	Type 1
QL4	Amphibolite	-6.443	-3.211	-1.193	0.063	0.829	1.273	1.507	1.604	1.614	1.446	1.201	0.804	0.591	0.492	0.448	0.428	Type 1
SB1	Fine-grained eclogite	0.725	1.484	1.840	1.947	1.905	1.779	1.609	1.423	1.237	0.822	0.507	0.144	-0.008	-0.068	-0.091	-0.099	Type 1
Sulu-YK1	Metagabbro	-0.665	-0.843	-0.766	-0.611	-0.449	-0.309	-0.199	-0.116	-0.055	0.028	0.062	0.078	0.079	0.079	0.079	0.079	Type 1
Sulu-YK2A	Metagabbro	3.738	-0.345	-1.421	-1.432	-1.136	-0.810	-0.539	-0.339	-0.198	-0.017	0.049	0.077	0.080	0.079	0.079	0.079	Type 1
Sulu-YK3B	Metagabbro	6.534	3.968	2.417	1.474	0.901	0.552	0.341	0.214	0.137	0.058	0.038	0.033	0.034	0.034	0.033	0.033	Type 1
YM1	Marble	11.146	6.200	3.375	1.768	0.865	0.368	0.102	-0.032	-0.094	-0.118	-0.097	-0.068	-0.060	-0.058	-0.057	-0.057	Type 1
YM4	Amphibolite	2.553	2.012	1.582	1.239	0.967	0.751	0.580	0.445	0.339	0.166	0.071	-0.003	-0.023	-0.028	-0.029	-0.029	Type 1
147-2-11	Dunite	6.931	5.856	4.390	3.095	2.104	1.400	0.921	0.605	0.400	0.161	0.083	0.054	0.051	0.051	0.051	0.050	Type 2a
151-14-16	Grt harzburgite	0.124	3.885	5.039	5.004	4.470	3.778	3.091	2.479	1.965	1.088	0.609	0.256	0.172	0.153	0.148	0.146	Type 2a
166-42-43	Phl dunite	-2.718	5.793	6.477	5.227	3.798	2.642	1.807	1.232	0.847	0.370	0.196	0.118	0.109	0.107	0.106	0.106	Type 2a
210-15-21	Granitic gneiss	3.374	4.578	4.169	3.332	2.506	1.829	1.318	0.948	0.688	0.344	0.208	0.141	0.132	0.130	0.129	0.129	Type 2a
26-10-17	Granitic Gneiss	6.775	5.591	3.983	2.670	1.754	1.163	0.799	0.581	0.453	0.325	0.292	0.281	0.279	0.277	0.276	0.274	Type 2a
B1536R6P41e	Hbl-Phn eclogite	16.362	7.512	3.424	1.523	0.655	0.278	0.129	0.083	0.080	0.113	0.137	0.151	0.152	0.152	0.152	0.151	Type 2a
B1608R27P12e	Grt-Bt-Pl amphibolite	-0.721	3.218	4.296	4.172	3.600	2.927	2.299	1.770	1.347	0.684	0.360	0.155	0.116	0.109	0.107	0.107	Type 2a
MB34	Coarse-grained garnetite	3.699	3.382	3.029	2.671	2.326	2.005	1.712	1.451	1.221	0.774	0.467	0.141	0.012	-0.036	-0.054	-0.060	Type 2a
Sulu-YK22	Metagabbro	6.309	4.665	3.483	2.624	1.996	1.534	1.194	0.943	0.758	0.484	0.353	0.266	0.246	0.241	0.239	0.237	Type 2a
Sulu-YK9	Serpentinite	8.393	5.996	4.086	2.790	1.955	1.429	1.101	0.896	0.768	0.624	0.577	0.557	0.553	0.551	0.549	0.547	Type 2a
TF3	Granitic gneiss	9.442	6.452	4.427	3.047	2.102	1.455	1.011	0.707	0.499	0.230	0.128	0.084	0.083	0.084	0.084	0.084	Type 2a
XG3	Serpentinite	14.685	9.041	5.596	3.492	2.209	1.429	0.956	0.672	0.502	0.324	0.276	0.265	0.265	0.265	0.264	0.263	Type 2a
125-15-18	Qtz eclogite	13.535	10.610	8.087	6.053	4.479	3.295	2.421	1.786	1.328	0.688	0.409	0.251	0.224	0.218	0.216	0.215	Type 2b
125-8-18	Qtz eclogite	32.260	18.095	10.251	5.856	3.381	1.986	1.201	0.763	0.520	0.294	0.245	0.237	0.237	0.236	0.235	0.234	Type 2b
160-12-11	Grt harzburgite	39.610	21.620	11.842	6.500	3.583	1.995	1.133	0.666	0.413	0.184	0.132	0.119	0.118	0.117	0.117	0.116	Type 2b
178-6-6	Bt dioritic gneiss	9.101	8.828	7.785	6.523	5.298	4.218	3.315	2.588	2.014	1.104	0.641	0.324	0.255	0.240	0.236	0.234	Type 2b
203-5-15	Amphibolite	11.197	8.780	6.847	5.300	4.071	3.104	2.351	1.770	1.326	0.642	0.303	0.077	0.032	0.023	0.021	0.020	Type 2b
315-1-11	Phn eclogite	12.582	12.014	9.820	7.501	5.525	3.978	2.816	1.962	1.343	0.461	0.065	-0.172	-0.215	-0.222	-0.222	-0.221	Type 2b
B2078R63P9r	Felsic orthogneiss	42.143	16.986	6.341	1.846	0.054	-0.556	-0.670	-0.599	-0.478	-0.227	-0.102	-0.038	-0.030	-0.029	-0.029	-0.029	Type 2b
B2168R85P2a	Bt-Hbl-Pl-Kfs paragneiss	25.706	14.575	8.482	4.994	2.945	1.723	0.987	0.542	0.272	-0.023	-0.112	-0.144	-0.145	-0.144	-0.143	-0.142	Type 2b
JC2	Fine-grained eclogite	5.259	4.800	4.204	3.577	2.979	2.436	1.961	1.555	1.215	0.610	0.247	-0.066	-0.158	-0.183	-0.189	-0.189	Type 2b
MB23	Coarse-grained eclogite	7.804	6.351	5.176	4.220	3.439	2.799	2.275	1.847	1.496	0.881	0.506	0.159	0.041	0.003	-0.010	-0.014	Type 2b
MB25	Coarse-grained eclogite	13.740	9.781	7.006	5.043	3.646	2.648	1.933	1.419	1.049	0.523	0.284	0.137	0.110	0.105	0.104	0.103	Type 2b
TF1	Granitic gneiss	6.009	5.057	4.235	3.533	2.939	2.440	2.026	1.683	1.402	0.911	0.617	0.358	0.278	0.253	0.245	0.242	Type 2b
150-3-20	Lherzolite	13.296	14.432	12.821	10.488	8.220	6.285	4.734	3.530	2.615	1.225	0.545	0.089	-0.010	-0.031	-0.035	-0.036	Type 2c
19-13-13	Granitic Gneiss	24.948	18.624	12.622	8.265	5.345	3.445	2.223	1.440	0.940	0.352	0.150	0.066	0.057	0.056	0.055	0.055	Type 2c
219-1-2	Granitic gneiss	29.419	21.037	14.681	10.075	6.842	4.626	3.130	2.132	1.472	0.660	0.368	0.238	0.222	0.219	0.218	0.217	Type 2c
703-29	Grt-Bt-Hbl dioritic gneiss	17.875	18.161	13.994	9.944	6.861	4.686	3.196	2.186	1.506	0.638	0.303	0.138	0.115	0.111	0.110	0.109	Type 2c
B1578R14P18t	Bt-Ms-Pl-Kfs orthogneiss	27.177	15.285	8.898	5.302	3.218	1.990	1.259	0.823	0.561	0.284	0.205	0.180	0.178	0.178	0.177	0.177	Type 2c
B2184R88P4s	Bt-Hbl-Pl-Kfs paragneiss	-2.145	6.303	8.669	8.576	7.537	6.235	4.974	3.875	2.971	1.487	0.720	0.200	0.092	0.070	0.065	0.064	Type 2c
JZ1	Fine-grained eclogite	2.802	4.425	5.148	5.333	5.201	4.891	4.492	4.059	3.626	2.659	1.910	1.014	0.608	0.432	0.356	0.323	Type 2c
QL2	Eclogite	7.054	6.582	6.014	5.409	4.806	4.227	3.685	3.188	2.740	1.830	1.171	0.420	0.095	-0.038	-0.090	-0.110	Type 2c

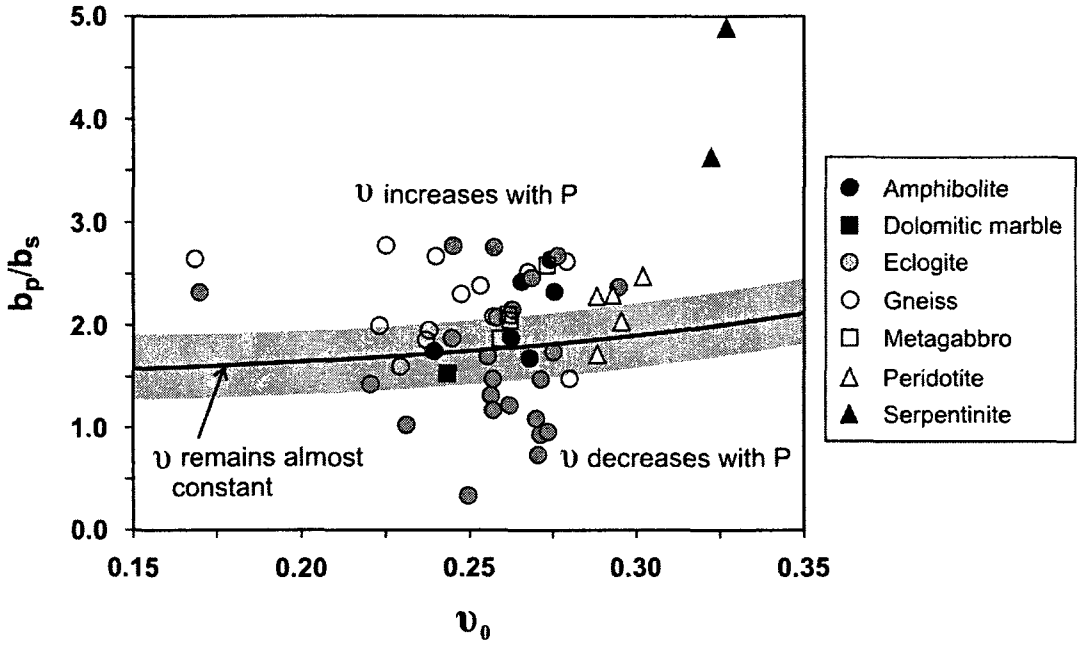

Figure 4.7 Ratio of b_p to b_s versus υ_0 for 54 samples from the Dabie-Sulu UHP metamorphic terrane. υ_0 is the Poisson's ratio of a crack-free rock. With increasing pressure, Poisson's ratio of a rock increases (above the solid line), decreases (below the solid line), and remains unchanged (on the solid line) or almost unchanged (in gray zone).

Based on the theory of continuum elasticity, Walsh (1965) shows that the closure pressure for thin-disk-shaped cracks with aspect ratio of α in a homogeneous, isotropic material is approximated by:

$$P_c = \frac{\pi \alpha E_0}{4\left(1-\upsilon_0{}^2\right)} \tag{4.22}$$

where E_0 and υ_0 are the Young's modulus and Poisson's ratio of the rock matrix without porosity, and $\alpha = W/L$, and W and L are the thickness and length of the cracks, respectively.

$$E_0 = a_p^2 \rho \frac{(1+\upsilon_0)(1-2\upsilon_0)}{(1-\upsilon_0)} \tag{4.23}$$

or

$$E_0 = 2a_s^2\rho(1+\upsilon_0) \tag{4.24}$$

At a constant porosity, thin-disk-shaped cracks with small α are more readily suppressed by the application of confining pressure than more spherical voids with $\alpha \approx 1$. In other words, flatter cracks yield a larger k value while more spherical pores yield a smaller k value. The decay constant k is a parameter to quantify the facility of the successive closure and collapse of cracks of varying aspect-ratio spectra with increasing pressure (Ji et al., 2007).

Substituting Eq. (4.20) into Eq. (4.22), we obtain:

$$\alpha = \frac{24.86\left(1-\upsilon_0{}^2\right)}{\pi k_p E_0} \tag{4.25}$$

Then the α value can be estimated for each sample according to Eq. (4.25). The estimated value (Table 4.1, Fig. 4.9) should be regarded as a mean aspect-ratio for the microcracks within the initial sample.

It is necessary to point out that the values of $P_c(P)$ and $P_c(S)$ or k_p and k_s for a given rock sample depend also on its past pressure history because the seismic velocities are very sensitive to the state of microcracks within the sample (Ji et al., 2007). For 3 cores cut from each sample in the X, Y and Z directions, $V_p(X)$, $V_p(Y)$ and $V_p(Z)$ were measured during the first run, $V_s(XY)$, $V_s(YX)$, $V_s(ZX)$ during the second run, and $V_s(XZ)$, $V_s(YZ)$, $V_s(ZY)$ during the third run. Each run was separated in time by an interval of a few days or weeks. A pressurization-depressurization cycle was applied to the cores during each run. Thus the difference between k_s and k_p or $P_c(P)$ and $P_c(S)$ can be attributed to modification of microstructures, particularly porosity and microcrack geometry during the pressurization-depressurization cycles. $k_s > k_p$ (Table

4.1) and $P_c(P) > P_c(S)$ indicate: (1) some microcracks closed during the first run (V_p measurements) did not reopen during the second and third runs (V_s measurements); (2) some pores which collapsed during the first run did not recover their original shapes or dimensions during the second and third runs; and (3) the contact conditions were improved by local ductile cushions of weak, alteration materials (e.g., chlorite, sericite, or serpentine) along grain boundaries and microcracks during successive pressurization.

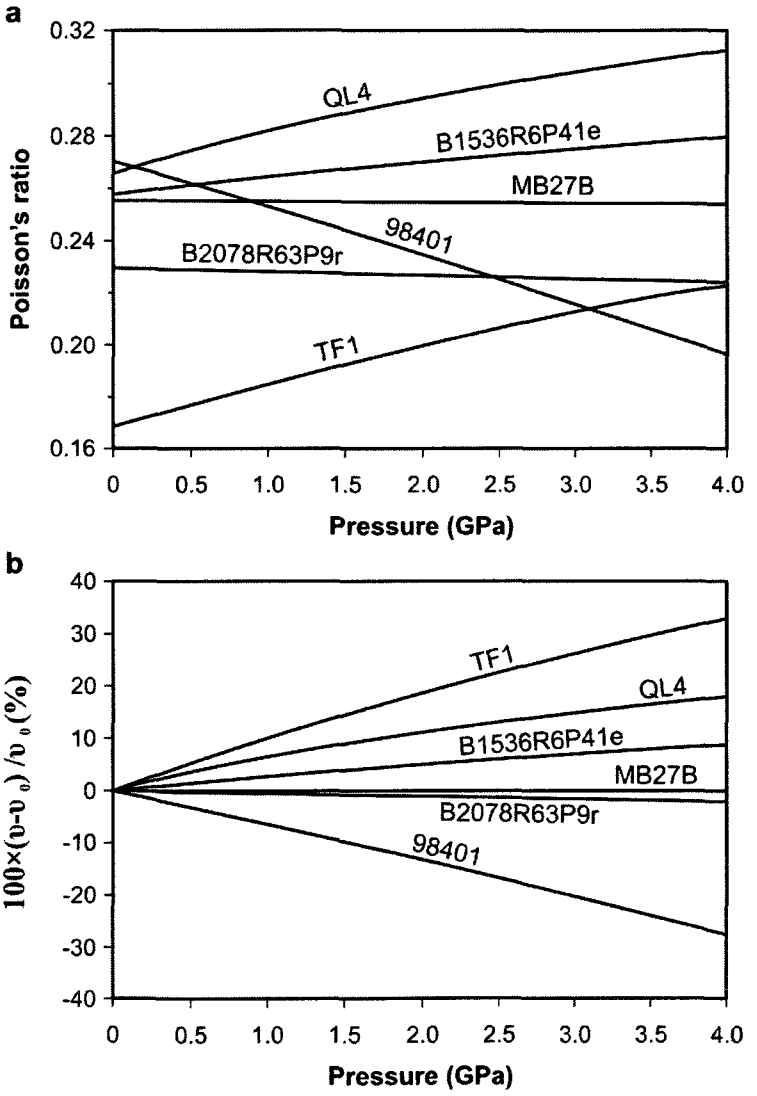

Figure 4.8 Variations of Poisson's ratio as a function of pressure (up to 4.0 GPa) for samples QL4, MB27B, 98401, TF1, B1536R6P41e and B2078R63P9r, which are presumably crack-free in the linearly elastic regime. (a) Absolute values, and (b) relative values for Poisson's ratios.

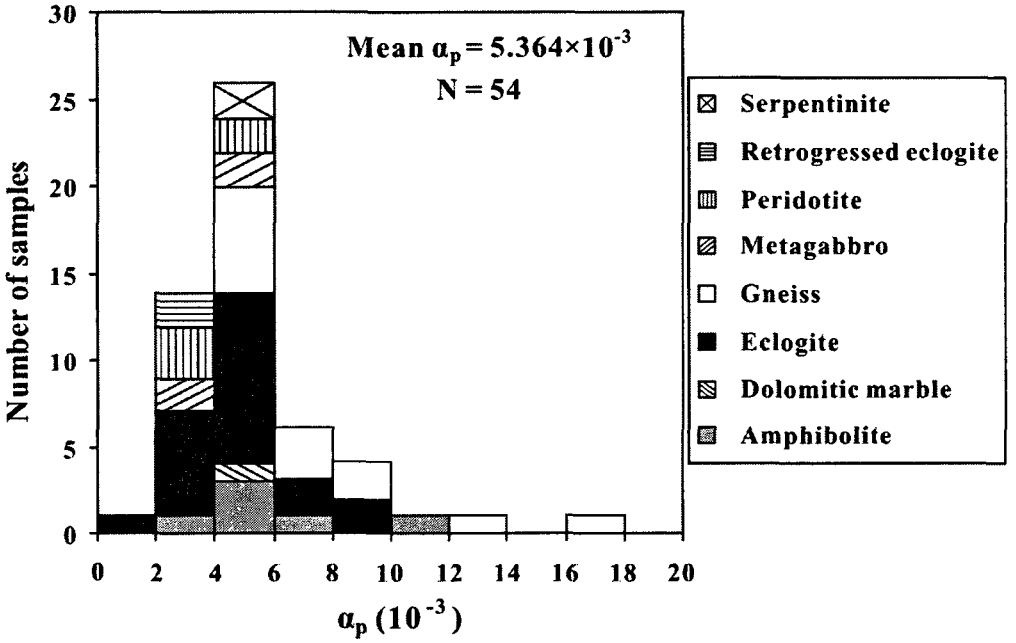

Figure 4.9 Histogram showing the distribution of disk-shaped pore aspect ratios in 54 samples from the Dabie-Sulu UHP metamorphic terrane. Calculations were based on the theory of Walsh (1965).

4.6.2 Effect of porosity

In the following, we analyze whether the variation of Poisson's ratio with hydrostatic pressure can be explained by the effect of crack porosity on the effective Poisson's ratio of a porous material. The Poisson's ratio for an isotropic solid material can be calculated according to the following equation:

$$\upsilon = \frac{E}{2G} - 1 \qquad (4.26)$$

E and G are the Young's and shear moduli of the material, respectively.

$$E = E_0(1 - P)^m \qquad (4.27)$$

$$G = G_0(1-P)^n \qquad (4.28)$$

where E_0 and G_0 are the Young's and shear moduli of the nonporous material, respectively; P is the porosity. The exponents m and n are the microstructural parameters that depend on the geometrical shape, spatial arrangement, orientation and size distribution of pores, and in turn on the formation and deformation processes of the rock. Eq. (4.27) was first proposed by Balshin (1949) as an empirical equation. Recently, Ji et al. (2006) showed that Eqs. (4.27)-(4.28) can be derived directly from the generalized mixture rule (Ji et al., 2003; Ji, 2004). Based on an assumption that a porous material consists of a three dimensional (3D) intertwined, continuous network of material chains and open-pore channels, Wong et al. (1984) and Wagh et al. (1991) derived Eq. (4.27) as a theoretical formula for the porosity dependence of the Young's modulus. In the materials science, the physical meaning of m and n has been investigated. In the elastic field, the exponents have been related to the stress concentrations that develop around pores (Haynes, 1971; Griffiths et al., 1979), and named as the elastic stress concentration factor of the pores (Ichitsubo et al., 2002; Phani, 1986; Boccacini et al., 1995; Blanks et al., 1998). Based on 3D elasticity theory for the stress concentration around spheroidal pores (Z is the axis of revolution and X is the axis perpendicular to Z) in a material under uniaxial stress, Boccaccini et al. (1995) obtained the following results: For spherical pores (Z/X=1), m=2. For infinitely long cylindrical pores ($Z/X \to \infty$) oriented perpendicular to the stress direction, m=3. For lotus-type porous materials with long cylindrical or hexagonal pores ($Z/X \to \infty$) oriented parallel to the stress direction, there is no stress concentration effect (Rice, 1997) and $m \to 1$.

Substituting Eqs. (4.27)-(4.28) into Eq. (4.26), we obtain:

$$\upsilon = (\upsilon_0 + 1)(1-P)^{m-n} - 1 \qquad (4.29)$$

where υ_0 is the Poisson's ratio of the non-porous material [$\upsilon_0 = E_0/(2G_0) - 1$], and $(1-P)$ is always ≤ 1.

From Eq. (4.29), we can draw the following conclusions:

(1) If $m = n$, $\upsilon = \upsilon_0$, the effective Poisson's ratio of the porous material is independent on porosity. In this case, the rock Poisson's ratio remains invariable with change in pressure (Type 1, Fig. 4.4).

(2) If $m > n$, $(1-P)^{m-n} < 1$, then $\upsilon < \upsilon_0$. Hence the Poisson's ratio decreases with increasing porosity. Because an increase in hydrostatic pressure leads to a reduction in porosity, the rock Poisson's ratio should increase with increasing pressure in this case (Type 2, Fig. 4.5).

(3) If $m < n$, $(1-P)^{m-n} > 1$, then $\upsilon > \upsilon_0$. The effective Poisson's ratio of the porous material increases with increasing the porosity. In this case, the rock Poisson's ratio should decrease with increasing pressure.

Therefore, to the first approximation, the relative dependence of E and G on porosity controls the dependence of Poisson's ratio on porosity.

Using the Mori and Tanaka (1973) mean-field approach, Dunn and Ledbetter (1995) theoretically analyzed the effective Poisson's ratio of macroscopically isotropic solids containing randomly distributed and randomly oriented spheroidal pores. Similar conditions were also used by O'Connell and Budiansky (1974) in their self-consistent approximation. The pore shape, which is defined by the aspect ratio (width/length) of the voids (α), varies from spherical ($\alpha = 1$), thin-disk-shaped ($\alpha << 1$) and needle-shaped ($\alpha \to \infty$). For the material containing spherical voids ($\alpha = 1$), Dunn and Ledbetter (1995) obtained:

$$\upsilon = \frac{2\upsilon_0(5\upsilon_0 - 7) + P(5\upsilon_0 - 3)(\upsilon_0 + 1)}{2(5\upsilon_0 - 7) + P(15\upsilon_0 - 13)(\upsilon_0 + 1)} \tag{4.30}$$

In Eq. (4.30), P is the porosity, and υ_0 is the Poisson's ratio of the non-porous solid.

Figure 4.10 plots the effective Poisson's ratio of porous solids with various υ_0 values as a function of the volume fraction of spherical pores (i.e., porosity). The effective Poisson's ratio decreases with increasing porosity for the solid with $\upsilon_0 > 0.20$ (e.g., calcite, serpentine, plagioclase, biotite, muscovite, hornblende, diopside, olivine, garnet) whereas υ increases with increasing porosity for the solid with $\upsilon_0 < 0.20$ (e.g., quartz and pyrite). For a material with $\upsilon_0 \approx 0.20$ (e.g., staurolite, diallage and enstatite), the effective Poisson's ratio remains unchanged as a function of porosity. As shown in Fig. 4.10, there is only a slight decrease (when $\upsilon_0 > 0.20$) or increase (when $\upsilon_0 < 0.20$) in the effective Poisson's ratio for a solid with a porosity of $\leq 1\%$. Thus, the remarkable increases in υ with increasing pressure (Fig. 4.5), observed in the crystalline rocks, cannot be attributed to the closure of spherical pores during the hydrostatic pressurization.

For the material containing needle-shape pores ($\alpha \to \infty$), Dunn and Ledbetter (1995) obtained:

$$\upsilon = \frac{-15\upsilon_0 + P(8\upsilon_0 - 5)(\upsilon_0 + 1)}{-15 + 4P(4\upsilon_0 - 5)(\upsilon_0 + 1)} \tag{4.31}$$

The variations in the effective Poisson's ratio of porous solids as a function of the volume fraction of needle-shaped pores and υ_0 value are illustrated in Fig. 4.11. The effective Poisson's ratio decreases with increasing porosity for the solid with $\upsilon_0 > 0.20$ whereas υ increases with increasing porosity for the solid with $\upsilon_0 < 0.20$. For a material

with $\upsilon_0 \approx 0.20$, the effective Poisson's ratio is almost a constant. The change in υ is barely significant for a solid with a porosity of $<1\%$. Accordingly, the remarked changes in υ with increasing pressure (Fig. 4.5), observed in the highly compacted UHP metamorphic rocks, cannot be explained by the closure of needle-shaped pores during the hydrostatic pressurization.

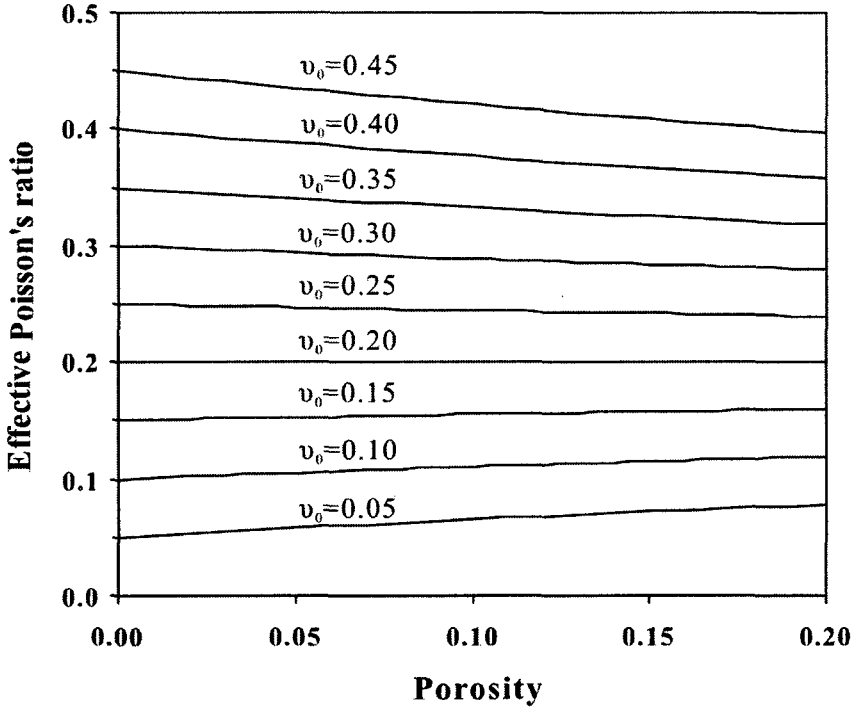

Figure 4.10 Effective Poisson's ratio of a porous material containing randomly distributed spherical pores as a function of porosity (P) and intrinsic Poisson's ratio of the porosity-free solid (υ_0). Each curve is calculated using Eq. 4.30 for a different υ_0.

For the material containing thin-disk-shaped pores ($\alpha << 1$), Dunn and Ledbetter (1995) obtained:

$$\upsilon = \frac{15\alpha\pi\upsilon_0(2-\upsilon_0) + P\upsilon_0\left[-4\upsilon_0^{\,2} + 15\alpha\pi\upsilon_0 + 2(2-15\alpha\pi)\right]}{15\alpha\pi(2-\upsilon_0) + P\left[12\upsilon_0^{\,3} - 40\upsilon_0^{\,2} + 3(5\alpha\pi-4)\upsilon_0 + 10(4-3\alpha\pi)\right]} \qquad (4.32)$$

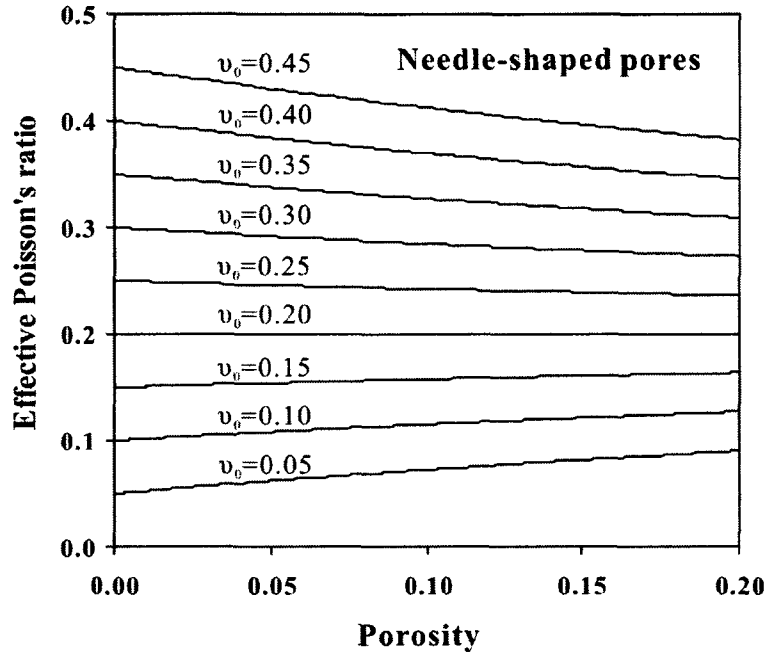

Figure 4.11 Effective Poisson's ratio of a porous material containing randomly distributed and randomly oriented needle-shaped pores as a function of porosity (P) and intrinsic Poisson's ratio of the porosity-free solid (υ_0). Each curve is calculated using Eq. 4.31 for a different υ_0.

The results computed using Eq. (4.32) are shown in Fig. 4.12a ($\alpha = 0.001$), Fig. 4.12b ($\alpha = 0.005$), Fig. 4.12c ($\alpha = 0.01$), and Fig. 4.12d ($\alpha = 0.1$), respectively. Three facts can be clearly observed:

(1) The presence of thin-disk-shaped pores in a solid material with $0 < \upsilon_0 < 0.5$ always reduces its effective Poisson's ratio (Figs. 4.12a-d).

(2) The porosity-dependence of the effective Poisson's ratio is much more pronounced for the material with a larger υ_0.

(3) Pores with a smaller α value play a much more important role in the reduction of the effective Poisson's ratio than those with a larger α value (Fig. 4.12). The

progressive closure of a small volume fraction (0.1%-0.5%) of thin-disk-shaped pores with aspect ratios as shown in Fig. 4.12 is sufficient to interpret the increase in υ for the samples of type 2 (Fig. 4.5). In Fig. 4.5, the linear slopes result from intrinsic properties, and the gap between the linear slopes and the nonlinear curves reflect the effects of microcracks. The microcracks include intragranular cracks (e.g., cleavage cracks in omphacite, amphibole, phengite and feldspar; intragranular cracks in garnet and quartz, radial cracks around coesite inclusions) and intergranular cracks (e.g., grain boundary cracks, foliation-parallel cracks, lineation-perpendicular or oblique cracks). The progressive reduction of the gap correlates with the progressive closure of microcracks with different aspect ratios at different confining pressures.

Dunn and Ledlbetter (1995) and later Roberts and Garboczi (2000) and Yeheskel and Tevet (2000) suggested that the effective Poisson's ratio of a porous material depends only on porosity, pore shape and the Poisson's ratio of the solid medium. In other words, the effective Poisson's ratio of a porous material is independent of any other elastic constants than the Poisson's ratio of the solid medium. However, the mechanical model of Dunn and Ledbetter (1995), which assumed a macroscopically isotropic solid containing randomly distributed and randomly oriented spheroidal pores, cannot successfully explain the invariability in υ with increasing P in the poro-elastic regime (Fig. 4.4).

4.6.3 Effect of anisotropy

In the naturally deformed rocks, both intra- and inter-granular microcracks are in general preferentially oriented and heterogeneously distributed (Siegesmund et al., 1993; Ji et al., 1997). The rocks may be anisotropic due to the presence of shape-preferred and lattice-preferred orientations and compositional layering. Elastic wave propagation in an anisotropic medium results in 3 velocities in each given direction. For example, $V_p(X)$,

$V_s(XY)$ and $V_s(XZ)$ in the X direction, $V_p(Y)$, $V_s(YX)$ and $V_s(YZ)$ in the Y direction, and $V_p(Z)$, $V_s(ZX)$ and $V_s(ZY)$ in the Z direction. Hence there are two velocity ratios for each propagation direction: $V_p(X)/V_s(XY)$ and $V_p(X)/V_s(XZ)$ for the X direction, $V_p(Y)/V_s(YX)$ and $V_p(Y)/V_s(YZ)$ for the Y direction, and $V_p(Z)/V_s(ZX)$ and $V_p(Z)/V_s(ZY)$ for the Z direction. For each sample, we computed the six velocity ratios as a function of hydrostatic pressure. Figure 4.13 shows the calculated results for 2 representative samples. For sample Sulu-YK1 (metagabbro, Type 1), $V_p(X)/V_s(XY)$ and $V_p(X)/V_s(XZ)$ decrease while $V_p(Z)/V_s(ZX)$ and $V_p(Z)/V_s(ZY)$ increase with pressure below ~150 MPa (Fig. 4.13a). With increasing pressure, $V_p(Y)/V_s(YX)$ increases at low pressures (<100 MPa), then decreases at moderate pressures (100-300 MPa), and finally increases slowly at high pressures (>300 MPa). $V_p(Y)/V_s(YZ)$ decreases with increasing pressure at P<100 MPa, then increases slowly above this pressure. At 600 MPa, $V_p(X)/V_s(XZ)$ (1.789) > $V_p(Y)/V_s(YZ)$ (1.779) > $V_p(Y)/V_s(YX)$ (1.771) > $V_p(X)/V_s(XY)$ (1.768) > $V_p(Z)/V_s(ZY)$ (1.751) > $V_p(Z)/V_s(ZX)$ (1.730) with an average value of 1.765. Interestingly, the average value of the six velocity ratios, which corresponds to the rock Poisson's ratio, displays little variation with pressure in the range of 40-800 MPa (Fig. 4.13a). For sample MB25 (coarse-grained eclogite, Type 2), the 6 velocity ratios all have similar shapes of the variation curves: a rapid, nonlinear rise below ~200 MPa, followed by a quasi-constant above this pressure (Fig. 4.13b). As a result, the average velocity ratio for this sample increases rapidly below ~200 MPa and then remains quasi constant at higher pressures. At 600 MPa, $V_p(X)/V_s(XY)$ (1.812) > $V_p(X)/V_s(XZ)$ (1.772) > $V_p(Z)/V_s(ZY)$ (1.758) > $V_p(Z)/V_s(ZX)$ (1.755) > $V_p(Y)/V_s(YZ)$ (1.742) > $V_p(Y)/V_s(YX)$ (1.715) with an average value of 1.759. Thus, the ratio of P- to S-wave velocities of an anisotropic rock measured along a selected pair of propagation-vibration directions may be significantly different from the true value for its isotropic counterpart. Furthermore, the variations of the velocity ratios in different

directions with confining pressure may oppose or enhance each other. With progressively increasing the confining pressure from 0 to 200-300 MPa, the averaged velocity ratio or the Poisson's ratio for the bulk sample can remain unchanged (Type 1) or increase (Type 2).

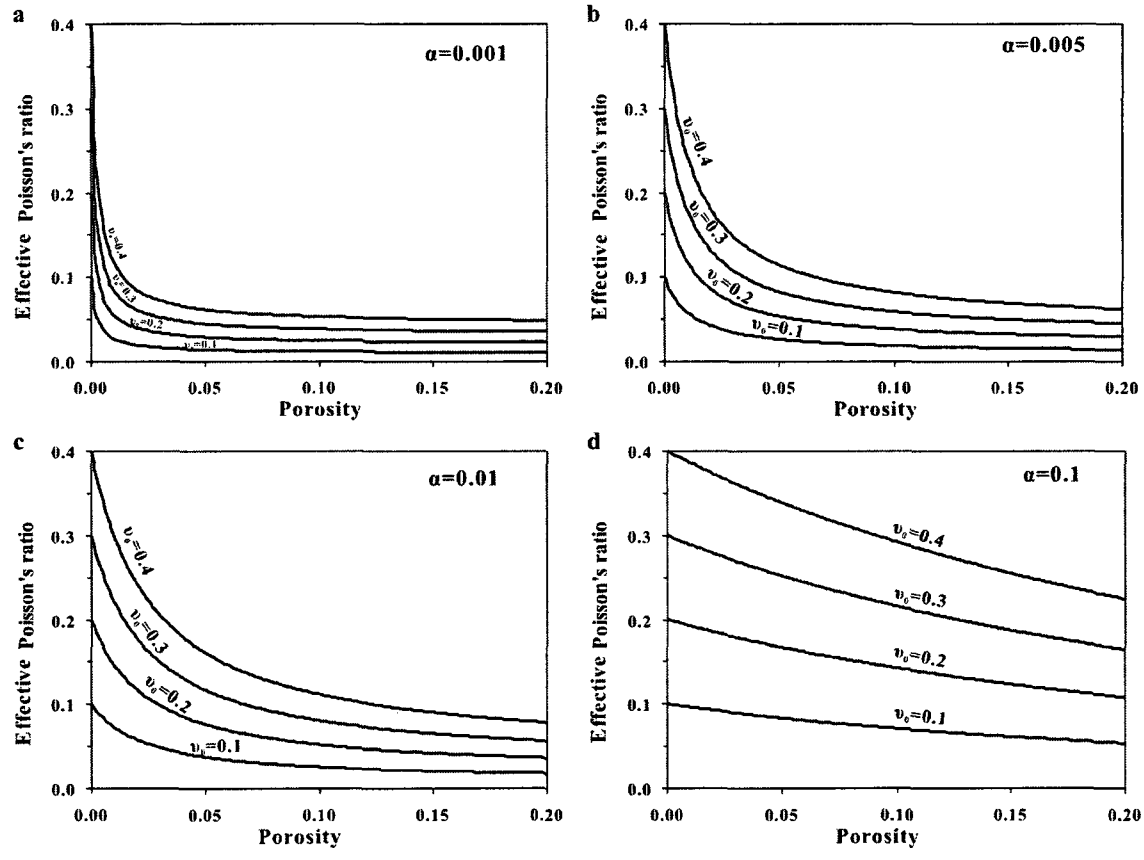

Figure 4.12 Effective Poisson's ratio of a porous material containing randomly distributed and randomly oriented disk-shaped pores as a function of porosity (P) and intrinsic Poisson's ratio of the porosity-free solid (υ_0). Each curve is calculated using Eq. 4.32 for a different υ_0. Aspect ratio of the pores: α =0.001 (a), 0.005 (b), 0.01 (c), and 0.1 (d).

4.7 Conclusions

Poisson's ratios of the rocks have been used to constrain the composition of the Earth's interior. In order to constrain the effects of hydrostatic confining pressure (P) on

the Poisson's ratios (υ), we measured both P- and S-wave velocities (V_p and V_s) up to 850 MPa for 54 crystalline rocks from the Sulu-Dabie orogenic belt (China) using the pulse transmission techniques (Birch, 1960; Ji and Salisbury, 1993). The experimental results display 2 main types of the υ-P relationships in the range of 40-850 MPa: (1) υ shows little variation with P in the range of 40-850 MPa. (2) With increasing pressure, υ increases rapidly below ~200 MPa and then becomes quasi-constant at higher pressures. Types 1 and 2 are observed in 22 and 32 samples, respectively. The origin of type 2, which has been observed in 59% of the samples studied, can be reasonably interpreted by a small volume fraction (0.1%-0.5%) of thin-disk-shaped pores that are progressively closed during pressurization. The effects of seismic anisotropy due to the presence of microcrack preferred orientation, and mineral shape and lattice preferred orientations are needed to be taken into consideration for interpreting the origins of the first type.

The experimental data were analyzed using two four-parametric exponential equations: $V_p = a_p + b_p P - c_p \exp(-k_p P)$ and $V_s = a_s + b_s P - c_s \exp(-k_s P)$, where the subscripts p and s denote the P- and S-waves, respectively; a is the intrinsic velocity at zero pressure if pores/cracks were absent; b is the intrinsic pressure derivative of velocity in the linear elastic regime; c is the initial velocity drop caused by the presence of pores/cracks at zero pressure; and k is the decay constant of the velocity drop, which controls the shape of the velocity-pressure curves in the nonlinear poro-elastic regime (Ji et al., 2007). In the linear elastic regime (P>200-300 MPa), Poisson's ratio increases with increasing P if $(b_p/b_s) > (a_p/a_s)$, decreases with increasing P if $(b_p/b_s) < (a_p/a_s)$, and remains almost unchanged if $(b_p/b_s) \approx (a_p/a_s)$. In the nonlinear poro-elastic regime (P<200-300 MPa), however, the variation in Poisson's ratio depends on the competition between terms $V_s(dV_p/dP)$ and $V_p(dV_s/dP)$. Poisson's ratio increases with increasing P if $V_s(dV_p/dP) > V_p(dV_s/dP)$, decreases with increasing P if $V_s(dV_p/dP) < V_p(dV_s/dP)$, and remains constant if the two terms

are equal. Thus, the mineralogy and confining pressure all play an important role in influencing the Poisson's ratio of the crystalline rocks.

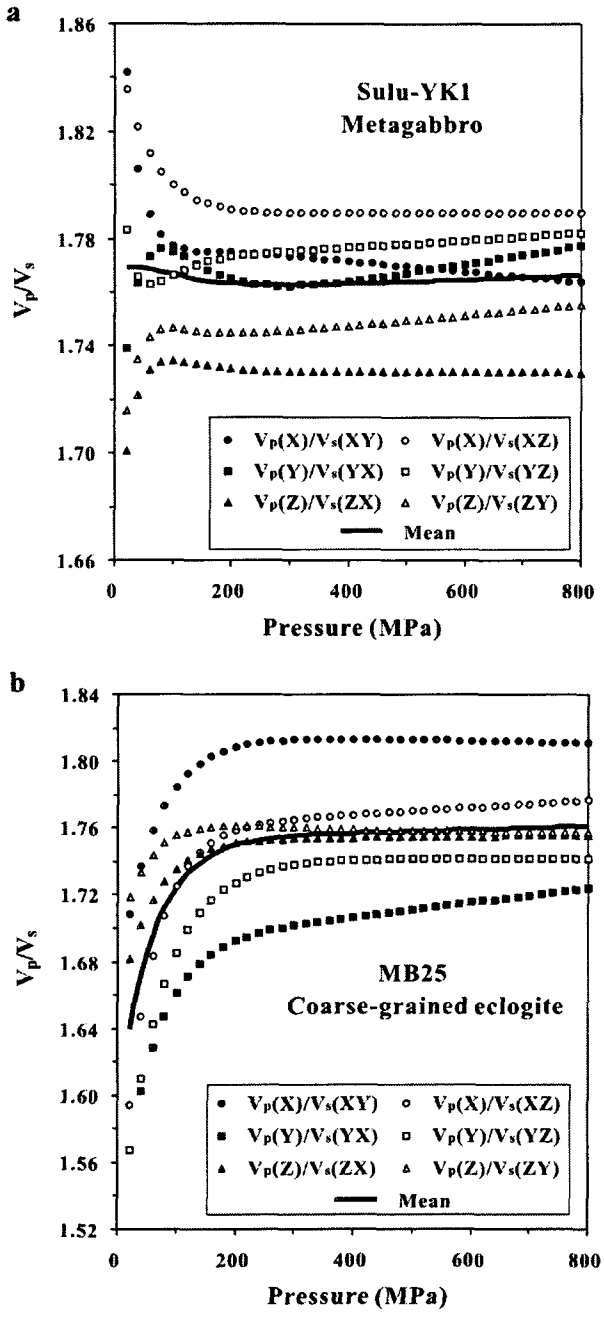

Figure 4.13 V_p/V_s ratios calculated for different pairs of propagation-vibration directions as a function of pressure. (a) Metagabbro (Sulu-YK1), and (b) coarse-grained eclogite (MB25).

Chapter 5

Composition and tectonic evolution of the Chinese continental crust constrained by Poisson's ratio

5.1 Abstract

We have measured P- and S-wave velocities (V_p and V_s) and determined the Poisson's ratios (υ) of 60 typical ultrahigh pressure (UHP) metamorphic rock samples from the Chinese Continental Scientific Drilling (CCSD) main and pre-pilot holes and surface outcrops in the Sulu-Dabie orogenic belt at hydrostatic confining pressures up to 850 MPa. The experimental results, together with those compiled in Handbook of Seismic Properties of Minerals, Rocks and Ores (Ji et al., 2002), reveal that except for monomineralic rocks such as quartzite, serpentinite, anorthosite, limestone and marble, the rest of the rock types have Poisson's ratios falling along an upward convex curve determined from the correlations between elastic moduli and density. Poisson's ratios increase with density as the lithology changes from granite, felsic gneiss and schist, through diorite-syenite, intermediate gneiss and metasediment, to gabbro-diabase, amphibolite and mafic gneiss, and then decrease as the rocks become ultramafic in composition. Eclogite has a higher density but a lower Poisson's ratio than peridotite. The results were applied to constrain the crustal composition and tectonic evolution of the Chinese continental crust based on crustal thickness (H) and Poisson's ratio data from 248 broadband seismic stations, measured using teleseismic receiver function techniques.

The North China, Yangtze, South China and Northeast China blocks and Songpan-Ganzi Terrane are dominated by low ($\upsilon < 0.26$) and moderate ($0.26 \leq \upsilon < 0.28$) υ values (>70%), suggesting the crust is predominantly felsic. The Lhasa terrane, Qiangtang terrane, and Indochina block are characterized by high proportions (33-42%) of measurements with very high υ values (≥ 0.30), suggesting that the crust is partially molten due to high temperatures. A negative correlation between υ and H is found for the South China block, Northeast block, Lhasa block, Qiangtang terrane and Indochina block, indicating either tectonic thickening of the felsic upper and middle crust by folding and thrusting or the removal of mafic layers from the lower crust into the upper mantle by delamination.

5.2 Introduction

Seismic properties of rocks provide important constraints for the chemical composition and structure of the Earth's interior. Among the properties, Poisson's ratio (υ) or the ratio of P- to S-wave velocities (V_P/V_S) is the least studied, but may be the most diagnostic (e.g., Kern, 1982; Ji and Salisbury, 1993; Christensen, 1996; Kumar et al., 2003; Gercek, 2007). Poisson's ratio is regarded as an important indicator for pore geometry and porosity of sedimentary rocks (e.g., Vernik, 1997; Mavko et al., 1998; Hamada, 2004). Poisson's ratio is also used to determine the carbonate content in reservoir rocks (e.g., Hamilton, 1979; Wilkens et al., 1984), to discriminate quartz- from plagioclase-rich rocks (Tarkov and Vavakin, 1982; Holbrook et al., 1988; Zandt and Ammon, 1995; Christensen, 1996; Julia and Mejia, 2004; Musacchio et al., 2004; Nair et al., 2006), to detect solid-solid phase transitions in constituent minerals (e.g., the α-β phase transition of quartz, Kern, 1979) and partial melting of rocks (e.g., Owens and Zandt, 1997), and to study fluid distribution at earthquake hypocenters (e.g., Mishra and Zhao, 2003).

In the present study, Poisson's ratio as a function of density and lithology has been investigated in detail for 60 representative ultrahigh pressure (UHP) metamorphic rocks

sampled by the Chinese Continental Scientific Drilling (CCSD) main and pilot holes and collected from surface outcrops in the Sulu-Dabie orogenic belt (China). P- and S-wave velocities of the rock samples were measured at hydrostatic pressures up to 850 MPa. The Poisson's ratios of the samples, together with those compiled in the Handbook of Seismic Properties of Minerals, Rocks and Ores (Ji et al., 2002), have been used to interpret the crustal thickness (H) and V_P/V_S or Poisson's ratio (υ) data from teleseismic receiver functions from 248 broadband seismic stations in China in terms of crustal chemical composition, physical state and tectonic evolution. The errors in V_P/V_S ratio are generally less than 0.06, and the errors in H are generally less than 2-3 km. The Poisson's ratio measured from receiver functions is the average value for the whole crust beneath a seismic station.

Previous studies demonstrated that υ does not vary significantly with confining pressure above about 100-200 MPa for compact crystalline rocks that contain no open microcracks (e.g., Christensen, 1996; Kern et al., 1999). In addition, υ shows little variation with temperature for most common rock types except quartzite (Christensen, 1996; Kern et al., 1999). The Poisson's ratio of quartzite varies appreciably near the temperature of the α-β quartz transition. At 200 MPa, the Poisson's ratios of a quartzite consisting of 100% quartz are 0.08 at 300 °C, 0.02 at 500 °C, -0.17 at 650 °C, and 0.21 at 700 °C (Kern, 1979). However, quartz-bearing granite and felsic gneiss show only slight decreases in υ within the temperature range from 200 °C to 600 °C (Kern and Richter, 1981, Kern et al., 1999; Kern et al., 2002). As confirmed in Chapiter 4, laboratory-measured Poisson's ratios should be directly applicable over a wide range of crustal depths because pressure dependences are relatively small for most rocks at pressures higher than about 200 MPa.

5.3 Samples

The locality, recovery depth, lithology and density as well as geological setting for each of the 60 UHP metamorphic rocks studied were given in Ji et al. (2007), and Wang

et al. (2005a and b). Twelve of the 60 samples were collected from the Chinese Continental Scientific Drilling (CCSD) main borehole between 3000 and 4600 m depth. These core samples represent typical lithologies (orthogneiss, paragneiss, amphibolite and retrogressed eclogite) in these depth intervals. Nineteen samples were collected from the cores of the CCSD pre-pilot hole in the 10-700 m depth interval. In this uppermost portion of the crust beneath the CCSD site, typical lithologies are eclogites with various extents of retrogression, ultramafic rocks (e.g., dunite, garnet harzburgite, lherzolite), and felsic orthogneiss. Twenty two samples were collected from fresh surface outcrops in quarries at Dugou, Jianchang, Jiangzhuang, Qinglongshan, Maobei and Xugou in Donghai County, Yanmachang in Ganyu County and Tuofeng in Lianyungang City. Two dark eclogite samples were collected from the Bixiling complex, which is the largest coesite-bearing mafic-ultramafic boudin (1.5 km^2) in the Dabie Mountains.

Five samples were collected from a layered UHP complex at Yangkou Beach, Qingdao. The complex consists of eclogite-facies metagabbro and serpentinized garnet peridotite blocks enclosed in granitic gneiss (Zhang and Liou, 1997). The metagabbro blocks display various degrees of transformation from incipiently metamorphosed gabbro with relict igneous textures and mineral assemblages (i.e., plagioclase + augite + bronzite + biotite + ilmenite) to completely recrystallized coesite-bearing eclogite-facies rocks (omphacite + zoisite + kyanite + garnet + phengite).

Figures 5.1a, b, and c show plots of rock densities as a function of SiO_2, MgO and Na_2O+K_2O, respectively. Two groups of rocks can be clearly distinguished: the eclogite group and the normal series that includes all other types of rocks with the exception of eclogites. For a given content of SiO_2, MgO or Na_2O+K_2O, the eclogite group always shows remarkably higher densities than the normal series. For both groups, the densities increase nearly linearly with decreasing SiO_2 (Fig. 5.1a) and Na_2O+K_2O (5.1c). Figure 5.1b demonstrates a nonlinear increase of ρ with increasing MgO. The variation of

rock densities as a function of CaO is more complicated: eclogite and peridotite seem to form a series and all the other types of rocks constitute another series. In both series, rock densities increases rather linearly with CaO (Fig. 5.1d).

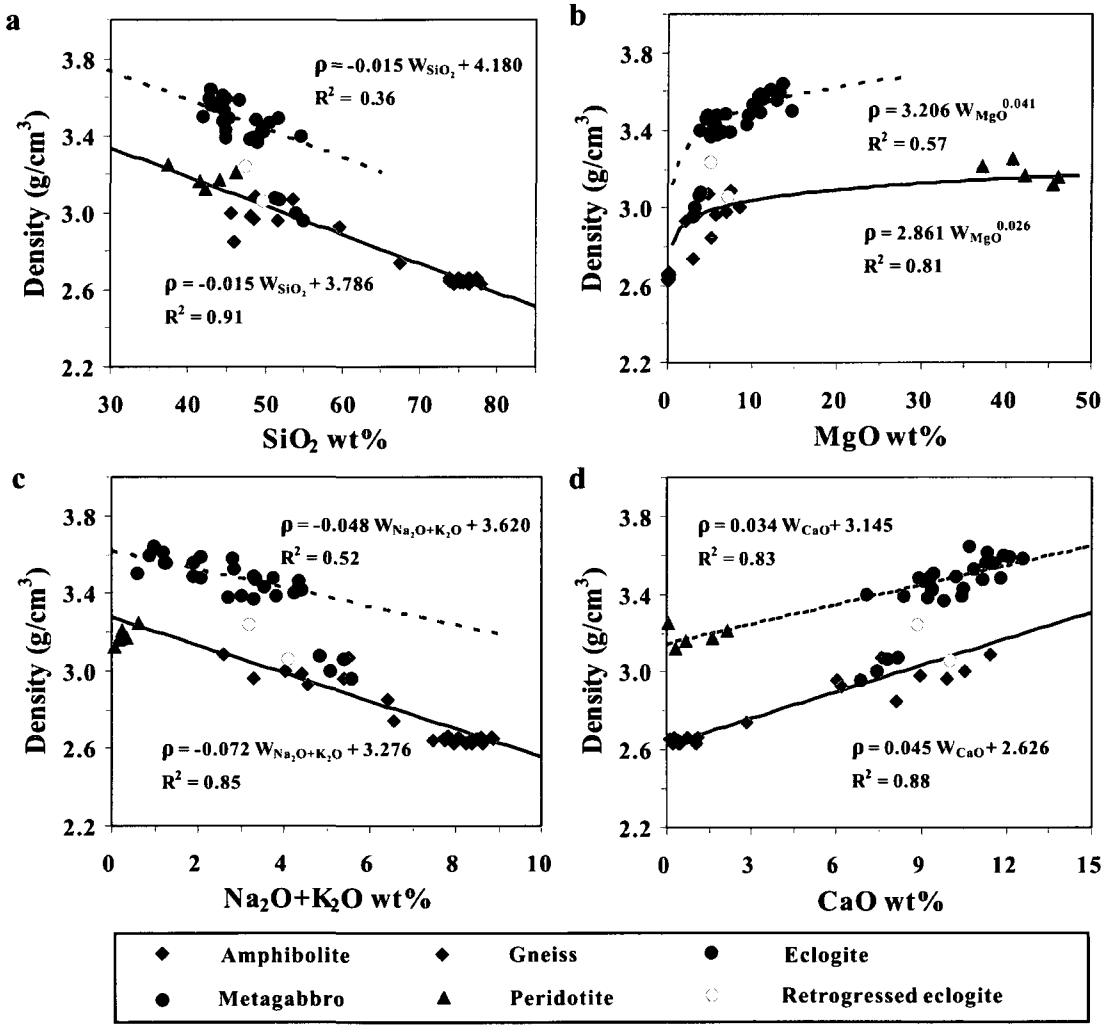

Figure 5.1 Density as a function of SiO_2 (a), MgO (b), Na_2O+K_2O (c) and CaO (d) contents for Sulu-Dabie UHP metamorphic rocks.

5.4 Experimental details

P- and S-wave velocities were measured at room temperature and hydrostatic pressures ranging from 10 to 850 MPa on jacketed dry samples using the pulse

transmission technique (Birch, 1960; Christensen, 1974). For most samples, three cylindrical minicores (2.54 cm in diameter and 3-5 cm in length) were cut in orthogonal directions with the X direction parallel to the stretching lineation, the Y direction perpendicular to lineation and parallel to foliation, and the Z direction normal to foliation. For CCSD core samples, only one (usually the Z-direction) or two directions (usually parallel to the X and Z directions) were taken. The high pressure experiments were carried out at the GSC/Dalhousie High Pressure Laboratory in Halifax, Nova Scotia (Ji et al., 1993; Ji et al., 1997; Wang et al., 2005a and b). The principal vessel is a seven-ton, double-walled steel vessel with a 40 cm long × 10 cm diameter working chamber, which can operate to a pressure up to 1.4 GPa. The pressure medium consists of light hydraulic oil pumped into the working chamber by means of a two-stage intensifier. P- and S-waves were generated and received by lead zirconate-titanate transducers with a 1 MHz resonance frequency. To prevent the pressure medium from invading the sample during the pressure run, the mini-cores were sheathed in impermeable thin copper foil and the entire sample/transducer/electrode assembly was enclosed in neoprene tubing. Once the sample assembly was sealed in the pressure vessel and the pressure was raised, a high voltage spike from a pulse generator excited the sending transducer and the time of flight to the receiving transducer was measured using a digital oscilloscope. The accuracy is estimated to be 0.5% for V_p and 1% for V_s (Christensen, 1985; Ji et al., 1993; Ji and Salisbury, 1993; Kern et al., 1999, 2002) and 2.5% for calculated Poisson's ratios (Christensen, 1996). The densities of the samples (Table 5.1) were determined using the immersion method with an accuracy of ±0.005 g/cm^3 at room conditions.

5.5 Experimental results

Although the velocity measurements were performed during both pressurization and then depressurization, only the velocity values measured during depressurization correspond to the stable microstructural state (e.g., Burke and Fountain, 1990; Ji et al.,

2007) and thus these were used for the computations of υ. The mean P-wave velocity of each sample is calculated according to the following equation:

$$V_p = [V_p(X) + V_p(Y) + V_p(Z)]/3 \qquad (5.1)$$

where $V_p(X)$, $V_p(Y)$ and $V_p(Z)$ represent the P-wave velocities along the propagation directions X, Y and Z, respectively. The mean S-wave of each sample is computed from the results of six measurements which are designed XY, XZ, YX, YZ, ZX, and ZY. The first letter refers to the propagation direction and the second to the polarization direction and the mean S-wave velocity is calculated from the equation,

$$V_s = [V_s(XY) + V_s(XZ) + V_s(YX) + V_s(YZ) + V_s(ZX) + V_s(ZY)]/6 \qquad (5.2)$$

The mean V_p and V_s values calculated from Eqs. (5.1) and (5.2) give values very close to true isotropic elastic properties even in highly anisotropic rocks (e.g., Christensen and Ramananantoandro, 1971; Ji et al., 2003). Mean velocities and elastic constants calculated for drill core samples may have larger errors, however, because sufficient material was not always available to measure velocities in all three directions.

The mean P- and S-wave velocities as a function of confining pressure were analyzed using the following equation (e.g., Zimmerman et al., 1986; Greenfield and Graham, 1996; Ji et al., 2007):

$$V(P) = V_0 + DP - B_0 \exp(-kP) \qquad (5.3)$$

where V_0 is the projected velocity of a non-porous or crack-free compacted rock at zero pressure, which is determined from extrapolation of the linear velocity-pressure relationship obtained at high pressures to zero pressure (Fig. 5.2); D, which is the intrinsic pressure derivative of velocity in the linear elastic regime; B_0, which is the

ambient velocity drop caused by the presence of pores/microcracks at zero pressure, determines the maximum magnitude of the velocity increases due to the closure of pores and microcracks; k, which is the decay constant of the velocity drop, controls the shape of the nonlinear segment of the velocity-pressure curve. The zero-pressure velocity of the rock containing microcracks and pores equals V_0-B_0. In Eq. (5.3), V_0 and D are thus two parameters which describe the intrinsic seismic property of the microcrack- or pore-free solid matrix, while B_0 and k are parameters related to the porosity and geometrical shape of pores (e.g., aspect ratio, spatial arrangement, orientation and size distribution) and thus the formation and deformation processes of the rocks. The physical significance of Eq. (5.3) was discussed in detail by Ji et al. (2007).

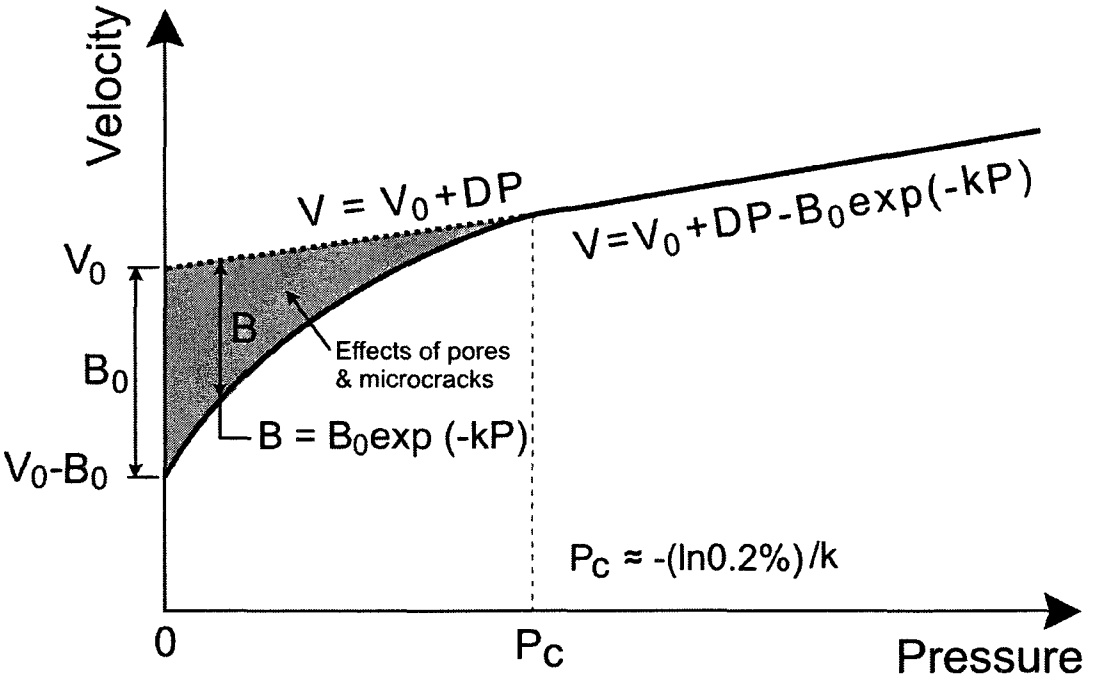

Figure 5.2 Physical significance of 4 parameters in Eq. (5.3). Each parameter is defined in the text. The effects of microcracks/pores on the velocity are illustrated by the shadowed area.

Parameters V_0, D, B_0 and k determined for the mean P- and S-wave velocities of each sample during depressurization, using a least square regression method, are given

in Table 5.1. As indicated by the goodness-of-fit coefficients (R^2), the pressure-velocity curves for P- and S-waves can be well fitted by Eq. (5.3), with more than 95% and 97% of the 60 samples having $R^2 \geq 0.90$, respectively (Table 5.1).

The calculated E (Young's modulus), G (shear modulus), K (bulk modulus) and υ values for each porosity-free sample at zero and 600 MPa are listed in Table 5.2. The correlation between an elastic modulus and density (ρ) can be well fitted by an equation:

$$M = a\rho^3 + b\rho^2 + c\rho \qquad (5.4)$$

where M is a given elastic modulus (i.e., E, G or K), and a, b and c are adjustable coefficients (Table 5.3). The convincible ability of Eq. (5.4) to best-fit the relationship between elastic moduli and density implies that both V_p and V_s vary linearly with density (Figs. 5.3 and 5.4), as suggested by Birch's law (Birch, 1960; Chung, 1972; Campbell and Heinz, 1992).

Poisson's ratios as a function of ρ for porosity-free samples are plotted in Fig. 5.5. Excluding two serpentinites that have anomalously high υ values, all the samples can be described by the trend lines calculated from the correlations between the elastic moduli (i.e., G and K) and density (Table 5.3). Poisson's ratios show systematically high values in serpentinized peridotites and then decrease with either decreasing or increasing rock density. It is worth noting that the variations of intrinsic υ with ρ are almost the same between zero and 600 MPa when microcracks are closed. As shown in Fig. 5.5, the maximum υ values of 0.326-0.335 are obtained for serpentinites, and the minimum υ value of 0.179 is observed in a quartz-rich orthogneiss (sample TF1). The mean υ values for felsic gneisses, eclogites, metagabbros, amphibolites, serpentinized peridotites, and serpentinites at 600 MPa are 0.247, 0.256, 0.266, 0.267, 0.295, and 0.330, respectively.

Table 5.1 Parameters of V_p-pressure and V_s-pressure curves measured during depressurization for Sulu UHP rocks

Sample No.	Lithology	Density	Vp					Vs				
			V_0	D	B_0	k	R^2	V_0	D	B_0	k	R^2
		(g/cm^3)	(km/s)	(10^{-4} km/s/MPa)	(km/s)	(10^{-2} MPa^{-1})		(km/s)	(10^{-4} km/s/MPa)	(km/s)	(10^{-2} MPa^{-1})	
203-5-15	Amphibolite	3.07	5.746	3.088	1.479	1.732	0.988	3.363	1.764	0.638	2.063	0.999
B1608R27P12e	Grt-Bt-Pl amphibolite	2.98	6.965	1.892	1.006	1.709	0.961	3.875	0.815	0.568	2.949	0.995
B1651R37P41c	Amphibolite	3.00	6.592	1.708	0.691	2.483	0.981	3.675	0.648	0.618	3.599	0.962
QL4	Amphibolite	2.96	6.177	6.053	1.175	1.006	0.980	3.489	2.497	0.728	1.336	0.983
YM4	Amphibolite	3.09	7.056	2.019	0.548	1.474	0.969	3.972	1.205	0.236	1.590	0.973
B2068R61P20h	Bt-Pl amphibolite	2.85	6.244	1.313	0.890	2.843	0.998	3.544	0.701	0.368	2.895	0.993
86351	Coarse-grained eclogite	3.49	8.335	1.769	0.885	1.096	0.965	4.652	1.849	0.514	1.705	0.959
98401	Eclogite	3.48	7.627	1.371	0.760	1.355	0.983	4.277	1.863	0.367	1.725	0.964
98501	Eclogite	3.47	7.299	1.674	0.553	1.123	0.963	4.145	1.373	0.269	1.728	0.975
125-15-18	Qtz eclogite	3.48	8.024	3.669	1.106	1.814	0.912	4.512	1.489	0.250	3.018	0.982
125-8-18	Qtz eclogite	3.38	7.694	3.188	2.174	2.559	0.979	4.277	1.192	0.447	2.211	0.896
315-1-11	Phn eclogite	3.43	7.952	1.637	1.220	1.682	0.988	4.463	1.502	0.382	4.378	0.984
315-4-11	Fine-grained Phn eclogite	3.53	8.107	2.007	1.068	2.358	0.959	4.635	1.720	0.687	2.792	0.998
C397 PC 2a	Eclogite	3.39	7.879	2.455	0.964	2.870	0.997	4.303	1.427	0.977	2.646	0.992
C398 PC 5b	Qtz eclogite	3.39	7.796	2.691	0.971	1.746	0.945	4.319	1.315	0.953	2.079	0.977
DG1	Fine-grained eclogite	3.46	7.842	1.957	0.861	1.322	0.938	4.393	2.099	0.357	1.379	0.983
JC2	Fine-grained eclogite	3.40	7.623	1.375	0.989	1.323	0.984	4.507	1.344	0.373	1.838	0.979
JZ1	Fine-grained eclogite	3.49	7.590	3.671	1.205	0.867	0.984	4.410	1.326	0.453	1.782	0.988
MB22	Coarse-grained eclogite	3.50	8.111	2.446	0.950	1.300	0.995	4.715	1.307	0.617	1.377	0.964
MB23	Coarse-grained eclogite	3.48	8.384	2.417	1.134	1.187	0.976	4.669	1.389	0.356	1.390	0.963
MB25	Coarse-grained eclogite	3.59	8.316	3.296	1.392	1.496	0.958	4.746	1.587	0.397	1.390	0.970
MB26	Coarse-grained eclogite	3.56	8.419	2.873	0.747	1.096	0.943	4.775	1.336	0.349	1.341	0.973
MB27B	Coarse-grained eclogite	3.58	8.405	1.715	0.684	1.032	0.881	4.817	1.014	0.308	1.162	0.961
MB2B	Coarse-grained garnetite	3.61	8.506	0.252	0.853	1.293	0.975	4.912	0.756	0.298	1.040	0.892
MB30	Coarse-grained eclogite	3.60	8.250	2.069	0.831	1.132	0.922	4.720	1.581	0.380	1.243	0.980
MB34	Coarse-grained garnetite	3.64	8.476	1.712	0.797	1.055	0.927	4.846	1.161	0.275	1.418	0.968
MB62	Coarse-grained garnetite	3.56	7.621	3.219	0.640	1.399	0.956	4.805	1.388	0.346	1.330	0.974
MB-OU-14	Garnetite	3.56	7.914	6.224	1.079	0.595	0.867	4.545	2.530	1.027	1.152	0.998
QL2	Eclogite	3.42	7.128	3.323	1.562	0.980	0.985	4.267	2.331	0.620	1.335	0.966
SB1	Fine-grained eclogite	3.37	7.943	2.325	0.613	0.972	0.917	4.448	1.578	0.247	1.681	0.982
178-6-6	Bt dioritic gneiss	2.74	5.814	2.729	1.072	1.599	0.995	3.277	1.083	0.407	2.518	0.984
19-13-13	Granitic Gneiss	2.64	6.186	2.548	1.273	2.241	0.997	3.632	1.372	0.381	6.812	0.755
210-15-21	Granitic gneiss	2.63	6.157	1.902	0.597	2.029	0.993	3.567	0.826	0.302	3.754	0.970
219-1-2	Granitic gneiss	2.63	6.290	2.528	1.586	2.171	0.996	3.482	0.963	0.326	3.767	0.996
26-10-17	Granitic Gneiss	2.64	6.172	2.871	0.932	2.988	0.995	3.611	1.073	0.460	4.072	0.959

Table 5.1 (continued)

Sample No.	Lithology	Density	Vp					Vs				
			V_0	D	B_0	k	R^2	V_0	D	B_0	k	R^2
		(g/cm^3)	(km/s)	(10^{-4} km/s/MPa)	(km/s)	(10^{-2} MPa^{-1})		(km/s)	(10^{-4} km/s/MPa)	(km/s)	(10^{-2} MPa^{-1})	
703-29	Grt-Bt-Hbl dioritic gneiss	2.93	6.685	2.721	1.436	1.988	0.995	3.824	1.305	0.771	6.336	0.984
B1578R14P18t	Bt-Ms-Pl-Kfs orthogneiss	2.65	6.198	1.691	2.629	2.250	0.996	3.692	0.608	1.063	2.156	0.952
B1628R33P24	Hbl-Mag felsic orthogneiss	2.65	6.378	1.923	1.726	2.103	0.997	3.667	0.804	1.213	2.495	0.980
B1694R49P7s	Felsic orthogneiss	2.63	6.394	1.710	1.500	0.739	0.871	3.697	0.685	1.076	1.457	0.957
B2078R63P9r	Felsic orthogneiss	2.63	6.315	1.932	3.449	3.012	0.997	3.743	1.212	1.170	2.355	0.982
B2168R85P2a	Bt-Hbl-Pl-Kfs paragneiss	2.65	6.129	1.870	2.171	2.522	0.978	3.393	1.319	0.757	2.556	0.997
B2184R88P4s	Bt-Hbl-Pl-Kfs paragneiss	2.66	6.062	1.502	1.992	1.618	0.974	3.619	0.753	1.233	2.793	0.987
B2242R100P16a	Hbl-Bt-Pl-Kfs paragneiss	2.66	6.357	1.970	1.545	1.592	0.998	3.597	0.729	1.089	1.302	0.940
B2339R122P1f	Hbl-Pl-Kfs paragneiss	2.65	6.193	1.779	0.902	1.173	0.951	3.616	0.859	1.019	2.689	0.984
TF1	Granitic gneiss	2.66	6.101	2.402	0.787	1.299	0.976	3.852	0.907	0.308	1.598	0.952
TF3	Granitic gneiss	2.66	6.096	2.527	0.878	1.577	0.955	3.575	1.296	0.314	1.421	0.946
YM1	Dolomitic marble	2.86	6.678	1.909	0.962	2.265	0.974	3.889	1.247	0.312	1.840	0.981
Sulu-YK1	Metagabbro	3.08	7.131	2.027	0.702	2.564	0.988	4.052	0.964	0.415	2.328	0.968
Sulu-YK22	Metagabbro	2.96	6.781	3.074	0.776	1.678	0.988	3.788	1.190	0.290	1.789	0.993
Sulu-YK2A	Metagabbro	3.07	6.985	2.328	0.718	3.909	0.990	3.967	1.137	0.275	2.245	0.978
Sulu-YK3B	Metagabbro	3.00	6.912	2.210	0.695	2.147	0.991	3.942	1.182	0.247	1.983	0.987
147-2-11	Dunite	3.16	7.356	2.408	0.947	2.495	0.989	3.963	1.184	0.388	3.519	0.943
150-3-20	Lherzolite	3.12	7.070	2.152	1.455	1.528	0.996	3.857	1.255	0.506	3.774	0.976
151-14-16	Grt-Harzburgite	3.21	7.670	2.580	1.150	1.487	0.923	4.085	1.044	0.570	2.694	0.993
160-12-11	Grt-Harzburgite	3.17	7.229	2.441	2.049	3.137	0.972	3.944	1.071	0.214	4.056	0.978
166-42-43	Phl dunite	3.25	6.835	2.114	0.932	2.139	0.966	3.697	0.924	0.796	5.081	0.977
B1536R6P41e	Hbl-Phn eclogite	3.11	7.087	1.718	2.152	2.850	0.997	4.050	0.623	0.861	2.549	0.998
C399 PC c1	Retrogressed Qtz eclogite	3.24	7.695	2.428	1.658	1.786	0.990	4.149	1.022	0.936	2.043	0.996
Sulu-YK9	Serpentinite	2.60	5.766	2.760	0.300	2.379	0.992	2.923	0.563	0.053	6.734	0.972
XG3	Serpentinite	2.66	5.622	1.683	0.587	2.287	0.974	2.879	0.464	0.077	1.827	0.984

Table 5.2 Young's (E), shear (G) and bulk (K) moduli and Poisson's ratio for microcrack-free UHP metamorphic rocks at hydrostatic pressures of zero and 600 MPa.

Lithology/	Density	E (GPa)		G (GPa)		K (GPa)		Poisson's ratio	
Sample	g/cm^3	0 MPa	600 MPa	0 MPa	600 MPa	0 MPa	600 MPa	0 MPa	600 MPa
Amphibolite									
203-5-15	3.07	86.08	91.63	34.73	36.95	55.07	58.75	0.239	0.240
B1608R27P12e	2.98	114.19	117.30	44.75	45.89	84.88	88.12	0.276	0.278
B1651R37P41c	3.00	103.30	105.76	40.52	41.39	76.35	79.29	0.275	0.278
QL4	2.96	91.35	100.12	36.09	39.25	64.98	74.35	0.266	0.276
YM4	3.09	123.49	127.95	48.69	50.48	88.74	91.67	0.268	0.267
B2068R61P20h	2.85	90.36	92.56	35.79	36.64	63.40	65.08	0.262	0.263
Eclogite									
86351	3.49	192.40	200.51	75.52	79.17	141.75	143.03	0.274	0.266
98401	3.48	161.64	168.81	63.60	66.97	117.48	117.36	0.271	0.260
98501	3.47	150.67	156.18	59.69	62.09	105.52	107.43	0.262	0.258
125-15-18	3.48	179.76	187.68	70.83	73.67	129.63	138.32	0.269	0.274
125-8-18	3.38	157.83	163.80	61.82	63.91	117.68	124.97	0.276	0.282
315-1-11	3.43	173.56	179.89	68.33	71.11	125.79	127.46	0.270	0.265
315-4-11	3.53	190.68	198.42	75.84	79.25	130.86	133.25	0.257	0.252
C397 PC 2a	3.39	161.61	168.02	62.76	65.28	126.77	131.35	0.288	0.287
C398 PC 5b	3.39	161.70	167.86	63.24	65.57	121.70	127.21	0.279	0.280
DG1	3.46	170.00	178.58	66.86	70.74	123.93	125.16	0.271	0.262
JC2	3.40	170.04	175.34	69.04	71.54	105.50	106.46	0.231	0.226
JZ1	3.49	168.99	176.19	67.86	70.33	110.54	118.72	0.245	0.253
MB22	3.50	193.87	200.53	77.87	80.47	126.62	131.54	0.245	0.246
MB23	3.48	193.54	200.43	75.88	78.61	143.54	148.38	0.275	0.275
MB25	3.59	203.49	212.17	80.85	84.12	140.42	147.99	0.258	0.261
MB26	3.56	205.09	212.44	81.20	83.95	144.14	150.86	0.263	0.265
MB27B	3.58	208.70	213.92	83.12	85.22	142.21	145.56	0.255	0.255
MB2B	3.61	217.86	220.85	87.16	88.76	145.10	143.87	0.250	0.244
MB30	3.60	201.35	208.89	80.11	83.36	137.91	140.95	0.257	0.253
MB34	3.64	215.11	221.03	85.55	88.03	147.64	150.63	0.257	0.255
MB62	3.56	192.15	200.29	82.11	84.98	97.05	103.82	0.170	0.178
MB-OU-14	3.56	184.42	197.97	73.53	78.49	124.95	138.09	0.254	0.261
QL2	3.42	151.98	161.48	62.25	66.39	90.72	94.83	0.221	0.216
SB1	3.37	169.46	176.39	66.63	69.49	123.70	127.31	0.272	0.269
Gneiss									
178-6-6	2.74	74.56	77.88	29.42	30.60	53.40	57.12	0.267	0.273
19-13-13	2.64	86.17	90.24	34.83	36.43	54.57	57.50	0.237	0.238
210-15-21	2.63	83.50	86.07	33.47	34.41	55.08	57.56	0.247	0.251
219-1-2	2.63	81.57	84.60	31.88	32.95	61.56	65.22	0.279	0.284
26-10-17	2.64	85.35	88.97	34.42	35.66	54.69	58.73	0.240	0.248
703-29	2.93	107.69	112.39	42.84	44.61	73.84	77.95	0.257	0.260
B1578R14P18t	2.65	88.49	90.65	36.12	36.83	53.66	56.06	0.225	0.230
B1628R33P24	2.65	89.29	91.91	35.62	36.57	60.29	62.97	0.253	0.257
B1694R49P7s	2.63	89.78	91.89	35.94	36.74	59.59	61.40	0.249	0.251
B2078R63P9r	2.63	90.60	94.08	36.85	38.30	55.76	57.72	0.229	0.228
B2168R85P2a	2.65	78.03	81.51	30.50	31.94	58.89	60.65	0.279	0.276
B2184R88P4s	2.66	85.23	87.52	34.84	35.72	51.29	53.05	0.223	0.225
B2242R100P16a	2.66	87.05	89.47	34.42	35.25	61.61	64.53	0.265	0.269
B2339R122P1f	2.65	86.03	88.66	34.66	35.65	55.43	57.61	0.241	0.243
TF1	2.66	92.38	95.82	39.53	40.65	46.45	49.69	0.169	0.179
TF3	2.66	84.10	87.97	33.97	35.46	53.47	56.45	0.238	0.240
Dolomitic marble									
YM1	2.86	107.60	111.63	43.27	44.95	69.90	72.07	0.243	0.242

Table 5.2 (continued)

Lithology/	Density	E (GPa)		G (GPa)		K (GPa)		Poisson's ratio	
Sample	g/cm^3	0 MPa	600 MPa	0 MPa	600 MPa	0 MPa	600 MPa	0 MPa	600 MPa
Metagabbro									
Sulu-YK1	3.08	127.45	131.32	50.51	51.97	89.09	92.54	0.262	0.263
Sulu-YK22	2.96	108.04	112.62	42.43	44.05	79.38	84.72	0.273	0.278
Sulu-YK2A	3.07	121.75	126.16	48.24	49.91	85.23	89.04	0.262	0.264
Sulu-YK3B	3.00	117.37	121.71	46.61	48.30	81.20	84.49	0.259	0.260
Peridotite									
147-2-11	3.16	128.60	133.35	49.63	51.43	104.81	109.20	0.296	0.296
150-3-20	3.12	119.56	124.20	46.41	48.24	94.06	97.37	0.288	0.287
151-14-16	3.21	139.48	144.08	53.56	55.22	117.43	122.91	0.302	0.305
160-12-11	3.17	127.02	131.43	49.31	50.93	99.90	104.52	0.288	0.290
166-42-43	3.25	114.90	118.55	44.42	45.77	92.58	96.48	0.293	0.295
Retrogressed eclogite									
B1536R6P41e	3.11	128.30	131.07	51.01	51.96	88.17	91.49	0.257	0.261
C399 PC c1	3.24	144.48	149.05	55.78	57.44	117.48	122.60	0.295	0.297
Serpentinite									
Sulu-YK9	2.60	58.97	60.69	22.22	22.74	56.82	61.16	0.327	0.335
XG3	2.66	58.34	59.65	22.06	22.49	54.73	57.21	0.322	0.326

Table 5.3 Relationship between elastic moduli (E, G, and K) and density of rocks at 0 and 600 MPa

Elastic modulus (GPa)	Pressure (MPa)	Relationship with density (ρ: g/cm^3)	R^2
E	0	$E = 26.133\rho^3 - 137.500\rho^2 + 213.310\rho$	0.953
	600	$E = 26.440\rho^3 - 138.350\rho^2 + 214.540\rho$	0.959
G	0	$G = 12.119\rho^3 - 65.522\rho^2 + 101.630\rho$	0.952
	600	$G = 12.310\rho^3 - 66.232\rho^2 + 102.590\rho$	0.958
K	0	$K = 2.414\rho^3 + 3.223\rho^2 - 4.638\rho$	0.889
	600	$K = 1.484\rho^3 + 9.220\rho^2 - 12.986\rho$	0.893

5.6 Causes of Poisson's ratio variations

The possible causes of υ variations with rock density are of special interest and have been discussed by Kern (1982), Tarkov and Vavakin (1982), Ji and Salisbury (1993), Christensen (1996), Brocher (2005) and others. Figure 5.6, plotting υ versus ρ, provides some interesting perspectives on the υ characteristics of common rock-forming minerals:

(1) Quartz and serpentinite have, respectively, the lowest (υ=0.080) and highest (υ=0.345) Poisson's ratios among the principal rock-forming minerals (Kern, 1979, Watanabe et al., 2007). Calcite also displays a high Poisson's ratio.

(2) K-feldspars and plagioclase have quite high Poisson's ratios. In the plagioclase series, there is a non-linear increase in υ with anorthite content (Christensen, 1996).

(3) The Poisson's ratios of sheet sillicates have a triangular distribution: phlogopite (relatively Mg-rich) has a relatively high υ but low density, biotite (Fe-rich) has a high density but moderate υ, and muscovite has a low υ and moderate density.

(4) Augite and omphacite have almost the same Poisson's ratios as olivine with Fo90. Diopside has a lower density but higher υ than augite, omphacite and jadeite.

(5) The Poisson's ratios of orthopyroxenes show a J-shaped distribution with a lower value for enstatite and a higher value for bronzite. The Poisson's ratio of orthopyroxene increases with increasing Fe-content.

(6) In the olivine group, Poisson's ratio increases with increasing FeSiO3 content. Fig. 5.6 illustrates only the Poisson's ratios of olivine with forsterite content Fo100 to Fo90, which represents the chemical composition of common olivine in the upper mantle.

(7) According to their elasticity, silicates garnets can be classified into two groups, pyralspite (pyrope-almandine-spessartine), and ugrandite (uvarovite-grassular-andradite) groups. Poisson's ratio decreases very slightly with increasing density for pyralspite, but increases significantly with increasing density for ugrandite (Wang and Ji, 2001).

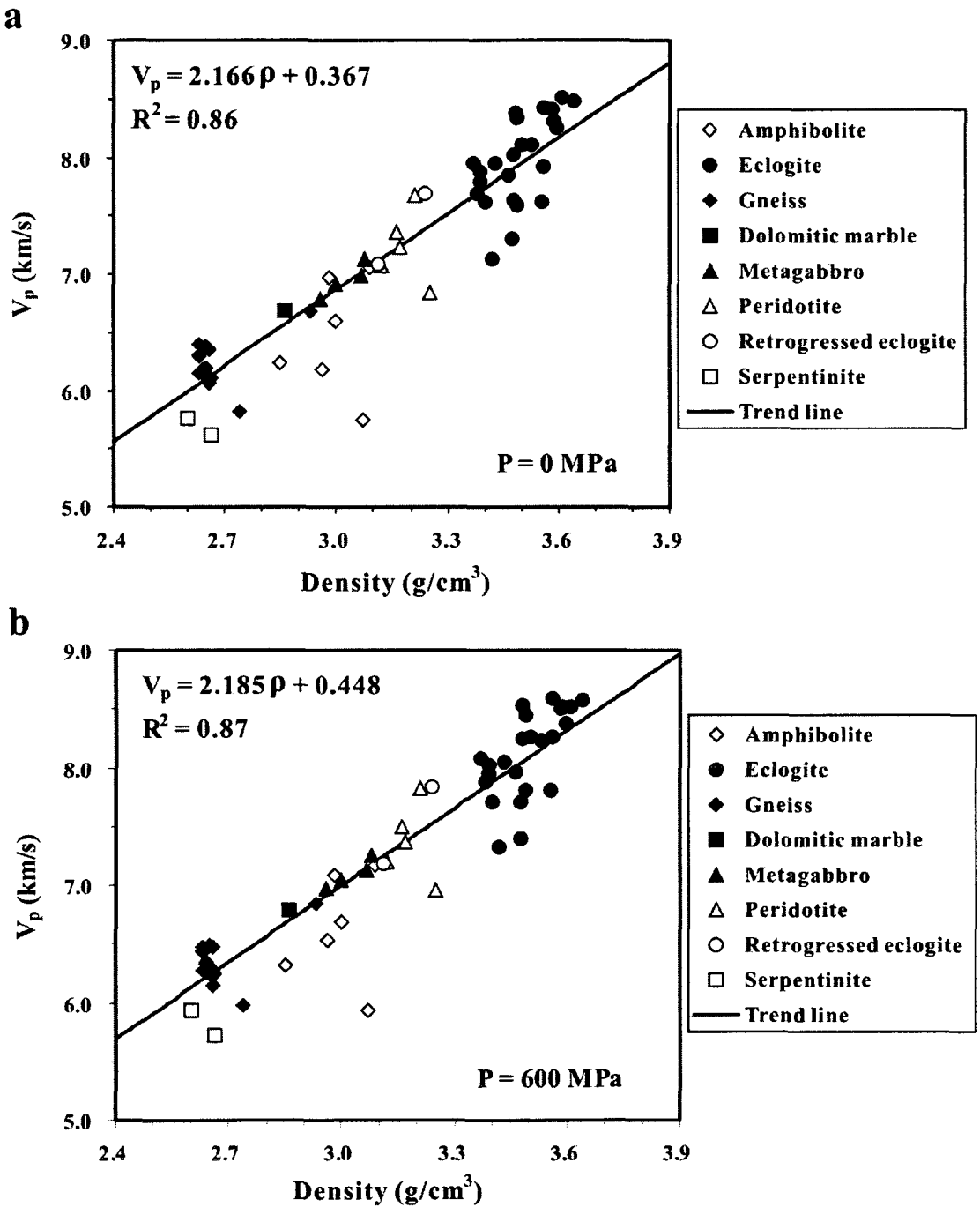

Figure 5.3 Plots of mean P-wave velocity versus density for Sulu-Dabie UHP metamorphic rocks at zero pressure (a) and 600 MPa (b).

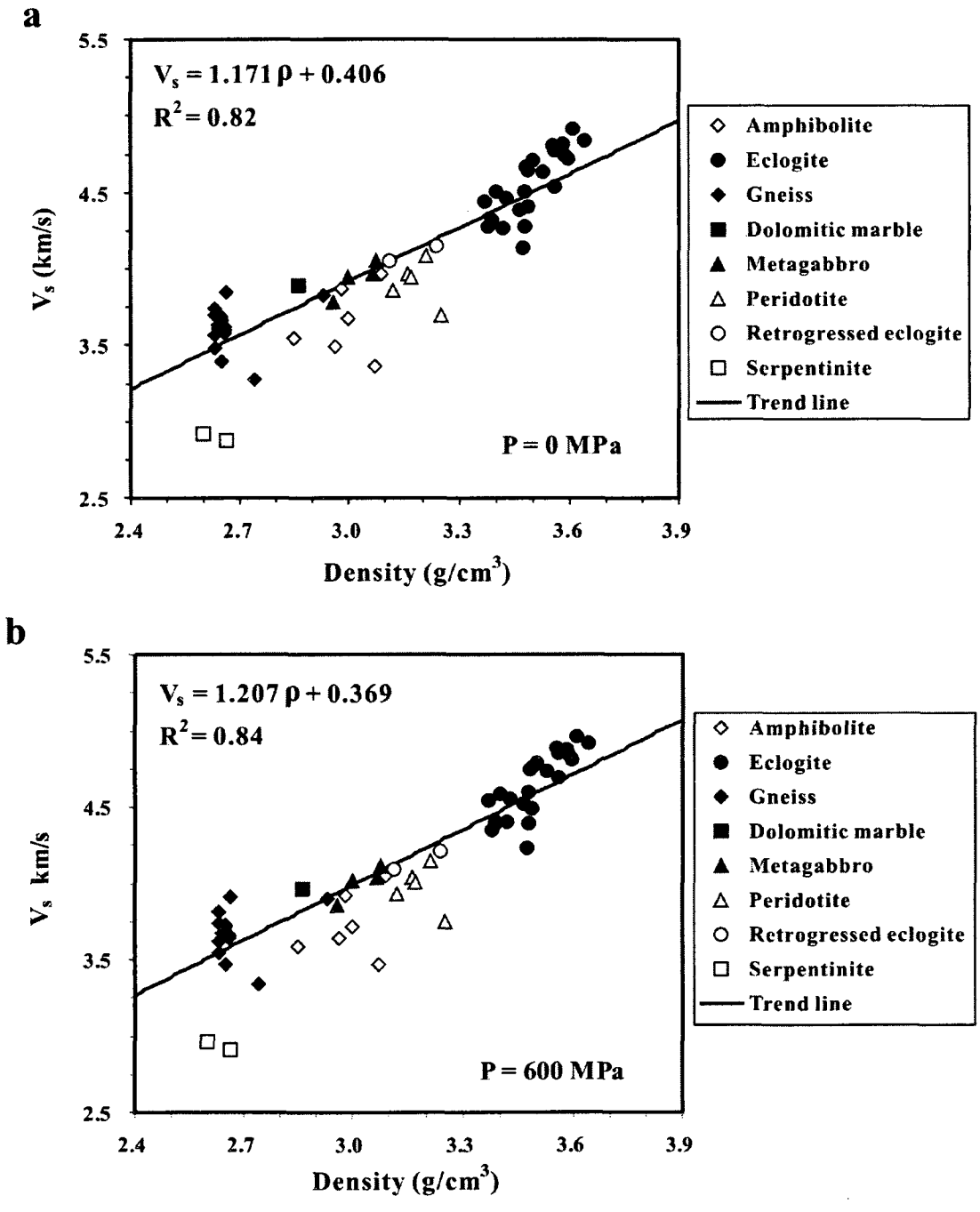

Figure 5.4 Plots of mean S-wave velocity versus density for Sulu-Dabie UHP metamorphic rocks at zero pressure (a) and 600 MPa (b).

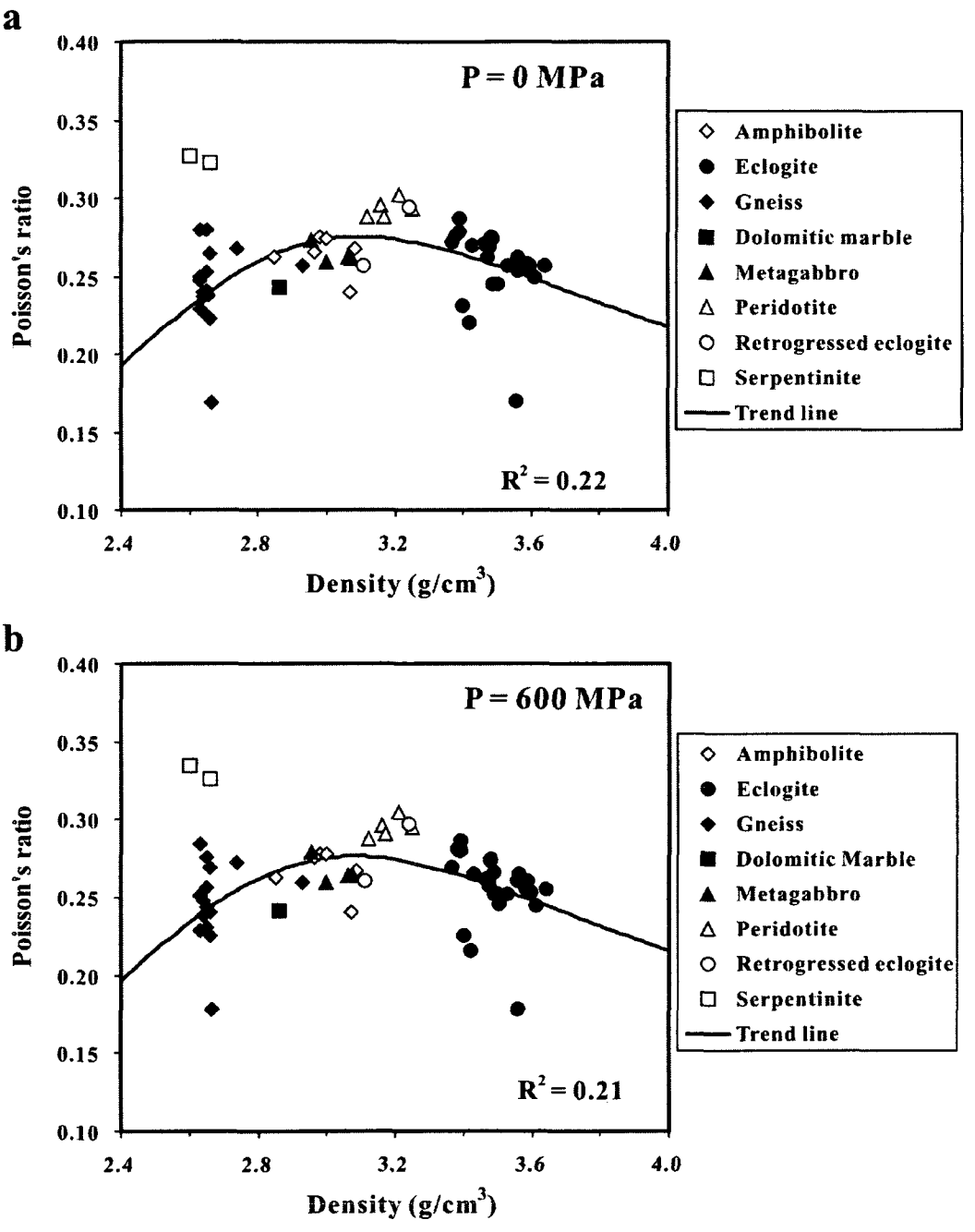

Figure 5.5 Poisson's ratio-density plots for Sulu-Dabie UHP metamorphic rocks at zero pressure (a) and 600 MPa (b). The trend line was calculated from the correlations between the elastic moduli and density for the studied UHP rocks (Table 5.3).

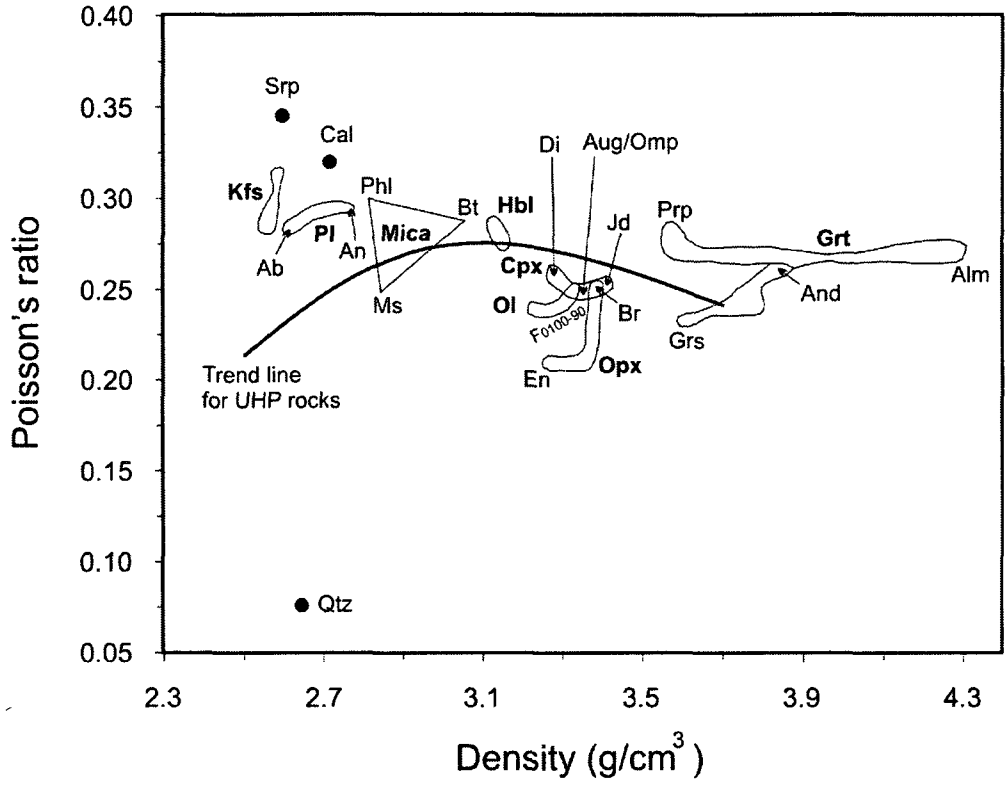

Figure 5.6 Poisson's ratio-density plots for common rock-forming minerals. Ab: albite; Alm: almandine; And: andradite; Aug: augite; Br: bronzite; Bt: biotite; Cal: calcite; Cpx: clinopyroxene; Di: diopside; En: enstatite; Grs: grossular; Grt: garnet; Hbl: hornblende; Jd: Jadeite; Kfs: K-feldspar; Ms: muscovite; Ol: olivine; Omp: omphacite; Opx: orthopyroxene; Phl: phlogopite; Pl: plagioclase; Prp: pyrope; Qtz: quartz; Srp: serpentinite. The trend line was calculated from the correlations between elastic moduli and density for the studied UHP rocks (Table 5.3).

Wang et al. (2005b) summarized all available mean P- and S-wave velocity and Poisson's ratio information at a confining pressure of 600 MPa for 18 common lithologies. The velocity data were from the Handbook of Seismic Properties of Minerals, Rocks and Ores (Ji et al., 2002). As shown in Fig. 5.7, except for quartzite, serpentinite, anorthosite, limestone, marble, and serpentinized peridotite, the other rock types all fall along the trend line determined for the metamorphic rocks from the Sulu-

Dabie orogenic belt. Poisson's ratio increases with density as the lithology changes from granite, schist, felsic gneiss, through diorite-syenite, intermediate gneiss and metasediment, to gabbro-diabase, amphobolite, and mafic gneiss, and then decreases as the rocks become ultramafic in composition (i.e., pyroxenite and peridotite). Eclogite has a higher density but a slightly lower υ than peridotite. Clearly, the transition from mafic granulite or gabbro to eclogite results in a significant increase in V_p, V_s and ρ, but a slight decrease in υ.

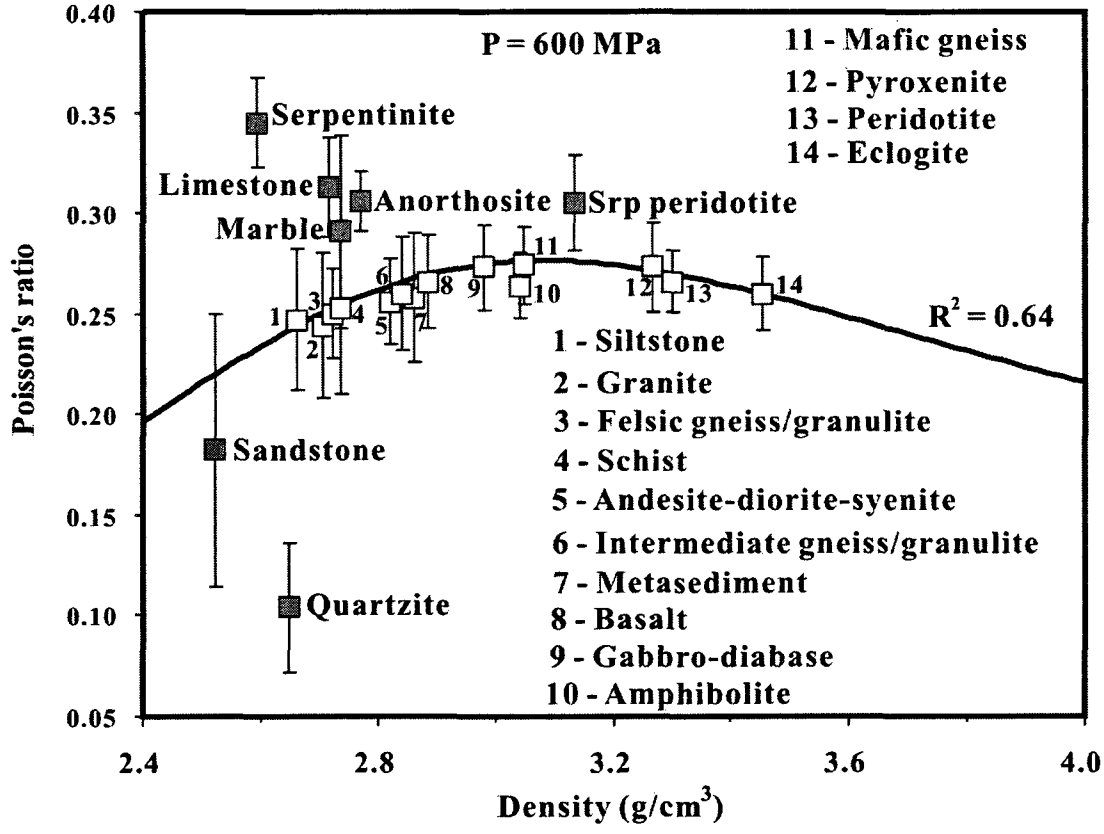

Figure 5.7 Poisson's ratio-density plots for major rock types. This figure was constructed based on the data from 620 samples, compiled in Handbook of Seismic Properties of Minerals, Rocks and Ores (Ji et al., 2002). The trend line was calculated from the correlations between elastic moduli and density for the Dabie-Sulu UHP rocks (Table 5.3). R^2 (0.64) indicates the fitting goodness of the trend line to the mean Poisson's ratios of 14 common lithologies (open squares) excluding monomineralic rocks such as serpentine, calcite and quartz (filled squares).

The contribution of each constituent mineral to the bulk Poisson's ratio of a polymineralic rock can be analyzed for the moment only in a qualitative manner because a relevant mixture rule for Poisson's ratio is not available. In other words, it is still unclear how to calculate the bulk Poisson's ratio of a composite rock from the Poisson's ratios and volume fractions of its constituent minerals. Even in a simple two-phase porous material, whether the effective Poisson's ratio varies with porosity (ϕ) or the matrix Poisson's ratio (υ_0) is still in debate (e.g., Wang, 1984; Ramakrishnan and Arunachalan, 1990; Dunn and Ledbetter, 1995; Arnold et al., 1996). For example, the analysis of Dunn and Ledbetter (1995) demonstrated that for spherical and needle-shaped pores, υ decreases with ϕ for materials with $\upsilon_0 > 0.2$ and increases with ϕ for materials with $\upsilon_0 < 0.2$ and shows no variation with porosity for materials with $\upsilon_0 = 0.2$. Their analysis also suggests that for disk-shaped pores, Poisson's ratio always decreases with increasing ϕ for any materials with $\upsilon_0 = 0-0.5$. These theoretical analyses suggest that the role of the second phase on the Poisson's ratio is complicated, depending on the geometrical shape, preferred orientation, connectivity/continuity, and the volume fraction of each phase.

Laboratory experiments have also shown that Poisson's ratio can decrease (e.g., for polycrystalline iron, Panakkal et al., 1990) or increases (e.g., for ZrO_2 aggregates, Smith and Crandall, 1964) with increasing ϕ. The comparison between sandstone and quartzite (Fig. 5.7) suggests an increase of υ and a decrease of ρ with increasing porosity for quartz aggregates. In nature, pores, microcracks and fractures are often filled with aqueous fluids. Generally speaking, very high Poisson's ratios coincide with regions with high heat flow where the lower crust is partially molten or with fault zones in which rocks are fractured and saturated with aqueous fluids. For the same reason, the presence of very thick porous sediments or volcanic materials may result in an increase in Poisson's ratio.

The correlations between a rock's Poisson's ratio and its modal composition can be summarized as follows: The increase in υ with density, ranging from felsic gneisses to metagabbro, is generally correlated with systematic variations of quartz and feldspar content in the rocks (Tarkov and Vavakin, 1982; Christenen, 1996). An increase in quartz content induces a decrease in υ while an increase in feldspar content causes an increase in υ (Figs. 5.6-5.7). An increase in the anorthite content of plagioclase may slightly increase the Poisson's ratio of the bulk rock. Fresh peridotites have lower υ values than metagabbro and amphibolite. However, serpentinized peridotites have larger υ values than metagabbro and amphibolite because serpentine possesses an extremely high value of υ (Christensen, 1966; Kern, 1993; Watanabe et al., 2007). It is evident that serpentinization can significantly raise the Poisson's ratio of peridotites.

Hence, rocks from the continental crust can be classified into 4 categories with low ($\upsilon < 0.26$), medium ($0.26 \leq \upsilon < 0.28$), high ($0.28 \leq \upsilon < 0.30$), and very high ($\geq 0.30$) Poisson's ratios. Poisson ratios higher than 0.30 are found only for serpentinite, limestone and anorthosite (Fig. 5.7), which are generally regarded as monomineralic aggregates of serpentine, calcite and plagioclase, respectively. These rocks represent only a very minor proportion of the continental crust (Rudnick and Gao, 2005) and in general are localized. When very high υ values (≥ 0.30) are observed, they tend to occur in the following regions: (1) large fault zones in which rocks are extensively fractured and the resultant cataclasites are saturated with water or other fluids; (2) thick unconsolidated sediments which are saturated with aqueous fluids; (3) lower crust with pervasive intrusions of mantle-derived mafic magmas; and (4) modern volcanic regions with magma chambers above hot, partially molten upper mantle, and melt-filled fractures or mafic dykes within the crust above magma chambers (Walck, 1988). To a first approximation, the 4 categories of continental crust with low ($\upsilon < 0.26$), medium ($0.26 \leq \upsilon < 0.28$), high ($0.28 \leq \upsilon < 0.30$), and very high ($\geq 0.30$) bulk Poisson's ratios thus correspond, respectively, to acid, intermediate, mafic, and fluid-filled

porous/fractured or partially molten rocks (Zandt and Ammon, 1995; Owens and Zandt, 1997; Chevrot and van der Hilst, 2000; Xu Lili et al., 2007).

5.7 Poisson's ratios of Chinese continental crust

5.7.1 Geological background

The Chinese continental crust was formed by the amalgamation of many blocks (Fig. 5.8). The North China, Yangtze and Tarim blocks, which display both Precambrian basement and sedimentary cover, are considered parts of Paleo-China. Evidence for the existence of cold, thick cratonic lithosphere of Archean age has been found for the North China block (e.g., Menzies et al., 2007). Three significant tectonic deformation events occurred between 2.6-2.4, 1.9-1.7 and 1.0-0.8 Ga in Paleo-China (e.g., Ren Jishun, 1996). Due to lithospheric thinning in the Mesozoic-Cenozoic, the eastern part of the North China block is characterized by thin crust adjacent to the Bohai Bay basin. The Northeast China and Kazakhstan blocks, which are considered to have Siberian-affiliations, were located to the north of Paleo-China prior to the Permian. The Indochina, Lhasa and Qiangtang terranes are Gondwana-affiliated continental blocks. During most of the Paleozoic, these blocks were a part of eastern Gondwana. After the early Mesozoic Indosinian orogeny, these blocks moved to the north of the Tethys and then collided with the southern Eurasian continental margin.

The Indochina block is bounded by two major strike slip faults: the sinistral Red-River fault to east and the dextral Gaoligong fault to west. The transcurrent shears caused the southeastward extrusion of the Indochina block and a significant clockwise rotation of the block with respect to the Yangtze and South China blocks during the continuous indentation of the rigid Indian plate into the Eurasian continent from ~45 Ma ago to the present (Wu Haiwei et al., 1989; Tapponnier et al., 1990; Leloup et al., 1995).

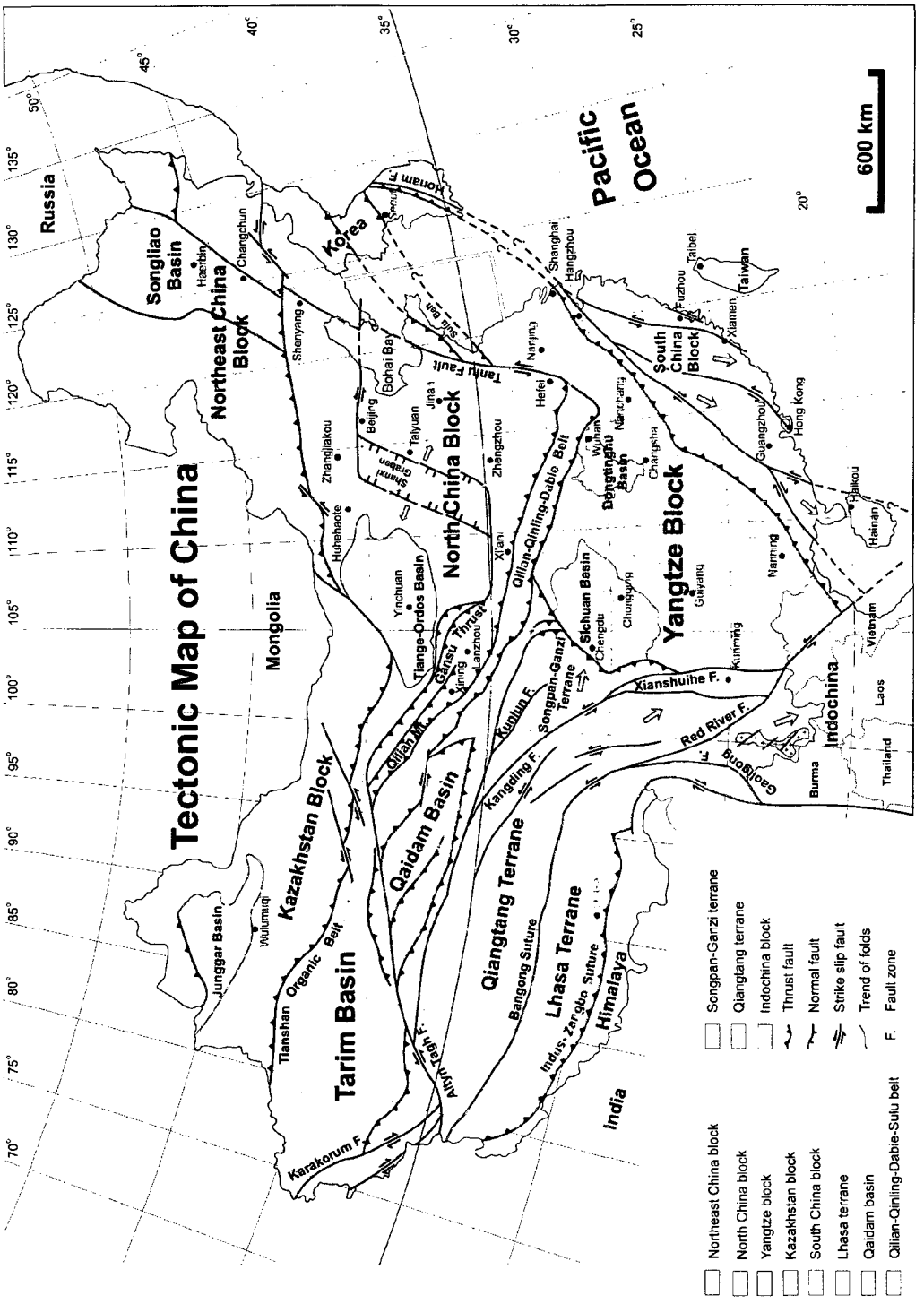

Figure 5.8 Simplified map showing the major tectonic provinces in China.

The Yangtze block is characterized by a metamorphosed Precambrian crystalline basement and an overlying sequence composed of weakly metamorphosed latest Precambrian (Sinian) to middle Triassic marine sedimentary rocks. These sedimentary rocks were folded with fold axes aligned NE40-60° (Fig. 5.8). The collision between the Yangtze and North China blocks took place in the Triassic, forming the spectacular Qinling-Dabie-Sulu UHP belt. Recent studies suggest that the peak UHP metamorphism and subsequent exhumation-related amphibolite-facies retrograde metamorphism occurred at 220-240 Ma and 180-210 Ma, respectively (e.g., Zhang Zeming et al., 2005). After the collision, mollasse sediments (sandstones, conglomerates and red beds) were deposited in foreland basins in Jurassic to lower Cretaceous times. Late Cretaceous and Cenozoic sediments were deposited mainly in pull-apart and rifted basins.

The boundary between the Yangtze and South China blocks is marked by the Qinzhou-Pingxiang-Shanghai fault zone. To the southeast of the boundary, the South China block is characterized by a dense array of Jurassic-Cretaceous granites and Late Triassic to Early Cretaceous continental basins. The granites and basins are less densely distributed in the Yangtze block, northwest of the boundary (Zhou Xinmin et al., 2005). The basement of the South China block is assumed to be Paleo- to Neoproterozoic continental crust (e.g., Jahn et al., 1990; Li Xianhua et al., 2003; Chen and Jahn, 1998). Based on zircon inheritance ages of the Phanerozoic granitoids, previous workers suggested five stages of Precambrian accretion for the South China block, which occurred at 2.5, 2.1., 1.9-1.7, 1.4-1.2., and 1.1-0.8 Ga (Yui et al., 1996; Jahn et al., 1990; Xu Xisheng et al., 2005; Chen Chenghong et al., 2006). The South China block may include Archean microcontinet fragments. The collision between the Yangtze and South China blocks is thought to have taken place at 1000-900 Ma (Chen Jiangfeng et al., 1991; Li Xianhua et al., 2003).

The Lhasa terrane is bounded by the Indus-Yalu suture to the south and the Bangong suture to the north. The collision between the Lhasa and Qiangtang terranes took place

in the late Jurassic to the middle Cretaceous (e.g., Hodges, 2000; Matte et al., 1996). Continuing north-south contraction lasted until the early Late Cretaceous within the Lhasa terrane, resulting in >180 km of shortening (Yin and Harrison, 2000). The Qiangtang terrane lies between the Bangong suture to the south and the Kangding fault to the northeast. This terrane is about 500-600 km wide in central Tibet, but tapers towards the eastern syntaxis of Yunnan. Both the Qiangtang Terrane and Indochina block developed a crystalline basement of metamorphic rocks covered by Late Paleozoic (Carboniferous and Permian) shallow marine strata and Triassic-Jurassic shallow marine carbonates interbedded with terrestrial clastic and volcaniclastic strata. The basement metamorphic complexes consist of highly deformed flysch sediments and mafic and ultramafic igneous rocks. The Songpan-Ganzi terrane is a triangular region among the Yangtze block in the east, the Qaidam Basin-Qilian zone in the north, and the Qiangtang terrane in the south. During the mid- to late-Triassic, the block subducted southward beneath the Qiangtang along the Jinsha Jiang suture (Zhong Dalai, 2000). The 12 May 2008 M_w=8.0 Wenchuan earthquake that devastated several cities of Sichuan and killed ~87,165 people originated from right-lateral thrusting of the Songpan-Ganzi Terrane over the Sichuan Basin along the Longmen Shan fault zone.

5.7.2 Crustal Poisson's ratio data

Using joint analysis of teleseismic receiver functions and Rayleigh wave dispersion, Ma Yanlu and Zhou Huilan (2007) investigated the crustal thicknesses and average Poisson's ratios beneath 36 permanent broadband seismic stations in China. The authors showed good agreement between the results from the teleseismic receiver functions and deep seismic sounding profiles. Xu Weiwei and Zheng Tianyu (2005) determined the crustal thicknesses and Poisson's ratios beneath 58 broadband seismic stations in the Beijing region and Hebei province. The stations were distributed in the basin-range region northwest of Bohai Bay (Fig. 5.9). Zhang Xuemin et al. (2001a) conducted a detailed study of V_p and V_s structures in Tangshan where a magnitude 7.8 earthquake

took place on July 28, 1976, killing 250,000 people. The crusts beneath the Douhe and Luanxian stations have the same thickness of 38 km, but different Poisson's ratios: 0.273 beneath Luanxian station and 0.285 beneath Douhe station, which locality is closer to the focus of the Tangshan earthquake (N39.60°, E118.79°). The crustal thicknesses and Poisson's ratios beneath the Donglang (N40.43°, E115.52°) and Chicheng (N40.91°, E115.84°) stations in Northwest Hebei province were calculated from the V_p and V_s structures and reported by Zhang Xuemin et al. (2001b). Tong Weiwei et al. (2007) measured the crustal thicknesses and Poisson's ratios beneath 12 seismic stations in the region of Liupanshan.

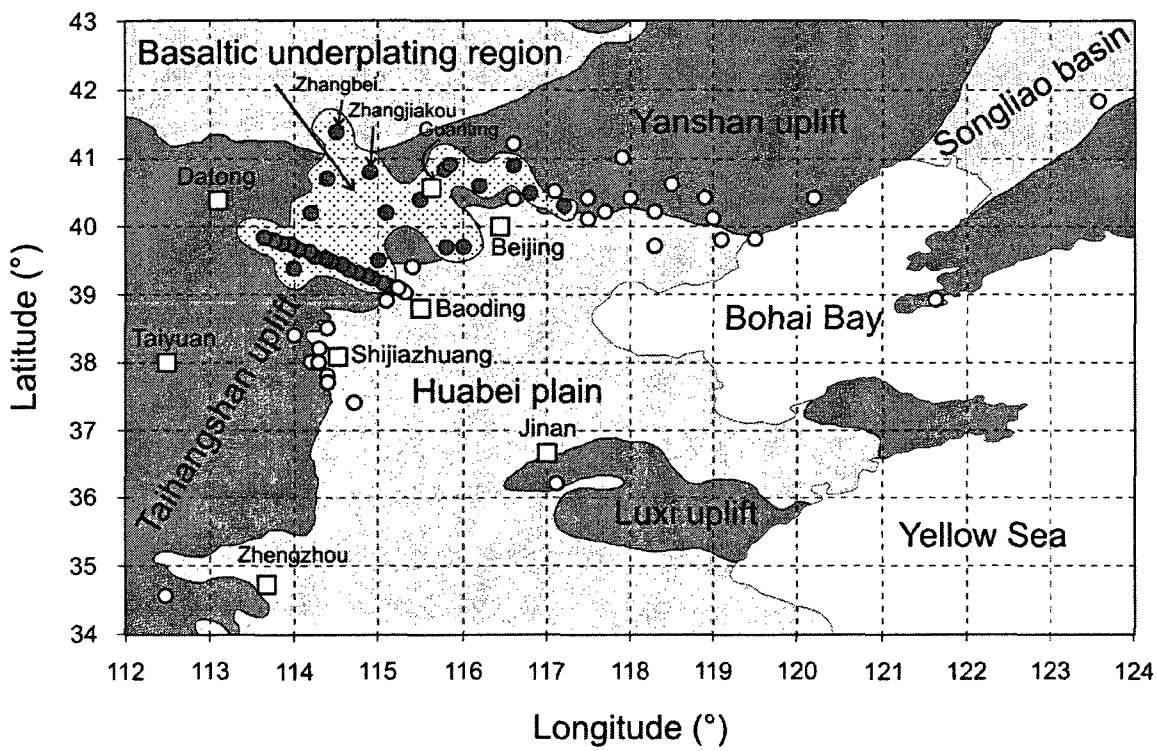

Figure 5.9 Map of seismic stations in the North China block. In the region where the stations are indicated by solid circles, v increases gently and linearly with increasing crustal thinning. In the region where the stations are indicated by open circles, v increases abruptly and nonlinearly with increasing crustal thinning. See Fig. 5.13.

Wang Xiaoping et al. (2006) measured the depths of Moho and crustal Poisson's ratios beneath 17 permanent seismic stations in Jiangsu Province, 10 stations in Shanghai, and 14 in Zhejiang Province. Hu Jiafu et al. (2003) reported the crustal thicknesses and Poisson's ratios beneath 23 broadband seismic stations in Yunnan province and found an obvious trend of decreasing crustal thickness from north (62 km at Zhongdian) to south (30.2 km at Jinghong). Fourteen of the stations display Poisson's ratios higher than 0.30. Xu Mingjie et al. (2005) measured the depths to Moho and crustal Poisson's ratios beneath 6 seismic stations in a corridor which crossed, from northeast to southwest, the Yangtze block, the Red-River fault zone, and the Indochina block. Using broadband teleseismic waveform data recorded by 16 seismic stations in Gansu province, Li Yonghua et al. (2006a) investigated the variations in crustal thickness and Poisson's ratio for the Songpan-Ganzi terrane.

Owens and Zandt (1997) measured crustal thickness and Poisson's ratio beneath 9 sites across the Tibetan plateau using shear-coupled teleseismic P-waves from deep earthquakes. Li Yonghua et al. (2006b) analyzed teleseismic converted and multiple waves recorded by the INDEPTH-III seismic array in the central Tibetan plateau. They obtained crustal thicknesses and Poisson's ratios beneath 11 stations in the Lhasa terrane and 10 stations in the Qiangtang terrane. Their results show that the crustal thickness is 65±5 km beneath the central plateau with the Moho 5-6 km shallower in the Qiangtang terrane than the Lhasa terrane. Very high Poisson's ratio values (>0.30) were observed at stations (St20, St22 and St23) near the Bangong suture or strike-slip fault zone and at 4 stations (ST37-40) in the northern part of the Qiangtang terrane.

Recently, Xu Lili et al. (2007) reported the crustal thicknesses and Poisson's ratios beneath 22 temporary broadband seismic stations: 5 stations were located in the Yangtze block, 2 in the Indochina block, 3 in the Songpan-Ganzi terrane, and 12 in the eastern portion of the Qiangtang terrane. The authors found that the crustal thickness decreases gradually from the Songpan-Ganzi terrane (~60 km) to the western Sichuan basin (~46

km) and the southwestern Yangtze block (~40 km). The Indochina block has a crustal thickness of 38-46 km. In Yunnan Province, Poisson's ratios generally decrease from the eastern Qiangtang terrane to the southwestern Yangtze block.

Teleseismic receiver functions have proven to be a powerful tool for estimating crustal thickness and bulk Poisson's ratio beneath individual seismic stations (Zandt and Ammon, 1995; Chevrot and van der Hilst, 2000; Julia and Mejia, 2004). Figure 5.10 shows the distribution histogram of Poisson's ratios measured from each main tectonic province in China using teleseismic receiver functions. The prominent characteristics are summarized below:

The Yangtze block, South China block and Songpan-Ganzi terrane are characterized by low mean υ values: 0.249, 0.243 and 0.236, respectively. The mean υ value for the North China block is 0.268. Large mean υ values are found for the Lhasa (0.285) and Qiangtang (0.293) terranes and the Indochina block (0.283).

The North China block and particularly the Yangtze and South China blocks and the Songpan-Ganzi Terrane are dominated by low ($\upsilon < 0.26$) and moderate ($0.26 \leq \upsilon < 0.28$) Poisson's ratios (>70%). The data imply that these crusts have dominantly felsic composition. The present results are remarkably consistent with the seismic refraction profile across the Songpan-Ganzi terrane (Liu Mingjun et al., 2006). Their data suggest that mafic lower crust is likely absent in the NE margin of the Tibetan plateau, from the Songpan-Ganzi terrane to the Ordos basin. The Songpan-Ganzi terrane appears to be an accreted crustal terrane which has been squeezed among the advancing Tibetan plateau, the North China block and the Yangtze block. The squeezing induced an intensively shortened felsic crust and formed a new seismic Moho after the lower-crustal mafic materials were delaminated and recycled into the underlying hot mantle.

The modern orogenic regions such as the Lhasa, Qiangtang and Indochina terranes have an unusually high proportion of measurements with $\upsilon \geq 0.30$ (Fig. 5.10 and Table 5.4). The Qiangtang terrane displays a significantly higher percentage of high υ values (0.28-0.30) than the Lhasa terrane and particularly the Indochina block (Fig. 5.10). These high υ values may represent either crystalline mafic rocks or a mixture of felsic rocks with fluids. The crust is 10-20 km thinner beneath the Qiangtang terrane than the Lhasa terrane (Fig. 5.11). Changes in the υ distribution appear to be related to differences in partial melting depth within the crust and in the source of heat causing the partial melting. In the Lhasa terrane, partial melts of hydrous granites occur in the felsic middle crust (Nelson et al., 1996; Unsworth et al., 2005), and the heat which causes the partial melting results from crustal thickening rather than underplating of partial melts derived from the upper mantle below. The volume fraction of melts is estimated to be in the range of 5-14% (Unsworth et al., 2005). The fast upper mantle and the lack of Neogene to recent mafic volcanism in the Lhasa terrane also suggest that no intrusion of mantle-derived melts into the crust has occurred. The mid-crustal partial melt layer (10-15 km thick) with its top at a depth of 15-20 km, acts as a rheologically weak flow channel (Shapiro et al., 2004; Beaumont et al., 2004), which on the time scale of Himalayan deformation promotes large-scale upward, eastward extrusion of the Lhasa terrane. The above interpretation agrees with the now widely held view of Nelson et al. (1996) that partial melt is widely developed within the middle crust of the southern Tibetan Plateau, based largely on INDEPTH seismic reflection profiling (Brown et al., 1996) and magnetotelluric surveying results (Pham et al., 1986; Chen Leshou et al., 1996; Alsdorf and Nelson, 1999; Wei Wenbo et al., 2001; Unsworth et al., 2005) as well as heat flow data (Francheteau et al., 1984).

In the Qiangtang terrane, however, there are important proportions of measurements with high (υ=0.28-0.30, 29%) and very high ($\upsilon \geq 0.30$, 37%) values. The high υ values imply that crystalline mafic rocks are probably important in the crust while the very high υ values suggest that partial melt and/or aqueous fluids are widespread within

the crust. Previous magnetotelluric data show that the conductive layer is at a depth of 30 to 40 km and is due to partial melting (Wei Wenbo et al., 2001). Thus the Poisson's ratio data from the Qiangtang terrane can be reasonably attributed to the intrusion of mantle-derived mafic magmas into the lower crust. This interpretation accords with the fact that mantle-derived, post Mid-Miocene potassic basalts are widespread in this terrane (Turner et al., 1993). There is overwhelming evidence, such as inefficient regional upper mantle S-wave (S_n) propagation, low regional upper mantle P-wave (P_n) velocity and strong shear-wave splitting (Ni and Barazangi, 1983; McNamara et al., 1994, 1995; Owens and Zandt, 1997), to indicate that the upper mantle beneath the Qiangtang terrane is hot and partially molten.

Hot springs, indicative of high heat flow, are a ubiquitous feature of the Indochina block. Quaternary (<0.95 Ma) volcanism (basalt, andesite and dacite) occurs in the region of Tengchong, Yunnan Province. The unusually high proportion of measurements with $\upsilon \geq 0.30$ indicates the presence of partial melts or aqueous fluids in the lower crust beneath the Indochina block. Limited sampling prevents any attempt to constrain the crustal composition for the Northeast China block, the Tarim basin and the Kazakhstan terrane.

Table 5.4 Poisson's ratios and their interpretation in terms of lithology for the main tectonic provinces in China

Lithology Poisson's ratio	N	Mean υ	Acid <0.26	Intermediate 0.26-0.28	Mafic 0.28-0.30	Presence of fluid / melt ≥0.30
North China block	99	0.268	28%	43%	26%	3%
Yangtze block	44	0.249	75%	11%	7%	7%
South China block	20	0.243	80%	15%	5%	0%
Northeast China block	3	0.271	0%	100%	0%	0%
Lhasa block	18	0.285	17%	28%	22%	33%
Indochina block	12	0.283	17%	33%	8%	42%
Qiangtang terrane	41	0.293	12%	22%	29%	37%
Songpan-Ganzi terrane	8	0.236	88%	12%	0%	0%
Tarim basin	1	0.266	0%	100%	0%	0%
Kazakhstan block	2	0.259	50%	50%	0%	0%

N – number of seismic stations

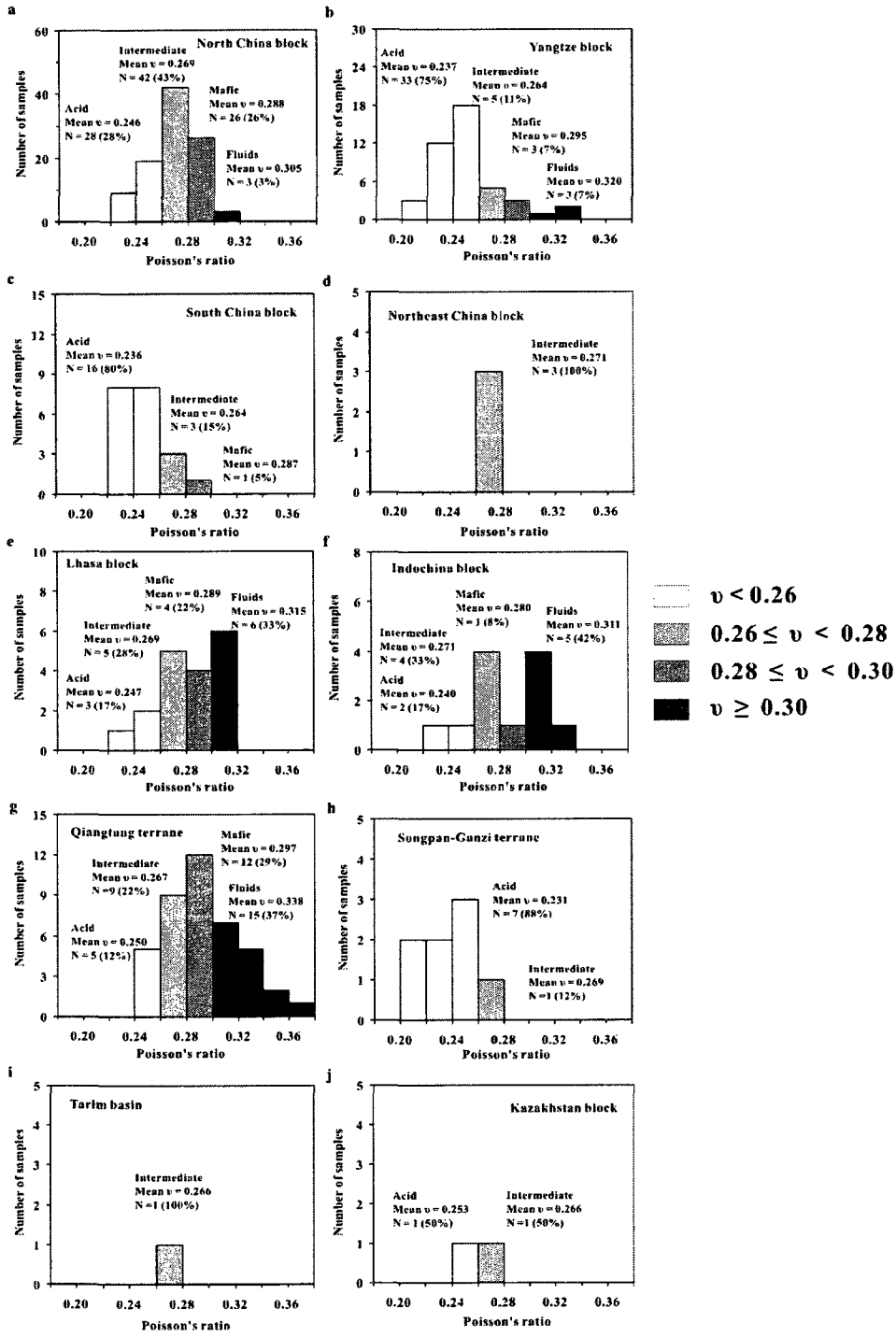

Figure 5.10 Histogram of crustal Poisson's ratios for each tectonic province in China. (a) North China block; (b) Yangtze block; (c) South China block; (d) Northeast China block; (e) Lhasa block; (f) Indochina block; (g) Qiangtang terrane; (h) Songpan-Ganzi terrane; (i) Tarim basin; and (j) Kazakhstan block.

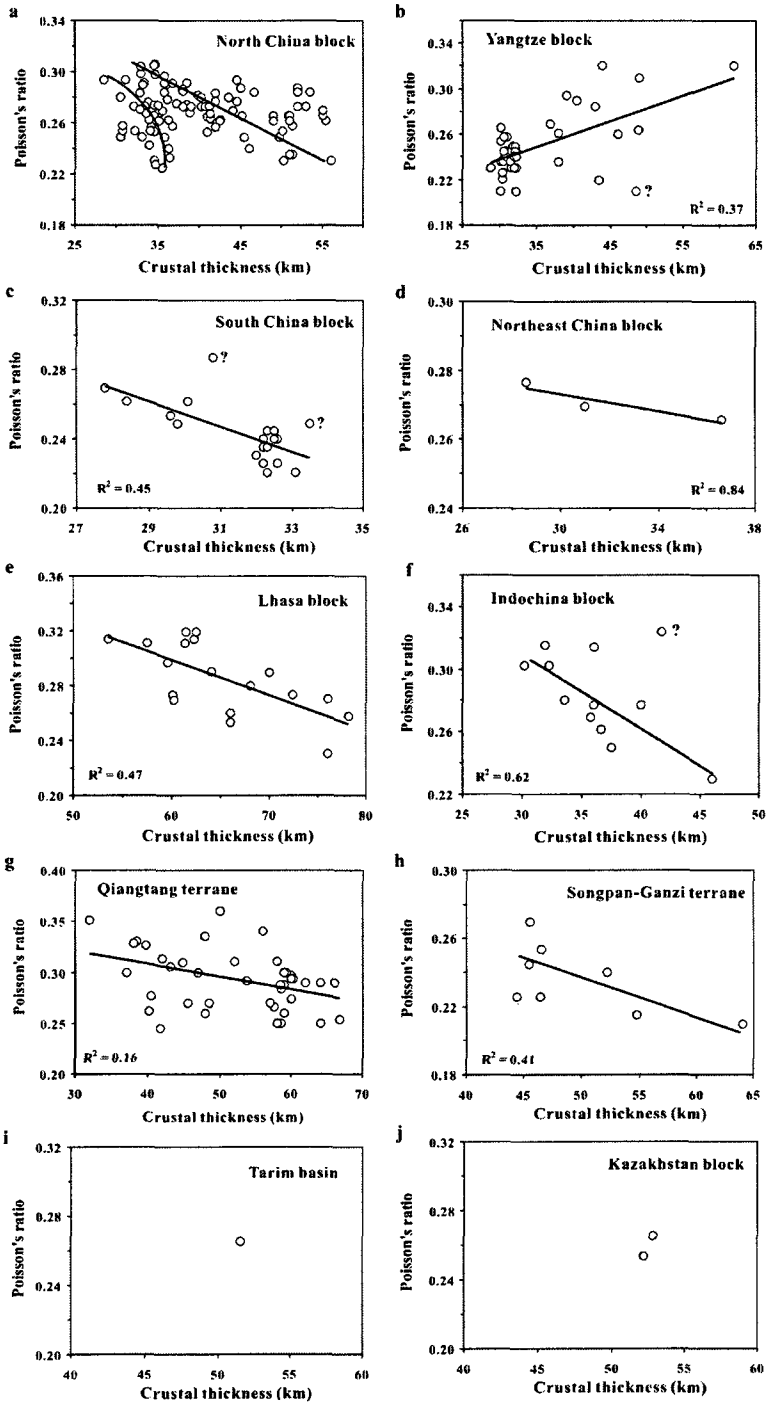

Figure 5.11 Measured Poisson's ratios as a function of crustal thickness for the seismic stations in each tectonic province in China. (a) North China block; (b) Yangtze block; (c) South China block; (d) Northeast China block; (e) Lhasa block; (f) Indochina block; (g) Qiangtang terrane; (h) Songpan-Ganzi terrane; (i) Tarim basin; and (j) Kazakhstan block.

5.7.3 Correlation between crustal thickness and Poisson's ratio

The correlation between crustal thickness (H) and Poisson's ratio can provide a valuable constraint on the building processes and tectonic evolution of the continental crust. If the continental crust has the same composition from the surface to the Moho, thickening or thinning should have little or no effect on the measured bulk Poisson's ratio. If the crust has strong lateral heterogeneity in both composition and thickness, there is no simple relationship between υ and H. If the crust is composed of horizontal layers with distinct compositions and thus different rheological properties, tectonic thickening or thinning would occur preferentially in weak layers rather than strong layers, and one would expect to see some correlation between υ and H. If shortening and thickening occur preferentially in felsic upper crust (low υ) rather than mafic lower crust, for example, the tectonic process will result in a decrease in υ with increasing H. If the lower crust is thickened by the addition of mafic materials through basaltic underplating, this process will result in an increase in υ with increasing H.

The Tibetan plateau has a crustal thickness approximately double the global average (Sapin and Hirn, 1997). If the seismic Moho beneath the plateau represents the boundary of the transformation from mafic materials to eclogite, then the crust has become more felsic in composition and has a smaller value of average Poisson's ratio due to delamination (Fig. 5.12a). Crustal thickening related to folding and imbricate thrusting of felsic rocks has induced a reduction in υ with increasing crustal thickness (Fig. 5.12a). The negative correlation between H and υ in the South China block, and the Lhasa, Qiangtang and Songpan-Ganzi terranes (Fig. 5.11) can also be interpreted as due to both mafic lower crustal delamination and felsic upper and middle crustal thickening. The Indochina block displays a similar negative correlation between υ and H if values of $\upsilon > 0.30$ are not taken in account (Fig. 5.11f). Obviously, the negative correlation is related to crustal thickening caused by the folding and thrusting of felsic upper and middle crust with a low Poisson's ratio. Similarly, in the area between the Ailaoshan-

Red River fault zone and the Gaoligong shear zone, EW-trending shortening during the Indosinian orogeny and the Himalayan SE extrusion event was largely accommodated by NS- and NW-SE-trending folds and thrust faults.

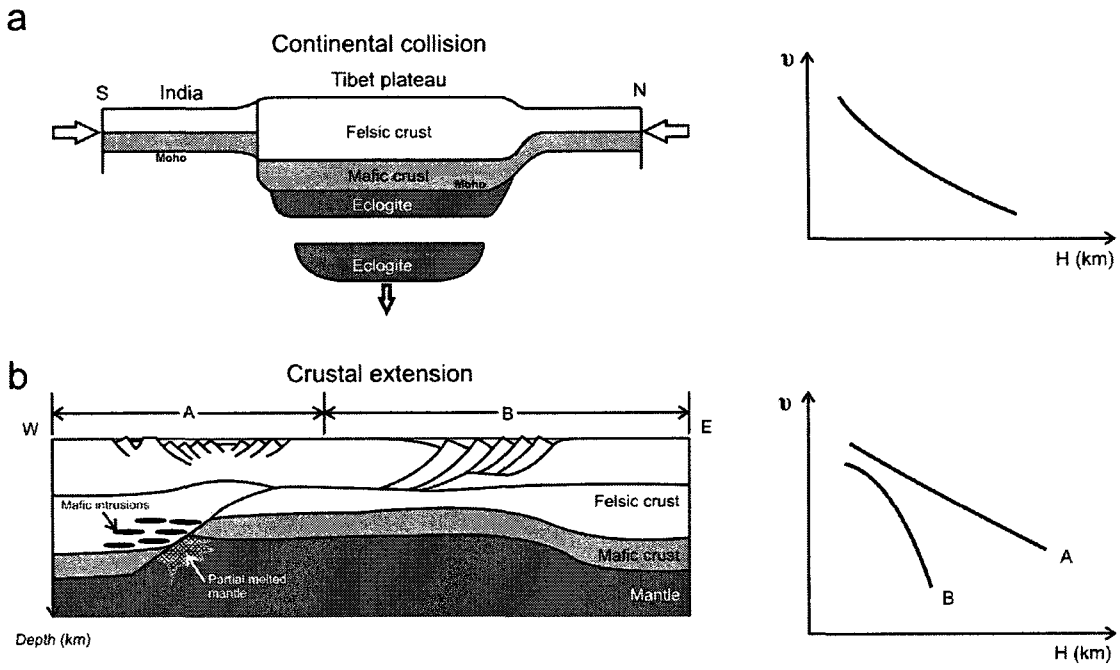

Figure 5.12 Rheology-based tectonic models for the interpretation of the correlation between crustal thickness and Poisson's ratio. (a) Mafic crustal delamination beneath a thickened felsic crust such as the Tibetan plateau; (b) Asymmetrical extension of the crust beneath the North China block. Basaltic underplating thickens the crust and also raises the crustal Poisson's ratio.

In the North China block (Fig. 5.9), υ decreases linearly with increasing H in the Baoding-Datong and Guanting-Zhangjiakou-Zhangbei regions while υ decreases nonlinearly with increasing H in the Northeastern Hebei province, Liaoning province and the southern Taihangshan area near Shijiazhuang (Fig. 5.13). These two different trends should reflect different crustal formation and evolution processes. The rapid increase in υ with crustal thinning, which requires a rapidly decreasing proportion of felsic material in the crust, is interpreted as the result of much larger thinning strains in the felsic upper and middle crust than in the mafic lower crust during the Mesozoic-

Cenozoic tectonic extension (Fig. 5.12b). This assumption implies that tectonic deformation occurs mainly in felsic parts of the crust because felsic materials are rheologically much weaker than mafic rocks under the prevailing conditions of deformation. The bulk crustal Poisson's ratio increases abruptly with increasing crustal thinning because no mafic material has been added into the crust through underplating. In contrast, the gentle increase in υ with crustal thinning in the Baoding-Datong and Guanting-Zhangjiakou-Zhangbei regions is thought to result from simultaneous underplating of mafic magmas from partially molten upper mantle into deep crust which was likely intermediate in composition during the extensional event (Fig. 5.12b). As argued above, the crustal thinning is compensated by the addition of gabbroic rocks crystallized from underplated mafic magmas. As a result, the Poisson's ratio gently increases with increasing crustal thinning (Fig. 5.13). If this is correct then it can be inferred that the underplating has been localized mainly in the Zhangjiakou and adjacent regions, where Mesozoic-Cenozoic basalts are widespread, whereas the rest of the North China Block is characterized by thinning of the felsic upper and middle crust without basaltic underplating (Fig. 5.9).

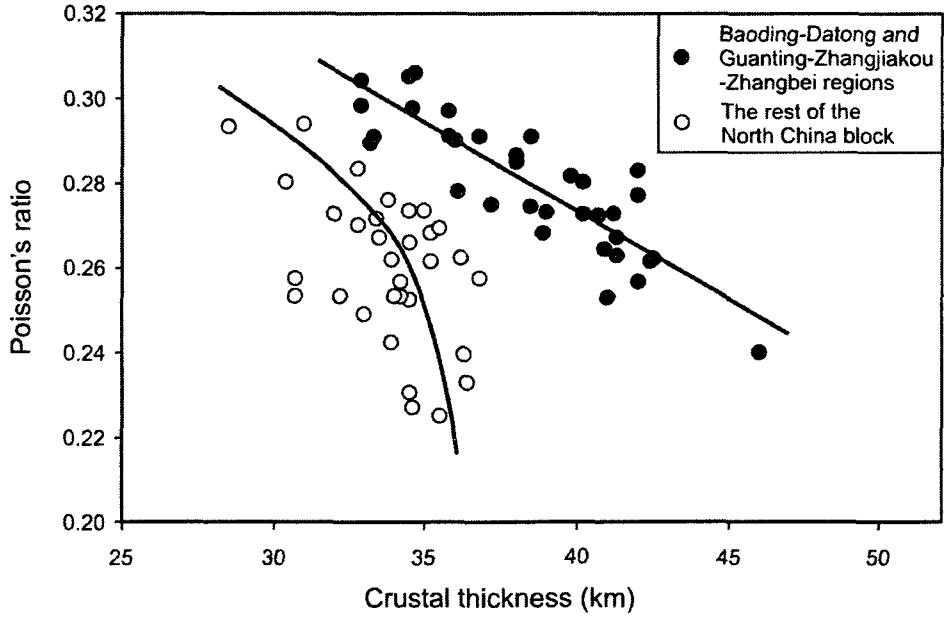

Figure 5.13 Two types of correlation between υ and H observed in the North China block

The Yangtze block seems to display a positive correlation between H and v (Fig. 5.11b). This unusual pattern needs to be confirmed by more measurements. If such a correlation indeed exists, it can be explained by an increase in thickness of the mafic lower crust, as advocated by Chevrot and van der Hilst (2000) for the Proterozoic crust of the North Australian craton. The timing of the basaltic underplating from the fertile upper mantle to the lower crust beneath the Yangtze block is unclear.

5.8 Conclusions

To obtain full information on the elastic constants (i.e., Young's modulus, shear modulus, bulk modulus and Poisson's ratio) of a rock requires measurements of its density and both average P- and S-wave velocities. In the literature, however, it is relatively rare that both P- and S-wave velocities have been determined on the same set of samples using the same laboratory equipment and the same methods (e.g., Kern, 1982; Kern et al., 1999, 2002; Ji et al., 1993; Ji and Salisbury, 1993). Usually only P- or S-wave velocity is measured. We have experimentally determined P- and S-wave velocities of 60 typical UHP metamorphic rock samples of which 31 were collected from the CCSD main and pre-pilot holes and 29 were from surface outcrops in the Sulu-Dabie orogenic belt, at ambient temperature and hydrostatic confining pressures up to 850 MPa. The velocity-pressure curves can be well described by a four-parameter expression derived directly from general principles (Ji et al., 2007). The elastic constants of each sample were then computed from average P- and S-wave velocities measured during depressurization. At each given pressure, the correlation between an elastic modulus (M) and density (ρ) can be quantitatively fitted by an empirical equation: $M = a\rho^3 + b\rho^2 + c\rho$, where a, b and c are adjustable coefficients. Synthesis of the present results and the data compiled in the Handbook of Seismic Properties of Minerals, Rocks and Ores (Ji et al., 2002) reveals that except for serpentinized peridotite and monomineralic rocks such as quartzite, serpentinite, anorthosite, limestone and

marble, all of the other types of rocks have Poisson's ratios falling along an upward convex curve determined from the correlations between elastic moduli and density. Poisson's ratios increase with density as the lithology changes from granite, schist, felsic gneiss, through diorite-syenite, intermediate gneiss and metasediment, to gabbro-diabase, amphibolite, and mafic gneiss, and then decrease again as the rocks become ultramafic in composition (i.e., pyroxenite and peridotite). Eclogite has a higher density but a lower Poisson's ratio than peridotite. The increase in υ with density and rock type, ranging from felsic gneisses to metagabbro, is correlated with systematic variations in the quartz and feldspar contents in the rocks. An increase in quartz content causes a decrease in υ while an increase in feldspar content causes an increase in υ. An increase in the anorthite content of plagioclase also increases the Poisson's ratio of the bulk rock. Serpentinization significantly raises the Poisson's ratio of peridotites because serpentine possesses an extremely high value of υ. The results also suggest that if V_s measurements are unavailable, reasonable estimates of υ can be made for a candidate rock with a given density using the measured V_p data and the trend line. The experimental results are believed to provide a complete set of basic information for the interpretation of field seismic data.

Data on the crustal thickness (H) and Poisson's ratio (υ) determined for 248 broadband seismic stations across China using the techniques of teleseismic receiver function analysis, have been carefully examined. The North China, Yangtze and South China blocks and the Songpan-Ganzi Terrane are dominated by low ($\upsilon < 0.26$) and moderate ($0.26 \leq \upsilon < 0.28$) Poisson's ratios (>70%), suggesting the dominance of felsic composition in the crust. The Lhasa terrane, Qiangtang terrane, and Indochina block are characterized by high proportions (33-42%) of measurements with very high υ values ($\geq$0.30), suggesting that the crust is partially molten due to high temperatures. Partial melting occurs in the middle crust of the Lhasa terrane and in the lower crust of the Qiangtang terrane. The heat to cause partial melting is probably from crustal thickening in the Lhasa terrane and from underplating of mantle-derived basaltic melts in the

Qiangtang terrane. The negative correlation between v and H, which is found for the South China block, Northeast China block, Lhasa block, Qiangtang terrane, Songpan-Ganzi terrane and Indochina block, indicates either tectonic thickening of the felsic upper and middle crust by folding and thrusting or the removal of mafic layers from the lower crust into the upper mantle by delamination.

Two types of correlation between v and H have been observed in the North China block: with decreasing H, v increases gently and linearly in the Baoding-Datong and Guanting-Zhangjiakou-Zhangbei regions, while increasing abruptly and nonlinearly in the rest of the block (e.g., Northeastern Hebei province and the southern Taihangshan area near Shijiazhuang). The linear correlation is interpreted as due to the summed, opposing contribution of tectonic thinning of felsic crust and the addition of mafic rocks crystallized from underplated magmas to the bulk crustal v. The abrupt increase of v with decreasing H suggests that much larger thinning strains have taken place in the felsic upper and middle crust than in the mafic lower crust during Mesozoic-Cenozoic tectonic extension. It is further inferred that basaltic underplating has been localized mainly in the Zhangjiakou and adjacent regions.

Chapter 6

Correlations between compressional and shear wave velocities and corresponding Poisson's ratios for some common rocks and sulfide ores

6.1 Abstract

The correlations between V_p and V_s and corresponding Poisson's ratios are important in modeling and interpreting seismic data in terms of chemistry and lithology. Data from high-pressure laboratory measurements of compressional and shear wave velocities (V_p and V_s) are analyzed for 12 common categories of rocks (amphibolite, anorthosite, basalt, diorite, eclogite, felsic gneiss, gabbro-diabase, granite, intermediate gneiss, limestone, mafic gneiss, and peridotite) and 4 types of massive sulfide ores (chalcopyrite, pyrite, sphalerite and pyrrhotite). The analysis reveals that the linear correlation provides good descriptions for the V_s-V_p and $\ln V_s$ - $\ln V_p$ relationships. Poisson's ratio is linearly correlated with V_s, V_p, shear modulus (G) and Young's modulus (E) for these rocks and sulfide ores. A decrease in Poisson's ratio is associated with increases in V_s, G and E. However, the variation of Poisson's ratio with V_p depends on the logarithmic ratio $R_{s/p}$ (i.e., $\partial \ln V_s / \partial \ln V_p$). Poisson's ratio increases or decreases with V_p when $R_{s/p}$ <1 or >1. $R_{s/p}$ varies systematically with lithology (0.300 for granite, 0.573 for diorite, 0.602 for felsic gneiss, 0.631 for intermediate gneiss, 0.721 for gabbro-diabase, 0.768 for mafic gneiss, 0.866 for eclogite, 0.890 for amphibolite, and 1.391 for peridotite). It is suggested that $R_{s/p}$ can be used as a proxy for the composition of the deep continental crust and the upper mantle.

6.2 Introduction

Seismic properties of rocks provide important constraints for the chemical composition, physical state and structure of the Earth's interior, especially for depths greater than 10-12 km (i.e., depths below which rock samples have not yet obtained by drilling). Successful interpretation of seismic data in terms of radial and lateral variations of chemical composition, mineralogy, temperature and pressure requires statistical information on the relationships between P- and S-wave velocities (V_p and V_s) and corresponding Poisson's ratio of each main category of lithology under the elevated conditions that characterize the Earth's interior (e.g., Zandt and Ammon, 1995; Christensen, 1996; Chevrot and van der Hilst, 2000; Ji et al., 2009).

For a statistically isotropic (i.e., texture-free polycrystalline rocks), linearly elastic solid, only two of the following elastic constants are required to characterize the seismic properties: the Young's (E), shear (G) and bulk (K) moduli and Poisson's ratio (υ). Once two independent constants are known, other constants can be calculated according to the well-known equations in elastic mechanics. The magnitudes of the elastic constants reflect crystal interatomic bonding, grain boundary strength, and microstructural characteristics (e.g., microcracks, porosity, phase connectivity and continuity) of rocks during uniaxial extension/compression, simple shear and hydrostatic compression. If any new relationship is found to exist between these elastic constants for a given isotropic material, it would be possible to reduce the number of required independent elastic constants from 2 to 1. This subject has received much attention in materials science. For example, by plotting G against E for 34 metals including body-centred cubic (bcc), face-centred cubic (fcc) and hexagonal close-packed (hcp) crystal structures, Ledbetter (1977) obtained $G/E \approx 3/8$. Gorecki (1980) carried out a statistical study on the relationships between E, G, and K for polycrystalline metals with different structures (Table 6.1). Kumar et al. (2003) reported a negative correlation between Poisson's ratio and ultrasonic shear wave velocity for metals, alloys, intermetallics,

ceramics, glasses, and polymers. Whether does such a correlation exist for natural polymineralic rocks that constitute the Earth's crust and upper mantle? The first objective of the present study is to seek some hidden relationship between the two independent elastic constants for common categories of crustal and upper mantle rocks.

Table 6.1 Statistical results of the relationships between E, G, and K for polycrystalline metals with different structures. Original data from Gorecki (1980).

Structure	G/E	G/K	E/K
Face-centred cubic (fcc)	0.385	0.379	0.944
Body-centred cubic (bcc)	0.357	0.373	1.041
Hexagonal close-packed (hcp)	0.389	0.527	1.314

The elastic constants of a rock are usually determined through acoustic measurements of P- and S-wave velocities (V_p and V_s) using the pulse transmission technique (Birch, 1960; Christensen, 1974; Kern, 1982; Burlini and Fountain, 1993; Ji and Salisbury, 1993; Watanabe et al., 2007), along with the density (ρ). In the literature, however, there are much more laboratory measurements of V_p than V_s for rock samples (see Handbook of Seismic Properties of Minerals, Rocks and Ores, Ji et al., 2002). This is in part because measurements of V_s met appreciable difficulties at low pressures, as the transduction of shear wave through the specimen requires a firm contact between the transducer and the end surfaces of the specimen. In-situ seismic refraction experiments often report only V_p data because the experiments commonly use short period vertical seismometers from which it is difficult to pick the S arrivals (e.g., Chevrot and van Hilst, 2000). V_p and V_s structures of the Earth's interior for a given region are usually determined separated with typical frequency of ~1 s for P waves and ~20 s or longer for S waves. Moreover, raypaths used to constrain these velocity structures may not be uniform (e.g., Song and Helmberger, 2007). As pointed out by Brocher (2005), it has been a common practice in many regions that seismologists who do earthquake hazard analyses first develop V_p models and then convert those to V_s models for two reasons: (1) There are much more V_p data than V_s data. (2) A V_s model is more important than a V_p model because shear and surface waves have much larger amplitudes, excite strong

ground motions, and consequently cause most of damage (Joyner, 2000). During the last decade, S-wave velocity information became increasingly available through VSP analysis, full-waveform logging, multicomponent seismic data, and the analysis of teleseismic receiver functions. The non-unique interpretation of seismic data in terms of rock type becomes inevitable when P- or S-wave velocities alone are available. Thus, the second objective of this investigation is to establish some empirical relations between V_s and V_p and between $\ln V_s$ and $\ln V_p$, and to characterize the variations of Poisson's ratio as a function of seismic velocities V_p and V_s and elastic moduli for common rock types. Such relationships are useful to constrain the full elastic properties and characteristics of formation and deformation of rocks using available V_p or V_s only. The scaling factor $\partial \ln V_s / \partial \ln V_p$ is of particular interest because it is used as a diagnostic for the origin of heterogeneities in the Earth's interior since the factor, derived from seismic inversions, is less ambiguous than the absolute values of the V_p and V_s anomalies.

6.3 Data for statistic analysis

The data used for the statistic analysis were taken from the samples on which both P- and S-wave velocities and density have been determined at relatively high hydrostatic pressures (≥ 300 MPa) using the same laboratory equipment and the same methods (e.g., the pulse transmission technique, Birch, 1960; Christensen, 1974; Kern, 1982). The confining pressures are high enough to close the microcracks and pores with small aspect ratios (width/length) so that the measured values can represent the intrinsic properties. The literature data were taken from Handbook of Seismic Properties of Minerals, Rocks and Ores (Ji et al., 2002) and Wang et al. (2005a, b) and Ji et al. (2007) and Ji et al. (2009). Only the velocities measured during depressurization were selected for the statistic study because the values correspond to the stable microstructural state (Burke and Fountain, 1990; Ji et al., 1993; Wang et al., 2005a, b; Ji et al., 2007). In order to minimize the influence of seismic anisotropy, the arithmetical mean P- and S-

wave velocities were used for the computations of elastic moduli for the bulk rock. The mean P-wave velocity of each sample is calculated according to the following equation:

$$V_p = [V_p(X) + V_p(Y) + V_p(Z)]/3 \qquad (6.1)$$

where $V_p(X)$, $V_p(Y)$ and $V_p(Z)$ represent the P-wave velocities along the propagation directions X, Y and Z, respectively. The X direction is parallel to the stretching lineation, the Y direction is perpendicular to lineation and parallel to foliation, and the Z direction is normal to foliation. The mean S-wave of each sample is computed from the results of six measurements that are designed XY, XZ, YX, YZ, ZX, and ZY. The first letter refers to the propagation direction and the second to the polarization direction.

$$V_s = [V_s(XY) + V_s(XZ) + V_s(YX) + V_s(YZ) + V_s(ZX) + V_s(ZY)]/6 \qquad (6.2)$$

The mean V_p and V_s values calculated from Eqs. (6.1) and (6.2) give values very close to true isotropic elastic properties even in highly anisotropic rocks (Christensen and Ramananantoandro, 1971; Ji et al., 2003). The accuracy is estimated to be better than 0.5% for V_p and 1% for V_s (Christensen, 1985; Ji and Salisbury, 1993) and 2.5% for calculated Poisson's ratio (Christensen, 1996). The measurements of densities of the samples, using the immersion method, have an accuracy of ±0.005 g/cm^3 at room conditions.

6.4 Linear relationship between V_p and V_s

Previous authors (e.g., Pickett, 1963; Castagna et al., 1985; Castagna et al., 1993; Mavko et al., 1998) reported that the relationship between V_p and V_s for sedimentary rocks (e.g., sandstone, limestone, dolomite, shale, and mudstone), which are generally porous, can be described by a linear correlation. Brocher (2005, 2008) plotted thousands of V_p and V_s data for a wide variety of lithologies (from unconsolidated sediments to

very low porosity igneous rocks, and from non-welded volcanic tuffs to highly compact metamorphic rocks) all together on a single figure to draw a nonlinear fitting curve by eye. His empirical curve is described by

$$V_p = 0.9409 + 2.0947V_s - 0.8206V_s^2 + 0.2683V_s^3 - 0.0251V_s^4 \quad (6.3)$$

or

$$V_s = 0.7858 - 1.2344V_p + 0.7949V_p^2 - 0.1238V_p^3 + 0.0064V_p^4 \quad (6.4)$$

Equations (6.3) and (6.4) are valid for V_s between 0.3373 km/s and 5.0 km/s and V_p between 1.5 km/s and 8.5 km/s, respectively. Equation (6.4) indicates that V_s=0.3373 km/s when V_p=1.5 km/s (In fresh water, P-wave travels at about 1.5 km/s at 25 °C). The V_p and V_s data used for Brocher's regression fit, obtained from various methods (wireline borehole logs, vertical seismic profiles, laboratory or field measurements on hand samples at various effective confining pressures, in-situ estimates from seismic tomography studies, and regional velocity models) and are of different qualities, are extremely scattered. Furthermore, in Brocher's (2005, 2008) compilation, most of the velocity measurements were made on samples from California, USA.

Here we show that the high-pressure V_p and V_s data of dry igneous and metamorphic rocks can be equally best fitted by the linear correlation. A goodness-of-fit coefficient (R) is used as a statistical measure of how well the experimental data are fitted by the empirical relation. R ranges between 0 and 1. If there is no fit at all, R is zero. A perfect fit gives a value of R=1.0. The higher R is, the better the fit is. The statistically fitting results for 12 common lithologies (i.e., amphibolite, anorthosite, basalt, diorite, eclogite, felsic gneiss, gabbro-diabase, granite, intermediate gneiss, limestone, mafic gneiss, and peridotite) and 4 common sulfide ores (i.e., chalcopyrite, pyrite, sphalerite and pyrrhotite) are summarized in Table 6.2.

Table 6.2 Parameters of the linear relations for best-fitting the V_s-V_p and LnV_s-LnV_p data

Lithology	P (MPa)	N	Density	$V_s=aV_p+b$			$LnV_s=aLnV_p+b$		
			g/cm^3	a	b	R	a	b	R
Rocks									
Amphibolite	600	29	3.01	0.501	0.451	0.718	0.890	-0.356	0.724
Anorthosite	600	8	2.78	0.632	-0.678	0.847	1.159	-0.936	0.841
Basalt	600	21	2.89	0.622	-0.382	0.916	1.096	-0.755	0.916
Diorite	600	9	2.76	0.337	1.555	0.820	0.573	0.248	0.822
Eclogite	600	55	3.47	0.496	0.580	0.789	0.866	-0.286	0.782
Felsic gneiss	600	67	2.70	0.346	1.462	0.593	0.602	0.183	0.592
Gabbro-diabase	600	47	2.98	0.401	1.068	0.770	0.721	-0.047	0.771
Granite	600	31	2.66	0.172	2.575	0.215	0.300	0.744	0.218
Intermediate gneiss	600	14	2.76	0.366	1.371	0.419	0.631	0.140	0.419
Limestone	600	26	2.72	0.482	0.217	0.645	0.916	-0.506	0.647
Mafic gneiss	600	70	3.06	0.426	0.924	0.751	0.768	-0.132	0.756
Peridotite	600	65	3.09	0.728	-1.380	0.976	1.391	-1.400	0.981
Sulfide ores									
Chalcopyrite	600	11	3.57	1.032	-2.764	0.913	1.846	-2.080	0.924
Pyrite	300	12	4.18	0.908	-2.111	0.968	1.524	-1.524	0.968
Pyrrhotite	600	24	4.16	0.403	0.965	0.966	0.695	-0.027	0.964
Sphalerite	600	9	3.76	0.704	-0.872	0.932	1.280	-1.086	0.924

Figure 6.1a shows the V_s-V_p plots for 65 peridotites with various degrees of serpentinization, measured at a hydrostatic confining pressure of 600 MPa. The least-squares linear fit gives $V_s = 0.728V_p - 1.380$ (R=0.976) and $V_p = 1.310V_s + 2.149$ (R=0.976), where both V_p and V_s are in km/s. These relations are valid when V_p ranges from 4.8 to 8.8 km/s and V_s ranges from 2.2 to 5.0 km/s. The trends of velocity variation from high to low values reflect essentially a progressive increase in serpentine content.

Figure 6.1b shows the V_s-V_p variations for 55 eclogite samples at 600 MPa. The linear fitting yield: $V_s = 0.496V_p + 0.580$ (R=0.789) in the V_p range between 7.3 and 8.7 km/s, and $V_p = 1.257V_s + 2.327$ (R=0.789) in the V_s range between 4.2 and 5.0 km/s. When only V_p data exist, these V_s-V_p relations seem to give a reasonable estimate for the average V_s values.

The linear regressions to V_s-V_p (Fig. 6.1c) and V_p-V_s data of 70 mafic gneisses give: $V_s = 0.426V_p + 0.924$ (R=0.751) in the V_p range from 6.5 to 7.6 km/s and

$V_p = 1.325V_s + 1.872$ (R=0.751) in the V_s range from 3.6 to 4.3 km/s, respectively. Although the linear correlation is clear, the data are somewhat scattered about the trend line. This is not surprising in view of the highly variable composition and microstructure of the gneisses deformed and metamorphosed under various conditions. Some points in Fig. 6.1c deviated markedly from the regression lines, probably implying that these samples were inaccurately classified in term of lithology.

Figure 6.1d plots 21 sets of seismic velocity data for basalts at a hydrostatic confining pressure of 600 MPa. The scattering of data around the trend line reflects mainly the variations in both porosity and pore geometry of the basalts. It is worthy to note that the small pores with larger aspect-ratios (width/length) may remain at pressures as high as 600 MPa.

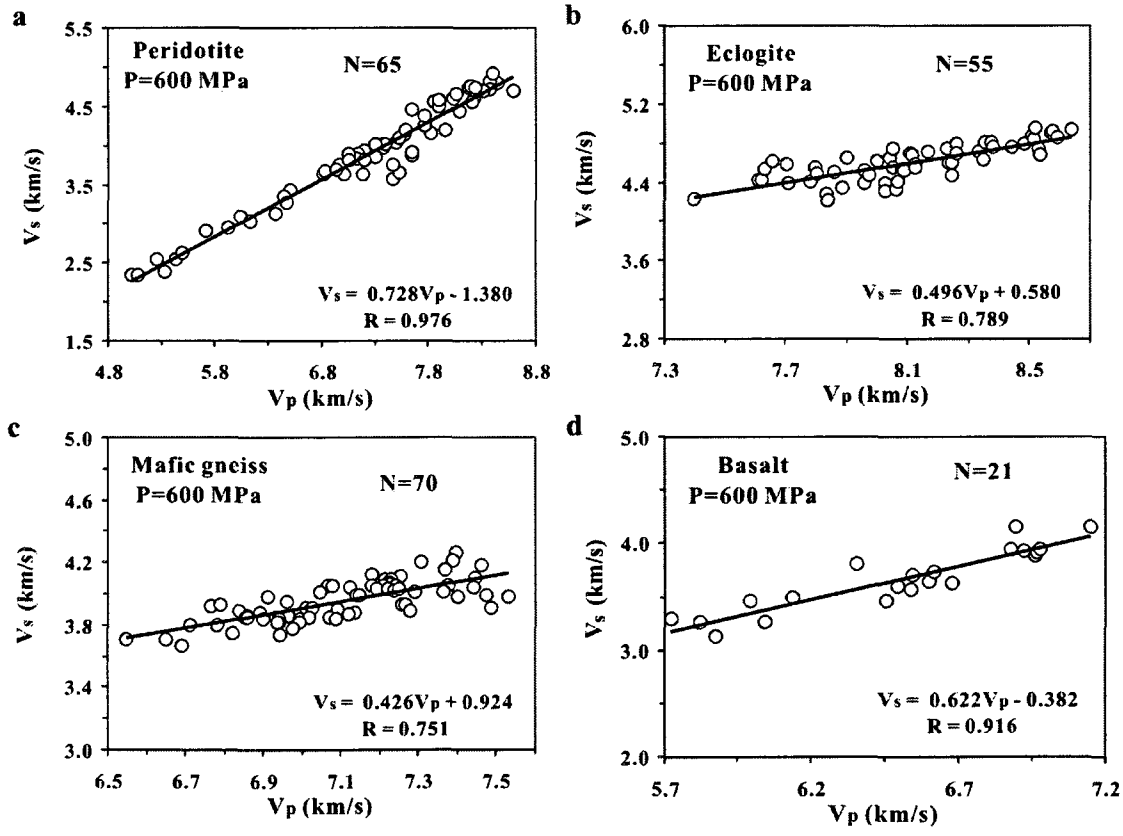

Figure 6.1 V_s-V_p plots for peridotite (a), eclogite (b), mafic gneiss (c) and basalt (d) samples at 600 MPa. The experimental data are fitted using linear correlation.

We also investigated the correlation between V_p and V_s for massive ores of chalcopyrite, pyrite, pyrrhotite and sphalerite (Table 6.2). These data were measured in Dr. Matt Salisbury's laboratory (Salisbury et al., 1996; Salisbury et al., 1997; Salisbury et al., 2000) and incorporated in Handbook of Seismic Properties of Minerals, Rocks and Ores (Ji et al., 2002). For chalcopyrite ores (Fig. 6.2a), $V_s = 1.032V_p - 2.764$ (R=0.913) in the V_p range from 5.0 to 6.6 km/s, and $V_p = 0.807V_s + 3.208$ (R=0.913) in the V_s range from 2.5 to 4.2 km/s. For pyrite ores (Fig. 6.2b), $V_s = 0.908V_p - 2.111$ (R=0.968) in the V_p range from 6.3 to 7.7 km/s, and $V_p = 1.033V_s + 2.623$ (R=0.968) in the V_s range from 3.4 to 5.0 km/s. For sphalerite ores (Fig. 6.2c), $V_s = 0.704V_p$—0.872 (R=0.932) in the V_p range from 5.4 to 6.7 km/s, and $V_p = 1.235V_s$+1.856 (R=0.932) in the V_s range from 2.7 to 4.2 km/s. For pyrrhotite ores (Fig. 6.2d), $V_s = 0.403V_p + 0.965$ (R=0.966) in the V_p range from 4.7 to 6.5 km/s, and $V_p = 2.319V_s - 1.880$ (R=0.966) in the V_s range from 2.7 to 3.6 km/s. The above relations between V_p and V_s may help the mining industry to search for deep massive sulfide ores using seismic methods.

6.5 Scaling factor $R_{s/p}$

Scaling factor $R_{s/p}$ is defined as

$$R_{s/p} = \frac{\partial V_s / V_s}{\partial V_p / V_p} = \frac{\partial \ln V_s}{\partial \ln V_p} \qquad (6.5)$$

where $\partial V_s / V_s$ and $\partial V_p / V_p$ are the S and P wave velocity anomalies, respectively. Clearly, $R_{s/p}$ is a logarithmic ratio to describe the relative variation in V_s and V_p for a given lithology. $R_{s/p}$ can be estimated from the data of P wave travel time delay (∂t_p)

and S wave travel time delay (∂t_s) at a given depth: $R_{s/p} \approx (V_s/V_p)(\partial t_s/\partial t_p)$. The velocity heterogeneities in the Earth's interior can be caused by the variations in temperature, chemical composition or phase transformation. $R_{s/p}$ has been used as a diagnostic for the origin of heterogeneities in the Earth's interior because this factor, derived from seismic inversions, is less ambiguous than the absolute values of the anomalies (e.g., Kennett et al., 1998; Karato and Karki, 2001). Robertson and Woodhouse (1996) found a quasi-linear increase in $R_{s/p}$ with depth from 1.7 in the upper mantle to >2.5 in the lower mantle deeper than 2000 km. To our knowledge, the $R_{s/p}$ values have not been systematically investigated for the common crustal rocks although these values are potentially important constrains on the composition, physical state and structure of the deep continental crust.

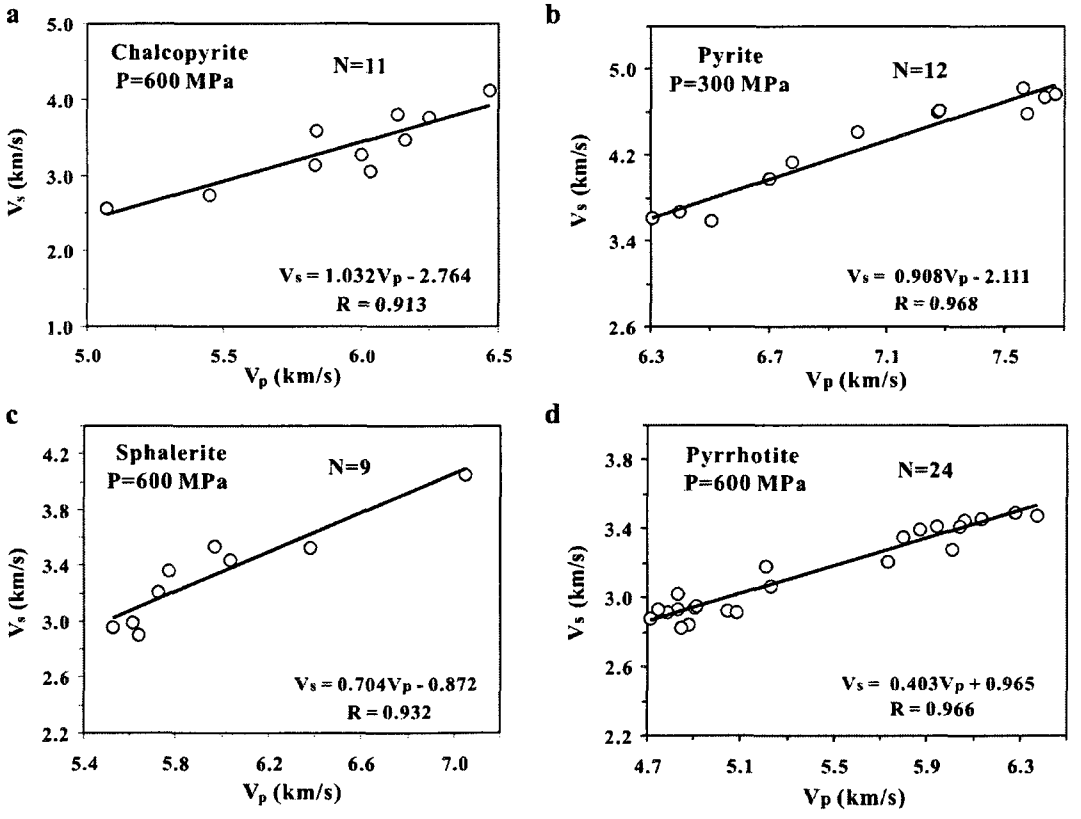

Figure 6.2 V_s-V_p plots for chalcopyrite (a), sphalerite (c) and pyrrhotite (d) samples at 600 MPa and pyrite (b) at 300 MPa. The experimental data are fitted using linear correlation.

Figure 6.3 illustrates the $\ln V_s - \ln V_p$ plots for 65 peridotites, 55 eclogites, 70 mafic gneisses, and 21 basalts at 600 MPa. The least-squares linear fit yields: $\ln V_s = 1.391 \ln V_p - 1.400$ (R=0.981) for peridotite (Fig. 6.3a), $\ln V_s = 0.866 \ln V_p - 0.286$ (R=0.782) for eclogite (Fig. 6.3b), $\ln V_s = 0.768 \ln V_p - 0.132$ (R=0.756) for mafic gneiss (Fig. 6.3c), and $\ln V_s = 1.096 \ln V_p - 0.755$ (R=0.916) for basalt (Fig. 6.3d). As shown in Fig. 6.4a, $R_{s/p}$ varies systematically with lithology: 0.300 for granite, 0.573 for diorite, 0.602 for felsic gneiss, 0.631 for intermediate gneiss, 0.721 for gabbro-diabase, 0.768 for mafic gneiss, 0.866 for eclogite, 0.890 for amphibolite, 1.096 for basalt, 1.159 for anorthosite, and 1.391 for peridotite. Obviously, $R_{s/p}$ increases globally with decreasing the content of SiO_2 from acidic, intermediate, through mafic to ultramafic rocks. Basalt displays a higher $R_{s/p}$ value than gabbro-diabase although these mafic rocks have similar chemical compositions, indicating the effect of porosity (Table 6.2). As porous basalt exists only in the uppermost part of the crust, $R_{s/p}$ should allow better constrains on lithological composition of the deep continental crust that with the absolute value of V_p or V_s alone. Furthermore, a volumically important mass of eclogite that was delaminated from the lowermost part of the thickened continental crust and sunk into the upper mantle should be distinguished from its surrounding peridotitic mantle in term of $R_{s/p}$. Otherwise discrimination of eclogite from peridotite seems to be impossible using the absolute values of V_p or V_s.

Figure 6.5 shows the $\ln V_s$ - $\ln V_p$ plots for massive ores. For chalcopyrite, pyrite, sphalerite and pyrrhotite $\ln V_s = 1.846 \ln V_p - 2.080$ (R=0.924), $\ln V_s = 1.524 \ln V_p - 1.524$ (R=0.968), $\ln V_s = 1.280 \ln V_p - 1.086$ (R=0.924), and $\ln V_s = 0.695 \ln V_p - 0.027$ (R=0.964), respectively. $R_{s/p}$ increases progressively from pyrrhotite (0.695), sphalerite

(1.280), pyrite (1.524) to chalcopyrite (1.846), suggesting that the scaling factor is indeed a diagnostic for the chemical composition of sulfide ores.

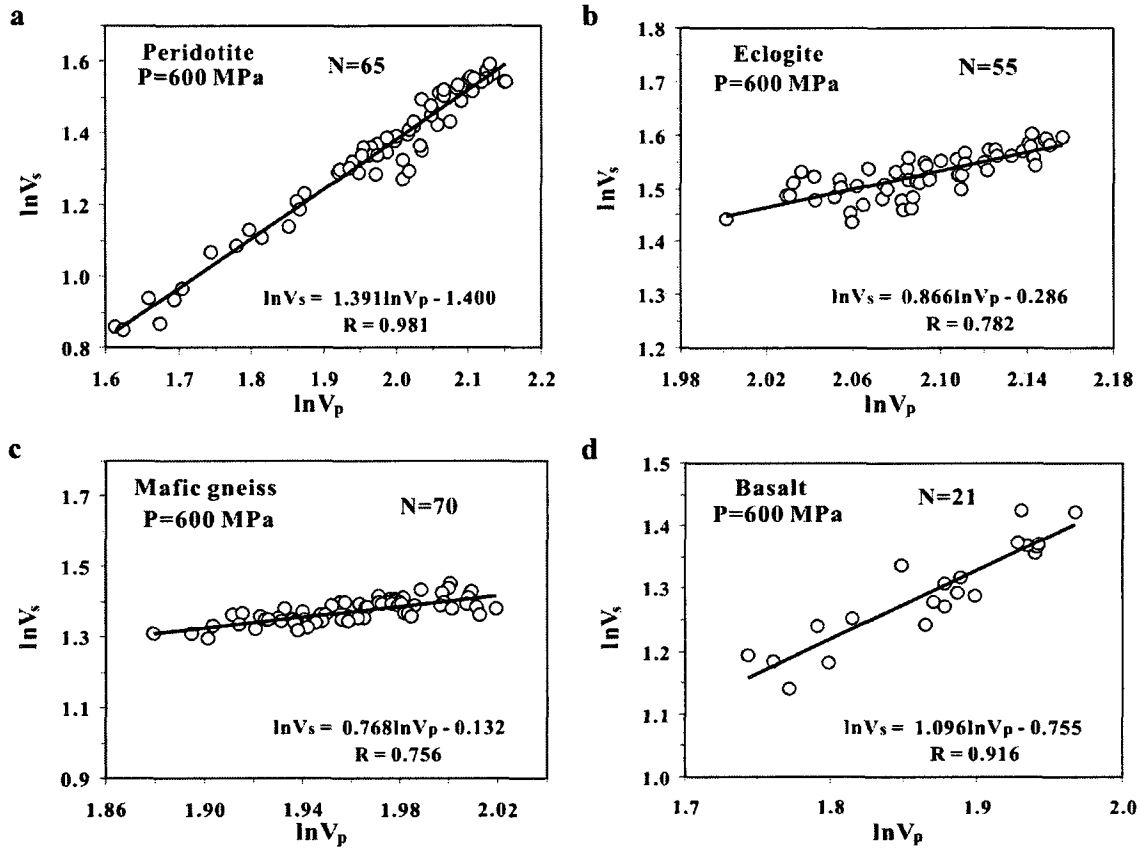

Figure 6.3 $\ln V_s$-$\ln V_p$ plots for peridotite (a), eclogite (b), mafic gneiss (c) and basalt (d) samples at 600 MPa. The experimental data are fitted using linear correlation.

Figures 6.6-6.7 give two examples for the $\ln V_c$ - $\ln V_s$ (V_c is the bulk wave speed and $V_c = \sqrt{K/\rho} = \sqrt{V_p^2 - 4V_s^2/3}$), $\ln\rho$ - $\ln V_s$ (ρ is the density) and $\ln\rho$ - $\ln V_p$ plots. The linear regression of these data yields the following logarithmic ratios: $R_{c/s} = \partial \ln V_c / \partial \ln V_s$, $R_{\rho/s} = \partial \ln \rho / \partial \ln V_s$, and $R_{\rho/p} = \partial \ln \rho / \partial \ln V_p$. These ratios, which are usually derived from seismic and geodynamical inversions, have been used jointly with $R_{s/p}$ as diagnostics for the origin of heterogeneities in the Earth's interior.

Karato and Karki (2001) suggests that $R_{s/p}$>1.5 along with $R_{\rho/s}$<0 or $R_{\rho/s}$>0 should indicate a dominant chemical or thermal origin of the mantle heterogeneity. For peridotite (Fig. 6.6), $\ln V_c = 0.515 \ln V_s + 1.039$ (R=0.919), $\ln \rho = 0.443 \ln V_s + 0.528$ (R=0.862), and $\ln \rho = 0.631 \ln V_p - 0.121$ (R=0.865). Thus $R_{c/s}$=0.515, $R_{\rho/s}$=0.443 and $R_{\rho/p}$=0.631 for peridotite. For pyrrhotite (Fig. 6.7), $\ln V_c = 1.619 \ln V_s$—0.470 (R=0.922), $\ln \rho = -1.359 \ln V_s + 2.977$ (R=0.935), and $\ln \rho = -0.966 \ln V_p$+3.049 (R=0.922). Hence $R_{c/s}$=1.619, $R_{\rho/s} = -1.359$ and $R_{\rho/p} = -0.966$ for pyrrhotite. It is of interest to note that different from pyrite and sphalerite, pyrrhotite and chalcopyrite have negative values for $R_{\rho/s}$ and $R_{\rho/p}$.

6.6 Correlations of Poisson's ratio with V_s, V_p, G and E

For the rocks studied, there is generally a negative linear correlation between Poisson's ratio and V_s, G or E (Table 6.3 and Figs. 6.8-6.9). However, Poisson's ratio displays distinct trends of variation with V_p for different lithologies: υ decreases with increasing V_p for anorthosite, basalt and peridotite, but increases with increasing V_p for amphibolite, diorite, eclogite, felsic gneiss, gabbro-diabase, granite, intermediate gneiss, limestone, and mafic gneiss. The increases of υ with increasing V_p in general are not great but continuous.

Figure 6.8 shows the variation in υ with V_s, V_p, G and E for 65 peridotites at 600 MPa. Poisson's ratio decreases linearly with increase in V_s, V_p, G and E. It is evident that υ displays a better correlation with V_s (R=0.911) than V_p (R=0.802). Poisson's ratio also shows a lightly better correlation with G (R=0.901) than E (R=0.886). For granite, Poisson's ratio displays a decrease with increasing V_s but a slight increase with increasing V_p. Poisson's ratio reveals also a slight decrease with increase in G and E (Fig. 6.9). Similar correlations between υ and V_s, V_p, G or E are observed for eclogite.

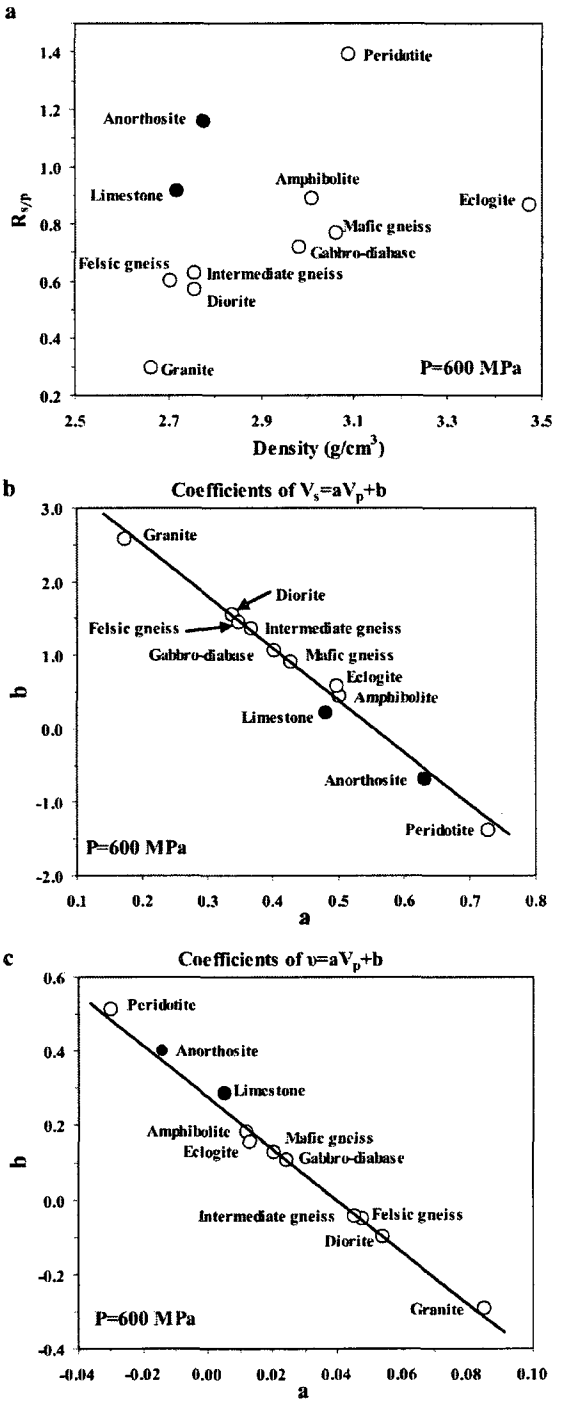

Figure 6.4 (a) Variation of $R_{s/p}$ versus density for each lithology, (b) b-a plots for the relation $V_s = aV_p + b$, and (c) b-a plots for the relation $\upsilon = aV_p + b$.

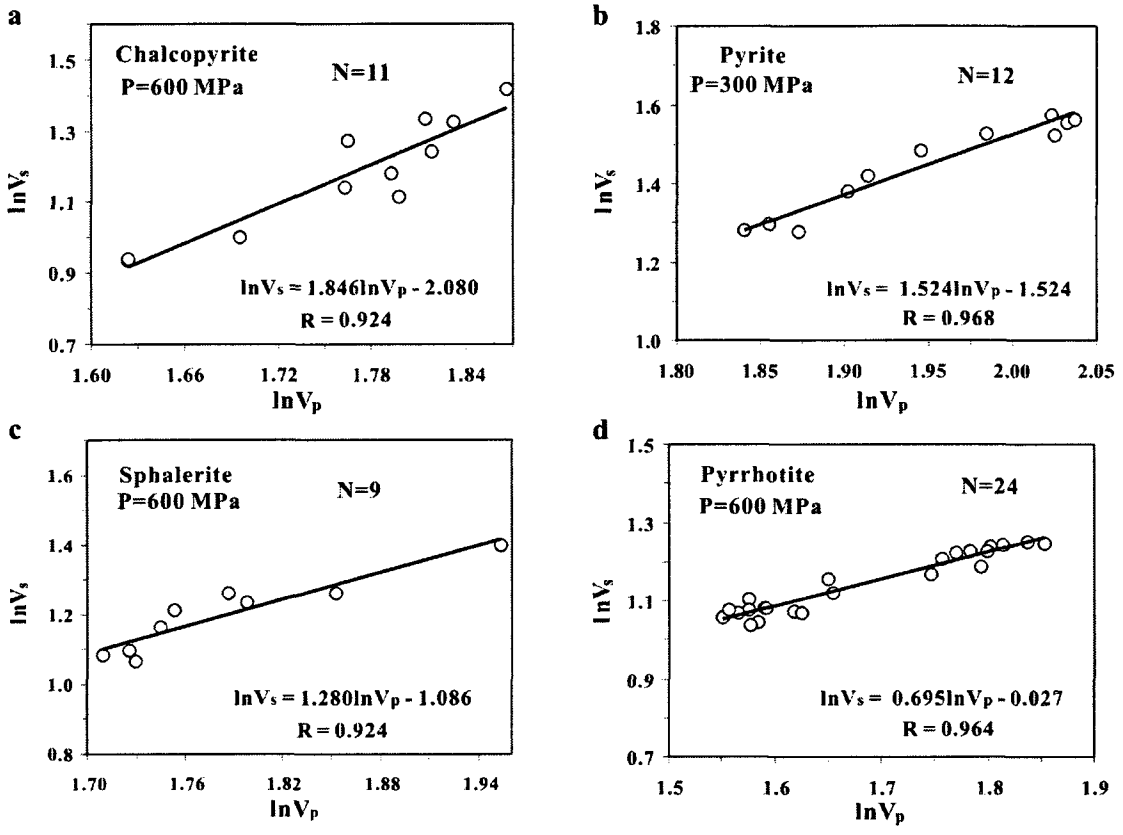

Figure 6.5 lnV_s-lnV_p plots for chalcopyrite (a), sphalerite (c) and pyrrhotite (d) samples at 600 MPa and pyrite (b) at 300 MPa.

The linear-regression results for the sulfide ores (chalcopyrite, pyrite, pyrrhotite and sphalerite) are given in Table 6.3. Poisson's ratio decreases linearly with increase in V_s, V_p, G and E for chalcopyrite, pyrite (Fig. 6.10), and sphalerite. For pyrrhotite (Fig. 6.11), however, Poisson's ratio displays a trend of linear increase with increasing V_s, V_p, G and E. We hope that this new finding will encourage the search for the physical significance of these correlations.

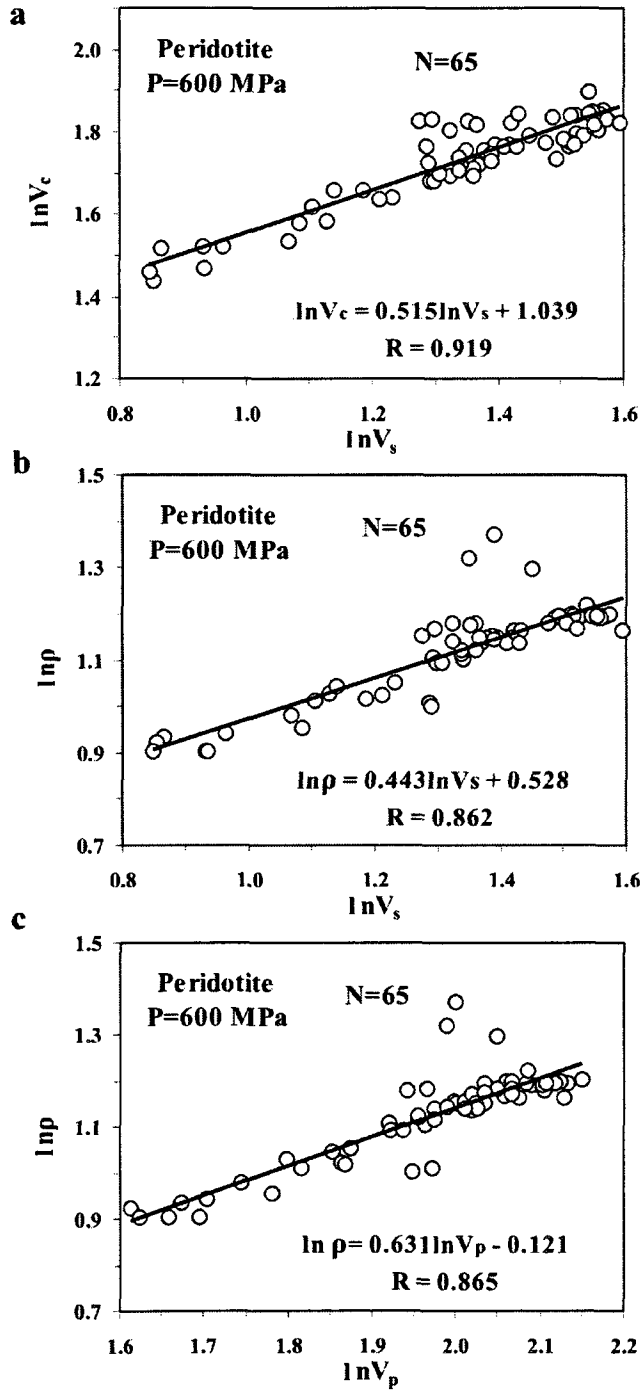

Figure 6.6 $\ln V_c$ - $\ln V_s$ (a), $\ln \rho$ - $\ln V_s$ (b) and $\ln \rho$ - $\ln V_p$ plots for peridotite at 600 MPa. V_c is the bulk wave speed, and ρ is the density.

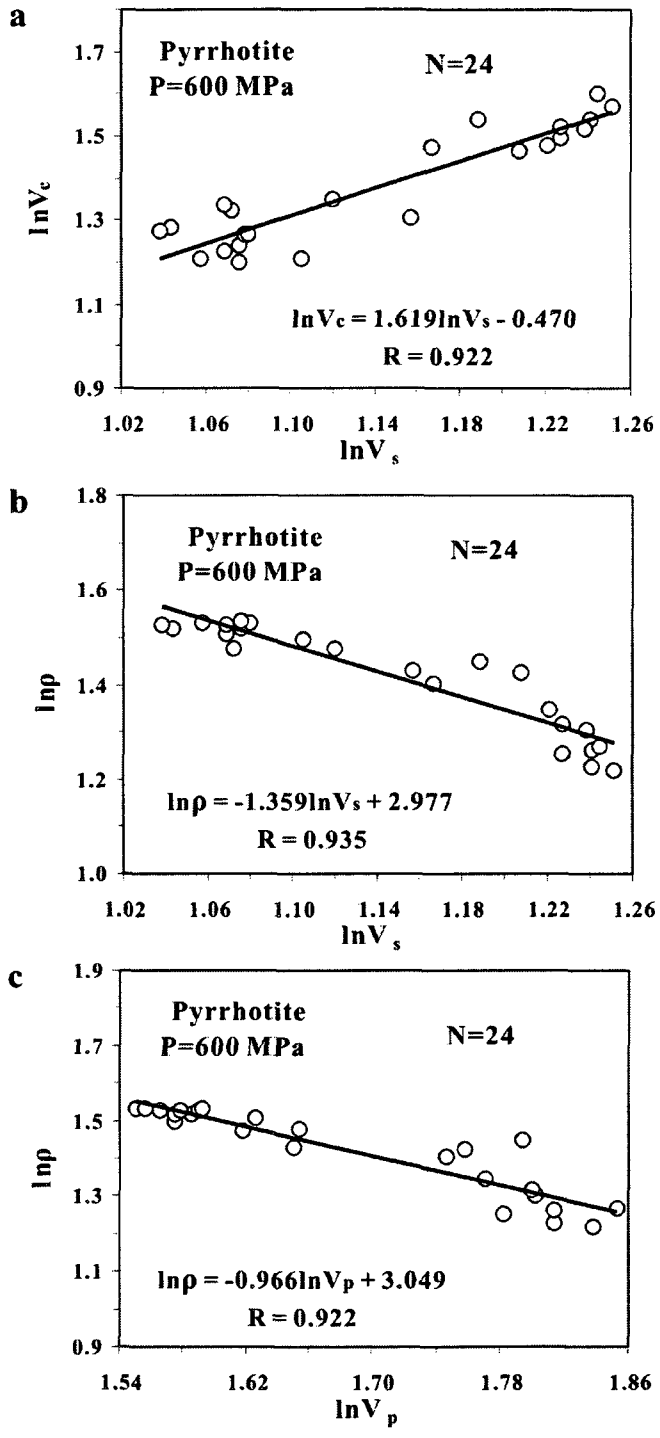

Figure 6.7 $\ln V_c$ - $\ln V_s$ (a), $\ln \rho$ - $\ln V_s$ (b) and $\ln \rho$ - $\ln V_p$ plots for pyrrhotite at 600 MPa. V_c is the bulk wave speed, and ρ is the density.

Table 6.3 Parameters of the correlations between Poisson's ratio (υ) and V_s, V_p, G or E

Lithology	P (MPa)	N	$\upsilon=aV_s+b$			$\upsilon=aV_p+b$			$\upsilon=aG+b$			$\upsilon=aE+b$		
			a	b	R	a	b	R	a	b	R	a	b	R
Rocks														
Amphibolite	600	29	-0.071	0.541	0.591	0.012	0.184	0.136	-0.002	0.354	0.420	-0.001	0.325	0.270
Anorthosite	600	8	-0.058	0.516	0.719	-0.014	0.400	0.239	-0.002	0.373	0.562	-0.001	0.367	0.487
Basalt	600	21	-0.045	0.431	0.569	-0.010	0.333	0.191	-0.002	0.331	0.528	-0.001	0.325	0.451
Diorite	600	9	-0.042	0.093	0.240	0.054	-0.099	0.752	0.003	0.150	0.430	0.001	0.131	0.557
Eclogite	600	55	-0.042	0.454	0.431	0.013	0.157	0.212	-0.001	0.338	0.422	-0.0003	0.319	0.300
Felsic gneiss	600	67	-0.084	0.556	0.458	0.047	-0.050	0.443	-0.003	0.359	0.335	-0.0003	0.277	0.079
Gabbro-diabase	600	47	-0.030	0.391	0.264	0.024	0.108	0.410	-0.001	0.314	0.261	-0.0002	0.298	0.150
Granite	600	31	-0.174	0.880	0.761	0.085	-0.290	0.467	-0.007	0.497	0.642	-0.002	0.430	0.394
Intermediate gneiss	600	14	-0.155	0.815	0.770	0.045	-0.043	0.257	-0.009	0.561	0.850	-0.004	0.596	0.716
Limestone	600	26	-0.083	0.597	0.724	0.005	0.287	0.058	-0.004	0.443	0.732	-0.002	0.444	0.661
Mafic gneiss	600	70	-0.043	0.446	0.383	0.021	0.131	0.321	-0.001	0.323	0.294	-0.0002	0.304	0.173
Peridotite	600	65	-0.046	0.476	0.911	-0.030	0.516	0.802	-0.002	0.380	0.901	-0.001	0.382	0.886
Surfide ores														
Chalcopyrite	600	11	-0.117	0.649	0.942	-0.101	0.860	0.724	-0.007	0.532	0.894	-0.003	0.580	0.826
Pyrite	300	12	-0.080	0.549	0.914	-0.064	0.660	0.784	-0.001	0.320	0.856	-0.001	0.325	0.829
Pyrrhotite	600	24	0.084	-0.023	0.668	0.044	0.004	0.834	0.005	0.043	0.414	0.003	-0.018	0.659
Sphalerite	600	9	-0.060	0.472	0.730	-0.027	0.433	0.434	-0.001	0.313	0.378	-0.0003	0.308	0.315

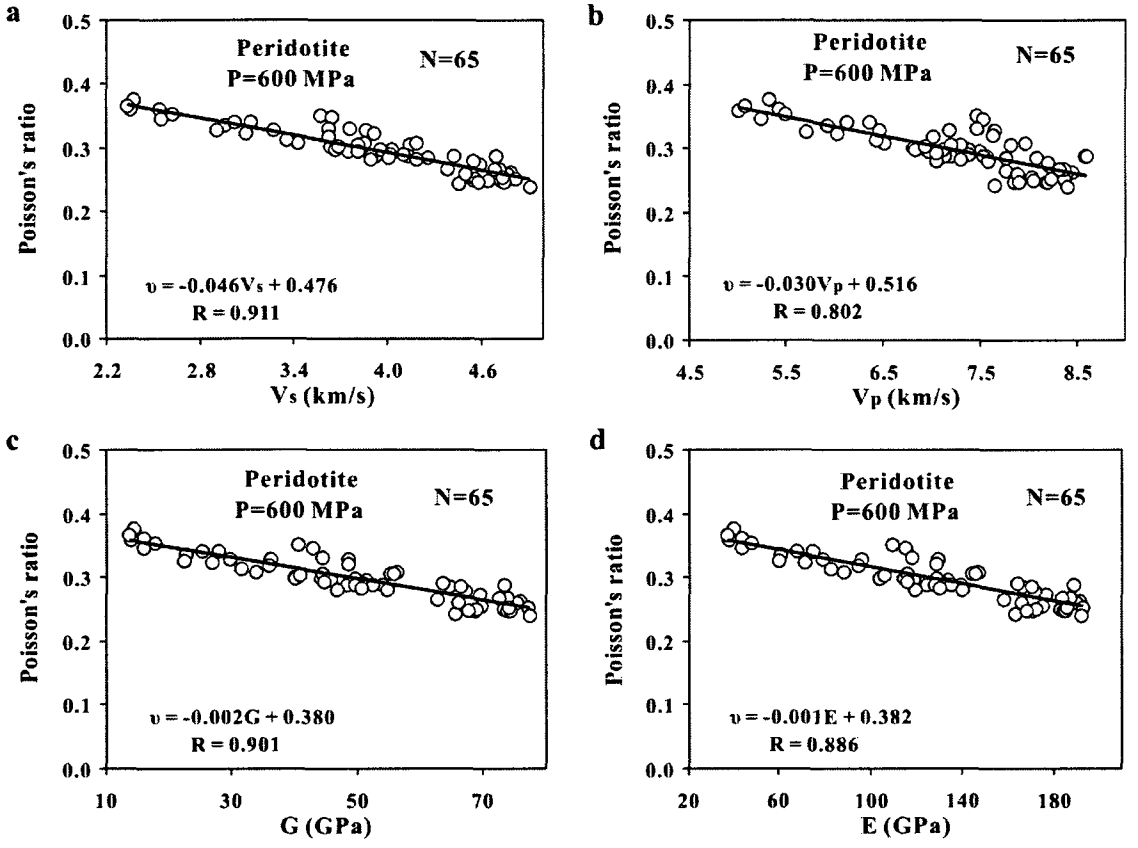

Figure 6.8 Variations in Poisson's ratio with V_s (a), V_p (b), G (c) and E (d) for peridotite at 600 MPa.

The relation between Poisson's ratio (υ) and V_p is defined by $\upsilon = aV_p + b$, where a and b are two parameters to describe the slope and intercept, respectively. It is surprising to see that in the b-a diagram (Fig. 6.4c) felsic rocks (i.e., granite, diorite, felsic gneiss and intermediate gneiss), mafic rocks (i.e., amphibolite, gabbro-diabase, eclogite, and mafic gneiss) and ultramafic rocks (i.e., peridotite) are characterized by high a and low b, moderate a and b, and low a and high b values, respectively. An opposite trend is observed for the $V_s = f(V_p)$ linear function (Fig. 6.4b). The sulfide ores can be placed in the following order of increasing the a-value and decreasing the b-value: chalcopyrite,

pyrite, sphalerite and pyrrhotite when $\upsilon = aV_p + b$. The exact reason for the above evolution remains unclear and is an interesting theme for further study.

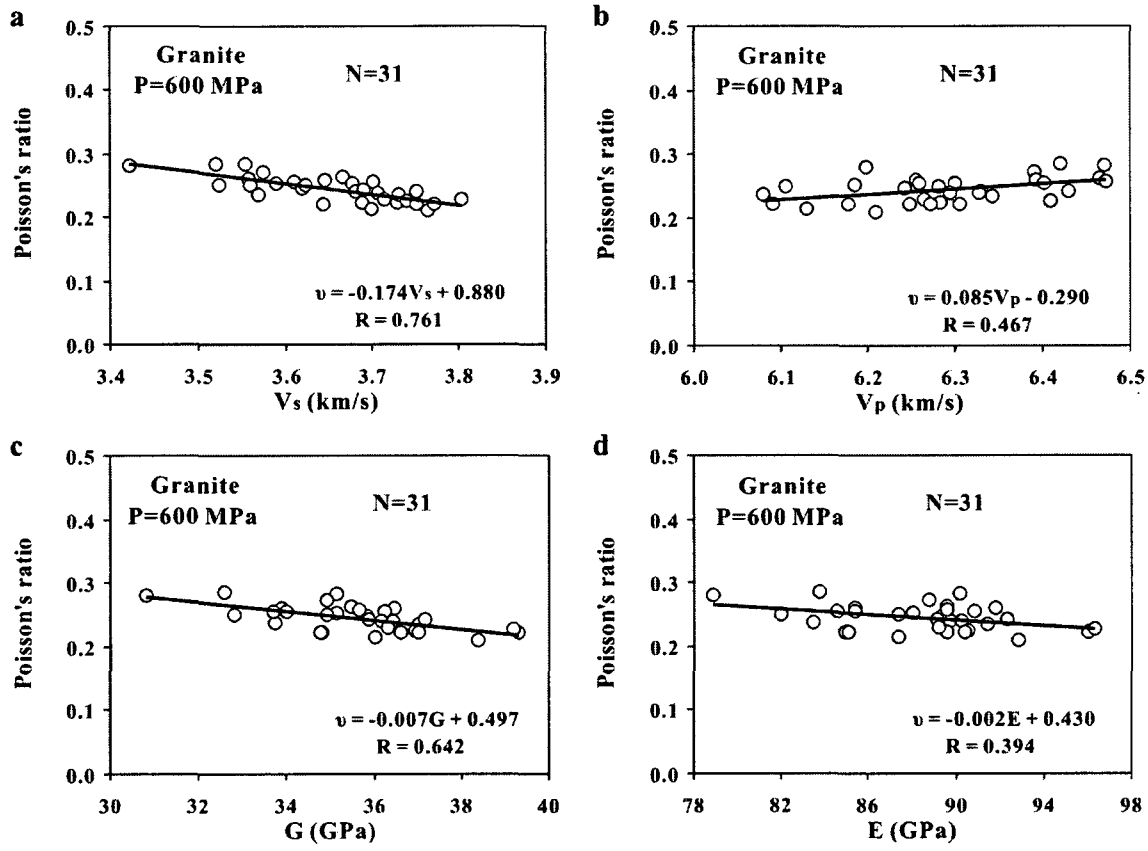

Figure 6.9 Variations in Poisson's ratio with V_s (a), V_p (b), G (c) and E (d) for granite at 600 MPa.

6.7 Discussion

It is generally described in the textbook of geophysics and materials science that Poisson's ratio depends on only the ratio of V_p/V_s and is insensitive to the absolute values of V_p and V_s (e.g., Gercek, 2007). Such impression rises probably from the presentation:

$$\upsilon = \frac{1}{2}\left[1-\left(\left(\frac{V_p}{V_s}\right)^2 - 1\right)^{-1}\right] \qquad (6.6)$$

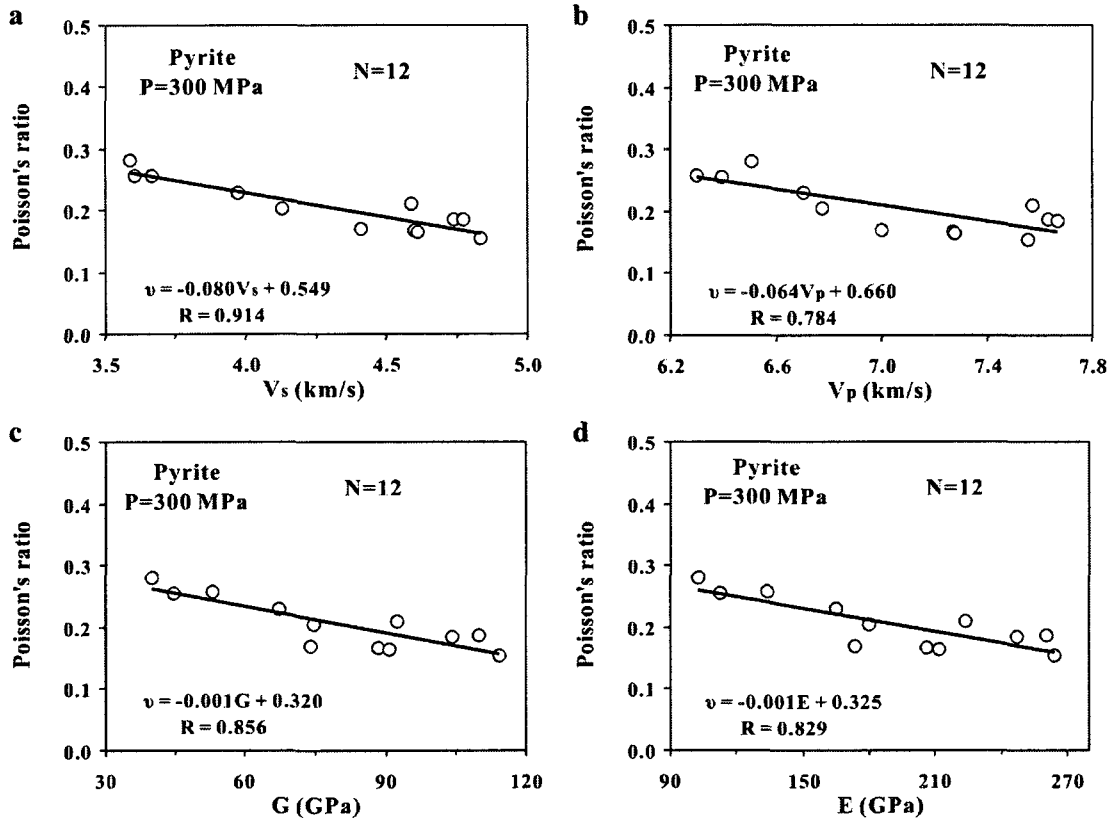

Figure 6.10 Variations in Poisson's ratio with V_s (a), V_p (b), G (c) and E (d) for pyrite ore at 300 MPa.

Here we have shown some obvious dependence of Poisson's ratio upon V_s and V_p for the common crustal and upper mantle rocks. Poisson's ratio decreases generally with increase in V_s, G and E. However, the dependence of υ on V_p seems to be complicated and to vary with lithology. At 600 MPa, amphibolite, diorite, eclogite, felsic gneiss, gabbro-diabase, granite, intermediate gneiss, limestone, and mafic gneiss (Table 6.3) display an increase in υ with increasing V_p. Anorthosite, basalt and peridotite, however,

reveals a negative correlation between υ and V_p. Moreover, the sulfide ores can be classified into two groups according to the $\upsilon - V_p$ relationship: a negative correlation for chalcopyrite, pyrite (Fig. 6.10) and sphalerite, whereas a positive correlation for pyrrhotite (Fig. 6.11).

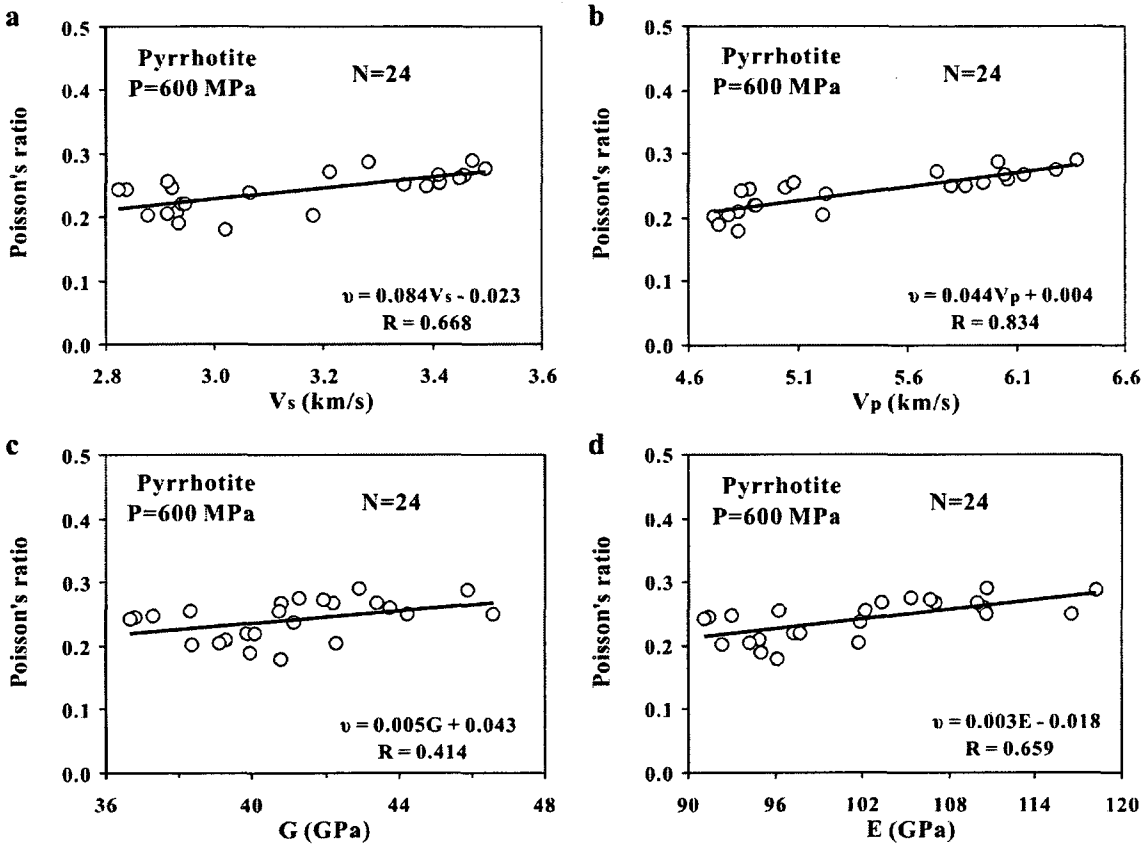

Figure 6.11 Variations in Poisson's ratio with V_s (a), V_p (b), G (c) and E (d) for pyrrhotite ore at 600 MPa.

Equation (6.6) can be written as:

$$\upsilon = \frac{V_p^{\,2} - 2V_s^{\,2}}{2\left(V_p^{\,2} - V_s^{\,2}\right)} \qquad (6.7)$$

Equation (6.7) indicates that υ is a function of both V_s and V_p. For a constant V_p, υ always decreases nonlinearly with increase in V_s. For a constant V_s, however, υ always increases nonlinearly with increase in V_p.

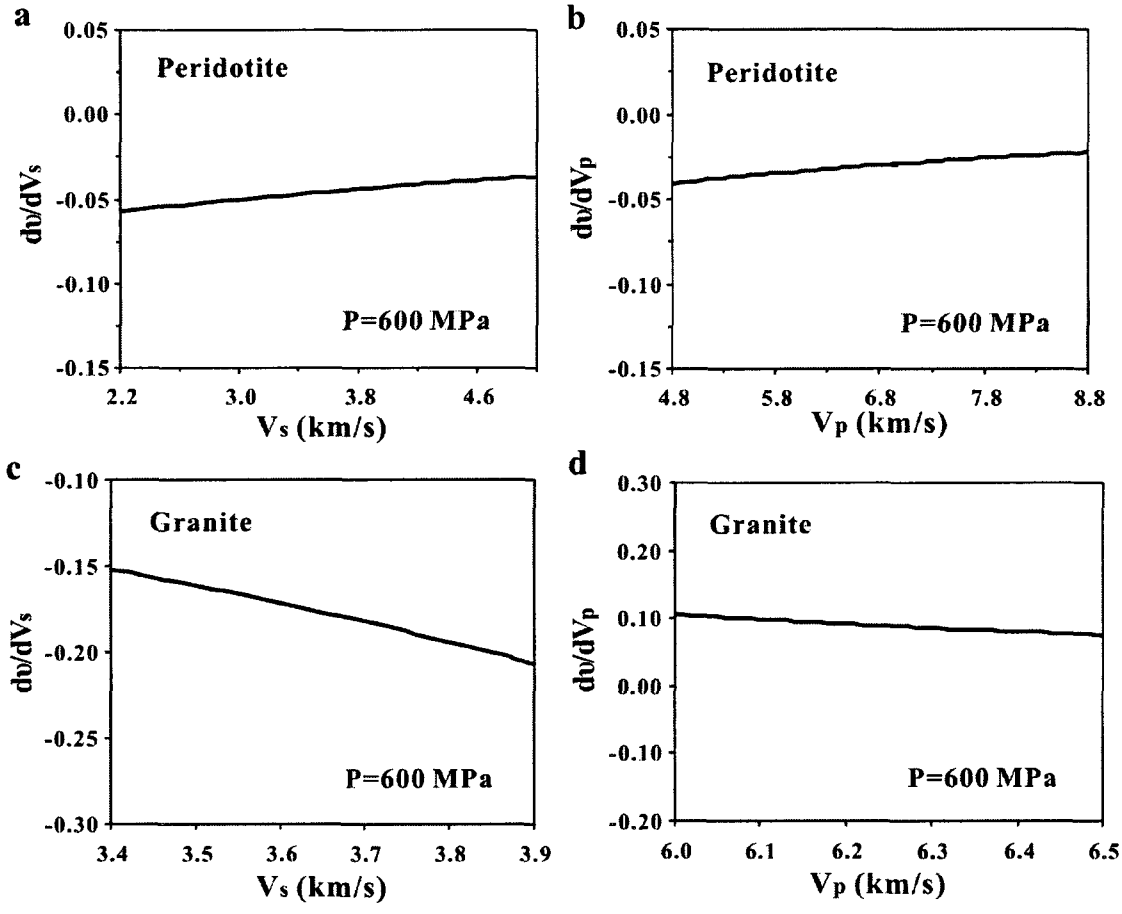

Figure 6.12 Variations in $d\upsilon/dV_s$ with V_s (a and c) and $d\upsilon/dV_p$ with V_p (b and d) for peridotite (a-b) and granite (c-d).

Differentiating Eq. (6.7) yields:

$$\frac{d\upsilon}{\upsilon} = \zeta\left(\frac{dV_p}{V_p} - \frac{dV_s}{V_s}\right) = \zeta\left(1 - R_{s/p}\right)\frac{dV_p}{V_p} \qquad (6.8)$$

where

$$\zeta = \frac{2V_p^{\,2}V_s^{\,2}}{\left(V_p^{\,2} - V_s^{\,2}\right)\left(V_p^{\,2} - 2V_s^{\,2}\right)} \tag{6.9}$$

As long as $\upsilon > 0$, then $\left(V_p^{\,2} - 2V_s^{\,2}\right) > 0$, and $\zeta > 0$. Hence Eq. (6.8) shows that the variation in Poisson's ratio depends on the relative variation rates in V_p and V_s. As long as the rate of increase in V_s is larger than that in V_p, $dV_s/V_s > dV_p/V_p$, $d\upsilon/\upsilon$ will be negative and thus υ decreases with increase of V_s and V_p (Kumar et al., 2003). Thus Eq. (6.8) indicates a positive correlation between Poisson's ratio and V_p (Table 6.3) when $R_{s/p} < 1$ (e.g., amphibolite, diorite, eclogite, felsic gneiss, gabbro-diabase, granite, intermediate gneiss, limestone, mafic gneiss and pyrrhotite). A negative correlation occurs between Poisson's ratio and V_p (Table 6.3) when $R_{s/p} > 1$ (e.g., anorthosite, basalt, peridotite, chalcopyrite, pyrite and sphalerite).

$$\upsilon = \frac{E}{2G} - 1 \tag{6.10}$$

We obtain:

$$\frac{d\upsilon}{\upsilon} = \frac{1}{\left(1 - \frac{2G}{E}\right)}\left(\frac{dE}{E} - \frac{dG}{G}\right) \tag{6.11}$$

Because $2G/E = 1/(\upsilon + 1)$ and $0 \le \upsilon \le 0.5$, $2G/E \le 1$. From Eq. (6.11), we can easily observe that if the rate of G increase is larger than that of E increase, $d\upsilon/\upsilon$ will be negative and hence υ will vary in the opposite direction as those of E and G. For the

rocks investigated, υ generally displays a negative correlation with G and E, indicating that dG/G is commonly larger than dE/E.

However, V_p and V_s are always mutually correlated and both tend to vary in the same direction (increase or decrease). Thus, the variation of υ with V_s and V_p may be complicated: υ may monotonically increase, monotonically decrease, first increase and then decrease (convex line), or first decrease and then increase (concave line) with increase in V_s or V_p.

Considering that V_p is linearly correlated with V_s:

$$V_p = aV_s + b \tag{6.12}$$

$$\frac{d\upsilon}{dV_s} = -\frac{b\left(a+\frac{b}{V_s}\right)}{\left[\left(a+\frac{b}{V_s}\right)^2 - 1\right]^2 V_s^2} \tag{6.13}$$

Poisson's ratio decreases with increasing V_s if $d\upsilon/dV_s$ calculated from Eq. (6.13) is negative. For example, the calculated $d\upsilon/dV_s$ values for peridotite (Fig. 6.12a) and granite (Fig. 6.12c) are always negative in the V_s ranges of experimental measurements (2.2-5.0 km/s for peridotite and 3.4-3.9 km/s for granite). These negative values of $d\upsilon/dV_s$ correspond to the continuous decrease in υ with increasing V_s for peridotite (Fig. 6.8a) and granite (Fig. 6.9a).

When V_s is correlated with V_p,

$$V_s = aV_p + b \tag{6.14}$$

$$\frac{d\upsilon}{dV_p} = \frac{\dfrac{V_p}{(b+aV_p)^2}\left(1-\dfrac{aV_p}{(b+aV_p)}\right)}{\left(\left(\dfrac{V_p}{b+aV_p}\right)^2-1\right)^2} \qquad (6.15)$$

Poisson's ratio decreases with increasing V_p if $d\upsilon/dV_p$ calculated from Eq. (6.15) is negative. In the case of peridotite (Fig. 6.12b), for example, the calculated $d\upsilon/dV_p$ values are negative in the V_p range of experimental measurements (4.8-8.8 km/s). This explains why Poisson's ratio of peridotite displays a clear trend of decrease with increasing V_p (Fig. 6.8b). For granite (Fig. 6.12d), the calculated $d\upsilon/dV_p$ values are positive in the V_p range from 6.0-6.5 km/s, corresponding to an increase in υ with increasing V_p (Fig. 6.9b).

6.8 Conclusions

Data from high-pressure laboratory measurements of V_p and V_s are statistically analyzed for 12 common categories of rocks (i.e., amphibolite, anorthosite, basalt, diorite, eclogite, felsic gneiss, gabbro-diabase, granite, intermediate gneiss, limestone, mafic gneiss, and peridotite) and 4 types of massive sulfide ores (i.e., chalcopyrite, pyrite, pyrrhotite, and sphalerite). The analysis shows that the linear correlation provides rather good descriptions for the relationships between V_s and V_p or $\ln V_s$ and $\ln V_p$. These empirical relations can give a reasonable estimate for the V_s value when only V_p data exist or vice versa. The logarithmic ratio $R_{s/p}$ (i.e., $\partial \ln V_s/\partial \ln V_p$) varies systematically with lithology: 0.300 for granite, 0.573 for diorite, 0.602 for felsic gneiss, 0.631 for intermediate gneiss, 0.721 for gabbro-diabase, 0.768 for mafic gneiss, 0.866 for eclogite, 0.890 for amphibolite, and 1.391 for peridotite. The trend of an obvious

increase in $R_{s/p}$ with decreasing the content of SiO_2 from acidic to intermediate, then through mafic to ultramafic rocks suggests that the ratio can be used as a diagnostic for the composition of the deep continental crust with less ambiguity than the absolute values of V_p and V_s. It is of particular interest that eclogite (0.866) displays a significantly lower $R_{s/p}$ value than peridotite (1.391). An eclogitic mass that was delaminated from the lowermost part of the thickened continental crust and sunk into the upper mantle, if its volume is sufficiently large, should be distinguishable from its surrounding peridotitic mantle in term of $R_{s/p}$. Otherwise the discrimination of eclogite from peridotite seems to be impossible using the absolute values of V_p or V_s alone.

Poisson's ratio, which is believed to provide much tighter constraints on lithological composition than either V_p or V_s alone, is found to be linearly correlated with V_s, V_p, G and E for the common rocks and sulfide ores. A decrease in Poisson's ratio is commonly associated with increases in V_s, G and E. The variation of Poisson's ratio with V_p depends on the scaling factor $R_{s/p}$. The positive and negative corrections between Poisson's ratio and V_p occur when $R_{s/p}<1$ and $R_{s/p}>1$, respectively. It is also found that different from pyrite and sphalerite, pyrrhotite and chalcopyrite have negative values for $R_{\rho/s}$ $(\partial \ln \rho / \partial \ln V_s)$ and $R_{\rho/p}$ $(\partial \ln \rho / \partial \ln V_p)$. Interesting theoretical problems arise to explain the results presented in the paper.

Chapter 7
Conclusions and future work

7.1 Concluding summary

There has been growing interest towards quantification of seismic properties of polyphase rocks that consist of the Earth's deep crust, subducting slabs and upper mantle. The properties are extremely important for geological interpretation of in-situ seismic data (e.g., reflections, refraction, received functions, tomography, P-wave anisotropy and shear-wave splitting) obtained from the continental and oceanic lithospheres and mantle. The Qinling-Dabie-Sulu ultrahigh pressure (UHP) metamorphic terrane, which is the world's largest UHP terrane exposed on the surface, is a deep root of the convergent orogenic belt formed by continent-continent collision between the North China Block and the Yangtze Block during the Triassic. The Chinese Continental Scientific Drilling (CCSD), which was the largest and most expensive geoscientific research project ever undertaken in the People's Republic of China before 2007, and drilled 5158 m into the Sulu UHP metamorphic terrane which consists of coesite-bearing eclogite, felsic gneiss, quartzite and garnet peridotite, provided us a unique and excellent opportunity to characterize the seismic properties (e.g., P- and S-wave velocities, anisotropy and Poisson's ratio) of HP and UHP rocks that came from the deep root of the mountain belt and subducted continental slab. Hence the present investigation offers a significant contribution to understanding the physical properties and their variations in terms of pressure and lithology of continental crustal materials subducted deeply into the upper mantle and then exhumated back into the crust.

The present thesis consists of two parts. The first part gave an introduction to the background of elasticity and mixture rules (Chapter 1), and the Sulu UHP metamorphic terrane and the CCSD project (Chapter 2). The main scientific results achieved from the CCSD project were summarized. The objective of the investigation was also presented

in this part. The second part of the thesis presented our experimental results and their applications (from Chapter 3 to Chapter 6).

Chapter 3 addressed the origin of seismic hysteresis, a phenomenon that rock velocities measured during depressurization are higher than those measured during pressurization. The comparison between the samples collected from surface outcrops and those from the CCSD deep drill cores (0-5158 m) indicates that the observed seismic hysteresis is caused by irreversible changes in grain contact, increases in microcrack aspect ratios and reduction of void space during the pressurization-depressurization cycle. It is found that the velocity-pressure curves can be well described by a four-parameter exponential equation [i.e., Equation (3.9)] that can be derived from the general principle. The theoretical derivation provides for the first time clarification of the physical meaning of each parameter in the equation. Equation (3.9) not only can be used in the interpolation and extrapolation of seismic velocities but also offers a basis for classification of lithologies according to the values of these 4 parameters and for comparison among experimental results for different lithologies or different geological settings. We believe that the statistical properties of P-wave velocities in the UHP rocks, obtained from this study, provide indeed an important set of basic information for the interpretation of field seismic data from the root zones of continental convergent orogenic belts and modern and ancient subduction zones. The results suggest that regionally extensive mantle reflectors observed beneath modern and ancient orogenic belts (e.g., Calvert et al., 1995; Cook et al., 1999) may imply the preservation of rapidly subducted, dry, metastable crustal mafic or felsic material within the lithospheric upper mantle.

Chapter 4 addresses the hydrostatic pressure (P) dependence of Poisson's ratios (υ) for 54 crystalline rocks from the Sulu-Dabie orogenic belt (China). The experimental results display two main types of the $\upsilon - P$ relationships in the range of 40-800 MPa: (1) υ shows little variation with P in the range of 40-850 MPa; and (2) with increasing

pressure, υ increases rapidly below ~200 MPa and then becomes quasi-constant at higher pressures. Types 1 and 2 are observed in 22 and 32 samples, respectively. The origin of type 2 can be reasonably interpreted by a small volume fraction (0.1-0.5%) of randomly distributed and randomly oriented thin-disk shaped pores that are progressively closed during pressurization. The effects of microcrack orientation, crystallographic preferred orientations, and compositional layering should be taken into consideration for interpreting the origin of type 1. The present study suggests that both mineralogy and confining pressure play a critical role in influencing the Poisson's ratio of the crystalline rocks particularly below 200-300 MPa.

Chapter 5 dealt with first Poisson's ratios of common minerals and rocks and then applied these experimental results to constrain the crustal composition and tectonic evolution of the Chinese continental crust based on crustal thickness (H) and Poisson's ratio data measured from 248 broadband seismic stations using teleseismic receiver function techniques. The combination of our experimental results with those compiled in Handbook of Seismic Properties of Minerals, Rocks and Ores (Ji et al., 2002) reveals that except for monomineralic rocks such as quartzite, serpentinite, anorthosite, limestone and marble, the rest of the rock types have Poisson's ratios falling along an upward convex curve determined from the correlations between elastic moduli and density. Poisson's ratios display an increase with density as the lithology changes from granite, felsic gneiss and schist, through diorite-syenite, intermediate gneiss and metasediment, to gabbro-diabase, amphibolite and mafic gneiss, and then decrease as the rocks become ultramafic in composition. Eclogite has a higher density but a lower Poisson's ratio than peridotite. The teleseismic receiver function data show that the North China, Yangtze, South China and Northeast China blocks and Songpan-Ganzi Terrane of China are dominated by low ($\upsilon < 0.26$) and moderate ($0.26 \leq \upsilon < 0.28$) υ values (>70%), indicating that the crust is predominantly felsic. The Lhasa terrane, Qiangtang terrane, and Indochina block of China are characterized by high proportions (33-42%) of measurements with very high υ values (≥ 0.30), suggesting that the crust

is partially molten due to high temperatures. A negative correlation between υ and H is observed for the South China block, Northeast block, Lhasa block, Qiangtang terrane and Indochina block, indicating either tectonic thickening of the felsic upper and middle crust by folding and thrusting or the removal of mafic layers from the lower crust into the upper mantle by delamination. The receiver function data from the North China block are particularly interesting: with decreasing H, υ increases gently and linearly in the Baoding-Datong and Guanting-Zhangjiakou-Zhangbei regions, while increasing abruptly and nonlinearly in the rest of the block (e.g., Northeastern Hebei province and the southern Taihangshan area near Shijiazhuang). The linear correlation is interpreted as due to the summed, opposing contribution of tectonic thinning of felsic crust and the addition of mafic rocks crystallized from underplated magmas to the bulk crustal υ. The abrupt increase of υ with decreasing H implies that much larger thinning strains have taken place in the felsic upper and middle crust than in the mafic lower crust during Mesozoic-Cenozoic tectonic extension. It is further inferred that basaltic underplating has been localized mainly in the Zhangjiakou and adjacent regions.

Chapter 6 is devoted to the correlations between P- and S-wave velocities (V_p and V_s) and corresponding Poisson's ratios (υ) for 12 common categories of rocks (amphibolite, anorthosite, basalt, diorite, eclogite, felsic gneiss, gabbro-diabase, granite, intermediate gneiss, limestone, mafic gneiss, and peridotite) and 4 types of massive sulfide ores (chalcopyrite, pyrite, sphalerite and pyrrhotite). Our analysis displays that the linear correlation provides good descriptions for the V_s - V_p and $\ln V_s - \ln V_p$ relationships. Poisson's ratio is linearly correlated with V_s, V_p, shear modulus (G) and Young's modulus (E) for these rocks and sulfide ores. A decrease in Poisson's ratio is associated with increases in V_s, G and E. However, the variation of Poisson's ratio with V_p depends on the logarithmic ratio $R_{s/p}$ (i.e., $\partial \ln V_s / \partial \ln V_p$). Poisson's ratio increases or decreases with V_p when $R_{s/p}<1$ or >1. $R_{s/p}$ is found to vary with lithology (0.300 for granite, 0.573 for diorite, 0.602 for felsic gneiss, 0.631 for intermediate gneiss, 0.721

for gabbro-diabase, 0.768 for mafic gneiss, 0.866 for eclogite, 0.890 for amphibolite, and 1.391 for peridotite). $R_{s/p}$ can be used as a proxy for the composition of the deep continental crust and the upper mantle. This study suggests that the correlations between V_p and V_s, and corresponding Poisson's ratios (υ) should be important in modeling and interpreting seismic data in terms of chemistry and lithology.

7.2 Further work: seismic properties of rocks from Yunkai Mountains-the northern continental margin of the South China Sea

7.2.1 Objectives

During my study period in École Polytechnique de Montréal, I also completed laboratory measurements of both P- and S-wave velocities at confining pressures up to 650 MPa for 31 rock samples collected from the Yunkai Mountains which constitutes the northern continental margin of the South China Sea. After my Ph.D. thesis defense, I will carefully analyze these experimental data and publish the results in international journals such as Tectonophysics and the Asian Journal of Earth Sciences.

The South China Sea is the largest marginal sea basin in Southeast Asia. It is located tectonically at the junctions of the Indo-Australian plate; the Eurasian plate and the Pacific plate (Fig. 7.1). Several tectonic models have been proposed for the formation and evolution of the South China Sea:

(1) The opening of the South China Sea was related to left-lateral shear along the Red-River fault zone in response to the India-Eurasia continent-continent collision and southeastward escape of the Indochina block during the Cenozoic (Tapponnier and Molnar, 1976; Tapponnier et al., 1982; Tapponnier et al., 1990). This model is based on plasticine experiments and field investigation of the Red-

River fault zone (Wu et al., 1989; Tapponnier et al., 1990; Leloup et al., 1995) and magnetic anomaly lineaments (Briais et al., 1993).

(2) The opening of the South China Sea was due to the extensional force from an upwelling mantle plume beneath the South China Sea during the Cenozoic after the closure of the Tethyan Ocean (Fan and Menzies, 1992; Li et al., 1998; Zhu et al., 2002). This model was based on petrological and geochemical data on Cenozoic basalts and mantle xenoliths.

(3) The South China Sea is a back-arc basin related to the subduction of the Pacific plate along the south-eastern margin of the Eurasia plate (Hawkins et al., 1990; Stern et al., 1990; Aubouin, 1990; Lan et al., 1996; Xia et al., 2006). However, the geochemical characteristics of volcanic rocks formed during the opening of the South China Sea display strong affinity to Indian Ocean mantle rather than to the Pacific subduction zone (Zhu et al., 2002).

So far no consensus has been reached about how the South China Sea was exactly formed. Many important questions have not been answered yet: How did the left-lateral shearing Red-River ductile shear zone extend in the South China Sea? Was the shear strain along the Red-River shear zone sufficient to have led to the opening of the South China Sea? Does a mantle plume or upwelling exist beneath the South China Sea? What was the extensional and thinning style of the crust beneath the South China Sea? What was the rift process? To answer these questions, one should use the existent seismic reflection and refraction data from the region. During the last 20 years, more than 10,000 km of seismic reflection and refraction lines have been carried out in the South China Sea for the exploration of petroleum and natural gas (e.g., Hayes et al., 1995; Nissen et al., 1995; Kido et al., 2001; Clift and Lin, 2001; Yan et al., 2001; Yao et al., 2005). However, the geological interpretation of the seismic data in terms of basement lithology, composition and structure has been limited due to lacking appropriate petrophysical data of the basement rocks from the region. For this purpose,

we are conducting the high pressure laboratory measurements on the P- and S-wave velocities and anisotropy of 31 representative samples (73 minicores) from the Yunkai Mountains at the northern continental margin of the South China Sea. The results provide basic constrains on the seismic properties and anisotropy of the basement beneath the South China Sea.

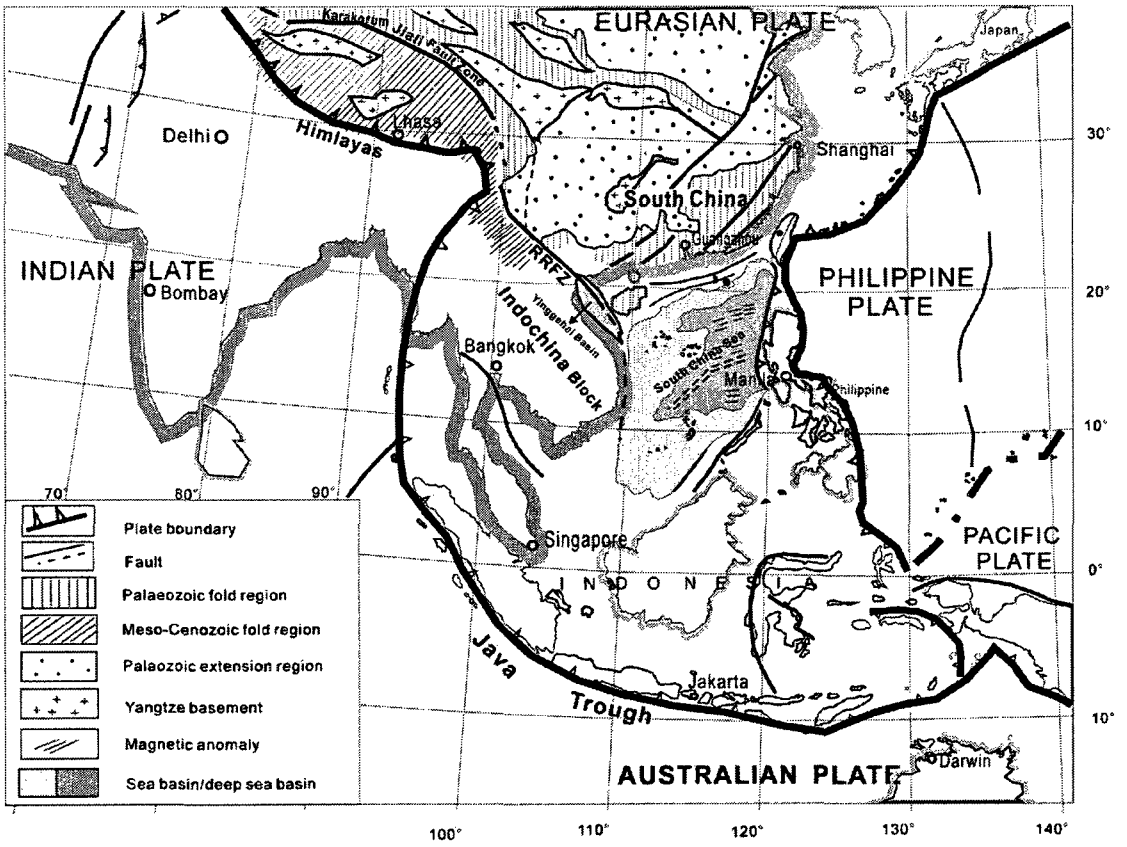

Figure 7.1 Tectonic map of the Southeast Asia and neighboring regions. (Modified from Xia et al., 2006)

7.2.2 Description of samples

The metamorphic rocks in the Yunkai Mountains (Fig. 7.2), which have been traditionally thought to be the Precambrian basement to the Paleozoic sedimentary strata of the South China Block, include banded and augen granitic gneisses (mylonites and

ultramylonites), amphibolite, mica-garnet gneiss, schist, migmatite, metapelite and deformed igneous rocks. The basement was reworked during the Indosinian orogeny (zircon $^{206}Pb/^{238}U$ age: 230 ± 10 Ma) which was related to the collision between the South China Sea and Indochina/Sibumasu blocks.

Two lateral shear zones have been mapped at the northern and southern margins of the Yunkai mountains: (1) Beihai-Luchuan shear zone. This zone, up to 10 km wide, developed a steep northwest-trending and southeast-dipping subvertical foliation with a subhorizontal lineation. Kinematic analyses based on various indicators such as rotating porphyroclasts, S-C structures, extensional shear bands and mica fishes suggest a dextral ductile strike-slip shear. (2) Wuchun-Sihui shear zone. This zone, up to 8-20 km wide, goes of N20-40E through Yangchun, Yunfu and Sihui. Tectonic lenses occur in this zone, reflecting the heterogeneity of ductile deformation. In the Yunfu region, the Devonian and Carboniferous limestone and dolomite have been metamorphosed into marble and dolomitic marble. This shear zone developed a subvertical foliation and a subhorizontal lineation and kinematic indicators display a sinistral shear. Xinyi massif is a granitic-gneissic and migmatitic dome that lies in a complex contractional duplex between these above-mentioned strike-slip shear zones. The metamorphism and ductile deformation as well as intrusion of magmatic rocks in the Yunkai Mountains mainly took place at 230 ± 10 Ma, corresponding to the Indosinian orogeny (Wang et al., 2007).

Detailed information about the samples used for measurements of seismic velocities is given in Table 7.1. Yanshanian (180-67 Ma) magmatic rocks (samples: YK25, YK52A, YK81, YK83, YK84, YK85, YK95), which are not deformed, and some Paleozoic sedimentary rocks (samples: YK90, YK101, YK102) were also sampled and investigated. The bulk chemical compositions of the samples from the Yunkai Mountains are listed in Table 7.2. The velocity-pressure curves were fitted by Eq. (3.9) using a least squares regression method. Tables 7.3 and 7.4 list the parameters of velocity-pressure curves measured during depressurization for the samples from the Yunkai Mountains.

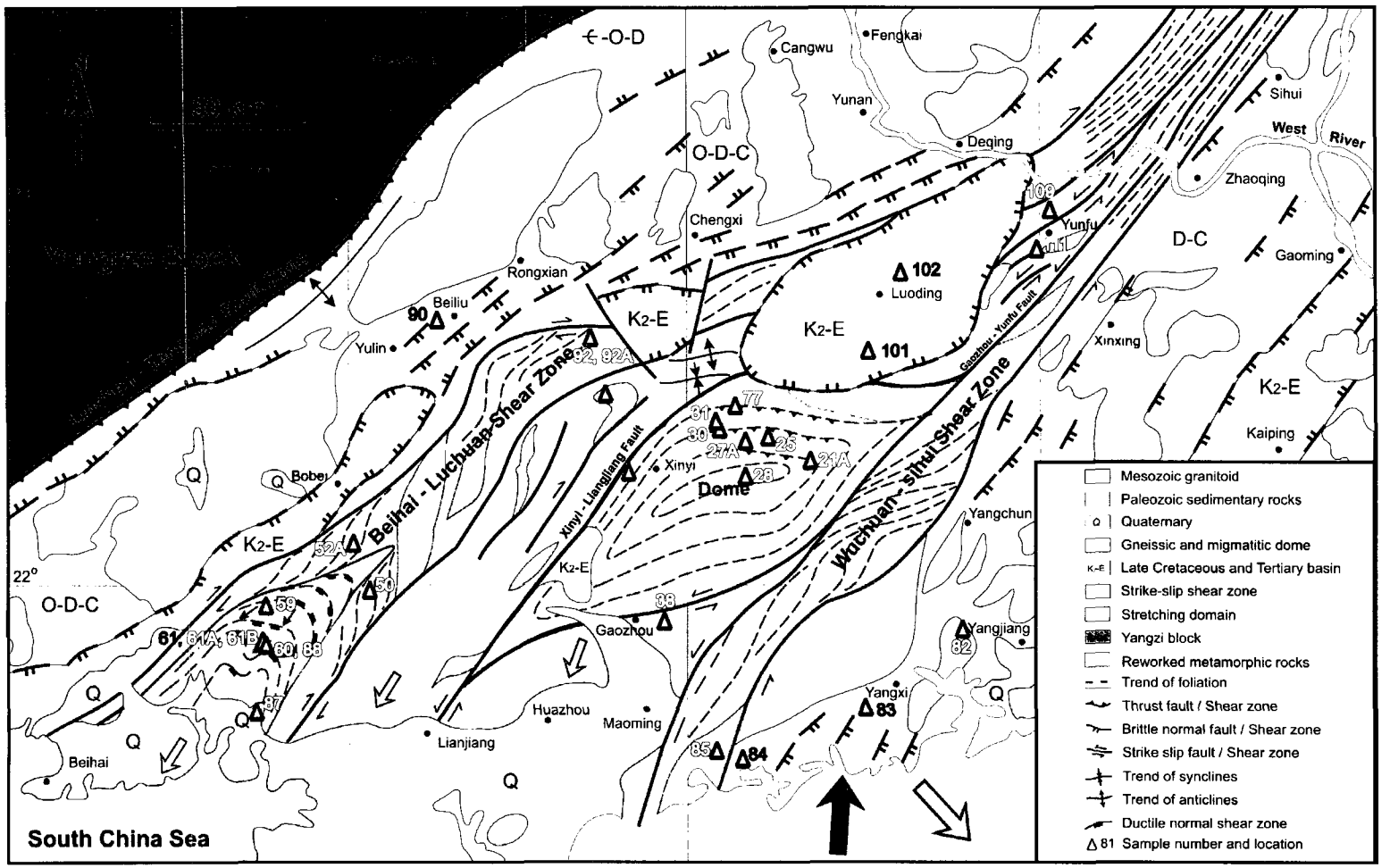

Figure 7.2 A simplified geological map of the Yunkai Mountains, South China.

Table 7.1 Description of Yunkai Mountains samples[a]

No.	Sample	Coordinates	Lithology	Density (g/cm^3)
1	YK21A	N22.330, E111.348	Qtz plagioclase schist	2.85
2	YK25	N22.386, E111.224	Granitic porphyrite (homogeneous)	2.56
3	YK27A	N22.377, E111.154	Felsic mylonite	2.66
4	YK28	N22.289, E111.158	Porphyroclastic plagiocalse-granitic gneiss	2.68
5	YK30	N22.409, E111.077	Granitic gneiss	2.69
6	YK31	N22.425, E111.067	Porphyroclastic granodioritic gneiss	2.71
7	YK38	N21.908, E110.920	Bt granitic gneiss	2.69
8	YK50	N21.987, E110.061	Porphyroclastic granitic mylonite	2.64
9	YK52A	N22.105, E110.013	Diorite (undeformed)	2.78
10	YK59	N21.948, E109.759	Granitic ultramylonite	2.64
11	YK60	N21.847, E109.759	Porphyroclastic granitic mylonite	2.64
12	YK61	N21.855, E109.746	Porphyroclastic granitic mylonite	2.62
13	YK61A	N21.855, E109.746	Granitic mylonite	2.61
14	YK61B	N21.855, E109.746	Granitic ultramylonite	2.62
15	YK73	N22.295, E110.810	Granitic gneiss (weakly deformed)	2.63
16	YK77	N22.467, E111.130	Granodioritic mylonite	2.71
17	YK81	N22.164, E112.224	Isotropic granite	2.64
18	YK82	N21.881, E111.794	Leucogranitic mylonite	2.61
19	YK83	N21.681, E111.508	Bt granodiorite	2.70
20	YK84	N21.548, E111.145	Granite (weakly deformed)	2.69
21	YK85	N21.564, E111.072	Granite	2.63
22	YK87	N21.664, E109.718	Limestone with calcite veins	2.71
23	YK88	N21.847, E109.755	Porphyroclastic gneiss	2.67
24	YK90	N22.697, E110.258	Siltstone	2.84
25	YK92	N22.631, E110.700	Amphibolite	3.04
26	YK92A	N22.631, E110.700	Granitic gneiss	2.64
27	YK95	N22.497, E110.754	Diorite (weakly deformed)	2.77
28	YK101	N22.614, E111.513	Limestone	2.77
29	YK102	N22.814, E111.609	Sandstone	2.67
30	YK109	N22.981, E112.048	Marble (coarse-grained)	2.71
31	YK111	N22.881, E112.005	Marble (fine-grained)	2.75

[a] Abbreviations: Bt: biotite; Qtz: quartz.

Table 7.2 Chemical composition (wt %) of samples from Yunkai Mountains

Sample	Lithology	SiO_2	TiO_2	Al_2O_3	Fe_2O_3	FeO	MnO	MgO	CaO	Na_2O	K_2O	P_2O_5	LOI	Total
YK21A	Qtz plagioclase schist	51.33	1.06	15.04	2.48	8.24	0.20	6.41	8.47	0.57	3.16	0.12	2.35	99.43
YK25	Granitic porphyrite (homogeneous)	78.58	0.07	11.39	0.44	0.68	0.05	0.00	0.59	3.33	4.69	0.00	0.85	100.67
YK27A	Felsic mylonite	74.56	0.26	13.85	0.73	1.07	0.03	0.52	1.97	4.14	2.00	0.08	0.89	100.10
YK28	Porphyroclastic plagiocalse-granitic gneiss	70.67	0.49	14.45	1.09	2.74	0.05	0.96	3.06	2.65	3.24	0.17	0.43	99.99
YK30	Granitic gneiss	69.47	0.57	14.68	1.04	3.26	0.06	1.34	2.24	2.22	4.15	0.12	0.66	99.82
YK31	Porphyroclastic granodioritic gneiss	68.69	0.60	15.11	1.45	3.16	0.06	1.28	3.44	2.56	3.09	0.17	0.82	100.42
YK38	Bt granitic gneiss	69.56	0.55	14.38	1.12	3.34	0.08	1.46	1.91	2.29	3.78	0.17	1.22	99.86
YK50	Porphyroclastic granitic mylonite	72.39	0.16	14.38	0.50	1.14	0.04	0.25	0.91	2.33	6.06	0.10	1.50	99.76
YK52A	Diorite (undeformed)	59.40	0.87	16.43	2.53	4.07	0.09	3.66	6.06	2.54	3.39	0.29	0.59	99.91
YK59	Granitic ultramylonite	76.74	0.13	13.02	0.41	0.32	0.00	0.13	0.30	2.33	5.36	0.14	0.97	99.86
YK60	Porphyroclastic granitic mylonite	74.67	0.12	13.63	0.72	0.94	0.05	0.16	0.94	2.67	5.10	0.10	0.90	100.00
YK61	Porphyroclastic granitic mylonite	76.95	0.09	12.54	0.92	0.44	0.02	0.16	0.26	2.15	5.59	0.13	0.62	99.87
YK61A	Granitic mylonite	76.93	0.09	12.80	0.84	0.30	0.01	0.05	0.35	2.77	4.97	0.14	0.74	99.99
YK61B	Granitic ultramylonite	77.65	0.06	12.10	0.54	0.79	0.10	0.04	0.35	2.90	4.40	0.14	0.91	100.00
YK73	Granitic gneiss (weakly deformed)	73.53	0.12	14.35	0.42	0.95	0.02	0.19	0.47	2.92	5.73	0.13	0.90	99.74
YK77	Granodioritic mylonite	68.81	0.63	14.35	3.52	1.21	0.06	1.76	1.95	2.05	4.08	0.13	1.02	99.57
YK81	Isotropic granite	71.81	0.28	14.57	0.00	2.11	0.04	0.68	2.23	3.16	4.15	0.07	0.74	99.85
YK82	Leucogranitic mylonite	76.39	0.04	13.36	0.26	0.39	0.07	0.00	0.57	2.92	5.83	0.01	0.36	100.20
YK83	Bt granodiorite	71.55	0.51	13.40	1.25	2.99	0.05	1.62	1.58	2.03	3.72	0.14	1.08	99.91
YK84	Granite (weakly deformed)	64.83	0.64	15.89	1.01	3.04	0.05	2.05	2.70	1.95	6.85	0.58	0.60	100.19
YK85	Granite	74.02	0.18	13.72	0.68	1.02	0.05	0.19	0.83	2.88	5.70	0.07	0.75	100.09
YK87	Limestone with calcite veins	0.00	0.03	0.26	0.00	0.12	0.00	0.39	56.67	0.25	0.06	0.00	41.95	99.74
YK88	Porphyroclastic gneiss	72.47	0.30	14.03	0.78	1.63	0.05	0.49	1.45	2.22	5.11	0.15	1.36	100.03
YK90	Siltstone	7.18	0.12	2.36	0.44	0.42	0.01	18.68	30.04	0.20	0.91	0.03	39.98	100.38
YK92	Amphibolite	48.93	1.50	14.44	4.83	8.28	0.21	7.21	11.43	1.44	0.72	0.12	0.65	99.77
YK92A	Granitic gneiss	77.20	0.21	12.09	0.76	1.09	0.01	0.30	0.83	2.67	4.29	0.06	0.55	100.06
YK95	Diorite (weakly deformed)	73.74	0.20	14.08	0.50	1.23	0.03	0.23	1.35	3.03	5.03	0.06	0.56	100.04
YK101	Limestone	15.29	0.16	1.29	0.26	0.19	0.01	14.82	32.18	0.21	0.49	0.00	35.32	100.20
YK102	Sandstone	56.38	0.36	7.33	1.65	0.63	0.08	1.64	16.64	0.80	1.27	0.08	13.46	100.30
YK109	Marble (coarse-grained)	0.25	0.03	0.16	0.00	0.09	0.05	0.25	57.18	0.26	0.01	0.00	40.93	99.20
YK111	Marble (fine-grained)	5.27	0.11	2.33	0.33	0.46	0.00	8.64	43.29	0.43	0.84	0.01	38.04	99.74

Table 7.3 Parameters of V_p-pressure curves measured during depressurization for the rock samples from the Yunkai Mountains.

Sample	Lithology	λ	Density	V_0	D	B_0	k	R^2	P_c	$P_{1/2}$
			(g/cm^3)	(km/s)	(10^{-4} km/s/MPa)	(km/s)	(10^{-2} MPa^{-1})		(MPa)	(MPa)
YK21A	Qtz-Pl schist	X	2.86	6.132	1.085	0.529	1.381	0.985	450	50
YK21A	Qtz-Pl schist	Y	2.84	6.006	1.618	0.427	1.163	0.994	534	60
YK21A	Qtz-Pl schist	Z	2.86	5.634	1.539	0.464	1.403	0.999	443	49
YK25	Granitic porphyrite (Homogeneous)	Z	2.56	5.758	1.276	0.368	1.050	0.997	592	66
YK27A	Felsic mylonite	X	2.66	6.268	2.854	0.611	1.837	0.999	338	38
YK27A	Felsic mylonite	Z	2.66	6.091	2.366	0.384	1.342	0.997	463	52
YK28	Porphyroclastic Pl-granitic gneiss	X	2.69	6.534	1.607	1.014	1.966	0.849	316	35
YK28	Porphyroclastic Pl-granitic gneiss	Y	2.67	6.845	2.827	1.188	1.638	0.888	379	42
YK28	Porphyroclastic Pl-granitic gneiss	Z	2.68	6.168	2.651	0.688	1.883	1.000	330	37
YK30	Granitic gneiss	X	2.70	6.156	3.371	0.799	1.476	1.000	421	47
YK30	Granitic gneiss	Y	2.69	6.082	3.217	1.160	1.784	0.999	348	39
YK30	Granitic gneiss	Z	2.69	5.635	3.611	1.044	1.651	0.982	376	42
YK31	Porphyroclastic granodioritic gneiss	X	2.71	6.063	3.350	1.001	1.313	0.947	473	53
YK31	Porphyroclastic granodioritic gneiss	Y	2.70	6.271	4.116	1.073	2.686	0.999	231	26
YK31	Porphyroclastic granodioritic gneiss	Z	2.71	5.852	3.124	1.590	3.792	0.976	164	18
YK38	Bt-granitic gneiss	X	2.69	6.243	3.327	0.906	1.538	0.997	404	45
YK38	Bt-granitic gneiss	Y	2.69	6.094	2.625	1.054	2.071	0.998	300	33
YK38	Bt-granitic gneiss	Z	2.70	6.178	2.779	0.633	1.775	1.000	350	39
YK50	Porphyroclastic granitic mylonite	X	2.65	6.216	3.046	0.420	1.613	0.990	385	43
YK50	Porphyroclastic granitic mylonite	Y	2.64	6.133	3.599	0.624	1.996	0.995	311	35
YK50	Porphyroclastic granitic mylonite	Z	2.64	5.857	3.797	0.730	1.855	0.994	335	37
YK52A	Diorite (Undeformed)	X	2.78	6.171	1.486	0.943	2.186	0.998	284	32
YK52A	Diorite (Undeformed)	Y	2.78	6.228	2.071	0.841	2.026	0.994	307	34
YK52A	Diorite (Undeformed)	Z	2.77	6.056	2.108	0.699	1.719	0.998	362	40
YK59	Granitic ultramylonite	X	2.64	5.966	4.444	0.652	2.304	0.982	270	30
YK59	Granitic ultramylonite	Z	2.65	5.956	3.333	1.045	2.050	0.978	303	34
YK60	Porphyroclastic granitic mylonite	X	2.64	6.201	2.033	0.695	2.394	0.990	260	29
YK60	Porphyroclastic granitic mylonite	Y	2.64	6.098	1.492	0.602	1.873	0.996	332	37
YK60	Porphyroclastic granitic mylonite	Z	2.64	6.201	1.923	0.536	2.131	0.989	292	33
YK61	Porphyroclastic granitic mylonite	X	2.63	6.011	2.193	0.717	2.307	0.999	269	30
YK61	Porphyroclastic granitic mylonite	Y	2.60	5.579	3.279	0.711	2.027	0.996	307	34
YK61	Porphyroclastic granitic mylonite	Z	2.63	5.674	3.329	0.980	1.933	0.999	321	36
YK61A	Granitic mylonite	X	2.63	6.112	2.046	0.806	1.820	0.988	341	38
YK61A	Granitic mylonite	Y	2.60	5.725	3.726	0.492	1.633	0.998	381	42
YK61A	Granitic mylonite	Z	2.60	5.827	3.279	0.762	1.734	0.998	358	40
YK61B	Granitic ultramylonite	X	2.62	6.013	2.133	0.473	1.707	0.998	364	41
YK61B	Granitic ultramylonite	Y	2.62	6.067	2.726	0.689	1.976	0.997	314	35
YK61B	Granitic ultramylonite	Z	2.62	5.847	4.093	0.677	1.556	0.989	399	45
YK73	Granitic gneiss (Weakly deformed)	Z	2.63	6.263	3.470	0.789	2.755	0.988	226	25
YK77	Granodioritic mylonite	X	2.71	6.504	2.552	1.348	2.681	0.989	232	26
YK77	Granodioritic mylonite	Y	2.71	6.080	2.953	1.237	2.771	0.991	224	25
YK77	Granodioritic mylonite	Z	2.72	6.062	2.213	0.809	2.250	0.997	276	31
YK81	Isotropic granite	Z	2.64	5.976	2.165	1.234	1.987	0.997	313	35
YK82	Leucogranitic mylonite	X	2.61	6.156	1.663	1.008	2.279	0.990	273	30
YK82	Leucogranitic mylonite	Y	2.61	6.001	2.393	0.943	2.045	0.998	304	34
YK82	Leucogranitic mylonite	Z	2.61	6.013	1.612	1.048	2.125	0.999	292	33
YK83	Bt granodiorite	Z	2.70	6.006	1.264	0.920	2.559	0.997	243	27
YK84	Granite (Weakly deformed)	X	2.68	6.425	1.707	0.673	2.486	0.991	250	28
YK84	Granite (Weakly deformed)	Y	2.69	6.437	2.512	0.832	2.081	0.997	299	33
YK84	Granite (Weakly deformed)	Z	2.69	6.211	2.356	1.035	2.091	0.980	297	33
YK85	Granite	Z	2.63	6.067	1.214	0.849	1.717	0.977	362	40
YK87	Limestone with calcite veins	Z	2.71	6.561	1.549	0.293	3.856	0.987	161	18

Table 7.3 (continued)

Sample	Lithology	λ	Density	V_0	D	B_0	k	R^2	P_c	$P_{1/2}$
			(g/cm^3)	(km/s)	(10^{-4} km/s/MPa)	(km/s)	(10^{-2} MPa^{-1})		(MPa)	(MPa)
YK88	Porphyroclastic gneiss	X	2.69	6.261	2.472	0.776	2.329	0.997	267	30
YK88	Porphyroclastic gneiss	Y	2.66	6.319	3.424	0.644	2.453	0.992	253	28
YK88	Porphyroclastic gneiss	Z	2.67	6.093	2.605	0.768	2.030	0.991	306	34
YK90	Siltstone	Z	2.84	6.788	3.008	0.547	3.002	0.992	207	23
YK92	Amphibolite	X	3.04	7.215	1.644	0.407	2.592	0.998	240	27
YK92	Amphibolite	Y	3.04	7.062	1.609	0.665	3.481	0.976	179	20
YK92	Amphibolite	Z	3.04	6.469	1.984	0.588	3.111	0.997	200	22
YK92A	Granitic gneiss	Z	2.64	6.134	3.609	0.626	2.560	0.997	243	27
YK95	Diorite (Weakly deformed)	Y	2.77	6.041	2.365	0.953	2.329	0.993	267	30
YK95	Diorite (Weakly deformed)	Z	2.77	6.009	1.880	1.194	2.125	0.988	292	33
YK101	Limestone	Y	2.76	6.565	1.863	0.429	2.217	0.996	280	31
YK101	Limestone	Z	2.77	6.297	2.138	0.460	2.800	1.000	222	25
YK102	Sandstone	Z	2.67	5.615	4.009	0.583	1.732	0.988	359	40
YK109	Marble (Coarse-grained)	X	2.71	6.776	2.203	0.903	2.237	0.986	278	31
YK109	Marble (Coarse-grained)	Y	2.72	6.523	2.854	1.653	3.758	0.992	165	18
YK109	Marble (Coarse-grained)	Z	2.71	6.524	3.492	3.461	3.198	0.999	194	22
YK111	Marble (Fine-grained)	X	2.75	6.520	1.583	0.609	3.449	0.989	180	20

[a] λ is the propagation direction.

Table 7.4 Parameters of V_s-pressure curves measured during depressurization for the rock samples from the Yunkai Mountains.

Sample	Lithology	λ	Density	V_0	D	B_0	k	R^2	P_c	$P_{1/2}$
			(g/cm^3)	(km/s)	(10^{-4} km/s/MPa)	(km/s)	(10^{-2} MPa^{-1})		(MPa)	(MPa)
YK21A	Qtz-Pl schist	XY	2.86	3.522	0.896	0.232	2.409	0.992	258	29
YK21A	Qtz-Pl schist	XZ	2.86	3.166	1.489	0.246	2.883	0.928	216	24
YK21A	Qtz-Pl schist	YX	2.84	3.543	0.589	0.195	2.910	0.911	214	24
YK21A	Qtz-Pl schist	YZ	2.84	3.064	1.227	0.285	2.765	0.957	225	25
YK21A	Qtz-Pl schist	ZX	2.86	3.207	2.726	1.045	1.827	0.993	340	38
YK21A	Qtz-Pl schist	ZY	2.86	3.129	1.385	0.219	4.166	0.885	149	17
YK25	Granitic porphyrite (Homogeneous)	ZX	2.56	3.327	0.609	0.222	2.226	0.966	279	31
YK27A	Felsic mylonite	XY	2.66	3.733	1.127	0.264	2.038	0.993	305	34
YK27A	Felsic mylonite	XZ	2.66	3.595	1.167	0.383	1.509	0.996	412	46
YK27A	Felsic mylonite	ZX	2.66	3.701	0.906	0.553	2.024	0.992	307	34
YK27A	Felsic mylonite	ZY	2.66	3.659	0.954	0.582	3.819	0.994	163	18
YK28	Porphyroclastic Pl-granitic gneiss	XY	2.69	3.798	1.181	0.278	1.121	0.998	554	62
YK28	Porphyroclastic Pl-granitic gneiss	XZ	2.69	3.188	0.601	0.267	1.462	0.998	425	47
YK28	Porphyroclastic Pl-granitic gneiss	YX	2.67	3.637	0.728	0.611	2.265	0.996	274	31
YK28	Porphyroclastic Pl-granitic gneiss	YZ	2.67	3.413	0.980	0.317	1.522	0.991	408	46
YK28	Porphyroclastic Pl-granitic gneiss	ZX	2.68	3.752	0.861	1.347	4.211	0.993	148	16
YK28	Porphyroclastic Pl-granitic gneiss	ZY	2.68	3.553	0.944	0.761	3.125	0.998	199	22
YK30	Granitic gneiss	XY	2.70	3.694	1.883	0.490	1.655	0.997	375	42
YK30	Granitic gneiss	XZ	2.70	3.401	1.351	0.524	1.826	0.975	340	38
YK30	Granitic gneiss	YX	2.69	3.684	1.699	0.497	1.653	0.996	376	42
YK30	Granitic gneiss	YZ	2.69	3.399	1.710	0.617	2.106	0.963	295	33
YK30	Granitic gneiss	ZX	2.69	3.413	1.510	0.482	1.443	0.993	431	48
YK30	Granitic gneiss	ZY	2.69	3.420	1.091	0.399	1.704	0.979	365	41
YK31	Porphyroclastic grantic gneiss	XY	2.71	3.886	1.083	0.702	2.326	0.977	267	30
YK31	Porphyroclastic grantic gneiss	XZ	2.71	3.605	1.650	0.617	1.822	0.995	341	38
YK31	Porphyroclastic grantic gneiss	YX	2.70	3.846	1.357	0.500	1.802	0.999	345	38
YK31	Porphyroclastic grantic gneiss	YZ	2.70	3.647	1.080	0.663	2.300	0.996	270	30
YK31	Porphyroclastic grantic gneiss	ZY	2.71	3.509	2.506	0.336	2.360	0.911	263	29

Table 7.4 (continued)

Sample	Lithology	λ	Density	V_0	D	B_0	k	R^2	P_c	$P_{1/2}$
			(g/cm^3)	(km/s)	(10^{-4} km/s/MPa)	(km/s)	(10^{-2} MPa^{-1})		(MPa)	(MPa)
YK50	Porphyroclastic granitic mylonite	XY	2.65	3.828	1.418	0.259	2.023	0.995	307	34
YK50	Porphyroclastic granitic mylonite	XZ	2.65	3.643	0.915	0.279	3.075	0.996	202	23
YK50	Porphyroclastic granitic mylonite	YX	2.64	3.701	0.959	0.787	5.061	0.989	123	14
YK50	Porphyroclastic granitic mylonite	YZ	2.64	3.595	0.722	0.270	2.193	0.966	283	32
YK50	Porphyroclastic granitic mylonite	ZX	2.64	3.545	0.989	0.614	3.319	0.984	187	21
YK50	Porphyroclastic granitic mylonite	ZY	2.64	3.601	0.703	0.203	2.546	0.966	244	27
YK52A	Diorite (Undeformed)	XY	2.78	3.555	1.058	0.363	1.903	0.993	327	36
YK52A	Diorite (Undeformed)	YX	2.78	3.592	0.840	0.407	2.383	0.998	261	29
YK52A	Diorite (Undeformed)	ZX	2.77	3.590	0.781	0.451	2.567	0.973	242	27
YK59	Granitic ultramylonite	XY	2.64	3.591	1.265	0.395	2.440	0.983	255	28
YK59	Granitic ultramylonite	XZ	2.64	3.561	1.548	0.266	2.044	0.998	304	34
YK59	Granitic ultramylonite	ZX	2.65	3.628	1.757	0.276	1.855	0.976	335	37
YK59	Granitic ultramylonite	ZY	2.65	3.549	1.288	0.317	1.771	0.997	351	39
YK60	Porphyroclastic granitic mylonite	XY	2.64	3.744	0.655	0.182	2.180	0.925	285	32
YK60	Porphyroclastic granitic mylonite	XZ	2.64	3.440	0.808	0.342	3.706	0.987	168	19
YK60	Porphyroclastic granitic mylonite	YX	2.64	3.704	1.008	0.243	2.562	0.978	243	27
YK60	Porphyroclastic granitic mylonite	YZ	2.64	3.446	0.564	0.279	2.727	0.970	228	25
YK60	Porphyroclastic granitic mylonite	ZX	2.64	3.645	1.047	0.308	2.069	0.990	300	34
YK60	Porphyroclastic granitic mylonite	ZY	2.64	3.380	0.752	0.522	3.951	0.896	157	18
YK61A	Granitic mylonite	XY	2.63	3.652	1.289	0.759	4.499	0.995	138	15
YK61A	Granitic mylonite	XZ	2.63	3.531	1.511	0.572	3.075	0.985	202	23
YK61A	Granitic mylonite	YX	2.60	3.586	1.140	0.339	1.946	0.994	319	36
YK61A	Granitic mylonite	YZ	2.60	3.492	0.954	0.356	1.462	0.996	425	47
YK61A	Granitic mylonite	ZX	2.60	3.487	0.894	0.332	1.441	0.997	431	48
YK61A	Granitic mylonite	ZY	2.60	3.494	0.779	0.479	1.808	0.978	344	38
YK77	Felsic mylonite	XY	2.71	3.833	0.951	0.639	2.617	0.994	237	26
YK77	Felsic mylonite	XZ	2.71	3.801	1.541	0.616	2.870	0.918	217	24
YK77	Felsic mylonite	YX	2.71	3.663	1.035	0.435	2.045	0.996	304	34
YK77	Felsic mylonite	YZ	2.71	3.537	2.013	0.580	3.791	0.999	164	18
YK77	Felsic mylonite	ZX	2.72	3.646	1.428	0.627	2.288	0.985	272	30
YK77	Felsic mylonite	ZY	2.72	3.560	1.130	0.669	3.773	0.971	165	18
YK81	Isotropic granodiorite	ZX	2.64	3.667	1.669	0.494	1.118	0.996	556	62
YK82	Leucogranitic mylonite	XY	2.61	3.619	1.295	0.365	3.617	0.998	172	19
YK82	Leucogranitic mylonite	XZ	2.61	3.607	1.028	0.438	4.162	0.976	149	17
YK82	Leucogranitic mylonite	YX	2.61	3.734	0.593	0.402	2.185	0.997	284	32
YK82	Leucogranitic mylonite	YZ	2.61	3.700	0.913	0.499	2.315	0.989	268	30
YK82	Leucogranitic mylonite	ZX	2.61	3.464	0.592	0.379	2.685	0.994	231	26
YK83	Bt granodiorite	ZX	2.70	3.743	1.507	0.596	2.625	0.984	237	26
YK84	Granite (Weakly deformed)	XY	2.68	3.590	1.145	0.548	5.104	0.929	122	14
YK84	Granite (Weakly deformed)	YX	2.69	3.707	1.230	0.620	3.756	0.939	165	18
YK84	Granite (Weakly deformed)	ZX	2.69	3.677	1.219	0.397	1.576	0.999	394	44
YK85	Granite	ZX	2.63	3.683	2.862	0.534	2.522	0.997	246	27
YK87	Limestone with calcite veins	ZX	2.71	3.442	0.521	0.132	9.379	0.922	66	7
YK92	Amphibolite	XY	3.04	4.186	0.643	0.176	6.327	0.984	98	11
YK92	Amphibolite	XZ	3.04	3.909	0.655	0.067	4.926	0.907	126	14
YK92	Amphibolite	YX	3.04	4.186	0.219	0.336	3.496	0.445	178	20
YK92	Amphibolite	YZ	3.04	3.849	0.550	0.089	10.093	0.942	62	7
YK92	Amphibolite	ZX	3.04	3.859	0.584	0.234	4.541	0.956	137	15
YK92	Amphibolite	ZY	3.04	3.829	0.564	0.148	4.205	0.961	148	16
YK92A	Granitic gneiss	ZX	2.64	3.732	1.503	0.962	9.113	0.984	68	8
YK102	Sandstone	ZX	2.67	3.404	0.980	0.235	2.322	0.994	268	30
YK109	Marble (Coarse-grained)	XY	2.71	3.563	0.527	0.188	3.845	0.994	162	18
YK109	Marble (Coarse-grained)	XZ	2.71	3.564	0.509	0.216	4.105	0.910	151	17
YK109	Marble (Coarse-grained)	YX	2.72	3.466	0.896	0.899	23.097	0.978	27	3
YK109	Marble (Coarse-grained)	YZ	2.72	3.393	0.291	0.173	4.698	0.943	132	15
YK109	Marble (Coarse-grained)	ZX	2.71	3.450	0.647	0.177	5.672	0.972	110	12
YK109	Marble (Coarse-grained)	ZY	2.71	3.188	0.460	0.225	4.732	0.989	131	15

[a] λ is the propagation and polarization direction.

7.2.3 Analysis and interpretation of the experimental data

The experimental data obtained from the study will be used to investigate:

(1) Relationships between rock density and seismic velocities (V_p, V_s, average, and for each given propagation direction). Special attention will be given to the effect of anisotropy on the relationships.

(2) Quantitative correlation between seismic properties, mineralogy and chemical composition.

(3) Comparison between experimentally measured and theoretically calculated seismic properties using different mixture rules (e.g., Voigt, Reuss, Hill and geometrical means as well as generalized means). The calculations will be based on lattice preferred orientation, density, modal composition and elastic stiffness coefficients. The main merits of the calculations are: (a) The calculations can provide a complete 3D distribution of seismic properties (21 elastic constants) in the structural framework (foliation and lineation), whereas the experimental measurements are usually limited to three orthogonal directions (X, Y, and Z). (b) The calculations can offer information about the variations of the seismic properties of rocks as a function of mineralogical composition. (c) The calculated results can help us to estimate the magnitude and orientations of seismic velocities and anisotropy in rocks, which can be further used to constrain and calibrate seismologic observations.

(4) Correlation between seismic properties and finite strain axes (i.e., foliation and lineation). This correlation can provide a valuable tool to constrain the interpretation of seismic anisotropy and S-wave splitting.

(5) Correlations between seismic anisotropy and deformation mechanisms (i.e., dislocation creep, diffusion creep or superplasticity).

(6) Reflection coefficients at interfaces between various rocks and the effects of anisotropy on reflectivity.

(7) Application of the experimental data to explain the seismic reflection and refraction profiles in the South China Sea and its northern continental margin in terms of lithology and structure.

References

Ahrens, T. J. (1995). *Mineral Physics & Crystallography: A Handbook of Physical Constants* (Agu Reference Shelf, No 2).

Alsdorf, D., & Nelson, D. (1999). Tibetan satellite magnetic low: evidence for widespread melt in the Tibetan crust. *Geology*, 27, 943-946.

Ames, L., Tilton, G. R., & Zhou, G. (1993). Timing of collision of the Sino-Korea and Yangtze cratons: U-Pb dating of coesite-bearing eclogites. *Geology*, 21, 339-342.

Archie, G. E. (1942). The electrical resistivity log as an aid in determining some reservoir characteristics. *Petrochemical Technology*, 1, 55-62.

Arnold, M., Boccaccini, A. R., & Ondracek, G. (1996). Prediction of the Poisson's ratio of porous materials. *Journal of Materials Science*, 31(6), 1643-1646.

ASME. (1953). Pressure-viscosity report: viscosity and density of over 40 lubricating fluids of known composition at pressures to 150,000 PSI and temperatures to 425 F. American Society of Mechanical Engineers, New York.

Aubouin, J. (1990). Dynamic model of the western Pacific. *Tectonophysics*, 183, 1-7.

Babuska, V., & Cara, M. (1991). *Seismic anisotropy in the Earth.* Kluwer Academic Publishers, Dordrecht/Boston/London, 217 pp.

Balshin, M. Y. (1949). Relation of mechanical properties of powder metals and their porosity and the ultimate properties of porous metal-ceramic materials. *Doklady Akademii Nauk* (SSSR), 67, 831-834.

Barberini, V., Burlini, L., & Zappone, A. (2007). Elastic properties, fabric and seismic anisotropy of amphibolites and their contribution to the lower crust reflectivity. *Tectonophysics*, 445, 227-244.

Barruol, G. (1993). Pétrophysique de la croûte inférieure — Rôle de l'anisotropie sismique sur la réflectivité et le déphasage des ondes S. Ph.D. Thesis. Université de Montpellier II, France, 239-258.

Beaumont, C., Jamieson, R. A., Nguyen, M. H., & Medvedev, S. (2004). Crustal channel flow: Numerical models with applications to tectonics of the Himalayan-Tibetan orogen. *Journal of Geophysical Research*, 109, B06406.

Birch, F. (1960). The velocity of compressional waves in rocks to 10 kilobar, Part 1. *Journal of Geophysical Research*, 65, 1083-1102.

Blanks, K. S., Kristoffersson, A., Carlstrom, E., & Clegg, W. J. (1998). Crack deflection in ceramic laminates using porous interlayers. *Journal of the European Ceramic Society*, 18, 1945-1951.

Boccaccini, A. R., Ondracek, G., & Mombello, E. (1995). Determination of stress concentration factors in porous materials. *Journal of Materials Science Letters*, 14, 534-536.

Bostock, M. G. (1997). Anisotropic upper-mantle stratigraphy and architecture of the Salve craton. *Nature*, 390, 392-395.

Briais, A., Patriat, P., & Tapponnier, P. (1993). Updated interpretation of magnetic anomalies and seafloor spreading in the South China Sea: implications for the Tertiary Tectonics of Southeast Asia. *Journal of Geophysical Research*, 98(B4), 6299-6328.

Brocher, T. M. (2005). Empirical relations between elastic wavespeeds and density in the Earth's crust. *Bulletin of the Seismological Society of America*, 95(6), 2081-2092.

Brocher, T. M. (2008). Key elements of regional seismic velocity models for long period ground motion simulations. *Journal of Seismology*, 12(2), 217-221.

Brown, J. M., Abramson, E. H., & Angel, R. J. (2006). Triclinic elastic constants for low albite. *Physics and Chemistry of Minerals*, 33, 256-265.

Brown, L. D., Zhao, W., Nelson, K. D., Hauck, M., Alsdorf, D., Cogan, M., Clark, M., Liu, X., & Che, J. (1996). Bright spots, structure, and magmatism in southern Tibet from INDEPTH seismic reflection profiling. *Science*, 274, 1688-1690.

Budiansky, B., & O'Connell, R. J. (1976). Elastic moduli of a cracked solid. *International Journal of Solids and Structures*, 12, 81-97.

Burke, M. M., & Fountain, D. F. (1990). Seismic properties of rocks from an exposure of extended continental crust-new laboratory measurements from the Ivrea Zone. *Tectonophysics*, 182, 119-146.

Burlini, L., & Kunze, K. (2000). Fabric and seismic properties of Carrara marble mylonite. *Physics and Chemistry of the Earth*, 25, 133-139.

Burlini, L., & Fountain, D. M. (1993). Seismic anisotropy of metapelites from the Ivrea-Verbano zone and Serie dei Laghi (northern Italy). *Physics of the Earth and Planetary Interiors*, 78, 301-317.

Calvert, A. J., Sawyer, E. W., Davis, W. J., & Ludden, J. N. (1995). Archean subduction inferred from seismic images of a mantle suture in the Superior Province. *Nature*, 375, 670-674.

Campbell, A. J., & Heinz, D. L. (1992). A high-pressure test of Birch's law. *Science*, 257, 66-67.

Castagna, J. P., Batzle, M. L., & Eastwood, R. L. (1985). Relationship between compressional and shear wave velocities in clastic silicate rocks. *Geophysics*, 50, 571-581.

Castagna, J. P., Batzle, M. L., & Kan, T. K. (1993). Rock physics-the link between rock properties and AVO response. In: Castagna, J.P., Backus, M.M. (Eds.), Offset-Dependent Reflectivity — Theory and Practice of AVO Analysis. Society of Exploration Geophysicists, 124-157.

Chen Chenghong, Lu Hsueh-Yu, Wayne Lin, & Chiyu Lee. (2006). Thermal event records in SE China coastal areas: constraints from monazite ages of beach sands from two sides of the Taiwan Strait. *Chemical Geology*, 23, 118-134.

Chen Jiangfeng, Foland, K. A., Xing Fengming, Xu Xiang, & Zhou Taixi. (1991). Magmatism along the southeast margin of the Yangtze block: Precambrian collision of the Yangtze and Cathaysian blocks of China. *Geology*, 19, 815-818.

Chen Jiangfeng, & Jahn, B. M. (1998). Crustal evolution of Southeastern China: Nd and Sr evidence. *Tectonophysics*, 284, 101-133.

Chen Leshou, Booker, J., Jones, A. G., Wu Nong, Unsworth, M. J., Wei Wenbo, & Tan Handong. (1996). Electrically conductive crust in southern Tibet from INDEPTH magnetotelluric surveying. *Science*, 274, 1694-1696.

Cheng, Y. Q., & Chang, Y. F. (2004). *The Positional Map of Compilation Area of the Dabie-Sulu Orogen (Dabie Shan area)*. Geological Publishing House, Beijing.

Chevrot, S., & Van der Hilst, R. D. (2000). The Poisson's ratio of the Australian crust: geological and geophysical implications. *Earth and Planetary Science Letters*, 183(1-2), 121-132.

Christensen, N. I. (1966). Elasticity of ultrabasic rocks. *Journal of Geophysical Research*, 71, 5921-5931.

Christensen, N. I., & Ramananantoandro, R. (1971). Elastic moduli and anisotropy of dunite to 10 kilobars. *Journal of Geophysical Research*, 76, 4003-4010.

Christensen, N. I. (1965). Compressional wave velocities in metamorphic rocks at pressures to 10 kilobars. *Journal of Geophysical Research*, 70, 6147-6164.

Christensen, N. I. (1974). Compressional wave velocities in possible mantle rocks to pressures of 30 kilobars. *Journal of Geophysical Research*, 79, 407-412.

Christensen, N. I. (1985). Measurement of dynamic properties of rock at elevated temperatures and pressures. In: ASTM STP 869, American Society of Testing and Materials, Philadelphia, 93-107.

Christensen, N. I. (1996). Poisson's ratio and crustal seismology. *Journal of Geophysical Research*, 101, 3139-3156.

Chung, D. H. (1972). Birch's law: Why is it so good? *Science*, 177, 261-263.

Clarke, T. J., & Silver, P. G. (1993). Estimation of crustal Poisson's ratio from broad-band teleseismic data. *Geophysical Research Letters*, 20, 241-244.

Clift, P. D., & Lin, J. (2001). Preferential mantle lithospheric extension under the South China margin. *Marine and Petroleum Geology*, 18, 929-945.

Collins, M. D., & Brown, J. M. (1998). Elasticity of an upper mantle clinopyroxene. *Physics and Chemistry of Minerals*, 26, 7-13.

Cong, B. L. (Ed.). (1996). *Ultrahigh-Pressure Metamorphic Rocks in the Dabieshan-Sulu Region of China*. Kluwer Academic Publishing, London, 224 pp.

Cong, B. L., & Wang, Q. C. (1999). The Dabie-Sulu UHP rocks slice: Review and prospect. *Chinese Science Bulletin*, 44, 1074-1085.

Cook, F. A., van der Velden, A. J., & Hall K. W. (1999). Frozen subduction in Canada's Northwest Territories: Lithoprobe deep lithospheric reflection profiling of the western Canadian Shield. *Tectonics*, 18, 1-24.

Coyle, D. A., Wagner, G. A., Hejl, E., Brown, R., & Van de Haut, P. (1997). The Cretaceous and younger thermal history of the KTB site (Germany): apatite fission-track data from the Vorbohrung. *International Journal of Earth Sciences* (Geol Rundsch), 86, 203-209.

Crampin, S., & Peacock, S. (2008). A review of our current understanding of shear-wave splitting and common fallacies in interpretation. *Wave Motion*, 45, 675-722.

Crampin, S., & Peacock, S. (2005). A review of shear-wave splitting in the compliant crack-critical anisotropic Earth. *Wave Motion*, 41, 59-77.

Dewey, J. M. (1947). The Elastic Constants of Materials Loaded with Non-rigid Fillers. *Journal of Applied Physics*, 18, 578-581.

Duffy, T. S., & Anderson, D. L. (1989). Seismic velocities in mantle minerals and the mineralogy of the upper mantle. *Journal of Geophysical Research*, 94, 1895-1912,

Dunn, M. L., & Ledbetter, H. (1995). Poisson's ratio of porous and microcracked solids: Theory and application to oxide superconductors. *Journal of Materials Research*, 10, 2715-2722.

Dzeiwonski, A. M. & Anderson, D. L. (1981). Preliminary reference earth model. *Physics of the Earth and Planetary Interiors*, 25, 297-356.

Eberhart-Phillips, D., Han, D. H., & Zoback, M. D. (1989). Empirical relationships among seismic velocity, effective pressure, porosity, and clay content in sandstone. *Geophysics*, 54, 82-89.

Fan, W., & Menzies, M. A. (1992). The lithospheric mantle composition of volcanism in extension settings: the geochemical evidence of Cenozoic basalts in Leiqiong area. In: Liu Ruoxin (Ed.), *The ages and geochemistry of Cenozoic volcanic rocks in China*. Seismological Publishing House, Beijing, 320-329.

Fountain, D. M. (1987).Geological and geophysical nature of the lower continental crust as revealed by exposed cross sections of the continental crust. In: Noller, J. S., Kirby, S. H., Nielson-Pike, J. E. (Eds.), *Geophysics and Petrology of the deep Crust and Upper Mantle*. United States Geological Survey Circular, 956, 25-26.

Fountain, D. M., Hurich, C. A., & Smithson, S. B. (1984). Seismic reflectivity of mylonitic zones in the crust. *Geology*, 12, 195-198.

Fountain, D. M., Salisbury, M. H., & Percival, J. (1990). Seismic structure of the continental crust based on rock velocity measurements from the Kapuskasing uplift. *Journal of Geophysical Research*, 95, 1167-1186.

Fourmaintrax, D. (1976). *Characterization of rocks – Laboratory test*, Chapter IV, Paris.

Francheteau, J., Jaupart, C., Xian, J. S., Wen-Hua, K., De-Lu, L., Jia-Cha, B., Hun-Pin, W., & Hsia-Yeu, D. (1984). High heat flow in southern Tibet. *Nature*, 307, 32-36.

Freedman, R., & Vogiatzis, J. P. (1979). Theory of microwave dielectric constant logging, using the lectromagnetic propagation method. *Geophysics*, 44, 969-986.

Freund, D. (1992). Ultrasonic compressional and shear velocities in dry clastic rocks as a function of porosity, clay content, and confining pressure. *Geophysical Journal International*, 108, 125-135.

Gardner, G. H. F., Gardner, L. W., & Gregory, A. R. (1974). Formation velocity and density the diagnostic basics for stratigraphic maps. *Geophysics*, 39, 370-380.

Gardner, G. H. F., Wyllie, M. R. J., & Droschak, D. H. (1965). Hysterisis in the velocity-pressure characteristics of rocks. *Geophysics*, 30, 111-134.

Gebrande, H. (1982). Elastic wave velocities and constants of elasticity of rocks and rock-forming minerals. In: Hellwege, K. H. (Ed.), Landolt-Börnstein - Group V Geophysics, Numerical Data and Functional Relationships in Science and

Technology, 1b, Physical Properties of Rocks, Springer-Verlag, Berlin, Heidelberg, New York, 1-99.

Gercek, H. (2007). Poisson's ratio values for rocks. *International Journal of Rock Mechanics and Mining Sciences*, 44, 1-13.

Gorecki, T. (1980). The relations between the shear modulus, the bulk modulus and Young's modulus for polycrystalline metallic elements. *Materials Science and Engineering*, 43, 225-230.

Greenfield, R. J., & Graham, E. K. (1996). Application of the simple relation for describing wave velocity as a function of pressure in rocks containing microcracks. *Journal of Geophysical Research*, 101, 5643-5652.

Griffiths, T. J., Davies, R., & Bassett, M. B. (1979). Analytical study of effects of pore geometry on tensile strength of porous materials. *Power Metallurgy*, 3, 119-123.

Guéguen, Y., & Palciauskas, V. (1992). *Introduction à la Physique des Roches*, Hermann Éditeurs des Sciences et des Arts, 299 pp.

Guo, J. H., Chen, F. K., Zhang, X. M., Siebel, W., & Zhai, M. G. (2005). Evolution of syn- to post-collisional magmatism from north Sulu UHP belt, eastern China: zircon U-Pb geochronology. *Acta Petrologica Sinica*, 21, 1281-1301.

Guyer, R. A, & Johnson, P. A. (1999). Nonlinear mesoscopic elasticity: evidence for a new class of materials. *Physics Today*, April, 30-36.

Hacker, B. R., Ratschbacher, L., & Webb, L. (1998). U/Pb zircon ages constrain the architecture of the ultrahigh-pressure Qingling-Dabie Orogen, China. *Earth and Planetary Science Letters*, 161, 215-230.

Hacker, B. R., Ratschbacher, L., Webb, L. E., McWilliams, M. O., Ireland, T., Calvert, A., Dong, S. W., Wenk, H. R., & Chateigner, D. (2000). Exhumation of ultrahigh-pressure continental crust in east central China: Late Triassic-early Jurassic tectonic unroofing. *Journal of Geophysical Research*, 105, 13,339-13,364.

Hamada, G. M. (2004). Reservoir Fluids Identification Using V_p/V_s Ratio. *Oil and Gas Science and Technology*, 59 (6), 649-654.

Hamilton, E. L. (1979). V_p/V_s and Poisson's ratios in marine sediments and rocks. *Journal of the Acoustical Society of America*, 66, 1093-1101.

Hashin, Z. (1962). Elastic moduli of heterogeneous materials. *Journal of Applied Mechanics*, 29(1), 143-155.

Hashin, Z., & Shtrikman, S. (1963). A variation approach to the theory of the elastic behavior of multiphase materials. *Journal of the Mechanics and Physics of Solids*, 11, 127-140.

Hawkins, J. W., Lonsdale, P. F., Macdougall, J. D., & Volpe, A. M. (1990). Petrology of the axial ridge of Mariana Trough back-arc spreading center. *Earth and Planetary Science Letters*, 100, 226-250.

Hayes, D. E., Nissen, S. S., Buhl, P., Diebold, J., Yao, B., Zeng, W., & Chen, Y. (1995). Through-going crustal faults along the northern margin of the South China Sea and their role in crustal extension. *Journal of Geophysical Research*, 100(B11), 22435-22446.

Haynes, R. (1971). Effect of porosity content on the tensile strength of porous materials. *Power Metallurgy*, 14, 64-70.

He, L. J., Hu, S. B., Yang, W. C., Wang, J. Y., Yang, S. C., Yuan, Y. S., & Cheng, Z. Y. (2006). Temperature measurement in the main hole of the Chinese Continental Scientific Drilling. *Chinese Journal of Geophysics*, 49(3), 745-752.

Hill, R. (1963). Elastic properties of reinforced solids: some theoretical principles. *Journal of the Mechanics and Physics of Solids*, 11, 357-372.

Hodges, K. V. (2000). Tectonics of the Himalaya and southern Tibet from two perspectives. *Geological Society of America Bulletin*, 112, 324-350.

Holbrook, W., Mooney, W., & Christensen, N. I. (1992). The seismic velocities of the deep continental crust. In: Fountain, S. D., Arculus, R., Kay, R. W. (Eds.), *Continental Lower Crust*, Elsevier, Amsterdam, 1-43.

Holbrook, W. S., Gajewski, P., Krammer, A., & Prodehl, C. (1988). An interpretation of wide-angle compressional and shear wave data in southwest Germany: Poisson's ratio and petrological implications. *Journal of Geophysical Research*, 93, 12081-12106.

Holcomb, D. J. (1981). Memory, relaxation and microfracturing in dilatant rock. *Journal of Geophysical Research*, 86, 6235-6248.

Hu Jiafu, Su Youjin, Zhu Xiongguan, & Chen Yun. (2003). S-wave velocity and Poisson's ratio structure of crust in Yunnan and its implication. *Science in China* (Series D-Earth Sciences), 48(2), 210-218.

Ichitsubo, T., Tane, M., Ogi, H., Hirao, M., Ikeda, T., & Nakajima, H. (2002). Anisotropic elastic constants of lotus-type porous copper: measurements and micromechanics modeling. *Acta Materialia*, 50, 4105-4115.

Jackson, P. D., Taylor Smith, D., & Stanford, P. N. (1978). Resitivity-porosity-particle shape relationships for marine sands. *Geophysics*, 43, 1250-1268.

Jahn, B. M., Zhou, X. H., & Li, J. L. (1990). Formation and tectonic evolution of southeastern China and Taiwan: isotopic and geochemical constraints. *Tectonophysics*, 183, 145-160.

Ji, S. C., & Mainprice, D. (1988). Natural deformation fabrics of plagioclase: Implications for slip systems and seismic anisotropy. *Tectonophysics*, 147, 145-163.

Ji, S. C. (2004). Generalized means as an approach for predicting Young's moduli of multiphase materials. *Materials Science and Engineering* (A), 366, 195-201.

Ji, S. C., & Wang, Z. C. (1999). Elastic properties of forsterite-enstatite composites up to 3.0 GPa. *Journal of Geodynamics*, 28, 147-174.

Ji, S. C., Long, C. X., Martignole, J., & Salisbury, M. H. (1997). Seismic reflectivity of a finely layered, granulite-facies ductile shear zone in the southern Grenville province (Quebec). *Tectonophysics*, 279, 113-133.

Ji, S. C., Saruwatari, K., Mainprice, D., Wirth, R., Xu, Z. Q., & Xia, B. (2003). Microstructures, petrofabrics and seismic properties of ultrahigh-pressure eclogites from Sulu region, China: Implications for rheology of subducted continental crust and origin of mantle reflections, *Tectonophysics*, 370, 49-76.

Ji, S. C., & Salisbury, M. H. (1993). Shear-wave velocities, anisotropy and splitting in high-grade mylonites. *Tectonophysics*, 221, 453-473.

Ji, S. C., Wang, Q., & Xia, B. (2002). *Handbook of Seismic Properties of Minerals, Rocks and Ores*, Polytechnic International Press, Montreal, 630 pp.

Ji, S. C., Wang, Q., Marcotte, D., Salisbury, M. H., & Xu, Z. Q. (2007). P-wave velocities, anisotropy and hysteresis in ultrahigh-pressure metamorphic rocks as a function of confining pressure. *Journal of Geophysical Research*, 112, B09204.

Ji, S. C. (2004). A generalized mixture rule for estimating the viscosity of solid-liquid suspensions and mechanical properties of polyphase rocks and composite materials. *Journal of Geophysical Research*, 109, B10207.

Ji, S. C., Gu, Q., & Xia, B. (2006). Porosity dependence of mechanical properties of solid materials. *Journal of Materials Science*, 41, 1757-1768.

Ji, S. C., Saruwatari, K., Mainprice, D., Wirch, R., Xu, Z. Q., & Xia, B. (2003). Microstructures, petrofabrics and seismic properties of ultrahigh-pressure eclogites from Sulu region, China: implications for rheology of subducted continental crust and origin of mantle reflections. *Tectonophysics*, 370, 49-76.

Ji, S. C., Wang, Q., Xia, B., & Marcotte, D. (2004). Mechanical properties of multiphase materials and rocks: a simple phenomenological approach using generalized means. *Journal of Structural Geology*, 24, 1377-1390.

Ji, S. C., & Long, C. X. (2006). Seismic reflection response of folded structures and implications for the interpretation of deep seismic reflection profiles. *Journal of Structural Geology*, 28, 1380-1387.

Ji, S. C., Salisbury, M., & Hanmer, S. (1993). Petrofabric, P-wave anisotropy and seismic reflectivity of high grade tectonites. *Tectonophysics*, 222, 195-226.

Ji, S. C., Saruwatari, K., Mainprice, D., Wirch, R., Xu, Z. Q., & Xia, B. (2003). Microstructures, petrofabrics and seismic properties of ultra high-pressure eclogites from Sulu region, China: Implications for rheology of subducted continental crust and origin of mantle reflections. *Tectonophysics*, 370, 49-76.

Ji, S. C., Wang, Q., & Salisbury, M. H. (2009). Composition and tectonic evolution of the Chinese continental crust constrained by Poisson's ratio. *Tectonophysics*, 463, 15-30.

Ji, S. C., Wang, Q., & Xia, B. (2003). P-wave velocities of polymineralic rocks: comparison of theory and experiment and test of elastic mixture rules. *Tectonophysics*, 366(1-2), 165-185.

Ji, S. C., Wang, Q., & Xu, Z. Q. (2007). Reply to the comments of S. Karato on "Petrofabrics and seismic properties of garnet peridotite from the UHP Sulu terrane (China)". *Tectonophysics*, 429, 291-296.

Ji, S. C., & Xia, B. (2002). *Rheology of Polyphase Earth Materials*, Polytechnic International Press, Montreal, 260 pp.

Jones, L. A., & Wang, H. F. (1981). Ultrasonic velocities in Cretaceous shales from the Williston basin. *Geophysics*, 46, 288-297.

Joyner, W. B. (2000). Strong motion from surface waves in deep sedimentary basins. *Bulletin of the Seismological Society of America*, 90, S95-S112.

Julia, J., & Mejia, J. (2004). Thickness and Vp/Vs ratio variation in the Iberian crust. *Geophysical Journal International*, 156, 59-72.

Kaneshima, S., & Ando, M. (1988). Crustal anisotropy inferred from shear-wave splitting. The Third International Workshop on Seismic Anisotropy, Berkeley, USA.

Kaneshima, S. (1990). Origin of crustal anisotropy: shear wave splitting studies in Japan. *Journal of Geophysical Research*, 95, 121-133.

Karato, S. (2003). Mapping water content in the upper mantle. In: Eiler, J. (Ed.), *Inside the subduction factory*. AGU, Washington, D.C., Geophysical Monograph, 138, 135-152.

Karato, S. I., & Karki, B. B. (2001). Origin of lateral variation of seismic wave velocities and density in the deep mantle. *Journal of Geophysical Research*, 106 (B10), 21,771-21,783.

Kennett, B. L. N., Widiyantoro, S., & van der Hilst, R. D. (1998). Joint seismic tomography for bulk sound and shear wave speed in the Earth's mantle. *Journal of Geophysical Research*, 103(B6), 12,469-12,493.

Kern, H., Gao, S., Jin, Z. M., Popp, T., & Jin, S. Y. (1999). Petrophysical studies on rocks from the Dabie ultrahigh-pressure (UHP) metamorphic belt, central China: implications for the composition and delamination of the lower crust. *Tectonophysics*, 301, 191-215.

Kern, H., Jin, Z. M., Gao, S., Popp, T., & Xu, Z. Q. (2002). Physical properties of ultrahigh-pressure metamorphic rocks from the Sulu terrain, eastern central China: implications for the seismic structure at the Donghai (CCSD) drilling site. *Tectonophysics*, 354, 315-330.

Kern, H. (1990). Laboratory seismic measurements: an aid in the interpretation of seismic field data. *Terra Nova*, 2(6), 617-628.

Kern, H., & Wenk, H. R. (1990). Fabric-related velocity anisotropy and shear wave splitting in rocks from the Santa Rosa mylonite zone, California. *Journal of Geophysical Research*, 95(B7), 11,213-11,223.

Kern, H. (1979). Effect of high-low quartz transition on compressional and shear wave velocities in rocks under high pressure. *Physics and Chemistry of Minerals*, 4, 161-171.

Kern, H. (1982). P- and S-wave velocities in crustal and mantle rocks under the simultaneous action of high confining pressure and high temperature and the effect of the rock microstructure. In: Schreyer, W. (Ed.), *High-Pressure Research in Geosciences*, E. Schweizerbart'sche Verlagsbuchhandlung, Stuttgart, 15-45.

Kern, H. (1993). P- and S-wave anisotropy and shear-wave splitting at pressure and temperature in possible mantle rocks and their relation to the rock fabric. *Physics of the Earth and Planetary Interiors*, 78, 245-256.

Kern, H., Gao, S., Jin, Z. M., Popp, T., & Jin, S. Y. (1999). Petrophysical studies on rocks from the Dabie ultrahigh-pressure (UHP) metamorphic belt, central China:

implications for the composition and delamination of the lower crust. *Tectonophysics*, 301, 191-215.

Kern, H., Jin, Z. M., Gao, S., Popp, T., & Xu, Z. Q. (2002). Physical properties of ultrahigh-pressure metamorphic rocks from the Sulu terrain, eastern central China: implications for the seismic structure at the Donghai (CCSD) drilling site. *Tectonophysics*, 354, 315-330.

Kern, H., & Richter, A. (1981). Temperature derivatives of compressional and shear wave velocities in crustal and mantle rocks at 6 kbar confining pressure. *Journal of Geophysics*, 49, 47-56.

Ketcham, R. A., Donelick, R. W., & Carlson, W. D. (1999). Variability of apatite fission-track annealing kinetics: III. Extrapolation of geological time scales. *American Mineralogist*, 84, 1235-1255.

Kido, Y., Suyehiro, K., & Kinoshita, H. (2001). Rifting to spreading process along the northern margin of the South China Sea. *Marine Geophysical Researches*, 22, 1-15.

Knight, R. J., & Endres, A. (1990). A new concept in modeling the dielectric response of sandstones: defining a wetted rock and bulk water system. *Geophysics*, 55, 586-594.

Kobranova, V. N. (1989). *Petrophysics*, Springer-Verlag, 375 pp.

Koster, W., & Franz, H. (1961). Poisson's ratio for metals and alloys. *Metallurgical Reviews*, 6 (21), 1-55.

Kumar, A., Jayakumar, T., Raj, B., & Ray, K. K. (2003). Correlation between ultrasonic shear wave velocity and Poisson's ratio for isotropic solid materials. *Acta Materialia*, 51, 2417-2426.

Lakes, R. S. (1987). Foam structures with a negative Poisson's ratio. *Science*, 235, 1038-1040.

Lakshtanov, D. L., Sinogeikin, S. V., & Bass, J. D. (2007a). High-temperature phase transitions and elasticity of silica polymorphs. *Physics and Chemistry of Minerals*, 34, 11-22.

Lakshtanov, D. L., Litasov, K. D., Sinogeikin, S. V., Hellwig, H., Li, J., Ohtani, E., & Bass, J. D. (2007b). Effect of Al^{3+} and H^{+} on the elastic properties of stishovite. *American Mineralogist*, 92(7), 1026-1030.

Lan, C. Y., Chen, C. H., Chung, S. L., Lee, T., Wang Lee, C. M., & Yui, T. F. (1996). The crustal evolution of continental Taiwan. *Journal of the Geological Society of China*, 39, 337-353.

Leary, P. (1991). Deep borehole log evidence for fractal distribution of fractures in crystalline rock. *Geophysical Journal International*, 107, 615-627.

Ledbetter, H. M. (1977). Ratio of the shear and Young's Moduli for polycrystalline metallic elements. *Materials Science and Engineering*, 27, 133-135.

Leloup, P. H., Lacassin, R., Tapponnier, P., Scharer, U., Zhong, D. L., Liu, X., Zhang, L., Ji, S. C., & Phan, T. T. (1995). The Ailao Shan-Red River shear zone (Yunnan, China): Tertiary transform boundary of Indochina. *Tectonophysics*, 251, 3-84.

Li Xianhua, Li, Z. H., Ge, W., Zhou, H., Li, W., Liu, Y., & Wingate, M. T. D. (2003). Neoproterozoic granitoids in South China: crustal melting above a mantle wedge at ca. 825 Ma? *Precambrian Research*, 122, 45-83.

Li Yonghua, Tian Xiaobo, Wu Qingju, Zeng Rongsheng, & Zhang Ruiqing. (2006a). The Poisson's ratio and crustal structure of the central Qinghai-Xizang inferred from INDEPTH-III telseismic waveforms: Geological and geophysical implications. *Chinese Journal of Geophysics*, 49(4), 1037-1044.

Li Yonghua, Wu Qingju, An Zhanghui, Tian Xiaobo, Zeng Rongsheng, Zhang Ruiqing, & Li Hongquang. (2006b). The Poisson's ratio and crustal structure across the NE Tibetan Plateau determined from receiver functions. *Chinese Journal of Geophysics*, 49(5), 1359-1368.

Li, S., Lin, C., Zhang, Q., Yang, S., & Wu, P. (1998). The dynamic process of screen rift of continental marginal basin in northern South China Sea and the tectonic events since 10Ma. *Chinese Science Bulletin*, 43(8), 797-810.

Li, S. G., Hart, S. R., Zhang, S. G., Liu, D. L., Zhang, G. W., & Guo, A. L. (1989). Timing of collision between north and south China blocks-The Sm-Nd isotopic age evidence. *Science in China* (Series D-Earth Sciences), 32, 1393-1400.

Li, S. G., Jagoutz, E., Chen, Y. Z., & Li, Q. L. (2000). Sm-Nd and Rb-Sr isotope chronology and cooling history of ultrahigh-pressure metamorphic rocks and their country rocks at Shuanghe in the Dabie Mountains, Central China. *Geochim Cosmochim Acta*, 64, 1,077-1,093.

Li, S. G., Jagoutz, E., & Lo, C. H. (2000). Sm/Nd, Rb/Sr and $^{40}Ar/^{39}Ar$ isotopic systematics of ultrahigh-pressure metamorphic rocks in the Dabie-Sulu slice, central China: A retrospective view. In: Ernst, G., Liou, J. G. (Eds.), *Ultrahigh-pressure Metamorphism and Geodynamics in Collision-type Orogenic Belt.* International Book Series, 4. Geological Society of America, California, Bellwether Publishing, 234-244.

Li, S. G., Sun, W. D., Zhang, G. W., Chen, Y. J., & Yang, Y. C. (1996). Chronology and geochemistry of metavolcanic rocks from Heigouxia Valley in Mianlue tectonic arc, South Qinling: Observation for a Paleozoic oceanic basin and its close time. *Science in China* (Series D-Earth Sciences), 39, 300-310.

Lin, J. X., Tan, D. J., & Chi, X. G. (1992). *Mesozoic Granites in Jiao-Liao Peninsula*, Scientific Publication House, Beijing.

Lin, L. H., Wang, P. L., Lo, C. H., Tsai, C. H., & Jahn, B. M. (2006). ^{40}Ar-^{39}Ar thermochronological constraints on the exhumation of ultrahigh-pressure metamorphic rocks in the Sulu Terrane of Eastern China. In: Liou, J. G., Cloos, M., Ernst, W. G. (Eds.), *Phase Relations, High-pressure Terranes, and Plate Pushing*. A tribute to W. G. Ernst, International Book Series, 9. Geological Society of America, California, Bellwether Publishing, 275-289.

Liou, J. G., & Zhang, R. Y. (1996). Occurrence of intragranular coesite in ultrahigh-P rocks from the Sulu region, eastern China: implications for lack of fluid during exhumation. *American Mineralogist*, 81, 1217-1221.

Liou, J. G., Hacker, B. R., & Zhang, R. Y. (2000). Into the forbidden zone. *Science*, 287, 1,215-1,216.

Liou, J. G., Zhang, R. Y., Ernst, W. G., Rumble, D., & Maruyama, S. (1998). High-pressure minerals from deeply subducted metamorphic rocks. *Review in Mineralogy and Geochemistry*, 37, 33-96.

Liu Mingjun, Mooney, W.D., Li Songlin, Okaya, N., & Detweiler, S. (2006). Crustal structure of the northern margin of the Tibetan plateau from the Songpan-Ganzi terrane to the Ordos basin. *Tectonophysics*, 420, 253-266.

Liu, F. L., Xu, Z. Q., & Song, B. (2003). Determination of UHP and retrograde metamorphic ages of the Sulu terrane: evidence from SHRIMP U-Pb dating on zircons of gneissic rocks. *Acta Geologica Sinica*, 77, 229-237.

Liu, F. L., Gerdes, A., Liou, J. G., Xue, H. M., & Liang, F. H. (2006). SHRIMP U-Pb zircon dating from Sulu-Dabie dolomitic marble, eastern China: Constraints on prograde, UHP and retrograde metamorphic ages. *Journal of Metamorphic Geology*, 24, 569-590.

Liu, F. L., Xu, Z. Q., Ikuo, K., Yang, J. S., Shigenori, M., & Liou, J. G. (2001). Mineral inclusions in zircons of para- and orthogneiss from pre-pilot drillhole CCSD-PP1, Chinese Continental Scientific Drilling Project. *Lithos*, 59, 199-215.

Liu, F. L., Xu, Z. Q., Liou, J. G., Dong, H. L., & Xue, H. M. (2007). Ultrahigh-pressure Mineral Assemblages in Zircons from the Surface to 5158 m Depth in Cores of the Main Drill Hole, Chinese Continental Scientific Drilling Project, SW Sulu Belt, China. *International Geology Review*, 49, 454-478.

Liu, F. L., Xu, Z. Q., Liou, J. G., Katayama, I., Masago, H., Maruyama, S., & Yang, J. S. (2002). Ultrahigh-pressure mineral inclusions in zircons from gneissic core samples of the Chinese continental scientific drilling site in eastern China. *European Journal of Mineralogy*, 14, 499-512.

Liu, F. L., Xu, Z.Q., Liou, J. G., & Song, B. (2004). SHRIMP U-Pb ages of ultrahigh-pressure and retrograde metamorphism of gneisses, South-western Sulu terrain, Eastern China. *Journal of Metamorphic Geology*, 22, 315-326.

Liu, F. L., Xu, Z. Q., & Song, B. (2003). Determination of UHP and Retrograde metamorphic ages of the Sulu terrane: Evidence from SHRIMP U-Pb dating on Zircons of gneissic rocks. *Acta Geologica Sinica*, 2, 229-239.

Liu, F. L., Xu, Z. Q., & Song, B. (2003). Precise restriction of none-UHP granitic gneiss from the UHP metamorphic belt in the Sulu terrane, Eastern China: Evidence from mineral inclusion, Cathodoluminescence images and SHRIMP U-Pb dating in zircon domains. *Acta Geologica Sinica*, 4, 534-540.

Liu, F. L., Xu, Z. Q., & Xue, H. M. (2004). Tracing the protolith, UHP metamorphism, and exhumation ages of orthogneiss from the SW Sulu terrane (eastern China): SHRIMP U–Pb dating of mineral inclusion-bearing zircons. *Lithos*, 78, 411-429.

Liu, F. L., Xu, Z. Q., Yang, J. S., Zhang, Z. M., Xue, H. M., & Li, T. F. (2004). Geochemical characteristics and UHP metamorphism of granitic gneisses in the main drilling hole of Chinese Continental Scientific Drilling Project and its adjacent area. *Acta Petrologica Sinica*, 20, 9-26.

Liu, L. G., Chen, C. C., Lin, C. C., & Yang, Y. J. (2005). Elasticity of single-crystal aragonite by Brillouin spectroscopy. *Physics and Chemistry of Minerals*, 32, 97-102.

Liu, S. S., Weber, U., Glasmacher, U. A., Xu, Z. Q., & Wagner, G. A. (2009). Fission track analysis and thermotectonic history of the main borehole of the Chinese Continental Scientific Drilling project. *Tectonophysics*, in press.

Liu, X. W., & Jin, Z. M. (2006). Microstructure features ultrahigh pressure garnet peridotite from the Donghai district in the Sulu terrane: new evidence of rapid exhumation. *Acta Petrologica Sinica*, 22, 1810-1816.

Lu, Z. Q. (2005). Role of hysteresis in propagating acoustic waves in soils. *Geophysical Research Letters*, 32, L14302.

Ma Yanlu, & Zhou Huilan. (2007). Crustal thicknesses and Poisson's ratios in China by joint analysis of telseismic receiver functions and Rayleigh wave dispersion. *Geophysical Research Letters*, 34, L12304.

Mackenzie, J. K. (1950). The elastic constants of a solid containing spherical holes. *Proceedings of the Physical Society* (b), 63, 2-11.

Mainprice, D., & Humbert, M. (1994). Methods of calculating petrophysical properties from lattice preferred orientation data. *Surveys in Geophysics*, 15, 575-592.

Mainpricea, D., Tommasia, A., Ferréb, D., Carrezb, P., & Cordierb, P. (2008). Predicted glide systems and crystal preferred orientations of polycrystalline silicate Mg-Perovskite at high pressure: Implications for the seismic anisotropy in the lower mantle. *Earth and Planetary Science Letters*, 271(1-4), 135-144.

Mao, Z., Jiang, F., & Duffy, T. S. (2007). Single-crystal elasticity of zoisite $Ca_2Al_3Si_3O_{12}$ (OH) by Brillouin scattering. *American Mineralogist*, 92, 570-576.

Matte, P., Mattauer, M., Oliver, J. M., & Griot, D. A. (1996). Continental subductions beneath Tibet and the Himalayan orogeny. *Terra Nova*, 9, 264-270.

Matthies, S., & Humbert, M. (1993). The Realization of the Concept of a Geometric Mean for Calculating Physical Constants of Polycrystalline Materials. *Physica Status Solidi* (b), 177, K47-K50.

Mavko, G., Mukerji, T., & Dyorkin, J. (1998). *The Rock Physics Handbook: Tools for Seismic Analysis of Porous Media*, New York, Cambridge University Press, 339 pp.

McCaffree-Pellerin, C. L., & Christensen, N. I. (1998). Interpretation of crustal seismic velocities in the San Gabriel – Mojave region, southern California. *Tectonophysics*, 286, 253-271.

McNamara, D. E., Owens, T. J., Silver, P. G., & Wu, F. T. (1994). Shear wave anisotropy beneath the Tibetan Plateau. *Journal of Geophysical Research*, 99, 13655-13665.

McSkimin, H. J., & Andreatch, P. (1962). Analysis of the pulse superposition method for measured ultrasonic wave velocities as a function of temperature and pressure. *Journal of the Acoustical Society of America*, 34, 609-637.

Meissner, R., Rabbel, W., & Kern, H. (2006). Seismic lamination and anisotropy of the lower continental crust. *Tectonophysics*, 416, 81-99.

Mendelson, K. S., & Cohen, M.H. (1982). The effect of grain anisotropy on the electrical properties of sedimentary rocks. *Geophysics*, 47, 257-263.

Menzies, M., Xu, Y. G., Zhang, H. F., & Fan, W. M. (2007). Integration of geology, geophysics and geochemistry: a key to understanding the North China craton. *Lithos*, 96, 1-21.

Mishra, O. P., & Zhao, D. P. (2003). Crack density, saturation rate and porosity at the 2001 Bhuj, India, earthquake hypocenter: A fluid-driven earthquake? *Earth and Planetary Science Letters*, 212, 393-405.

Mori, T., & Tanaka, K. (1973). Average stress in matrix and average elastic energy of materials with misfitting inclusions. *Acta Materialia*, 21 (5), 571-574.

Musacchio, G. D., White, J., Asudeh, I., & Thomson, C. J. (2004). Lithospheric structure and composition of the Archean western Superior Province from seismic refraction/wide-angle reflection and gravity modeling. *Journal of Geophysical Research*, 109 (b3), B03304.

Nair, S. K., Gao, S. S., Liu, K. H., & Silver, P. G. (2006). Southern African crustal evolution and composition: Constraints from receiver function studies. *Journal of Geophysical Research*, 111(b2), B02304.

Nelson, K. D., 27 others. (1996). Partially molten middle crust beneath southern Tibet: Synthesis of project INDEPTH results. *Science*, 274, 1684-1688.

Ni, J., & Barazangi, M. (1983). High-frequency seismic wave propagation beneath the Indian shield, Himalayan arc, Tibetan Plateau and surrounding regions: High uppermost velocities and efficient propagation beneath Tibet. *Geophysical Journal of the Royal Astronomical Society*, 72, 665-689.

Nissen, S. S., Hayes, D. E., Yao, B. C., Zeng, W. J., Chen, Y. Q., & Nu, X. (1995). Gravity, heat flow, and seismic constraints on the processes of crustal extension: northern margin of the South China Sea. *Journal of Geophysical Research*, 100(B11), 22447-22483.

Norris, A. N. (2006). Extreme values of Poisson's ratio and other engineering moduli in anisotropic materials. *Journal of Mechanics of Materials and Structures*, 1(4), 793-812.

Nur, A., & Simmons, G. (1969). The effect of saturation on velocity in low porosity rocks. *Earth and Planetary Science Letters*, 7, 183-193.

Nye, J. F. (1957). *Physical Properties of Crystals: Their Representation by Tensors and Matrices*, London, Oxford University Press, Amen House. 82-92.

O'Connell, R. J., & Budiansky, B. (1974). Seismic velocities in dry and saturated cracked solids. *Journal of Geophysical Research*, 86, 5412-5425.

Okay, A. I., Xu, S. T., & Sengor, A. M. C. (1989). Coesite from the Dabie Shan eclogites, central China. *European Journal of Mineralogy*, 1, 595-598.

Owens, T. J., & Zandt, G. (1997). Implications of crustal property variations for models of Tibetan plateau evolution. *Nature*, 387, 37-43.

Pacalo, R. E. G., & Weidner, D. J. (1997). Elasticity of majorite, $MgSiO_3$ tetragonal garnet. *Physics of the Earth and Planetary Interiors*, 99, 145-154.

Panakkal, J. P., Willems, H., & Arnold, W. (1990). Nondestructive evaluation of elastic parameters of sintered iron powder compacts. *Journal of Materials Science*, 25, 1397-1402.

Peacock, S., McCann, C., Sothcott, J., & Astin, T. R. (1994). Seismic velocities in fractured rocks: an experimental verification of Hudson's theory. *Geophysical Prospecting*, 42, 27-80.

Perrillat, J. P., Nestola, F., Sinogeikin, S. V., & Bass, J. D. (2007). Single-crystal elastic properties of $Ca_{0.07}Mg_{1.93}Si_2O_6$ orthopyroxene. *American Mineralogist*, 92, 109-113.

Peselnick, L., & Wilson, W. H. (1968). Wave velocities and hysteresis in Solenhofen limestone for pressures up to 12 kbar. *Journal of Geophysical Research*, 73, 3271-3286.

Pham, V. N., Boyer, D., Therme, P., Yuang, X. C., Li, L., & Jin, G. Y. (1986). Partial melting zones in the crust in southern Tibet from magnetotelluric results. *Nature*, 311, 310-314.

Phani, K. K. (1986). Young's modulus-porosity relation in gypsum systems. *American Ceramic Society Bulletin*, 65, 1584-1586.

Phani, K. K., & Sanyal, D. (2005). Critical reevaluation of the prediction of effective Poisson's ratio for porous materials. *Journal of Materials Science*, 40(21), 5685-5690.

Pickett, G. R. (1963). Acoustic character logs and their application in formation evaluation. *Journal of Petroleum Technology*, 15, 650-667.

Postma, G. W. (1955). Wave propagation in a stratified medium. *Geophysiques*, 20, 780-806.

Qiu, H. J., Xu, Z. Q., Zhang, Z. M., Yang, J. S., Yang, T. N., Zhang, J., & Li, H. B. (2002). New mineral evidence of high-pressure metamorphism of the Subei high-

pressure belt: aragonite inclusions in garnet from greenschist. *Geological Bullitin of China*, 21, 617-624.

Ramakrishnan, N., & Arunachalam, V. S. (1990). Effective elastic moduli of porous solids. *Journal of the American Ceramic Society*, 25, 3930-3937.

Rathschbacher, L., Hacker, B. R., Webb, L. E., Williams, M. M., Ireland, T., Dong, S., Calvert, A., Chateigner, D., & Wenk, H. R. (2000). Exhumation of the ultrahigh-pressure continental crust in east central China: Cretaceous and Cenozoic unroofing and the Tan-Lu fault. *Journal of Geophysical Research*, 105, 13,303-13,338.

Ren Jishun. (1996). The continental tectonics of China. *Journal of Southeast Asian Earth Sciences*, 13, 197-204.

Rey, E., Jongmans, D., Gotteland, P., & Garambois, S. (2006). Characterisation of soils with stony inclusions using geoelectrical measurements. *Journal of Applied Geophysics*, 58, 188-201.

Reynolds, J. M. (1997). *An Introduction to Applied and Environmental Geophysics*, John Wiley & Sons, 796 pp.

Rice, R. W. (1997). Limitations of pore-stress concentrations on the mechanical properties of porous materials. *Journal of Materials Science*, 32, 4731-4736.

Riznichenko, Y. V. (1949). Seismic quasi-anisotropy. *Isw. Akad Nauk SSSR*, 13, 518-544.

Roberts, A. P., & Garboczi, E. J. (2000). Elastic properties of model porous ceramics. *Journal of the American Ceramic Society*, 83, 3041-3048.

Robertson, G. S., & Woodhouse, J. H. (1996). Constrains on lower mantle physical properties from seismology and mineral physics. *Earth and Planetary Science Letters*, 143, 197-205.

Rudnick, R. L., & Gao, S. (2005). Composition of the Continental Crust. In: Rudnick, R. L. (ed.), *The Crust —Treatise on Geochemistry* (eds. Holland, H. D., Turekian K. K.), Elsevier-Pergamon, Oxford, 3, 1-64.

Ruffet, C., Gueguen, Y., & Darot, M. (1991). Complex conductivity measurements and fractal nature of porosity. *Geophysics*, 56 (6), 758-768.

Salisbury, M. H., & Fountain, D. M. (1994). The seismic velocity and Poisson's ratio structure of the Kapuskasing uplift from laboratory measurements. *Canadian Journal of Earth Sciences*, 31, 1052-1063.

Salisbury, M. H., Milkereit, B., Ascough, G., Adair, R., Matthews, L., Schmitt, D. R., Mwenifumbo, J., Eaton, D. W., & Wu, J. J. (2000). Physical properties and seismic imaging of massive sulfides. *Geophysics*, 65(6), 1882-1889.

Salisbury, M. H., Milkereit, B., Ascough, G. L., Adair, R., Schmitt, D., & Matthews, L. (1997). Physical properties and seismic imaging of massive sulphides. In: Proceedings of Exploration 97, 4th Decennial International Conference on Mineral Exploration. Gubins, A. G. (Ed.), Prospectors and Developers Association of Canada (PDAC), Toronto, 383-390.

Salisbury, M. H., Milkereit, B., & Bleeker, W. (1996). Seismic imaging of massive sulphide deposits: Part I. Rock properties. *Economic Geology*, 91, 821-828.

Salje, E. K. H. (2007). An empirical scaling model for averaging elastic properties including interfacial effects. *American Mineralogist*, 92(2-3), 429-432

Sapin, M., & Hirn, A. (1997). Seismic structure and evidence for eclogitization during the Himalayan convergence. *Tectonophysics*, 273, 1-16.

Schon, J. H. (1996). *Physical Properties of Rocks*, Pergamon, 583 pp.

Sen, P. N., Scala, C., & Cohen, M. H. (1981). A self-semilar model for sedimentary rocks with application to the dielectric constant of fused glass beads. *Geophysics*, 46, 781-795.

Seront, B., Mainprice, D., & Christensen, N. I. (1993). A determination of the three-dimensional seismic properties of anorthosite: comparison between values calculated from the petrofabric and direct laboratory measurements. *Journal of Geophysical Research*, 98, 2209-2221.

Shapiro, N. M., Ritzwoller, M., Molnar, P., & Levin, V. (2004). Thinning and flow of Tibetan crust constrained by seismic anisotropy. *Science*, 305, 233-236.

Shapiro, S. A. (2003). Elastic piezosensitivity of porous and fractured rocks. *Geophysics*, 68, 482-486.

Siegesmund, S., Vollbrecht, A., & Pros, Z. (1993). Fabric changes and their influence on P-wave velocity patterns: examples from a polyphase deformed orthogneiss. *Tectonophysics*, 225, 477-492.

Sinogeikin, S. V., Schilling, F. R., & Bass, J. D. (2000). Single crystal elasticity of lawsonite. *American Mineralogist*, 85, 1834-1837.

Smith, C. F., & Crandail, W. B. (1964). Calculated high-temperature elastic constants for zero porosity monoclinic zirconia. *Journal of the American Ceramic Society*, 47, 624-627.

Song, T. R. A., & Helmberger, D. V. (2007). P and S waveform modeling of continental sub-lithospheric detachment at the eastern edge of the Rio Grande Rift. *Journal of Geophysical Research*, 112, B07319.

Stern, R. J., Lin, P. N., & Morris, J. D. (1990). Enriched back-arc basin basalts from the northern Marianna Trough: Implications for the magmatic evolution of back-arc basin. *Earth and Planetary Science Letters*, 100, 210-225.

Stierman, D. J., Healy, J. H., & Kovach, R. L. (1979). Pressure-induced velocity gradient: An alternative to a Pg refractor in the Gabilan range, central California. *Bulletin of the Seismological Society of America*, 69, 397-415.

Tapponnier, P., Lacassin, R., Leloup, P. H., Schaerer, U., Zhong, D., Wu, H., Liu, X., Ji, S. C., Zhang, L., & Zhong, J. (1990). The Ailao Shan/Red River metamorphic belt: Tertiary left-lateral shear between Indochina and South China. *Nature*, 343, 431-437.

Tapponnier, P., & Molnar, P. (1976). Slip-line field theory and large scale continental tectonics. *Nature*, 264, 319-324.

Tapponnier, P., Peltzer, G., Le Dain, A. Y., Armijo, R., & Cobbold, P. (1982). Propagating extrusion tectonics in Asia: new insights from simple experiments with plasticine. *Geology*, 10, 611-616.

Tarkov, A. P., & Vavakin, V. V. (1982). Poisson's ratio behaviour in various crystalline rocks: application to the study of the Earth's interior. *Physics of the Earth and Planetary Interiors*, 29, 24-29.

Ting, T. C. T., & Chen, T. Y. (2005). Poisson's ratio for anisotropic elastic materials can have no bounds. *The Quarterly Journal of Mechanics and Applied Mathematics*, 58(1), 73-82.

Tong Weiwei, Wang Liangshu, Mi Ning, Xu Mingjie, Li Hua, Yu Dayong, Li Cheng, Li Shaowen, Liu Mian, & Sandvol, E. (2007). The upper mantle structure beneath the Liupanshan region characterized by receiver functions. *Science in China* (Series D-Earth Sciences), 37, 193-198.

Turner, S., Hawkesworth, C., Liu, J. Q., Rogers, N., Kelley, S., & van Calsteren, P. (1993). Timing of Tibetan uplift constrained by analysis of volcanic rocks. *Nature*, 364, 50-54.

Unsworth, M. J., Jones, A. G., Wei, W., Marquis, G., Gokarn, S. G., Spratt, J. E., the INDEPTH-MT team. (2005). Crustal rheology of the Himalaya and southern Tibet inferred from magnetotelluric data. *Nature*, 438, 78-81.

Vernik, L. (1997). Predicting porosity from acoustic velocities in siliciclastics. *Geophysics*, 62, 118-128.

Wagh, A. S., Poeppel, R. B., & Singh, J. P. (1991). Open pore description of mechanical properties of ceramics. *Journal of Materials Science*, 26, 3862-3868.

Walck, M. C. (1988). Three-dimensional V_p/V_s variations for the Coso region, California. *Journal of Geophysical Research*, 93, 2047-2052.

Wallis, S. R., Ishiwatari, A., Hirajima, T., Ye, K., Guo, J., Nakamura, D., Kato, T., Zhai, M., Enami, M., Cong, B., & Banno, S. (1997). Occurrence and field relationships of UHP meta-granitoid and coesite eclogite in the Su-Lu terrane, Eastern China. *Journal of the Geological Society*, 154, 45-54.

Walsh, J. P. (1965). The effects of cracks on the compressibility of rocks. *Journal of Geophysical Research*, 70, 381-389.

Wang Xiaoping, Zhu Yuanqing, & Yu Haiying. (2006). Crust velocity structure in Shanghai and its neighboring area inversed by teleseismic receiver function. *Journal of Seismological Research*, 29, 239-244.

Wang, J. C. (1984). Young's modulus of porous materials, Part 1, Theoretical derivation of modulus-porosity correlation. *Journal of Materials Science*, 19, 801-808.

Wang, Q., Burlini, L., Mainprice, D., & Xu, Z. Q. (2009). Geochemistry, microstructure and seismic properties of eclogites from the Chinese Continental Scientific Drilling boreholes in the Sulu UHP terrane, eastern China. *Tectonophysics*, in press.

Wang, Q., & Ji, S. C. (2009). Poisson's ratio of crystalline rocks as a function of hydrostatic confining pressure. *Journal of Geophysical Research*, in press.

Wang, Q., Ji, S. C., Salisbury, M. H., Pan, M. B., Xia, B., & Xu, Z. Q. (2005a). Pressure dependence and anisotropy of P-wave velocities in ultrahigh-pressure metamorphic rocks from the Dabie-Sulu orogenic belt (China): implications for seismic properties of subducted slabs and origin of mantle reflections. *Tectonophysics*, 398, 67-99.

Wang, Q., Ji, S. C., Salisbury, M. H., Xia, B., Pan, M. B., & Xu, Z. Q. (2005b). Shear wave properties and Poisson's ratios of ultrahigh-pressure metamorphic rocks from the Dabie-Sulu orogenic belt: Implications for crustal composition. *Journal of Geophysical Research*, 110, B08208.

Wang, Q., Ji, S. C., Sun Shengsi, & Marcotte, D. (2009). Correlations between Poisson's ratio and seismic wave velocities for some common rocks and sulfide ores. *Tectonophysics*, 469, 61-72.

Wang, Q., Ji, S. C., & Xu, Z. Q. (2007). Lattice-preferred orientation, water content and seismic anisotropy of olivine: Implications for deformation environment of continental subduction zones. *Acta Petrologica Sinica*, 23(12), 3065-3077.

Wang, Q., Ji, S. C., & Xu, Z. Q. (2009). V_p/V_s anisotropy and implications for crustal composition identification and earthquake prediction. *Acta Geologica Sinica*, 83(4), 801-815.

Wang, X. M., Liou, J. G., & Mao, H. G. (1989). Coesite-bearing eclogites from the Dabie mountains in central China. *Geology*, 17, 1085-1088.

Wang, Y. J., Fan, W. M., Zhao, G. C., Ji, S. C., & Peng, T. P. (2007). Zircon U-Pb Geochronology of gneissic rocks in the Yunkai massif and its implications on the Caledonian event in the South China Block. *Gondwana Research*, 12(4), 404-416.

Wang, Z. C., & Ji, S. C. (2001). Elasticity of six polycrystalline silicate garnets at pressure up to 3.0 GPa. *American Mineralogist*, 86, 1209-1218.

Watanabe, T., Kasami, H., & Ohshima, S. (2007). Compressional and shear wave velocities of serpentinized peridotites up to 200 MPa. *Earth Planets Space*, 59, 233-244.

Watt, J. P., Davies, G. F., & O'Connell, R. J. (1976). The elastic properties of composite materials. *Reviews of Geophysics and Space Physics*, 14, 541-563.

Wei, W. B., Unsworth, M., Jones, A., Booker, J., Tan, H. D., Nelson, D., Chen, L. S., Li, S. H., Solon, K., Bedrosian, P., Jin, S., Deng, M., Ledo, J., Kay, D., & Roberts, B. (2001). Detection of widespread fluids in the Tibetan crust by magnetotelluric studies. *Science*, 292, 716-719.

Wepfer, W. W., & Christensen, N. I. (1991). A seismic velocity-confining pressure relation, with applications. *International Journal of Rock Mechanics and Mining Sciences & Geomechanics Abstracts*, 28, 451-456.

Wharton, R. P., Hazen, G. A., Rau, R. N., & Best, D. L. (1980). Electromagnetic propagation logging: advances in technique and interpretation. SPE, Paper 9267, Dallas.

Wilkens, R., Simmons, G., & Caruso, L. (1984). The ratio Vp/Vs as a discriminant of composition for siliceous limestone. *Geophysics*, 49, 1850-1860.

Wong, P., Koplik, J., & Tomanic, J. P. (1984). Conductivity and permeability of rocks. *Physical Review*, B30, 6606-6614.

Wu Haiwei, Zhang Liangshen, & Ji Shaocheng. (1989). Himalayan ductile shear in the large sinistral strike-slip of Honghe-Ailaoshan. *Scientia Geologica Sinica*, 1, 1-7.

Wu, H. W., Zhang, L. S., & Ji, S. C. (1989). The Red River-Ailaoshan Fault Zone – A Hymalayan large sinistral strike-slip intercontinental shear zone. *Scientia Geologica Sinica*, 1, 1-8.

Wyllie, M. R. J., & Gregory, A. R. (1953). Formation factors of unconsolidated porous media: influence of particle shape and effect of cementation. AIME Petroleum Transactions, 198, 103-110.

Wyllie, M. R. J., Gregory, A. R., & Gardner, L. W. (1956). Elastic wave velocities in hetero-geneous and porous media. *Geophysics*, 21, 41-70.

Xia, B., Zhang, Y. Cui, X. J., Liu, B. M., Xie, J. H., Zhang, S. L., & Lin, G. (2006). Understanding of the geological and geodynamic controls on the formation of the South China Sea: a numerical modeling approach. *Journal of Geodynamics*, 42, 63-84.

Xu Lili, Rondenay, S., & van der Hilst, R. D. (2007). Structure of the crust beneath the southeastern Tibetan Plateau from teleseismic receiver functions. *Physics of the Earth and Planetary Interiors*, 165, 176-193.

Xu Mingjie, Wang Liangshu, Liu Jianhua, Zhong Kai, Li Hua, Hu Dezhao, & Xu Zhen. (2005). The crust and upper mantle beneath Ailaoshan-Red-River Fault Zone characterized by teleseismic receiver functions. *Science in China* (Series D), 35(8), 729-737.

Xu Weiwei, & Zheng Tianyu. (2005). Distribution of Poisson's ratios in the northwestern basin-mountain boundary of the Bohai Bay Basin. *Chinese Journal of Geophysics*, 48(5), 1077-1084.

Xu Xisheng, O'Reilly, S. Y., Griffin, W. L., Deng Ping, & Pearson, N. J. (2005). Relict proterozoic basement in the Nanling mountains (SE China) and its tectonothermal overprinting. *Tectonics*, 24, TC2003.

Xu, L. L., Rondenay, S., & van der Hilst, R. D. (2007). Structure of the crust beneath the southeastern Tibetan Plateau from teleseismic receiver functions. *Physics of the Earth and Planetary Interiors*, 165, 176-193.

Xu, P. F., Liu, F. T., Wang, Q. C., Cong, B. L., & Chen, H. (2001). Slab-like high velocity anomaly in the uppermost mantle beneath the Dabie-Sulu orogen. *Geophysical Research Letters*, 28, 1847-1850.

Xu, S. T., Okay, A. I., Ji, S. C., Sengor, A. M. C., Su, W., Liu, Y., & Jiang, L. (1992). Diamond from the Dabie Shan metamorphic rocks and its implication for tectonicsetting. *Science*, 256, 80-82.

Xu, Z. Q., Liu, F. L., Qi, X. X., Zhang, Z. M., Yang, J. S., & Zeng, L. S. (2006). Record for Rodinia supercontinent breakup event in the south Sulu ultra-high pressure metamorphic terrane. *Acta Petrologica Sinica*, 22, 1745-1760.

Xu, Z. Q., Zhang, Z. M. Liu, F. L., Yang, J. S., Tang, Z. M., Chen, S. Z., Cai, Y. C., Li, T. F., & Chen, F. Y. (2004). The structure profile of 0-1200m in the main borehole, Chinese Continental Scientific Drilling and its preliminary deformation analysis. *Acta Petrologica Sinica*, 20, 53-72.

Xu, Z. Q. (1987). Etudes tectonique et microtectonique de la chaine Paleozoique et Triasique des Qinlings (Chine). Ph.D. thesis, Universite de Montpellier II, France, 162 pp.

Xu, Z. Q. (2004). The scientific goals and investigation progresses of the Chinese Continental Scientific Drilling project. *Acta Petrologica Sinica*, 20, 1-8.

Xu, Z. Q., Chen, J., Wang, Q., Zeng, L. S., Yang, J. S., Chen, F. Y., Li, T. F., & Liang, F. H. (2005). Type-C olivine fabric in the Zhimafang garnet peridotite of the southern Sulu ultrahigh-pressure metamorphic terrane: Formation conditions and tectonic implications. *Acta Petrologica Sinica*, 21, 389-397.

Xu, Z. Q., Wang, Q., Ji, S. C., Chen, J., Zeng, L. S., Yang, J. S., Chen, F. Y., Liang, F. H., & Wenk, H. R. (2006). Petrofabrics and seismic properties of garnet peridotite from the UHP Sulu terrane (China): Implications for olivine deformation mechanism in a cold and dry subducting continental slab. *Tectonophysics*, 421, 111-127.

Xu, Z. Q., Wang, Q., Tang, Z. M., & Chen F. Y. (2009). Fabric kinematics of the ultrahigh-pressure metamorphic rocks from the main borehole of the Chinese Continental Scientific Drilling Project: implications for continental subduction and exhumation. *Tectonophysics*, in press.

Xu, Z. Q., Yang, W. C., Ji, S. C., Zhang, Z. M., Yang, J. S., Wang, Q., & Tang, Z. M. (2009). Deep root of a continent-continent collision belt: Evidence from the Chinese Continental Scientific Drilling (CCSD) deep borehole in the Sulu ultrahigh-pressure (HP-UHP) metamorphic terrane, China. *Tectonophysics*, in press.

Xu, Z. Q., Zeng, L. S., Liu, F. L., Yang, J. S., Zhang, Z. M., McWilliaans, M., & Liu, Z. G. (2006). Polyphase subduction and exhumation of the Sulu high pressure-ultrahigh pressure metamorphic terrane. *Geological Society of America*, Special paper 403, 93-113.

Yan Pin, Zhou Di, & Liu Zhaoshu. (2001). A crustal structure profile across the northern continental margin of the South China Sea. *Tectonophysics*, 338, 1-21

Yang, J. S., Li, T. F., Chen, S. Z., & Wu, C. L. (2009). Genesis of garnet peridotites in the Sulu UHP belt: Examples from the Chinese Continental Scientific Drilling Project-Main hole, PP1 and PP3 drillholes. *Tectonophysics*, in press.

Yang, J. S., Liu, F. L., Wu, C. L., Xu, Z. Q., & Chen, S. Y. (2005). Two ultrahigh-pressure metamorphic events recognized in the central orogenic belt of China: evidence from the U-Pb Dating of coesite-bearing zircons. *International Geology Review*, 47, 327-343.

Yang, J. S., Wooden, J. L., Wu, C. L., Liu, F. L., Xu, Z. Q., Shi, R. D., Liou, J. G., & Maruyama, S. (2003). SHRIMP U-Pb dating of coesite-bearing zircons from the ultrahigh-pressure metamorphic rocks, Sulu terrane, east China. *Journal of Metamorphic Geology*, 21, 551-560.

Yang, J. S., Xu, Z. Q., Song, S. G., & Zhang, J. X. (2001). Discovery of coesite in the North Qaidam early Paleozoic ultrahigh pressure (UHP) metamorphic belt, NW China. Comptes Rendus de l'Académie des Sciences (Series IIA) Earth and Planetary Science, 333, 719-724.

Yang, J. S., Xu, Z. Q., Wu, C. L., Liu, F. L., Shi, R. D., Wooden, J., & Maruyama, S. (2002). SHRIMP U-Pb dating on coesite-bearing zircon: evidence for Indosinian ultrahigh-pressure metamorphism in Su-Lu, East China. *Acta Geologica Sinica*, 3, 354-372.

Yang, J. S., Zhang, R. Y., Li, T. F., Zhang, Z. M., & Liou. J. G. (2007). Petrogenesis of the garnet peridotite and garnet-free peridotite of the Zhimafang ultramafic body in the Sulu ultrahigh-pressure metamorphic belt, eastern China. *Journal of Metamorphic Geology*, 25, 187-206.

Yang, T. N., Chen, W., Li, J. Y., & Xu, Z. Q. (2002). Exhumation history of the Sulu UHPM terrane: evidence from dating and deformation on its northern boundary. *Geological Review*, 48, 176-182.

Yang, W. C. (2002). Geophysical profiling across the Sulu ultra-high-pressure metamorphic belt, eastern China. *Tectonophysics*, 354, 277-288.

Yang, W. C., Cheng, Z., Chen, G., Hu, Z., & Bai, J. (1999). Geophysical investigations of northern Sulu HPM Belt; (I), Deep seismic reflection. *Chinese Journal of Geophysics*, 42, 57-69.

Yang, W. C., Cheng, Z. Y., Chen, G. J., Hu, Z. Y., & Bai, J. (1999). Geophysical Investigations in Northern Sulu UHPM Belt, Part 1: Deep Seismic Reflection. Geophysics, 42(1), 41-52.

Yang, W. C., Yang, W. Y., & Chen, Z. (2004). Interpretation of 3D seismic refletion data in the Chinese Continental Scientific Drilling site. *Acta Petrologica Sinic*a, 20, 127-137.

Yao, B. C., Wan, L., & Wu, N. Y. (2005). Cenozoic tectonic evolution and the 3D structure of the lithosphere of the South China Sea. *Geological Bulletin of China*, 24(1), 1-8.

Ye, K., Cong, B. L., & Ye, D. N. (2000). The possible subduction of continental material to depths greater than 200 km. *Nature*, 407, 734-736.

Yeheskel, O., & Tevet, O. (2000). A new assessment method for the bulk modulus and the Poisson's ratio of porous Ceramics. *Journal of Testing and Evaluation*, 28(3), 189-198.

Yin, A., & Harrison, T. M. (2000). Geologic evolution of the Himalayan-Tibetan orogen. *Annual Review of Earth and Planetary Sciences*, 28, 211-280.

You, Z. D., Su, S. G., Liang, F. H., & Zhang, Z. M. (2004). Petrography and metamorphic deformational history of the ultrahigh pressure metamorphic rocks from the 100-2000 m core of Chinese Continental Scientific Drilling, China. *Acta Petrologica Sinica*, 20, 43-52.

Yui, T. F., Heaman, L., & Lan, C. Y. (1996). U-Pb and Sr isotopic studies on granitoids from Taiwan and Chinmen-Lieyu and tectonic implications. *Tectonophysics*, 261, 61-76.

Zandt, G., & Ammon, C. J. (1995). Continental crust composition constrained by measurements of crustal Poisson's ratio. *Nature*, 374, 152-154.

Zhang Xuemin, Shu Peiyi, Diao Guiling, Xia Luanbao, Wu Youwen, Li Guang, Wang Yuzhen, & Zhang Xuewen. (2001a). Study of the P- and S-wave velocity structure under Tangshan region with digital earthquake records. *North China Earthquake Sciences*, 19(1), 10-17.

Zhang Xuemin, Diao Guiling, Xia Luanbao, Wu Youwen, & Shu Peiyi. (2001b). Study on the structure of deep S-wave velocity inside and outside macroseismic region of Hebei province. *North China Earthquake Sciences*, 19(3), 1-14.

Zhang Zeming, Zhang Jinfeng, You Zhendong, & Shen Kun. (2005). Ultrahigh-pressure metamorphic P-T-t path of the Sulu orogenic belt, eastern central China. *Acta Petrologica Sinica*, 21(2), 257-270.

Zhang, R. Y., & Liou, J. G. (1997). Partial transformation of Gabbro to Coesite-bearing Eclogites from Yangkou, the Sulu Terrane, eastern China. *Journal of Metamorphic Geology*, 15, 183-202.

Zhang, R. Y., Liou, J. G., & Shu, J. F. (2002). Hydroxyl-rich topaz in high-pressure and ultrahigh-pressure kyanite quartzite with retrograde woodhouseite from the Sulu terrane, eastern China. *American Mineralogist*, 87, 445-455.

Zhang, R. Y., Liou, J. G., Yang, J. S., & Yui, T. F. (2000). Petrochemical constraints for dual origin of garnet peridotites from the Dabie-Sulu UHP terrane, eastern-central China. *Journal of Metamorphic Geology*, 18, 149-166.

Zhang, R. Y., Yang, J. S., Wooden, J. L., Liou, J. G., & Li, T. F. (2005). U-Pb SHRIMP geochronology of zircon in garnet peridotite from the Sulu UHP terrane, China: Implications for mantle metasomatism and subduction-zone UHP metamorphism. *Earth and Planetary Science Letters*, 237, 729-743.

Zhang, Z. M., Zhang, J. F., You, Z. D., & Shen, K. (2005). Ultrahigh-pressure metamorphic P-T-t path of the Sulu orogenic belt, eastern central China. *Acta Petrologica Sinica*, 21, 257-270.

Zhang, Z. M., Xu, Z. Q., Liu, F. L., You, Z. D., Meng, F. C., & Li, T. F. (2003). Petrology and petrochemistry of UHP metamorphic rocks from the Sulu orogenic belt, Eastern Central China. *Acta Geologica Sinica*, 77, 478-491.

Zhang, Z. M, Shen, K., Xiao, Y. L., Hoefs, J., & Liou, J. G. (2006). Mineral and fluid inclusions in zircon of UHP metamorphic rocks from the CCSD-main drill hole: A record of metamorphism and fluid activity. *Lithos*, 92, 378-398.

Zhang, Z. M., Shen, K., & Liu, Y. S. (2007). Petrogenesis and mineralization of the Maobei complex from the southern Sulu ultrahigh-pressure metamorphic belt, eastern China. *Acta Petrologica Sinica*, 12, 3095-3115.

Zhang, Z. M., Shen, K., Wang, J. L., & Dong, H. L. (2009). Petrological and geochronological constraints on the formation, subduction and exhumation of the continental crust in the southern Sulu orogen, eastern-central China. *Tectonophysics*, in press.

Zhang, Z. M., Shen, K., Zhao, X. D., & Shi, C. (2006). Fluid during the UHP metamorphism: constrains from the petrology, oxygen isotope and fluid inclusion studies of the Sulu UHP metamorphic rocks. *Acta Petrologica Sinica*, 22, 1985-1998.

Zhang, Z. M., Xu, Z. Q., & Liu, F. L. (2004). Geochemistry of eclogites from the main hole (100-2050m) of the Chinese Continental Scientific Drilling Project. *Acta Petrologica Sinica*, 20, 27-42.

Zhang, Z. M., Xu, Z. Q., Liu, F. L., Liou, J. G., & Hoefs, J. (2005). Petrogenesis of UHP metamorphic rocks from Qinglongshan, southern Sulu, east-central China. *Lithos*, 81, 189-207.

Zhao, X. O. (1997). Microstructure et pétrofabrique des minéraux à haute température : exemple du terrain de Morin, province de Grenville, Québec. Ph.D. thesis, Université de Montréal, 199 pp.

Zhao, Y., & Anderson, D. L. (1994). Mineral physics constraints on the chemical composition of the Earth's lower mantle. *Physics of the Earth and Planetary Interiors*, 85, 273-292,

Zhong Dalai. (2000). *Paleotethysides in west Yunnan and Sichuan, China*, Science Press, Beijing, 248 pp.

Zhou Xinmin, Sun Tao, Shen Weizhou, Shu Liangshu, & Niu Yaoling. (2005). Petrogenesis of Mesozoic granitoids and volcanic rocks in South China: a response to tectonic evolution. *Episodes*, 29, 26-33.

Zhu, B., Wang, H., Chen, Y., Chang, X., Hu, Y., & Xie, J. (2002). Geochronological and geochemical constraint on the Cenozoic extension of Cathaysian lithosphere and tectonic evolution of the border sea basins in East China. *Geochimica*, 31(3), 213-221.

Zimmerman, R. W., Somerton, W. H., & King, M. S. (1986). Compressibility of porous rocks. *Journal of Geophysical Research*, 91, 12765-13277.